Structural response of corrosion damaged RC members: numerical analyses and experimental investigation

Dissertation

submitted to and approved by the

Department of Architecture, Civil Engineering and Environmental Sciences
University of Braunschweig – Institute of Technology

and the

Department of Civil and Environmental Engineering
University of Florence

in candidacy for the degree of a
Doktor-Ingenieur (Dr.-Ing.) /
Dottore di Ricerca in Processes, Materials and Constructions in Civil and Environmental Engineering and for the Protection of the Historic-Monumental Heritage[*)]

by

Irene Barbara Nina Finozzi
born 19 March 1986
from Thiene, Italy

Submitted on	10/09/2015
Oral examination on	19/11/2015
Professorial advisors	Prof. Anna Saetta Prof. Harald Budelmann

2016

*) Either the German or the Italian form of the title may be used.

ACKNOWLEDGEMENTS

“Seule compte la démarche, car c'est elle qui dure et non le but qui n'est que l'illusion du voyage.”

ANTOINE DE SAINT-EXUPERY

This PhD has been a surprising journey, studded of difficulties but also of small satisfactions. But above all, it gave me the opportunity to meet wonderful and unexpected people.

First of all, I would like to thank my family, for their patience and continued support. Additionally, I would like to thank both colleagues and friends, with whom I have shared so many things, for making these last years memorable. Furthermore, I would like to express my thankfulness to the technicians of both iBMB and Stahlbau Institutes of the Technische Universität Braunschweig for helping me with the experimental tests. And finally, my gratitude goes to my two supervisors: Professor Dr-Ing. Harald Budelmann for introducing me into the German research system and always showing me politeness and availability and Prof. Anna Saetta for the time spent in the fruitful discussions and the pleasant environment created.

ABSTRACT

This thesis deals with the development of a comprehensive approach for the assessment of the structural response of corroded reinforced concrete (RC) structures and of the appropriate numerical tools. Corrosion of steel reinforcement in concrete is one of the most severe causes of deterioration of RC structures, because it may affect both their serviceability and load-carrying capacity. In order to evaluate the residual level of safety of damaged structures, non-linear analyses, able to describe the evolution of the structural degradation, are required. To achieve this result, a classical continuum damage model was adopted and enhanced with new formulations, developed in order to consider the main structural consequences of reinforcement corrosion on RC members.

First, a comprehensive modelling approach able to take into account the main local effects of corrosion on concrete, steel reinforcement and their composite interaction was proposed. The approach combines original formulations with some empirical/analytical models derived from the literature. In detail, the concrete material was modelled with a coupled environmental–mechanical damage model, developed by Saetta et al.[224][225] and enhanced for considering concrete degradation due to reinforcement corrosion. Indeed, as consequences of the volume expansion of corrosion products around steel bars, cracking and spalling of concrete covers may occur. Regarding the effect of corrosion on reinforcement, the results of tensile tests made by the Author on locally damaged steel bars were presented and compared with different models proposed in literature for the estimation of both residual area and mechanical properties of corroded reinforcement. Further, a model for considering premature buckling in corroded steel bars in compression was also developed. To take into account bond deterioration between steel bars and surrounding concrete, a new approach was proposed, able to predict the maximum bond strength in degraded condition through a scalar parameter. Furthermore, three different bond stress-slip laws were introduced to consider different bond mode failure, which may occur in case of different degrees of reinforcement corrosion and levels of confinement. These laws were then validated through numerical simulations of experimental pull-out tests available in the literature.

Finally, a number of corroded RC elements, at different levels of degradation, were simulated in order to validate the new formulations proposed. The results of the numerical analyses were compared with the experimental tests made by Rodriguez et al.[221][222] and Lee et al.[153]. In detail, in a first phase (calibration phase) the main parameters involved in the proposed relationships, characterizing the effects of corrosion, were verified referring to one degraded beam. Then, in the prediction phase, in order to demonstrate the robustness of the modelling procedure and its ability to predict the structural response of deteriorated elements, several corroded beams and columns were analysed keeping the values of the main parameters equal to the ones obtained in the calibration phase. Regarding corrosion effects on RC beams, through the numerical analyses, it was clarified that the reduction of load-carrying capacity in corroded RC structures can be mainly related to the residual area of reinforcing bars, to concrete degradation and to anchorage efficiency of tensile bars. The reduction of global ductility of corroded structures wad noted to be instead dependent on the residual ductility of degraded concrete and of steel bars affected by pitting corrosion and on bond degradation. Further, it was observed that bond degradation and failure of transverse reinforcement may lead to a change of the resistant mechanisms. Therefore, bond loss and cracking of concrete cannot be neglected. Regarding RC columns, the numerical analyses evidenced that the environmental-mechanical damage model implemented to simulate cracking and spalling of concrete covers, stirrups failure and the law proposed for considering premature buckling phenomena of longitudinal bars, allow to better capture their structural response. For the RC members analysed, the numerical results agreed well with the experimental ones: in particular, the proposed model properly predicted the structural response in terms of both failure mode and load-deflection curves, with increasing corrosion level.

In conclusion, the ability of the numerical model to capture the behaviour of corroded RC members, at different levels of degradation, has been demonstrated. Therefore, the numerical model and in particular the comprehensive approach proposed can be considered a suitable numerical tool for the evaluation of the residual safety of corroded existing structures.

TABLE OF CONTENTS

LIST OF PUBLICATIONS

This thesis is based on the work contained in the following papers:

I. Finozzi I.B.N, Berto L., Saetta A., Budelmann H. (2014). Numerical modeling of the corrosion effects on reinforced concrete beams. WCCM XI, Proceedings, Barcelona, Spain; II: 880-891.

II. Finozzi I.B.N., Saetta A. (2014). Damage model for the analysis of structural response of RC columns subjected to corrosion phenomena. Concrete Solutions 5th International Conference on Concrete Repair, 1-3 September 2014, Belfast; pag. 793 -800.

III. Finozzi I.B.N., Berto L., Saetta A. (2015). Structural response of corroded RC beams: a comprehensive damage approach. Computers and Concrete, Vol.15, No.3, pag. 141-166.

IV. Berto, L., Finozzi, I.B.N., Saetta, A., Scotta, R., Talledo, D., Tesser, L., Vitaliani, R. (2015). Development of a computational tool for f.e. analysis of RC structures affected by environmental degradation. OpenSees Days Italy, 2nd Italian Conference, Salerno, 10-11 June 2015.

V. Berto, L., Budelmann, H., Finozzi, I.B.N., Saetta, A. Talledo, D.A. (2015). Coupled Damage Model for RC elements Assessment under environmental degradation. International Workshop on Durability and Sustainability of Concrete Structures, 1-3 October 2015, Bologna, Italy.

NOTATION

Roman upper case letters

A^* = strain-hardening deformation work [J/mm^3], area underneath the strain-hardening stress-strain curve of steel until the maximum load

A_{eq} = equivalent residual cross-sectional area of corroded bar [mm^2]

A_r = average residual cross-sectional area of corroded bar [mm^2]

A_s = cross-sectional area of uncorroded bar [mm^2]

A'_s = minimum residual cross-sectional area of corroded bar [mm^2]

A'_s/A_s = residual area ratio [-]

A_{pit} = maximum cross-sectional area of a pit in corroded bars [mm^2]

δ_s = percentage of maximum section loss by corroded bars [%]
-pitting corrosion (A_{pit}/A_s)

A^- = first parameter for the definition of the damage law for concrete in compression

A^+ = parameter for the definition of the damage law for concrete in tension

B^- = second parameter for the definition of the damage law for concrete in compression

C/Φ = cover-to-bar diameter ratio [-]

E_c = Young's modulus for the elastic deformation of the concrete material [MPa]

E_s = Young's elastic modulus of steel material [MPa]

E_{sh} = hardening or post-yielding modulus of steel material [MPa]

L = bar length between two consecutive stirrups [mm]

L_b = embedment length [mm]

R = pitting ratio (p/x)

W = total energy [J/mm^3], area underneath the stress-strain curve of steel until the maximum load

X = percentage of mass loss by corroded bars [%]

Z = lever arm [mm]

Roman lower case letters

a	=	shear span length [mm]
a/d	=	shear span-depth ratio [-]
d	=	effective beam high [mm]
d^+	=	internal damage variable for tensile stresses
d^-	=	internal damage variable for compressive stresses
d_{max}	=	maximum size of the concrete aggregate [mm]
d_τ	=	corrosion bond strength damage parameter
d^+_{env}	=	environmental damage parameter in tension
d^-_{env}	=	environmental damage parameter in compression
e	=	ultimate elongation of steel bar [%]
f_c	=	compressive strength of concrete [MPa]
f_{ck}	=	characteristic compressive strength of concrete [MPa]
f_{cm}	=	average compressive strength of concrete [MPa]
$f_{c,cracked}$	=	average compressive strength of cracked concrete [MPa]
f_0^-	=	elastic limit for mono-axial compression of concrete
$f_{0,2D}^-$	=	elastic limit for mono-axial l compression of concrete
f_0^+	=	elastic limit for mono-axial traction of concrete
f_t	=	tensile strength of concrete [MPa]
i_{corr}	=	corrosion current density [$\mu A/cm^2$]
p	=	maximum penetration of pitting corrosion [mm]
p/Φ	=	corrosion penetration ratio [-]
s	=	slip [mm]
x	=	penetration of uniform corrosion [mm]
x_{mean}/Φ	=	mean corrosion penetration ratio [-]
p/Φ	=	maximum corrosion penetration ratio [-]
w_{cr}	=	crack width [mm]

Greek letter

α	=	pitting ratio (p/ x_{mean})
β	=	plastic parameter for deformation in compression for concrete
δ_s	=	damage index referring to the corrosion penetration [-]
ε_c	=	strain of concrete material [-]
ε_{co}	=	peak strain of concrete in compression [-]
ε_{cu}	=	ultimate strain of concrete in compression [-]
ε_{sh}	=	strain at the beginning of the strain-hardening phase [-]
ε_{sm}	=	strain at the maximum strength of the virgin bar, ultimate strain [-]
ε_{sr}	=	strain at the bar rupture [-]
ε_{sy}	=	yield strain of uncorroded steel bar [-]
ε_{su}	=	ultimate strain of uncorroded steel bar [-]
λ	=	geometrical slenderness ratio of reinforcing bars (L/Φ)
λ_{corr}	=	geometrical slenderness ratio of corroded reinforcing bars [-]
λ_{crit}	=	critical geometrical slenderness ratio of reinforcing bars [-]
Φ	=	original diameter of a bar [mm]
Φ'	=	remaining diameter of a uniformly corroded bar [mm]
ρ	=	reinforcement ratio [%]
σ_c	=	compressive stress in concrete [MPa]
σ_{crit}	=	buckling strength of reinforcing bars under compression loads [MPa]
σ_t	=	tensile stress in concrete [MPa]
σ_{max}	=	ultimate or maximum strength for steel bars [MPa]
σ_y	=	yield strength for steel bars [MPa]
$\bar{\boldsymbol{\sigma}}^+$	=	tensile effective stress tensor [MPa]
$\bar{\boldsymbol{\sigma}}^-$	=	compressive effective stress tensor [MPa]
τ	=	bond stress [MPa]
τ_{max}	=	maximum bond strength [MPa]
τ_f	=	residual bond strength [MPa]
υ	=	Poisson's ratio [-]

CHAPTER 1
INTRODUCTION

1.1. Introduction

Reinforced concrete (RC) constructions are the most common and widespread type of civil engineering structures present in our territory, both for building and infrastructures. The use of this composite material, consisting of concrete and embedded reinforcement, started at the end of the nineteenth century and became soon popular, thanks the good mechanical performances exhibited and the intrinsically durability attributed. Only from the second half of the twentieth century, RC structures, particularly those built in aggressive environments, have exhibited evidences of material and structural deterioration. As a consequence, the evaluation of the durability of RC structures has started then to be analysed and considered an important issue, also due to the high costs for rehabilitation and safety problems connected. Nowadays, the problem of durability of RC structures is still a critical issue in civil engineering, due to the complexity of the phenomena involved and the uncertainties still related to the structural response of degraded elements. Engineers are required for durable design of RC constructions, for maintenance, inspection, assessment of their structural response and evaluation of rehabilitation interventions under economic restrictions.

Among the different causes of degradation, reinforcement corrosion has been identified as being the predominant deterioration mechanism for reinforced concrete structures. In normal conditions, the concrete is un-cracked and provides an effective cover to protect reinforcement from corrosion, delaying the ingress of the aggressive substances, such as carbon dioxide and chlorides. Furthermore, the alkalinity of concrete allows the reinforcing bars to be protected by a film of oxide. Due to service loads, physical processes, chemical and environmental attacks, concrete may crack and this enables rapid ingress of aggressive substances and an accelerated depassivation of reinforcing bars, leading to corrosion initiation. During the propagation period, reinforcement corrosion proceeds, leading to loss of bar section and deterioration of concrete, because the expansive corrosion products provoke cracks along the reinforcement, and subsequently cracking and eventually spalling of concrete cover. In addition, reinforcement corrosion alters the composite interaction between the steel bars and the surrounding concrete. Because of the presence of corrosion products and de-confinement due to opening of corrosion cracks, loss of bond at the steel-concrete interface may occur. All these consequences are known as “local” effects of corrosion and their understanding is particularly important in order to capture the global behaviour of corroded RC members. Indeed, the response of RC structures to external loads depends also on the level of damage reached in the structures themselves. Several studies have been made on the assessment of the residual service life of corroded RC elements, considering the penetration of chlorides and/or carbonation, establishing a limit to the service life when reinforcement depassivation occurs. These studies however, do not allow to establish the real behaviour of deteriorated structures. More researches are necessary for the comprehension of the single local effects of corrosion on the global behaviour of corroded RC elements at different stages of degradation. It is indeed important to estimate when it is needed to make a repair.

Reinforcement corrosion is a long-term process that weakens the structural elements, increasing their vulnerability with the time. Sudden failures of degraded elements have to be predicted and prevented, because they may lead to the collapse of full structures, e.g. bridges or frames. Only in this way the risks associated to loss of human lives, financial losses, social and environmental problems may be mitigated.

1.2. Motivation and scope of the research

Structural performances of RC constructions have to be considered time-dependent. Indeed, the progressive deterioration of material properties may affect the resistant mechanisms of the different structural elements, compromising their capability to withstand the loads for which they were designed. Therefore, structural assessment is required at different stages of the life of a construction and respect to serviceability and ultimate limit states, in order to assess respectively its reliability to fulfil its task for a given time period and to carry current and future loads. Through the assessment of existing structures, life cycle management and cost-efficient allocation of structural rehabilitation can be enhanced. A reliable prognosis of the condition and behavior of a structure is an important base for an effective service life management. In order to determine the most economic point in time for repair measures to be taken along the life-time of a structure, knowledge on the deterioration process at exposed regions as well as detailed knowledge about the current condition of the whole structure is essential, Kurz et al.[149]. In the case of corrosion damaged RC structures, the assessment of their static and seismic response is particularly important, due to the severe reduction of load-carrying capacity and ductility at which this kind of attack may lead. A study made by Çağatay[46] demonstrated how reinforcement corrosion induced by the presence of sea sand inside concrete mix, may lead to a greater seismic vulnerability and may anticipate the time to structural failure up to a period of 10-20 years, even under static loads. In this research field, many issues still need to be better investigated, such as the value of the residual area of reinforcing bars subjected to pitting corrosion, premature brittle failure mechanisms or the effect of bond degradation on the global structural response of RC beams.

In view of these remarks, the present dissertation has the purpose of better investigate the relationship between corrosion level and material mechanical properties of steel and concrete and their composite interaction. For the estimation of residual mechanical properties and area of steel bars subjected to pitting corrosion and validation of literature models, some tensile tests on locally damaged bars are also made. Basing on these observations, appropriate constitutive laws for degraded materials and bond capacity are proposed. Another aim of this thesis is the investigation of the consequences of the local effects of corrosion on the global behaviour of corroded RC structures. Indeed, during the recent years several researches have been carried out to develop models suitable to investigate the effects of corrosion by the finite element method. However, most of these models have the goal to simulate the local effects of corrosion. Only a limited numbers of models have been developed for the assessment of the global response of corroded RC structures. To this aim, a non-linear model able to describe the evolution of the structural degradation and the progressive redistribution of stress in corroded RC structures is adopted and enhanced with new formulations. In this way, the residual load- carrying capacity, deflection at service, stiffness and ductility of the damaged structures can be evaluated.

1.3. Overview

In the first part of this thesis (chapter 2), a brief introduction on the behaviour of concrete material and on the continuum damage approaches for its modelling is given. A more detailed description is provided for the adopted mechanical damage model, which is based on the work of Faria et al.[102] and has been recently improved by Berto et al.[34]. Furthermore, a number of numerical results are compared with experimental tests, in order to validate some new aspects introduced in the damage model, such as the *shear retention factor* and the technique adopted for the mesh-objectivity in compression.

The main part of the thesis is focused on the study and the modelling of the local and global effects of corrosion on RC structures.

In chapter 3, the corrosion phenomenon is briefly introduced, paying attention to the characteristics of different types of corrosive attacks. Then, a literature review of the effects of corrosion on steel and concrete materials and on their composite interaction is made. Finally, some remarks carried out by other researchers on the consequences of corrosion on the structural response of RC elements are reported, together with the description of some experimental tests. In particular, the experimental campaigns reported in this chapter, will represent the basis for some innovative proposals and their validation. Such experimental campaigns will be used as benchmark for the numerical analyses that will be carried out on corroded RC members.

In chapter 4 some improvements regarding the modelling of the local effects of corrosion with respect to the models available in the literature are carried out, in order to better reproduce the experimental evidences found in the last years. Concerning the effects of corrosion on reinforcing bars, the results of the tensile tests made by the Authors on locally damaged bars are presented and some remarks are pointed out. The modelling of concrete material degradation is made with the coupled environmental-mechanical damage model developed by Saetta et al.[225], here enhanced for considering the specific consequences of reinforcement corrosion on concrete. Finally, different bond stress-slip laws for the modelling of bond degradation due to corrosion and of different bond failures are proposed and validated against experimental data. These new proposals represent the different dowels of a more general comprehensive modelling approach, developed with the intent to make available a standard procedure, which considers the variables with the most important impact on the structural response of corrosion-damaged members.

The comprehensive modelling approach introduced in chapter 4 is validated in chapter 5 of this thesis, which is focused on the analysis of some structural elements subjected to different levels of corrosion. Here, the consequences of the local effects of corrosion on the structural response of RC beams and columns are discussed and the results of the numerical analyses compared with the available experimental data. A detailed numerical investigation is made on the consequences of bond loss in tensile bars of corroded RC beams on their structural behaviour.

In the last chapter (chapter 6), a summary of the achievements and some recommendations for further researches in this field are made.

CHAPTER 2
OVERVIEW ON CONCRETE MATERIAL MODELLING

2.1. Introduction

The response of reinforced concrete structures is partially defined by the behaviour of concrete material of which they are composed. Therefore, knowledge about the mechanical characteristics of concrete are required in order to predict and assess the static and dynamic response of RC constructions. To this aim, standard experimental tests of concrete specimens subjected to simple loads are commonly exploited. In particular, the results of these experimental investigations define a set of data that can be used in the development and calibration of analytical models. Development of constitutive models able to describe the non-linear behaviour of concrete material, considering its physical mechanisms and composition, remains a difficult task in structural engineering. At present, constitutive laws for concrete modelling have been developed basing on plasticity theory, smeared crack models and continuum damage mechanisms. In this section a brief description of the concrete behaviour in compression and in tension is given and some of the most common approaches to model concrete elements are summarized. After the attention will be focused on continuum constitutive laws for concrete and in particular on the mechanical damage model adopted in this research work.

2.2. Concrete behaviour

Concrete material is a heterogeneous and multiphase material composed of a mixture of coarse aggregate, sand and hydrated cement paste (*hcp*), which is the hydration product of portland cement and water (*Figure 2-1*).

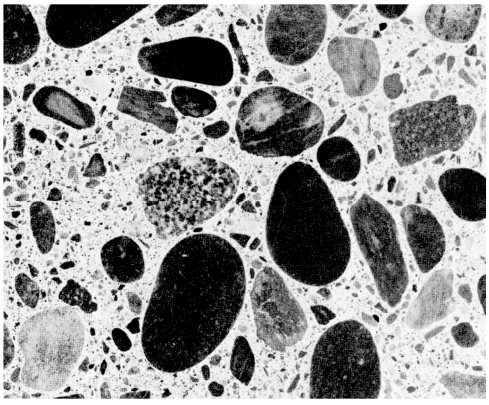

Figure 2-1. The Concrete Composite (Mehta et al.[180])

The area close to the coarse aggregate particles is instead defined as transition zone (*tz*) and it represents the weakest point of the material, because it is the physical boundary between the different components and it has a higher water to cement ratio. Under moderate levels of load, the concrete response is mainly controlled by microcracks that develop in the *tz (Figure 2-2 a))*; under increasing loads, microcracks propagate from the *tz* to the *hcp (Figure 2-2 b))*, Lowes[162].

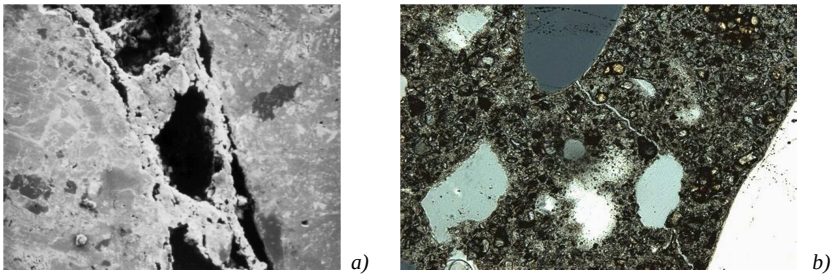

Figure 2-2. a) Cracks initiating at the tz; b) Cracks propagation in the hcp

Finally, microcracks may localize in relatively narrow zones, known as fracture process zones. The localization of strain and damage eventually leads to a gradual development of macroscopic stress-free cracks, Jirásek[132]. Because of this behaviour, the concrete is defined a quasi-brittle material. From a macroscopic point of view, it exhibits moderate strain hardening prior to the attainment of ultimate tensile strength and tension softening thereafter, mainly related to the fracture processes. Due to its non-homogeneous nature and that the primary mechanism of response is the development and prorogation of cracks, concrete behaviour may be modelled at different scales. Wittmann[270] proposed three scale levels for the concrete investigation and modelling: micro-, meso- and macro- level, *Figure 2-3*. At the micro-level, the physical and chemical processes in cement paste are considered at a molecular level. At the meso-level, individual aggregate particles, pores, inclusions and cracks are distinguished. At the macro-level, concrete is regarded as a homogeneous isotropic material, no material structure is distinguished, and all non-linear behaviour is included in the constitutive law.

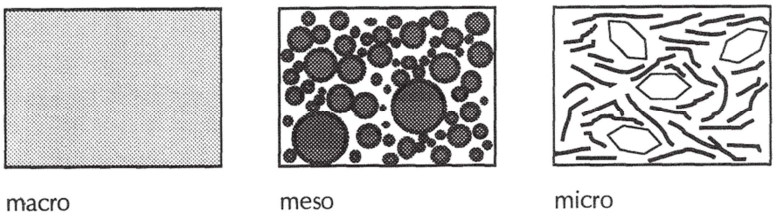

Figure 2-3. Macro-, meso-, micro- level for concrete modelling, van Mier[257]

In this thesis the attention will be focused on macro-level, which is the most global approach to model the concrete material. The concrete behavior is described by a stress-strain response, which reflects the propagation of internal micro-cracks and micro-voids and that can be calibrated from tests performed on larger specimens. The advantage, from a numerical point of view, to consider concrete as an equivalent continuum is that the structure that is analysed can be divided in relatively large finite elements, which tends to reduce the computational effort.

2.2.1. Uniaxial compression response

For the characterization of concrete material properties, standard testing procedures have to be adopted. Regarding the behaviour of concrete in compression, a typical stress-strain response of a specimen subjected to monotonically increasing compressive strain is shown in *Figure 2-4*. As outlined by Mehta and Monteiro[180], the behaviour of concrete is almost linear-elastic until the stress reaches about 30% of the peak strength (Zone A), because of the presence of marginal stable cracks within the *tz*. With load increasing, the behaviour starts to deviate from the linear response and the stiffness to reduce due to the increase in crack initiation and growth in the *tz* (Zone B). In concrete modelling, these two phases are commonly represented together and simplified with a linear-elastic response. Loading to compressive stress between 50% and 75% of peak strength results in higher reduction in material stiffness (Zone C), as a result of crack

initiation and growth in the *hcp.* Around the peak strength, increasing compressive strain under constant loading (Zone D) characterize the concrete response. This results from spontaneous crack growth in the *tz* and *hcp* and from the consolidation of microcracks into continuous crack systems, which may include cracks that transverse the coarse aggregate. The concrete behaviour of phases C and D up to the peak strength is commonly modelled through a non–linear response including material stiffness reduction. After this point, concrete exhibits increasing deformation while load decreases, because of the development of unstable cracks that continue to grow when subjected to a constant load and tend to localize (Zone E). This phase is displayed in the stress-strain curve by a softening branch.

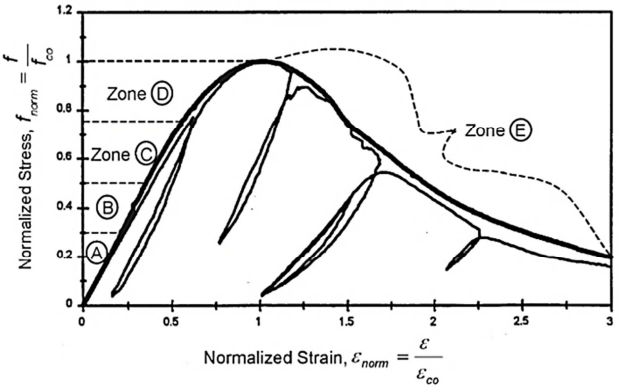

Figure 2-4. Concrete Response to Monotonic and Cyclic Compression Load, Bahn and Hsu[17]

Previous researches suggest that the post-peak softening response may be influenced by various factors, such as the slenderness of the specimen and the boundary conditions in the loading tests. In detail, especially rigid loading platens may affect the stress field inside the specimen, leading to formation of triaxial compression regions or more complex multiaxial stress states, Vonk[265][266]. Van Mier[257][258] carried out compression tests on specimens of different height using brush loading platens in order to reduce the influence of the boundary conditions. The author found different softening responses but a resembling compressive fracture energy between specimens of different slenderness. Similar conclusions were made by Jasen and Shah[129]. The authors tested concrete cylinders of different height with a feedback-control method using a linear combination of displacement and force that partially subtracts the elastic response of the specimen to give a stable feedback signal. Higher specimens exhibited a more brittle postpeak response, *Figure 2-5 a).* The amount of energy required to propagate the compression failure during postpeak was instead found to be independent from the specimen length, *Figure 2-5 b).*

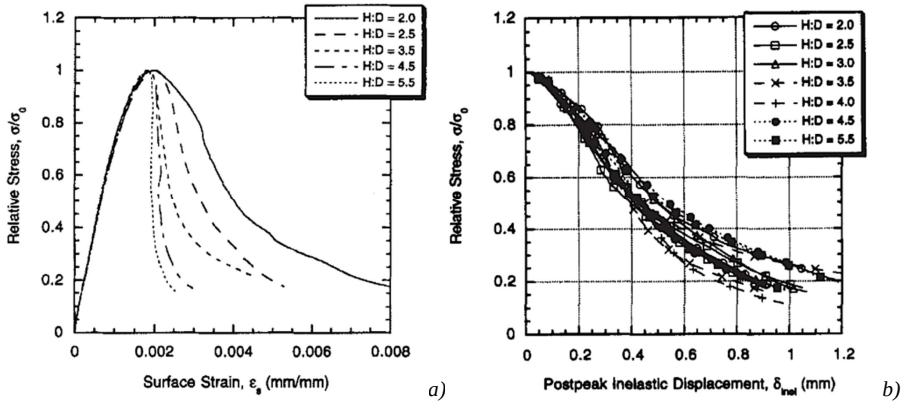

Figure 2-5. a) Stress-strain curves and b) post-peak stress displacement curves for concrete specimens of different height loaded in uniaxial compression, Jasen and Shah[129]

These remarks implies that compression failure is a localized phenomenon, otherwise there is a fracture region of limited width in which compression strains are concentrated, CEB-FIP MC90[61]. Due to the discontinuity, the stress-strain response of concrete becomes dependent on the size of the structure. Therefore, the strain softening response of concrete cannot be considered as a material property, but it represents a structural response, Vonk[266].

Figure 2-4 shows also the response of concrete under uniaxial, cyclic compression loading. It is possible to observe that, under moderate strain levels, stiffness of the unload-reload cycles is approximately equal to the elastic modulus; under higher strain levels stiffness deteriorates.

2.2.2. Tension Response

As well known, the structural response of concrete in tension is weaker than in compression. Almost all the codes suggest to calculate tensile strength as a fraction of the compressive strength, of a value between 5% and 15%. CEB-FIP MC90[61] pointed out that tensile strength is more influenced by the shape and the surface texture of the aggregates than the compressive strength, therefore its value may greatly vary. Further, the value of tensile strength is highly reduced by environmental effects, making the role of reinforcement particularly important. Therefore, deterioration of concrete tensile strength should be considered in a concrete constitutive model. *Figure 2-6* shows the typical stress-strain response of concrete prisms subjected to uniaxial tensile deformation under monotonically increasing loading. Approximately until the achievement of the peak tensile strength, concrete responds in an essentially linear-elastic manner. Near the peak, a small number of stable microcracks within the *tz* initiates and this lead to a slightly non-linear behaviour. Further increasing in load results in loss of load capacity, displayed by a strain softening post-peak response. This corresponds to the development and growth of continuous crack systems in the *tz* and in the *hcp*.

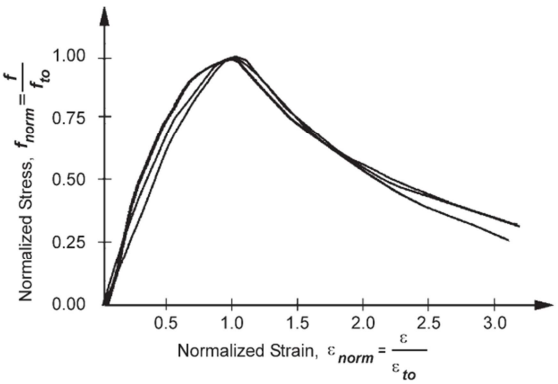

Figure 2-6. Tensile monotonic concrete tensile stress-strain curve, Yankelevsky et al.[275]

To observe the tension softening behavior, displacement control must be applied to the experiment or loading must be applied in parallel to other specimens that are stiffer than the steepest negative tangential stiffness of the post-peak curve, Evans and Marathe[99]. If load control is applied without special care, the experiment will yield a brittle fracture as soon as the tensile strength is reached. Indeed, under tensile loading, increased load acts directly to increase the stress at the crack tip and drive crack propagation. For this reason, the sequence of cracking leading up to the development of a continuous crack system and loss of strength occurs in a very rapidly way, in comparison with the specimen under compression loading. For this reason, also if uniaxial tensile testing is the most appropriate method to determine the tensile strength of concrete, in many instances the splitting tensile strength or flexural tensile strength are instead determined. Finally, the background documentation of *fib* MC2010[106] states that tension

softening can have a large influence on the tensile capacity of a tested member. However, it is also pointed out that the influence of this effect is very small, if not negligible, in large scale members with sufficient reinforcement in bending and shear.

Similarly to concrete compression, also in tension the strain softening response is nearly always accompanied by non-homogenous and highly localized deformations of the specimen, Van Mier[259]. Therefore the strain softening behaviour should be considered a structural response, as in compression. Instead, researchers agree that the area under stress-displacement curves, known as fracture energy G_F, can be considered a material characteristic. CEB-FIP MC90[61] defines the fracture energy as the energy required to propagate a tensile crack of unit area. There is still some controversy on the measurement of absolute values of G_F because the results may partially depend on the size of the structural member as well as on measurement procedure, Elices and Planas[97][203][204]. Further, *fib* MC2010[106] underlines the role played by concrete properties: for normal weight concrete, G_F may depend on the water-cement ratio, the maximum aggregate size, the age of concrete and curing conditions.

Finally, *Figure 2-7* shows the stress-strain curve for concrete prisms subjected to cyclic loading. Unload-reload cycles that initiate at strains in excess of that corresponding to the peak tensile strength occur at a material stiffness that is significantly less than the original material modulus. This reduced material stiffness is a result of cracks that formed under peak tensile load remaining open as long as the prism is carrying tensile stress.

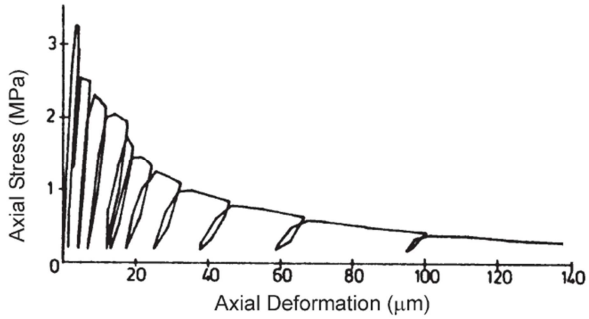

Figure 2-7. Stress-Deformation for Concrete Subjected to Cyclic Tensile Loading, Reinhardt[212]

2.2.3. Multiaxial response

In a number of RC structures, concrete is subjected to multiaxial stress state (σ_2 and/or σ_3 as well as σ_1 are finite). Therefore, in the years researchers have made experimental tests on concrete specimens under multi-axial loading and developed analytical model for characterizing the corresponding yield/failure surfaces. A typical failure envelope under biaxial stress (σ_3=0) found by Kupfer et al.[148] is shown in *Figure 2-8*, in which the applied stresses σ_1 and σ_2, are normalised respect to the uniaxial compressive strength. Under biaxial compressive stresses, strength of concrete has been found to be greater than the uniaxial compressive strength. Kupfer et al.[148] found that with ratio $\sigma_{1/}$ σ_2 of 0.5 and 1, the strength under biaxial stresses was respectively 1.25 and 1.16 times the uniaxial strength. The crack pattern reported by Vile[263], evidences cracks forming in the plane of the applied loads, splitting the specimen into slabs (*Figure 2-8 –type 3*). Specimens under bi-axial tensile stress have instead shown the lower strength, quite similar to the uniaxial tensile strength. Combined tension and compression stresses reduce the compressive stress needed for failure even if the tensile stress is low. The corresponding cracking pattern is a single tensile crack (*Figure 2-8 -type 1*), indicating that the

failure criterion is one of maximum tensile strain. In the region of near uniaxial compressive stress, close to the compressive stress axes cracks form all around the specimen approximately parallel to the compressive load (*Figure 2-8 -type 2*).

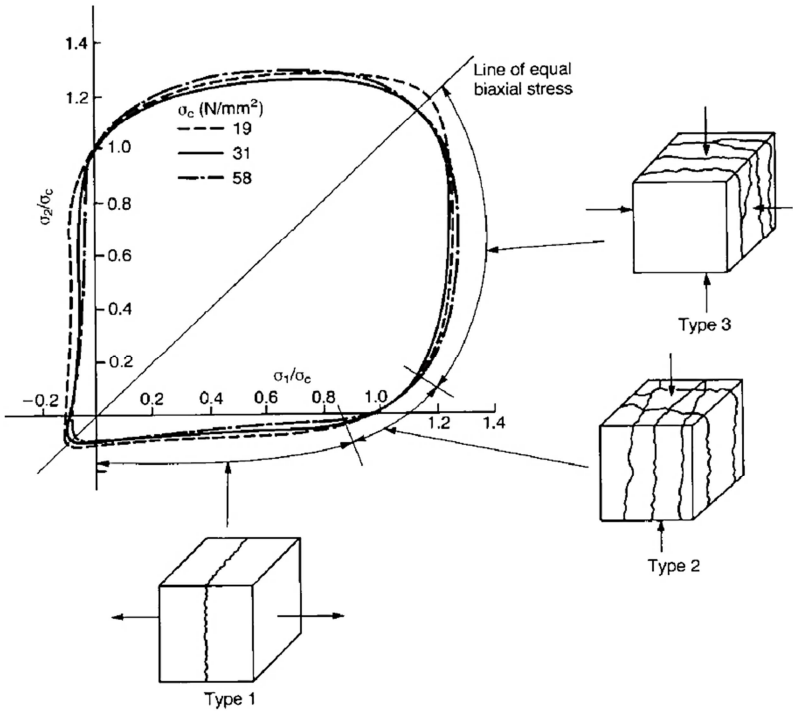

Figure 2-8. Failure envelopes and typical fracture patterns for concrete under biaxial stress σ_1 and σ_2 relative to uniaxial stress, Kupfer et al.[148], Vile [263]

With triaxial stresses, if all three stresses are compressive then the lateral stresses (σ_2 and σ_3) act in opposition to the lateral tensile strain produced by σ_1. This in effect confines the specimen, and results in increased values of σ_1 being required for failure, as illustrated in *Figure 2-9 a)* for the case of uniform confining stress (i.e. $\sigma_2 = \sigma_3$). In general, under tri-axial stress states the compressive strength may be even 10 to 20 times higher than the uniaxial compressive strength, see *Figure 2-9 b).*

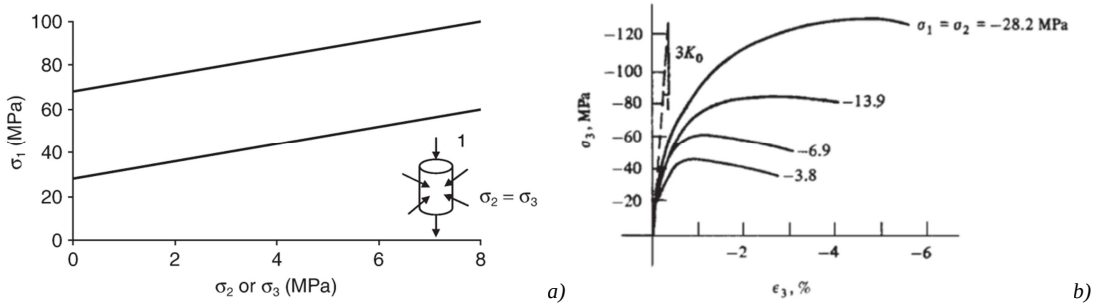

Figure 2-9. a) The effect of lateral confining stress (σ_2, σ_3) on the axial compressive strength (σ_1) of concretes of two different strengths; b)Stress-Strain curve under compression from the tests made by Richart et al.[215]

A particular case of triaxial stress can be found in compression uniaxial test. Here the load is applied to a specimen by the steel plate of a test machine. The lateral (Poisson effect) strains induce restraint forces in the concrete near the platen owing to the mismatch in elastic modulus between the concrete and the steel. This is therefore the cause of the higher strength of cubes compared to longer specimens such as cylinders.

2.3. Literary review: numerical models

Concrete exhibits a complex structural response with various important nonlinearities: among the others, a nonlinear stress-strain behavior, tensile cracking and compression crushing material failures, Bathe et al.[20]. Over the years many analytical models have been developed in order to accurately predict its behaviour. In particular, given that the primary mechanism of response of concrete is the development and propagation of discrete cracks, as described in 2.2, fracture processes assume a primary role. Most models for crack formation and propagation rely on Fracture Mechanics principles, either classical linear elastic fracture mechanics (LEFM) or non-linear fracture mechanics (NLFM). However, these principles are often superimposed onto a constitutive representation based on plasticity theory, damage theory or their combination. In practice, the approaches proposed for the simulation of fracture processes in concrete can be divided in two big groups: the discrete and the continuum approaches, *Figure 2-10*. In discrete approaches, a displacement discontinuity along an interface endowed with a cohesive constitutive behavior is artificially introduced in the model at a loading level, in a direction, with a length and at a position which have to be determined according to physically motivated criteria (Bocca et al.[41], Comi et al.[71], Jirásek[130], Mariani and Perego[173], Moës and Belytschko[183], Xu and Needleman[273]). In continuum approaches, the fracture is treated as the end of a process of accumulation and localization of damage without creating a real discontinuity in the material (Bazant and Cedolin[23], Carpinteri[57], Cervera et al.[62], Comi et al.[71], Jirásek[130][132], Mazars and Pijaudier-Cabot[177], Peerlings et al.[200]). Among these models, the Continuum Damage Mechanics is the most popular. A new trend is to combine these two methodologies: at first, the analysis begins with the application of a continuum damage model, which allows to describe the evolution of the mechanical properties of the continuum as micro-cracking develops. From a given damage value or from a critical size of the strain localization bandwidth, a displacement discontinuity is introduced and the evolution of the process is modelled with a cohesive crack law (Comi et al.[72], Oliver et al.[194], Wells[269]).

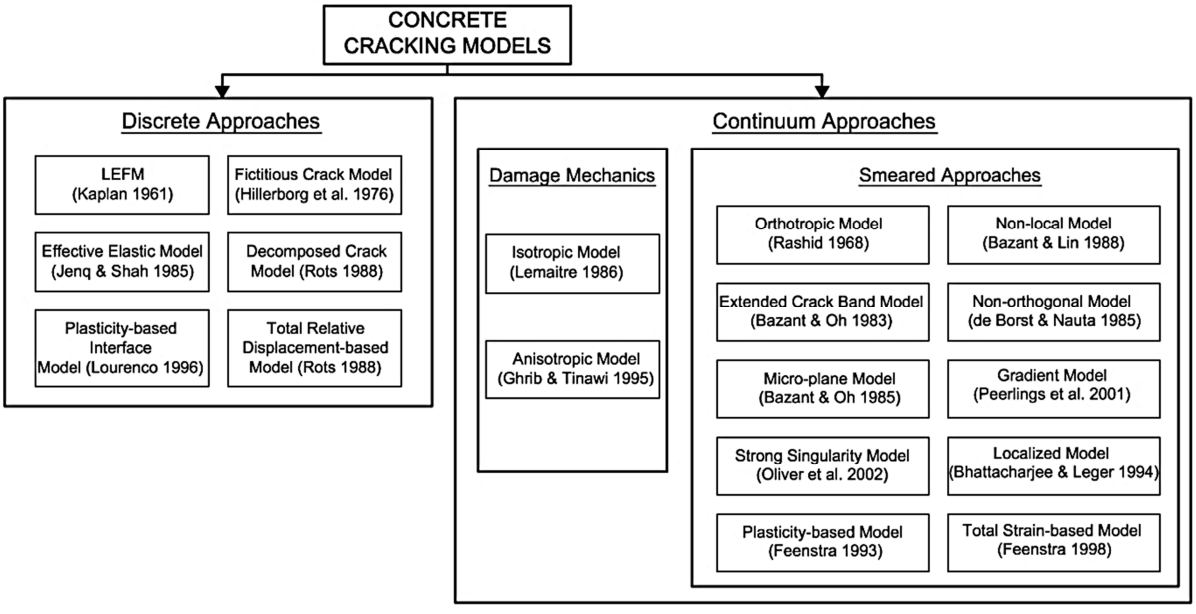

Figure 2-10. Overall models proposed for concrete fracture, Cai[47]

2.3.1. Discrete approaches

Linear elastic fracture mechanics is only applicable when the size of the Fracture Process Zone (F) at the crack tip is small when compared to the size of the crack and to the size of the specimen, Bazant[29]. In quasi-brittle materials, microcracks develop in a quite large zone at the crack tip, *Figure 2-11*. Therefore, linear elastic fracture mechanic is not applicable to concrete, and hence the nonlinear fracture mechanics (NLFM) based studies become essential. Among them, in the cohesive (fictitious) crack model, crack propagation is governed by a traction-displacement relation across the crack faces near the tip. Hillerborg et al.[121] proposed a number of traction-displacement relationships for concrete and introduced for first the concept of fracture energy into the cohesive crack model. Two main strategies are adopted to model the cohesive fracture with the finite element method. The first is the discrete inter-element cracks approach, where the crack evolves between elements and re-meshing operations are required (Bocca et al.[41], Camacho and Ortiz[55], Xu and Needleman[273]). The second is the discrete intra-element cracks approach, where instead the crack propagation is modelled through the finite elements, introducing embedded discontinuities in order to avoid re-meshing (Huang et al.[123], Moës and Belytschko[183], Simo et al.[233], Sukumar and Prévost [239], Wells[268]). A comparative study of such approaches can be found in Jirásek [133].

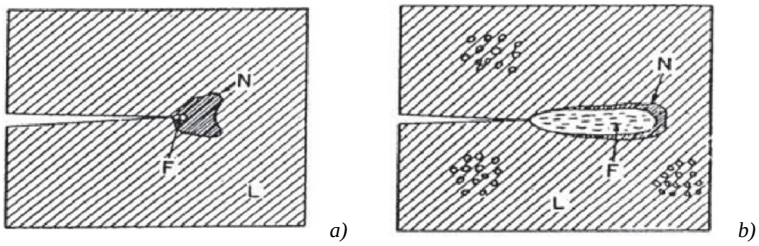

Figure 2-11. F size in a)ductile material ; b)quasi-brittle material, Murphy et al.[188]

2.3.2. Continuum approaches

Discrete models are unable to simulate the first phase of diffused damage; therefore, theories based on continuum damage mechanics have been developed. Continuum damage mechanics is able to describe the progressive loss of material integrity due to the propagation and coalescence of microcracks and defects, which lead to a degradation of material stiffness at a macro scale level, Jirásek[130]. In practice, the crack is represented by a change of the constitutive equations instead of changes on the finite element mesh, *Figure 2-12*. The concept of damage was first introduced by Kachanov[138][139]. Then, Rabotnov[209] defined the effective stresses and introduced the idea of affecting the initial stiffness of the material by a factor depending directly on the actual value of the damage variable. Some years later, thermodynamic laws have been used to set up the theoretical basis for the development of continuum damage mechanics models (Chaboche[63], Lemaitre[155], Lemaitre and Chaboche[156]).

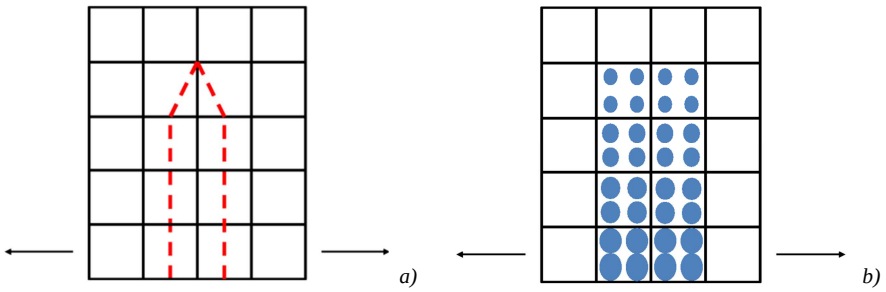

Figure 2-12. Crack propagation in: a) Discrete approach; b) Continuum approach

The isotropic damage models assume a uniform degradation of properties in all directions. In these models only some (one or two) variables are used to describe the deterioration of the material (Comi[69], Comi and Perego[73], Mazars[176], Mazars et al.[178]). To take into account the anisotropy induced by the development of diffuse micro-cracking, more sophisticated models have to be considered (Cordebois and Sidoroff[77], Krajcinovic and Fonseka[147], Proença and Pituba[207], Ramtani et al.[210]). Complex models in which the damage is represented with a second or fourth order tensor have also been developed, among others Ortiz[195] and Vakulenko and Kachanov[255]. De Borst[90] also demonstrate that smeared crack models can be considered as a special case of anisotropic damage models. Actually "smeared crack models" can be found in literature also to indicate a class of constitutive models which share some common features with but are different from plasticity and damage models, *Figure 2-10*. Many other authors have proposed models, in which damage and plasticity are coupled, e.g. Addessi et al.[3], Bazant and Jirásek[30], Lee and Fenves[151], Lu et al.[163], Lubliner et al.[164], Proença and Balbo[208]. For a more complete description of these models, refer to Jirásek[132]. In continuum approaches the constitutive law is expressed in terms of average stress and average strains, representing the crack by cracking strain distribuited on the finite element. Therefore they are based on the definition of a material law with softening post-peak behaviour. Due to the development of damage the material state is in the softening part of the stress-strain curve. The strain distribution obtained with finite element computations tends to localize into a narrow band whose width depends on the element size and tends to zero as the mesh is refined. The corresponding softening branch results arbitrarily close to the elastic branch of the load-displacement diagram. Since damage localizes in a region of zero volume the total amount of energy dissipated vanishes, which is not an admissible situation from the physical point of view. From a mathematical point of view, these features are related to the loss of ellipticity of the governing differential equations and the boundary value problem describing the structural response becomes ill-posed. Therefore, regularization techniques in order to avoid mesh dependence and to recover the well posedness of boundary value problem have to be used, Jirásek[134], Pijaudier-Cabot[202]. A technique frequently used is based on the adjustment of the softening modulus according to the element size, called fracture energy based regularization, Bazant and Oh [26]. This technique takes into account the quantity of energy which must be released in order to propagate a crack and can be implemented by adjusting the post-peak slope of the stress-strain diagram as a function of the element size. In detail, the area under the uniaxial stress-strain curve corresponds to the energy dissipated per unit volume, *gf*. The product of this energy density per unit volume with the thickness of the localized softening band gives the energy dissipation per unit area of the resulting stress-free crack, the fracture energy, which is considered a material property, paragraph 2.2.2. Obviously if the mesh adopted is too coarse, some discretization errors can be introduced, but the important property is that the total dissipation and the global load-displacement curve converge to a physically meaningful limit as the mesh is refined and that the energy dissipated in a band of cracking elements does not depend on its width, Bazant and Oh[26], Jirásek[132], Oliver[193]. In this technique however the global behaviour is regularized but the material behaviour remains dependent on the adopted discretization. A better computationally efficient and theoretically sound regularization technique is provided by the concept of non-local averaging, Bazant[22], Bazant and Jirásek[24], Bazant and Lin[25], Bazant and Pijaudier-Cabot [27][28][201]. In the integral non-local models some of the local physical quantities present in the constitutive relation and in the potential of dissipation definition are replaced by corresponding weighted averages defined over the whole domain, Borino et al.[42], Comi and Perego[75][76], Jirásek[131], Jirásek and Patzak[136]. The normalized Gauss function is usually used as weight function and the

procedure must be able to correctly reproduce local uniform fields. A correct choice of the physical quantities to be averaged is an important issue to ensure the efficiency and the coherence of the regularization procedure, Jirásek[130]. Other technique ensuring objectivity is based on the definition of gradient models, where the constitutive relation is enhanced through the definition of gradients of the state variables, Comi[69], Comi and Driemeier[70], Pamin[199]. A detailed review of damage models and their evolution can be found in Barros[18][19], Cotterell and Mai[82], Elices and Planas[97], Geers[111], Jirásek[135], Lemaitre and Desmorat[157].

2.4. Mechanical damage model

Within the framework of continuum damage mechanics, in the present work an isotropic damage model based on the work of Faria et al.[102] is adopted for the modelling of concrete material. It worth noting that for most of the concrete structures and loading conditions the use of damage isotropic models leads to accurate results. The numerical implementations are usually based on the use of such models, because they combine simplicity and robustness. In this paragraph, the basics of the mechanical damage model adopted are briefly described and the methods proposed to partially overcome the problem of mesh-dependency in tension and compression are introduced. In the next paragraph, the introduction of the *shear retention factor* and the criterion adopted for the mesh-objectivity in compression will be better investigated, considering the results of a number of experimental tests. Indeed, experimental data will be here used to provide additional information for refinement and calibration of the adopted model.

2.4.1. Isotropic model: basic assumptions

In a damaged body, for example a volume element which develops in the surrounding of a point M but enough large to contain micro-defects (or micro-cracks), as shown in *Figure 2-13*, the damage variable can be defined as:

$$D(M,\boldsymbol{n}) = \lim_{A\to 0}\frac{A_D}{A} \qquad \textit{Equation 2-1}$$

where A is the overall area of an element defined by the normal $\boldsymbol{n}$ and A_D is the area occupied by the micro-defects. When micro-defects are randomly distributed in all directions, D does not depend anymore on n, and the isotropic intrinsic variable is a scalar. In these conditions, D=0 corresponds to the undamaged state and D=1 to the completely damaged state.

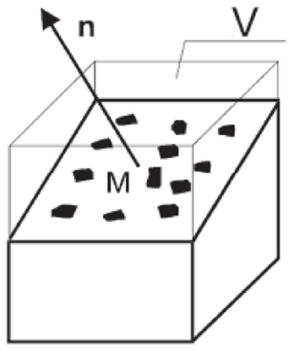

Figure 2-13. Definition of scalar damage variable in a finite volume

In the isotropic case, the general stress tensor, taken as the density of force with regard to the cross-sectional area A, is called the Cauchy stress tensor $\boldsymbol{\sigma}$. In a damage case, the actual stress tensor has to be taken as the density of force with regard to the effective area (A-A_D) and is called

effective stress tensor $\bar{\boldsymbol{\sigma}}$. In order to further simplify the problem, the hypothesis of strain equivalence proposed by Lemaitre[155][156] can be adopted. In detail, this hypothesis states that "*every strain behaviour of a damaged material is represented by constitutive equations of the undamaged material in the potential of which the stress is simply replaced by the effective stress*". Considering a 1D state as in *Figure 2-14*, due to the fact that the internal forces acting on any damaged section are the same as before damage, the following relationship can be written:

$$\sigma A = \bar{\sigma}(A - A_D) \qquad \textit{Equation 2-2}$$

Substituting $(A - A_D) = (1 - D)A$:

$$\sigma = \bar{\sigma}(1 - D) \qquad \textit{Equation 2-3}$$

Basing on the Hooke's law $\sigma = E \cdot \varepsilon$:

$$\varepsilon = \frac{\sigma}{E(D)} = \frac{\bar{\sigma}}{E_0} \qquad \textit{Equation 2-4}$$

where E_0 and $E(D)$ are the Young's modulus in the initial and damaged state respectively. The effective stress can then be defined alternatively as:

$$\bar{\sigma} = \frac{E_0}{E(D)}\sigma \qquad \textit{Equation 2-5}$$

which represents the basis of the hypothesis of strain equivalence for 1D case.

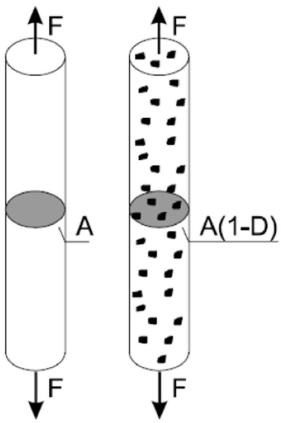

Figure 2-14. Undamaged and damaged configuration for uniaxial tensile test

The concrete model adopted in this work is based on the isotropic mechanical damage model originally developed by Faria et al.[102] and then modified and enhanced by Berto et al.[34][35], Scotta[227] and Talledo[240]. The model is based on the hypothesis of "strain equivalence" and the total strain tensor is split into "elastic-damage" and "plastic-damage" parts:

$$\boldsymbol{\varepsilon} = \boldsymbol{\varepsilon}^{\boldsymbol{e}} + \boldsymbol{\varepsilon}^{\boldsymbol{p}} \qquad \textit{Equation 2-6}$$

Therefore the effective stress tensor is defined as:

$$\bar{\boldsymbol{\sigma}} = \boldsymbol{C_0} : \boldsymbol{\varepsilon}^{\boldsymbol{e}} = \boldsymbol{C_0} : (\boldsymbol{\varepsilon} - \boldsymbol{\varepsilon}^{\boldsymbol{p}}) \qquad \textit{Equation 2-7}$$

where $\boldsymbol{C_0}$ denotes the fourth-order elastic stiffness tensor.

Further, the model encloses two independent internal damage variables d^+ and d^- relating respectively to the tensile and the compressive stresses. In this way, the different non-linear

behaviour of the concrete material, under tensile and compressive loading can be well captured, as well as the crack closure effect upon loading reversal. According to such a formulation, the effective stress tensor is split into two components $\bar{\boldsymbol{\sigma}}^{+}$, $\bar{\boldsymbol{\sigma}}^{-}$, related respectively to the tensile and the compressive behavior. The damage and plastic unloading/reloading processes are assumed to be elastic. The locally averaged free energy potential can be expressed as:

$$\Psi(\boldsymbol{\varepsilon}, \boldsymbol{\varepsilon^p}, d^+, d^-) = (1-d^+)\Psi_0^+(\boldsymbol{\varepsilon}, \boldsymbol{\varepsilon^p}) + (1-d^-)\Psi_0^-(\boldsymbol{\varepsilon}, \boldsymbol{\varepsilon^p}) = \\ = (1-d^+)\frac{1}{2}\bar{\boldsymbol{\sigma}}^{+}\!:\boldsymbol{\varepsilon^e} + (1-d^-)\frac{1}{2}\bar{\boldsymbol{\sigma}}^{-}\!:\boldsymbol{\varepsilon^e} \qquad \textit{Equation 2-8}$$

In agree with the first thermodynamic principle, during any physical process the energy dissipation shall be non-negative, therefore:

$$\dot{\boldsymbol{\varepsilon}}\!:\left[\boldsymbol{\sigma} - \frac{\partial\Psi}{\partial\boldsymbol{\varepsilon}}\right] - \left[\frac{\partial\Psi}{\partial d^+}\!:\dot{d}^+ + \frac{\partial\Psi}{\partial d^-}\!:\dot{d}^-\right] - \frac{\partial\Psi}{\partial\boldsymbol{\varepsilon^p}}\!:\dot{\boldsymbol{\varepsilon}}^p \geq 0 \qquad \textit{Equation 2-9}$$

The first term has to be zero, with the total strain a free variable:

$$\boldsymbol{\sigma} = \frac{\partial\Psi}{\partial\boldsymbol{\varepsilon}} = \frac{\partial\Psi}{\partial\boldsymbol{\varepsilon^e}} = (1-d^+)\frac{\partial\Psi_0^+}{\partial\boldsymbol{\varepsilon^e}} + (1-d^-)\frac{\partial\Psi_0^-}{\partial\boldsymbol{\varepsilon^e}} = \\ = (1-d^+)\bar{\boldsymbol{\sigma}}^{+} + (1-d^-)\bar{\boldsymbol{\sigma}}^{-} = (\boldsymbol{I}-\boldsymbol{D})\!:\bar{\boldsymbol{\sigma}} \qquad \textit{Equation 2-10}$$

This equation expresses the relationship between the Cauchy stress tensor and the effective stress tensor and basically represents the constitutive law of concrete material in analogy with *Equation 2-3*. The second and the third terms of *Equation 2-9* provide the damage and the plastic dissipation inequalities, which are demonstrated in Faria et al.[102]:

$$-\frac{\partial\Psi}{\partial d^+}\!:\dot{d}^+ - \frac{\partial\Psi}{\partial d^-}\!:\dot{d}^- = \frac{\partial\Psi}{\partial\boldsymbol{d}}\!:\dot{\boldsymbol{d}} \geq 0 \qquad \textit{Equation 2-11}$$

$$-\frac{\partial\Psi}{\partial\boldsymbol{\varepsilon^p}}\!:\dot{\boldsymbol{\varepsilon}}^p \geq 0 \qquad \textit{Equation 2-12}$$

Then developing *Equation 2-11*, the energy dissipated by the damage process must be defined. The thermodynamic force, which characterizes the damage evolution considering the progressive degradation of the mechanical properties of the material, is expressed as:

$$-\boldsymbol{Y} = \frac{\partial\Psi}{\partial\boldsymbol{d}} \qquad \textit{Equation 2-13}$$

The thermodynamic forces can be also defined as equivalent effective stresses $\bar{\tau}^{+}$ $\bar{\tau}^{-}$, since they provide two scalar measures of the effective stress tensor, Faria et al.[102]. Here they are defined following the proposal of Berto et al.[34] and Talledo[240], in which a unique damage criterion was proposed in order to improve the mixed tension-compression domain and therefore to better capture the behaviour of concrete under biaxial stress state as well as shear failures:

$$g(\bar{\tau}^{+}, \bar{\tau}^{-}, r^{+}, r^{-}) = \left(\frac{\bar{\tau}^{+}}{r^{+}}\right)^2 + \left(\frac{\bar{\tau}^{-}}{r^{-}}\right)^2 - 1 \leq 0 \qquad \textit{Equation 2-14}$$

$$\bar{\tau}^{-} = \sqrt{3}(K\bar{\sigma}_{oct}^{-} + \bar{\tau}_{oct}^{-}) \qquad \textit{Equation 2-15}$$

$$\bar{\tau}^{+} = \sqrt{E\bar{\boldsymbol{\sigma}}^{+}\!:\boldsymbol{C_0^{-1}}\!:\bar{\boldsymbol{\sigma}}^{+}} \qquad \textit{Equation 2-16}$$

where r^+ and r^- are the scalar damage thresholds monitoring the size of the damage surface in tension and compression respectively (for more details refer to Talledo[240]); $\bar{\sigma}_{oct}^-$and $\bar{\tau}_{oct}^-$ are respectively the octahedral normal and shear stresses; E is Young modulus of concrete; K is a material property that accounts for the uniaxial compressive strength increase due to biaxial compression, defined in Faria et al.[102].

In *Figure 2-15* the new mixed domain proposed by Berto et al.[34] is represented in the σ_1-σ_2 plane and compared with the one provided by Faria et al.[102]. It is possible to observe that the only differences between the two proposals reside in the tension-compression domain, where the original criterion of Faria et al.[102] neglects the influence of orthogonal tensile stress/strain on the compressive strength.

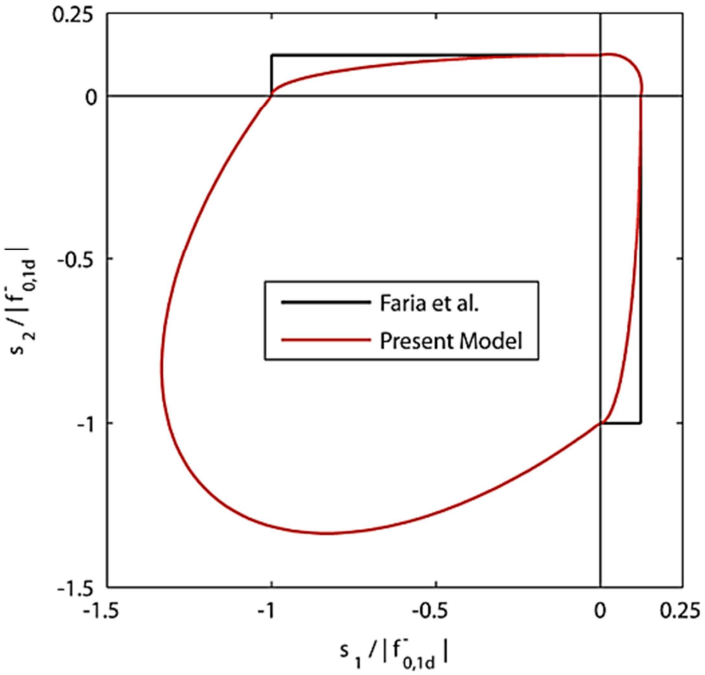

Figure 2-15. Comparison between mixed tension domains of Berto et al.[34]and Faria et al. [102]

Regarding the two internal damage variables, depending on the current damage thresholds, can be expressed as proposed by Berto et al.[35]:

$$d^+ = 1 - \frac{r_0^+}{r^+} \cdot exp\left[A^+ \cdot \left(1 - \frac{r^+}{r_0^+}\right)\right] \qquad \textit{Equation 2-17}$$

$$d^- = 1 - \sqrt{\frac{r_0^+}{r^+}} \cdot (1 - A^-) - A^- \cdot exp\left[B^- \cdot \left(1 - \sqrt{\frac{r^-}{r_0^-}}\right)\right] \qquad \textit{Equation 2-18}$$

where r_0^+ and r_0^- are the initial thresholds variables; A^+, A^-, B^- are model parameters: A^+ is related to the specific dissipated energy on a uniaxial tensile tests; A^-, B^- characterize the compressive damage evolution law and they based on a uniaxial compressive test, *Figure 2-16*.

In *Figure 2-17* is shown the monotonic behaviour of concrete under tensile and compressive loading. With the assumptions made, the model well reproduces the brittle behaviour of concrete in tension and the hardening effect of material under compression, followed by a softening branch after the achievement of the compressive strength.

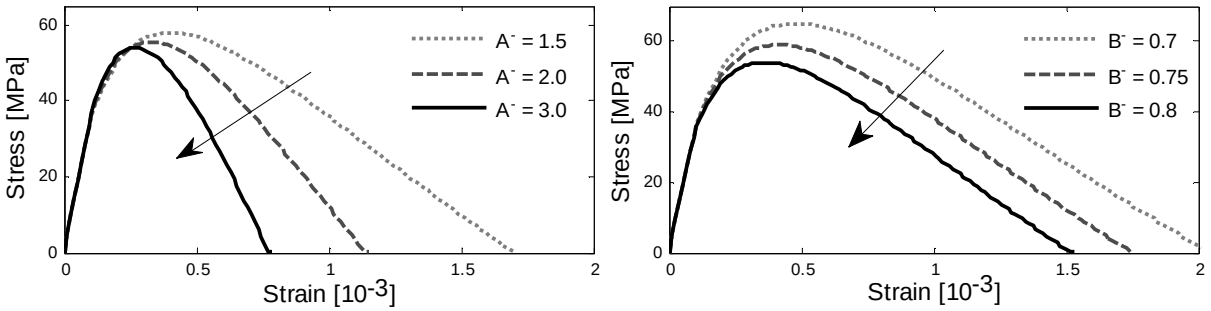

Figure 2-16. Effects of different values of A^-, B^- parameters on the compressive constitutive law

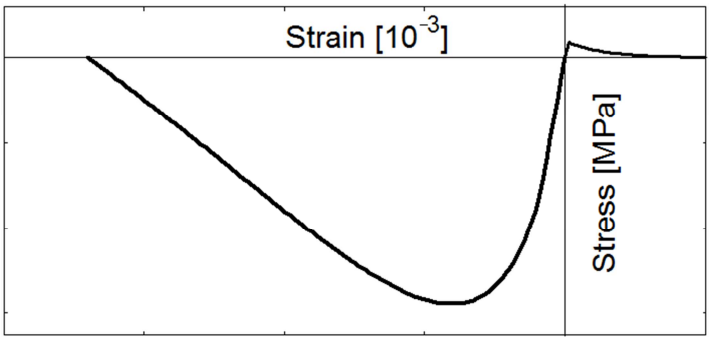

Figure 2-17. Monotonic constitutive law of concrete in tension and compression

Finally, the model considers that the damage criterion describes also the plastic surface. Therefore, the accumulation of irreversible plastic deformation is considered in the model for compression and tension states simultaneous to the development of material damage (Tesser et al.[246]), through the following relationship:

$$\dot{\boldsymbol{\varepsilon}}^p = \beta\, E\, H(\dot{d})\, \frac{\langle \bar{\boldsymbol{\sigma}} : \dot{\boldsymbol{\varepsilon}} \rangle}{\bar{\boldsymbol{\sigma}} : \bar{\boldsymbol{\sigma}}}\, \boldsymbol{C_0^{-1}} : \bar{\boldsymbol{\sigma}} \qquad \textit{Equation 2-19}$$

where β, with $\beta \geq 0$ and $\beta < 1$, is a material parameter controlling the rate intensity of inelastic strain; $H(d^- -)$ is the Heaviside step function and $\dot{d} = \dot{d}^+ + \dot{d}^-$ indicates the evolution of positive or negative damage. In this way, the plastic strain rate is parallel to the direction of total strain and the coupling between damage and plasticity simplified. In *Figure 2-18* is shown the effect of different values of β parameter on the constitutive law of concrete in compression and in tension.

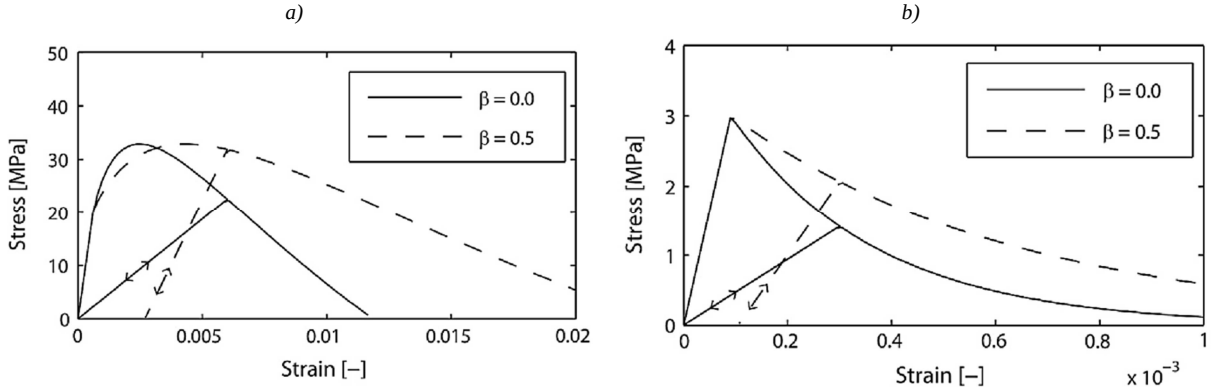

Figure 2-18. Effects of different values of β on a) compressive; b) tensile constitutive law of concrete, Berto et al.[34]

2.4.2. Shear retention factor

The original formulation of the adopted damage model implicitly considered only some secondary shear transfer mechanisms, such as the arch mechanism and the concrete cantilevers mechanism. In order to take into account also of the dowel action and of the aggregate interlock mechanism, a *shear retention factor* β_s was introduced by Scotta et al.[227]. This formulation is adopted also in the present work and extended for the two-parameter scalar damage model.

In detail, the *shear retention factor* β_s is directly introduced in the constitutive law modifying the stiffness matrix of the material only in the case of shear stresses, according to the following relationship:

$$\sigma_{ij} = \left[1 - d^+ + (1 - \delta_{ij}\delta_{kl})\beta_s d^+\right]\bar{\sigma}_{ij}^+ + \left[1 - d^- + (1 - \delta_{ij}\delta_{kl})\beta_s d^-\right]\bar{\sigma}_{ij}^- \qquad \textit{Equation 2-20}$$

Indeed, for normal stresses ($i = j$ and $k = l$) the constitutive law remains unaffected by β_s:

$$\sigma_{ij} = (1 - d^+)\bar{\sigma}_{ij}^+ + (1 - d^-)\bar{\sigma}_{ij}^- \qquad \textit{Equation 2-21}$$

while for shear stresses ($i \neq j$ and $k \neq l$), the β_s introduces a reduction of the damage action in order to assure a minimum shear strength, also in case of total damaged material ($d^+ = d^- = 1$):

$$\sigma_{ij} = \beta_s\bar{\sigma}_{ij}^+ + \beta_s\bar{\sigma}_{ij}^- \qquad \textit{Equation 2-22}$$

From an energetic point of view, the introduction of the *shear retention factor* implies a greater storage of free energy, Scotta et al.[227]. The authors firstly proposed a constant *shear retention factor*: *βs* could assume values between 0.0 (no *shear retention factor*) and 1.0 (damage ineffective for shear stress). The authors simulated some RC beams and found out that the results were almost identical for each value of *βs* greater than 0.2, while lower values were ineffective. Therefore they implemented a new formulation for *βs*, able to take into account that shear stress transfer decreases with increasing opening of the crack. The *shear retention factor* evolution law was defined as:

$$\beta_{s,ij} = 1 - \left|\frac{\varepsilon_{ij}}{\varepsilon_{ref}}\right| \geq 0 \qquad i \neq j \qquad \textit{Equation 2-23}$$

where ε_{ij} denotes the shear deformation and ε_{ref} is a reference value of deformation. With this formulation, Scotta et al.[227] found a better agreement with the experimental results analysed.

Finally, it is worth noting that theoretically the value of ε_{ref} depends on the relevance of the secondary mechanisms of shear resistance. In particular should depend on the diameter and distribution of the tensile reinforcement and on the aggregate size and the crack opening, in order to properly take into account respectively of the dowel action and of the aggregate interlock mechanism, *Figure 2-19*.

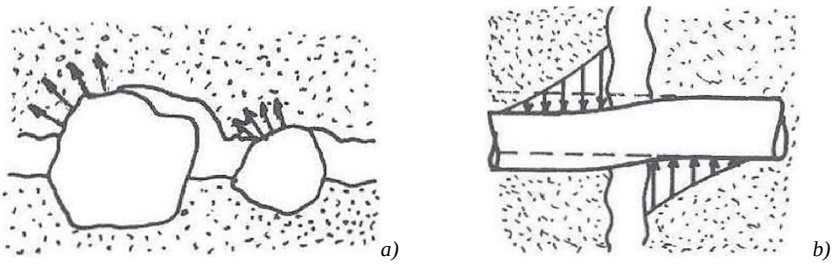

Figure 2-19. a) Aggregate interlock; b) Dowel action, Walraven[267]

A sensitivity analysis regarding the values of ε_{ref}, which should be adopted, will be made in the next paragraph, comparing the numerical results with the experimental data available of RC beams characterized by shear failure. Finally, a range of admissible values for the ε_{ref} will be proposed in order to avoid further calibration.

2.4.3. Softening behaviour and mesh objectivity

As introduced in paragraph 2.3.2, continuum approaches are based on the definition of a material model with softening post-peak behaviour, therefore they require a regularization to avoid mesh dependence due to the strain localization into a narrow band. In this work, the "fracture energy based regularization technique" is adopted in order to partially overcome these problems. In detail, the post-peak slope of the stress-strain diagram is adjusted as a function of the element size.

2.4.3.1. In tension

Concerning the tensile behaviour, the specific fracture energy (energy dissipated per unit volume) g_f is introduced and defined as the ratio of energy dissipation per unit area G_F (which is considered a material property) to the thickness of the localized softening band *h*:

$$g_f = \frac{G_F}{h} \qquad \textit{Equation 2-24}$$

where the thickness of the localized softening band *h* is assumed dependent on the mesh size:

$$h = \sqrt{A_e} \qquad \textit{Equation 2-25}$$

where A_e is the mesh element area, e.g. Oliver[193].

Then the parameter A^+ that controls the softening branch of the constitutive law of concrete in tension is correlated to the specific fracture energy through the follow relationship:

$$A^+ = \left[(1-\beta)\cdot\left(\frac{g_f E}{f_0^{+2}} - \frac{1}{2}\right)\right]^{-1} \qquad \textit{Equation 2-26}$$

In *Figure 2-20 a)* is shown the effect of different mesh refinement on the stress-strain response of concrete in tension, adopting a constant value of G_F. The adoption of such a technique of regularization makes the load-displacement curves for tension field not influenced by the mesh refinement. This technique has been widely used in the last years, and its effectiveness demonstrated in various work, among others in Berto et al.[34], *Figure 2-20 b),* where the hatched area represents two weaker elements aimed to induce the localization.

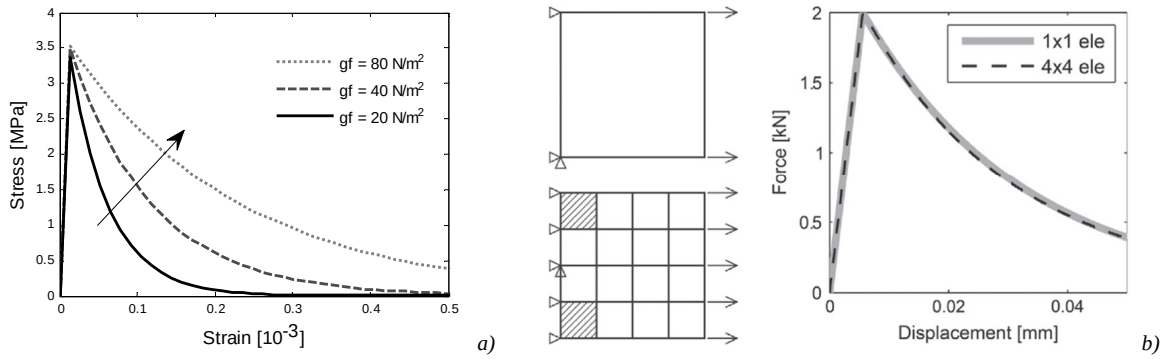

Figure 2-20. a) Influence of gf on the constitutive response of concrete in tension; b) load-displacement curves in tension for different mesh refinement, Berto et al.[34]

It is worth noting that the technique is effective regarding mesh objectivity but does not completely solve the problem of strain localization. However, it can be considered acceptable for the analysis of large structures, Talledo[240].

2.4.3.2. In compression

Strain localization mainly influences the behaviour of concrete in tension. Some authors have recently pointed out that also the compressive response of quasi-brittle materials may be affected by the same phenomenon. In particular, they proposed to introduce the concept of fracture energy also in compression, G_C, and to adopt a fracture energy based regularization technique similar to the one presented in tension, by defining a specific fracture energy g_c, among others Comi and Perego[74].

In this work, an approach similar to the one proposed by Hanjari et al.[119] is assumed. In detail, the compression softening behaviour of the stress-strain curve of concrete in compression is influenced especially by the specimen length, as reported in CEB-FIP MC90[61], *fib* MC2010[106], van Mier[257] and paragraph 2.2.1. Consequently, as the stress-strain curves proposed by different authors based on compressive tests made on concrete specimens of different sizes, the softening branch needs to be modified for the concrete element size used in the FE model, *Figure 2-21*. This can be done by assuming that the compression failure takes place in one element row and verifying this hypothesis *"a posteriori"*. The main difficulty of this method is that the number of elements in which the compressive region will localise is not known in advance. While in tension, it seems reasonable to assume that a crack will localise in one element row, Hanjari et al.[119].

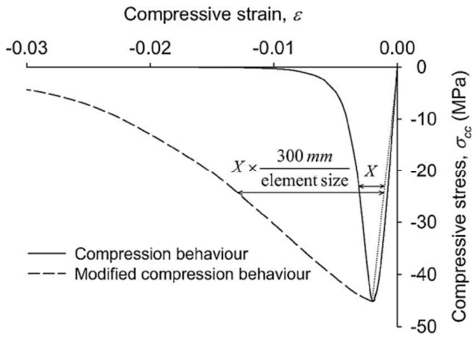

Figure 2-21. Modification of softening branch of stress-strain curve of concrete in compression, with respect to the concrete element size in the FE model, Hanjari et al.[119]

In this work, the stress-strain curve of the damage model for concrete in compression is calibrated on the constitutive relationship provided by CEB-FIP MC90[61], *Figure 2-23-dotted blue line.* In detail, the stress-strain curve proposed by CEB-FIP MC90[61] is based on the tests made by van Mier[258] and is expressed by the following equations:

$$\sigma_c = -\frac{\frac{E_{ci}}{E_{c1}}\frac{\varepsilon_c}{\varepsilon_{c1}} - \left(\frac{\varepsilon_c}{\varepsilon_{c1}}\right)^2}{1 + \left(\frac{E_{ci}}{E_{c1}} - 2\right)\frac{\varepsilon_c}{\varepsilon_{c1}}} f_{cm} \qquad \text{for } |\varepsilon_c| < |\varepsilon_{c,lim}| \qquad \textit{Equation 2-27}$$

$$\sigma_c = -\left[\left(\frac{1}{\varepsilon_{c,lim}/\varepsilon_{c1}}\xi - \frac{2}{\left(\varepsilon_{c,lim}/\varepsilon_{c1}\right)^2}\right)\left(\frac{\varepsilon_c}{\varepsilon_{c1}}\right)^2 + \left(\frac{4}{\varepsilon_{c,lim}/\varepsilon_{c1}} - \xi\right)\left(\frac{\varepsilon_c}{\varepsilon_{c1}}\right)\right]^{-1} f_{cm} \qquad \text{for } |\varepsilon_c| \geq |\varepsilon_{c,lim}| \qquad \textit{Equation 2-28}$$

Where f_{cm} is the mean compressive strength; E_{ci} is the tangent modulus; σ_c and ε_c respectively the compression stress and strain; ε_{c1}=-0.0022 the strain at the compressive peak; $E_{c1}=f_{cm}/\varepsilon_{c1}$ is the secant modulus; $\varepsilon_{c,lim}$ is the strain at $0.5f_{cm}$ in the softening branch; and ξ is defined as:

$$\xi = \frac{4\left[\left(\frac{\varepsilon_{c,lim}}{\varepsilon_{c1}}\right)^2\left(\frac{E_{ci}}{E_{c1}}-2\right)+2\frac{\varepsilon_{c,lim}}{\varepsilon_{c1}}-\frac{E_{ci}}{E_{c1}}\right]}{\left[\frac{\varepsilon_{c,lim}}{\varepsilon_{c1}}\left(\frac{E_{ci}}{E_{c1}}-2\right)+1\right]} \qquad \textit{Equation 2-29}$$

It is possible to note that the stress-strain curve defined by *Equation 2-27-Equation 2-30* is able to take into account of the brittleness of higher strength concrete in compression, *Figure 2-22*.

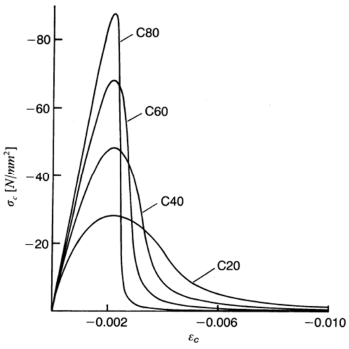

Figure 2-22. Stress-strain curves in compression for concrete with various f_{cm}, CEB-FIP MC 90[61]

However, this law can be reasonably accurate only for a length of the member subjected to compression of approximately 200 mm (CEB-FIP MC90[61]), which represents the specimen size on which the proposed law has been found. In this work, the descending portion of the stress-strain law defined by *Equation 2-28-Equation 2-29* is amplified by a parameter named *mesh size factor* (*m.s.f*) and the constitutive law for concrete in compression calibrated on the law so obtained, *Figure 2-23-continuous blue line.* The *m.s.f* is related to the localized softening band *h* (*Equation 2-25*), to the 200 mm length of the CEB FIP MC90's specimen and to the peak strain ε'_{c0}:

$$m.s.f. = \frac{speciment\ length\ (200mm)}{h}\cdot\frac{1}{\varepsilon'_{c0}} \qquad \textit{Equation 2-30}$$

where *h* in [mm]; ε'_{c0} is expressed [‰] and it refers to the peak strain of the amplified law.

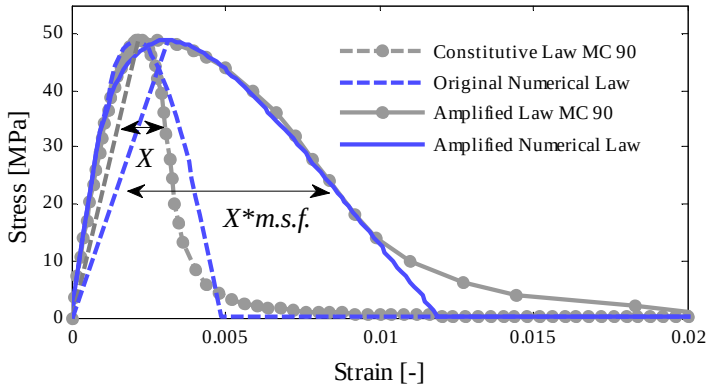

Figure 2-23. Amplification of the softening branch of σ-ε law of concrete in compression

In order to validate this approach, the uniaxial compression test made by Van Mier[258] on the prism specimen of 200 mm height is here simulated, using different mesh refinement. In detail,

the stress-strain curves obtained with *Equation 2-30* are reported in *Figure 2-24 a)* together with the mesh sizes adopted. Similarly to the validation tests made for the tensile behaviour of concrete, one weaker element is introduced, with the aim to induce localization. The results obtained in terms of Mean-stress - Mean-strain curves and of negative damage maps are reported in *Figure 2-24 b)* and *Figure 2-25* respectively. It is possible to observe that the strain localizes in one element and that the global response is almost not influenced by the mesh size.

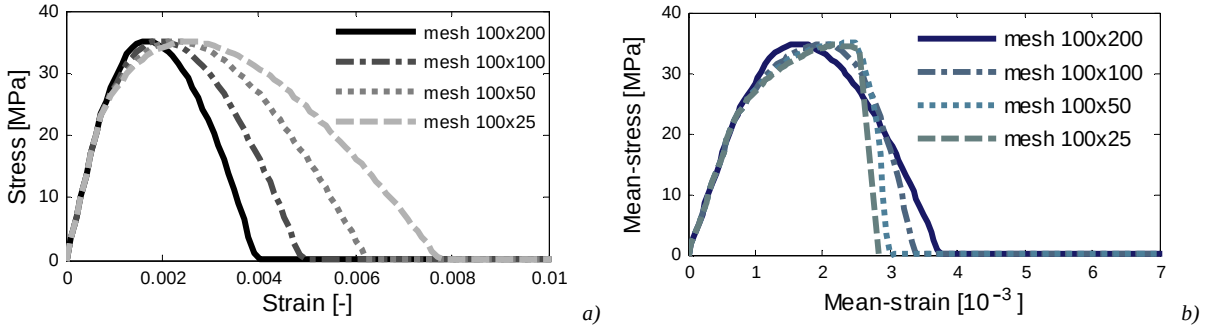

Figure 2-24. a)Stress-strain curves and b) Mean-stress – mean-strain curves, for different mesh sizes

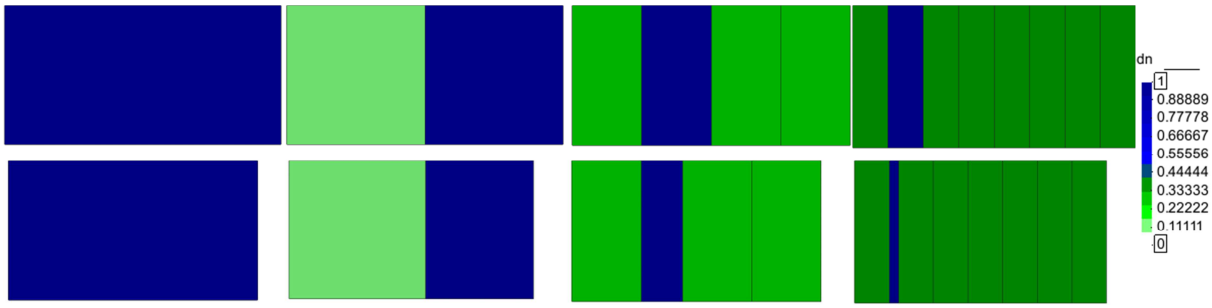

Figure 2-25. Negative damage maps and axial deformation for different mesh refinement

It should be noted that in *Equation 2-30*, a dependency of the *m.s.f.* on the value of ε'_{c0} has been introduced. This is due to the fact that the peak strain of the amplified law can assume different values, due to the law for damage evolution adopted. For this reason, the area under the pre-peak branch, which expresses a part of the compressive fracture energy (shown in *Figure 2-26 a)* considering an unload path with the secant modulus), results to be dependent on the value of peak strain. Therefore the global behaviour of concrete elements results to be influenced by the value of ε'_{c0}. In order to prove this statement, the same analyses made for the previous concrete specimen, are made calculating *m.s.f.* with *Equation 2-30* but without introducing the term ε'_{c0}. The results obtained in terms of Mean-stress - Mean-strain curves are displayed in *Figure 2-26 b)*. This time, the global response is influenced by the mesh size.

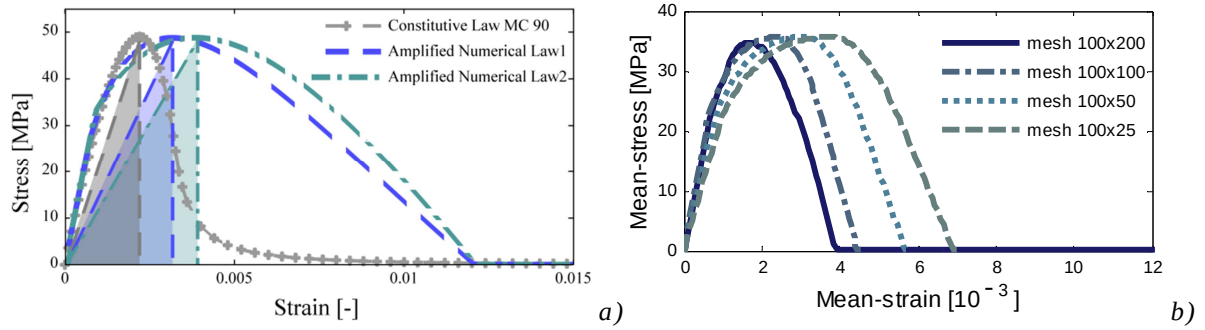

Figure 2-26. a) Stress-strain curves; b) Mean-stress – mean-strain curves, different mesh sizes

A further validation of the proposed approach, will be presented in the next paragraphs, taking into account the experimental results obtained by Leonhardt and Walther[158] on RC beams that are designed to fail in compressive crushing under flexural loading.

2.5. Validation of the mechanical damage model

The damage model briefly described in paragraph 2.4 requires a validation phase, especially regarding the new aspects introduced, such as the *shear retention factor* and the *mesh size factor*. In order to find a range of admissible values of ε_{ref}, the tests made by Bresler and Scordelis[43] on sound RC beams without stirrups and designed to fail in shear are firstly simulated. Regarding the approach proposed for the mesh objectivity in compression, the values of *m.s.f.* found with *Equation 2-30* are validated considering the tests made by Leonhardt and Walther[158] on RC beams designed to fail in bending by compressive crushing of concrete. Further, through the numerical simulation of these tests, the ability of the mechanical damage model to reproduce different types of failures in sound conditions will be proved, before applying the model for the simulation of corroded RC structures. Indeed, loaded RC beams may fail in bending or in shear, depending mainly on the amount of longitudinal and shear reinforcement and on the shear span value and corrosion attack may lead to a change of failure mechanism from a ductile to a brittle one. In order to have a ductile member with plenty of warning before the collapse, yielding of tensile reinforcement before crushing of concrete in compression is necessary for allowing an extensive cracking and deflection before failure. If a beam is over-reinforced, it fails by concrete compression before yielding of the tensile bars and it shows a lower structural ductility. Unlike flexural failures, shear failures are relatively brittle and lead to abrupt and dangerous collapses. Therefore the prediction of the failure type is a crucial issue in analysing structural response of RC members.

2.5.1. Finite element modeling

In the numerical simulations, concrete material is modelled with the mechanical damage model described and with 2D plane stress elements in order to reduce the computational effort of the analyses. The stress-strain curve of reinforcing steel bars is taken as for an elasto-plastic material with linear strain hardening and ultimate strength. The reinforcing bars and stirrups are modelled with truss elements and connected to the nodes of the concrete material. In this way, a condition of perfect adherence between steel bars and surrounding concrete is assumed. Due to symmetry, only half of the beam is modelled with the proper boundary conditions. In order to develop a reliable and effective working tool, all the aforementioned formulations are implemented in the finite element framework OpenSEES (Open System for Earthquake Engineering Simulation) [179]. This software is an open-source platform for research that enables user to combine existing libraries with new components, in fact one can add both material and element classes.

2.5.2. Tests made by Bresler and Scordelis

The tests made by Bresler and Scordelis[43] for analyzing the shear behavior of RC beams are considered in order to investigate the introduction of the *shear retention factor* in the damage model. The authors tested 12 beams with different geometrical characteristics and amount of reinforcement. The stirrups ratio ranged between 0.0 and 0.2%. The beams were designed and loaded such as to be critical in shear, being heavily reinforced for flexure and containing light amount of stirrups. The OA beams (*Table 2-1*) without stirrups are here analyzed, *Figure 2-27*.

Table 2-1. Details of Bresler and Scordelis' et al.[43] beams

Beam	*bxh [mm]*	*Total span [mm]*	*d [mm]*	*Bottom reinforcement*	*ρ [%]*	*a/d*
OA-1	*310X556*	*3660*	*461*	*4 No.9*	*1.84*	*3.97*
OA-2	*305X561*	*4570*	*466*	*5 No.9*	*2.30*	*4.90*
OA-3	*307X556*	*6400*	*462*	*6 No.9*	*2.70*	*5.80*

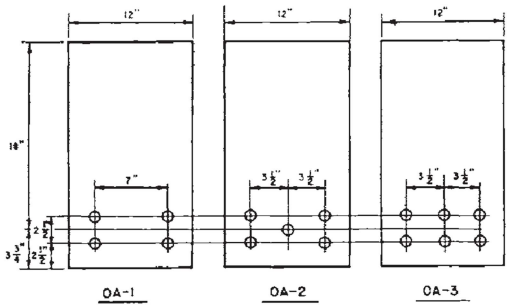

Figure 2-27. Beam cross sections (series OA, B, A and C), Bresler and Scordelis[43]

The beams are simply supported, subjected to a concentrated midspan load (*Figure 2-28*) and characterized by different shear span-depth ratios. In *Figure 2-29* is reported the typical crack pattern exhibited by the OA beams tested. These beams presented a sudden failure, immediately after the development of a diagonal critical crack (diagonal tension failure).

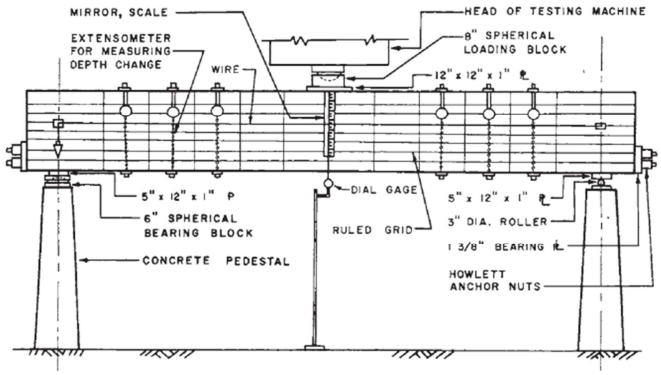

Figure 2-28. Loading arrangement and instrumentation, Bresler and Scordelis[43]

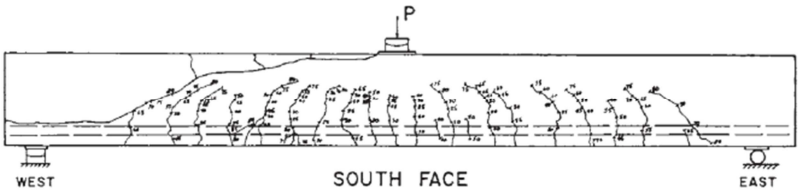

Figure 2-29. Typical crack pattern for diagonal tension failure, Bresler and Scordelis[43]

The characteristics of the materials, adopted in the numerical analyses, are reported in *Table 2-2*. The only data not provided by the authors are: the modulus of elasticity of concrete, here evaluated with ACI code[2]; and the tensile fracture energy, evaluated with CEB-FIP MC90[61].

Table 2-2. Material properties of Bresler and Scordelis beams

Beam	f_c *[MPa]*	E_c *[MPa]*	f_t *[MPa]*	G_F *[N/m]*	σ_y *[MPa]*	σ_{max} *[MPa]*	E_s *[MPa]*
OA-1	*22.6*	*22486*	*3.96*	*0.062*	*555*	*958*	*217874*
OA-2	*23.7*	*23027*	*4.33*	*0.064*	*555*	*958*	*217874*
OA-3	*37.6*	*28985*	*4.14*	*0.089*	*555*	*958*	*217874*

A sensitivity analysis is carried out for each of the OA beams respect to different values of ε_{ref} . In *Figure 2-30* the values of ε_{ref} considered in the numerical analyses are plotted versus the corresponding ultimate load obtained. The ultimate loads of the beams, provided by the experimental tests, are also indicated in *Figure 2-30 -dotted lines.* It is possible to observe that, in order to obtain a good correspondence between numerical and experimental results, reliable values of ε_{ref} are included between 0.00055 and 0.0007, in agree with the value of $\varepsilon_{ref} = 0.8‰$ found by Scotta et al.[227]. In *Figure 2-31* the best values found for ε_{ref} are reported versus the characteristics that should mainly influence the secondary mechanisms of shear resistance, such as the tensile reinforcement ratio ρ (which considers both bar diameter and amount of reinforcement), the maximum aggregate size d_{max}, concrete strength in tension f_t, fracture energy (which implicitly considers both d_{max} and f_t). Due to the fact that d_{max} was 19 mm for all the beams, the greater influence on ε_{ref} is respect to the reinforcement ratio. Instead, ε_{ref} seems not directly related to f_t.

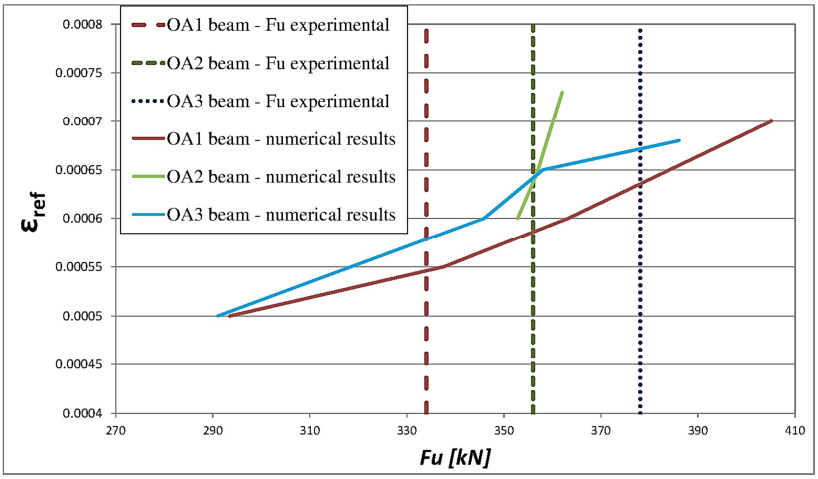

Figure 2-30. Values of ε_{ref} versus ultimate load Fu[kN], for OA beams

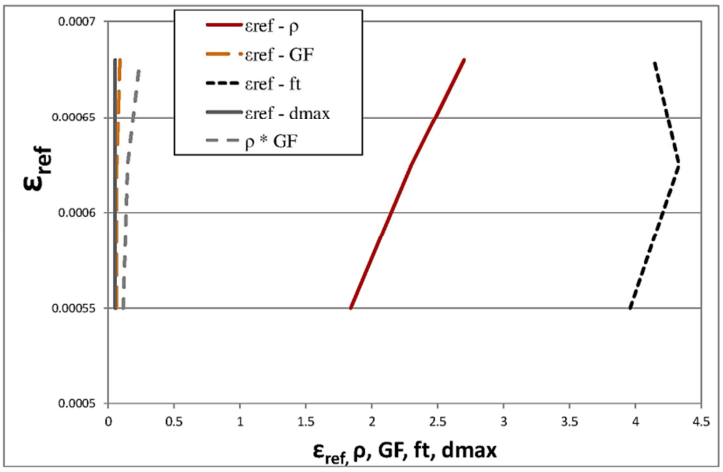

Figure 2-31. Values of ε_{ref} versus ρ, G_F, ft, d_{max} and $\rho \cdot G_F$

In *Figure 2-32* the numerical results in terms of Load-deflection curves (*blue dotted lines*), for the different values of ε_{ref} found, are reported and compared with the experimental curves (*grey continuous lines*). The model reproduces the experimental results with high-quality performance, in terms of ultimate load and stiffness of the elements. Further, the numerical curves are compared with those obtained without *shear retention factor* (*Figure 2-32 –dotted red lines*) confirming that the introduction of this parameter assures a real improvement of the damage model.

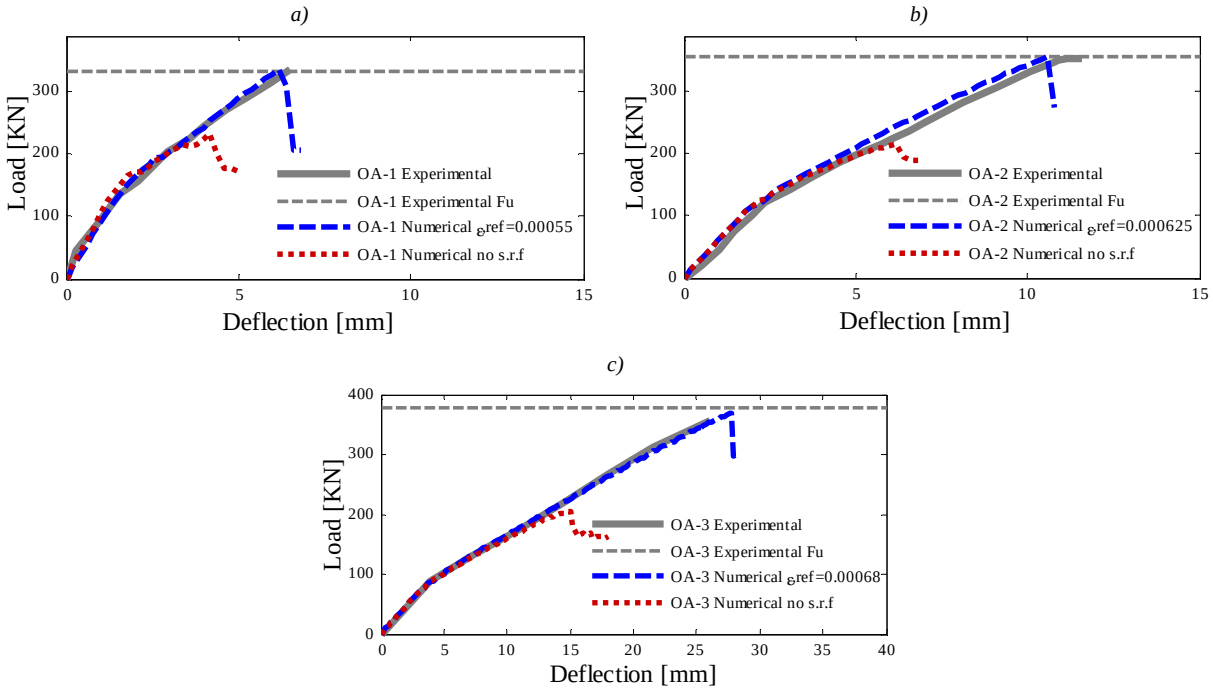

Figure 2-32. Load-midspan deflection for: a)OA-1 beam; b)OA-2 beam; c)OA-3 beam; comparison between experimental and numerical results.

Regarding the failure mode, as stated by Bresler and Scordelis[43], in beams wherein shear effects are significant, diagonal cracks formed due to "diagonal tension", resulting from a combination of shearing and flexural tension stresses, after the development of flexural vertical cracks of minor entity. The numerical model exhibits the same type of failure, as displayed by *Figure 2-33*, where the positive and the negative damage contours for the beam OA2 are reported. As we can see, a critical diagonal crack develops and leads to the failure of the beam, before that the compressive damage reaches a value close to 1. Similar results are found also for the OA1 and OA3 beams, here not reported for the sake of brevity.

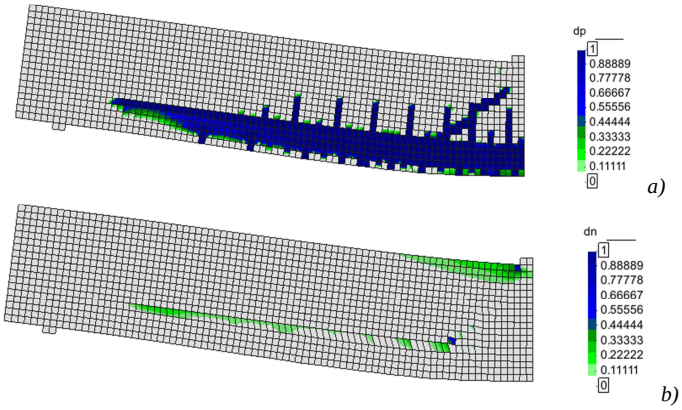

Figure 2-33. a) Tensile (dp) and b) compressive (dn) damage contours for OA2 beam at failure

Finally, a comparison between experimental, theoretical and numerical results is made and reported in *Table 2-3*. It is possible to observe that the better correspondence with the experimental data is given by the numerical results, because of the calibration phase made on the ε_{ref} value. The theoretical values of ultimate load P_u and diagonal tension cracking load P_{cr}, calculated with both the ACI[1] and the NTC2008[192] (which based on UNI EN 1992-1-1:2005[251]) codes, instead differ from the experimental results. This was observed also by Bresler and Scordelis[43]. The authors explained the difference between the calculated values and

the experimental results (found between 30% and 50%), stating that this higher strength is due to the dowel action, which is only partially considered in the calculations. In these beams the shear rigidity of the multilayered tensile reinforcement contributes for a significant portion to the higher strength. Indeed, when diagonal cracks develop within the shear span, the shear force is carried by the concrete in the compression zone, by the aggregate interlock action along the crack surface and by the dowel action of the longitudinal bars. For this reason, the introduction of the shear retention factor assumes a great importance in these numerical analyses. It should be noticed that for beams without multilayered tensile reinforcement, ε_{ref} can assume lower values due to the lower relevance of the dowel action.

Table 2-3. Comparison between experimental, theoretical and numerical results, OA beams

	Test		*Theoretical values - ACI-ASCE Commitee 426 (326)*				*Theoretical values - NTC2008*				*Numerical*			
Beam	*Pcr [kN]*	*Pu [kN]*	*Pcr [kN]*	*ΔPcr [%]*	*Pu [kN]*	*ΔPu [%]*	*Pcr [kN]*	*ΔPcr [%]*	*Pu [kN]*	*ΔPu [%]*	*Pcr [kN]*	*ΔPcr [%]*	*Pu [kN]*	*ΔPu [%]*
OA-1	*266.9*	*333.6*	*244.7*	*8.3*	*244.7*	*26.7*	*224.7*	*15.8*	*224.7*	*32.6*	*266.6*	*0.1*	*335.5*	*-0.6*
OA-2	*289.1*	*355.9*	*245.5*	*15.1*	*245.5*	*31.0*	*241.3*	*16.5*	*241.3*	*32.2*	*280.4*	*3.0*	*355.8*	*0.0*
OA-3	*311.4*	*378.1*	*296.3*	*4.9*	*296.3*	*21.6*	*344.2*	*-10.5*	*344.2*	*9.0*	*301.7*	*3.1*	*369.4*	*2.3*

2.5.3. Tests made by Leonhardt and Walther

The experimental campaign made by Leonhardt and Walther[158] is considered with a double purpose. From one side, the values of ε_{ref} previously defined for the beams tested by Bresler and Scordelis[43] have to be proved. On the other side, some of these beams exhibite a flexural failure by compressive crushing of the concrete, therefore they represent a good benchmark for the validation of the approach proposed for the mesh objectivity in compression (*m.s.f.* calculated by *Equation 2-30)*. Finally, the ability of the damage model to reproduce different types of failures will be proved.

Leonhardt and Walther[158] conducted an experimental campaign on RC beams without stirrups of different shear span-depth ratios in order to study the influence of the moment-shear interaction. The authors tested rectangular RC beams with the same cross section (190x320mm) and tensile reinforcement (2Φ26 rippentorstahl BstIIIb) but different values of *a/d*, *Figure 2-34* and *Figure 2-35*.

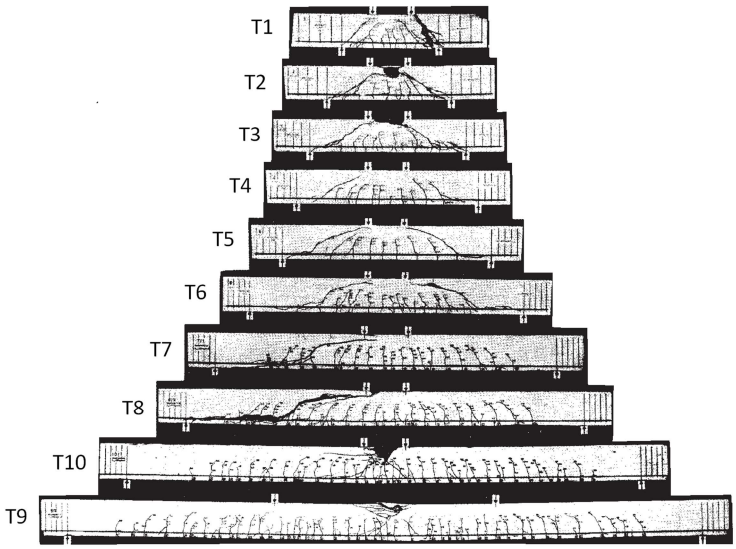

Figure 2-34. Cracks and failure pictures of beams, Leonhardt and Walther[158]

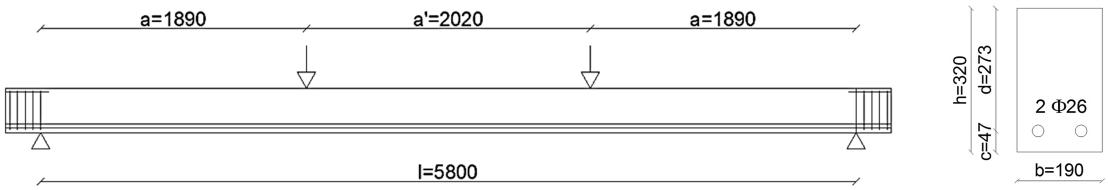

Figure 2-35. Loading arrangement and geometry of beam T9

The beams were subjected to four-point bending test. The geometry properties of the beams here analysed and the material characteristics given by the authors are reported in *Table 2-4*. The material characteristics adopted in the numerical analyses are reported in *Table 2-5*.

Table 2-4. Details of Leonhardt and Walther[158] beams

Beam	*L [mm]*	*a [mm]*	*h [mm]*	*b [mm]*	*a/d*	*ρ [%]*	*f_c [MPa]*	*σ_y [MPa]*	*σ_{max} [MPa]*
T3	*1450*	*540*	*320*	*190*	*1.98*	*2.05*	*28.90*	*465*	*550*
T4	*1700*	*670*	*320*	*190*	*2.45*	*2.05*	*28.90*	*465*	*550*
T5	*1950*	*810*	*320*	*190*	*2.97*	*2.05*	*28.90*	*465*	*550*
T6	*2350*	*1100*	*320*	*190*	*4.03*	*2.05*	*28.90*	*465*	*550*
T7	*3100*	*1350*	*320*	*190*	*4.95*	*2.05*	*30.28*	*465*	*550*
T9	*5800*	*1890*	*320*	*190*	*6.92*	*2.05*	*31.58*	*465*	*550*
T10	*4700*	*2160*	*320*	*190*	*7.91*	*2.05*	*29.38*	*465*	*550*

Table 2-5. Material properties adopted for the simulation of the Leonhardt and Walther's beams

f_c [MPa]	*E_c [MPa]*	*f_t [MPa]*	*G_F [N/m]*	*σ_y [MPa]*	*σ_{max} [MPa]*	*E_s [MPa]*
29	*25471*	*3.00*	*0.060*	*465*	*550*	*208000*

Regarding the *shear retention factor*, also for these beams a sensitivity analysis is carried out respect to different values of ε_{ref}, obtaining graphs similar to *Figure 2-30 a)*. For the sake of brevity, in *Figure 2-36* only the values of ε_{ref} that better fit the experimental results are reported. A mean value of ε_{ref} =0.00043 is found to be enough accurate for all the beams. Indeed, only one value of ε_{ref} was here expected, because all the beams have the same tensile reinforcement ratio ρ and maximum aggregate size d_{max}, factors that have been found to greatly influence the secondary mechanisms of shear resistance, see *Figure 2-30 b)*. The value of ε_{ref} found is slightly lower than the values found for the beams tested by Bresler and Scordelis[43]. This is probably due to the fact, that the beams tested by Leonhardt and Walther[158] have only one layer of tensile reinforcement and the maximum aggregate size in concrete is lower. However, in order to quantify these aspects, more analyses are required. Basing on the remarks made, a proposal for the prediction of a sufficiently accurate value of ε_{ref} is here made and reported in *Table 2-6*.

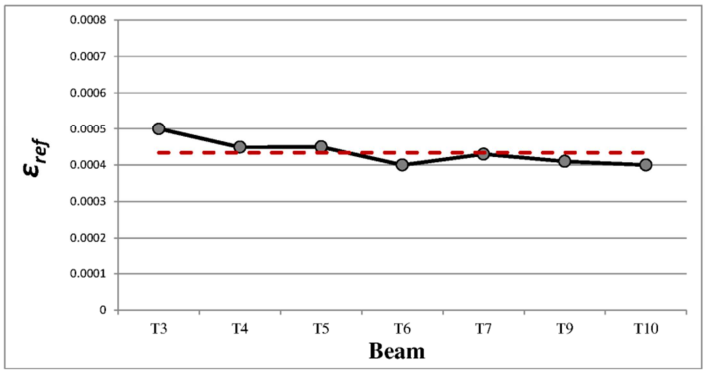

Figure 2-36. Values of ε_{ref} for the beams tested by Leonhardt and Walther[158]

Table 2-6. Proposal for the value of ε_{ref}

$\rho \leq 2$ %	$\rho > 2$ %	n°layer of tensile bars · d_{max}
0.00055	0.00065	≥20
0.0004	0.0005	<20

To conclude, a value of ε_{ref} between 0.0004 and 0.0007 is recommended for RC beams, as function of tensile reinforcement ratio, number of layer of tensile bars and maximum aggregate size. In *Figure 2-37* the load-mid span deflection curves obtained for T4 beam, with the values of ε_{ref} reported in *Table 2-6* and the value of ε_{ref} =0.00043 previously defined, are compared. The range of variability of the ultimate load is found to be 30%. Adopting ε_{ref} =0.00043, the numerical analysis better capture the experimental ultimate load.

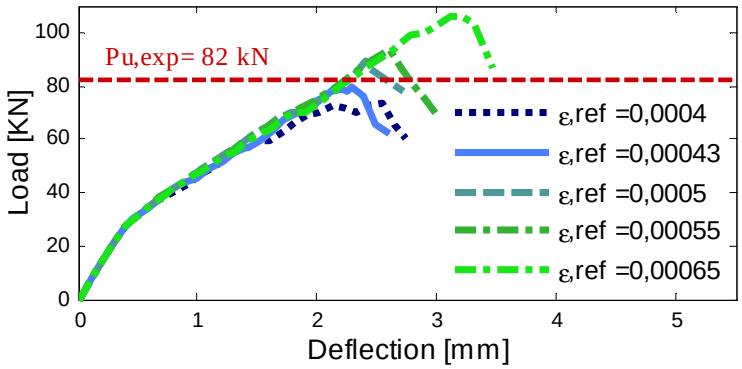

Figure 2-37. Load-midspan deflection curve for different values of ε_{ref}, T4 beam

In *Figure 2-38* a comparison between experimental (*dotted grey lines*) and numerical results (*continuous black lines*) in terms of load-mid span deflection curves for the beams analysed is reported. It is worth noting that the ultimate displacement of the beam and the full load-mid span deflection curves were not always provided by Leonhardt and Walther[158]. In general, the numerical analysis well reproduces the initial stiffness and the ultimate load ($\Delta F_u = F_{u,exp} - F_{u,num}$ is between 0 and 16%). Further, in *Figure 2-39* the experimental and numerical results are compared with the theoretical flexural and shear strengths. The change in failure mode, from shear to flexural with increasing values of *a/d* is very evident.

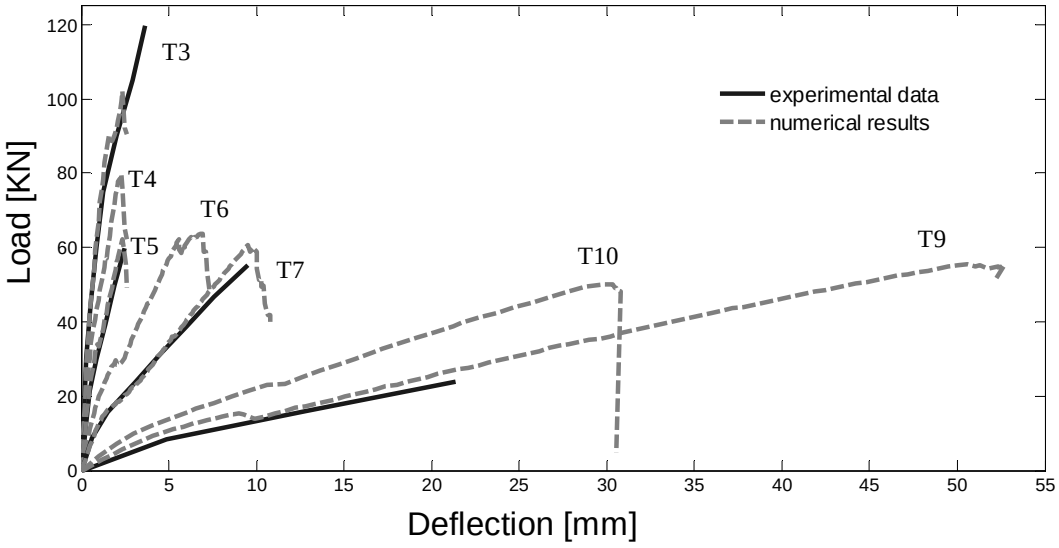

Figure 2-38. Load-mid span deflection curves for T3-T4-T5-T6-T7-T9-T10 beams: comparison between experimental, numerical and theoretical results

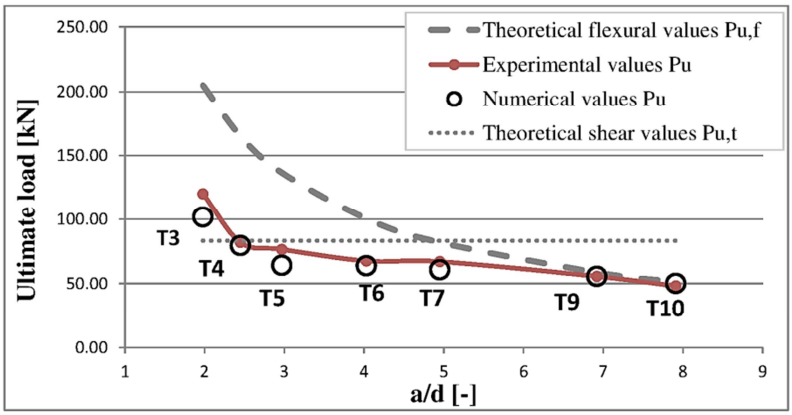

Figure 2-39. Ultimate load versus a/d, for T3-T4-T5-T6-T7-T9-T10 beams: comparison between experimental, numerical and theoretical results

Regarding the failure modes exhibited by the beams analysed, the development of cracks through the inclined compression strut of a beam and their influence on the member's strength depend on the value of shear span-depth ratio *a/d*, see *Figure 2-40*. In this picture, the Kani's valley[141] and position of the beams tested by Leonhardt and Walther[158] inside the Kani's valley are displayed.

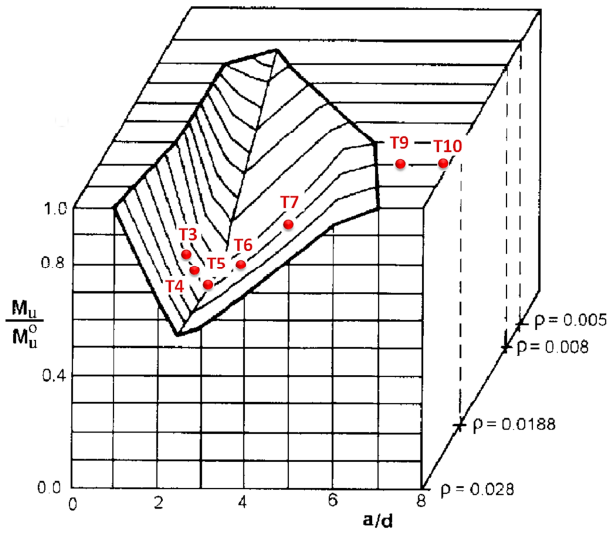

Figure 2-40. Kani's valley and beams tested by Leonhardt and Walther[158]

In specimens characterized by *a/d* lower than 2.0 (T3 beam), the so called "shear compression failure" takes place, *Figure 2-41*. In this kind of failure, shear cracks develop beyond the bending cracks at a quite high load and they proceed slowly over several load increments until the compression zone is destroyed. Although the concrete is destroyed in the zone of pure bending, it must be considered a shear failure because the height of the zone of compression due to bending is decreased much more by the shear crack than by the bending cracks, Leonhardt and Walther[158].

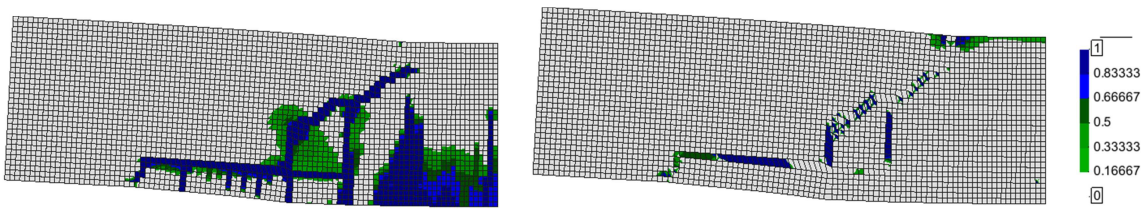

Figure 2-41. Tensile (dp) and compressive (dn) damage contours for T3 beam

Beams with a value of *a/d* between 2 and 7 (T4-T5-T6-T7 beams) are characterized by diagonal tension failure, exhibited also by the beams tested by Bresler and Scordelis[43]. In this case, it is possible to observe the development of important shear cracks, which extends under the load into the zone of pure bending and through the inclined struts, *Figure 2-42*. These shear cracks lead to the beam failure, decreasing the strength of the members. In beams with the greater values of *a/d*, the shear cracks are flatter, e.g. T7 beam, *Figure 2-43*. In *Figure 2-42* and *Figure 2-43* the tensile and the compressive damage contours of T5 and T7 beams are shown: the development of the diagonal crack that leads to the shear failure is evident, while the compressive damage is still at low values. Similar contours were found in the numerical simulation of T4 and T6 beams.

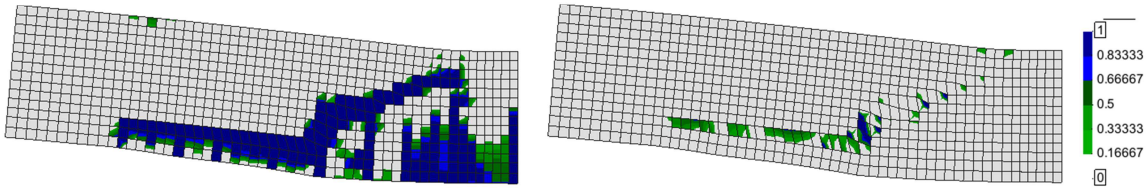

Figure 2-42. Tensile (dp) and compressive (dn) damage contours for T5 beam

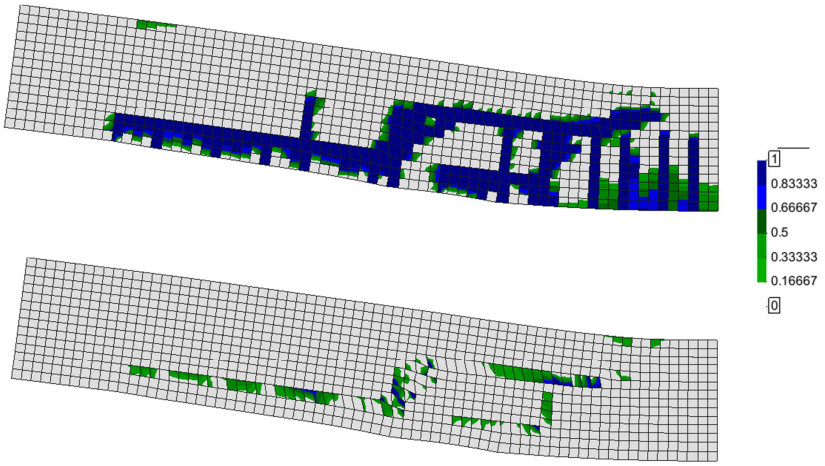

Figure 2-43. Tensile (dp) and compressive (dn) damage contours for T7 beam

Finally, beams characterized by a value of *a/d* greater than 7 exhibited a bending failure, due to the crushing of the concrete before that the tensile bars had achieved the yield strength. In these beams, the flexural strength is reached before that the critical crack can develop. The damage contours found with the numerical analysis for the T9 beam, are reported in *Figure 2-44*. The numerical analysis evidences the occurrence of flexural vertical cracks which develop from the bottom of the beam and the crushing of the concrete in the upper zone of the beam. Similar contours were found in the numerical simulation of T10 beam. The same response was found by Leonhardt and Walther[158] and can be seen in the experimental crack pattern reported in *Figure 2-34*. Finally, in *Figure 2-45* are reported the stresses in the tensile bars at the failure step. It is possible to observe that the yield strength is never reached because the concrete crushes before. Speaking of which, this aspect confirms the approach proposed for the mesh objectivity in compression, and in particular the value of *m.s.f.* found with *Equation 2-30*. Indeed, an over-estimation of the value of *m.s.f.* could lead to the achievement of the yield strength in the tensile bars. On the contrary, lower values of *m.s.f.* could lead to a lower value of ultimate load, in disagreement with the experimental data. A further validation regarding the value of *m.s.f.* calculated with *Equation 2-30*, will be done in chapter 5, comparing the numerical results of

sound RC beams that fail in bending by concrete crushing with the experimental data supplied by Rodriguez et al.[220][221].

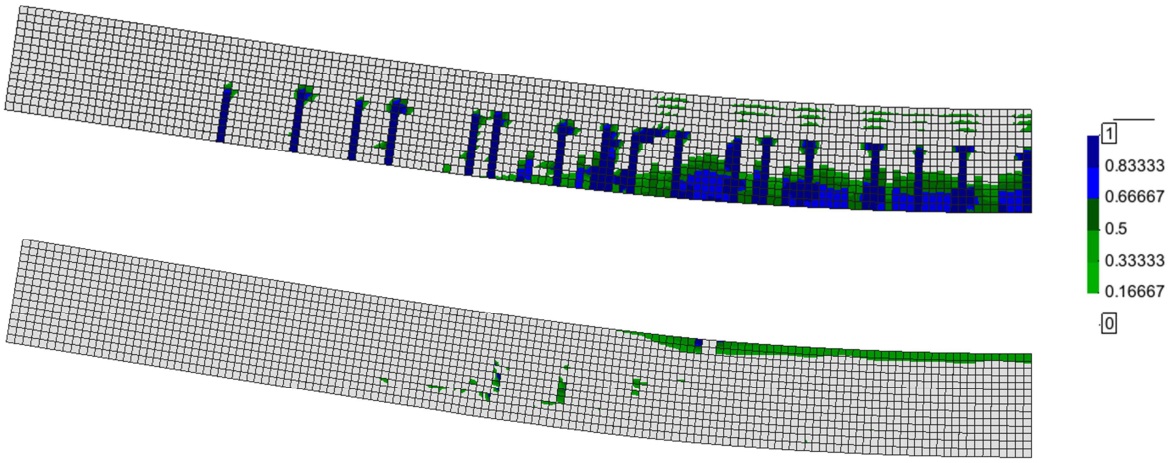

Figure 2-44. Tensile (d+) and compressive (d-) damage contours of T9 beam

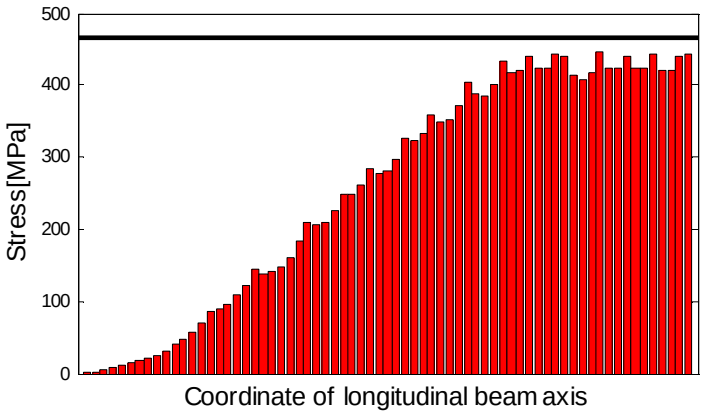

Figure 2-45. Stresses of the tensile reinforcement of the beam T9

CHAPTER 3
REINFORCEMENT CORROSION: RESULTS AND MODELS FROM LITERATURE

3.1. Introduction

One of the most severe causes of deterioration of RC structures is certainly corrosion of steel reinforcement, which may lead to a reduction of their level of safety and in most serious cases to their structural collapse (*Figure 3-1*). In normal conditions, the alkalinity of the concrete allows the reinforcing bars to be protected by a passive film, which prevents the beginning of corrosion, but the interaction with the carbon dioxide in the atmosphere (i.e. carbonation process) or the penetration of chlorides, may create the conditions for the initiation and propagation of the corrosion phenomenon. Indeed, both carbonation and chloride attacks dissolve the passive film that protects the reinforcement and in presence of oxygen and water, steel gets rusty.

The main consequence of corrosion attack is the reduction of the cross-sectional area of the affected reinforcing bars, in a homogeneous way in the case of carbonation attack and in a localized way in the case of chlorides attack. Steel corrosion leads also to a reduction of the mechanical properties of the affected bars, as ductility, yield strength and ultimate strength. Furthermore, the increases in volume of the corrosion products (oxides) may cause cracking of the concrete surrounding the damaged bars and eventually spalling of the concrete cover, which leads to a reduction of concrete section. At last, loss of composite interaction between steel bars and surrounding concrete may take place, due to the weakening of the bar confinement produced by both concrete cracking and area reduction of the transverse reinforcement.

In this chapter, after a brief introduction regarding corrosion mechanisms, a literature review of the local effects of corrosion is proposed. In detail, the consequences of corrosion attack on steel bars, on concrete material and on steel bars-concrete interaction, studied by different authors in the last decades, are summarized. In this way the most important effects that should be simulated in the numerical analyses are underlined and considered for the development of a comprehensive procedure that allow the assessment of corroded RC structures.

Figure 3-1. Partial collapse of the Pipers Row Multi-storey car park in 1997 due to corrosion of steel reinforcement through carbonation, HSE.

3.2. Corrosion phenomenon

In normal conditions the environment of concrete is alkaline, pH around 12-13, thanks to the alkaline solution contained in the pores of the cement paste. At this high pH, a thin oxyhydroxide layer forms on the surface of the reinforcing bars (*Figure 3-2*) and prevents metal atoms from dissolving. This passive film does not actually avoid corrosion but it reduces the corrosion rate to an insignificant level, also in presence of oxygen and moisture (Arup[15], Gouda[115]). Reinforcement corrosion may start after the depassivation of the protective layer. The destruction of the passive layer occurs when the alkalinity of the concrete is reduced due to carbon dioxide or when the chloride concentration in concrete is increased to a certain level. The two attacks act in a completely different ways: respectively in a uniform and in a localized way. In this paragraph, after a short introduction about corrosion phenomena, the two different corrosion mechanisms are examined in detail.

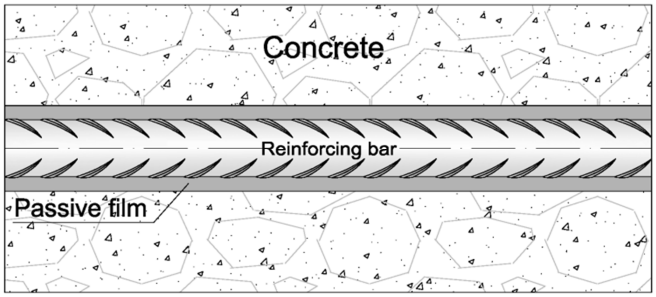

Figure 3-2. Passive film on reinforcement in alkaline concrete

Corrosion is an electrochemical process, which may arise only in presence of both oxygen and water. It is characterized by two reactions, the anodic and the cathodic one. In particular, reinforcement corrosion occurs only when both reactions are possible and therefore when there are the conditions that allow a flux of ions and electrons between the anode and the cathode. Ions are transported through the environment or the electrolyte and they create a flow from the anodic to the cathodic area. Electrons instead migrate via metallic connection, from the cathodic area to the anodic area, in order to complete the circuit (*Figure 3-3*), Bertolini et al.[36], Hunkeler[124].

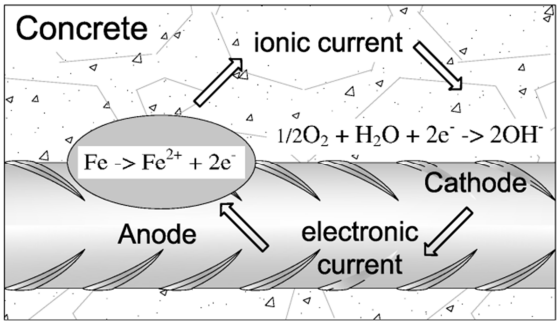

Figure 3-3. The anodic and cathodic reactions

In the anode, metallic iron is oxidized and electrons are generated (depassivation of the steel bar):

$$Fe \rightarrow Fe^{++} + 2e^{-} \qquad \textit{Equation 3-1}$$

The hydrolysis of the iron ions produces acidity:

$$Fe^{++} + 2H_2O \rightarrow Fe(OH)_2 + 2H^{+} \qquad \textit{Equation 3-2}$$

In the cathode, the electrons are consumed to reduce the oxygen into hydroxide ions via the following electrochemical cathodic reaction and so to produce alkalinity:

$$H_2O + {}^1/_2\, O_2 + 2e^- \rightarrow 2(OH)^- \qquad \textit{Equation 3-3}$$

The oxygen is naturally presents in the concrete: due to concrete porosity, O_2 easily enters, diffuses and dissolves in the pore solution, and finally reaches the steel bars. The product of the two equations *Equation 3-1* and *Equation* 3-3 is Ferrous hydroxide, which forms on bar surface:

$$Fe^{++} + 2(OH)^- \rightarrow Fe(OH)_2 \qquad \textit{Equation 3-4}$$

The Ferrous hydroxide is called also whitish rust, and tends to further react in presence of oxygen and water to form Ferric hydroxide:

$$Fe(OH)_2 + H_2O + O_2 \rightarrow 4Fe(OH)_3 \qquad \textit{Equation 3-5}$$

Ferric hydroxide becomes next hydrated ferric oxide, the usual known orange/red-brown rust, Roberge[218] :

$$2Fe(OH)_3 \rightarrow Fe_2O_3 \cdot H_2O + 2H_2O \qquad \textit{Equation 3-6}$$

The un-hydrated Ferric oxide Fe_2O_3 has a volume of about twice as that of the steel that it replaces and may have higher volume up to 10 times when it becomes hydrates, Mietz et al.[182].

It is worth noting that different corrosion processes lead to different types of corrosion damage in reinforcement. Environmental conditions, concrete composition, steel material, geometry of the RC structures, are all parameters that can influence the nature of the corrosive attack. Song et al.[235] proposed the following categories for corrosion types:

- Uniform corrosion: anodic and cathodic areas are very close each other and uniformly distributed along the bar length. This corrosion type may slow down with the time, due to the barrier effect that corrosion products may develop on steel surface.
- Galvanic corrosion: occurs when two or more metals of different nature are coupled, or even of the same nature but with a different internal structure (e.g. heterogeneity of concrete). Here, in some sites the cathodic process is stronger than the anodic process while at other places the anodic reaction is much faster than the cathodic one. The distance between anodic and cathodic areas is significant. It generally plays an important role in large dimensioned concrete structure.
- Localized corrosion is considered as a particular case of galvanic corrosion and it refers to the corrosion damage morphology. In this case the anodic area is smaller than the cathodic one and it has a very high corrosion penetration rate; the cathodic area is bigger and around the anodic zone. Contrariwise of uniform corrosion, localized corrosion is self-catalysis and the barrier effect of corrosion products may lead to an acceleration of the corrosion process with the time.
- External current (e.g. due to electric trams, trains, etc…) leads to corrosion due to the different conductivity of steel and concrete materials. The external current is conducted by steel bars: where the external current flows into the bars through the surrounding concrete, cathodic reactions occurred. The steel acts as an anode and where the current leaves the bars to return to the external environmental, iron dissolution takes place.
- Stress corrosion cracking and hydrogen induced embrittlement are caused by the combination of particular corrosion media and stresses. Their initiation and development are not easy to

recognize but they lead to very brittle and unexpected failure of the reinforcement in concrete. Fortunately they are very rare phenomena that involve mainly the high strength steel.

Uniform and localized corrosion are the most commons in reinforcing steel bars, due to respectively carbonation and chloride attacks; therefore they are considered in the present work.

3.2.1. Carbonation-induced corrosion

With the increasing of industrial areas, the emission of acid gases such as CO_2, SO_x, H_2S and NO_x has grown. High concentration of CO_2 and rainwater with dissolved acid gases lead to degradation of concrete structures. In detail the main cause of neutralization of concrete alkalinity is carbonation but also other acid gases present in the atmosphere, e.g. SO_2, may lead to carbonation. Acid rain has become a relevant phenomenon in areas with high environmental pollution: it is composed of H_2SO_4, HCl and HNO_3 that react with $Ca(OH)_2$ and form $CaSO_4$, $2H_2O$, $Ca(NO_3)_2 \cdot 4H_2O$ and $CaCl_2 \cdot 6H_2O$. Because of the high solubility of these products, they easily penetrate into the inner pores of concrete with the rainwater. After the evaporation of the water, the salts sediment and give rise to stress in the concrete. Concrete carbonation instead is a complex physicochemical process typical of urban and industrial areas or zones near transport activities, where environmental pollution results in a significant concentration of carbon dioxide. CO_2 diffuses inside the concrete and reacts with the solid reactants, mainly $Ca(OH)_2$, forming an acid aqueous solution with the water always present in the pores of the hardened cement paste. The amount of water is crucial for the carbonation process: on one side it provides a medium for reaction between CO_2 and $Ca(OH)_2$, on the other hand it can inhibit the full process. At very low ambient relative humidity levels, CO_2 can diffuse fast but pores are mainly dry, therefore the rate of carbonation is very slow. At high ambient relative humidity levels all the pores are filled with water, therefore diffusion of CO_2 is slowed down (Apostolopoulos et al.[14]). The main reactions of the carbonation process are following reported:

$$CO_2 + H_2O \rightarrow H_2CO_3 \qquad \textit{Equation 3-7}$$

$$Ca(OH)_2 + H_2CO_3 \rightarrow CaCO_3 + 2H_2O \qquad \textit{Equation 3-8}$$

The chemical reaction between carbon dioxide and calcium hydroxide leads to the formation of calcium carbonate $CaCO_3$ and so to a reduction of the pH value in concrete from around 13 to below 9, which is too low for the stability of the oxyhydroxide film. In detail, at the beginning of the process, the reactions are limited to a thin layer of the concrete cover. With the time, the front of carbonation diffuses inward into the concrete until reaching the reinforcing bars. With a low value of pH, the passive film is being dissolved and the dissolved Fe^{++} ions in pore solution tend to move away from the steel surface, *Figure 3-4*. This allows Fe^{++} ions to join with dissolved oxygen in water to produce rust and the process of corrosion of the reinforcing steel commences (*Equation 3-1 - Equation 3-6*). The anodic reaction is the most important process for the damage of reinforcement, indeed with the proceeding of the reaction, the cross section of reinforcement starts decreasing and finally the bar can break.

In the case of carbonated concrete, the cathodic reaction may be in the form of hydrogen evolution, *Figure 3-4*:

$$2H_2O + 2e^- \rightarrow H_2 + 2OH^- \qquad \textit{Equation 3-9}$$

Moreover, in moist environments, the carbonic acid formed may directly attack the steel:

$$H_2CO_3 + Fe \rightarrow FeCO_3 + H_2$$ *Equation 3-10*

It is commonly assumed that carbonation of concrete leads to uniform corrosion in reinforcing bars. Indeed, carbonation phenomena involve in equal way large areas of the structures and so lead to an equal reduction of the concrete pH. Therefore "uniform" is related to the constant distribution of anodic-cathodic processes along the steel bar and the resulting uniform dissolution of steel.

It is worth noting that carbonation does not lead to any damage of the concrete itself, rather to a reduction of its porosity and so to an increase of its strength. Indeed, the oxidation products that formed in the corrosion process, mainly Ferrous and Ferric hydroxide and Hematite, at near neutral pH have a very low solubility so they precipitate in the pores of the concrete microstructure directly adjacent to the reinforcement. Their volume is higher than the original steel material, therefore they generate an expansive pressure on the concrete which may crack. A loss of composite interaction between steel bars and concrete is then likely to occur in the entire bar length, due to the generalized nature of the corrosive attack. In carbonation-induced corrosion, rust can easily reach the external side of the concrete cover and so be detected during inspections.

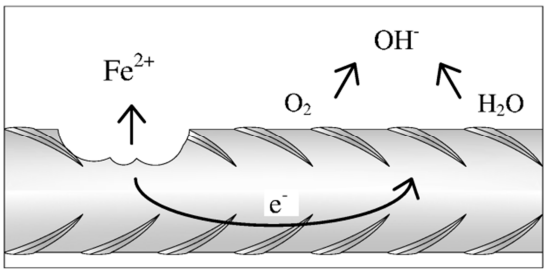

Figure 3-4. Dissolution of the passive film: anodic and cathodic reactions

3.2.2. Chloride-induced corrosion

Chloride ions come from several sources: they can be already cast in concrete, they can penetrate into concrete pores as a result of sea salt spray and direct seawater wetting or they can diffuse into concrete due to the application of chloride de-icing salts. Therefore chloride attack predominates in marine environments, in coastal areas and in pavements or bridge decks, floors of parking garage, etc. When chloride ions penetrate into the concrete cover and reach a critical level at the depth of the reinforcement, the passive layer is locally destroyed, even in alkaline concrete. In presence of moisture and oxygen a rapid anodic dissolution of steel, in a localized way in the areas subjected to the chloride attack, takes place. The cathodic areas (reinforcement surfaces with passive film intact) result protected by the cathodic reaction and the consequent leaving of the chloride, which leads to a strengthening of the passive film, *Figure 3-5*. Due to its localized nature, this attack is known as pitting corrosion. In detail, the anodic reaction inside the pit is the same reported in *Equation 3-1*. The electrons given up by the anode flow to the cathode where they are discharged in the cathodic reaction, *Equation 3-3*. As a result of these reactions the electrolyte enclosed in the pit gains positive electrical charge in contrast to the electrolyte surrounding the pit, which becomes negatively charged. The positively charged pit attracts negative ions of chlorine Cl^- increasing acidity of the electrolyte according to the reaction:

$$FeCl_2 + 2H_2O \rightarrow Fe(OH)_2 + 2HCl$$ *Equation 3-11*

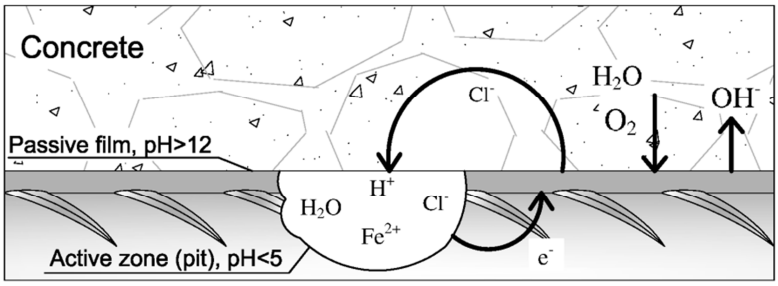

Figure 3-5. Local dissolution of the passive film by chloride ions

The pH of the electrolyte inside the pit decreases from 6 to 2-3, which causes further acceleration of corrosion process. For high levels of chlorides concentration, corrosion attack may be particularly severe and may lead to high damages in the steel bar, because the pitting corrosion becomes an auto-catalytic process. For the pit survival it is necessary that anions other than hydroxide move into the pit in order to maintain the aggressive pit chemistry and avoid repassivation, Pourbaix[206]. The presence of sufficient chlorides with respect to hydroxide is thus not only crucial for pit initiation but also for propagation of localized reinforcement corrosion, Angst et al.[12].

Especially in stainless steel, depending on the quantity of chromium and carbon in the steel composition, chloride ions tend to accumulate inside the pits, the environmental becomes more aggressive and this accelerates the anodic dissolution of steel. Corrosion products ($Fe(OH)_3$) form around the pit resulting in further separation of its electrolyte and often cover the pits surface, see *Figure 3-6*. The mouth of the pits can result open or also covered with a semi-permeable membrane of corrosion products, during that the pit grows in depth.

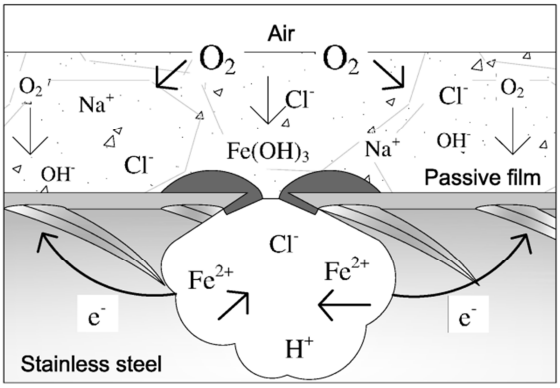

Figure 3-6. Example of pit development in stainless steel

The pit morphology has been studied by different authors. For example, Ribeiro et al.[214] found that pits grow more rapidly in depth than in width, assuming mainly near- hemispherical, -conical or -cylindrical shapes in stainless steel, see *Figure 3-7*. They also found that even if irregular pits are less frequent, are the most dangerous because they are the deepest ones.

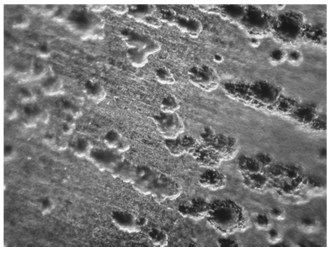

Figure 3-7. Pitting corrosion on stainless steel (x500 magnification), Haukka et al.[120]

Du et al.[93], doing a visual inspection of artificial corroded reinforcement, observed that pits may develop in different ways on the bar surface: some just increase in number and expand in size, while some others join up with each other creating an apparent uniform corrosion. Apostolopolous et al.[13] proved this, capturing stereoscopical images using a x35 magnification lens, see *Figure 3-8*. Furthermore, three-dimensional surface plots were derived by the authors in order to get a visual representation of the pit size, *Figure 3-9*. From these pictures it is possible to observe how the pits can grow up in different shapes, leading to different residual cross sections in a corroded bar. Also the ASTM G46 and the ASTM G15 standard guides recognise and classify different morphologies for the characterization of pitting corrosion, *Figure 3-10*.

Figure 3-8. Stereoscopic images (35x) of reinforcing bar: evolution of pitting corrosion, Apostolopoulos et al.[14]

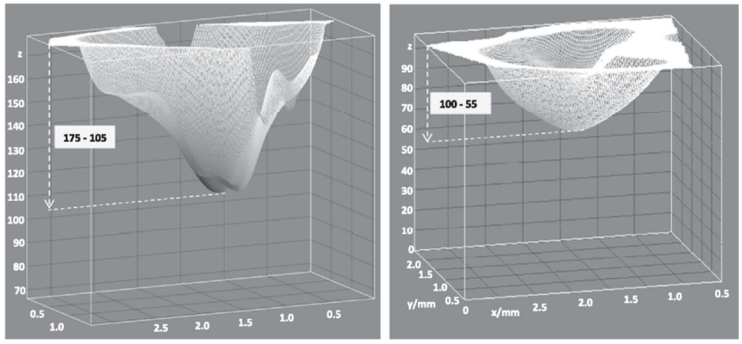

Figure 3-9. 3D surface plots of a pit in a) embedded bar and b) bare bar, Apostolopoulos et al.[13]

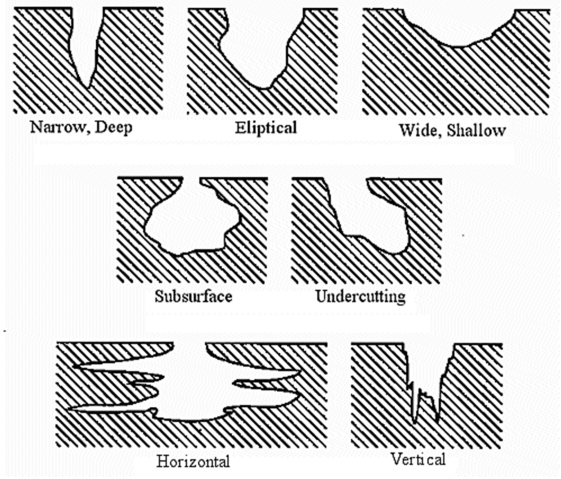

Figure 3-10. ASTM G46 – Variations in cross sectional shape of pits.

In *Figure 3-11* are shown some reinforcing bars affected by pitting corrosion. In particular, it is possible to notice that, for low levels of corrosion attack, pits develop mainly with a circumferential cross section shape *a)* and *d)*. For high levels of corrosion attacks, pits develop in different ways, involving all the cross section, etc. *g), h), l)* or big parts of the steel bar in a not homogenous way: *f), i), m).*

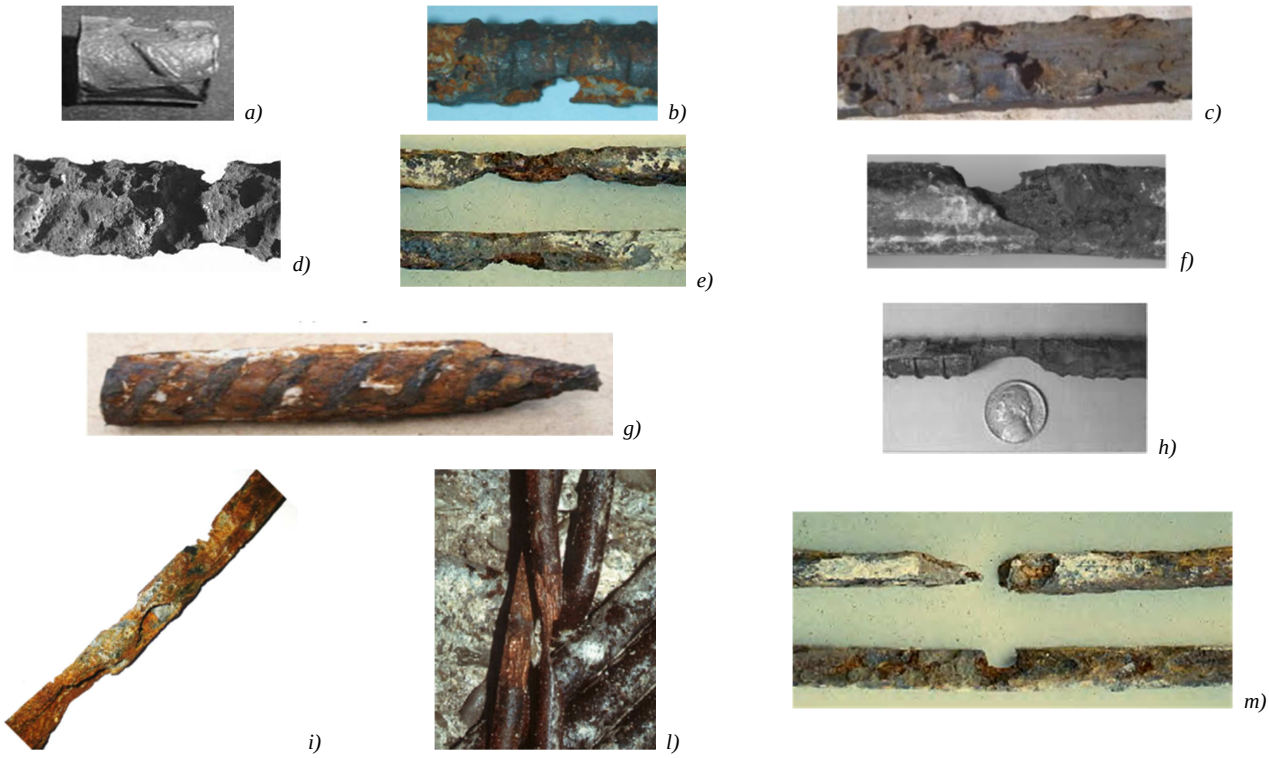

Figure 3-11. Various shapes of pitting corrosion on reinforcing bars

The residual cross sections in a corroded bar vary significantly also along its length and they are extremely irregular. This was proved by the measurement made by Tang et al.[241], that evaluated the residual cross section areas and the complete surface morphology of artificial corroded reinforcement with a 3D laser scanner, see *Figure 3-12.*

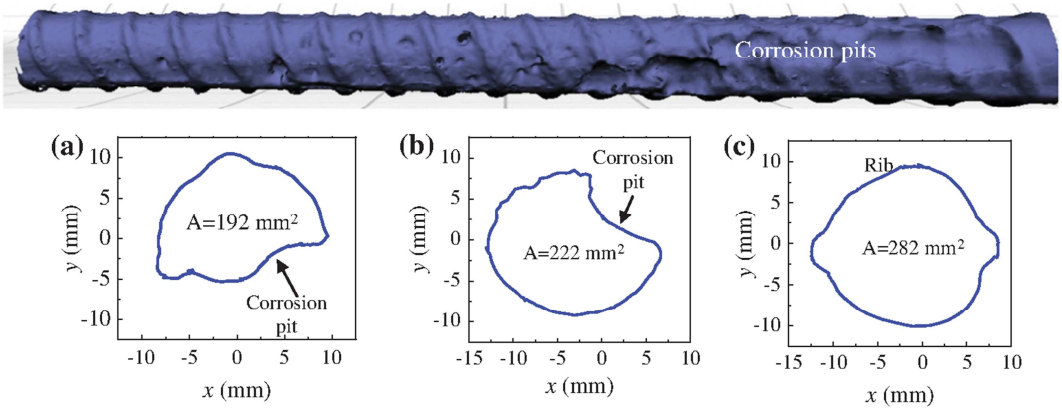

Figure 3-12. 3D images and cross sections of corroded bars at different locations, Tang et al.[241]

Chloride penetration is a process which takes place in totally or partly water-filled pores. For this reason, the process is much slower than carbonation, where CO_2 molecule may penetrate faster via air-filled pores. However it is more dangerous because it leads to a greater reduction of the cross-sectional area of the rebars and it is more difficult to detect. Experience from several practical cases has indeed demonstrated that significant, localized steel cross section loss may take place without giving any visual evidence on the surface of the concrete member, Angst et al.[12]. The authors gave also a theoretical explanation of the phenomenon, based on the very complex situation that characterized the zone around the pits. Briefly, a high alkalinity of the concrete and the presence of chlorides, allow a relatively high solubility of iron ions. The authors distinguished

three zones: the zone inside the pit, with low pH and considerable amount of chloride ions; the zone immediately outside the pit, with high pH and high amount of chloride ions; the zone external to the pit, with high pH, where instead the iron ions might meet hydroxide and precipitate in the form of solid corrosion products, if the chloride concentrations is low. Basing on these considerations, the most likely location for the precipitation of corrosion products results to be the internal part of a concrete structure, where the chloride content is negligible, rather than the cover zone. Furthermore, in order to produce a sufficient expansion stress level for concrete cracking, the iron dissolution required in chloride-induced corrosion is greater than in a uniform corrosion process, due to the localized nature of the attack. It was found that in carbonated concrete, 0.5 mm of cross-sectional loss can already lead to concrete cover cracking and spalling; instead for chloride-contaminated concrete, several millimetres of cross section loss in bars are required before concrete cover may crack, Hunkeler et al.[125]. Other factors may influence of course concrete cracking, as the porosity of the concrete material, the moisture content inside the concrete, the corrosion rate, geometric factors and mechanical properties of the concrete material, that have to be always taken into consideration.

For localized corrosion, many authors (e.g. Val et al.[256]) have proposed to do not take into account of the bond strength reduction around the corroded rebar, due to the lower amount of rust produced in this kind of corrosive attack.

3.3. Effects of corrosion on steel reinforcement

3.3.1. Reduction of cross-sectional area

In carbonation-induced corrosion, reinforcing bars mostly show uniform corrosion penetrations at the whole surface of the metal (*Figure 3-13*). For this reason this type of corrosive attack is called uniform or general corrosion and the corrosion rate can be expressed as mean loss of metal per unit over time, or units of mm per year.

From the relationship between corrosion current and weight losses by the steel, it is possible to estimate the corrosion rate of reinforcement. In particular, basing on the Faraday's law, a corrosion current density i_{corr} equal to 1 μA/cm^2 corresponds to a steel section loss of 11.6 μm/yr. As proposed by Thoft-Christensen et al.[247] for the estimation of the residual diameter of a corroded bar Φ', the following equation may be assumed, based on the Faraday's law and for a constant corrosion rate:

$$\emptyset'(T) = \Phi - 0.0232(T - T_i)i_{corr} \qquad \textit{Equation 3-12}$$

where Φ is the initial diameter of rebar [mm], T_i is the time of corrosion initiation [yr] and i_{corr} the corrosion current density [μA/cm^2]. If an average value of the corrosion penetration x [mm] is instead known (e.g. derived from gravimetric methods, *Figure 3-13*) at a specific time, it is possible to evaluate the residual cross-sectional area A'_s [mm^2] of each corroded bar, as proposed in e.g. Biondini et al.[40], Finozzi et al.[109]:

$$A'_s = \frac{\pi(\Phi - 2x)^2}{4} \qquad \textit{Equation 3-13}$$

Uniform corrosion is characterized by lower values of penetration attack than pitting corrosion, but by a higher amount of weight loss by the rebars, because the corrosion process involves the

full length of the reinforcement, see *Figure 3-13.* For this reason, the models available in literature assume a constant residual cross section for the full length of the corroded bar.

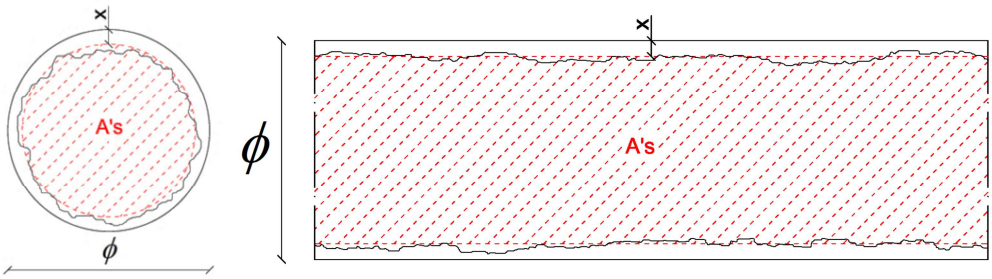

Figure 3-13. Cross and longitudinal section: real situation and modelling of uniform corrosion

In the case of chloride-induced corrosion, as result of the localized nature of the attack, corrosion tends to proceed in very specific forms, known as "pits", which are holes in the steel surface. For this reason, it is denominated localized or pitting corrosion. Pitting corrosion is a particularly severe kind of corrosion, because in spite of a small weight loss, there is a significant reduction in cross section size. Once defined the pitting ratio *R* as the ratio between the maximum pit depth *p* and the uniform corrosion penetration *x*, some authors have tried to define possible ranges for the value of *R* parameter. Gonzales et al.[114] found for example that *R* in a natural environment is between 4 and 8; in accelerated corrosion tests, *R* ranges between 5 and 13.

For the evaluation of the residual cross-sectional area of steel bars in the case of pitting corrosion, the most known model is the one proposed by Val et al.[256]. The authors proposed to consider a hemispherical form for the pits (*Figure 3-14)*, for sake of simplicity and to estimate the radius of the pit *p* [mm], at time *T*, as:

$$p(T) = 0.0116(T - T_i)i_{corr}R \qquad \textit{Equation 3-14}$$

where the value of *R* is suggested between 4 and 8. With this approach, for an equal average corrosion rate, pitting corrosion leads to a penetration attack between 4 and 8 times the uniform attack penetration.

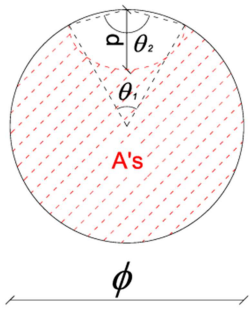

Figure 3-14. Val's et al. [256] model

The residual area of the steel bar at the time *T*, can be estimated by the following equations:

$$A'_s(T) = \begin{cases} \dfrac{\pi\Phi^2}{4} - A_1 - A_2 & p(T) \le \dfrac{\sqrt{2}}{2}\Phi \\ A_1 - A_2 & \dfrac{\sqrt{2}}{2}\Phi < p(T) \le \Phi \\ 0 & p(T) > \Phi \end{cases} \qquad \textit{Equation 3-15}$$

where:

$$A_1 = \frac{1}{2}\left[\theta_1\left(\frac{\Phi}{2}\right)^2 - a\left|\frac{\Phi}{2} - \frac{p(T)^2}{\Phi}\right|\right]$$
$$A_2 = \frac{1}{2}\left[\theta_2 p(T)^2 - a\frac{p(T)^2}{\Phi}\right]$$
$$a = 2p(T)\sqrt{1 - \left[\frac{p(T)}{\Phi}\right]^2}$$
$$\theta_1 = 2arcsin\left(\frac{a}{\Phi}\right)$$
$$\theta_2 = 2arcsin\left(\frac{a}{2p(T)}\right)$$

Equation 3-16

Val's et al.[256] model well simulates a real pitting corrosion attack for low levels of corrosion and in stainless reinforcement because the pits assume mainly a circular shape. This remark is verified by the tests made by Cairns et al.[54]. A series of steel bars of 16 mm diameter were casted in concrete, conditioned under a cyclic wetting/drying regime and subjected to an accelerated corrosion through an impressed current density between 0.01 and 0.05 mA/cm^2. The corrosive attack was of a low intensity (mean section loss of up to 4%) and characterized by a mixture of general and pitting corrosion. The authors measured the dimensions of the largest pits with a graduated magnifier and a micrometer. They found a maximum section loss of around 8%, at a singular pit and that the breadth of pits was approximately twice the depth, confirming the assumption of circular shape of pits in cross section. The hemispherical shape proposed by Val et al.[256] for the pits, however is only one of the possible shapes that the pits may have, as seen in paragraph 3.2.2. In some of these cases, the pits assume forms far away from a hemispherical one and the residual cross sectional area may be under or upper estimated with this model.

The residual cross-sectional area in the case of pitting corrosion may be evaluated also with the model proposed by Rodriguez et al.[221] (*Figure 3-15*):

$$A'_s = \frac{\pi(\Phi - \alpha \cdot x)^2}{4}$$

Equation 3-17

Where the bar attack penetration *x* can be estimated with the Faraday's law considering an average value of the corrosion rate and the coefficient α is the pitting ratio *R* previously defined. It should be noticed that *Equation 3-17* corresponds to *Equation 3-13* if α is equal to 2, general corrosion. The authors specified that the proposal model estimates a conservative value of the residual cross section at pits.

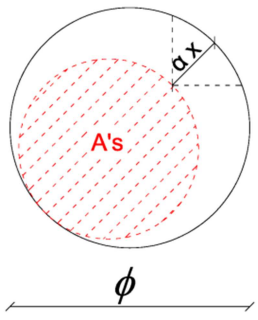

Figure 3-15. Rodriguez' et al.[221] model

The Rodriguez' et al.[221] proposal has been assumed by a number of authors for safety reasons, e.g. Saether et al.[223] and Khan et al.[145]. Other authors have instead pointed out that the Rodriguez' et al.[221] model overestimates too much the corroded area and they have adopted the same model for the assessment of the residual cross-sectional area in the case of concomitance between uniform and pitting corrosion, e.g. Biondini et al.[40] and Finozzi et al.[109]. This mixed corrosion type is quite common in all the experimental specimens subjected to an accelerated corrosion procedure. However, the coexistence of carbonation and chloride penetration in concrete is less common in practice and, in any case, one of these two attacks is predominant, Sirivivatnanon et al.[234], Zhang et al. Finally, a different approach was proposed by Coronelli et al.[80], who assumed no reduction of steel area, considering a sort of balance between the strength loss due to steel area reduction and the strength increase due to hardening of the undamaged steel in the pit section.

Regarding the spatial distribution of pits in corroded bars, the most common approach is to consider pit forms only at the location of maximum action or other critical sections. Only recently, some studies have been done in order to assess the spatial variability of pitting corrosion with probabilistic models, because reinforcement corrosion is essentially a stochastic process. For example, Stewart[237] proposed to characterize the pitting ratio R by a Gumbel distribution, basing on the results of some literature experimental tests. Then the stochastic model of pitting corrosion was applied to a simply supported RC office floor beam, in order to predict the maximum pit depth as function of bar diameter and length. It was found that the probability of failure increases of about 70% considering spatial variability of pitting corrosion. In Stewart et al.[238], the model was improved to incorporate the spatial variability of pitting corrosion in a time-dependent structural reliability analysis, for RC beams in flexure. More experimental data to improve the extreme value statistic for pitting and the corrosion effect on the mechanical properties of steel were considered. It was found that the maximum corrosion loss in a reinforcing bar conditional on beam collapse was no more than 16%. The probabilities of failure considering spatial variability of pitting corrosion were up to 200% higher than probabilities of failure obtained from a non-spatial analysis after 50 years of corrosion. These results however must be taken with caution, because the model bases on few accelerated corrosion tests made with very high corrosion rate, instead more tests are necessary, especially for a right evaluation of the Gumbel statistical parameters.

3.3.2. Deterioration of the mechanical properties of reinforcing bars

Over the last few years many researchers have studied the effects of corrosion on the residual mechanical properties of reinforcing bars. For a better understanding of corrosion effects, the two different kinds of corrosion types, uniform and localized, must be distinguished. In the case of uniform corrosion, researchers (e.g. Cairns et al.[54], Du et al.[93]) agree that the mechanical properties of reinforcing bars do not change and only the reduction of the cross-sectional area must be considered. Regarding pitting corrosion, the structural implications on reinforcement bars are more complex to define, due to the localized and asymmetric nature of this attack.

A review of the studies carried out in the last year is following made, for a better understanding of the effects of pitting corrosion on the residual mechanical properties of steel bars. Two mechanical parameters must first be defined: the nominal strength (yield or ultimate), calculated referring to the nominal cross-sectional area of the sound bar and the effective strength (yield or ultimate), calculated with respect to the residual cross-sectional area of the corroded bar.

Rodriguez et al.[220] (1996) proposed a simple equation for the evaluation of the critical buckling strength of corroded longitudinal bars in RC columns. Indeed, the authors observed that at the end of compressive axial tests made on RC columns, many longitudinal bars presented buckling, where the stirrups failed due to corrosion. They proposed to adopt the classical Euler's equation to calculate the buckling strength, with *s* the space between two consecutive stirrups intact and *Φ'* the residual bar diameter; for the estimation of the slenderness ratio they proposed to adopt a value of 0.75:

$$\sigma_{crit} = \frac{\pi^2 \cdot E_s \cdot (0.25\Phi')^2}{(0.75\ s)^2} \qquad \textit{Equation 3-18}$$

If this value results lower than the yield strength, the critical buckling strength should be calculated as:

$$\sigma_{crit} = k \cdot \sigma_y \qquad \textit{Equation 3-19}$$

where *k*=0.5, 0.2 or 0, depending if one, two or more consecutive stirrups fail.

Almusallam et al.[7] (2001) conducted tensile tests on corroded reinforcing steel bars in order to find a relationship between the degree of corrosion and their mechanical properties. Ribbed steel bars of 6 and 12 mm diameter were considered, embedded in concrete specimens and corroded with an accelerated technique by impressing an anodic current of 2 mA/cm^2 for different periods. After the desired level of corrosion was obtained, the steel bars were extracted and tested in tension. The degree of corrosion was measured as gravimetric loss in weight of the bars. The results obtained for the 6 mm diameter bars indicate that the load carried decreases with increasing levels of corrosion, as evidenced by *Figure 3-16*.

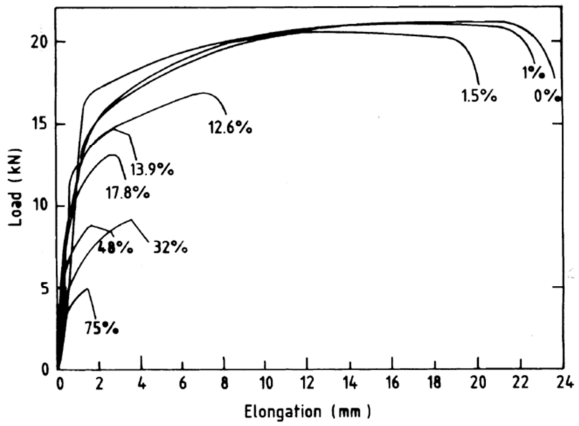

Figure 3-16. Load versus elongation curves for 6 mm diameter bars, Almusallam et al. [7].

In the same way, the nominal tensile strength of the bars was found to be much lower for corroded bars than for uncorroded bars, *Figure 3-17 a) -red curve*. Due to the decrease in cross-sectional area, the effective tensile strength was instead marginally affected by corrosion, *Figure 3-17 a) - blue curve*. Analogous results were found for the 12 mm diameter bars, see *Figure 3-17 b)*, demonstrating that the influence of different degrees of corrosion on the bar tensile strength is insignificant, when the residual cross-sectional area is considered. The authors observed that corrosion greatly affects the ductility of the steel bars: their elongation before failure was found to be lower for higher levels of corrosion and the bars failed with decreasing amounts of yield strain (*Figure 3-16*). This indicates that corrosion increases their brittleness: for corrosion levels greater than 12.6%, the bars abruptly fractured with very little elongation. Indeed, when a locally thinned

section of a steel bar is stretched by a tensile force, the strains are concentrated at the notch and the overall strain of the bar will be lower at failure than in an uncorroded bar. Hence, as the notch becomes deeper, the stress concentration here progressively increases and the bar may fail without yielding.

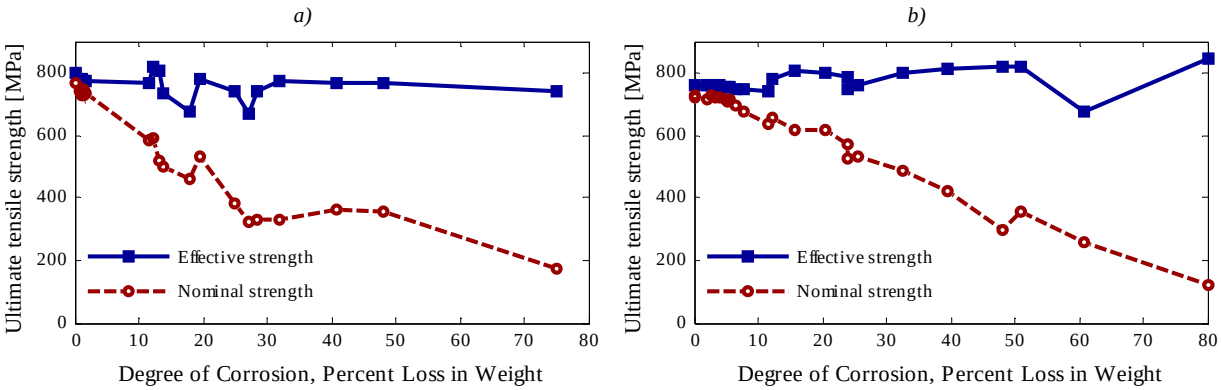

Figure 3-17. Tensile strength versus degree of corrosion: a) 6 mm diameter bar; b) 12 mm diameter bar, based on the data of Almusallam et al.[7].

Palsson et al.[198] (2002) carried out tensile tests on reinforcing bars extracted from an abandoned, deteriorated bridge in Montreal, Canada in order to study how the mechanical properties of real bars are affected by natural corrosion. The condition of the bars taken from the bridge varied greatly: few bars were found uncorroded, others presented uniform corrosion and some were pitted. Indeed, a high content of chloride-ions was detected in the concrete due to the frequent use of de-icing salt. The reinforcing bars were inspected in order to establish maximum, minimum and average losses of cross-sectional area. During the tensile tests, cross-head displacement and elongation were recorded. The yield and the ultimate tensile strengths calculated on the smallest cross-sectional area of the unloaded specimens were found to be similar for all the specimens. Instead, the ductility of the reinforcing bars was found to be dramatically decreased for increasing levels of corrosion. This is shown in *Figure 3-18 a)*, where the ultimate strains are plotted versus the percentage of area loss by the bars. In *Figure 3-18 b)* the ultimate strains are instead plotted versus the ratio between minimum and maximum cross-sectional areas. The authors demonstrated that a non-uniform distribution of cross sections along the bar length leads to lower values of the ultimate strains.

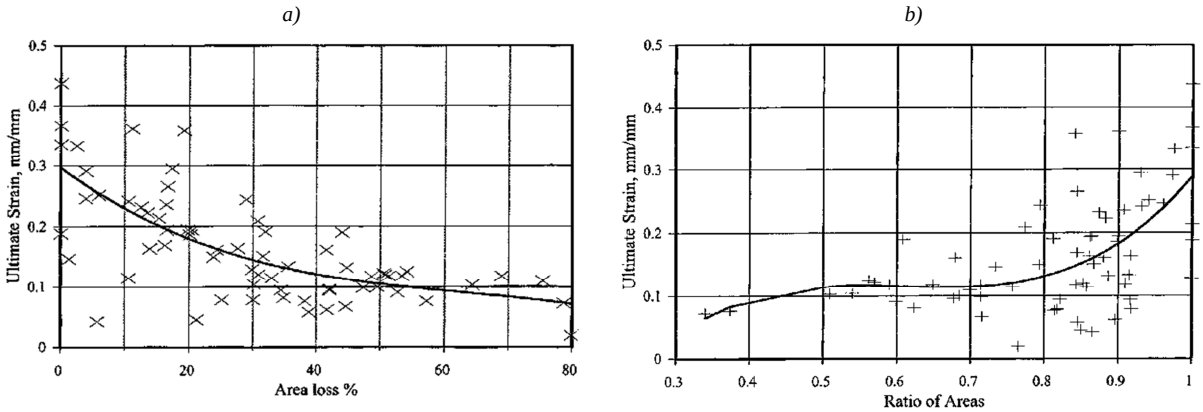

Figure 3-18. a) Ultimate strain (gage length of 25 mm) with loss in average cross-sectional area; b) Ultimate strain with ratio of minimum and maximum cross-sectional area; Palsson et al.[198].

Coronelli et al.[80] (2004) proposed a model to predict the residual ductility of corroded bars when the maximum loss of cross section is known. Also in their opinion, the most important aspect that should be considered for corroded bars is the reduction of the ductility in the case of pitting corrosion due to the notch effect. Indeed, the bar likely breaks in the short length where the local damage is located, due to the localisation of high strains, while the average strain over the length of the bar is smaller than the local strains at the pit. Basing on the experimental results of Cairns et al.[53] and Castel et al.[59], a linear reduction of the average ductility of the bars with the percent of reduction of the bar cross section was proposed:

$$\varepsilon'_{su} = \varepsilon_{sy} + (\varepsilon_{su} - \varepsilon_{sy})\left(1 - \frac{\alpha_{pit}}{\alpha_{pit}^{max}}\right) \qquad for\ \alpha_{pit} < \alpha_{pit}^{max} \qquad Equation\ 3\text{-}20$$

Where α_{pit} is the ratio between the reduction of cross-sectional area due to pitting and the sound area. The ultimate strain of the corroded bars ε'_{su} may assume values between the ultimate strain ε_{su} and the yield strain ε_{sy} of the sound bar. The value of α_{pit}^{max} parameter, which corresponds to a complete loss of bar ductility, was experimental found to be between 0.1 and 0.5.

Cairns et al.[54] (2005) experimentally studied the effects of corrosion on the mechanical properties of steel bars. Firstly, they reproduced the local damage of pitting corrosion by partially removing a section of bar using a multifluted, hemispherical and mill with a cylindrical shank on 12, 16, 20, 24 mm diameter deformed B500B bars (*Figure 3-19*). Sound and damaged steel bars were then subjected to tensile testing and load and displacement data recorded, *Figure 3-20*. The authors found a reduction of the maximum load proportional to the damaged area and a reduction of the force at yield slightly less-than-proportional to the section loss. The main effect of the local damage was found to be the reduction in the bar ductility (up to 80%).

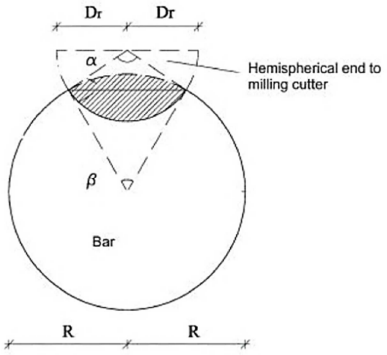

Figure 3-19. Schematic of machined defect geometry, Cairns et al. [54].

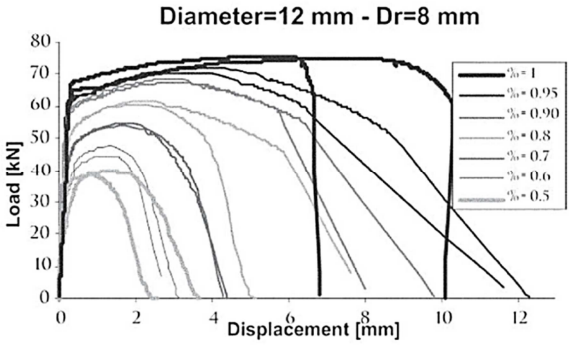

Figure 3-20. Load vs elongation from tensile tests made on 12 mm diameter bars, Cairns et al. [54].

In order to investigate bars subjected to both uniform and localized corrosion, a second series of tests was conducted, in which corrosion was accelerated by means of anodic polarization. In detail, 16 mm plain round bars (HW specimens) were tested and the results are reported in *Figure 3-21*. In order to obtain the maximum section loss, the authors examined the bars in detail and measured the largest reduction of cross section with a graduated magnifier and micrometer. *Figure 3-21 a)* shows that no loss in yield strength took place, while the ultimate tensile strength (UTS) slightly increases with increasing section loss. The authors specified that if the effective strength is plotted against the mean loss section, the change in peak strength with corrosion results not significant, confirming the remarks of Almusallam et al.[7]. In *Figure 3-21 b)* ultimate strains are plotted versus the maximum section loss, confirming the strong reduction of the bar ductility due to corrosion.

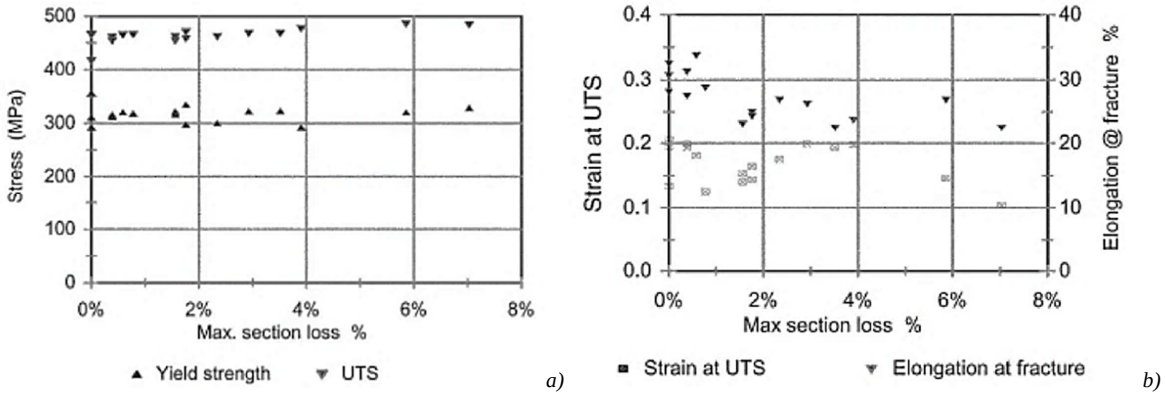

Figure 3-21. a) Effective tensile strength vs maximum section loss %; b) Strain and elongation at the ultimate tensile strength vs maximum section loss %, Cairns et al.[54].

Du et al.[94] (2005) made an experimental investigation into the residual properties of corroded reinforcing bars by performing accelerated corrosion tests and considering the influence of bar type, diameter and specimen type (bare bar or bar embedded in concrete). In detail, currents of 0.5, 1.0 and 2.0 mA/cm^2 were impressed onto 8, 16 and 32 mm diameter bars for different durations. The percentage of weight loss due to corrosion and the residual cross sections were measured. Uniaxial tension tests were performed and the results reported in terms of force-elongation curves. Regarding the residual effective yield and ultimate strengths calculated respect to the average residual cross-sectional area, the authors found a slightly reduction of values with increasing mass loss by the bars, see *Figure 3-22 R-T bars*. Similar results were found also for the corroded bars embedded in concrete, *Figure 3-22 RC-TC bars.* The results found were in contrast with remarks made by Almusallam et al.[7] and Cairns et al.[54]. The authors explained this dissimilarity as result of the different experimental measurement techniques adopted. If an electrical extensometer is used, the local tensile deformation is captured. If the testing machine is adopted, the tensile deformation along the reinforcement is obtained and the local strains become less relevant.

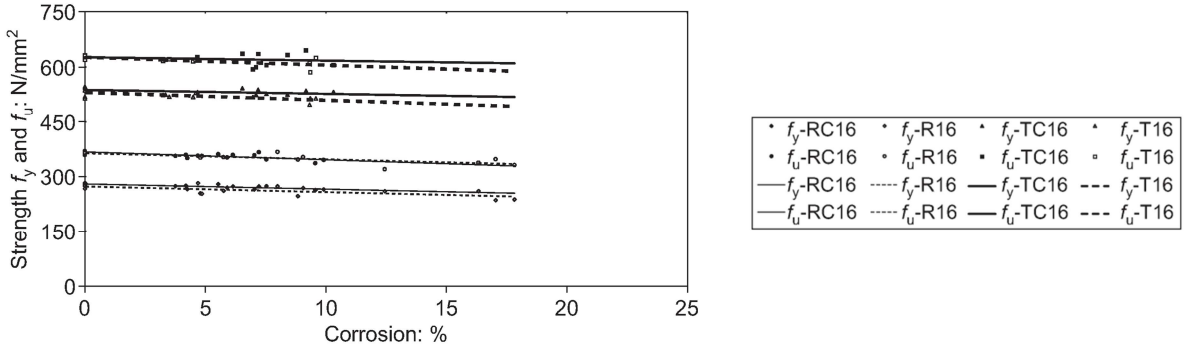

Figure 3-22. Residual strength of corroded bare and embedded in concrete bars, Du et al. [94]

The ultimate strain of bare reinforcing bars was found strongly influenced by corrosion, especially for bars embedded in concrete (*Figure 3-23)* due to more irregular residual sections induced. Furthermore, the authors made some tests on bars of different type and bar diameter, demonstrating that the residual capacity of smaller diameter and plain reinforcement decreases faster, but the differences in values are negligible.

The authors proposed also equations for the prediction of the effective residual properties of corroded reinforcement as function of the average section loss [%], based on regression analyses:

$$f'_y = (1 - \alpha_y \cdot X) f_y \qquad \textit{Equation 3-21}$$

$$f'_u = (1 - \alpha_u \cdot X) f_u \qquad \textit{Equation 3-22}$$

$$\varepsilon'_{su} = (1 - \alpha_{su} \cdot X) \varepsilon_{su} \qquad \textit{Equation 3-23}$$

where f'_y, f'_u, ε'_{su} and f_y, f_u, ε_{su} are yield and tensile effective strengths and ultimate strains of corroded and sound bars; X is the average section loss[%]; α_y, α_u, α_{su} are empirical coefficients: α_y, α_u, α_{su} suggested equal to 0.0012, 0.0015 and 0.029 (bare bars) or 0.044 (embedded bars).

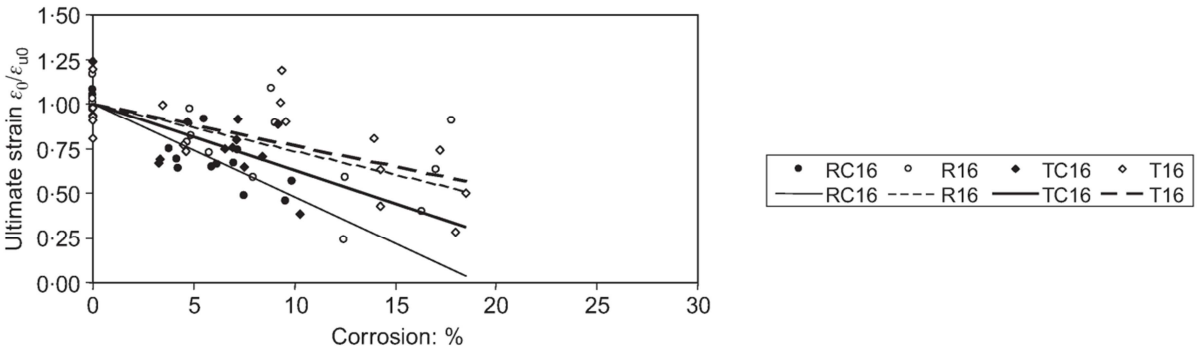

Figure 3-23. Effect of corrosion on ultimate strain ratio of bars in concrete

Kobayashi[146] (2006) made an experimental campaign to evaluate quantitatively the effect of chloride-induced corrosion on the mechanical properties of RC beams. Some specimens were sprayed with sodium chloride solution for different periods, in order to simulate a marine environment, while in others chloride ions were added on the concrete to accelerate corrosion. The longitudinal reinforcing bars of 10 mm diameter, were extracted from the beams, weighted in order to find the average mass loss due to corrosion and finally subjected to tensile tests. The relationship between the mechanical properties of the bars and the mass loss due to corrosion X (%) is reported in *Equation 3-24* and *Figure 3-24*. The results confirm the linear dependency of yield and tensile strength of the corroded bar to the mass loss and the more severity consequence of corrosion on the ductility of the bars. The authors proposed a linear relationship also for the elongation-mass loss correlation, confirming the approach of Du et al.[94]:

$$F'/F\ (\%) = 100 - \alpha \cdot X \qquad \textit{Equation 3-24}$$

where F' and F are respectively the degraded and the virgin properties of reinforcing bars: yield tensile strength f_y, ultimate tensile strength f_u and ultimate elongation e; and α are experimental constants that depend on the property considered, respectively: α_y=4.84, α_u=4.09, α_e=18.1. It should be noticed that the maximum mass loss found was of 3.27%, which is a very low value.

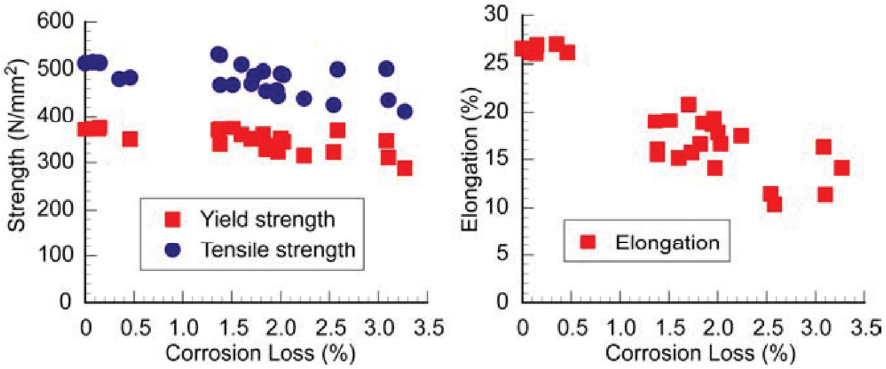

Figure 3-24. a)Yield and tensile strength vs mass loss (%); b)Elongation (%) vs mass loss (%), Kobayashi [146]

Apostolopoulos et al.[14] (2008) made tensile tests on both artificially and natural corroded bars. Regarding the first, ribbed bars of 10 mm diameter were corroded using laboratory salt spray tests for several exposure times. Also if an extensive pitting corrosion was detected in all the specimens, the authors assumed a uniform production of the oxide layer around the bar, in order to calculate an equivalent reduction of the bar diameter related to the mass loss. In this way, the results in terms of yield and ultimate stress could be plotted against the mean value of area loss, *Figure 3-25 a)*. The effective yield and ultimate strengths were found moderately influenced by the corrosion level, while the nominal yield and ultimate strengths were observed more sensible to the percentage of mass loss by the bars, confirming the remarks of Almusallam et al.[7]. A significant loss of ductility, expressed as elongation to failure, was observed with increasing damage levels, *Figure 3-26 –green dots.* The authors then compared these results with the results obtained carrying out tensile tests on natural corroded reinforcement of the same type of the previous bars. Specimens from a house located in a coastal area (chloride environment) and specimens from an industrial building (exposed mostly in carbonating and high humidity environment) were extracted. The mass loss was calculated as percentage of weight loss. The results reported in *Figure 3-25 b)* show that the nominal strengths moderately decrease with corrosion increment as in the artificial test, while in *Figure 3-26 –blue and red dots* the elongation of the bars was found dependent on the mass loss mainly in the industrial building. The authors also observed that in both natural and artificial corroded bars yield and ultimate stress reduction were proportional to the corresponding mass loss.

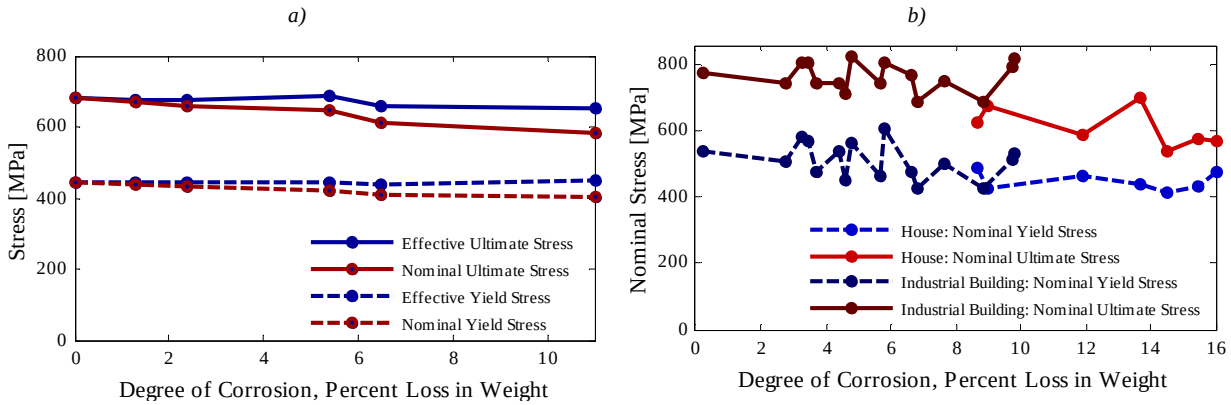

Figure 3-25. Effect of corrosion on yield and tensile strength of a) artificial corroded bars; b) natural corroded bars, based on the data of Apostolopoulos et al.[14]

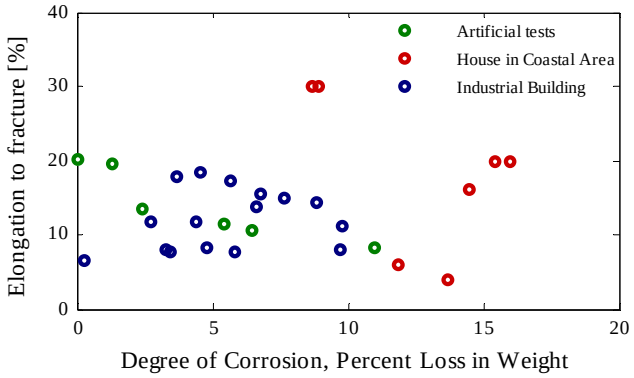

Figure 3-26. Elongation to fracture of corroded bars, data of Apostolopoulos et al.[14].

Lee et al.[152] (2009) made two experimental campaigns of tensile tests for the evaluation of the mechanical properties of corroded bars. In the first one, a quite uniform corrosion was induced in the bars embedded in concrete (Φ=13 mm) with an electrical method. In the second one, the RC

specimens were subjected to wetting-drying cycles at high temperature in chloride environment in order to reproduce pitting corrosion in bars of 13 and 10 mm diameter. The amount of corrosion was expressed as percentage of weight loss by the bars. The authors found for bars with pitting corrosion lower values of the residual mechanical properties, confirming the importance of the maximum section loss. Equations for the evaluation of the residual mechanical properties as function of the percentage of mass loss were also proposed, of the same kind of *Equation 3-24*. In this case, *F'* and *F* are respectively the degraded and the virgin following properties of reinforcing bars: yield tensile strength f_y, ultimate tensile strength f_u elastic modulus E_s and ultimate elongation *e*; α are experimental constants that depend on the property considered, respectively: α_y , α_u , α_E , α_e . The values found by the authors are reported in *Figure 3-27*. The residual yield and tensile strength are nominal values.

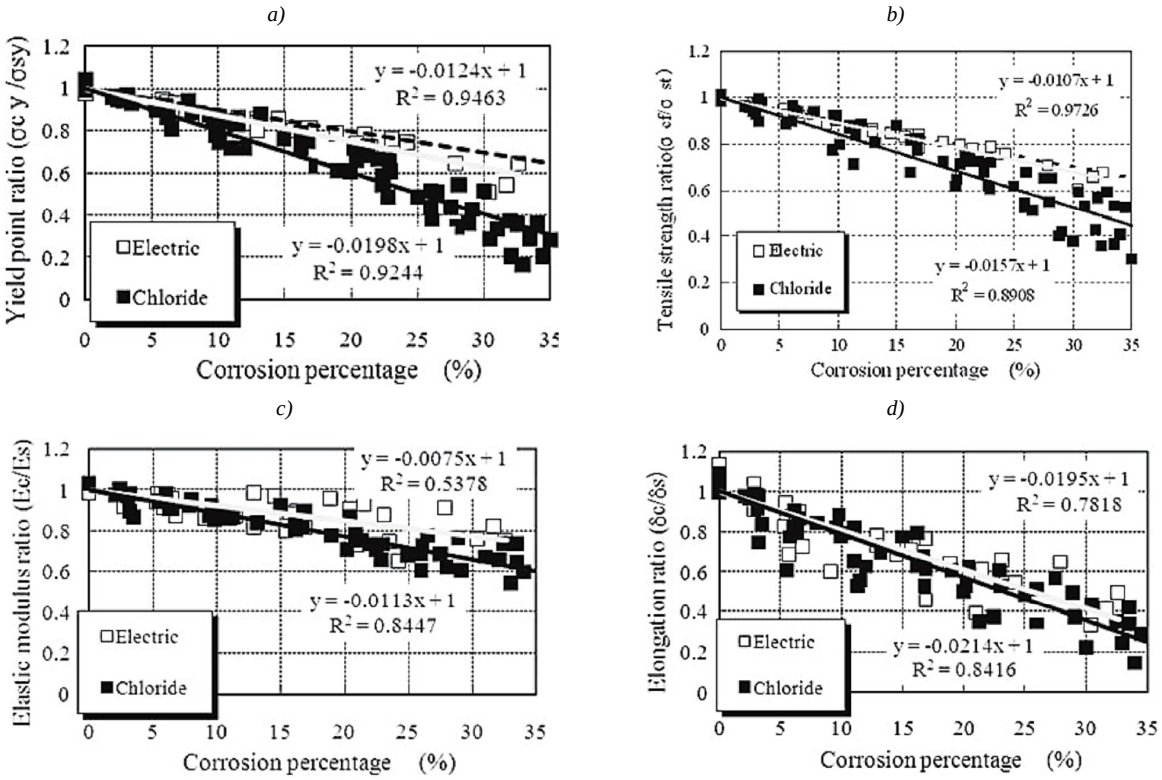

Figure 3-27. Relationships between mass loss X[%] and mechanical properties of corroded bars: a)Yield strength; b)Tensile Strength; c)Elastic modulus; d)Elongation(%); Lee et al.

Kashani et al.[143][144] (2012-2013) studied the response of corroded bars in tension and in compression including buckling. RC specimens with 8mm and 12mm diameter bars were subjected to an accelerated corrosion procedure by using external currents. Then the mass loss by the bars was measured and the average reduction of the bar diameter was estimated. Regarding the tension tests, a decrease in both ductility and strength was observed for corrosion levels greater of 15%. The most interesting results were obtained in the monotonic compression tests, carried out on corroded bars with different effective lengths. The average strain over the entire length of the bars was measured with external LVDT. The bars with low effective length L to bar diameter D ratio had a stable behaviour and the stress-strain curves showed only a decrease in the maximum stress with increasing corrosion levels, *Figure 3-28 a).* For L/D=8-10 (*Figure 3-28 b))* and predominant pitting corrosion, a premature yielding before buckling and a reduction of the buckling strength were noticed, while the post-buckling softening behaviour was found similar to the sound bars. In the case of high uniform corrosion, the bars showed a quicker transition from

the linear elastic to the non-linear plastic response, a high reduction of buckling strength and a steeper post-yield softening branch. For L/D=15-20 (*Figure 3-28 c)*), both sound and corroded bars displayed a quicker transition from linear elastic to post-yielding softening behaviour and a high reduction of the buckling strength. The authors proposed also a relationship between the buckling strength and the percentage of mass loss based on linear regression analysis:

$$f'_b = f_y(1 - \alpha \cdot X) \qquad \textit{Equation 3-25}$$

Where f'_b is the buckling strength of corroded bars, f_y is the yield strength of sound bars, X is the percentage of mass loss and α a is a constant that depends on *L/D* (greater values for greater L/D ratios) and if the strength is nominal or effective: $\alpha_{nominal}$ = 0.016-0.020, $\alpha_{effective}$ = 0.0065-0.0124.

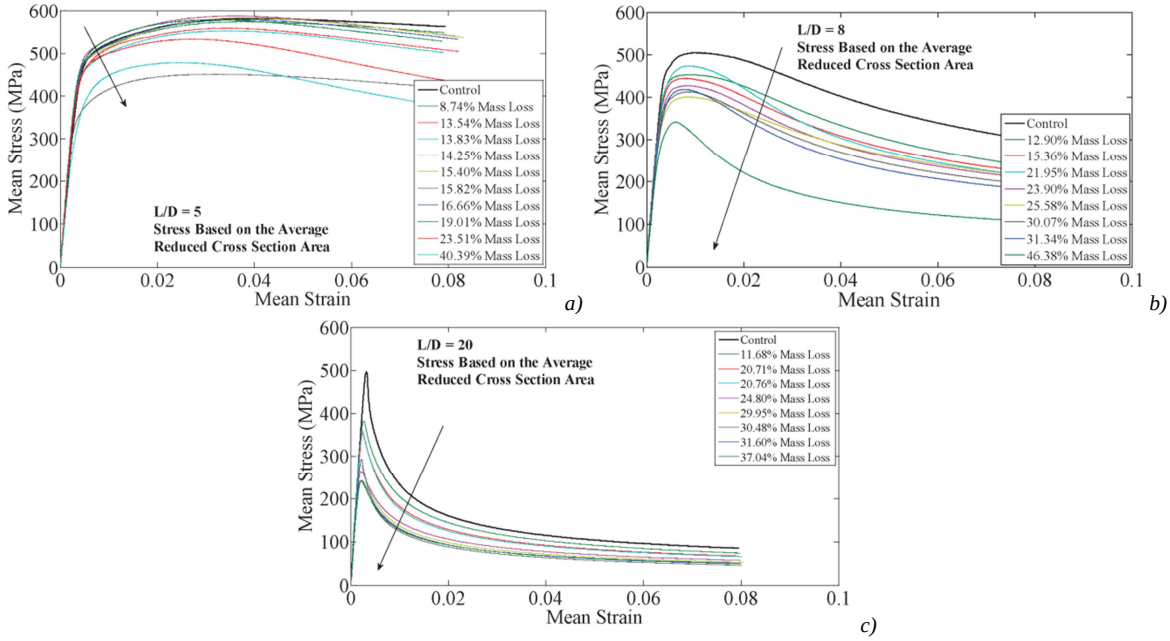

Figure 3-28. Effective stress-strain curves of corroded bars in compression; a) L/D=5; b) L/D=8; c) L/D=20, Kashani et al.[143]

Biondini et al.[40] (2012) proposed a formula to evaluate the reduction of reinforcement ductility as function of the cross section loss, which takes place in the case of pitting corrosion. Firstly, the authors defined a dimensionless damage index δ_s, which provides a measure of cross section reduction in the range [0; 1] and depends on the type of corrosion, uniform or localized. In the case of pitting corrosion, δ_s is the ratio between the area of the pit, calculated with the Val's et al.[256] model and the cross-sectional area of the undamaged bar. In practice, Equation 3-15 can be re-written as:

$$\delta_s = \begin{cases} \delta_{s1} + \delta_{s2} & 0 \le \delta \le 1/\sqrt{2} \\ 1 - \delta_{s1} + \delta_{s2} & 1/\sqrt{2} < \delta \le 1 \end{cases} \qquad \textit{Equation 3-26}$$

Once defined $\delta = {}^{p}/_{\Phi}$ and $\beta = {}^{a}/_{\Phi}$, *Equation 3-16* becomes:

$$\delta_{s1} = \frac{A_1}{A_0} = \frac{1}{2\pi}(\theta_1 - 2\beta\,|1 - 2\delta^2|) \qquad \beta = 2\delta\sqrt{1-\delta^2}$$

$$\delta_{s2} = \frac{A_2}{A_0} = \frac{2\,\delta^2}{\pi}(\theta_2 - \beta) \qquad \theta_1 = 2\,arcsin\,\beta \qquad \textit{Equation 3-27}$$

$$\theta_2 = 2arcsin\left(\frac{\beta}{2\delta}\right)$$

Then they interpolated the experimental results of the tests made by Apostolopoulos et al.[14] through an exponential function, deducing the following relationships that correlate the damage index with the residual ultimate strain of the corroded bars:

$$\varepsilon'_{su} = \begin{cases} \varepsilon_{su} & 0 \le \delta \le 0.016 \\ 0.1521\delta_s^{-0.4583}\,\varepsilon_{su} & 0.016 < \delta \le 1 \end{cases} \qquad \textit{Equation 3-28}$$

where ε_{su} and ε'_{su} are respectively the ultimate strain of the undamaged and corroded bars.

Tang et al.[241] (2014) evaluated the mechanical properties of corroded bars, referring to both the average and the minimum cross sections. To this aim, the distribution of residual cross-sectional areas was determined using a 3D laser scanner along the bar length. Ribbed reinforcing bars of 19 mm bar diameter were used. Only the middle part of each bar was subjected to an accelerated corrosion procedure in order to induce here the fracture during the tensile tests. The load-displacement curves obtained are reported in *Figure 3-29.* With the increasing of corrosion the yield plateau fast disappear, both the yield and the ultimate loads decrease and the elongation abruptly reduce, confirming the remarks of Du et al. [94]. A comparison between the residual yield and ultimate strength evaluated respect to the average and the minimum cross-sectional area was made, *Figure 3-30 a).* Both yield and ultimate strengths decrease respect to the average cross-sectional area loss and they slightly increase respect to the minimum cross-sectional area loss. Therefore, the minimum cross-sectional area is more relevant for the evaluation of the residual mechanical properties because both yielding and fracture occurred firstly here. Regarding the ductility of corroded bars, the elongation at the maximum load decrease exponentially with increasing corrosion levels. The exponential decay models were found more accurate if associate to the minimum section, *Figure 3-30 b).*

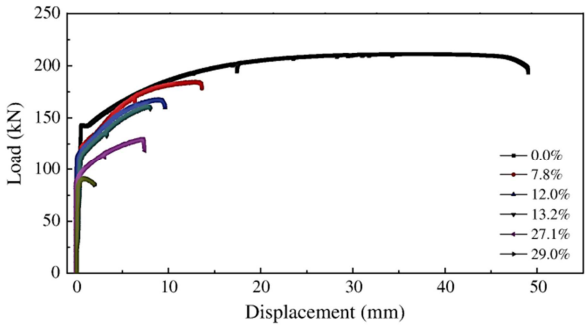

Figure 3-29. Load-displacement curves, different corrosion levels, Tang et al.[241]

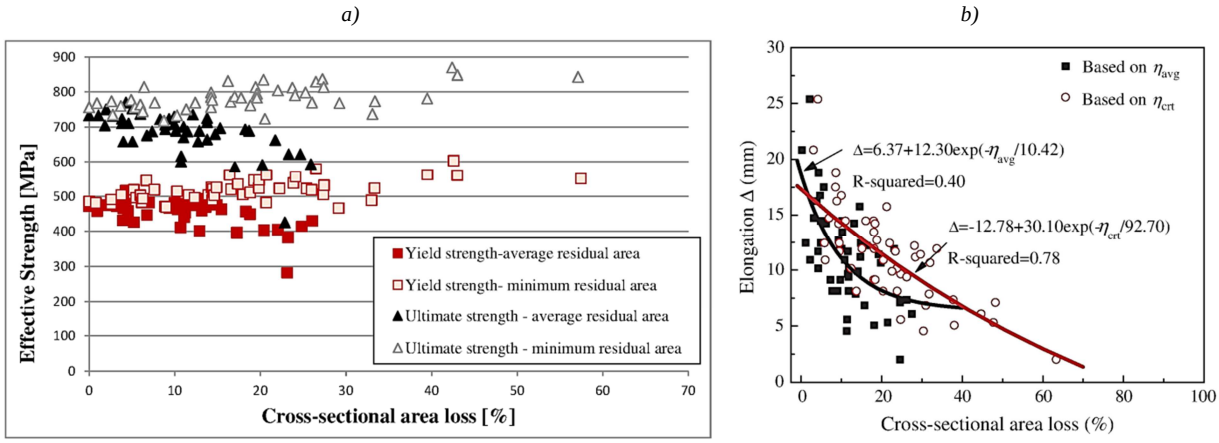

Figure 3-30. a) Effective yield and ultimate strengths, b) Elongation, as function of X[%], Tang et al.[241]

3.4. Effects of reinforcement corrosion on concrete

3.4.1. Concrete degradation

Concrete deterioration can be caused by several factors, of mechanical, physical, chemical or biological type. The main mechanisms start to act during the first year of the service life of structures, but while the mechanical and physical ones show immediately their effects, chemical and biological attacks display their consequences on concrete later, as observed by Apostolopoulos et al.[14] (*Figure 3-31*) and they are highly influenced by the presence of previous damages. In detail, chemical attacks lead to deterioration and durability problems on concrete, promoting corrosion in the reinforcing bars embedded. Carbonation, chlorides and acids attacks on concrete structures are the widespread chemical attacks affecting nowadays RC structures. Their action in promoting corrosion has been object of numerous researchers, while their effect on the mechanical properties of concrete material has been less studied, and in particular no data are available on their combined action. Below, the results of some studies are reported for the understanding of the consequences of different chemical attacks on the concrete material. An exhaustive review of the literature is thus beyond the scope of this work.

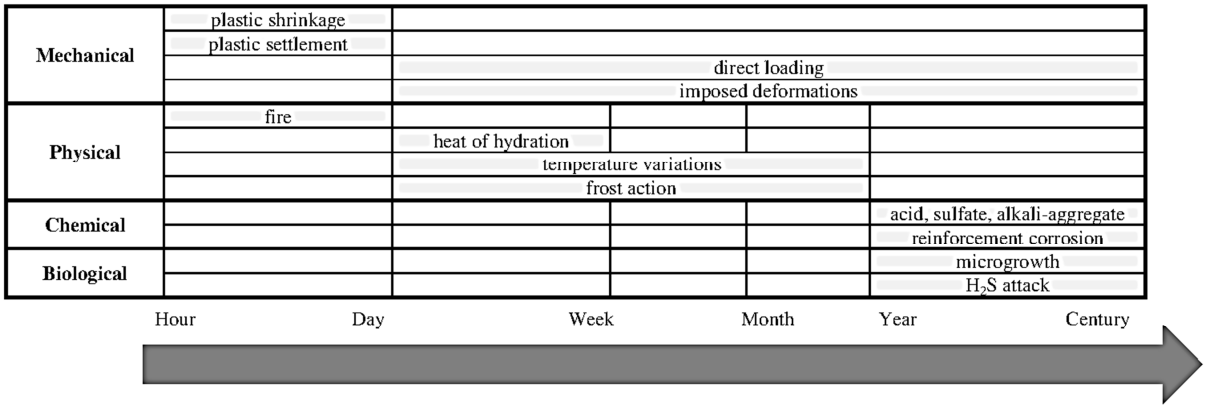

Figure 3-31. Factors that lead to concrete deterioration and possible time of action

- ***Carbonation***

It has been proved by many authors, e.g. Ngala and Page[189], that carbonation changes the microstructure of the concrete material reducing its porosity. This leads to a higher density, decrement in permeability, increment in hardness and in general to an improvement of its mechanical properties. Among others, Chang et al.[64] demonstrated through several mechanical experiments, made in different carbonation environments, that carbonation enhances compressive strength, splitting tensile strength, elastic modulus, bond strength and hardness of concrete specimens. Some results obtained by the authors are reported in *Figure 3-32*. It is possible to observe that compressive strength of concrete increases with the carbonation time, especially for two-ends coated, *Figure 3-32 a).* This is due to the higher strength of carbonation products ($CaCO_3$) respect to $Ca(OH)_2$. Splitting tensile strength, which indicates indirectly the concrete's capability to endure tensile stress, was also measured, *Figure 3-32 b). A*lso in this case, an increment of values with increasing levels of carbonation was observed, but less significant than for compressive strength. Finally, the influence of carbonation on the elastic modulus of concrete was investigated, *Figure 3-32 c).* It was found a strong dependency of concrete stiffness on the proportion of carbonated and uncarbonated zones, but in general carbonated concrete was observed stiffer.

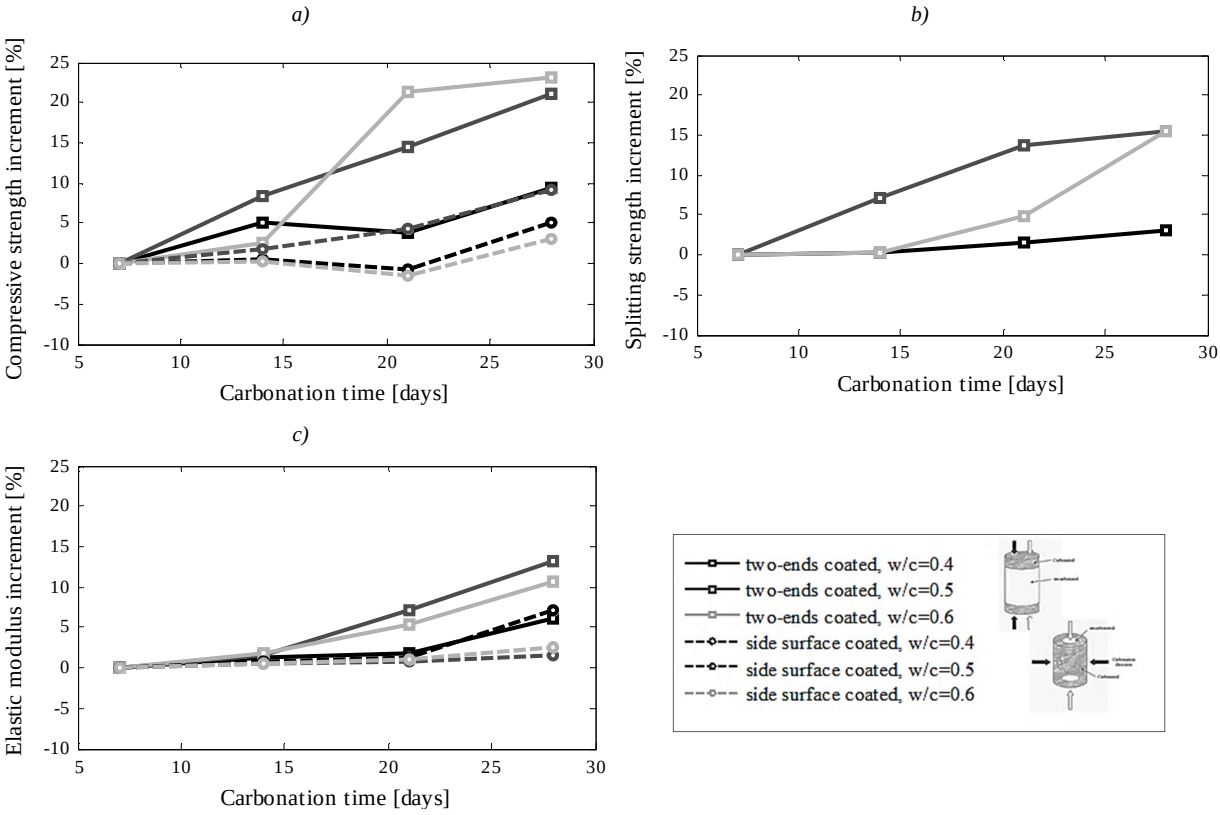

Figure 3-32. Mechanical properties of carbonated concrete, data from Chang et al.[64]

It should be underlined that enhancement in mechanical properties does not imply a more durable concrete. Once carbonation of concrete reaches the rebar-concrete interface, it may result in corrosion and consequently mechanical properties will be degraded, Chang et al.[64].

- ***Acid rain***

Zhang et al.[278] carried out an experimental campaign in order to study the uniaxial properties of concrete exposed to acid rain environment. As introduced in paragraph 3.2.1, acid rainwater may penetrate in concrete pores and lead to pH reduction in concrete, promoting the development of uniform corrosion. The authors simulated acid rain in laboratory, submitting a series of dumbbell-shaped specimen to an aggressive environment for different periods. Thereafter the specimens were tested in tension. The results obtained are reported in *Figure 3-33 a)*. The tensile strength was found higher for low levels of concrete degradation, because the fracture surface mainly passed through the aggregate or the aggregate-mortar interfaces. For severe deterioration, the tensile strength was found considerably lower because the fracture surface failure mode was coarse aggregates bond failure. The authors subjected to accelerate corrosion procedure also cubic specimens with 100 mm length, then tested in compression. The experimental results showed that compressive strength is more sensitive than tensile strength to aggressive environments. The authors reported also the ascending branch of stress-strain curves of the concrete specimens in tension *Figure 3-33 b).* For specimens under aggressive environments for less than 11 days, uniaxial tensile strength, peak strain, and elastic modulus were found greater than the undamaged specimens. For higher corrosion periods, the uniaxial tensile strength and elastic modulus decreased, but the peak strain continued to increase. Zhang et al.[278] did not measure the post peak softening behaviour of concrete in tension but they specified the brittle post peak response observed: once the peak strain was reached a visible crack developed and in a very short time the specimens failed.

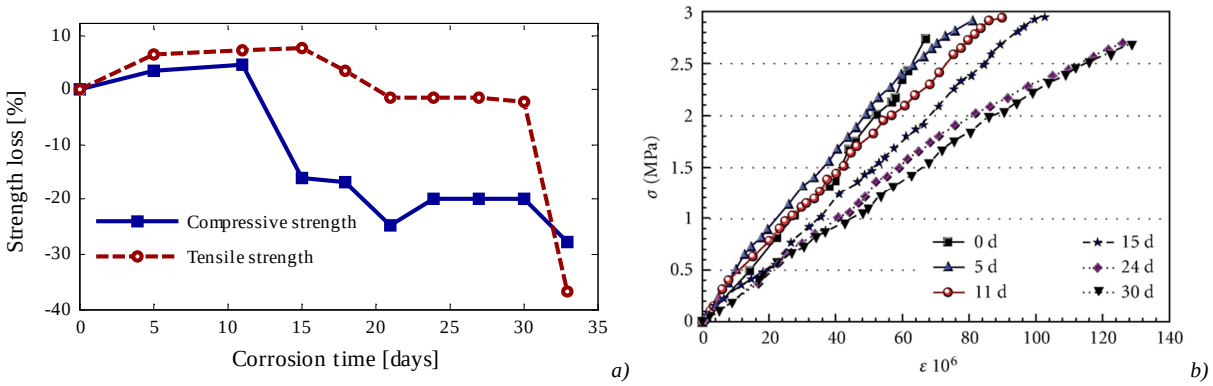

Figure 3-33. a)Tensile and compressive strength loss versus corrosion time; b)Ascending branch of stress-strain curves of concrete specimens in tension subjected to acid rain corrosion, Zhang et al.[278]

- ***Chloride salts***

Chloride salts are various, e.g. hydrochloric acid (HCl), potassium chloride (KCl), calcium chloride ($CaCl_2$), sodium chloride (NaCl), etc…and their effect on concrete has not still fully understood. Some studies have been carried out by the U.S. Federal Highway Administration and National Department of Transportation[254] in order to assess the effect of different types of de-icing salts on Portland Cement Concrete. It was found that concrete specimens exposed to $CaCl_2$ and especially to $MgCl_2$ had a very significant compressive strength loss. The laboratory tests demonstrated that the $CaCl_2$ deicer chemically reacted with phases in the hardened cement paste, producing calcium oxychloride, which damages mortar and concrete causing expansion, volume change, loss of compressive strength, and microcracking. On the contrary, samples exposed to NaCl solutions exhibited no loss in compressive strength. There remarks have been confirmed also by the experimental tests made by Fan et al.[100]. The authors first exposed concrete cubes on different corrosive environments for different days; then they tested the specimens in compression. Specimens exposed to hydrochloric acid (HCl) solution showed lower values of compressive strength, elastic modulus and increase of maximum strain, see *Figure 3-34 a).* Specimens exposed to sodium chloride (NaCl) displayed only a slightly decrease in compressive strength and only after long time, *Figure 3-34 b).*

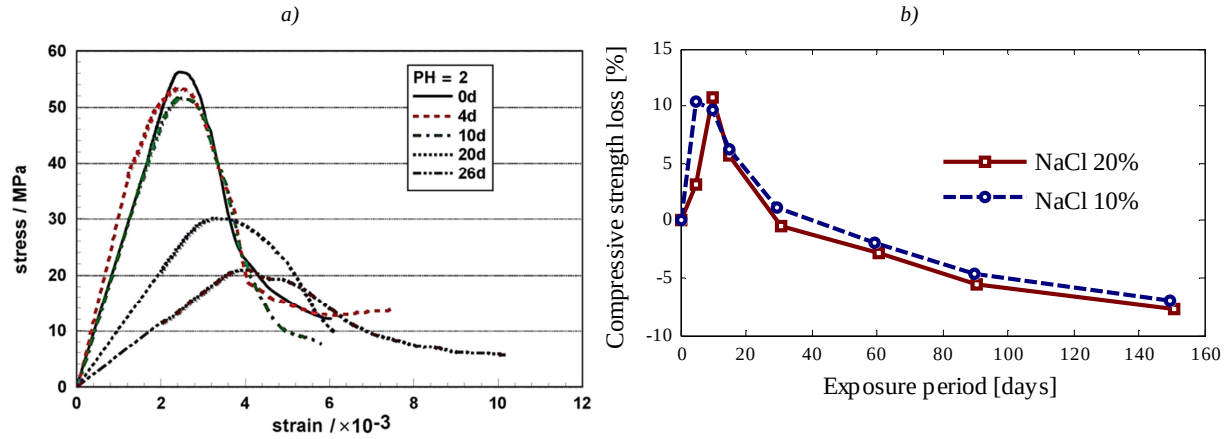

Figure 3-34. a) Stress-strain curves of concrete in hydrochloric acid solution; b) Compressive strength of concrete exposed to sodium chloride solution, Fan et al.[100]

From the tests, it is possible to conclude that while carbonation improves the mechanical properties of concrete, the effect of chlorides and acids is the opposite. A quantification of the effect of simultaneous chemical attacks, how actually happens in real structures, is complicated at

the moment due to the lack of more detail information. Fortunately, in RC structures experience shows that the most dangerous deterioration mechanisms are not those related to the degradation of the concrete itself, but corrosion of the embedded steel reinforcement. Chemical deterioration on concrete can create favourable conditions for the beginning of reinforcement corrosion and vice versa, corrosion in reinforcing bars can lead to damage of the surrounding concrete. This is certainly true for carbonation-induced corrosion, where the development of rust is diffused along the reinforcement length and the amount of oxide products is high. Regarding chloride-induced corrosion instead, researchers agree that localized corrosion often does not cause cracking of the concrete cover, due to the lower amount of corrosion products generate, while cracks in the protective concrete cover play a fundamental role for the penetration of chlorides in concrete, facilitating the initiation of localized corrosion, *Figure 3-35*.

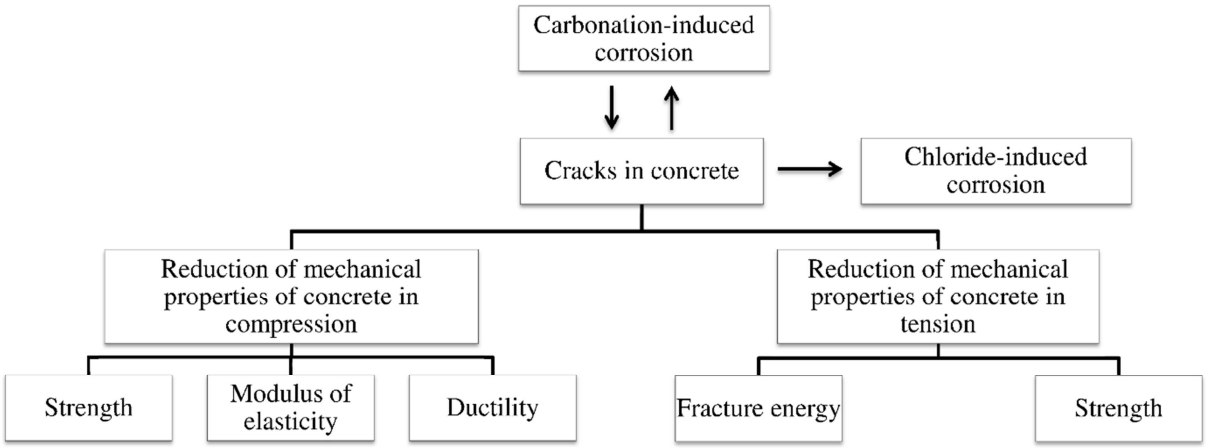

Figure 3-35. Diagram of the effects of reinforcement corrosion into concrete

The main effect of reinforcement corrosion on concrete is the formation of micro and macro cracks; for severe deterioration also spalling of concrete cover may occur (*Figure 3-36*). The cracked concrete is characterized by lower mechanical properties than the virgin material (*Figure 3-35*), and this should be considered in the assessment of corroded RC structures. In the next paragraph, some studies regarding the effects of reinforcement corrosion on concrete are introduced. In detail the reduction of strength and ductility of degraded concrete are analysed both in tension and in compression. It should be noticed that only the most significance studies, useful for the development of the damage model for degraded concrete, are here reported.

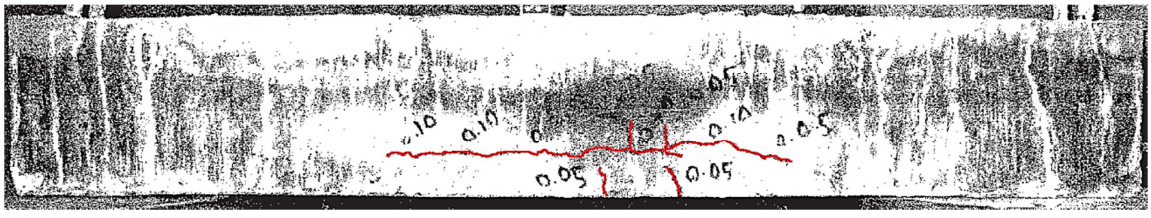

a)

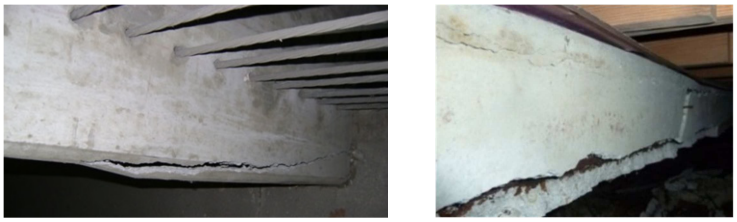

b)

Figure 3-36. a) Crack pattern due to reinforcement corrosion in RC beam, Joyce[137]; b) spalling of concrete cover in corroded RC beams

3.4.2. Crack width – corrosion level relationships

The relationship between crack width in concrete cover and quantity of oxide generated by corrosion, expressed as penetration of corrosion in the steel bars or loss of bar diameter, has been subjected to several researches by means of experimental corrosion tests and analytical models.

After corrosion initiation in steel, corrosion products accumulate around the bar. Hydrated rust of greater volume causes pressure on concrete and leads to formation of microcracks in the cement past, at the beginning, and then to concrete cover cracking and eventually spalling. As the concrete cracks, steel corrosion process increases due to additional exposure. The expansion of the corrosion products can be many times the initial steel volume. The most diffuse and qualified model to predict the damage caused by corroding reinforcing bars on concrete is the concrete ring model, (*Figure 3-37*): the radial stresses on concrete resulting from the volume expansion of corrosion products, can be regarded as an uniform pressure acting on a thick-walled concrete ring. The thickness of the ring corresponds to the thinnest concrete cover around the bar, giving the shortest crack path from the bar to the free surface. The concrete ring well approximates the effect of surrounding concrete, but due to differences in geometry between the cover ring model and the real cover, the stresses will only approximate the stresses in the real situation. However, the stresses are likely to be reasonable where the cover is thinnest, which is likely to be the critical section, so the concrete ring model can be accepted for the analysis (Bažant[21], Martin-Perez et al.[175], Tepfers[244]). Many analytical and numerical proposals basing on the concrete ring model have been developed with satisfactory results in the last years, e.g. Bažant[21], Bhargava et al.[37], Dagher and Kulendran[86], Liu and Weyers[161], Maaddaay et al.[166], Molina et al.[184], Ueda et al.[250]. Other models have been developed basing on empirical relationships, e.g. Alonso et al.[8], Andrade et al.[10][11], Cabrera et al.[44], Duracrete et al.[95], Vidal et al.[262].

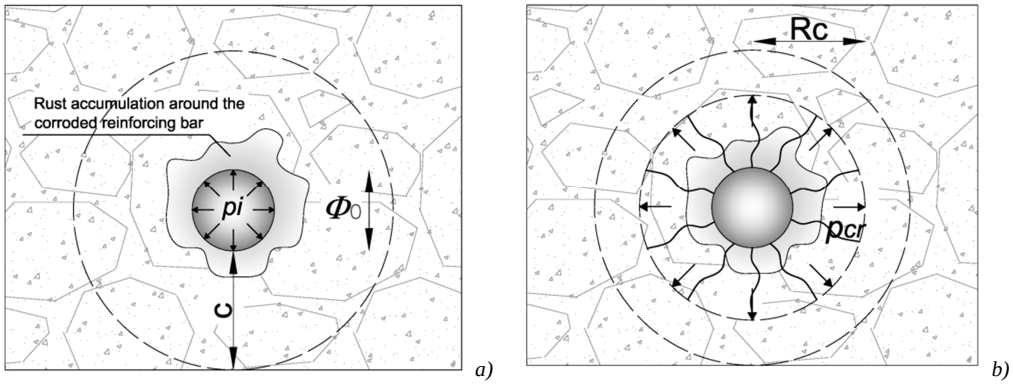

Figure 3-37. a)Pressure on concrete of corrosion products expansion and b) partially cracked cover.

Regarding the work of Molina et al.[184], the authors carried out non-linear finite element analyses to model cover cracking and they compared the results with the tests made by Andrade et al.[10]. Reinforcement corrosion was modelled by considering the superposition of two effects: a decrease in stiffness and an increase in specific volume of the reinforcement. In detail, the first effect was achieved by varying linearly the properties from those of steel to those of rust. Given the lack of experimental data, rust was assumed to have elastic properties similar to water based on the assumption that water is one of the main components of rust. The second effect was achieved by imposing an initial strain on the elements to be corroded. The rust was assumed to occupy twice the volume of the virgin steel ($\upsilon_{r/s}$=2). The results obtained showed that the

numerical model overestimates the deformation at a given section loss: a higher strain rate than the experimental data was in generally found for the all the specimens simulated. This is probably due to the fact that the rust product filling the surrounding concrete with significant deformation not occurs until the pores are full. However, the analyses showed also that although the strain at the main crack differed from specimen to specimen considered, the summation of strains (or crack-width rates $\Sigma\, w_{cr} / x$) at the three principle cracks was similar among the specimens. This was proved also by a theoretical point of view: the sum of crack-width rates has to be stable between the specimens, because if the fracture energy is completely released in all the cracks and an ideal stress-free state is assumed, the problem becomes a purely geometric one, Molina et al.[184]. Assuming a finite number of already opened cracks in the concrete surrounding the corroded bar and a uniform corrosion penetration equal to *x* (*Figure 3-38*) the net increment of volume of the rusted bar is equal to:

$$dV_{net} = (\upsilon_{r/s} - 1) \cdot 2\pi r \cdot H \cdot dx \qquad \textit{Equation 3-29}$$

where *r* is the current radius of the sound bar and *H* is the depth of the plane model. From *Equation 3-29* the increment of the external radius can be calculated:

$$dR = \frac{dV_{net}}{2\pi R \cdot H} = (\upsilon_{r/s} - 1) \cdot \frac{r}{R} \cdot dx \qquad \textit{Equation 3-30}$$

Assuming that the elongation of *Equation 3-30* is absorbed in the concrete by merely incrementing the crack widths, results that:

$$\sum \frac{dw_{cr,i}}{dx} = 2\pi(\upsilon_{r/s} - 1) \cdot \frac{r}{R} \qquad \textit{Equation 3-31}$$

where $dw_{cr,i}$ are the differential increments in the crack widths. If *r/R* is approximated by unity and a backward integration is performed to zero:

$$\sum \frac{w_{cr,i}}{x} = 2\pi(\upsilon_{r/s} - 1) \qquad \textit{Equation 3-32}$$

Equation 3-32 allows evaluating the total crack width respect to the radius loss by the corroded bar:

$$w_{cr} = 2\pi(\upsilon_{r/s} - 1) \cdot x \qquad \textit{Equation 3-33}$$

Equation 3-33 bases on a number of simplifying assumptions, e.g. the rust is considered incompressible, but it allows calculating a conservative value of the crack width basing only on the value of the uniform corrosion penetration *x*.

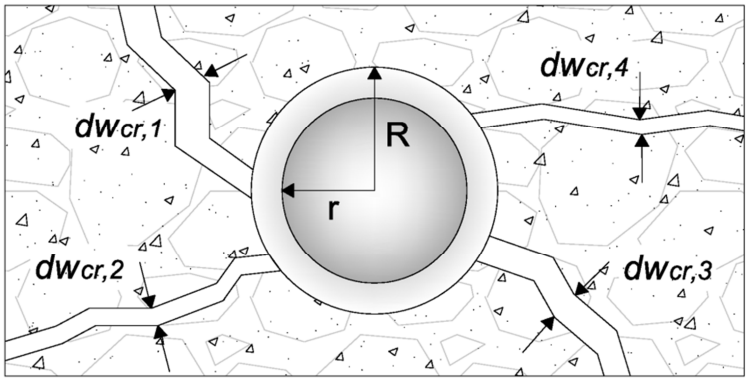

Figure 3-38. Geometrical model of Molina et al.[184]

3.4.3. Mechanical properties of cracked concrete

Concrete cracking should be taken into account even before the detachment of concrete cover and the consequent reduction of resistant section. One method consists on considering the reduction of the mechanical properties of the concrete material, according to analytical and numerical model and experimental data.

3.4.3.1. Residual strength and ductility of cracked concrete in compression

Concrete cracking in compression can be considered by reducing concrete strength. Coronelli et al.[80] modelled the concrete material by means of four-node plane-stress elements with a thickness equal to the section width. The authors proposed to adopt a degraded constitutive law for concrete elements belonging to the cover, *Figure 3-39* and to calculate the residual compressive strength of cracked concrete through the following equation, based on the more general Vecchio and Collins' [260] model for cracked concrete:

$$f_c^{res} = \frac{f_c}{1 + k\,{\varepsilon_1}/{\varepsilon_{co}}} \qquad \textit{Equation 3-34}$$

where k is a coefficient proposed by Capè[56] and Coronelli et al.[80], which depends on bar roughness and diameter, a typical value is 0.1; ε_{co} is the strain at the compressive stress peak f_c and ε_1 is the average tensile strain in the cracked concrete at right angles to the direction of the applied compression. Basically the reduction of compressive strength is function of the amount of the average tensile strain in the transverse direction that leads to longitudinal microcracks. The average tensile strain ε_1 can be calculated as:

$$\varepsilon_1 = \frac{(b_f - b_0)}{b_0} = \frac{n_{bars} \cdot w_{cr}}{b_0} \qquad \textit{Equation 3-35}$$

Where b_0 the original concrete section width; b_f is the final concrete section width, increased by corrosion cracking; n_{bars} is the number of reinforcing bars and w_{cr} is the total crack width for a give corrosion penetration x. It should be noticed that w_{cr} results the only one variable that link the corrosion level with the concrete degradation, therefore its estimation is of considerable importance. Coronelli et al.[80] proposed also to reduce the width of the transverse concrete section, in order to taken into account the possible delamination of the outer layers of concrete due to stirrups corrosion.

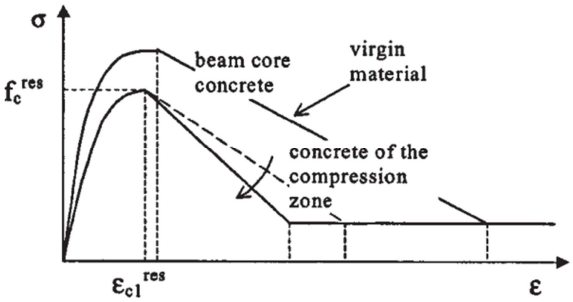

Figure 3-39. Constitutive law of concrete in compression, Coronelli et al.[80]

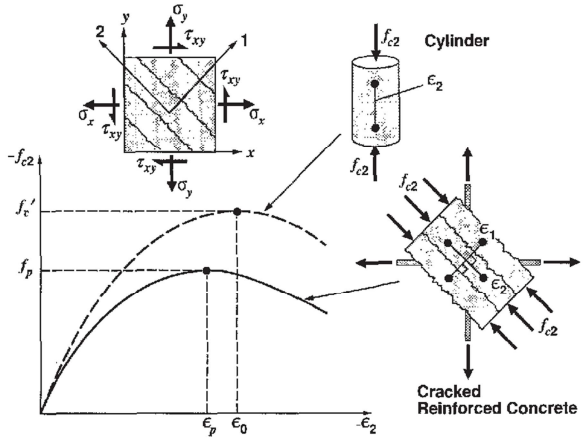

Figure 3-40. Deteriorate Compression Response in Cracked RC Elements, Vecchio et al. [260]

Vergani[261] formulated a three-dimensional reinforced concrete beam finite element, which accounts of concrete degradation due to reinforcement corrosion. The author suggested to consider damage of concrete material through a reduction of the compression strength only in the concrete surrounding the corroded bars. In detail the elements subject to degradation are those included in the circumference concentric to the corroded bar and of ratio equal to the concrete cover depth, located outside from the confined nucleus, *Figure 3-41*. The advantage of this approach consists on the automatic identification of the damaged elements and of the different fracture modes by the program: if the bars are close each other, the concrete cover detaches according to a horizontal fracture plane (*Figure 3-41 a)*), if the bars are only at the corners, the fracture plans are inclined (*Figure 3-41 b)*). For the assessment of residual compressive strength of degraded concrete, the authors adopted the approach of Coronelli et al.[80], *Equation 3-34*. In Biondini and Vergani[40] a critical crack width equal to 1 mm was introduced. For higher crack opening, the spalling of concrete cover was assumed to occur and therefore the residual compressive strength set equal to 0.

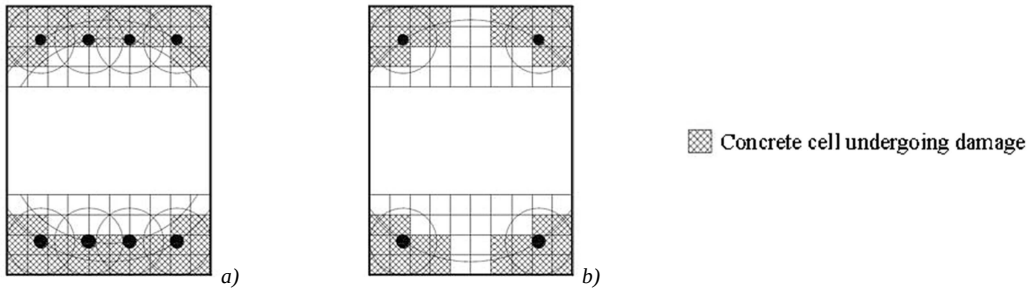

Figure 3-41. Concrete elements damaged by reinforcement corrosion, Biondini and Vergani[40]

Regarding the modulus of elasticity and the ultimate strain of degraded concrete, there are no experimental observations or analytical models specifically developed for the evaluation of the residual E_c and ε_{cu} of concrete damaged by reinforcement corrosion. In general, it is obvious that the degraded concrete will be characterized by a lower modulus of elasticity, due to the breakage of bonds in the microstructure of cement paste, the debonding between aggregates and cement pasta and sometimes the breaking of the aggregates themselves. However a right quantification of this effect is complicated due to the great numbers of variables involved, such the size of the aggregates, the porosity of the cement pasta, the quality of the adhesion between aggregate and mortar, etc…Moreover reinforcement corrosion in concrete is characterized by rust production, which fills concrete pores located at the concrete-steel interface (*Figure 3-42*) and causes micro and macro cracks mainly around the aggregate in the concrete surrounding the bar, which are not always filled by corrosion products (*Figure 3-43 a)*). On one side, not filled cracks behave like voids and therefore they lead to a decrease in the nominal Young's modulus of the concrete material. On the other side rust has an own elastic modulus, which contributes to the stiffness of concrete material. A numbers of authors have tried to define the mechanical properties of rust, e.g. Ouglova et al.[196] measured the Young's modulus of iron oxides by means of ultrasonic and mechanical measurements. These laboratory grown oxides were similar to oxides obtained from 40-year old corroded reinforced structures. The authors showed that the Young's modulus of these iron oxides was about 2 GPa. Šavija et al.[226] demonstrated instead that Young's modulus of rust layer is highly dependent on the level of confinement provided by the surrounding cement paste. In confined state, the rust layer exhibited a relative uniform modulus of elasticity of value between 49.4 GPa and 67.9 GPa (*Figure 3-43 b)*). Once extensive cracking occurred, the rust

layer was found no longer uniform and due to the presence of micro gaps, a precise value for the Young modulus could not be determined. Due to the complexity of the phenomena and to the fact that some aspects are not yet fully understood, it is difficult to adequately define the residual modulus of elasticity of concrete damaged by reinforcement corrosion and some simplifications must be introduced.

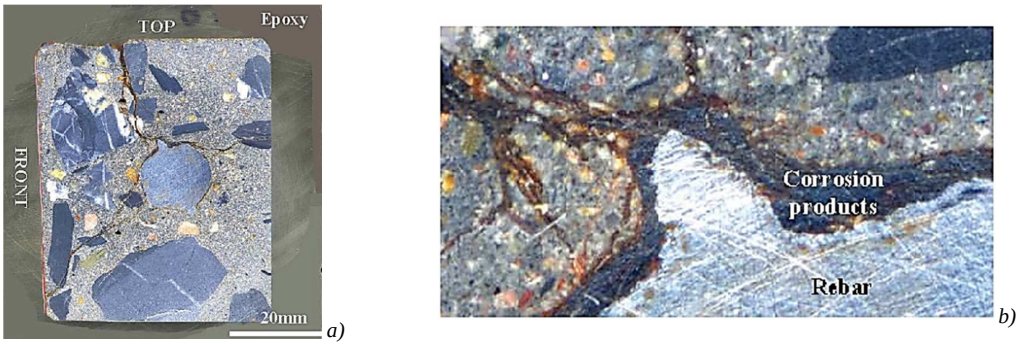

Figure 3-42. a)Concrete specimen with corroded reinforcing bar: crack propagation; b)Magnified portion of the boxed area, Wong et al.[271]

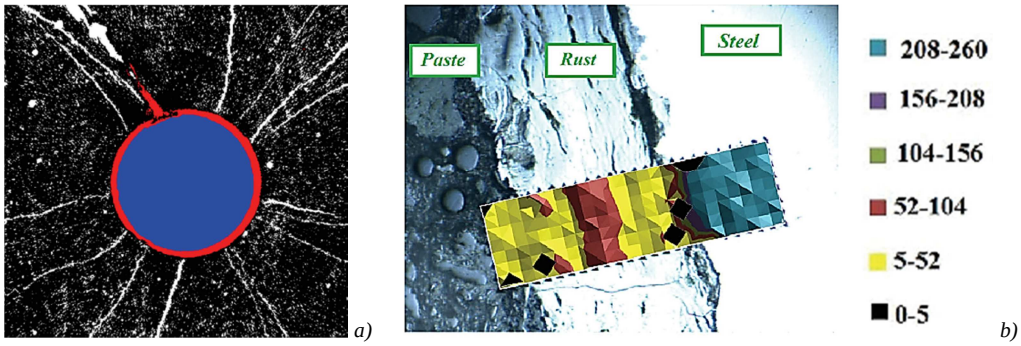

Figure 3-43. a) Penetration of corrosion products into an open crack in concrete; b) distribution of the Modulus of elasticity in steel-concrete interface, Šavija et al.[226]

The assessment of the deteriorated concrete ductility is even more complex, due to the difficulty to measure the post-peak response. Some researchers, who have modelled degraded concrete due to reinforcement corrosion, have proposed to reduce the compressive ultimate strain of the material to account for the ductility reduction due to microcraking phenomena, but they did not give a possible explanation or a relationship linked to the corrosion level. For example, Coronelli et al.[80] suggested to adopt a brittle postpeak behaviour for degraded concrete in compression, *Figure 3-39*. Kallias and Rafiq[140] modelled the post-peak response of concrete in compression using compressive fracture energy G_c, based on the recommendations of Nakamura and Higai[190]. In order to consider cracked concrete, for the elements of the top cover of corroded RC beams, the authors reduced the values of both compressive strength and G_c, *Figure 3-44*.

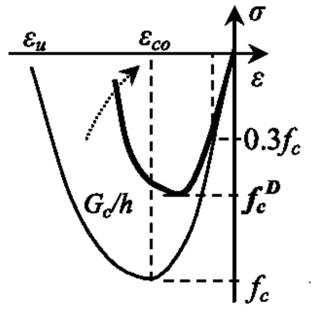

Figure 3-44. Constitutive models for concrete in compression, Kallias and Rafiq[140]

3.4.3.2. Residual strength and ductility of cracked concrete in tension

Regarding the modelling of degraded concrete in tension, some researchers have proposed to neglect the tensile strength for damaged concrete. For example, Vergani[261] obtained a better correspondence between the numerical modelling and the experimental data of corroded RC beams, adopting a null tensile strength in the elements subject to degradation, defined in *Figure 3-41*. On the contrary, Kallias and Rafiq[140] did not consider any reduction of concrete properties in tension, probably assuming that the effects of concrete deterioration are negligible in bottom cover of RC beams. Many other authors, e.g. Gestsdóttir and Guðmundsson[112] and Saether and Sand[223] adopted arbitrary reduced values of tensile strength and fracture energy of degraded elements in tension regions, in order to take the ageing and deterioration of the concrete into account. Finally Hanjari et al.[118] suggested another kind of approach: due to the fact that cracked concrete in regions outside the corroded stirrups may influence the shear capacity of RC beams, the authors adopted in these areas a lower tensile strength of concrete, as shown in *Figure 3-45*. The tensile strength of degraded concrete was calculated proportionally to the reduction of compressive strength, evaluated with the approach of Coronelli et al.[80]:

$$f_{ct,cracked} = \frac{f_{cc,cracked}}{f_{cc}} \cdot f_{ct} \qquad \textit{Equation 3-36}$$

Where f_{ct} and $f_{ct,cracked}$ are respectively the tensile strengths of virgin and cracked concrete and f_{cc} and $f_{cc,cracked}$ are the compressive strengths of virgin and cracked concrete. The concrete fracture energy G_F was also accordingly reduced.

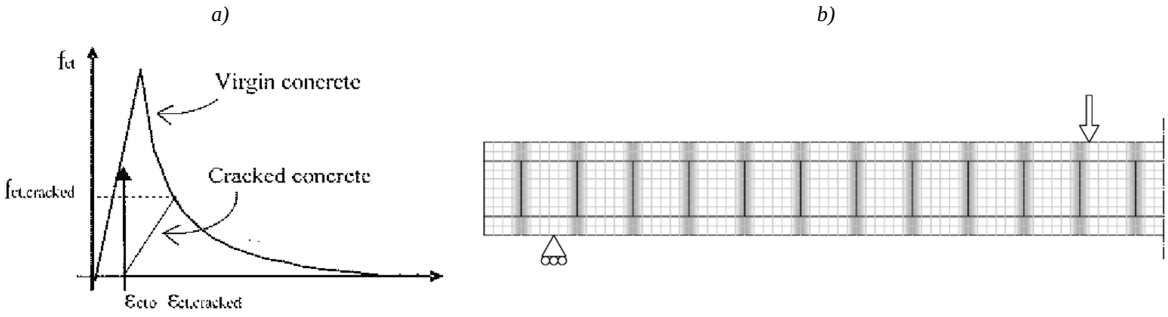

Figure 3-45. a) Stress-strain law in tension for concrete sound and degraded; b) FE model of half RC beam, Hanjari et al.[118]

These different approaches derive from the lack of available test data regarding the mechanical characterization of degraded concrete, especially in tension. Material models for deteriorated concrete structures are mainly based on assumptions or idealizations. In order to make computational results more accurate, some tests have been carried out for the assessment of the relationship among the level of reinforcement corrosion and tensile properties of degraded concrete. In Shimomura and Maruyama[231] uniaxial RC specimens with a single reinforcing bar were immersed in salt water and subjected to accelerated corrosion procedure, applying an electric current of 0.65 A. Thereafter tensile stress in concrete was obtained through uniaxial tensile tests of the specimens, *Figure 3-46.* Corrosion level was measured from weight loss by the bars, after being extracted. As well known, concrete around reinforcing bars carries tensile stress by bonding mechanisms, even after concrete cracking due to the aggregate interlocking. This effect, known as tension stiffening, is reduced in concrete damaged by reinforcement corrosion, due to the development of micro and macro cracks and the bond degradation.

The average tensile stress in concrete σ_c was calculated by the authors exploiting this effect, as:

$$\sigma_c = \frac{P - A_s E_s \varepsilon}{A_c} \qquad \textit{Equation 3-37}$$

Where P is the applied load, A_s is the cross sectional area of the steel bar, E_s is the elastic modulus of steel, ε is the average strain and A_c the cross sectional area of concrete.

The results obtained by the authors in term of average strain – average stress of concrete, are reported in *Figure 3-47*. It was observed that the tensile stress carried by concrete decreased with increasing levels of corrosion and that this effect was high even in specimens 1-2 and 1-4, in which no cracks formation had been observed. Starting from these results, the authors proposed to consider reduction of tension stiffening in corroded RC members.

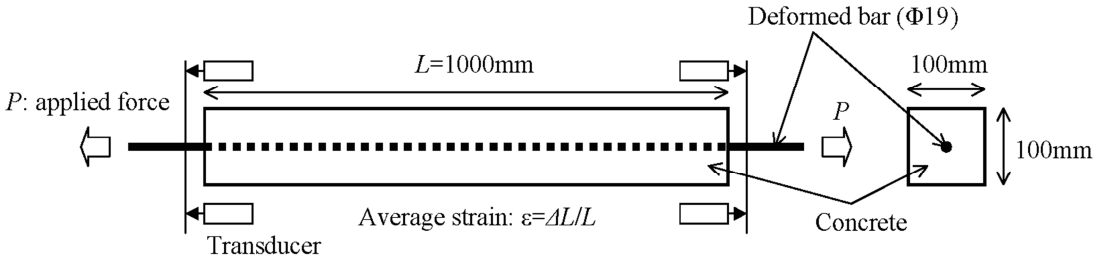

Figure 3-46. Uniaxial test on RC specimen, Shimomura and Maruyama[231]

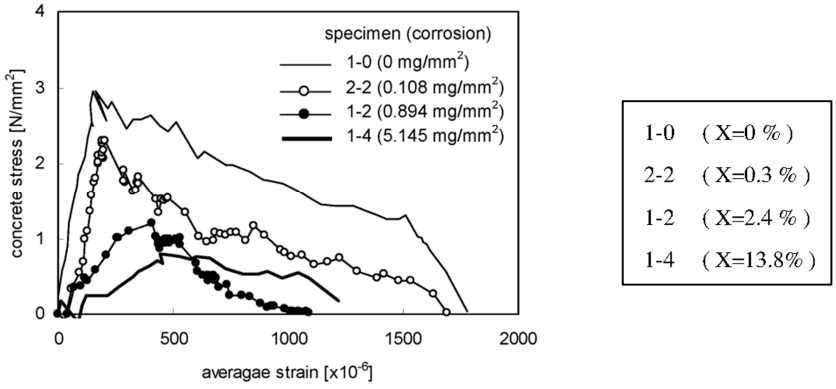

Figure 3-47. Tensile stress – average strain in concrete measured, Shimomura and Maruyama[231]

3.5. Effects of corrosion on steel-concrete interface

The structural response of RC members is considerably influenced by the stress transfer between reinforcement and concrete in the longitudinal direction of the bars, known as bond. Ductility requires bond to withstand large steel strains along the embedded reinforcement, in order to let the strains spread between two contiguous bending cracks, and to favour the formation of densely-spaced secondary cracks, *fib* MC2010[106]. In the case of reinforcement corrosion, because of the development of the rust layer, the reduction of the bar ribs, the lower confinement due to the cracking of the concrete cover, etc…a decreasing of the adherence between steel bars and surrounding concrete occurs. As a consequence, the structural response of RC members may change. In this paragraph, a short introduction about the bond mechanics is firstly given, in order to understand the phenomenon in absence of corrosion. Then, the effects of corrosion on the composite interaction between concrete and steel bars are discussed.

3.5.1 Steel-to-concrete bond mechanics

3.5.1.1 Local steel-concrete interactions

Bond and anchorage are terms used to denote the transfer of force between reinforcement and concrete. In particular, the change in force along the reinforcement divided by the area of the steel bar surface, over which this change takes place, is called bond stress. The length of a member required to develop the full bond is called anchorage length. An average value of bond stress throughout the anchorage length, in the case of one reinforcing bar, can be calculated as:

$$\tau_b = \frac{\Phi \cdot \Delta\sigma}{4 l_b} \qquad \textit{Equation 3-38}$$

where Φ is the bar diameter; l_b is the bond length; $\Delta\sigma$ the change in stress.

Anchorage is studied using a long bonded length (10 Φ): the level of steel stress is near yielding and the resulting bond strength is evaluated as the average value exerted along the anchorage length. For evaluating instead the local bond stress-slip relationship, the classical pullout test suggested by RILEM[217] consists of: reinforcing bar cast-in-place in a concrete specimen, loaded in its longitudinal direction at one end by an axial force *N*, while the other end is unloaded. A limited embedment length l_b (5 times Φ) is used. The reinforcement is in tension, while the concrete is in compression. As result of a pull-out test, the composite interaction between steel bars and surrounding concrete can be experimentally express in terms of tangential stress (bond stress) τ – slip displacement *s* relationship. The average bond stress can be calculated as *Equation 3-39*, see also *Figure 3-48 a)* and *b):*

$$\tau_b = \frac{N}{\pi \Phi l_b} \qquad \textit{Equation 3-39}$$

Averaging is only meaningful in the case of short anchorage. In normal case instead, due to the elasticity of the steel bar and the non-linearity of the bond, the shapes of the actual tensile stress and bond stress distribution increasingly deviate from the linear idealisation for larger anchorage lengths, Mahrenholtz[168] (dashes lines of *Figure 3-48 c)* and *d)).*

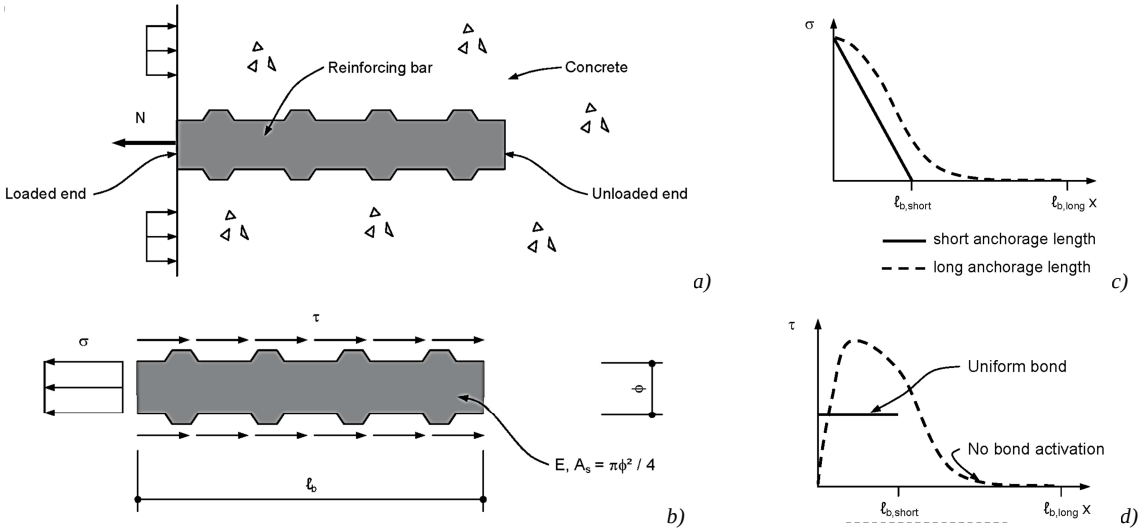

Figure 3-48: a) Schematic pullout test; b)Tensile stress and bond stress of a reinforcing bar element with one loaded end; Schematic distribution of c)tensile stress and b)bond stress, Mahrenholtz[168]

The scientists agree to recognise four different stages in the τ-s relationship through the pull-out test, *Figure 3-49*. The first stage corresponds to uncracked concrete and low bond stress values $\tau<\tau_1$: the bond efficiency is due mainly to the chemical adhesion and to the micromechanical interaction associated with the rough steel surface. No relative slip at the concrete-steel interface occurs in this phase, the small slip displacement is related only to the shear deformations in concrete. In the case of plain bars, these adhesions are soon broken and the sliding of the bars characterizes the so called "pull-out failure", described by the softening branch of the law (*stage IVa- Figure 3-49*). The slope of this branch highly depends on the level of transverse confinement because the force transfer is provided by friction. In the case of deformed bars, a second stage takes place, which is characterized by the breakage of the chemical adhesions and by higher bond stress. Due to the stresses caused by the presence of lugs (*p*- Figure 3-50*), transverse microcracks at the tips of the bars lugs develop and allow local slip between the steel bars and the concrete. In the third stage the bond stresses are higher and because of the wedging action and the crushed concrete located in front of the lugs, longitudinal cracks, called splitting cracks, develop. In particular, the crushed concrete acts as a wedge against the surrounding concrete, pressure *p*** of *Figure 3-50*. As a consequence, the surrounding concrete applies a confinement action on the bar, which insures good bond strength. When a good transverse confinement is present, the concrete splitting remains limited to the cracked cored around the bar and the bond failure is caused by bar pull-out (*stage IVc-Figure 3-49*). Instead, in the case of light transverse reinforcement, the splitting cracks spread through the concrete cover until they reach the outdoor surface and a sudden splitting failure occurs (*stage IVb-Figure 3-49*). Finally, the residual bond stress is reached (asymptotic behaviour), due to the friction between concrete and steel bar caused by the bars sliding.

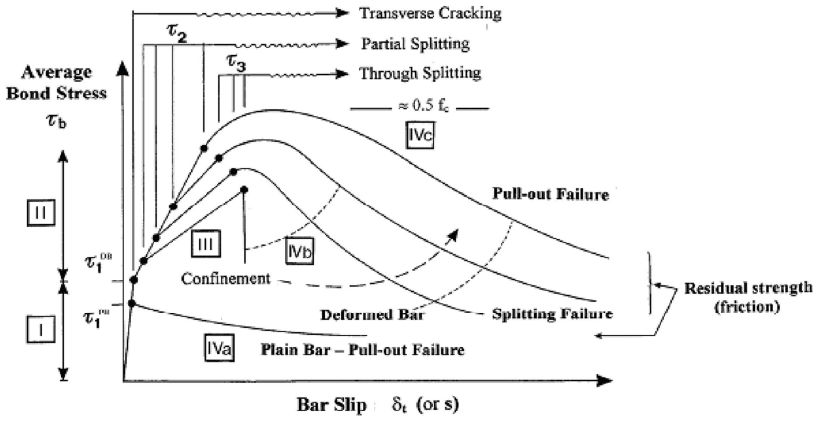

Figure 3-49: Local bond stress-slip law, Tassios[242]

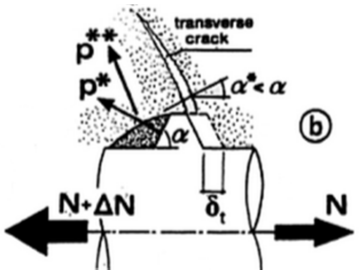

Figure 3-50: Bar-concrete slip and wedging action of the bar, Gambarova et al.[110]

The description of local bond behaviour has been reported for the better understanding of the two types of failure modes that characterize the composite interaction between concrete and steel reinforcement. In the case of pull-out mode, the failure is due to an interface collapse related to the shearing-off of the concrete keys. In the case of splitting mode, the bond reduces due to splitting and radial cracks, so the failure involves the area surrounding the reinforcement and lost the local nature, *Figure 3-51*. For long anchorages and splices, more complex failure modes may develop: for example pull-out failure induced by partial splitting, in which the shearing-off of the concrete keys is accompanied by concrete slip on rib faces, Addessi et al.[3], Cairns[48].

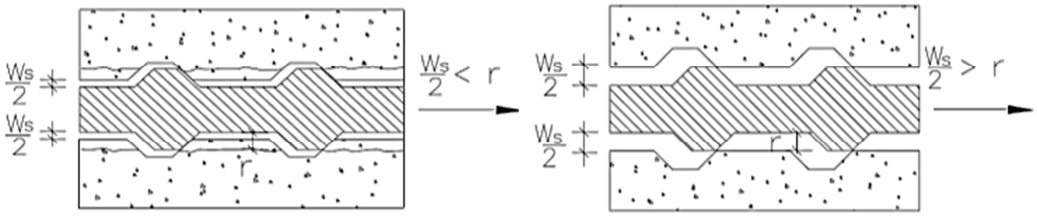

Figure 3-51: Pull-out and splitting local bond failure, Plizzari[205]

3.5.1.2 Factors affecting bond behaviour

According to the scope of this chapter to provide a brief recall of bond phenomenon, without aiming to give its complete description, in the next only the main factors affecting bond behaviour, which have importance in the definition of the bond stress-slip law, will be mentioned.

- Stress level and geometry of reinforcing bars: ribbed/plain bars, rib height, rib spacing and bar diameter, define the so called bond index, which provides an amount of the bond strength (Castel et al.[60], Daoud et al.[89], *fib* MC2010[106], *fib* Bullettin n°72[107], Hamad[116], Rehm[211]). The clear spacing between the bars, the number of bar layers and bundled bars, the bar position with the respect to the free surface have also a great influence on the bond properties, CEB-FIP MC90[61]. Finally, bond strength is dependent on the stress level in reinforcement: this has been demonstrated for plain reinforcing bars, e.g. in Bennett et al.[32] and still under investigation for ribbed bars. The experimental tests of Bigaj et al.[39] showed that the softening of the steel at yielding and the contraction of the steel bar have a negative influence on the bond-slip relationship. CEB-FIP MC90[61] takes implicitly into account the bar contraction, assuming a reduction of bond stress close to the crack, as proposed also by Eibl et al.[96].
- Concrete quality, strength and concrete section geometry: among others, Collepardi et al.[68] demonstrated that the concrete composition affects bond strength. The casting direction with respect to bar orientation is also important for the bond performances. In horizontal bars located at the bottom of the formwork and in vertical bars loaded perpendicular to the casting direction, the bond action is improved, *fib* MC2010[106]. The steel-concrete adherence depends also on both concrete multiaxial behaviour in compression and uniaxial strengths. In detail, the concrete uniaxial strength in compression and the concrete tensile strength, play the major role respectively, in pull-out and splitting failures (*fib* Bulletin n°10[105], Tassios[242]).
- Passive and active confinement: confinement is one of the most important parameters that influence bond efficiency. It can be active, resulting from loads transverse to the bar, e.g. resulting from a direct support, or passive, given by concrete cover and transverse reinforcement mainly. Den Uijl et al.[91] observed that the influence of confinement depends on the bond failure mode. Maeda et al.[167] noticed an increment of bond strength with the increasing of transverse reinforcement, for bond splitting failure. Eligehausen et al.[98] stated instead the non-influence of the amount of transverse reinforcement, once a transition from rib bearing to friction takes place. On the other hand, active confinement contributes always to increase bond strength, Eligehausen et al.[98] and Malvar[169].
- Environmental effects: among the environmental effects that influence bond behaviour, steel corrosion is the most important. This aspect will be amply discussed in paragraph 3.5.2.

3.5.1.3 Analytical models of the bond mechanism

A brief literary review regarding the τ-s laws for monotonic loading is here made. Following, ribbed bars and short anchorage conditions are considered, if not diversely specified. This implies that bars remain into the elastic field and the tangential stresses may be approximated as constant. Finally, it must be remember that the relationships available in literature to represent bond behaviour are not constitutive laws, but they represent a "structural" behaviour.

Tepfers[244] was the first to propose a model in which the concrete surrounding a single steel bar is characterized as a thick-walled cylinder subjected to internal shear and pressure. The bond strength is determined by the capacity of the concrete surrounding the reinforcing bars to carry the hoop stresses. In this way, the confinement effect of the stirrups and of the concrete cover is implicitly considered. Many authors have improved this model, among others the Den Uijl's et al.[91] model is able to considered both the pull-out and the splitting bond mechanics. The most qualified bond stress versus slip model, for monotonic loading, is the one proposed by Eligehausen et al.[98]. The model considers four different stages, which represent the four theoretical stages described in 3.5.1.1, *Figure 3-52*. CEB-FIP MC90[61] adopts the Eligehausen's et al.[98] model, distinguishing the splitting failure by the pull-out failure, through the definition of different values for the coefficients involved in the τ-s law, see *Table 3-1*.

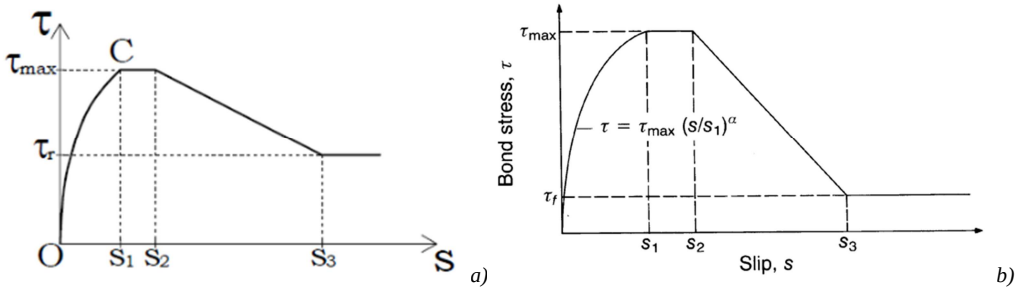

Figure 3-52. τ-s relationship-monotonic loading: a)Eligehausen et al.[98]; b)CEB-FIP MC90[61]

Table 3-1: Parameters for defining the mean bond stress-slip relationship

	*Unconfined concrete**		*Confined concrete†*	
	Good bond conditions	*All other bond conditions*	*Good bond conditions*	*All other bond conditions*
s1	*0.6 mm*	*0.6 mm*	*1.0 mm*	*1.0 mm*
s2	*0.6 mm*	*0.6 mm*	*3.0 mm*	*3.0 mm*
s3	*1.0 mm*	*2.5 mm*	*Clear rib spacing*	*Clear rib spacing*
α	*0.4*	*0.4*	*0.4*	*0.4*
τmax	$2.0\sqrt{fck}$	$1.0\sqrt{fck}$	$2.5\sqrt{f_{ck}}$	$1.25\sqrt{f_{ck}}$
τf	$0.15\,\tau max$	$0.15\,\tau max$	$0.40\,\tau_{max}$	τ_{max}

**Failure by splitting of the concrete; †Failure by shearing of the concrete between the ribs.*

The ascendant branch refers to penetration of the steel ribs into the concrete and the consequent local crushing and micro-cracking physical phenomena:

$$\tau = \tau_{max}\left(\frac{s}{s_1}\right)^{\alpha} \qquad 0 \le s \le s_1 \qquad \textit{Equation 3-40}$$

The second branch is the horizontal one, which occurs only for the confined concrete. Indeed, it represents the advancement of the concrete crushing and the shearing off of the concrete between the ribs, possible thanks a minimum amount of transverse reinforcement and concrete cover:

$$\tau = \tau_{max} \qquad s_1 < s \leq s_2 \qquad \textit{Equation 3-41}$$

The softening branch simulates the development of splitting cracks along the bar, for unconfined concrete, and the reduction of bond strength due to shearing of the concrete corbels between the ribs, for confined concrete:

$$\tau = \tau_{max} - (\tau_{max} - \tau_f)\left(\frac{s - s_2}{s_3 - s_2}\right) \qquad s_2 < s \leq s_3 \qquad \textit{Equation 3-42}$$

The last horizontal branch represents the residual bond stress, due to the presence of a minimum amount of transverse pressure:

$$\tau = \tau_f \qquad s > s_3 \qquad \textit{Equation 3-43}$$

Some authors have also introduced a reliance on the stress state of the steel bar, by discriminating the τ-s law for the steel yielded or in the elastic state. Among others, Shima et al.[229] added the dependency of the bond law, on to the deformation of the steel. *fib* MC2010[106] adopts the equations of CEB-FIP MC90[61], introducing some new aspects:

- In *fib* MC2010 the mean compressive strength of concrete f_{cm} is introduced in the bond definition, in place of the characteristic one f_{ck}. This leads to an increase of the bond strength respect to the past, for both pull-out and splitting failure, *Table 3-2*.
- In the case of pull-out failure, in CEB-FIP MC90 the change from "Good bond conditions" to "All other conditions" consists of a decreasing of bond strength. Instead, in *fib* MC2010 an extra-reduction of the stiffness of the ascendant branch and an extension of the plateau are also introduced, *Figure 3-53 a).*
- In the case of splitting failure, *fib* MC2010 distinguishes between the case of unconfined concrete – no presence of confining stirrups (no residual bond stress τ_f) and confined concrete – presence of confining stirrups (with residual bond stress τ_f), for both cases of "Good bond conditions" and "All other bond conditions". In CEB-FIP MC90 the splitting failure is distinguishes only between "Good bond conditions" and "All other bond conditions" and the residual bond strength is always provided, *Figure 3-53 b).*

CEB-FIP MC90[61] and *fib* MC2010 [106] specify that the laws proposed, have to be considered as an average formulation, due to the many parameters that influence the bond behaviour. The bond models do not necessarily concern uncracked concrete, so have a general validity.

Table 3-2: Parameters for defining the mean bond stress-slip relationship of deformed bars

	Pull-out (PO) $\varepsilon_s < \varepsilon_{s,y}$		*Splitting (SP)* $\varepsilon_s < \varepsilon_{s,y}$			
	Good bond conditions	*All other bond conditions*	*Good bond conditions*		*All other bond conditions*	
			unconfined	*stirrups*	*unconfined*	*stirrups*
τ_{bmax}	$2.5\sqrt{f_{cm}}$	$1.25\sqrt{f_{cm}}$	$2.5\sqrt{f_{cm}}$	$2.5\sqrt{f_{cm}}$	$1.25\sqrt{f_{cm}}$	$1.25\sqrt{f_{cm}}$
$\tau_{bu,split}$	-	-	$7.0\cdot\left(\frac{f_{cm}}{25}\right)^{0.25}$	$8.0\cdot\left(\frac{f_{cm}}{25}\right)^{0.25}$	$5.0\cdot\left(\frac{f_{cm}}{25}\right)^{0.25}$	$5.5\cdot\left(\frac{f_{cm}}{25}\right)^{0.25}$
s_1	*1.0 mm*	*1.8 mm*	$s(\tau_{bmax})$	$s(\tau_{bmax})$	$s(\tau_{bmax})$	$s(\tau_{bmax})$
s_2	*2.0 mm*	*3.6 mm*	s_1	s_1	s_1	s_1
s_3	*Clear rib spacing*	*Clear rib spacing*	$1.2\ s_1$	*0.5 Clear rib spacing*	$1.2\ s_1$	*0.5 Clear rib spacing*
α	*0.4*	*0.4*	*0.4*	*0.4*	*0.4*	*0.4*
τ_{bf}	$0.40\ \tau_{bmax}$	$0.40\ \tau_{bmax}$	*0*	$0.40\ \tau_{bmax}$	*0*	$0.40\ \tau_{bmax}$

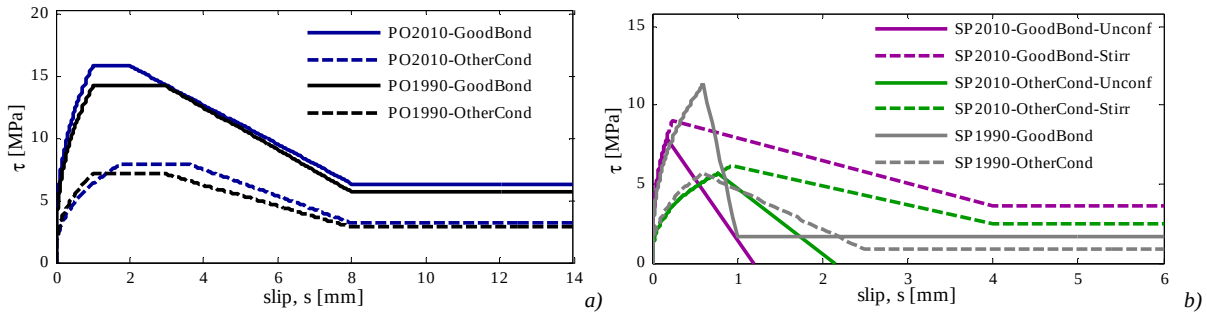

Figure 3-53: Comparison between bond stress-slip relationship-monotonic loading proposed in CEB-FIP MC90[61]and fib MC2010[106] – a) Pull-out failure: Good bond conditions and All other conditions; b) Splitting failure: Good bond conditions and All other conditions.

Nilson[191], Tassios et al.[243], KanKam[142] and many others, proposed experimental bond laws depending on the slip and on the distance from the crack. Langer[150] added to these models, the case of splitting failure. CEB-FIP MC90[61] and *fib* MC2010, suggest to reduce the parameters that define the τ-s relationship, in the zone close to a transverse crack. Moreover, in order to consider the influence of the reinforcement yielding, of the transverse pressure, of the cracking parallel to the bar axis and of the cyclic loading, the *Equation 3-40* to *Equation 3-43* may modified by the factors Ω_y, $\Omega_{p,tr}$, Ω_{cr}, Ω_{cyc} respectively. Finally, the bond model proposed by Giuriani et al.[113] considered also the concrete properties, the confinement effect and the width of the splitting cracks.

3.5.1.4 Changing of bond failure mode from pull-out to splitting

Both CEB-FIP MC90[61] and *fib* MC2010[106] consider the passive confinement effect on bond strength, differentiating the case of "unconfined concrete" and "confined concrete", *Figure 3-53*. In CEB-FIP MC90[61] the bond stress-slip law for unconfined concrete is defined for concrete cover/bar diameter (c/Φ) equal to 1 and a minimum amount of transverse reinforcement $A_{st,min}$. Instead, the conditions to define a well confined concrete are: $c/\Phi \geq 5$, clear spacing between bars $> 10\Phi$ or closely spaced transverse reinforcement with area greater than the total area of the bars enclosed by the stirrups or high transverse pressure $p \geq 7.5$ MPa. In *fib* MC2010[106] the definition of well confined concrete is: $c/\Phi \geq 5$, clear spacing between bars $\geq 10\Phi$, or suitable confining reinforcement. Moreover, in *fib* MC2010[106] also the influence of reinforcement yielding and transverse pressure on the bond stress-slip law are introduced. In particular, the positive effect of transverse compression pressure is highlighted (*Figure 3-54*): it retards the onset of splitting failure, especially in the case of low confinement from concrete cover and stirrups, and it increases the frictional force at the bar/concrete interface, Cairns[48].

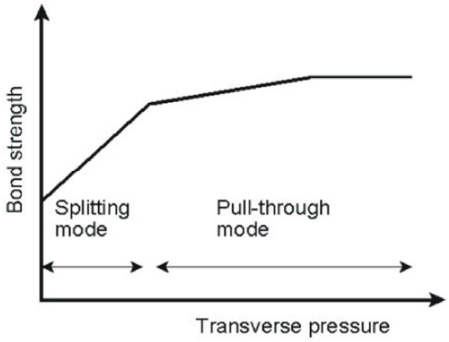

Figure 3-54: Influence of transverse pressure

In both CEB-FIP MC90[61] and *fib* MC2010[106], the τ-s relationship is not defined as a continuous function of the concrete cover value, but it is given for two discrete values of the concrete cover. For intermediate levels of confinement, the s_1, s_3, τ_{max} and τ_f parameters may be interpolated linearly between the values given for unconfined and confinement concrete, an example for good bond condition is shown in *Figure 3-55*.

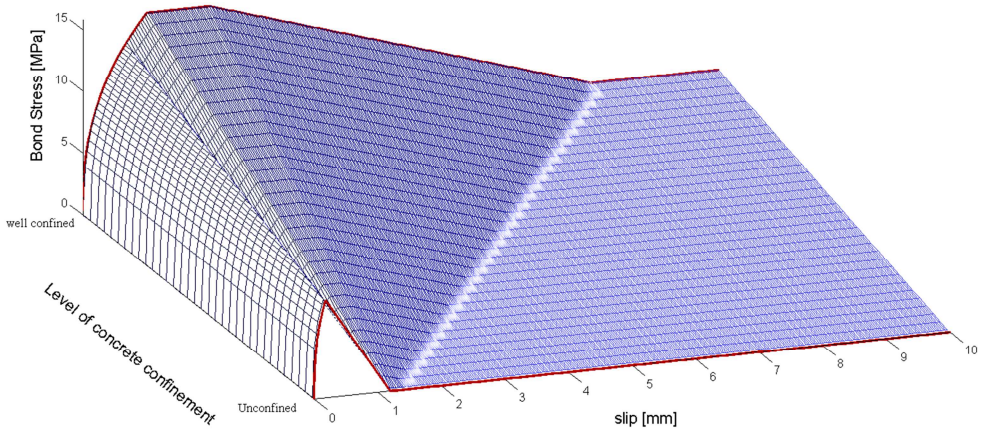

Figure 3-55: fib MC2010[106], analytical bond stress-slip relationship (monotonic loading) for different levels of concrete confinement and good bond condition

Torre-Casanova et al.[248] underlined and proved the effect of an increasing concrete cover depth on the changing of the bond failure mode from splitting to pulling. In detail, the authors carried out an experimental campaign in order to investigate the effects of active and passive confinement on the bond strength. A higher value of bond strength, in comparison with the values reported by other authors, was found. The authors attributed this result to the greater value of c/Φ (equal to 7) adopted in their experimental test. Moreover, they showed the non-influence of the active confinement on the bond strength, in the case of pull-out failure mode and high values of c/Φ. In order to prove these remarks, a numerical investigation was made, which has underlined the dependency of the bond strength and of the bond failure mode on the c/Φ value, *Figure 3-56*, in well agreement with what found by others authors, e.g. Tepfers[245].

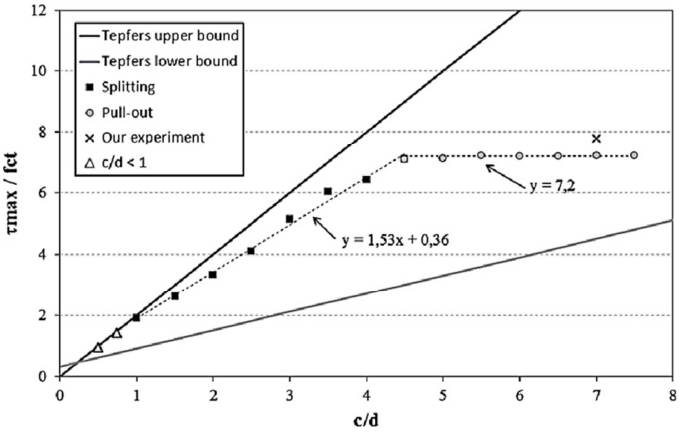

Figure 3-56 Bond strength evolution as function of c/Φ, Torre-Casanova et al.[248]

The authors proposed also a simply equation to determinate the concrete cover that corresponds to a change from a splitting failure to a pull-out failure, obtaining values similar to RILEM[216]:

$$\left(\frac{c}{\Phi}\right)_{splitting\ to\ pull-out} = 0.39\frac{f_c}{f_t} - 0.24 \qquad \textit{Equation 3-44}$$

Equation 3-44 was found considering the continuity of the the two bond failure mode, splitting and pull-out, given as function respectively of f_t and f_c. Indeed, the authors demonstrated that the splitting failure is governed by concrete tensile properties and the bond has a linear evolution respect to c/Φ (first branch of *Figure 3-56*). The pull-out strength is instead a constant function of the concrete compressive strength (second branch of *Figure 3-56*). Finally, the numerical analysis demonstrates the non-influence of an active confinement on bond strength in the case of thick concrete covers. The active confinement was found effective only for low c/Φ, for which it led to an increase of bond strength. These conclusions validate the previous experimental results.

Eligehausen et al.[98] carried out an extensive experimental campaign (125 pull-out specimens were tested) in order to find a local bond stress-slip relationship for deformed reinforcing bars subjected to generalized excitations. Among the other investigations made, the authors evaluated the influence of the passive confinement effect. A clear difference between the tests results with or without stirrups was found, *Figure 3-57 a).* Specimens without confining reinforcement failed by splitting of the concrete at a small bond stress. On the opposite side, confined specimens failed by bars pulling out: the vertical bars crossing the longitudinal splitting crack development were demonstrated to be the most effective in increasing bond strength. Furthermore, the authors proved the existence of an upper limit for an effective restraining reinforcement, beyond which the bond behaviour cannot be further improved. The authors did not test intermediate case of transverse confining in order to evaluate the transition point between pulling out and splitting bond failure. It is worth noting that the authors made pull-out tests for both tension and compression loading, finding that the bond stress-slip relationship is almost identical, *Figure 3-57 b).* This result could be expected because the bars were cast in a horizontal position and the steel stresses were below the yield. After yielding, the diameter of a bar in tension is reduced due to the Poisson effect, which may reduce the bond resistance. The opposite is true for a bar yielding in compression. Cowell et al.[83] and Viwathanatepa et al.[264] suggested that the Poisson effect increase the bond resistance of about 20-30%.

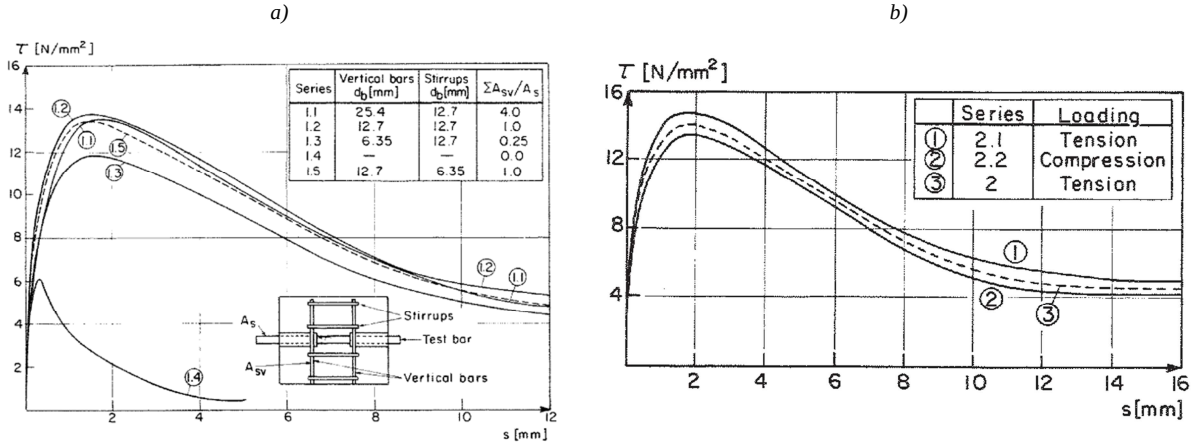

Figure 3-57: a)Influence of transverse reinforcement on τ-s relationship; b)Influence of the direction of loading (tension or compression) on τ-s relationship, Eligehausen et al.[98]

Giuriani et al.[113] evidenced the influence of transverse reinforcement on the bond failure mode by a theoretical point of view. The splitting of the concrete around the steel bar, produced by the radial action provoked by the ribs, at the beginning is controlled by the confining action given by the tensile strength of the uncracked concrete (*Figure 3-58*), as observed also by other authors, e.g. Tepfer[245]. When splitting cracks propagate and become wider, the transverse confinement (stirrups and residual tensile strength of cracked concrete) becomes the most important actions

that equilibrates the radial pressure, in particular for bigger bar diameters (Φ>14 mm) or higher slip values. The authors also stated that when the amount of transverse reinforcement is evenly distributed and not negligible in the cracked area, the local confinement of each transverse bar is more relevant with respect to that produced by restraints and external loads.

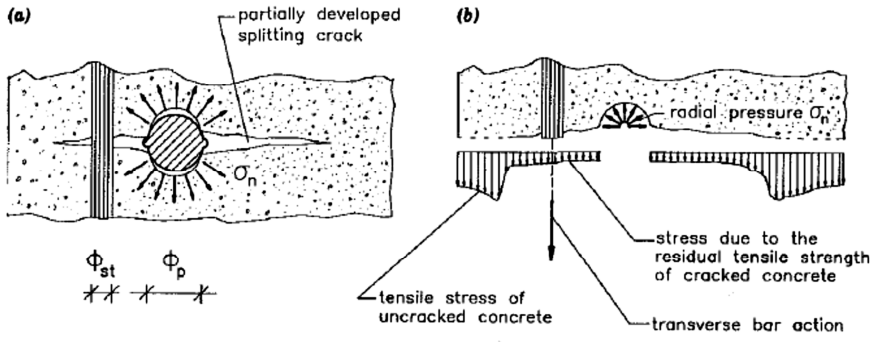

Figure 3-58: Splitting crack and confining actions around a ribbed bar, Giuriani et al.[113]

The authors proposed an equation in order to calculate the bond stress τ and the correspondent slip s, as function of the confining action provided by the transverse reinforcement and the residual tensile stress transmitted by the faces of the splitting crack, of width w_{cr}. The results proved that, a small amount of transverse reinforcement is sufficient to prevent the splitting failure, in well agreement with the experimental results found by Eligehausen et al.[98]. In detail, the authors showed how an increasing values of stirrups diameter, number of legs of stirrups and a reduction of the stirrup spacing, increase the bond resistance after splitting occur, *Figure 3-59.*

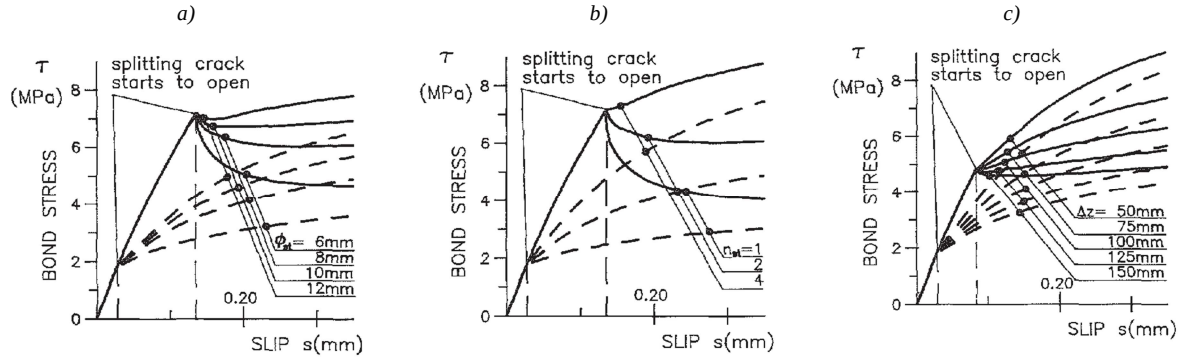

Figure 3-59: Role of stirrup a) diameter; b) leg number; c) spacing.Dashed curves refer to the case without any residual tensile strength of cracked concrete, Giuriani et al.[113]

3.5.2 Corrosion-induced bond degradation

Bond behaviour in corroded reinforced concrete has been well investigated in the last decades by many researches, experimentally and analytically. A wide literary production is available. However, due to the complexity of the phenomenon and the several parameters involved, it is difficult to generalize the results obtained. The majority of the researchers (Almusallam et al.[6], Al-Sulaimani et al.[9], Lee et al.[154], Mangat et al.[172], Shima et al.[230]) identified in the reduction of bond strength, the main consequence of reinforcement corrosion on the composite interaction between steel and concrete, *Figure 3-60*. Some authors (Bhargava et al.[38], Cabrera[45], Lee et al.[154]) proposed also empirical relationships between the level of corrosion and the ultimate bond strength. However these relationships depend on the type of test, on the characteristics of the concrete material and on the geometry of the specimen considered, so they must be analysed with a critical thinking. Almusallam et al.[6], Al-Sulaimani et al.[9], Cairns et

al.[52], Mangat et al.[172] noticed that for low levels of reinforcement corrosion, the bond strength increases, *Figure 3-60.* Only few authors, e.g. Lundgren[165] and Mancini et al.[170] tried to summarize the literature data available for the better understanding of the influence of reinforcement corrosion on bond.

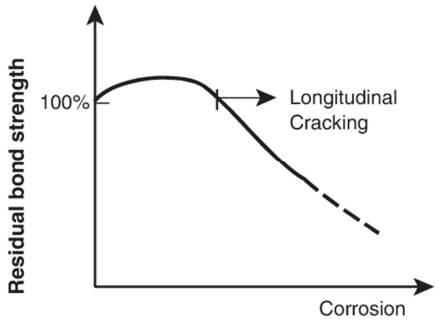

Figure 3-60: Influence of corrosion on residual bond strength, Cairns et al.[52]

Following these remarks, in the next paragraph the experimental results available from pull-out and beam tests are divided basing on the presence or the absence of transverse reinforcement. Particular attention will be paid also to the value of c/Φ ratio in the specimens, in order to consider also this parameter in the definition of the level of confinement.

3.5.2.1 Experimental test on specimens with stirrups

Specimens with transverse reinforcement and different values of c/Φ have been subjected to pull-out and beam-flexural tests by Al-Sulaimani et al.[9], Fang et al.[101], Lee et al.[154] and Shima [230]. Following, a brief description of the experimental tests made is reported.

Al-Sulaimani et al.[9] (1990) tested two types of RC beams with different sizes, 150x150x1000mm and 150x150x3000mm with respectively embedment length L_b of 144 mm and 300 mm (values recommended by ACI codes), in order to study the corrosion-bond behaviour in normal beams, failing respectively in bond or in flexure. The beam specimens were located in water and a constant current density of 2000 $\mu A/cm^2$ was impressed on the bar embedded, for different periods, in order to evaluate the bond behaviour in uncorroded, precracking, cracking and postcracking conditions. For the first type of beams and for low levels of corrosion, a considerable increase of bond strength was detected. When the longitudinal cracks appeared, a strong reduction of the bond strength was found (0.5% of corrosion). After that the bond strength decreases staying always 1.5 times above the values permitted by ACI codes, see *Figure 3-61*. This can be explained considering the confinement given by the stirrups in the beams (Φ6/50mm) and the high value of c/Φ (about 3).

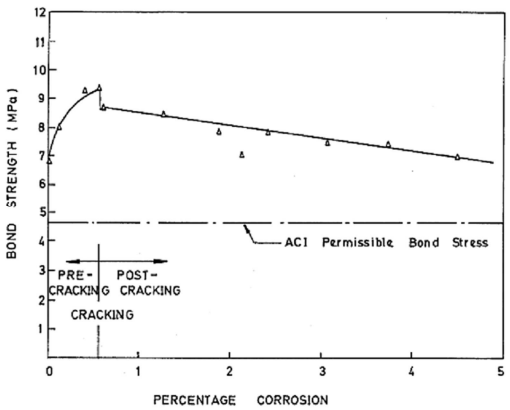

Figure 3-61: Bond stress-level of corrosion - beams 150x150x1000mm, Al-Sulaimani et al.[9]

Lee et al.[154] (2002) carried out pull-out tests, corroding the embedded reinforcement with an accelerated electric method, in order to find a relationship between the percentage of corrosion and the maximum bond strength and the bond stiffness. The pull-out tests were conducted at different degree of reinforcement corrosion, different compressive strength of concrete and different values of concrete cover. Specimen had dimensions of 8Φx8Φ, with Φ equal to 13 mm, and bonded length of the reinforcement equal to 6Φ. A constant current of around 800 μA/cm^2 was applied for different periods, then the corrosion percentage was determined by measuring the weight loss by the steel bars, after removing the rust. Specimens with stirrups were fractured by slipping of reinforcement due to the confinement effect, given also by the high c/Φ (equal to 3.5). As explained by the authors, the presence of transverse reinforcement prevented a splitting failure (*Figure 3-62*). As the corrosion percentage increased, the maximum bond stress τ_{max} decreased, before moderately (for a corrosion level of 13%, the bond strength reduction was of 11.6%) and after heavily (for a corrosion level of 24%, the bond strength reduction was of 38.6%).

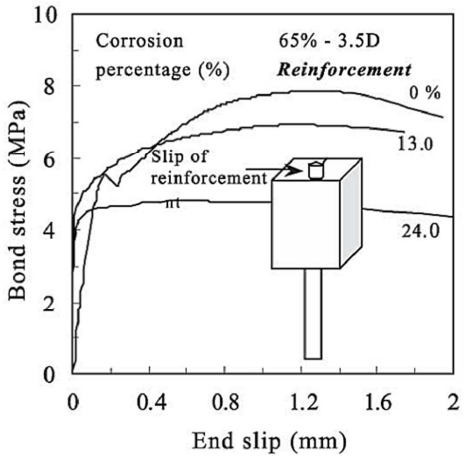

Figure 3-62: Bond stress-end slip curve- specimens with transverse reinforcement

Shima[230] (2002) carried out one-side pull-out tests of corroded steel bars with long embedment in order to study the effect of different values of concrete cover (10-25-40 mm) and degree of corrosion (from 0% to 30%) on the local bond stress-slip relationship. All the specimens tested had dimensions of 400x300x500 and transverse reinforcement (Φ10mm/100mm), except one single case. The longitudinal bar had diameter of 22.3 mm and yield and tensile strength respectively of 606 MPa and 796 MPa. Specimens were soaked in artificial salt solution of 3.3% weight concentration and subjected to a constant electric current of 2800 μA/cm^2 density. The degree of corrosion was represented by the ratio of weight loss. For low c/Φ and presence of stirrups, the bond strength slightly decreased with the increasing of corrosion level (*Figure 3-63 a)-series IV*). For higher c/Φ, the author found a rather high loss of bond strength (*Figure 3-63 a)-series II and III)* also in presence of transverse reinforcement, probably due to the fact that the stirrups were arranged only on one side *(Figure 3-63 b))*. The specimen without transverse reinforcement showed the highest degree of reduction with increasing corrosion levels (*Figure 3-63-series I*), until to reach the 40% of the original bond strength, after that the bond strength remained constant. The author also analysed the decrement ratio of stiffness for corroded bars, finding that it remains almost constant with increasing corrosion levels: the maximum reduction was found to be of 14%, for a corrosion level of 30% and no transverse reinforcement.

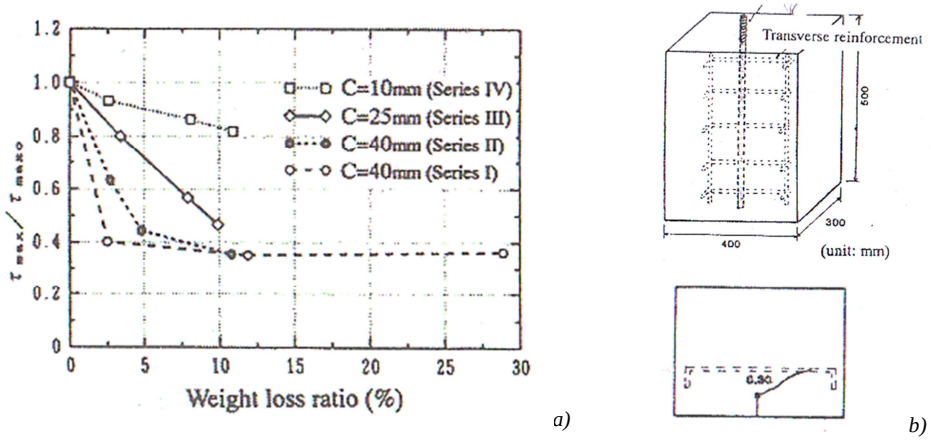

Figure 3-63:; a)Relation between corroded ratio and maximum local bond stress; b)Geometry of the tested specimens, Shima et al.[230]

Fang et al.[101] (2004) performed pull-out test on specimen of size 140x140x180mm, with one central bar of 20 mm diameter and presence of stirrups of 6 mm diameter located in the embedment length (L_b=80 mm) and with a spacing of 40 mm. The authors tested both smooth and deformed bars, here only the results obtained for the deformed ones are reported. The specimens were immersed in NaCl solution for 3 days and then subjected to an average current density of 1200 μA/cm^2. To avoid corrosion of the stirrups, these were isolated from the main bar. The authors carried out pullout tests until a steel mass loss of 6%. For this levels of corrosion, only a slightly reduction of the bond strength, of about 12%, was obtained, *Figure 3-64.* The authors underlined the positive effect of confinement on the control of the splitting cracks developed due to corrosion. Furthermore, they observed that the slope of the softening branch of the load-slip curves only slightly decreased between corrosion levels equal to 3.8% and 6.0%, confirming the non-influence of corrosion on the ultimate slip of the τ-*s* law, for specimens with stirrups.

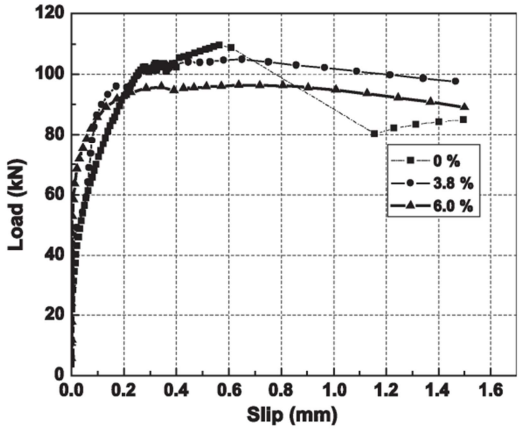

Figure 3-64: Load-slip relationship -specimens with stirrups, Fang et al.[101]

3.5.2.2 Experimental test on specimens without stirrups

Pull-out and beam-end tests on specimens without transverse reinforcement are the most common type of experiments. Several authors have studied the effects of corrosion on the local bond-slip relationships obtained with this type of tests.

Almusallam et al.[6] (1996) carried out a series of bond tests on 152x254x279mm cantilever beam specimens, with one reinforcement central deformed bar of 12 mm diameter and an embedment length L_b of 102 mm. The specimens were subjected to a high constant current of 3500 μA/cm^2, in order to accelerate the reinforcement corrosion. The amount of corrosion was

measured as gravimetric loss in weight by the reinforcing bars. It is worth nothing that two U shape shear reinforcing bars were collocated in the specimen, similarly to Shima et al.[230]. However, in this case the main bar was located outside of the confinement area (*Figure 3-65 a)*. The authors defined four stages of corrosion, similarly to Al-Sulaimani et al.[9]: a zero corrosion phase; a pre-cracking phase (0-4% of corrosion); a cracking phase (4-6% of corrosion) and a post-cracking phase (corrosion level beyond 6%). In *Figure 3-65 b)* is reported the relationship between the ultimate bond strength and the level of corrosion found by the authors. In the pre-cracking phase the bond strength visibly increases (+15%), due to the expansion of the corrosive products. Then, in the cracking phase, the bond strength falls rapidly down and the failure mode changes to a continuous slippage. Finally, the bond strength reaches an approximately constant value (at about 15% of corrosion level), due to the friction between the rusty bars and the concrete. In *Figure 3-66* are reported the Load-slip curves for the different phases. It is evident the decrease in the slip at which the maximum bond strength is reached, with the increasing of the corrosion level. The stiffness of the first branch instead does not present an evident decrease. The slope of the softening branch (which lies between the maximum bond strength and the beginning of the constant bond strength) decreases, confirming the changing from pullout to splitting failure, for high levels of corrosion.

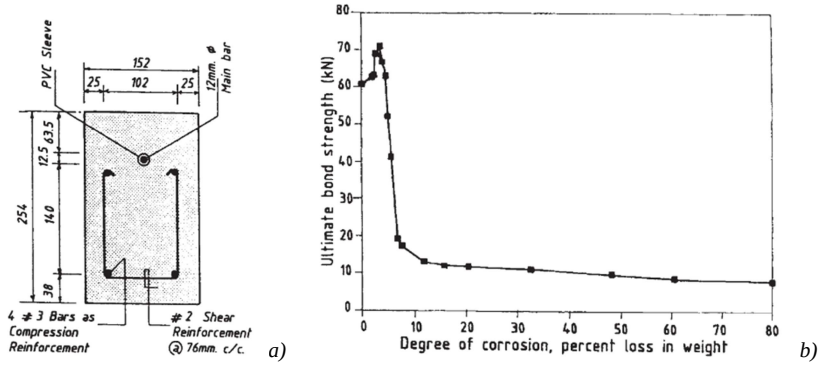

Figure 3-65: a) Tested specimens; b) Bond strength-corrosion level, Almusallam et al.[6]

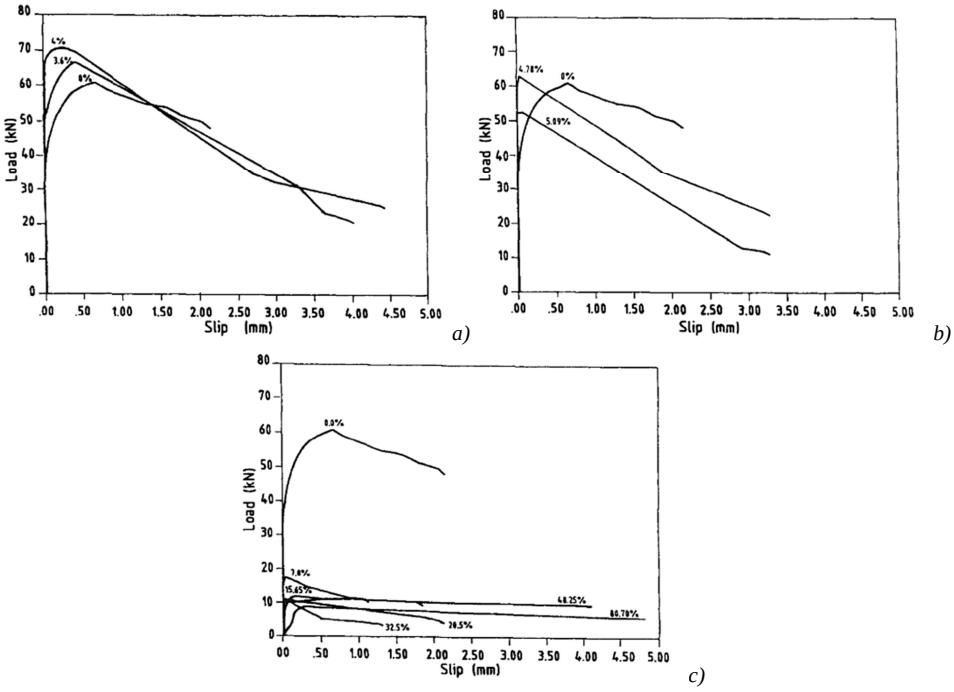

Figure 3-66: Load-slip curves: a)precracking stage; b)cracking stage; c)postcracking stage, Almusallam et al.[6].

Mangat et al.[172] (1999) made an experimental investigation on the bond strength in corroded reinforced concrete beams, made up of two halves RC beams linked by a hinge mechanism, in order to allow for rotation the two concrete parts. The two beams, each of size 100x150x430mm, were immersed in a 3.5% NaCl solution and subjected to an accelerated corrosion procedure, by impressing a direct current of intensity 800 μA/cm^2 (2400 μA/cm^2 only to reach the corrosion level of 5%) for different periods, in order to achieve diverse degrees of corrosion. Then the specimens were tested under four point bending to induce bond failure. Since no stirrups were provided inside the specimens, in order to avoid shear failure external steel collars were located for all the size of the shear spans. In *Figure 3-67 a)* load versus free-end slip curves at different degrees of corrosion, experimentally obtained, are reported. For the lower levels of corrosion, between 0% and 0.4%, a strong increase of the bond strength and none free-end slip can be observed, before the complete break-down of the bond. At higher degrees of corrosion, between 0.5% and 5%, free-end slip can be noticed from the onset of loading. In *Figure 3-67 b)* is reported the relationship between the maximum flexural load at bond failure and the degree of corrosion. In detail, for corrosion levels lower than 0.4%, the bond strength increases (+25% of τ_{max0}), despite the formation of small cracks along the reinforcement, caused by the expansion of the corrosion products. For degree of corrosion greater than 0.4%, the maximum bond strength decreases with the increasing of corrosion: at corrosion level of 5%, the maximum bond strength is reduced by over the 50% of the uncorroded capacity bond. In these tests, also the slip at the maximum load linearly increases with the increasing of the corrosion level, after 0.4%. The stiffness of the load-slip curves shows also a decrease with the increasing of corrosion level.

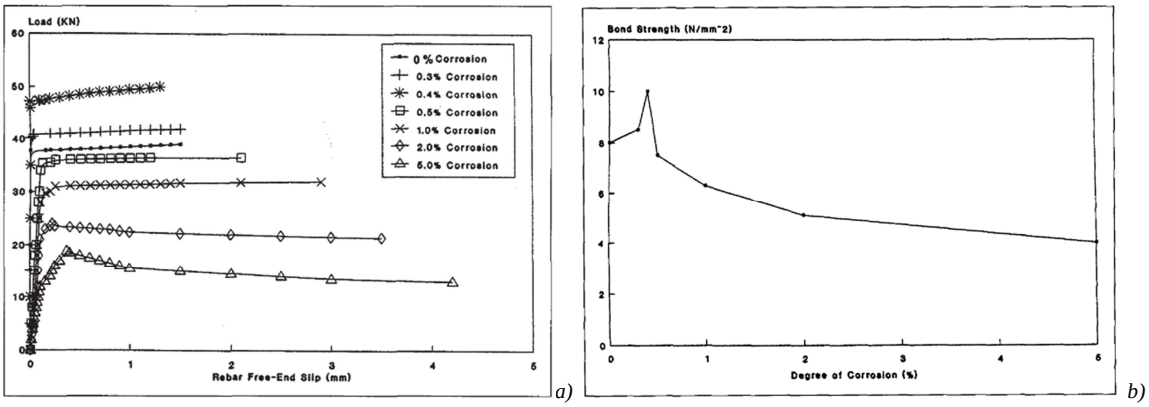

a) *b)*

Figure 3-67: a)Load-slip relationships of the flexural bond tests; Relationship between maximum bond strength and degree of corrosion, Mangat et al.[172].

Al-Sulaimani et al.[9] (1990) performed also pull-out tests. The specimens of size 150x150x150 mm, with one central embedded bar of 10-14-20 mm diameter and L_b/d=4, were subjected to a constant current density of 2000 μA/cm^2 and then to a pull-out test. In *Figure 3-68 a)* the bond stress versus free-end slip curves, for different levels of corrosion, are reported. *Figure 3-68 b)* shows instead the bond strength versus the level of corrosion. For low levels of corrosion (up to 1.5%), the bond strength is considerably higher than the bond strength detected in absence of corrosion (up to 50% more). For higher levels of corrosion, the bond strength drops down fast, until it reaches a residual value for corrosion levels around 6-9%. This is due to the degradation of the bar lugs, the reduction of the steel section, the lubricating effect of the flaky corroded metal and the reduction of the confinement effect due to the cracking of the concrete cover. In these pullout tests, the effect of different values of the c/Φ ratio was also investigated. The authors found that lower values of corrosion are required, to initiate concrete cracking, for lower value of the c/Φ ratio. From the experimental results, the main effect of corrosion results to be the

reduction of the bond strength, in the cracking stage. Also the bond stiffness decreases with increasing levels of corrosion, as also the slope of the softening branch. Beyond that, all the bar sizes lost bond strength at a similar rate. This suggests that the differences in bond strength may be linked to the amount of corrosion required to generate a sufficient level of internal micro-cracking necessary to start the bond degradation. Higher *c/Φ* ratios, require a greater amount of corrosion to develop the internal micro cracking.

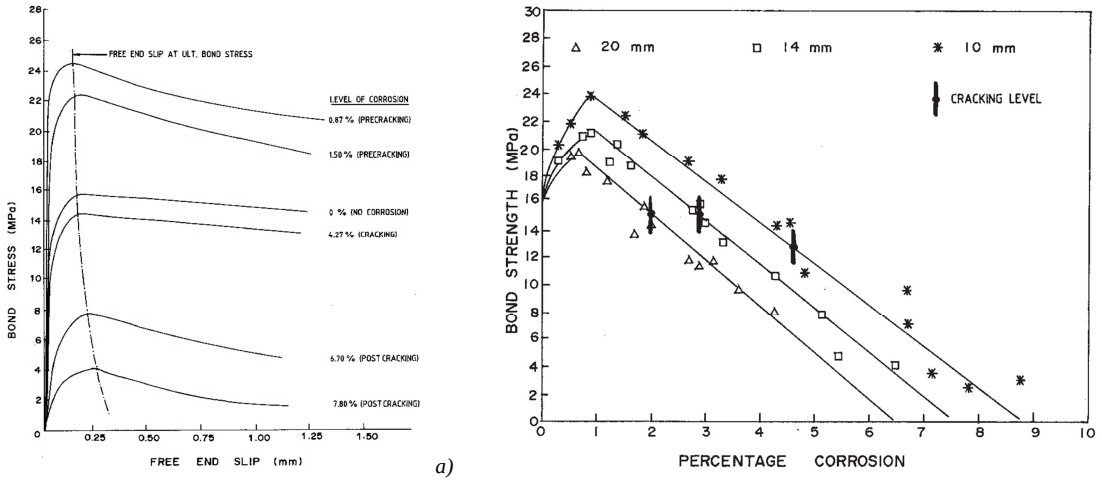

Figure 3-68: a)Bond stress versus free-end slip- different levels of corrosion, d=10 mm; b) Bond strength versus level of corrosion, d=10-14-20 mm; pullout specimens, Al-Sulaimani et al.[9].

Lee et al.[154] (22002) carried out pull-out tests with corroded embedded reinforcement also in absence of transverse reinforcement. The characteristics of the specimens and of the experimental tests have been already described in paragraph 3.5.2.1. In *Figure 3-69* are reported the experimental results, in terms of bond stress-slip curves and in terms of maximum bond strength versus corrosion percentage, found for the case of concrete strength of 24.7 MPa and *c/Φ*=3.5. The authors observed a reduction of bond strength due to the split of concrete when cracks developed. In the case of reinforcement corrosion, the bond strength is abruptly lost, due to the absence of transverse bars, and it happens earlier. It is worth noting that, if we apply *Equation 3-44*, given by Torre-Casanova[248] at this case, the value of the *c/Φ* is very close to the one that defines the transition from splitting to pull-out failure, in contrast with the other experimental tests reported until now by other authors. This explains both the splitting failure characterizing the tests and the rapidly loss of bond strength for low levels of corrosion.

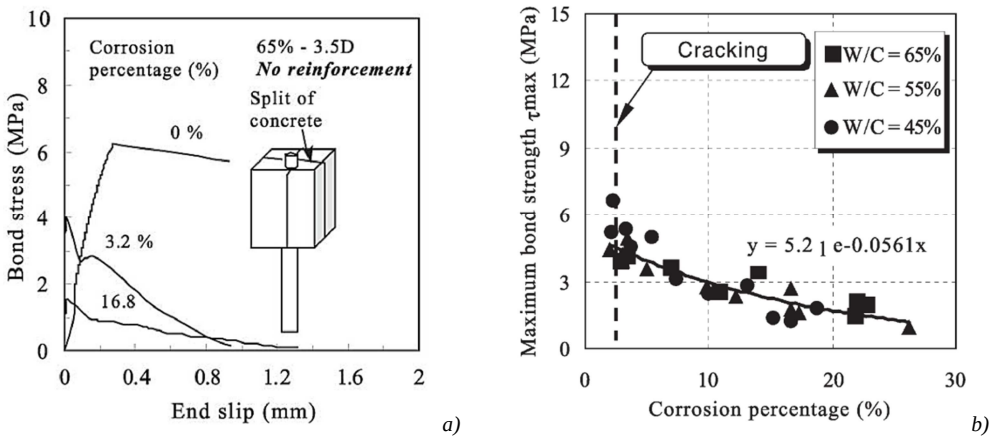

Figure 3-69: a) Bond stress-end slip curve: no lateral reinforcement; b) maximum bond strength - corrosion percentage, Lee et al.[154]

Fang et al.[101] (2004) made pull-out tests with specimens without transverse reinforcement. The characteristics of the specimens and of the experimental tests have been already described in paragraph 3.5.2.1. *Figure 3-70* shows the load versus free-end slip relationship for different corrosion levels: 0%, 4.0% and 9.0%. For the uncorroded specimen, a sudden drop at ultimate load can be observed in load–slip curve, caused by the sudden splitting of the concrete cover over the bar. As the corrosion level increases, a substantial degradation of the bond strength is noticed (-45.5% of the load for corrosion of 4%). Also the corresponding free-end slip at the ultimate load decreases: from 0.56 mm through 0.097 mm and then to 0.064 mm. In *Figure 3-71* is reported a comparison between the specimens with and without stirrups: the bond strength drops down fast in the case of absence of transverse reinforcement. In confined specimens, instead, corrosion does not substantial influence the bond strength. Finally, it must be noticed that also in these tests, the value of the c/Φ ratio of the specimens is near to the transition value from splitting to pull-out defined by Torre-Casanova[248] in *Equation 3-44*. Therefore a bond splitting failure and a dependency of bond strength on corrosion were expected.

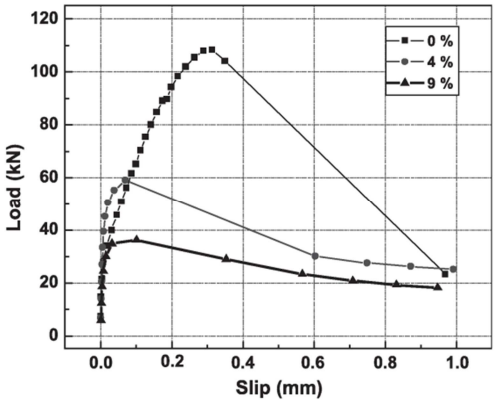

Figure 3-70: Load-slip curves for deformed reinforcing bar without stirrups, Fang et al.[101]

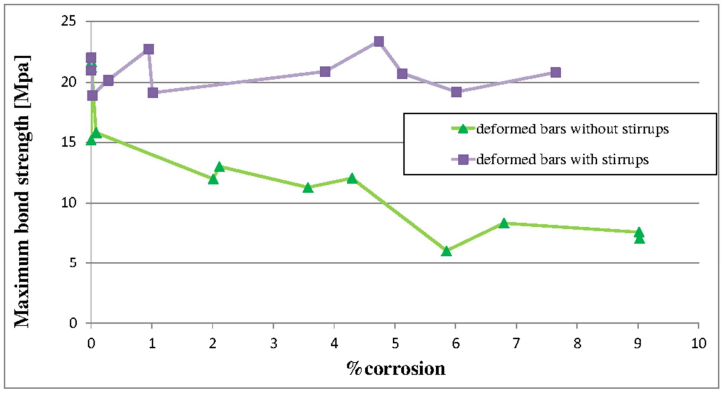

Figure 3-71: Effects of corrosion on bond strength, for deformed bars without and with stirrups, data of Fang et al.[101]

3.5.2.3 Modelling of bond degradation due to corrosion

The quantitative effect of corrosion on bond strength has been extensively studied also through a theoretical point of view and some empirical and analytical models have been proposed. It should be noticed that the amount of the bond strength decrease depends on numerous variables. Therefore the value of the degraded bond strength $\tau_{max}^{degraded}$ cannot be exactly defined. A summary of the equations provided by different authors for the evaluation of $\tau_{max}^{degraded}$ starting from the level of corrosion X (percentage of mass loss by corroded bars) is given in *Table 3-3*.

Most of the researchers have proposed linear or exponential correlations between the bond strength and the level of corrosion:

$$\tau_{max}^{degraded} = A + B \cdot X^{c} \qquad \textit{Equation 3-45}$$

$$\tau_{max}^{degraded} = A + B \cdot e^{C \cdot X} \qquad \textit{Equation 3-46}$$

where the parameters A, B and C are obtained by linear regression of the experimental data.

Table 3-3. Review of existing empirical and analytical equations proposed to account for the effects of corrosion (X) on bond strength

Author	*Equation*	*Test conditions*
Cabrera[45]	$\tau_{max}^{degraded} = 23.478 - 1.313X\ [MPa]$	*150mm cubes – Pull-out tests – Unconfined specimens*
Lee et al.[154]	$\tau_{max}^{degraded} = 0.34f_c - 1.93 \quad before\ cracking\ [MPa]$ $\tau_{max}^{degraded} = 5.21e^{(-0.0561X)} \quad after\ cracking\ [MPa]$	*8Φ cubes – Pull-out tests – Unconfined specimens*
Stanish et al. [236]	$\tau_{max}^{degraded} = \sqrt{f'_c}\,(0.77 - 0.027X)\ [MPa]$	*One-way slabs – Flexural tests – Unconfined specimens*
Chung et al. [66]	$\tau_{max}^{degraded} = \tau_{max}^{sound} \quad X \leq 2$ $\frac{\tau_{max}^{degraded}}{\tau_{max}^{sound}} = 2.09X^{(-1.06)} \quad X > 2$	*One-way slabs – Flexural tests – Unconfined specimens*
Chung et al. [67]	$\tau_{max}^{degraded} = \tau_{max}^{sound} \ X \leq 2\%\ [MPa]$ $\tau_{max}^{degraded} = 24.7X^{-0.55} \ X > 2\%\ [MPa]$	*150mm cubes – Pull-out tests – Unconfined specimens*
Bhargava et al.[38]	$\tau_{max}^{degraded} = \tau_{max}^{sound} \quad X \leq 1.5\%\ [MPa]$ $\frac{\tau_{max}^{degraded}}{\tau_{max}^{sound}} = 1.192X^{(-0.117X)} \quad X > 1.5$	*Literature review – Pull-out tests – Unconfined specimens*
	$\tau_{max}^{degraded} = \tau_{max}^{sound} \quad X \leq 1.5\%\ [MPa]$ $\frac{\tau_{max}^{degraded}}{\tau_{max}^{sound}} = 1.346e^{-0.198X} \quad X > 1.5$	*Literature review – Flexural tests – Unconfined specimens*
Rodriguez et al. [219]	$\tau_{max}^{degraded} = 0.6\left(0.5 + {}^{c}/_{\Phi}\right)f_{ct}(1 - \beta \cdot X^{\mu}) + \frac{k\,A_s\,f_y}{s\,\Phi}\ [MPa]$	*300mm cubes – Eccentric pull-out tests – Confined and Unconfined specimens*
Rodriguez et al. [221]	$\tau_{max}^{degraded} = 5.25 - 2.72X \quad X > 1mm\ \rho > 0{,}25 \ \ [MPa]$	*300mm cubes – Eccentric pull-out tests – Confined specimens*
	$\tau_{max}^{degraded} = 3 - 4.76X \quad X < 1mm\ [MPa]$	*300mm cubes – Eccentric pull-out tests –Unconfined specimens*
Li et al. [160] (2014)	$\frac{\tau_{max}^{degraded}}{\tau_{max}^{sound}} = 0.9959e^{0.0041X} + 0.0069e^{0.7858X} \quad X \leq 4$	*Based on the experimental tests of Almusallam et al.[6] - Unconfined specimens*
Coronelli[79] (2002)	$\tau_{max}^{degraded} = k(x)p^{max}(x) + \tau_b^0(x) + \mu(x)p_{corr}(x) \quad [MPa]$	*Analytical approach*
Hussein [126] (2011)	$\tau_{max}^{degraded} = \mu(x)p_{conf}(x) + \mu(x)p_{corr}(x) + \tau_{AD}(x) \quad [MPa]$	*Analytical approach*
Wu[272] (2012)	$\tau_{max}^{degraded} = \mu(x) \cdot \left[p_{c,c}(x) + p_{c,st}(x) + p_{corr}(x)\right] \quad [MPa]$	*Analytical approach*

As observed also by Chung et al.[66], the linear correlations do not properly capture the gradual bond strength reduction, see *Figure 3-72*. Furthermore, almost all the proposed formulas have been developed in the case of unconfined specimens. One experimental study that considers the parameters defining the confining action is the one of Rodriguez et al.[219]. The formula proposed by the authors, distinguishes the two terms related respectively to concrete and transverse reinforcement contribution. It was obtained by fitting a number of experimental tests on specimens with and without transverse reinforcement, different values of *c/Φ*, concrete strengths and amount of stirrups. However, as suggested by the authors, this expression must be used with caution due to the limited tests carried out until now.

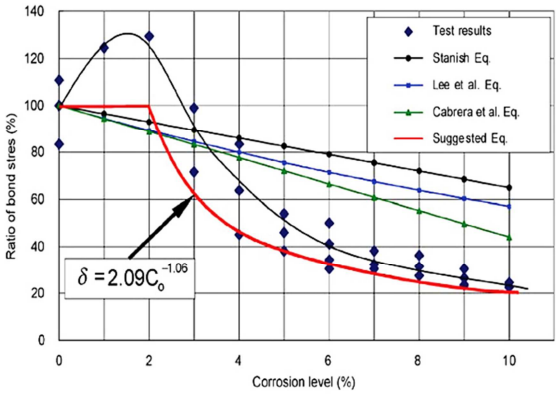

Figure 3-72. Relationship between bond stress and corrosion level, Chung et al.[66]

The effect of confining pressure on bond strength in corroded conditions was studied from a theoretical point of view by some authors. Among them, the approach proposed by Coronelli et al.[79] considers the confinement of concrete and stirrups p^{max}, the adhesive bond strength contribution τ_b^0 and the corrosion pressure p_{corr}, as function of the corrosion depth *x*. The model was developed basing on the one proposed by Cairns and Abdullah[51] for splitting bond failure, modified in order to account of corrosion. Hussein et al.[126] further modified the Coronelli's et al.[79] model in order to consider in addition to the adhesion and the corrosion pressure, also the confining pressure given by the cracked concrete p_{conf}. However in this formulation, the contribution of the confinement given by the stirrups was not included. Wu[272] therefore modified the equation for taking into account of this very important factor, distinguishing the confinement given by concrete $p_{c,c}$ and the confinement given by the stirrups $p_{c,st}$ and he validated the approach against experimental data.

Finally also the codes recognized strength bond degradation due to corrosion, e.g. *fib* MC2010[106] proposed the values reported in *Table 3-4* for the evaluation of $\tau_{max}^{degraded}$.

Table 3-4: Reduction in degraded bond strength for corroded reinforcement,fib MC2010

Corrosion penetration (mm)	**Equivalent surface crack** (mm)	**Confinement**	**Residual capacity** (as % of f_{bd}) Bar type	
			Ribbed	Plain
0.05	0.2-0.4	No links	50-70	70-90
0.10	0.4-0.8		40-50	50-60
0.25	1.0-2.0		25-40	30-40
0.05	0.2-0.4	Links	95-100	95-100
0.10	0.4-0.8		70-80	95-100
0.25	1.0-2.0		60-75	90-100

To the Author's knowledge, the only researchers that tried to evaluate the effects of reinforcement corrosion also on the other parameters that define the τ-s law, as the residual bond strength, the stiffness of the τ-s law or the bond failure mode, are Li et al.[160] and Lundgren[165]. In detail, Li et al.[160] proposed also some empirical relations for the evaluation of the residual bond stiffness and bond strength. In Lundgren[165] the author considered some experimental pull-out tests available in literature, highlighting the effects of different amount and type of reinforcement, concrete cover and transverse reinforcement on the bond type failure and on the bond strength. The literature review was accompanied with finite element analyses. An overview of the numerical results is reported in *Figure 3-73.*

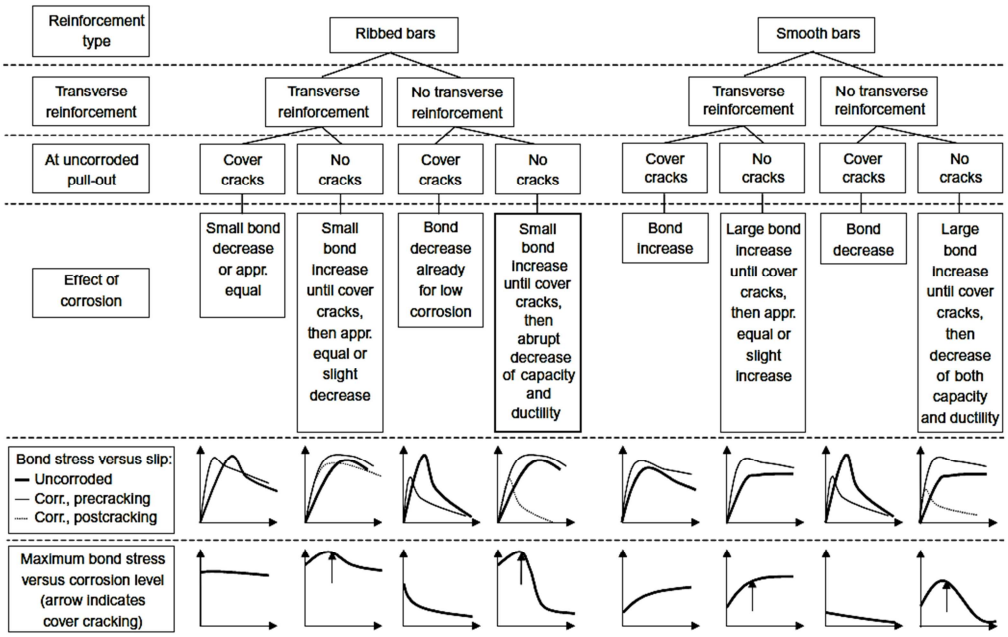

Figure 3-73: Influence Overview of effect of corrosion on bond, Lundgren[165]

Regarding the numerical modelling of the composite interaction between steel bars and surrounding concrete and more in detail of the effect of reinforcement corrosion on bond, in the last years many approaches have been proposed, depending on the level of accuracy that the researchers wanted to reach. Within the framework of the phenomenological models, adopted in this work, some approaches are mention, because they represent the base of the new proposal for the modelling of the corrosion effects on τ-s bond law that will be given in the next chapter.

Coronelli et al.[80] stated the no applicability of the assumption of plane sections in the case of bond deterioration and increasing slip values at the bar-concrete interface. The FE code used by the authors considered a different representation of concrete material, reinforcing bars and composite interaction. In particular, the concrete material was modelled with four-node plane-stress elements, the steel bars with two-node truss elements and their interaction through bond-link elements. These bond-links elements are characterized by a τ-s law defined by the authors, which in sound conditions corresponds to the one proposed by CEB-FIP MC90[61], *Equation 3-40* to *Equation 3-43,* and in the case of reinforcement corrosion was modified in order to consider splitting bond failure, *Figure 3-74*. The residual bond strength τ_{res}, the slip s_1 at the maximum bond stress and the softening branch were reformulated, as a function of the corrosion level. The postpeak behavior included the cover splitting through the elimination of both the plateau and the frictional strength. The degraded bond strength $\tau_{max}^{degraded}$ was calculated basing on the proposal of Rodriguez et al. [219].

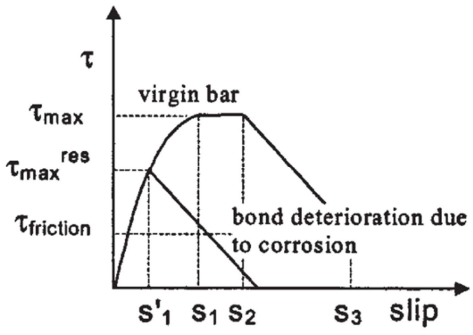

Figure 3-74: Bond stress-slip curves for sound and corroded conditions, Coronelli et al.[80]

Similar approaches have been adopted also by other authors, e.g. Saether and Sand[223], Kallias[140], Hanjari et al.[118], Berto et al.[33]. The authors adopted different kinds of interface elements, such as zero thickness or more general interface elements, triangular or quadrilateral contact elements, but always defining a bond strength-slip law. An interesting proposal is the one given by Berto et al.[33]. The authors developed two different types of τ-s laws in the numerical simulations: the first one was a frictional model, which allowed considering slip displacement between the steel bars and the surrounding concrete, see *Figure 3-75 a)*. However, this model was not able to reproduce the reduction of bond strength, experimentally observed after the achievement of the maximum bond strength. For this reason, the authors proposed a τ-s law based on a damage approach ("damage" type law), see *Figure 3-75 b)*. This bond stress-slip law is characterized by four stages as suggested by CEB-FIP MC90[61]: the initial branch that represents a linear elastic behaviour is followed by an ascending curve, which develops until the achievement of the maximum bond stress, and by a softening branch. Finally, the bond strength assumes a constant value, corresponding to the frictional resistance. In order to consider the loss of bond strength, the authors introduced a scalar damage parameter, d_{bond}. Berto et al.[33] obtained a good correspondence between numerical and experimental results in the simulation of both pull-out tests and four-point bending tests on corroded RC beams, made by Al-Sulaimani et al.[9], applying the "damage" type law. The damage bond model demonstrated therefore to be able to well describe the non-linear shape of the bond stress and the reduction of bond strength. However, the model does not consider the fact that minor corrosion can enhance the bond strength and the parameters that govern the effect of corrosion (d_{bond} and β) are obtained by direct calibration. Relationships between these bond parameters and the key characteristics of the materials (i.e. steel and concrete), depending on the degree of corrosion, are not proposed. Further, it allows simulating only a pull-out bond type failure.

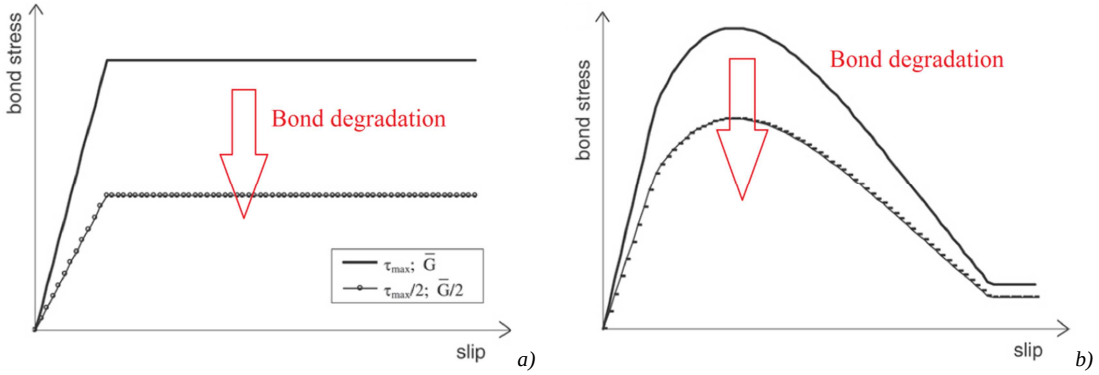

Figure 3-75: Bond stress-slip laws: a) Frictional type; b) Damage type, Berto et al.[33].

3.6. Corrosion effects on the structural response of RC members

The local effects of corrosion on steel bars, concrete and bond are in relation each other and modify the structural response of the corroded RC members. Many researchers have made experimental tests on corroded RC elements, in order to assess their global response. It has been found that reinforcement corrosion may affect the stiffness, the ultimate load, the ductility and the mode of failure of the structures themselves, leading to a reduction of their service life and level of safety. Following, a list of published experimental works and a briefly description of the main structural consequences of corrosion observed are reported. Some of the reported tests are fully described, because considered as reference for the numerical analyses made and reported in chapter five.

3.6.1 Corrosion effects on the flexural behavior of RC beams

A literature review of experimental tests made on the flexural capacity of RC beams damaged by reinforcement corrosion is reported in *Table 3-5*. It is possible to observe that corrosion may affect the mechanical properties of RC beams in different ways, depending on the type and level of attack. Indeed, corrosion may involve the longitudinal reinforcing bars, the stirrups or even both, leading to different degree of deterioration. In corrosion accelerated tests, which represents the standard type of tests made by most of researchers, both the longitudinal and the transverse reinforcement are attacked by corrosion and the damage is quite uniformly spatially distributed. In detail, the rebars are mainly affected by mixed corrosion type and in some cases pitting corrosion may be prevalent, leading to a reduction of steel ductility and therefore to lower values of ultimate deflection in the beams, as observed in Castel et al.[58], Dang and François[88], Daly[87], Rodriguez et al.[221][222], Torres-Acosta et al.[249]. When the stirrups are more affected by pitting corrosion, the RC beams may fail in shear, as demonstrated by Rodriguez et al.[221][222] and Uomoto et al.[253]. At the same time reinforcement corrosion may lead or not to cracking and spalling of concrete cover and therefore to a premature crushing of concrete in the compression zones, depending on the amount and on the spatial distribution of the corrosion products. This has been demonstrated by the tests carried out by Rodriguez et al.[221][222] and Uomoto and Misra[252]. Finally the composite interaction between steel bars and surrounding concrete may be degraded in a severe way or only slightly and can concern the anchorage areas or only the shear span of the beam. Almusallam et al.[5], Daly[87], Lee et al.[153], Uomoto et al.[253] showed that bond degradation in severe cases can lead to bond failure; in some beams tested by Rodriguez et al.[221][222] also anchorage failure of tensile bars was found. However, the main consequences of corrosion on RC beams designed to fail in bending, have been found to be the reduction of load-carrying capacity and ultimate deflection and especially the change of the failure mode. These are influenced by all the corrosion effects mentioned: reduction of steel area and ductility, concrete and bond degradation.

Following, the experimental tests made by Rodriguez et al.[221][222] and Lee et al.[153] will be better described, because considered as benchmark for the numerical simulations. In detail the tests made by Rodriguez et al.[221][222] are selected, due to the variety of corrosion effects and the different failure modes exhibited by the RC beams tested. Furthermore the authors measured both the mass loss by the corroded bars and the maximum pitting depth. The tests made by Lee et al.[153] are chosen due to the bond failure mechanism observed in some corroded RC beams tested.

Table 3-5: Summary of tests made on corroded RC beams designed to fail in bending

Researchers	Specimen type and size in mm [bxhxL]	Type of corrosion/maximum corrosion level	Type of loading test	Failure mechanism	Corrosion effects on structural behaviour
Uomoto et al.[339] (1984)	singly reinforced beams; 100x100x700	NaCl in mixing water +Impressed current	two point loading	from flexural failure to combination of shear and bond mechanisms	reduction in load-carrying capacity (-24% max)
Uomoto and Misra[338] (1990)	beams with tensile, compressive bars and stirrups; 100x200x2100	NaCl in mixing water +Impressed current / Xmax=1.4%	two point loading	from flexural failure with bar yielding to flexural failure coupled with spalling of concrete and buckling of bars in compression zone	reduction in flexure strength (-17% max) reduction in ductility (-33% max)
Daly[106] (1994)	singly reinforced beams; 120x240x3000	Impressed current/ X_{max}=22%	single point load	from flexural failure with long plateau after bar yielding to bond failure with short plateau after bar yielding/ flexural failure by tensile bar rupture with short plateau after bar yielding	reduction in flexure strength (-31% max) reduction in ductility
Almusallam et al.[3] (1996)	singly reinforced one-way slabs ; 305x63.5x771	NaCl solution + Impressed current/ X_{max}=75%	uniformly distributed load	from flexural failure to bond brittle failure mechanism before bar yielding	high reduction in flexure strength (-87% max) high reduction in ductility (-88% max)
Rodriguez et al. [286][287][288] (1996)	beams with tensile, compressive bars and stirrups; 150x200x2300	$CaCl_2$ in mixing water + Impressed current	two point loading	from flexural failure with long plateau after bar yielding to flexural failure with shorter plateau with bar yielding or premature compressive concrete crushing/shear failure/shear failure combined with anchorage failure of tensile bars	increase in deflections and crack widths at service load; reduction in load-carrying capacity and ductility;
Lee et al. [199] (1998)	singly reinforced beams; 100x100x800	Impressed current/ Xmax=7.9%	two point loading	flexural failure with long plateau after bar yielding	reduction in ultimate load (-10% max) reduction in stiffness after 50% peak load
	doubly reinforced beams; 100x100x800	saltirized concrete up to tensile bars +cyclic wet-dry curing at high temperature/ Xmax=14%	two point loading	flexural failure with long plateau after bar yielding	any
Lee et al. [201] (1999)	beams with tensile, compressive bars and stirrups; 200x250x2400	NaCl solution + Impressed current/ Xmax=25.3%	two point loading	from flexural failure with long plateau after bar yielding to bond failure with shorter plateau after bar yielding	reduction in flexural strength (-24% max) reduction in ductility (-37% max)
Castel et al. [67] (2000)	type B beams with tensile, compressive bars and stirrups; 150x280x3000	Salt fog environment (for 14 years)/ Xmax=10%	three-point bending	from flexural failure with long plateau after bar yielding to flexural failure with shorter plateau due to rupture of corroded tensile bars at deepest pit failure	reduction in flexural strength (-20% max) reduction in ductility (-70% max) decrease in stiffness (-35% max)
Torres-Acosta et al.[336] (2007)	singly reinforced beams; 100x150x1500	NaCl in mixing water + Impressed current/ Xmax=10%	three-point bending	from flexural failure with long plateau after bar yielding to flexural failure with shorter plateau due to rupture of corroded tensile bars at deepest pit failure	reduction in flexural strength (-60% max) reduction in ductility (-86% max)
Dang and François[107] (2013)	beams with tensile, compressive bars and stirrups; 150x280x3000	Salt fog environment +wetting–drying cycles (for 27 years)/ Xmax=50%	three-point bending	flexural failure due to concrete crushing with long plateau after bar yielding to flexural failure due to rupture of corroded tensile bars at deepest pit failure	reduction in ultimate load (-26% max) reduction in ductility (-50% max) decrease in stiffness

3.6.1.1 Experimental tests made by Rodriguez et al.[221][222]

Rodriguez et al.[221][222] investigated the influence of different levels of reinforcement corrosion on the flexural response of RC beams, by means of an extensive experimental work. In particular, six different types of beams, with different detailing, were casted, corroded and tested in order to evaluate the effect of different ratio of both tensile and compressive reinforcement, concrete spalling, shear reinforcement and curtailment of bars. The beams had all size of 150 by 200 by 2300 mm (a/d=4.7), except beam type 1 which was 2050 mm length; further details are given in *Table 3-6* and *Figure 3-76.* Type 1 beam was made to set up the artificial corrosion procedure.

Table 3-6: Details of the tested beams, Rodriguez et al.[221][222]

Beams		*Concrete*		*Reinforcement*		
Type	*Number*	*Type*	*Compressive strength [MPa]*	*Tensile bars*	*Compressive bars*	*Stirrups*
1	*1*	*-*	*42*	*2Φ12*	*2Φ8*	*Φ6/150 mm*
11	*2*	*1*	*50*	*2Φ10*	*2Φ8*	*Φ6/170 mm*
	4	*2*	*34*	*2Φ10*	*2Φ8*	*Φ6/170 mm*
12	*2*	*1*	*48*	*4Φ12*	*2Φ8*	*Φ6/170 mm*
	4	*2*	*35*	*4Φ12*	*2Φ8*	*Φ6/170 mm*
13	*2*	*1*	*52*	*2Φ12 + 2Φ12**	*2Φ8*	*Φ6/170 mm*
	4	*2*	*37*	*2Φ12 + 2Φ12**	*2Φ8*	*Φ6/170 mm*
21	*2*	*1*	*50*	*4Φ12*	*4Φ8*	*Φ6/170 mm*
	4	*2*	*35*	*4Φ12*	*4Φ8*	*Φ6/170 mm*
31	*2*	*1*	*49*	*4Φ12*	*4Φ8*	*Φ6/85 mm*
	4	*2*	*37*	*4Φ12*	*4Φ8*	*Φ6/80 mm*

**2Φ12 mm. cut-off bars*

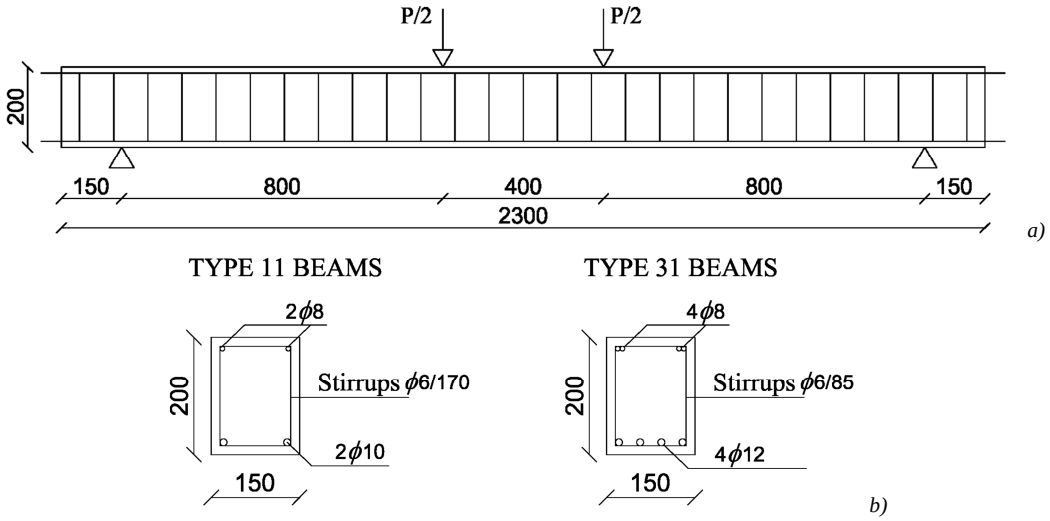

Figure 3-76. Scheme of the tested beams: a)Longitudinal section; b)Cross sections of type 11 and 31

Two types of concrete were employed: type 1 produced with siliceous sand and limestone crushed coarse aggregate of 12 mm maximum diameter; type 2 with the same composition but made adding calcium chloride (3% by weight of cement) in the mixing water, in order to accelerate the reinforcement corrosion. It should be noticed that the compressive concrete strength in beams without chlorides (sound beams) was significantly higher than in beams with $CaCl_2$.

After being casted and cured for 28 days, beams made with concrete type 2 were subjected to an accelerated corrosion procedure; *Figure 3-77* shows the test arrangement. In detail, the reinforcing bars were submitted to a a constant current density of about 100 μA/cm^2 for a period between 100 and 200 days, in order to obtain the required level of corrosion. This value of current density is very small respect to those used by other researchers and corresponds to ten times the corrosion intensity measured in highly corroding concrete structures. After the corrosion procedure, a detailed map of the concrete cracking was made by the authors, an example is shown in *Figure 3-78*.

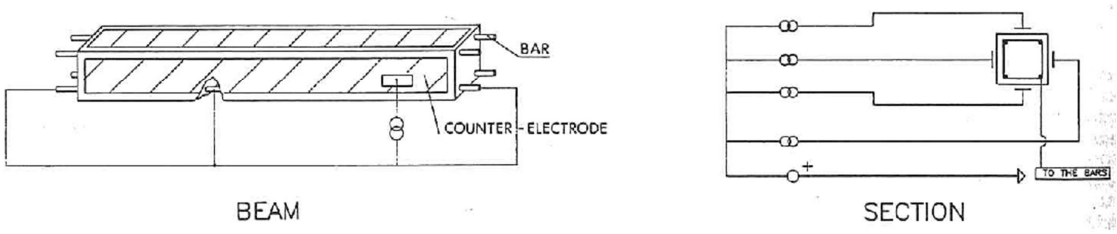

Figure 3-77. Scheme of test arrangement for accelerated corrosion, Rodriguez et al.[221]

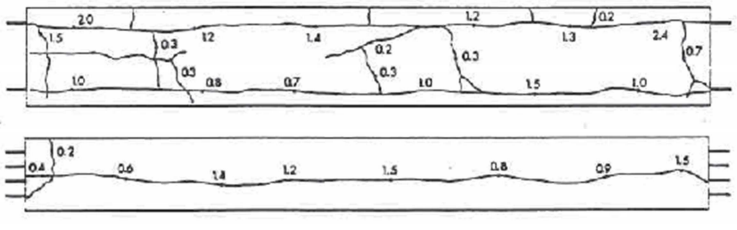

Figure 3-78. Cracks formation due to reinforcement corrosion: a) Longitudinal beam section; b) Bottom beam side, Rodriguez et al.[221]

Regarding reinforcing bars, ribbed bars of Spanish type AEH 500S were used, the mechanical characteristics reported by the authors are summarized in *Table 3-7*. The steel bars were corroded while the beams were unloaded, then the simply supported beams were tested up to failure under two monotonic symmetrical loads, as shown in *Figure 3-76*, applied by means of an hydraulic actuar at a constant displacement rate. During the tests, the mid-span deflection and the load were measured through load cella and displacement transducers (LVDTs). Dial-gauges were also placed to measure the slip between the ends of tensile bars and surrounding concrete. Finally extensiometers were located at top side of the mid-span section of the beams in order to measure compressive concrete strain.

Table 3-7. Mechanical characteristics of reinforcing steel

Bar diameter [mm]	*Yield stress [MPa]*	*Strength [MPa]*
6	*626*	*760*
8	*615*	*673*
10	*575*	*655*
12	*585*	*673*

The main experimental results obtained by the authors are reported in *Table 3-8*. In the firsts six columns of *Table 3-8* are shown the time of the accelerated corrosion for each beam and the values of the attack penetration, produced at main bars and at stirrups. The mean value of corrosion attack penetration *X* was obtained by gravimetric method, whereas the maximum value of pitting corrosion *p* was obtained by geometrical measurement on the pits of each bar.

Table 3-8. Time of accelerated corrosion and corresponding values of attack penetration and main experimental results

Beam type	Beam n°	N° of days	Attack penetration (mm) (+)			Service load	Ultimate load		
			Tensile bars	Compressive bars	Stirrups	Deflection at mid-span [mm]	Type of failure	Shear force [kN]	Bending Moment [kNm]
1	-	149	0.54	-	-	2.4	Bending (tensile bars)	34.5	17.8
11	111/112	-	-	-	-	3.5 / 3.2	Bending (concrete)	20.7 / 21.6	15.1 / 15.7
	115	101	0.36 (1.0)	0.26	0.37 (3.0)	4.0	Bending (tensile bars)	15.9	11.6
	114	117	0.45 (1.1)	0.52	0.39 (3.1)	3.2	Bending (tensile bars)	14.4	10.5
	113	160	0.49 (1.3)	0.56	0.49 (3.9)	3.6	Bending (tensile bars)	13.9	10.1
	116	190(*)	0.71 (2.1)	0.48	0.66 (5.0)	6.1	Bending (tensile bars)	11.9	8.6
12	121/122	-	-	-	-	5.2 / 5.2	Bending (concrete)	49.5 / 52.5	36.1 / 38.3
	126	104	0.32 (1.3)	0.27	0.39 (3.1)	5.7	Bending (concrete)	39.8	29.0
	123	115	0.35 (1.4)	0.44	0.39 (3.2)	5.8	Shear	37.3	27.2
	124	163	0.41 (1.6)	0.57	0.49 (3.8)	6.0	Shear	27.9	20.4
	125	175	0.40 (1.6)	0.41	0.53 (4.5)	6.3	Shear	31.4	22.9
13	131/132	-	-	-	-	5.1 / 5.3	Shear / Bond	50.1 / 52.8	36.6 / 38.5
	134	108	0.32 (1.3)	0.30	0.34 (2.7)	5.8	Shear / Bond	34.6	25.3
	133	116	0.35 (1.4)	0.31	0.36 (2.9)	5.8	Shear / Bond	34.5	25.2
	136	164	0.40 (1.6)	0.43	0.50 (3.8)	7.2	Shear	29.1	21.2
	135	175	0.39 (1.6)	0.56	0.53 (4.5)	6.7	Shear	33.9	24.7
21	211/212	-	-	-	-	5.3 / 5.3	Bending (concrete)	52.7 / 54	38.4 / 39.4
	215	108	0.37 (1.5)	0.24	0.37 (2.5)	5.5	Shear	38.6	28.2
	216	127	0.31 (1.2)	0.35	0.44 (3.5)	6.8	Shear	36.2	26.4
	213	154	0.43 (1.7)	0.38	0.52 (3.8)	6.5	Shear	26.6	19.4
	214	181	0.53 (2.1)	0.47	0.63 (5.0)	7.1	Shear	28.7	20.9
31	311/312	-	-	-	-	5.3 / 5.5	Bending (concrete)	52.3 / 53.2	38.1 / 38.8
	313	111	0.30 (1.3)	0.20	0.35 (2.8)	5.5	Bending (concrete)	38.7	28.2
	314	128	0.48 (1.5)	0.26	0.50 (4.0)	5.5	Bending (concrete)	39.0	28.5
	316	164	0.42 (1.8)	0.37	0.54 (4.3)	5.9	Bending (concrete)	37.7	27.5
	315	190(*)	0.51 (2.0)	0.34	0.63 (5.0)	7.7	Shear	27.7	20.2

(*) beams kept under natural corrosion conditions other 180 days

(+) Average value and maximum value at pitting (in brackets)

In the lasts four columns of *Table 3-8*, the deflection at mid-span measured, the failure mode observed, the maximum load measured and the maximum value of bending moment calculated by equilibrium, considering also horizontal reactions due to the friction at bearing supports, are reported. In *Figure 3-79* and *Figure 3-80* the load-deflection curves given by the authors are shown, unfortunately they refer only to type 11 and type 31 beams. The authors made the following remarks:

- Type 11 beams, sound and corroded, failed by bending and in particular mainly because the tensile reinforcement reached the ultimate strength. This type of failure is typical in beams with low ratio of tensile reinforcement, as type 11 beams. Due to reinforcement corrosion, stiffness, ultimate load and ultimate displacement decreased, see *Figure 3-79*;
- Sound and light corroded type 12 beams, failed by concrete crushing in compression. Indeed they had greater ratio of tensile reinforcement than type 11 beams. The remaining three corroded type 12 beams instead failed in shear;
- Type 13 and type 12 beams were identical, but type 13 had 50% of tensile bars curtailed before the supports. Therefore the sound beams and the two less corroded beams failed in a combination of shear and anchorage failure of tensile bars. The higher corroded beams failed in shear due to pitting corrosion in stirrups;
- Type 21 beams were also similar to type 12 beams, but characterized by twice the level of compressive reinforcement. The load-carrying capacity and the failure modes were similar: sound beams failed by concrete crushing in compression, corroded beams failed in shear;
- Type 31 beams had half the stirrups spacing of type 21 beams. All of the beams except the higher corroded failed in compression, but exhibiting different levels of ductility, see *Figure 3-80*. The most corroded beam failed in shear due to the significant reduction of stirrups area.

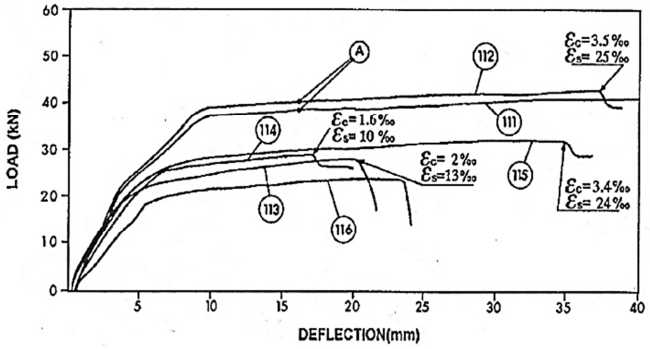

Figure 3-79. Load-deflection curves in type 11 beams, Rodriguez et al.[221]

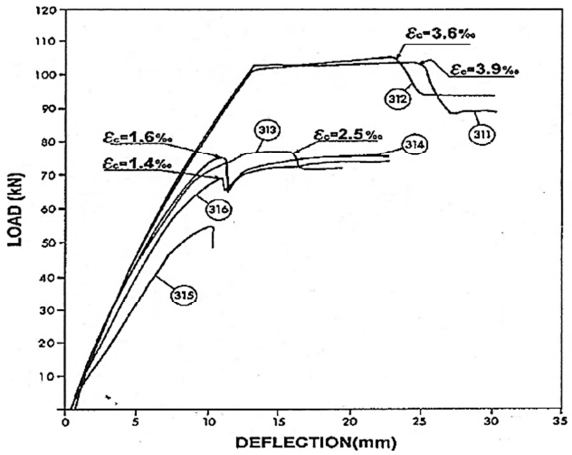

Figure 3-80. Load-deflection curves in type 31 beams, Rodriguez et al.[221]

3.6.1.2 Experimental tests made by Lee et al.[153]

Lee et al.[153] experimentally investigated the effect of different degrees of reinforcement corrosion on the flexural strength of RC beams. The authors carried out static loading tests on RC beams previously submitted to an accelerate corrosion procedure and they used the results to elaborate relationships that quantify the effect of the level of corrosion on both tensile and bond properties of the damaged bars.

Three types of beams were tested: sound specimen (BS); specimen with tension rebars of reduced size (BD); and corroded specimens (BCD1-0 corrosion level 1, BCD2-0 corrosion level 2 and BCD3-0 corrosion level 3), identical to BS specimen, except that their main tensile steel bars were corroded prior the loading test by an electrolytic corrosion method. The authors used an accelerated corrosion procedure (*Figure 3-81*) in order to induce reinforcement corrosion in a useful time. In detail, the bottom side of the beams was immersed in 3% NaCl solution. Then a direct current of 1A was impressed on the specimens using a constant electric current supplied for different periods, in order to reach the three defined levels of corrosion in the tensile bars. The level of corrosion reached was finally measured as the percentage of weight loss by the tensile bars, after being extracted from the beams at the end of the loading test.

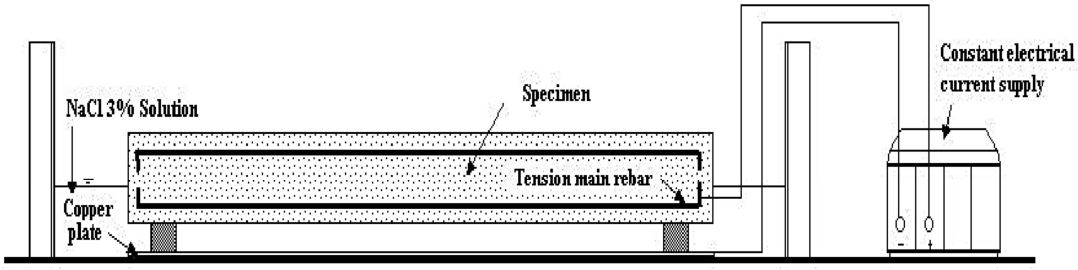

Figure 3-81. Electrolytic corrosion method, Lee et al.[153]

The RC beams had size of 200 x 250 x 2400 mm and a value of shear span-depth ratio equal to 3.4. The details of each type of beam are given in *Table 3-9* and *Figure 3-82*. In *Table 3-10* are reported the materials proprieties of the concrete and of the steel bars given by the authors.

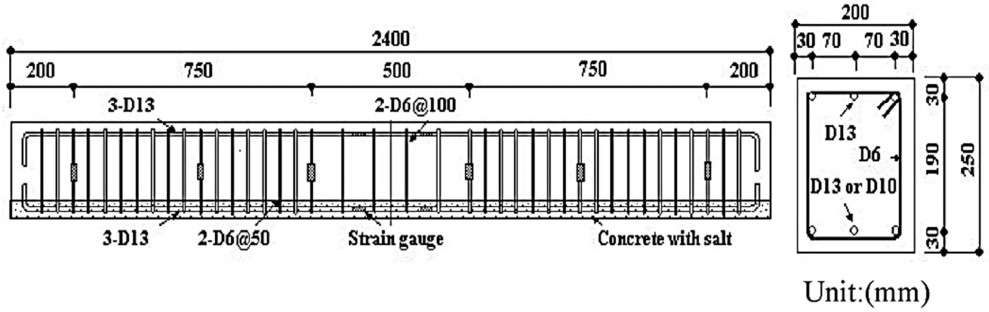

Figure 3-82. Details of the RC beams tested by Lee et al.[153]

Table 3-9. Characteristics of the RC beams tested by Lee et al.[153]

Name of the beam	*Type of specimen*	*Tensile bars*	*Compressive bars*	*Stirrups*
BS	*Sound*	*3 x D13*	*3 x D13*	*D6 / 50 mm*
BD	*Sound*	*3 x D10*	*3 x D13*	*D6 / 50 mm*
BCD1-0	*Corroded, level 1*	*3 x D13*	*3 x D13*	*D6 / 50 mm*
BCD2-0	*Corroded, level 2*	*3 x D13*	*3 x D13*	*D6 / 50 mm*
BCD3-0	*Corroded, level 3*	*3 x D13*	*3 x D13*	*D6 / 50 mm*

Table 3-10. Mechanical properties of concrete and steel bars

Concrete			*Steel*			
W/C=	*65*	*%*	*Type*	*fy [MPa]*	*fu [MPa]*	*Es [MPa]*
fc=	*39.2*	*MPa*	*D13*	*343*	*477*	*182000*
Ec=	*29419*	*MPa*	*D10*	*289*	*429*	*187000*
v=	*0.19*	*-*	*D6*	*226*	*415*	*194000*

The sound and the corroded beams were tested under two-point concentrated loads applied monotonically, see *Figure 3-83*. Beam deflections at the loading points, strains in the tensile bars and cracks width were recorded.

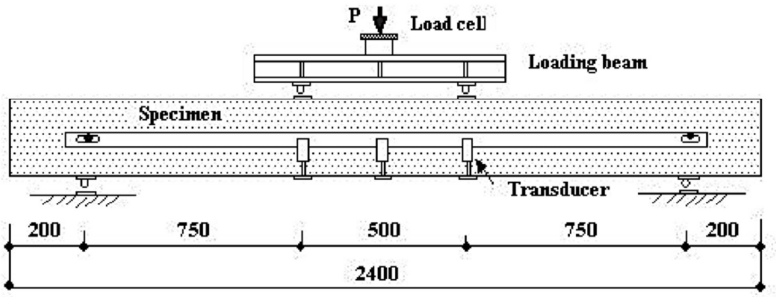

Figure 3-83. Static loading test, Lee et al.[153]

A summary of the test results is reported in *Table 3-11* and the experimental load-deflection curves found by the authors are shown in *Figure 3-84.* BD beam showed a maximum strength equal to 70% of the load-carrying capacity of the BS beam, related only to the reduction of the diameter of tensile bars. Regarding the corroded beams, as the corrosion in tensile bars progressed, the yield strength, the maximum strength and the deflection at the maximum strength decreased, but their maximum load was found to be always greater than the one of BD beam, *Figure 3-84.* The authors instead noticed that corrosion led to a change in failure mode: BS and BD beams failed by concrete crushing in compression after many flexural cracks occurred; the corroded beams failed with lower ductility due to the bond loss between tensile bars and surrounding concrete. This change of structural response was proved by the authors comparing the crack patterns of sound and corroded beams, *Figure 3-85*. In the sound BS beam, flexural cracks spread over to the shear zone, exhibiting a bending failure mode due to the collapse of the compressed concrete, see *Figure 3-85*. In corroded BCD1-0, BCD2-0, BCD3-0 beams cracks tended to concentrate on the equal bending moment zone. BCD2-0, BCD3-0 beams exhibited a bond failure mode associated with widening of longitudinal corrosion cracks due to corrosion expansion and spalling of concrete cover. The spalling of concrete at the bottom of the specimens indicated that the bond between tensile bars and concrete had really deteriorated.

Table 3-11. Test results, Lee et al.[153]

Name of the beams	*Δw [%]*	*Cracking Load [kN]*	*Yield Load [kN]*	*Maximum Load [kN]*	*Type of failure*
BS	*0*	*22.6 (1.00)*	*75.5 (1.00)*	*88.9 (1.00)*	*Flexure*
BD	*0*	*25.5 (1.13)*	*49.0 (0.65)*	*62.6 (0.70)*	*Flexure*
BCD1-0	*3.8*	*21.6 (0.96)*	*71.1 (0.94)*	*85.4 (0.96)*	*Bond and flexure*
BCD2-0	*7.9*	*20.6 (0.91)*	*69.6 (0.92)*	*78.8 (0.89)*	*Bond of rebar*
BCD3-0	*25.3*	*24.5 (1.09)*	*51.5 (0.68)*	*67.3 (0.76)*	*Bond of rebar*

Δw corrosion percentage by weight
( ) strength of specimen / strength of BS beam

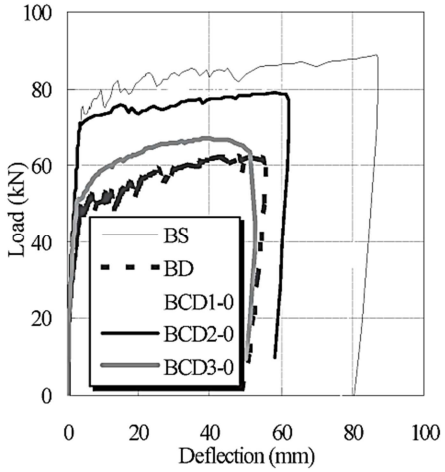

Figure 3-84. Load-deflection curves, Lee et al.[153]

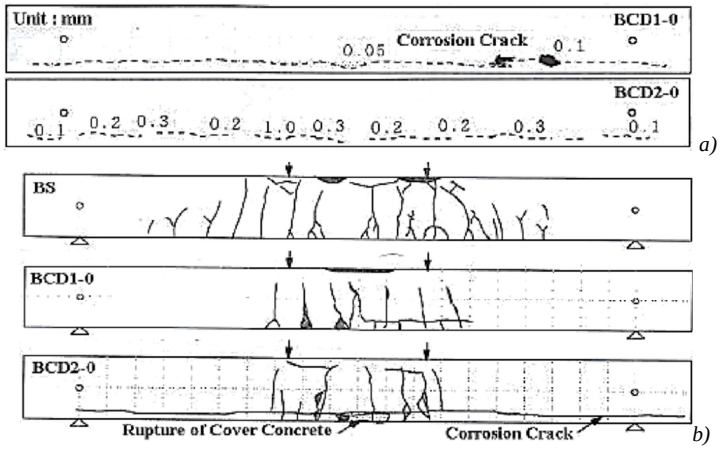

Figure 3-85. Map of the cracks in the RC beams: a) due to reinforcement corrosion; b)after being loaded, at the failure step, Lee et al.[153]

3.6.2 Corrosion effects on the structural behaviour of RC columns

A very limited literature exists on the structural response of corrosion damaged RC columns, despite their structural fundamental role in both RC frames and bridges and the high numbers of existing deteriorated members, e.g. bridge piers damaged by de-icing salt or carbonation.

Uomoto and Misra[252] (1990) tested ten columns under axial load, which were previously been subjected to accelerated corrosion procedure adding NaCl in the concrete mixing water and applying a current density. The columns has size 100x100x400 mm, therefore were stocky (h/b=4 $\leq$ 4), had a small c/Φ ratio (equal to 2) and stirrups Φ6/75 mm. The corroded columns were observed to fail after spalling of the concrete cover or buckling of the longitudinal reinforcement. The number of cracks formed during loading was small and the final cracks at the maximum load were mostly shear cracks close to the loading plates of the columns. No data were reported regarding the conditions of the bars in the sound columns or the level of corrosion reached in stirrups and longitudinal bars, therefore a comparison is difficult. However the authors reported the load-carrying capacity of the corroded columns: the two columns with least corrosion showed a small reduction of load-carrying capacity, between 2% and 12%. The other six columns tested had lower ultimate load, between 77% and 84% of the sound column. The authors found that the reduction in load-carrying capacity was greater than could be expected on the basis of area lost by the reinforcing bars, suggesting that other mechanisms may play a more important role in the assess of the residual load-carrying capacity of corroded bars.

Rodriguez et al.[220] (1996) tested a greater number of corroded slender columns under axial load, with different amount of reinforcement ratio and stirrups spacing. This experimental campaign will be following better described. Indeed, due to great amount of experimental data reported by the authors, it has been chosen as benchmark for the numerical analyses on corroded RC columns that will be presented in chapter 5.

Revathy et al.[213] (2009) carried out an experimental investigation on circular RC columns with corroding reinforcement to assess both their residual strength and ductility. The columns had a diameter of 150 mm and were 900 mm height, therefore they were slender (h/b=6 >4); they were reinforced with 6*Φ*8 and stirrups *Φ*6/115 mm. The accelerate corrosion procedure was made immersing the specimens in 3.5% NaCl solution and applying a high-density current, until to reach two corrosion levels equal to 10 and 25%. Then the columns were tested under axial compression test until failure. The results showed a marked reduction in axial strength and ductility, respectively within the range of 3-12% and 1.5-9% for the lower and the higher level of corrosion. The reduction of ultimate load was attributed to the loss of steel area. A reduction of stiffness was also found by the authors, analysing the slope of the axial stress- axial strain curves. Furthermore the authors measured the area under the load-deflection curves, which indicates the energy absorption. The energy absorption for corroded columns decreased as the level of corrosion damage increased, indicating the more brittle nature of the failure in the corroded columns.

To the best of the Author's knowledge, no test data are instead available regarding the effects of corrosion on combined flexural and axial behaviour.

3.6.2.1 Experimental tests made by Rodriguez et al.

Rodriguez et al.[220] tested 24 columns of three different types, to investigate the effects of accelerated corrosion on the structural response of these members. RC columns with different reinforcing details, without corrosion and with different levels of corrosion were tested. In particular, the columns had 200x200 mm cross section and were 2000 mm high (h/b=10>4, very slender) and they were characterized by end stiffening. The characteristics of each type of column are reported in *Table 3-12* and *Figure 3-86.* Concrete was produced with siliceous sand and limestone crushed coarse aggregates with particles of 12 mm maximum size. To accelerate corrosion in steel bars, 3% of calcium chloride by weight of cement was added to the concrete mixing water of the columns subjected to corrosion procedure. The compressive strength of concrete with chloride was found to be higher than the strength of concrete made without $CaCl_2$ (*Table 3-12).* For longitudinal and stirrups reinforcement, ribbed steel bars of Spanish type AEH 500S were employed. These bars have a yield stress between 550 MPa and 590 MPa and an ultimate strength between 600 MPa and 670 MPa.

Table 3-12. Characteristics of the RC columns

Columns	*Concrete*		*Reinforcement*	
type	*Chloride*	*Compressive strength [MPa]*	*Longitudinal bars*	*stirrups*
1	*No*	*30.0*	*2x2Φ8*	*Φ6/100*
	3% of $CaCl_2$	*35.8*	*2x2Φ8*	*Φ6/100*
2	*No*	*34.0*	*2x2Φ16*	*Φ6/150*
	3% of $CaCl_2$	*35.6*	*2x2Φ16*	*Φ6/150*
3	*No*	*34.3*	*2x4Φ12*	*Φ6/150*
	3% of $CaCl_2$	*39.4*	*2x4Φ12*	*Φ6/150*

After being cast and cured for 28 days, columns made with calcium chloride, were submitted to an accelerate corrosion procedure. In particular, a current of 0.1 mA/cm^2 was applied to the bars located in the central zone of the columns, for a number of days between 100 to 200. In *Figure 3-87* is shown the test arrangement. Once the corrosion process had finished, map of cracks at the concrete surface of each column was obtained. *Table 3-13* shows the time of the accelerated procedure, the maximum crack width at concrete surface measured and the amount of attack penetration in both longitudinal bars and stirrups. The mean values of the attack penetration shown in *Table 3-13* were obtained by gravimetric method, while the maximum values of pitting by geometrical measurement. Finally, the columns were tested under axial load and four displacement transducers (one for each side of the columns) were located to measure the average compressive strain. During the loading test, some eccentricities of relevant value (*Table 3-13)* were detected in the measurement of the strains on the four sides in most of the corroded columns, due to the non-uniformity of the corrosion, geometrical and testing imperfections and spalling phenomena.

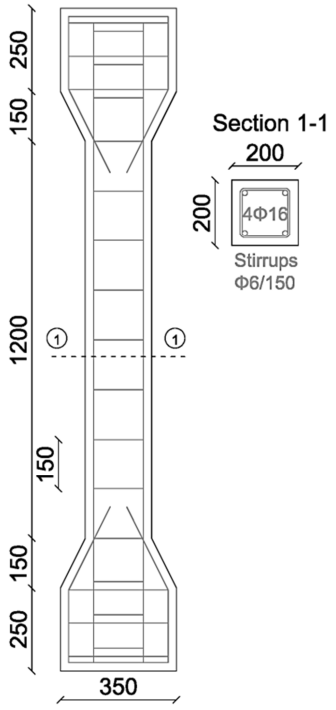

Figure 3-86. Scheme of columns type 2 (dimensions in mm)

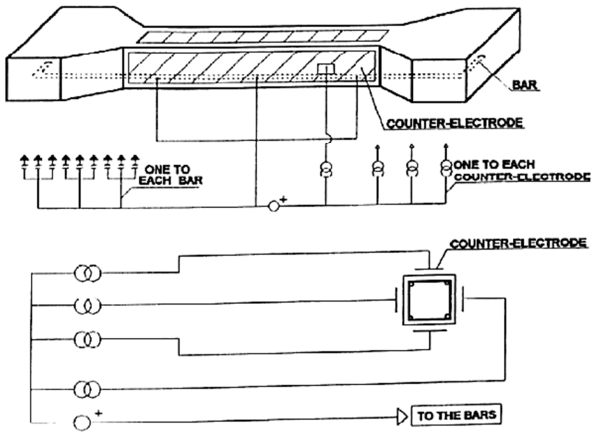

Figure 3-87. Scheme of test arrangement for accelerated corrosion , Rodriguez et al.[220]

In *Table 3-13* and *Figure 3-88* are reported the experimental results found by the authors. During the tests, delamination phenomena of the concrete cover were observed. The level of the load at which spalling of the concrete cover firstly occurred on one side is named “Delamination load”. The “Ultimate load” corresponds instead to the maximum load measured in the tests, close to this level of load, stirrups failures were observed. From *Table 3-13*, it is possible to observe that the Ultimate load of corroded columns is significantly lower than of the sound columns, in spite of the lower concrete compressive strength. The authors found a reduction of load-carrying capacity between 36% and 55% and they also observed that 55% was the maximum reduction of load-carrying capacity, beyond that further corrosion had little effect. The results confirmed also the remark of Uomoto and Misra[252]: the loss of load-carrying capacity was far greater than could be explained by loss of steel area. Corrosion leads also to a reduction of the ultimate strain and of the compressive stiffness of the columns, in particular of the first part of the P-ε curve, see *Figure 3-88*. Furthermore, for a load equal to the Delamination Load, a change of slope in the P-ε curve is visible. After this change, the load does not increase significantly although the concrete strain increases. The columns failure was experimentally observed initiated by the cracking and spalling of the concrete cover and the failure of one or more stirrups, heavily affected by corrosion, which leads to the buckling of the main bars under the applied axial load. The authors observed also that the reduction of the longitudinal bar section had a negligible influence on the results. The main important role in the column strength was attributed to the failure of the concrete cover and of the stirrups. Finally, the authors tried several methods for calculating the residual strength of corroded columns, considering eccentricities due to initial imperfections and geometry, as suggested in the codes and adding an additional value of eccentricity due to corrosion. They considered both the full cross section of concrete, with an allowance made for the buckling of bars, and reduced concrete sections corresponding to the concrete core with no one or more sides of concrete covers. On axial load-moment (N-M) interaction diagrams the test results fell between the full and reduced concrete sections. This suggests that more work is required to develop a suitable procedure for assessing corroded columns.

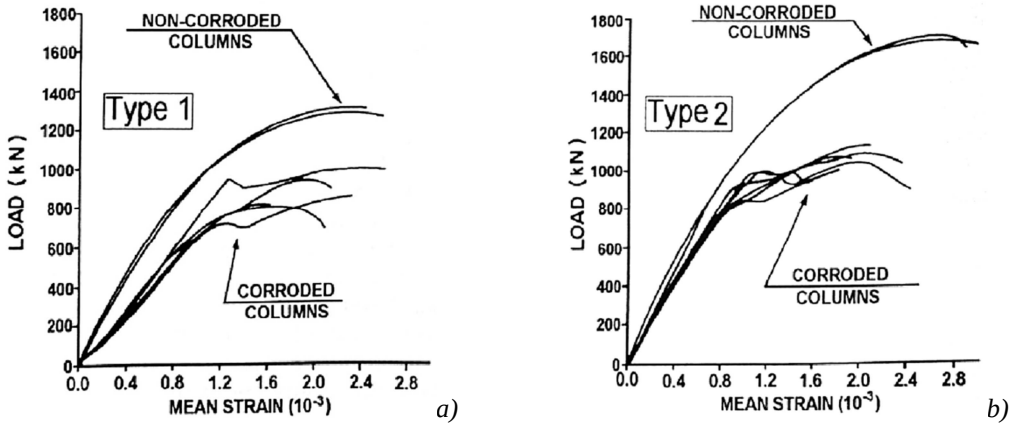

Figure 3-88. Load versus mean strain in column a)type 1; b)type 2, Rodriguez et al.[220]

Table 3-13. Summary of experimental results

Column n°	N° of days	Max crack width (mm)	Attack penetration (mm) (*)		Delamination load (+)		Ultimate load			Eccentricity [mm]	
			Main bars	Stirrups	Axial force (KN)	mean strain (.)	Axial force (KN)	Mean strain (.)	no. of broken stirrups	ex	ey
11	-	-	-	-	-	-	1300	2.4	-	4.9	8.8
12	-	-	-	-	-	-	1320	2.4	-	9.4	1.1
13	106	0.8	0.32	0.30 (1.4)	934	1.3	990	2.5	1	2.8	10.7
14	113		0.31	0.35 (1.4)	-	-	993	2.3	1	13.6	8.1
15	143	1.0	0.39	0.40 (2.4)	-	-	947	2.0	1-2	13.4	8.1
16	150	1.0	0.44	0.42 (3.2)	-	-	828	1.7	2-3	9.4	20.5
17	190	1.5	0.52	0.58 (3.9)	-	-	822	1.6	2-3	24.2	5.4
18	204	2.0	0.60	0.56 (3.7)	735	1.3	862	2.3	2-3	7.8	10.6
21	-	-	-	-	-	-	1680	2.7	-	8.2	2.3
22	-	-	-	-	-	-	1702	2.6	-	2.1	5.4
23	106	1.3	0.38	0.28 (2.8)	993	1.1	1080	2.2	1-2	22.2	15.6
24	113	0.9	0.37	0.30 (3.0)	999	1.2	1040	2.0	1	20.5	14.1
25	143	1.5	0.45	0.36 (3.9)	934	1.0	1091	1.8	3	13.8	16.4
26	150	1.6	0.46	0.41 (3.8)	890	1.1	1135	2.1	3-4	1.4	7.4
27	190	2.0	0.62	0.47 (4.7)	847	1.0	973	1.8	4	3.2	4.6
28	204	2.5	0.63	0.50 (4.7)	975	1.4	997	1.8	4	1.9	5.5
31	-	-	-	-	-	-	1728	2.5	-	1.2	5.2
32	-	-	-	-	-	-	1673	2.3	-	2.1	5.4
33	106	1.2	0.30	0.28 (3.0)	1258	1.3	1274	2.1	1	10.0	7.9
34	113	1.5	0.34	0.30 (3.5)	1130	1.2	1178	1.7	1	7.8	11.3
35	143	2.2	0.40	0.29 (3.4)	1164	1.1	1203	2.1	2-3	9.2	20.9
36	150	1.5	0.39	0.33 (3.4)	1145	1.3	1174	1.9	2-3	4.0	2.0
37	190	4.0	0.51	0.41 (4.4)	991	1.2	1038	1.7	4	4.8	4.6
38	204	1.8	0.56	0.40 (3.8)	1089	1.2	1170	1.5	2-3	21.1	4.0

** Maximum values of pitting are reported in bracket.*

+Load value when initiation of delamination of concrete cover was observed.

.Mean strain at the midspan zone, in ‰ on the four sides of the column.

3.7. Conclusions

The need to consider the different nature of the corrosive attack was initially pointed out. Especially in the case of pitting corrosion, some aspects regarding the reinforcing bars should be better investigated. In detail, different models to evaluate the residual area have been proposed making use of some simplifications regarding the pit morphology. Further, the influence of the pit shape on the residual steel area and mechanical properties of corroded bars has not been studied, because the researchers mainly refer to the average weight loss by the bars. For these reasons, some tests on locally damaged bars with different pit shapes are made by the Author. A comparison between the models for the assessment of the residual steel area and mechanical properties and the experimental data found will be made in chapter 4 in order to clarify their reliability. The influence of the pit spatial distribution on the bar length should be also more deeply investigated. Therefore, some sensitivity numerical analyses will be carried out. Finally, the tests examined evidenced the necessity to consider premature buckling phenomena in corroded bars in compression, which is an aspect that the models in literature have not well captured. Also in this case, a proposal will be made, based on previous models of literature.

In the case of concrete degradation due to reinforcement corrosion, the reduction of concrete strength in compression has been considered by many models. Instead, due to the lack of information, a unique generally approved approach for the evaluation of the residual ductility and modulus of elasticity of concrete damaged by reinforcement corrosion has not been proposed. Regarding the behaviour of degraded concrete in tension, some proposals have been made but due to the lack of experimental data, they are often in disagreement. In this work, basing on the tests made by Shimomura and Maruyama[231], reduction of both tensile strength and fracture energy are considered. In chapter 4 a proposal for the modelling of degraded concrete in tension and in compression, considering all the aspects here analysed will be given.

Bond degradation has been deeply studied through many experimental tests and a number of models, which consider bond strength degradation, have been proposed. However, only some researchers tried to identify the consequences of corrosion on the full bond strength-slip relationship, e.g. considering also bond stiffness, ultimate slip reduction or change in bond failure mode (from pull-out to splitting failure). Further, it is opinion of the Author that the effect of confinement on bond, and the consequences of corrosion on the confinement level, should be taken into consideration, due to the great relevance found in the experimental tests analysed. For these reasons, new τ-s laws considering confinement levels and consequences of corrosion are developed and will be presented in chapter 4.

Finally, the consequences of corrosion on RC members have been investigated through some experimental campaigns that allow however to study only the global response. The consequences of the single local effects of corrosion on RC beams and columns can be better investigated through numerical simulations. Especially the consequences of bond degradation and the causes that lead to a change of failure mechanism (e.g. from a flexural to shear one) need to be clarify. To the Author's knowledge, only some numerical models consider all the local effects of corrosion and even less simulated the behaviour of corroded columns. Many uncertainties related especially to the residual global ductility of corroded members are present. Therefore in chapter 5, making use of a comprehensive modelling approach, numerical analyses will be carried out on both RC beams and columns, trying to consider the different aspects here mentioned.

CHAPTER 4
REINFORCEMENT CORROSION: OWN TESTS AND MODEL IMPROVEMENTS

4.1. Introduction

The need for effective and accurate methods to anticipate the remaining service life of deteriorated reinforced concrete structures has become a priority for developing proper maintenance program and repair strategies. A number of studies have been devoted on the evaluation of the single effects of corrosion on steel, concrete and bond. However their interaction has not been deeply investigated, while it represents an essential aspect for the assessment of the structural response of corroded RC structures. For this reasons, in this work a comprehensive modelling approach is proposed, with the aim to take into account all the main effects of corrosion. The approach combines original formulations with some empirical/analytical models derived from the literature. In detail, the geometry changes caused by the damage evolution as well as the degradation of the material properties are taken into account. Concerning the effect of corrosion on steel, the results of some experimental tests made by the Author on locally damaged bars are presented and compared with different models proposed in literature for the estimation of the residual area and mechanical properties of corroded steel bars. Regarding concrete material, the coupled chemical – mechanical damage model developed by Saetta et al.[224][225] is here enhanced and used together with a new relationship proposed to account for the reduction of the compressive ductility of cracked concrete cover due to corrosion. To take into account of bond deterioration between steel bars and concrete, a new approach is proposed, able to predict the maximum bond strength in degraded condition, once the corrosion penetration is known. Furthermore, three different τ-s laws are introduced to consider different bond failure modes that may occur. The bond proposal is validated against the results of pull-out tests made by a number of researchers. The effectiveness of the proposed comprehensive modelling approach will be proved in chapter 5, through numerical analyses.

4.2. Corrosion effects on reinforcing steel bars

4.2.1. Experimental tests

The residual cross-sectional area and mechanical properties of corroded reinforcing bars play a primary role in the response of deteriorated RC structures; therefore their correct evaluation is fundamental. As observed in paragraph 3.3, the assessment of corrosion effects on reinforcing bars is still far away to be solved. Several experimental tests have been made and a number of models have been proposed, but the results are often in disagreement. This is mainly due to the fact that tests and models of literature are related to the average mass loss by corroded bars, without taking into account of the actual non-uniform nature of the corrosive attack, particularly important in the case of pitting corrosion. Only recently some authors, e.g. Tang et al.[241] have observed how, considering an average reduction of cross-sectional area evaluated from the total

weight loss of a corroded bar, the reduction of steel cross-sectional area is underestimated and this may lead also to an erroneous estimation of the residual mechanical properties of the corroded bars. Nevertheless, there is a lack of experimental tests that report the minimum cross-sectional area of corroded bars and the related residual mechanical properties, to the Author's knowledge only Cairns et al.[54], Palsonn et al.[198] and Tang et al.[241]. A brief description of their tests is reported in paragraph 3.3.2. Between these, only the tests made by Cairns et al.[54] on artificially damaged bars allow to establish a direct relationship between the minimum cross-sectional area and the residual mechanical properties of steel bar, without that the non-uniform distribution of pits along the bar length affects the results. However, Cairns et al.[54] did not take into account the possible influence of different shapes and lengths of the pits, which instead may be of certain relevance (paragraph 3.3). In order to consider also these aspects, an experimental campaign was made by the Author and the results are following reported.

4.2.1.1. Description of the experimental campaign

A number of tensile tests was made on locally damaged reinforcing bars, at the laboratory of the Institut für Baustoffe, Massivbau und Brandschutz (iBMB) of the Technische Universität Braunschweig. In detail, the tests were carried out on ribbed bars B550B type of 16 mm diameter. The total length of the bars was of 500 mm, the effective length of the bars between the jaws of the testing machine was of 335 mm. In order to simulate pitting corrosion, a part of the reinforcing bars was removed using a computer numerical control (CNC) milling machine provided by the Stahlbau Institut of the Technische Universität Braunschweig. This kind of machine is able to carve out materials based directly on a pre-existing design CAD, see *Figure 4-1*. In order to get the exact desired shape of the local damage, different tool heads were consecutively used, see *Figure 4-2*. An example of a bar made with two local damages is shown in *Figure 4-3*. A summary of the reinforcing bars with the different local damages designed is reported in *Table 4-1* and *Table 4-2*.

Figure 4-1. CAD design and computer station controlling of the CNC milling machine

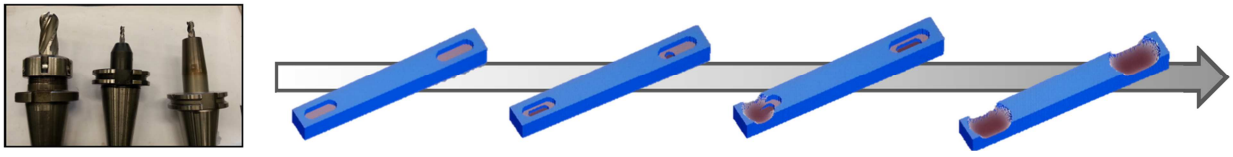

Figure 4-2. Example of the progressive procedure for the creation of two pits in a bar.

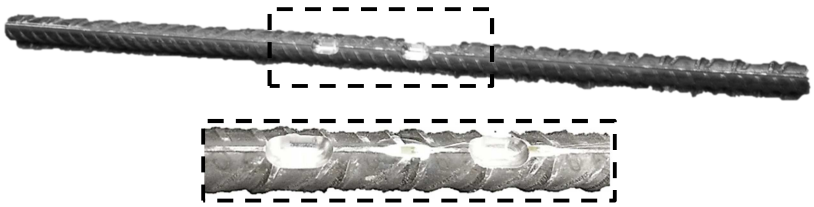

Figure 4-3. Example of two local damages created in a reinforcing bar

Eight locally damaged bars were created with one single pit of different shapes and lengths; other three bars were made with more than one pit; three reinforcing bars were let without damages (*SB* bars) in order to obtain the mechanical properties of sound bars. The name of the damaged bars is of type: *1DBc8p5*; the first number indicates the number of pits; the second number is the pit length in mm; the third number is the maximum pith depth in mm; *DB* stands for Damage Bar and *SB* for Sound Bar; *c* or *w* stand for circular or wedge-shaped pit cross section; *p* is the pit depth. It is worth noting that the *Pit length* is the bar length with maximum reduction of cross section, while the length of the full local damage is called *Total pit length*. In the following tables are reported the maximum percentage of cross-sectional area removed and a schematic representation of transverse and longitudinal sections. More details regarding the geometry of the locally damaged bars are reported in Appendix A.

Table 4-1. Geometrical characteristics of bars with one pit

Φ16							
Circular pit cross section				*Wedge-shaped pit cross section*			
Pit length= 8 mm		*Pit length= 32 mm*		*Pit length= 8 mm*		*Pit length= 32 mm*	
p=5 mm	*p=10 mm*	*p=5 mm*	*p=10 mm*	*p=5 mm*	*p=10 mm*	*p=5 mm*	*p=10 mm*
1DBc8p5	*1DBc8p10*	*1DBc32p5*	*1DBc32p10*	*1DBw8p5*	*1DBw8p10*	*1DBw32p5*	*1DBw32p10*
A'_s= 167.05 mm^2 -17%	A'_s= 87.53 mm^2 -56.5%	A'_s= 167.05 mm^2 -17%	A'_s= 87.53 mm^2 -56.5%	A'_s= 191.38 mm^2 -4.8%	A'_s= 163.46 mm^2 -18.7%	A'_s= 191.38 mm^2 -4.8%	A'_s= 163.46 mm^2 -18.7%
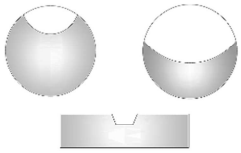		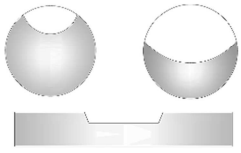		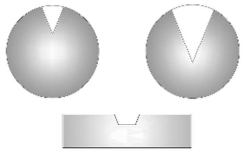		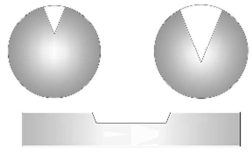	

A'_s = minimum cross-sectional area (grey background in the pictures)

Table 4-2. Geometrical characteristics of bars with more than one pit

Φ16		
Circular pit cross section		
N° pit =2	*N° pit =3*	*N° pit =3*
Pit length= 8 mm	*Pit length= 8 mm*	*Pit length= 8 mm*
p=5 mm	*p=5 mm*	*p=10 mm*
2DBc8p5	*3DBc8p5*	*2DBc8p10*
A'_s= 167.05 mm^2 -17%	A'_s= 167.05 mm^2 -17%	A'_s= 87.53 mm^2 -56.5%
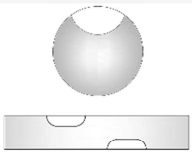	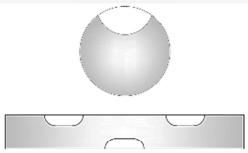	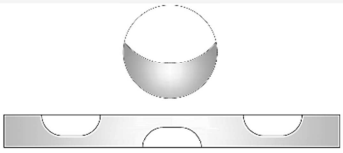

A'_s = minimum cross-sectional area (grey background in the pictures)

Sound and damaged reinforcing bars were then tested in tension. A Zwick ZA6 testing machine of 600 kN was used to apply the load to the steel bars. The load was monotonically applied till failure by displacement control and at loading rate of 2 mm/min, according to ISO/FDIS 15630-1 specification[128] and the tests made by Cairns et al.[54]. The testing machine was equipped with a data-processing computer, to record the applied load and reinforcement elongation, *Figure 4-4 a)*. Furthermore, the ARAMIS system, an optical deformation measuring system developed by GOM mbH, was used to recorder the deformations of the bar surface. ARAMIS is indeed able to elaborate different digital images and through their comparison to display the deformations of an object, *Figure 4-4 b)*. To verify the results of the ARAMIS system, some Strain Gauges (DMS) were also placed at different position of the bars (*Figure 4-5*). For the first sound bar tested, also an electrical extensometer over an effective gauge length of 100 mm was used to measure the linear elongation of the bar, to determine its elasticity, prior to the yielding of the bar, *Figure 4-4 c)* and to have data to compare with the ones given by the Strain Gauges. ISO/FDIS 15630-1 specification[128] indeed prescribes that extensometer may be unnecessary, if measurement of the strain with an adequate accuracy is possible by means of strain gauges. Finally, two marks with initial distance of 335 mm (length between the jaws) were made on reinforcement surface. After bar fracture, the extension between these two marks was measured and compared with the one given by the machine.

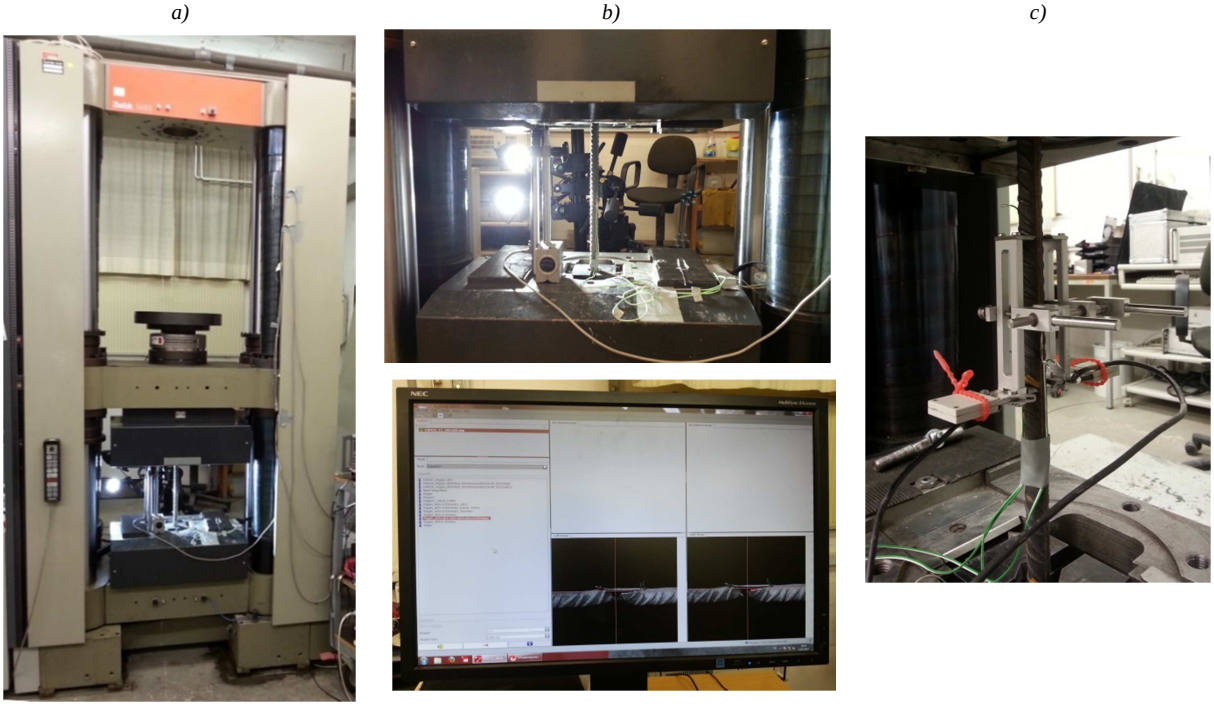

Figure 4-4. a)Tensile tests machine; b)Optical Measurement System and c) extensometer.

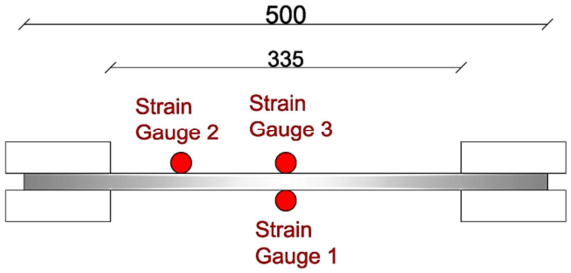

Figure 4-5. Positions of the Strain Gauges

4.2.1.2. Undamaged reinforcing bars

Three steel bars without damages (*SB* bars) were firstly tested in order to obtain the mechanical properties of undamaged reinforcement. The details regarding the geometry of the bar type is given in *Table 4-3.*

Table 4-3. Geometrical characteristics of SB bars

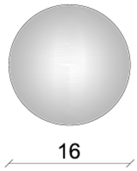

Bar diameter Φ *[mm]*	*Cross-sectional area* A_s *[mm²]*	*Initial total length* L *[mm]*	*Initial length between jacks* L_0 *[mm]*	*Volume between jacks* V_0 *[mm³]*
16	*201.06*	*500.00*	*335.00*	*67355.10*

For the *SB1* bar tested, both Strain Gauges and extensometer were used. The results for the elastic field in terms of stress-strain curves are compared in *Figure 4-6* and *Table 4-4*. The yield strength is taken as the stress at which the curve bends (plastic deformation begins to occur). The modulus of elasticity is calculated between one-third and two-thirds of the yield strength, as suggested by ISO/FDIS 15630-1 specification.

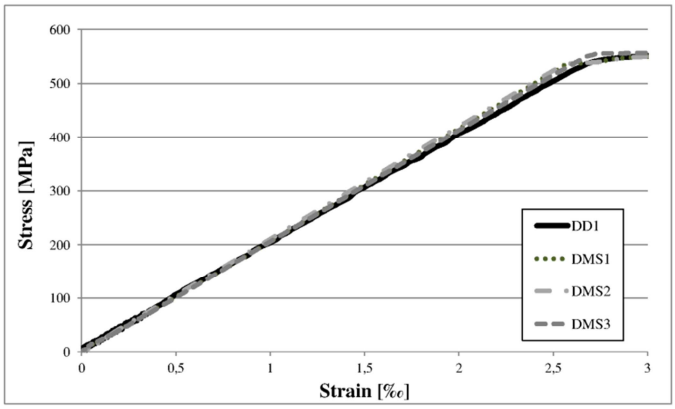

Figure 4-6. Stress-strain curves obtained from Strain Gauges (DMS1-2-3) and extensometer (DD1), elastic phase of SB1 bar.

Table 4-4. Experimental results of SB1 bar

Modulus of elasticity				*Yield strength*			
$E_{s,DMS1}$ *[MPa]*	$E_{s,DMS3}$ *[MPa]*	$E_{s,DMS3}$ *[MPa]*	$E_{s,DD1}$ *[MPa]*	$\sigma_{y,DMS1}$ *[MPa]*	$\sigma_{y,DMS2}$ *[MPa]*	$\sigma_{y,DMS3}$ *[MPa]*	$\sigma_{y,DD1}$ *[MPa]*
209759	*209794*	*207204*	*198432*	*556.21*	*554.49*	*555.78*	*555.59*
*206297**				*555.52**			
*4660.74***				*0.63***			

**Mean value*
***Standard Deviation*

It is possible to notice that the Strain Gauges give results in quite good agreement each other. The elastic modules evaluated with the Strain Gauges strains are slightly higher than the elastic modulus evaluated with the extensometer, because the extensometer measures elongation on a finite length instead to capture local strains. However, an accurate estimation of the elastic stiffness is possible with the Strain Gauges, so the extensometer will not be used for the other bars, in order also to obtain a better panoramic field of vision for the video camera of the Optical Measurement system.

In *Table 4-5* are reported the values of the modulus of elasticity and yield strength for each bar, found as an average values of the data of the three Strain Gauges. The maximum force and the

ultimate force and the corresponding displacements are also reported, obtained from the testing machine. In detail, the displacement at the rupture, $Disp._{Fu}$, is compared with the final elongation of the bar measured, E_{Fu}, in order to validate the displacements given by the testing machine. A good correspondence was obtained: the difference between $Disp._{Fu}$ and E_{Fu} is in percentage between 1.1 and 3.3% and it is probably due to small slips at the jaws or deformation inside the machine.

Table 4-5. Experimental results of SB bars

Bar	Modulus of elasticity E_s [MPa]	Yield strength σ_y [MPa]	Yield force F_y [kN]	Max force F_{max} [kN]	Max stress σ_{max} [MPa]	Ultimate force F_u [kN]	Disp. at F_{max}/ machine $Disp._{Fmax}$ [mm]	Strain at Fmax ε_{sm} [%]	Disp. at F_u /machine $Disp._{Fu}$ [mm]	Final elongation /measured E_{Fu} [mm]
SB1	206297	555.52	111.69	132.05	656.77	93.82	48.96	14.61	58.64	58.00
SB2	199832	574.34	115.48	131.59	654.48	97.18	36.25	10.82	46.35	45.00
SB3	193619	556.20	111.83	132.02	656.62	100.12	44.20	13.19	52.72	51.00
	199916*	562.02*	113.00*	131.89*	655.96*	97.04*	43.14*	12.88*	52.57*	51.33*
	5176.11**	8.72**	1.75**	0.21**	1.05**	2.57**	5.24**	1.57**	5.02**	5.31**

*Mean value
**Standard Deviation

The Force-elongation curves and the obtained stress-strain curves for each *SB* bar are compared in *Figure 4-7*. After the initial linear-elastic branch, the curves are characterized by a quite-long yield plateau typical of this type of steel. In the strain-hardening phase, until to arrive at the maximum strength, the bars show large plastic strains. After this point, the deformations along the gage section are not anymore uniformly: the softening branch shows indeed increasing deformations but for lower load because the deformation starts to localize, forming a neck, until to the bar rupture (*Figure 4-8*).

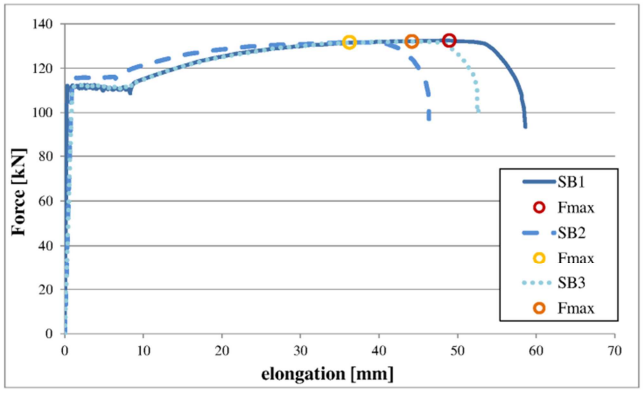

a)

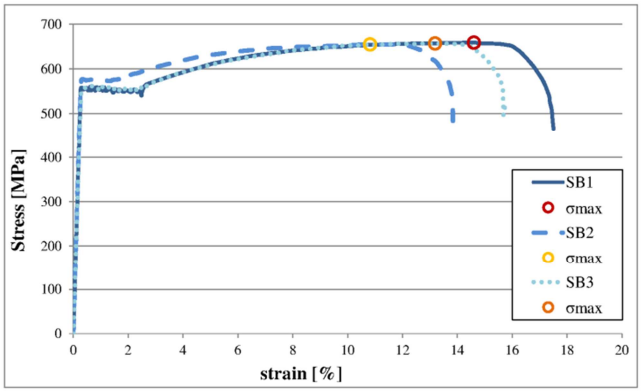

b)

Figure 4-7. a) Force-elongation curves; b) Stress-strain curves of SB bars.

Figure 4-8. Rupture of the SB3 bar.

Finally, some pictures captured by the ARAMIS system are compared with the stress-strain curve in order to evidence the differences between global measurements (Strain Gauges, extensometer, machine) with the local strains of the bar surface. The results obtained for some worthy stages during the tensile test of the *SB3* bar are shown in *Figure 4-9.* It worth noting that in the pictures a small part of the longitudinal profile is not visible (at half length) because a DMS was placed there.

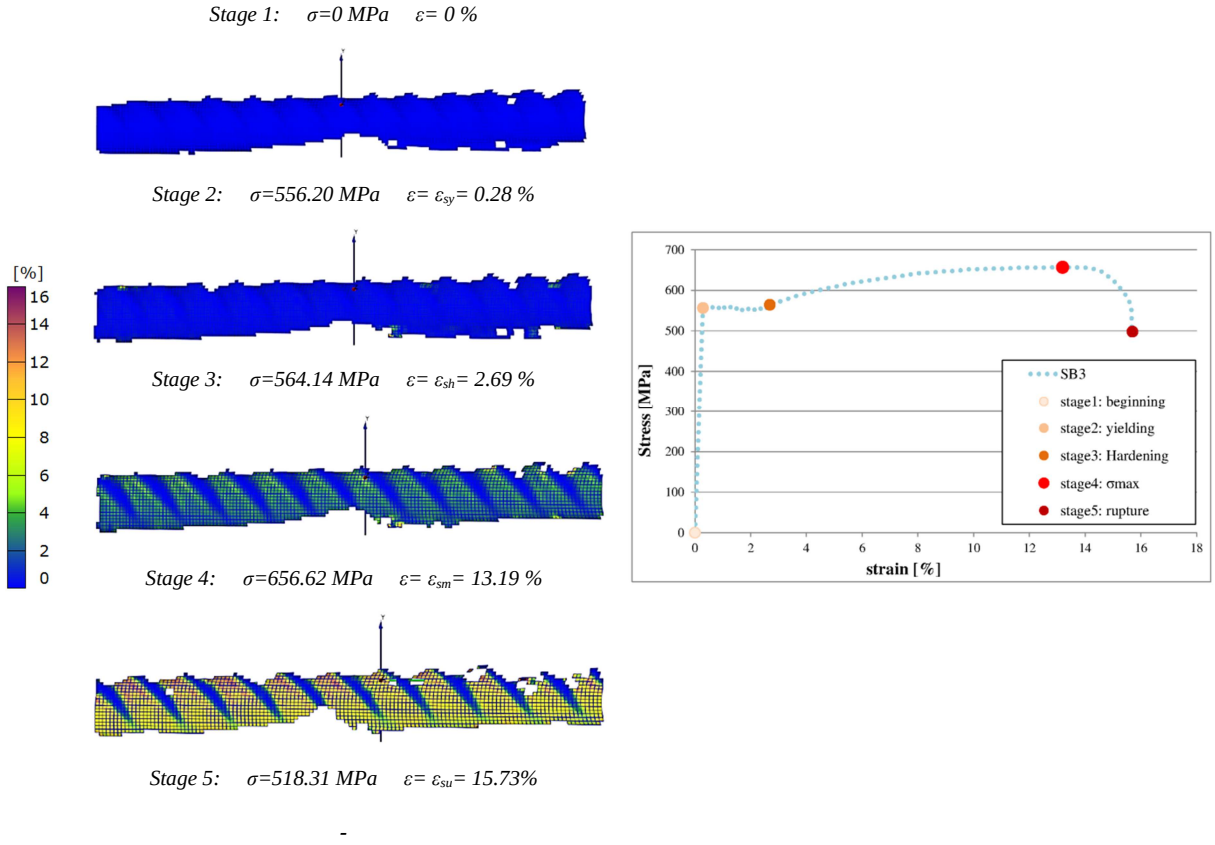

Figure 4-9. Optical Deformation Measurement System and stress-strain curve

The pictures elaborated by the ARAMIS system show how the local strains can strongly differ from the average global deformation measured by the test machine. In particular, strains concentrate between two consecutive ribs of the longitudinal profile, see *Figure 4-10.*

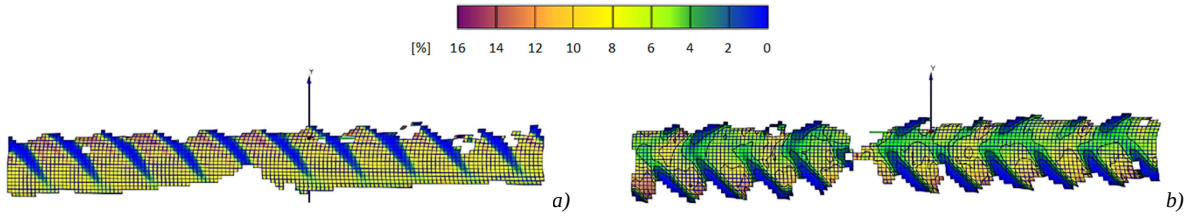

Figure 4-10. Optical Deformation Measurement System: a) longitudinal profile of SB3 bar and b) view from above of SB2 bar.

4.2.1.3. Reinforcing bars with local damages

Eight steel bars were locally damaged creating one single pit of different shapes and lengths, at the half length of each bar. In detail, for four bars the damage created had circular cross section, for the other four the damage was narrower than deep (wedge-shaped cross section). Three bars were made with more than one pit. In detail, bar *2DBc8p5* was made with two pits in opposite positions respect to the longitudinal axis, in order to verify if this particular configuration could lead to lower residual mechanical properties respect to the bar *1DBc8p5*, characterized by one pit with the same depth and length. For the same reason, two bars with three equal pits were also made: bars *3DBc8p5* and *3DBc8p10*. These last tests were useful also to verify the effects of more pits located in a small length of reinforcing bars. The geometrical characteristics and the experimental results are briefly reported in *Table 4-6* and *Table 4-7*. The force-elongation curves obtained from the tensile tests on locally damaged bars are shown in *Figure 4-11*. The comparison between the experimental results will be made in the next paragraph.

Table 4-6. Geometrical characteristics of locally damaged reinforcing bars

Bar	Max pit depth	Initial cross-sectional area	Max cross-sectional area of the pit	Min. residual cross-sectional area	Reduction of cross-sectional area	Residual volume between jacks	Volume of the pit	Reduction of volume
	p[mm]	A_s[mm^2]	A_p[mm^2]	A'_s[mm^2]	ΔA_s[%]	V_r[mm^3]	V_p[mm^3]	ΔV[%]
1DBc8p5	5	201.06	34.01	167.05	16.92	66852.15	502.95	0.75
1DBc8p10	10	201.06	113.53	87.53	56.47	64861.37	2493.73	3.70
1DBc32p5	5	201.06	34.01	167.05	16.92	66035.92	1319.18	1.96
1DBc32p10	10	201.06	113.53	87.53	56.47	62136.65	5218.45	7.75
1DBw8p5	5	201.06	9.68	191.38	4.81	67262.19	92.91	0.14
1DBw8p10	10	201.06	37.6	163.46	18.70	66954.03	401.07	0.60
1DBw32p5	5	201.06	9.68	191.38	4.81	67032.43	322.67	0.48
1DBw32p10	10	201.06	37.6	163.46	18.70	66051.63	1303.47	1.94
2DBc8p5	5	201.06	34.01	167.05	16.92	66349.20	1005.90	1.49
3DBc8p5	5	201.06	34.01	167.05	16.92	65846.25	1508.85	2.24
3DBc8p10	10	201.06	113.53	87.53	56.47	59873.91	7481.19	11.11

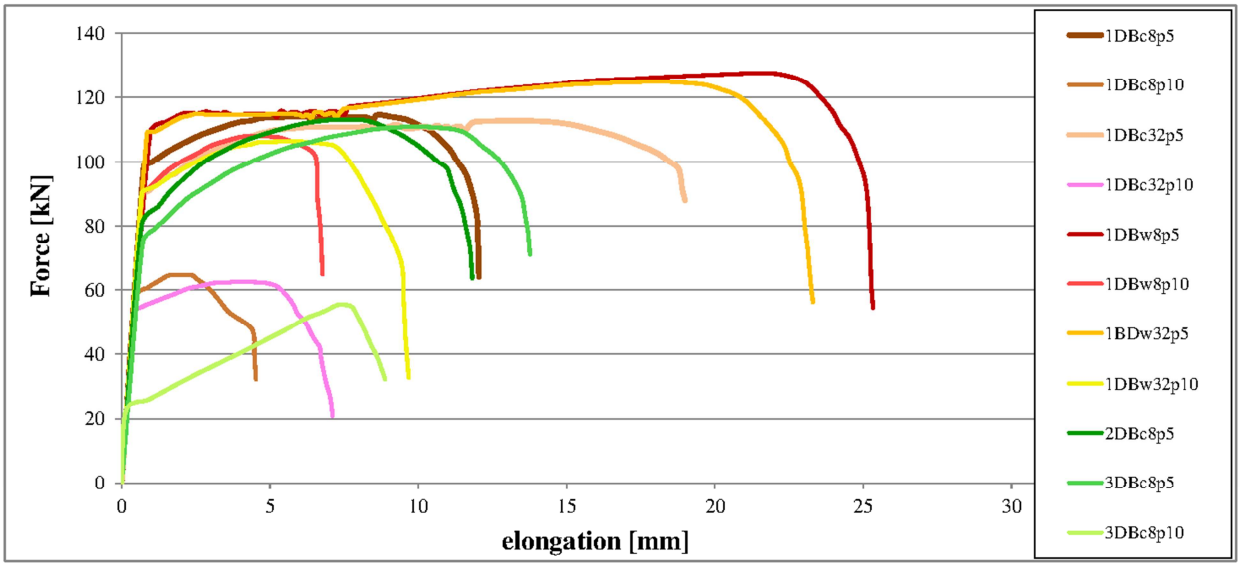

Figure 4-11. Force versus elongation curves from tensile tests of locally damaged reinforcing bars

Table 4-7. Experimental results of locally damaged reinforcing bars

Bar	Modulus of elasticity	Yield strength	Yield force	Max force	Max stress	Ultimate force	Disp. at F_{max} / machine	Strain at Fmax	Disp. at F_u /machine	Final elongation /measured	Total pit elongation /measured
	E_s [MPa]*	σ_y [MPa]	F_y [kN]	F_{max} [kN]	σ_{max} [MPa]	F_u [kN]	$Disp._{,Fmax}$ [mm]	ε_{sm} [%]	$Disp._{,Fu}$ [mm]	E_{Fu} [mm]	$E_{Fu,pit}$ [mm]
1DBc8p5	220894	489.60	98.44	114.61	570.03	64.14	8.62	2.57	12.04	12.50	7.90
1DBc8p10	193905	289.89	58.29	64.77	322.14	32.38	2.04	0.61	4.53	4.80	2.40
1DBc32p5	211057	453.3	91.14	112.86	561.32	88	13.34	3.98	18.99	19.10	12.60
1DBc32p10	210414	265.73	53.43	62.51	310.90	20.89	4.03	1.20	7.11	7.20	6.10
1DBw8p5	187445	542.58	109.09	127.61	634.69	54.53	21.34	6.37	25.33	25.80	8.40
1DBw8p10	214332	443.73	89.22	108.06	537.45	65.00	4.70	1.40	6.77	7.50	6.60
1DBw32p5	212302	541.10	108.79	124.95	621.45	56.26	17.99	5.37	23.30	24.00	11.90
1DBw32p10	225456	447.98	90.07	106.50	529.69	32.89	5.66	1.69	9.68	10.50	8.90
2DBc8p5	199345	399.31	80.29	113.19	562.97	63.70	7.56	2.26	11.82	12.10	8.20
3DBc8p5	176648	376.75	75.75	110.94	551.78	71.12	10.28	3.07	13.76	14.10	8.70
3DBc8p10	243531	107.52	21.62	55.43	275.69	32.37	7.54	2.25	8.88	8.90	6.00

**The values of E_s are obtained from Strain Gauge in position 2, Figure 4-5*

As an example, in *Figure 4-12* are reported the pictures elaborated by the ARAMIS system, that show the deformations in the *1DBc8p5* bar at different stages of the tensile test, specified in the adjacent stress-strain curve. It is possible to observe that the strains concentrate at the pit: at stage 3, local strains of value around 30% are detected in the damaged area, while the value of the overall strain is about 2.5%. This phenomenon intensifies in the final stages of the testing. At the second to last step recorded, local strains equal to 40% in the middle of the hole forewarn the occurrence of the bar rupture, shown in *Figure 4-13*. The elongation of the pit was found to be 63.2% of the total bar elongation, confirming these observations. In *Figure 4-14* the strains elaborated by the ARAMIS system for *SB3* and *1DBc8p5* bars, at the maximum strength of each bar, are compared. In detail, the colours highlight in which stage of the global stress-strain curve are situated the different areas of the bar, as shown by the legend on the left. In the sound bar *SB3* the strains are uniformly distributed along the bar length and differ only at the ribs. None portion exhibit strains greater than the global ultimate strain ε_{su} (violet colour). Instead, in the *1DBc8p5* bar, strains localise inside the pit while the zones immediately adjacent to the local damage are still not yielded (cyan colour). Similar results are obtained also for the other locally damaged bars. A comparison will be made in the next paragraphs.

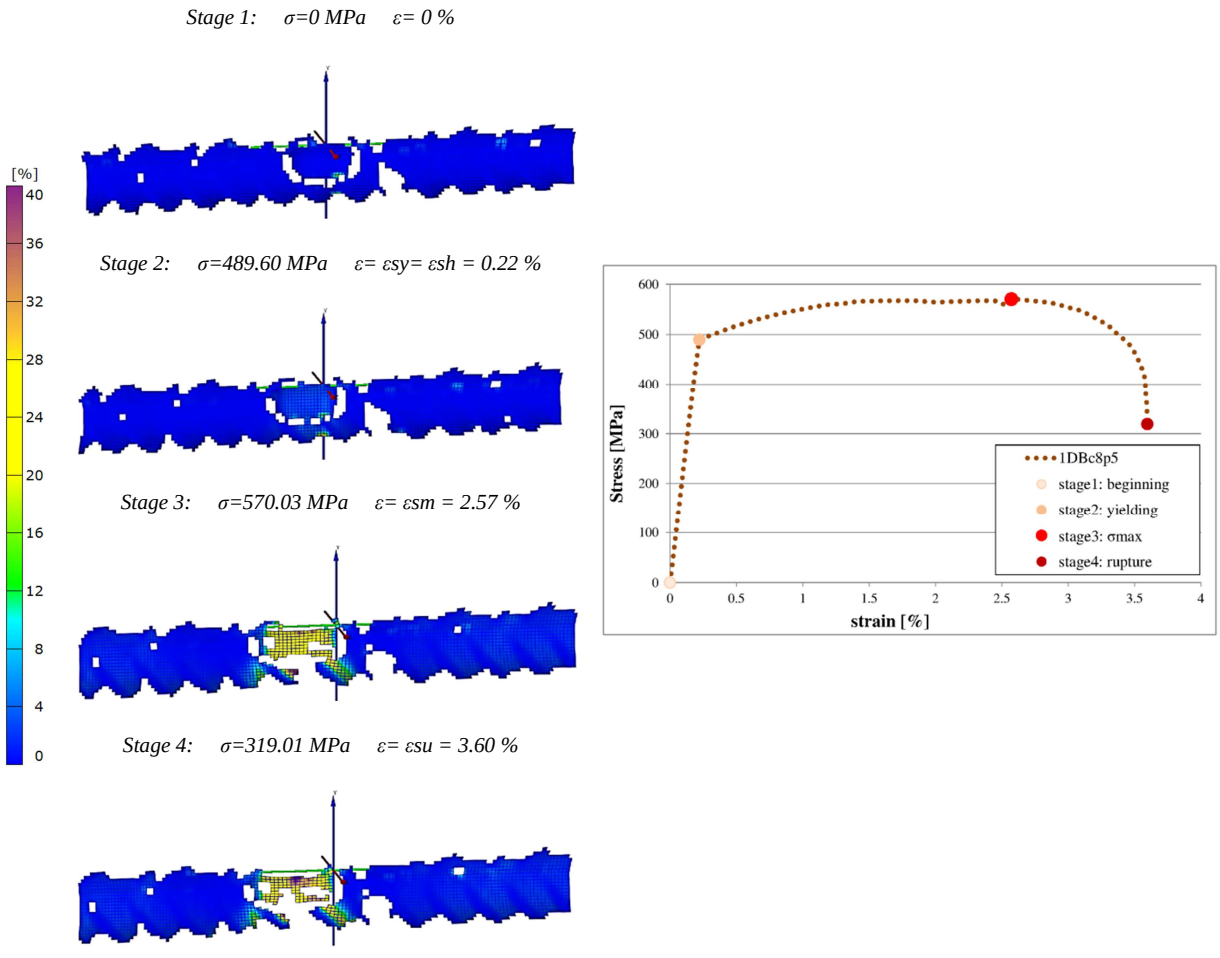

Figure 4-12. Optical Deformation Measurement System and Stress-strain curve, 1DBc8p5 bar

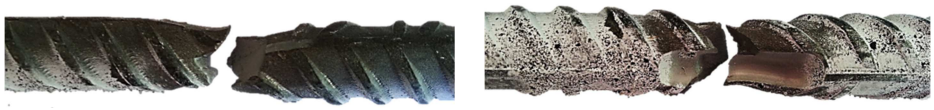

Figure 4-13. Rupture of 1DBc8p5 bar: longitudinal profile and two sides of the bar

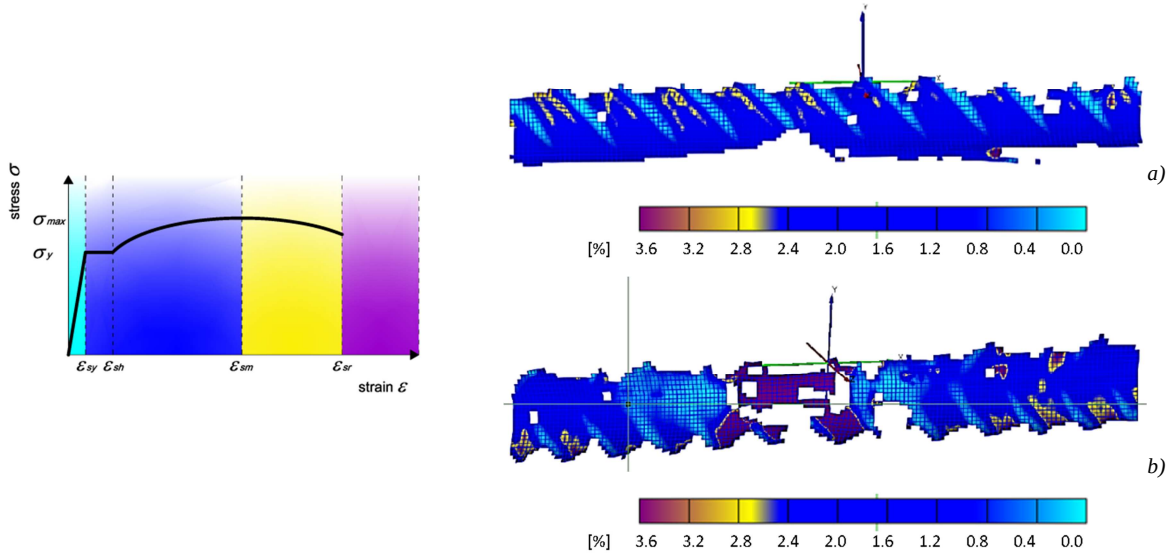

Figure 4-14.Comparison between strains: a) SB3 and b) 1DBc8p5 bars, ARAMYS system

4.2.1.4. Comparison between experimental results

A comparison between the behaviour of the different bars tested will be presented in the next paragraphs, basing on the obtained stress-strain curves, data measured and pictures elaborated by the ARAMIS system. It is worth noting that in this phase, the stresses shown in the graphs are nominal stresses, obtained dividing the forces by the initial cross-sectional area of sound bars (A_s = 201.06 mm^2) and not by the residual cross-sectional area. Furthermore, it should be considered that the results should be treated with caution. Indeed, it was possible to test only one locally damaged bar of each type, therefore a margin of error is likely.

In general, reinforcing bars with local damage exhibit lower global strength and ductility respect to sound bars, see *Figure 4-15*. In detail, a global reduction of strength between 3 and 60% is found. The highest reduction of strength is observed for pit of circular shape and depth equal to 10 mm. The global ductility of the damaged bars (expressed through W or A* following defined) decreases between 50 and 100% respect to the sound bars, with a great variability as function of pit depth, pit shape, pit length and number of pits. A more detailed analysis is given below.

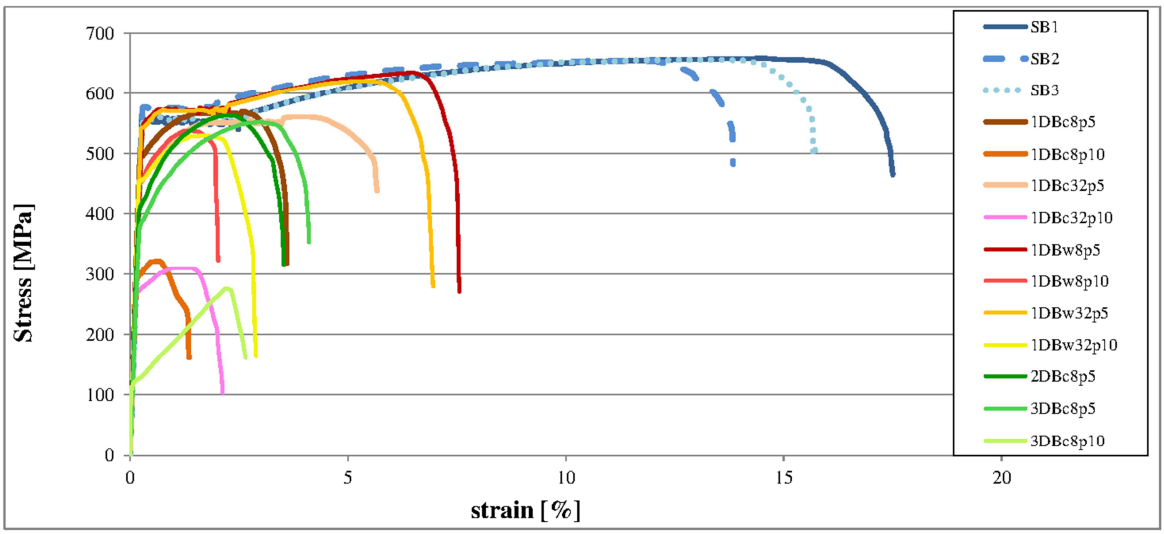

Figure 4-15. Stress-strain curves from tensile tests of sound and locally damaged reinforcing bars

Before to go ahead with the examination of the tests results, some definitions must be specified. In *Figure 4-16* it is reported a typical stress-strain curve which can be obtained through tensile tests on steel bars. In this work, yield strength and tensile strength (maximum strength) are respectively indicated with σ_y and σ_{max}. Regarding the strains, ε_{sy} is the strain corresponding to the achievement of the yield strength, ε_{sh} is the strain at the beginning of the strain-hardening phase, ε_{sm} is the strain at the maximum strength and ε_{sr} is the strain at the bar rupture. Another important definition that must be specified concerns the concept of steel ductility, i.e. the ability of steel bars to deform when loaded above its elastic limit without fracturing. A number of Codes defines the ductility of steel reinforcement through minimum values of different parameters. For example, CEB-FIP MC90[61] recommends a specific minimum value for both the strength ratio σ_{max}/σ_y and the strain ε_{sm}, *Figure 4-16 a)*. The three parameters involved can be easily found by tensile tests, without the need to define a stress-strain curve, therefore this definition of ductility is widespread among the researchers (paragraph 3.3.2). Others researchers have instead given proposals for defining steel ductility through a single parameter, able to take into account strength and deformation simultaneously. For example, Moreno et al.[186] proposed to consider the total energy W, defined as the area under the stress-strain curve until the maximum tensile strength, *Figure 4-16 b)*. This parameter corresponds to the toughness, which expresses the total energy absorbed by the steel per unit of volume during the deformation process up to elongation at maximum loading. Creazza et al.[84] proposed instead to define the steel ductility as A*, the area under the post yielding stress-strain curve until the tensile strength, see *Figure 4-16 c)*. A* represents the deformation work of the steel material during the strain-hardening phase and implicitly considers both the ductility in terms of strength, through σ_{max} and σ_y and the ductility in terms of elongation, through ε_{sh} and ε_{sm}. The authors specified that this definition of ductility is only an indicator of the performance of steel bars, while other criteria have been developed to consider their rotational capacity, e.g. Cosenza et al.[81] or Beeby et al.[31], and therefore their behaviour within concrete structures. All these criteria may be useful for a correct definition of ductility in corroded steel bars.

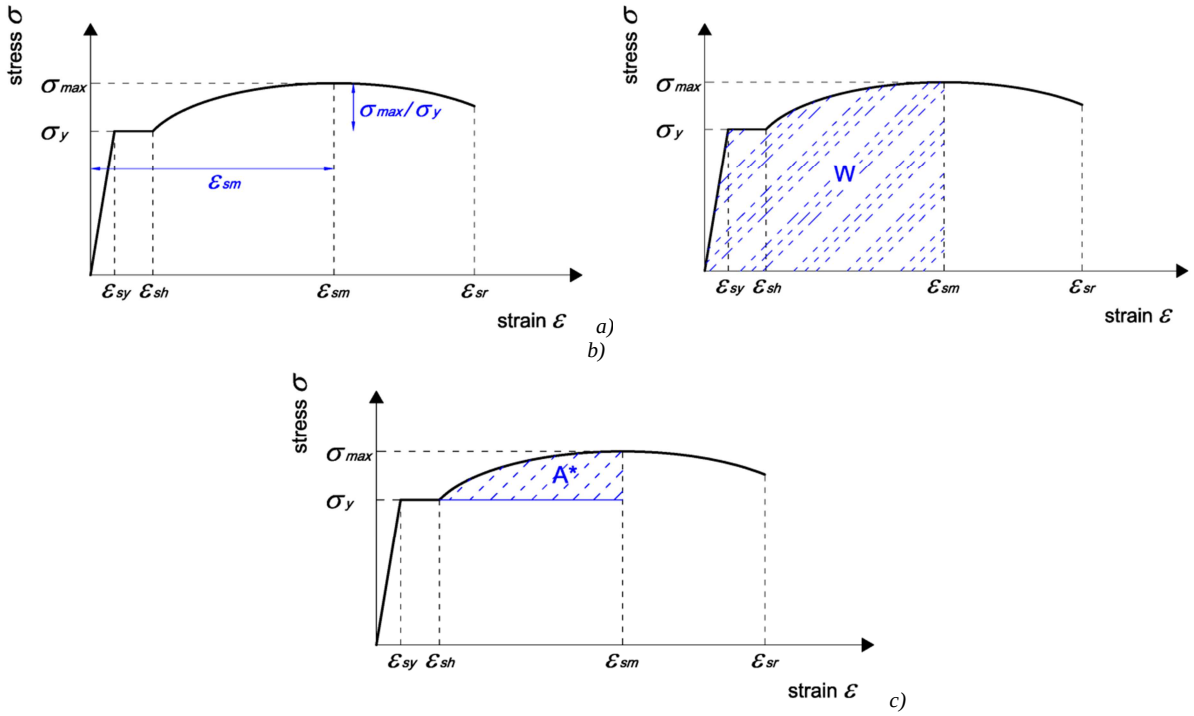

Figure 4-16. Typical stress-strain curve for reinforcing steel and ductility definition

Effect of different pit shapes

As previously described, pits with different cross section shapes were created in the reinforcing bars. In *Figure 4-17* and *Table 4-8* the global responses of bars with circular or wedge-shaped pits are compared and the following conclusions are gleaned:

- The tensile strength of damaged bars is higher when the pit is cuneiform instead of circular. This is more evident when pits are deeper. The range of variability found is about 10-70%.
- The ductility of damaged bars with cuneiform pit is also generally greater than the one of the bars with circular shape. This is always true if the definition of ductility W is considered: in this case the range of ductility variation is about 50-300%. When instead A* is considered, in one case the situation is reversed. This is due to the fact that considering A*, the plateau of the σ-ε law is neglected and the ductility refers only to the plastic-hardening branch.
- A possible explanation of the dependence of the overall response of damaged bars on the pit shape lies in the different way in which the areas near the pit work. When the pit is cuneiform, its lateral areas collaborate on the achievement of higher strength and ductility. Instead, in the case of circular shape, there is lower cross-sectional area that may collaborate and the rupture of the bar is brittler, see *Figure 4-18*, *Figure 4-19* and *Figure 4-20*.

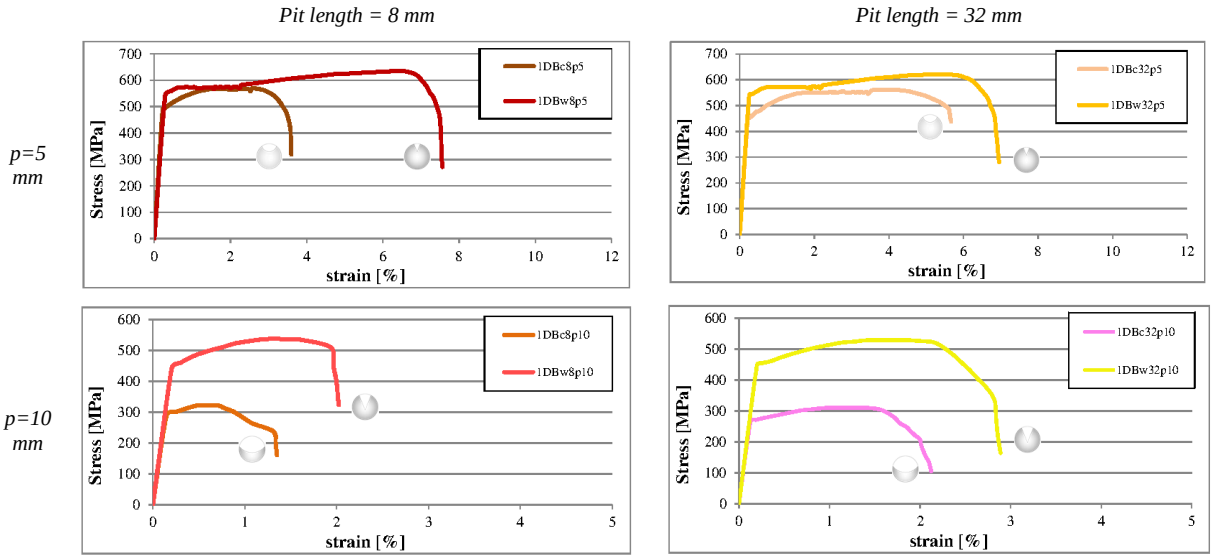

Figure 4-17. Stress-strain curves for reinforcing bars with different shapes of pit cross section

Table 4-8. Comparison between reinforcing bars with different pit cross section shapes

Bar	Pit cross section shape	Max strength		Area under σ-ε law / plastic branch, until σ_{max}		Area under σ-ε law / elastic-plastic branch, until σ_{max}	
		σ_{max}[MPa]	$\Delta\sigma_{max}$ [%]	A* [J/mm^3]	ΔA* [%]	W [J/mm3]	ΔW [%]
1DBc8p5	circular	570.03	11.34	1.44	141.69	13.48	176.28
1DBw8p5	wedge-shaped	634.69		3.47		37.26	
1DBc32p5	circular	561.32	10.71	3.14	-19.26	20.70	49.29
1DBw32p5	wedge-shaped	621.46		2.53		30.90	
1DBc8p10	circular	322.14	66.84	0.10	698.01	1.64	298.19
1DBw8p10	wedge-shaped	537.45		0.77		6.54	
1DBc32p10	circular	310.90	70.37	0.33	149.13	3.36	136.46
1DBw32p10	wedge-shaped	529.69		0.82		7.94	

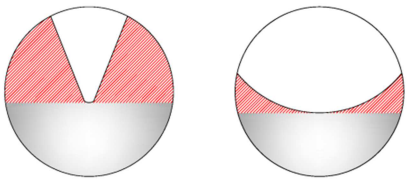

Figure 4-18. Comparison between wedge-shaped and circular pit– cross section of 1DBc8p10 and 1DBw8p10 bars

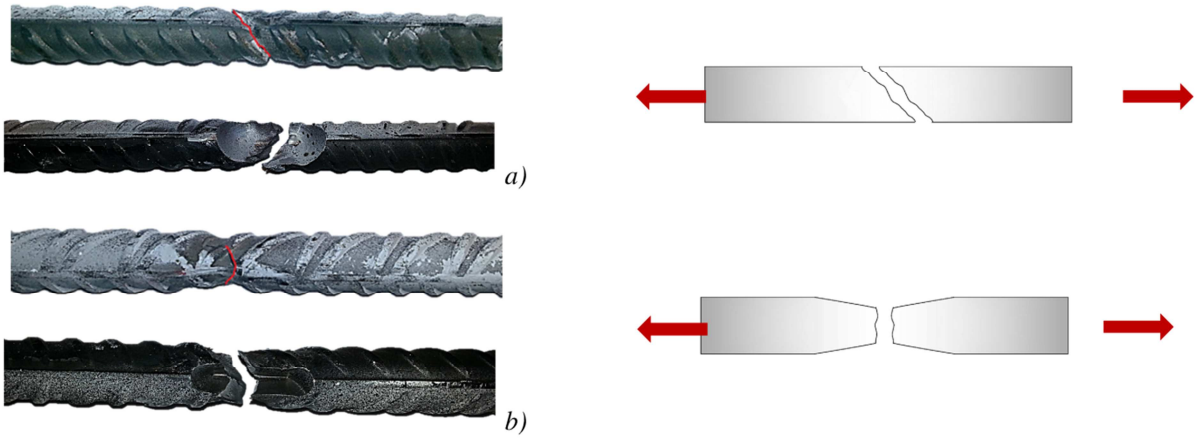

Figure 4-19. Comparison between circular and wedge-shaped pit –longitudinal profiles of a)1DBc8p10 and b)1DBw8p10 bars: shear fracture and ductile fracture.

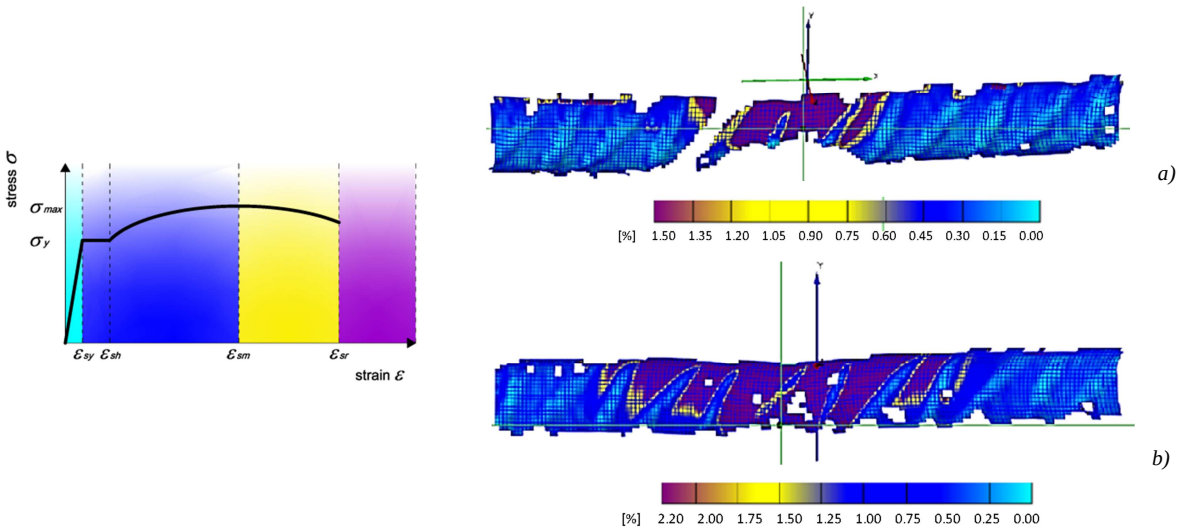

Figure 4-20. Comparison between circular and wedge-shaped pit –longitudinal profiles of a)1DBc8p10 and b)1DBw8p10 bars at stage 3, ARAMIS system

Effect of different pit lengths

Reinforcing bars with pits of different lengths were also tested. In *Figure 4-21* and *Table 4-9* the global response of damaged bars with *Pit length* of 8 or 32 mm are compared. It is possible to observe that:

- The tensile strength of reinforcing bars with longer pits is slightly lower respect to bars with shorter pits. However, this difference is around 2-3% so it can be neglected. A possible explanation is that the volume removed among these bars is quite similar.
- Steel bars with longer pits have in general greater ductility, in this case expressed only with W parameter in *Table 4-9*. Indeed, the pit length does not influence the

presence/absence of yield plateau so W or A* are equivalent. When the pits have greater length, the bars are able to dissipate more energy in the pit length before breaking. This is confirmed by the greater amount of elongation in longer pits respect to shorter pit, see last column *Table 4-9* and by the fact that the strains localise in a greater area when the pit is longer, *Figure 4-22* and *Figure 4-23*.

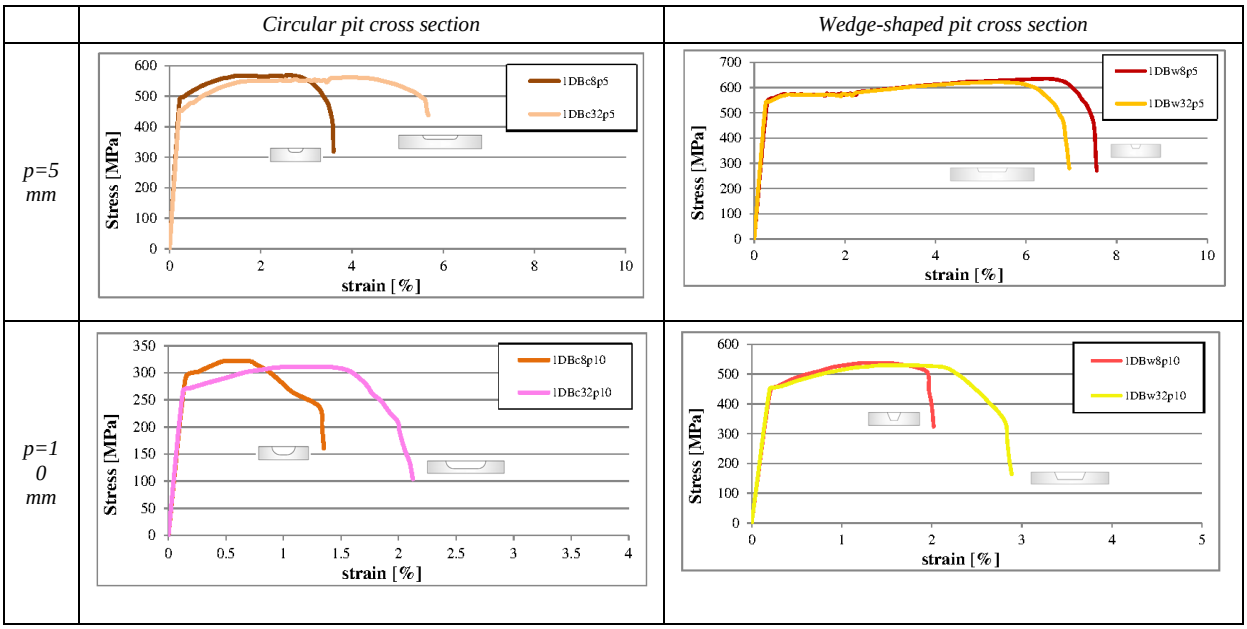

Figure 4-21. Stress-strain curves for reinforcing bars with different pit lengths

Table 4-9. Comparison between reinforcing bars with different pit lengths

Bar	Pit length	Max strength		Area under σ-ε law / elastic-plastic branch, until σ_{max}		Final elongation /measured	Pit elongation /measured	Percentage of pit elongation on the total bar elongation /measured
		σ_{max} [MPa]	$\Delta\sigma_{max}$ [%]	W [J/mm^3]	ΔW [%]	E_{Fu} [mm]	$E_{Fu,pit}$ [mm]	ΔE [%]
1DBc8p5	8	570.03	-1.53	13.48	53.51	12.50	7.90	63.20
1DBc32p5	32	561.32		20.70		19.10	12.60	65.97
1DBw8p5	8	634.69	-2.08	37.26	-17.05	25.80	8.40	32.56
1DBw32p5	32	621.46		30.90		24.00	11.90	49.58
1DBc8p10	8	322.14	-3.49	1.64	104.36	4.80	2.40	50.00
1DBc32p10	32	310.90		3.36		7.20	6.10	84.72
1DBw8p10	8	537.45	-1.44	6.54	21.36	7.50	6.60	88.00
1DBw32p10	32	529.69		7.94		10.50	8.90	84.76

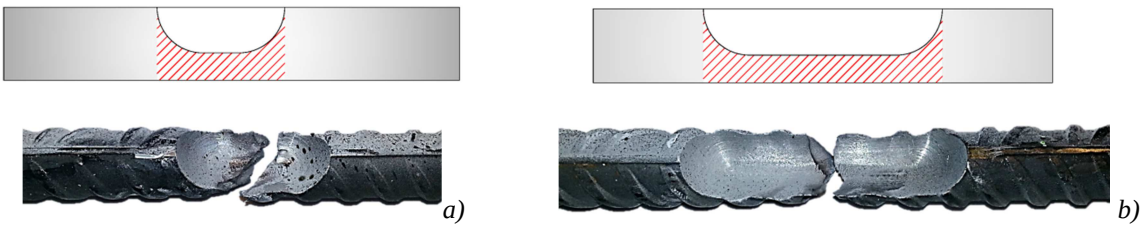

Figure 4-22. Comparison between bars with pits of different length –longitudinal profiles of a)1DBc8p10 and b)1DBc32p10 bars

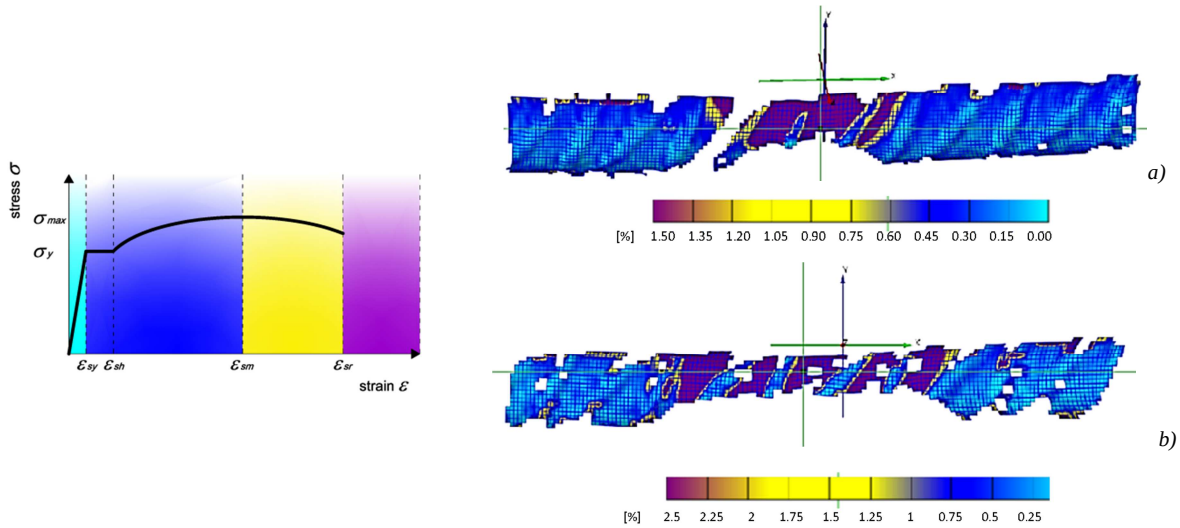

Figure 4-23. Comparison between pits of different length –longitudinal profiles of a)1DBc8p10 and b)1DBc32p10 bars, ARAMIS system

Effects of a different pit number

The presence of more than one pit in the bar length is also investigated. The structural response of bars with one, two or three pits is compared in *Figure 4-24* and *Table 4-10*. For steel bars damaged with pits of small depth (p=5 mm), no great differences in the global response are observed. It should be noticed that considering different definitions of bar ductility, different conclusions can be made. Indeed, A* is found greater for bars with more pits only because the ratio σ_{max}/σ_y increases; the strain at the maximum strength instead are more similar among them. Finally, it is possible to observe that in all the damaged bars, the deformations localize at one pit, where the bar rupture will take place, while in the other pits a lower final elongation is measured, see *Figure 4-26*. In the case instead of deeper pits (p=10 mm), the effect of more pits is evident: after the yielding of the steel bar, the stiffness highly decreases and due to the asymmetric disposition of the pits, bending develops (*Figure 4-24*). For this reason, the bar ductility increases, also if the strains localize in the central pit more than in the bar with one pit, see *Figure 4-27*.

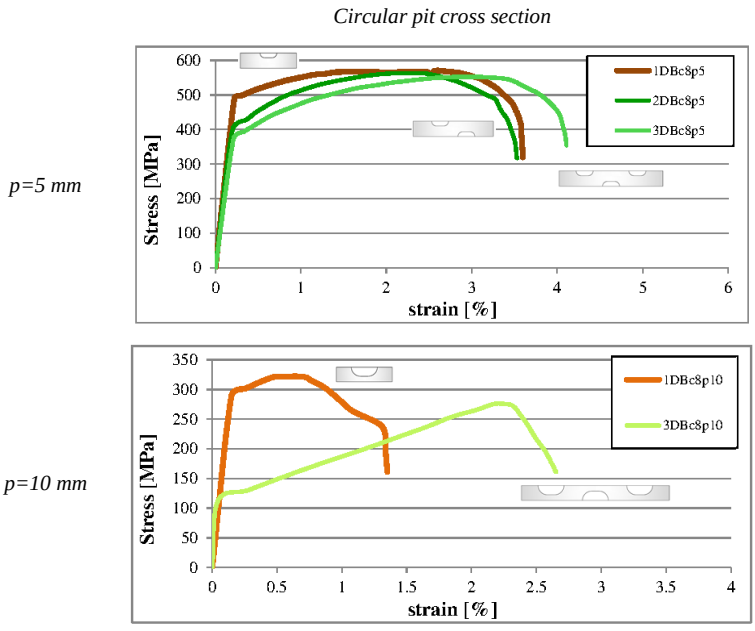

Figure 4-24. Stress-strain curves for reinforcing bars with different pit number

Table 4-10. Comparison between reinforcing bars with different pit lengths

Bar	Pit number	Max stress		Area under σ-ε law / plastic branch, until σ_{max}		Area under σ-ε law / elastic-plastic branch, until σ_{max}		Strain at σ_{max}	Percentage of pit elongation on the total bar elongation /measured
		σ_{max} [MPa]	$\Delta\sigma_{max}$ [%]	A* [J/mm^3]	ΔA* [%]	W [J/mm^3]	ΔW [%]	$\Delta\varepsilon_{sm}$ [%]	ΔE [%]
1DBc8p5	1	570.03		1.44		13.48			63.20
2DBc8p5	2	562.97	-1.24	2.36	64.10	10.97	-18.67	-12.2	67.77
3DBc8p5	3	551.78	-3.20	3.64	153.38	14.70	9.00	19.3	61.70
1DBc8p10	1	322.14	-14.42	0.10	1866.33	1.64	167.46	270.3	50.00
3DBc8p10	3	275.69		1.90		4.39			67.42

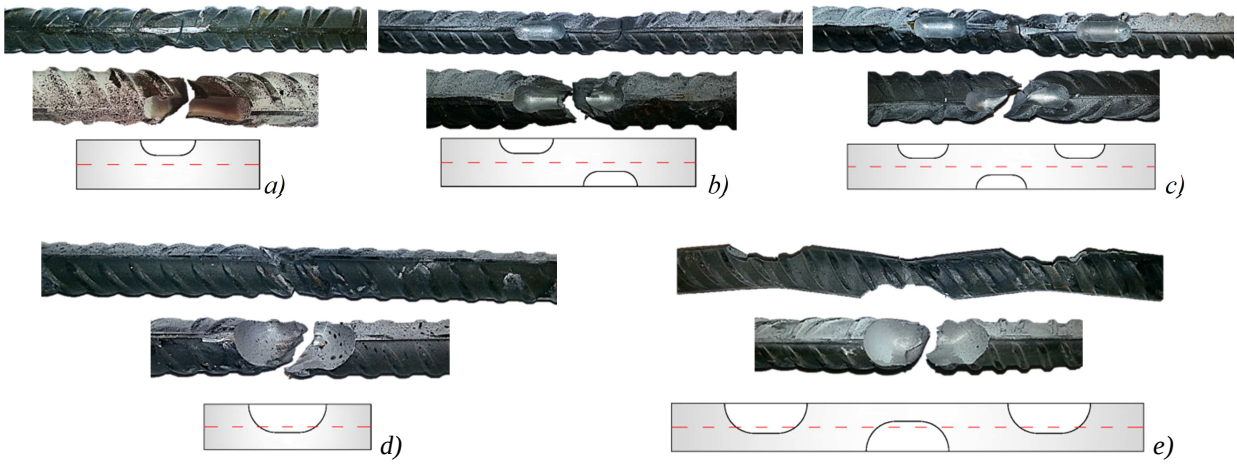

Figure 4-25. Comparison between bars with different number of pits –longitudinal profiles of a)1DBc8p5; b)2DBc8p5; c)3DBc8p5; d)1DBc8p10; e)3DBc8p10 bars

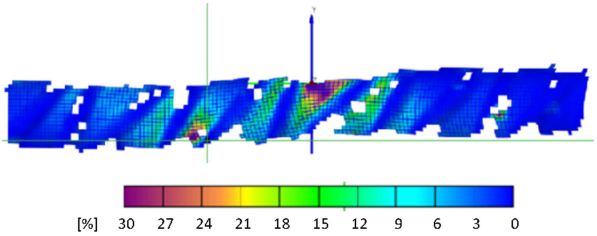

Figure 4-26. Longitudinal profile of 2DBc8p5 bar at stage 3, ARAMIS system

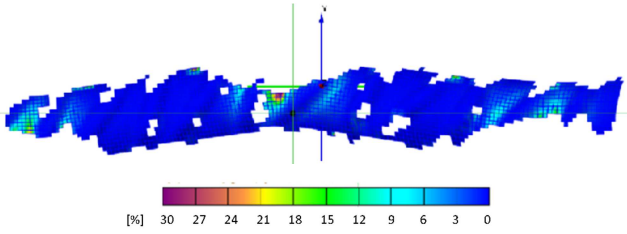

Figure 4-27. Longitudinal profile of 3DBc8p10 bar at stage 3, ARAMIS system

Comparison between damaged bars with equal pit depth

In order to quantify the amount of corrosion in reinforcing bars, many researchers measure the maximum pit depth, among others Rodriguez et al.[222]. However, the tests made indicate that also if the damaged bars have pits of equal depth, their global behaviour may be completely different, see *Figure 4-28.* In detail, when pits are 5 mm deep, the main difference between the damaged bars is the ductility. The reduction of ductility for these bars respect to the sound bars is

between about 50 and 80% (*Table 4-11*). When pits are 10 mm deep, the damaged bars have different maximum strength as well as different ductility. In this case, the maximum strength decreases between 20 and 60%, while the ductility decreases between 70 and 100% (*Table 4-11*). To conclude, when the residual mechanical properties of corroded bars are estimated basing on the pit depth, the great approximation made on the assessment should be considered.

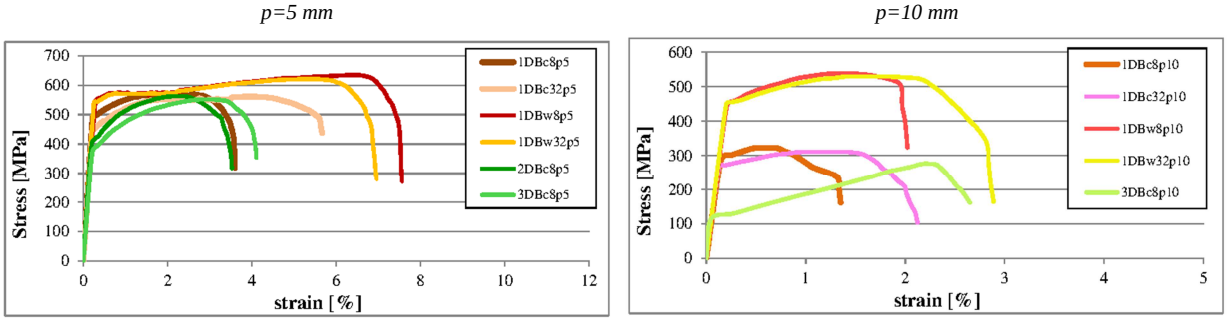

Figure 4-28. Stress-strain curves for reinforcing bars with equal pit depth

Table 4-11. Comparison between reinforcing bars with equal pit depth

Bar	Max strength		Area under σ-ε law / plastic branch, until σmax		Area under σ-ε law / elastic-plastic branch, until σmax	
	σmax [MPa]	Δσmax [%]	A* [J/mm3]	ΔA* [%]	W [J/mm3]	ΔW [%]
SB	655.97		7.38		78.92	
1DBc8p5	570.03	-13.10	1.44	-80.54	13.48	-82.91
1DBc32p5	561.32	-14.43	3.14	-57.50	20.70	-73.77
1DBw8p5	634.69	-3.25	3.47	-52.96	37.26	-52.79
1DBw32p5	621.46	-5.26	2.53	-65.69	30.90	-60.84
2DBc8p5	562.97	-14.18	2.36	-68.06	10.97	-86.10
3DBc8p5	551.78	-15.88	3.64	-50.68	14.70	-81.38
1DBc8p10	322.14	-50.89	0.10	-98.69	1.64	-97.92
1DBc32p10	310.90	-52.60	0.33	-95.54	3.36	-95.75
1DBw8p10	537.45	-18.07	0.77	-89.57	6.54	-91.71
1DBw32p10	529.69	-19.25	0.82	-88.89	7.94	-89.94
3DBc8p10	275.69	-57.97	1.90	-74.30	4.39	-94.43

Comparison between damaged bars with equal volume reduction

The second method used by almost all the researchers in order to quantify the amount of corrosion in reinforcing bars is to measure the loss of weight of the corroded bars respect to an equal sound bar. In *Figure 4-29* are shown the results of the tests made on bars with equal loss of volume. Damaged bars with volume lost [%] minor of 1, manifest similar residual strength but different residual ductility, which varies between 60 and 90% of the sound one (*Table 4-12*).

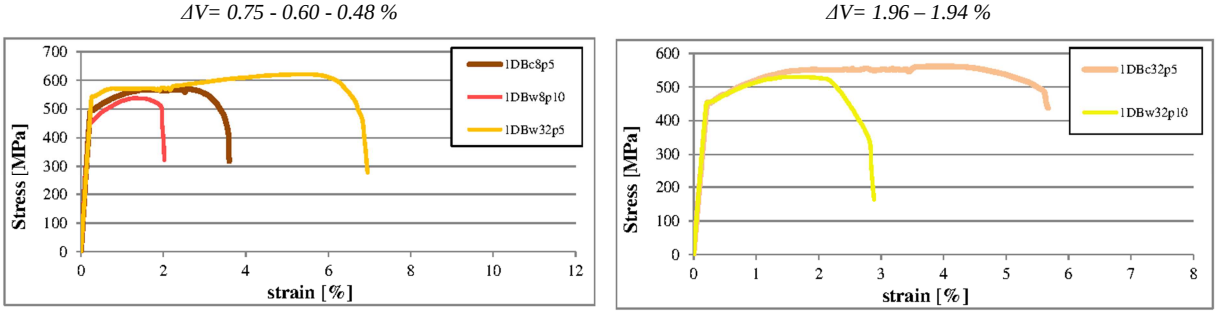

Figure 4-29. Stress-strain curves for reinforcing bars with equal loss of volume

The same remark is valid for damaged bars with 1.9% of volume lost: the two bars exhibit a similar maximum strength but a different residual ductility (*Table 4-12*). To conclude, basing on these remarks, the evaluation of the weight loss by the corroded bars may be a sufficiently approximate method for the evaluation of the residual strength but not for assessment of the residual ductility.

Table 4-12. Comparison between reinforcing bars with equal loss of volume

Bar	Max strength		Area under σ-ε law / plastic branch, until σ_{max}		Area under σ-ε law / elastic-plastic branch, until σ_{max}	
	σ_{max} [MPa]	$\Delta\sigma_{max}$ [%]	A* [J/mm^3]	ΔA* [%]	W [J/mm^3]	ΔW [%]
SB*	655.97		7.38		78.92	
1DBc8p5	570.03	-13.10	1.44	-80.54	13.48	-82.91
1DBw8p10	537.45	-18.07	0.77	-89.57	6.54	-91.71
1DBw32p5	621.46	-5.26	2.53	-65.69	30.90	-60.84
1DBc32p5	561.32	-14.43	3.14	-57.50	20.70	-73.77
1DBw32p10	529.69	-19.25	0.82	-88.89	7.94	-89.94

4.2.2. Modeling of corrosion effects on steel bars

4.2.2.1. Residual area

Corrosion phenomena are mainly due to carbonation or chloride attack. In the first case, corrosion is distributed more or less uniformly over the bar surface, *Figure 4-30 a)*. For the evaluation of the residual cross-sectional area in the case of **uniform corrosion**, *Equation 3-13* is reliable. In the case of **pitting corrosion** instead, a correct evaluation of the residual area of reinforcing bars is difficult, because the residual cross sections vary significantly along the bar length due to the different shapes that pits develop. Val et al.[256] and Rodriguez et al.[221] proposed simplified models for the evaluation of the residual steel area; a brief description of the two models has been given in paragraph 3.3.1. According to these approaches, once the maximum penetration of pitting *p* is known, the residual cross-sectional area of corroded bars can be estimated, see respectively *Figure 4-30 b)* and *Figure 4-30 c)* and assumed equal for all the bar length. The main difference between the two models is that Val et al.[256] assume a hemispherical shape for the pit cross section while Rodriguez et al.[221] take on a circular residual cross section. In practice, the Rodriguez's et al.[221] model overcomes the problem of the pit shape assuming that the "working" area of a corroded bar is only the central core. The models lead to two evaluations of the residual cross-sectional area of corroded bars that may strongly differ. In *Figure 4-31* a comparison between the two approaches is made: the residual bar section normalized with respect to the original area is plotted against the corrosion penetration ratio p/Φ. It is possible to observe that with the increasing of the corrosion penetration ratio p/Φ until a value of 0.42, the difference between the results obtained with the two models also increases, reaching a maximum of 37.5%. For p/Φ>0.42, the results again converge.

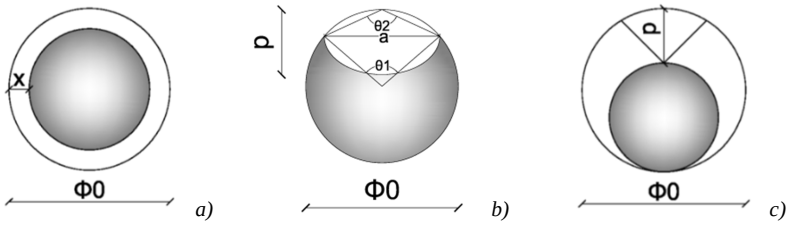

Figure 4-30. a)Uniform corrosion; b) Val's et al.[256] model; c) Rodriguez' et al.[221] model

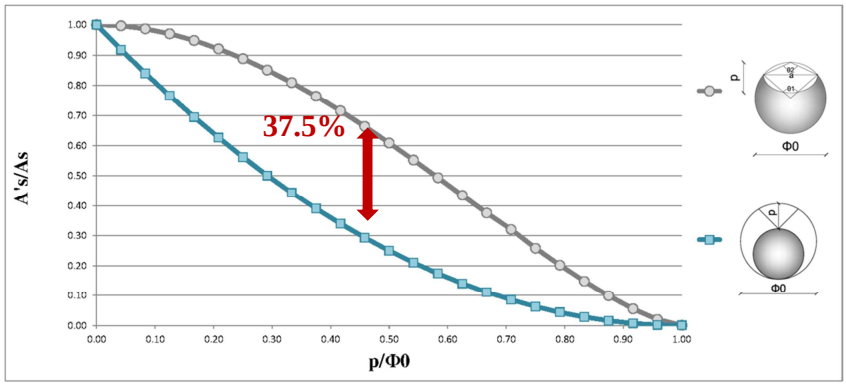

Figure 4-31. Residual area ratio A'_s/A_s versus Corrosion penetration ratio p/Φ

In order to establish which model should be adopted for the evaluation of the residual area of a bar subjected to pitting corrosion, the results of the experimental campaign made by the Author and described in paragraph 4.2, are here compared. Indeed, the locally damaged bars tested well simulate the case of steel bar with pitting corrosion. In this way, the effect of the presence of one pit on the assessment of the residual steel area can be understood disregarding from the spatial variability of the corrosve attack along the bar length. For this purpose, three different residual areas must be defined:

- A'_s is the already defined minimum residual cross-sectional area, which corresponds to the geometrical residual cross section (grey area of *Figure 4-30 b));*
- A_{eq} is the effective residual cross-sectional area, which may be estimated with the following equation, once the data of a tension test are available:

$$A_{eq} = {F_{max}}/{\sigma_{max,sound}} \qquad \textit{Equation 4-1}$$

  where F_{max} is the maximum force recorded during the tension test [N] and $\sigma_{max,sound}$ is the maximum strength of the sound bar, found with the tension test [MPa]. In practice this parameter gives an equivalent cross-sectional area [mm^2] equal for all the bar length, which expresses the area of the steel bar that is actually working;

- A_r is the average residual cross-sectional area, which corresponds to an average value estimated from the weight loss by a corroded bar. For the tests made, due to the fact that the volume of the local damage was known, may be calculated as:

$$A_r = {V_r}/{l_0} \qquad \textit{Equation 4-2}$$

  where V_r is the residual volume of the damaged bar and l_0 is the bar length, both defined between the jaws of the tested bar.

In practice, A_{eq} corresponds to the real value of the residual steel area; A'_s is the residual transverse area (in the experimental tests made is known, in general can be estimated through models) and A_r is the area that researchers usually measure during the tests, because of its simple determination. The results found with the experimental campaign made are compared through these three definitions of area. As we can see in *Figure 4-32*, the value of residual area may significantly diverge depending on which of the three definitions of area is considered, in particular for pits with greater depth. In general, the equivalent cross-sectional area A_{eq} is well estimated by the Val's et al.[256] model only when the pits are circular. The Rodriguez's et al.[221] model underestimates excessively the residual steel area for every pit shape. The average

residual cross-sectional area A_r upper estimates in all cases the residual area, especially when pits have great depth. Finally, the values of minimum residual cross-sectional area A'_s are very close to A_{eq}. This it means that if the pit shape is known, a good estimation of the equivalent cross-sectional area A_{eq} is possible. Following, more accurate comparisons are made.

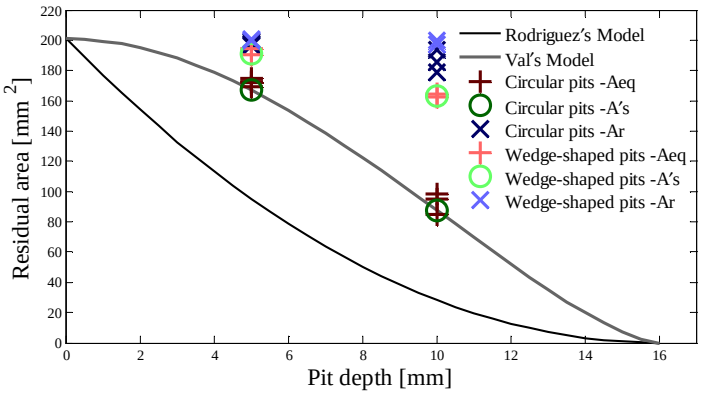

Figure 4-32. Residual area versus pit depth for locally damaged bars tested in tension

In the case of locally damaged bars with circular pits:

- All the three areas defined are slightly influenced by the pit length, *Table 4-13*.
- The Val's et al.[256] model well estimates A_{eq}, as expected, considering that the circular shape of the pits is quite close to the one of the Val's model. The maximum difference found between *Aeq* and the value given by the Val's model is of 12.81% (*Table 4-13*).
- The average residual cross-sectional area A_r, estimated from the weight loss by corroded bars, differs significantly from A_{eq} and from the values found with Val's model. In the worst case, p=10 mm, A_r is about +121.20% the value estimated with Val's model (*Table 4-13*), so cannot be considered a good estimation of the residual steel area.

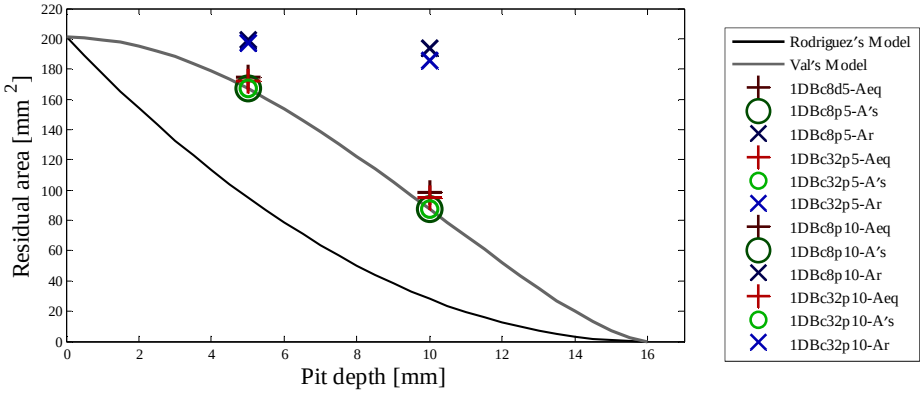

Figure 4-33. Residual area versus pit depth for locally damaged bars tested in tension

Table 4-13. Comparison between reinforcing bars with equal loss of volume

Bar	*Equivalent area*	*Min. residual cross-sectional area*	*Average residual cross-sectional area*	*Comparison - different pit length*			*Val's model: A'_s=167,05mm^2 p=5mm A'_s=87,53 mm^2 p=10mm*		
	A_{eq} [mm^2]	A'_s [mm^2]	A_r [mm^2]	ΔA_{eq} [%]	$\Delta A'_s$ [%]	ΔA_r [%]	ΔA_{eq} [%]	$\Delta A'_s$ [%]	ΔA_r [%]
1DBc8p5	174.72	167.05	199.56	-1.53	0.00	-1.22	+4.59	0.00	+19.46
1DBc32p5	172.05	167.05	197.12				+2.99	0.00	+18.00
1DBc8p10	98.74	87.53	193.62	-3.49	0.00	-4.20	+12.81	0.00	+121.20
1DBc32p10	95.29	87.53	185.48				+8.87	0.00	+111.91

In the case of locally damaged bars with wedge-shaped pits:

- The values of residual area are slightly influenced by the pit length (low values of ΔA_{eq}, $\Delta A'_s$ and ΔA_r of *Table 4-14)*.
- The Val's et al.[256] model underestimates the value of residual steel area. This is due to the great difference between the pit shapes of the model and the reality. The maximum difference between A_{eq} and the value found with the Val's model is of 88.20% (*Table 4-14*).
- In the case of low pit depth, A_r does not differ so much from A_{eq} and A'_s. The difference becomes greater for p=10 mm but is however lower than for damaged bars with circular pit.

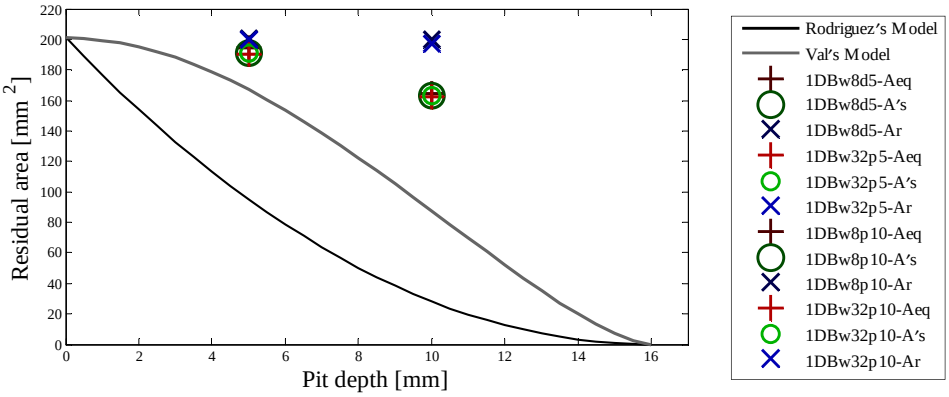

Figure 4-34. Residual area versus pit depth for locally damaged bars tested in tension

Table 4-14. Comparison between reinforcing bars with equal loss of volume

Bar	*Equivalent area*	*Min. residual cross-sectional area*	*Average residual cross-sectional area*	*Comparison - different pit length*			*Val's model: A's=167.05mm2 p=5mm A's=87.53 mm2 p=10mm*		
	Aeq [mm2]	*A's [mm2]*	*Ar [mm2]*	*ΔAeq [%]*	*ΔA's [%]*	*ΔAr [%]*	*ΔAeq [%]*	*ΔA's [%]*	*ΔAr [%]*
1DBw8p5	*194.54*	*191.38*	*200.78*	*-2.08*	*0.00*	*-0.34*	*+16.45*	*+14.56*	*+20.19*
1DBw32p5	*190.48*	*191.38*	*200.10*				*+14.03*	*+14.56*	*+19.78*
1DBw8p10	*164.73*	*163.46*	*199.86*	*-1.44*	*0.00*	*-1.35*	*+88.20*	*+86.75*	*+128.34*
1DBw32p10	*162.35*	*163.46*	*197.17*				*+85.48*	*+86.75*	*+125.26*

In the case of locally damaged bars with more than one pit:

- A_{eq} and A_r are slightly influenced by the number of pits when p=5 mm; in the case of p=10 mm, the values of equivalent and average residual cross-sectional area are instead more influenced: between one and three pits A_{eq} decreases of 14.42%, and the A_r of 7.69% (*Table 4-15*).
- The Val's et al.[256] model better estimates A_{eq}, when the number of pits is greater. However, for deeper pit, the Val's model can underestimate the residual area (*3DBc8p10* bar). This remark is important because the real corroded bars have more than one pit, therefore the Val's model may be not on the safety side.
- The difference between A_r and the values of residual area found with the Val's model decreases for an increasing number of pits. However, the error remains too high for considering this method reliable.

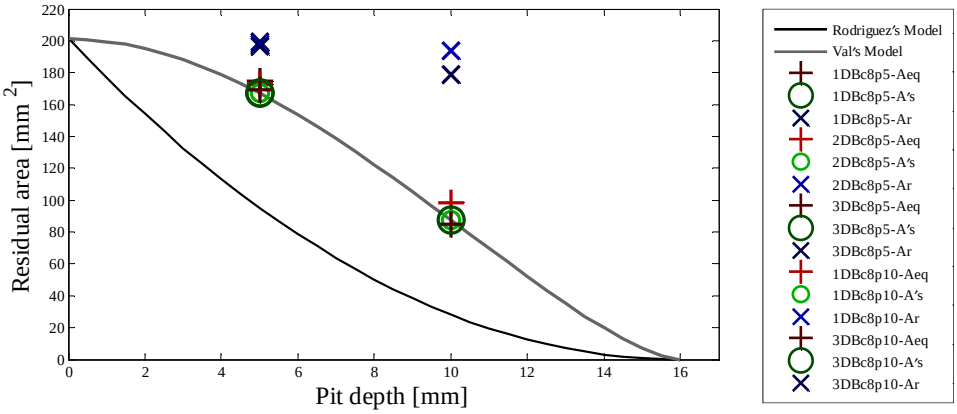

Figure 4-35. Residual area versus pit depth for locally damaged bars tested in tension

Table 4-15. Comparison between reinforcing bars with equal loss of volume

Bar	*Equivalent area*	*Min. residual cross-sectional area*	*Average residual cross-sectional area*	*Comparison - different pit number*			*Val's model: A'_s=167.05mm^2 p=5mm A'_s=87.53 mm^2 p=10mm*		
	A_{eq} [mm^2]	A'_s [mm^2]	A_r [mm^2]	ΔA_{eq} [%]	$\Delta A'_s$ [%]	ΔA_r [%]	ΔA_{eq} [%]	$\Delta A'_s$ [%]	ΔA_r [%]
1DBc8p5	174.72	167.05	199.56				4.59	0.00	19.46
2DBc8p5	172.55	167.05	198.06	-1.24	0.00	-0.75	3.29	0.00	18.56
3DBc8p5	169.12	167.05	196.56	-3.20	0.00	-1.50	1.24	0.00	17.66
1DBc8p10	98.74	87.53	193.62	-14.42	0.00	-7.69	12.81	0.00	121.20
3DBc8p10	84.50	87.53	178.73				-3.46	0.00	104.19

To conclude, the equivalent area is the cross-sectional area of reinforcing bar that is actually working. For a correct evaluation of this area, it is suggested to consider the minimum cross-sectional area A'_s, which leads to a good approximation and in major cases to be on the safety side. If A'_s is not known, because the exact morphology of the pits has not been detected, the Val's model gives its best approximation. The widespread evaluation of the residual cross-sectional area through the average loss of weight has been instead found totally unsafe because it leads to a strong over-estimation of the residual steel area of corroded bars. The method can be considered reliable only for pitting corrosion characterized by small pith depth, high number of pitting along all the length of the steel bar and preferable pits of wedge shape.

In general, pitting corrosion occurs in concomitance with uniform corrosion, **mixed corrosion type**. The approach here suggested is to consider the model proposed by Rodriguez et al.[221] for pitting corrosion (*Figure 4-30 c)*), for the evaluation of the residual area of steel bars subjected to mixed corrosion type. Indeed, from the analysis made, it is evident that the Rodriguez's model strongly underestimates the residual cross-sectional area of bars affected by pitting corrosion and may be instead more suitable for a more aggressive type of corrosion, like the mixed corrosion type. The formula proposed for the evaluation of the residual area in the case of mixed corrosion is therefore:

$$A'_s = \frac{\pi}{4} \cdot (\Phi - p)^2 \qquad \textit{Equation 4-3}$$

where p is the maximum depth of the localized corrosion attack and Φ is the initial diameter of the reinforcing bar. The value of p may be available from experimental test or evaluated according to the following relationship:

$$p = R \cdot x_{mean} \qquad \textit{Equation 4-4}$$

where R assumes values between 4-8 for natural corrosion and between 5-13 for accelerated corrosion tests, see paragraph 3.3.1. The parameter x_{mean} is an average corrosion penetration which can be estimated from loss in weight. In order to confirm this proposal, in *Figure 4-36* a comparison between the residual areas obtained for mixed corrosion type, pitting corrosion and pitting + uniform corrosion is made. In detail, in the ordinate is reported the residual area of a corroded bar normalized with respect to the original sound area, in the abscissa the corrosion penetration x_{mean} normalized with respect to the original bar diameter. The residual area in the case of pitting corrosion is calculated with the Val's model. The residual area for mixed corrosion type is evaluated with *Equation 4-3* and R equal to 4 or 8 and with Val's model removing the additional corroded area due to uniform corrosion. It is possible to observe that *Equation 4-3* gives values very close to the ones obtained with Val's model + uniform corrosion, especially for R=4. Concluding, the approach proposed is coherent with the physical phenomenon and it allows the valuation of the residual area of steel bars in the case of mixed corrosion type in a simple and effective way.

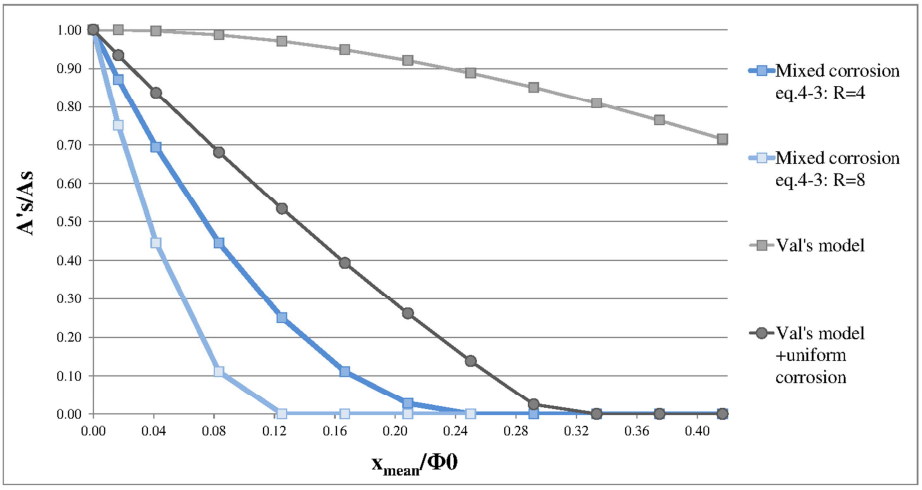

Figure 4-36. Residual area ratio A'_s/A_s versus Corrosion penetration ratio x_{mean}/Φ

To conclude this paragraph, it is opinion of the Author that when it is possible, the profile of the corroded bar should be considered. Especially in the case of pitting corrosion, the shape and the spatial distribution of the pits play an important role on the exact evaluation of the residual mechanical properties of corroded bars. In order to obtain the profile of corroded bars, in the last years non-destructive tests (NDT) methods have been developed and their use is strongly recommended for an adequate assessment of the structural response of existing RC corroded members. Instead, the evaluation of the residual area through the loss weight by a corroded bar leads to a strong underestimation of the corroded area, so cannot be considered a reliable method. Finally, in absence of detail data, the best way to evaluate the residual steel area is through the models here presented, chosen according to the type of corrosion: *Equation 3-13* for uniform corrosion, *Equation 3-15* and *Equation 3-16* for pitting corrosion (Val's model) and *Equation 4-3* for mixed corrosion type.

4.2.2.2. Degradation of the mechanical properties

Corrosion may influence the strength of reinforcing bars but it certainly leads to a high reduction of bar ductility. In paragraph 3.3 a literature review has been made for the understanding and quantification of the corrosion effect on the mechanical properties of reinforcing bars. However, researchers reported sometimes contradictory results and the quantification of the corrosion effects is still far away to be solved. For this reason, the results of the tensile tests made on locally damaged bars are here elaborated respect to such considerations and compared with the experimental results found by other authors. In detail, the results of the tests made show that the reduction of bar strength is mainly related to the decrease in area of reinforcing bars; therefore both pitting and uniform corrosion are relevant in the assessment of the residual bar strength. The reduction of ductility is instead function of the non-uniform reduction of cross-sectional area along the bar length, which leads to stress concentration and consequently to premature failures. For this reason, the bar ductility is more influenced by pitting corrosion.

Residual strengths of corroded reinforcing bars

The reduction of bar strength is mainly related to the decrease of the cross-sectional area of corroded bars. This is confirmed by *Figure 4-37 a)* and *b)* that report the results of the tensile tests made. In detail, the Yield and Maximum Load found for the locally damaged bars are normalized with respect to the same values found for the undamaged bar and plotted against the penetration of pitting corrosion p [mm], the loss of cross-sectional area ΔA [%] or the loss of volume ΔV [%]. It is worth noting that only the minimum residual cross-sectional area A'_s and the residual cross-sectional area estimated with Val's model A_{Val} are considered, because usually available. The average residual cross-sectional area A_r is equivalent to the volume loss, therefore it is not reported. Finally A_{eq} cannot be estimated a priori therefore it is also not shown.

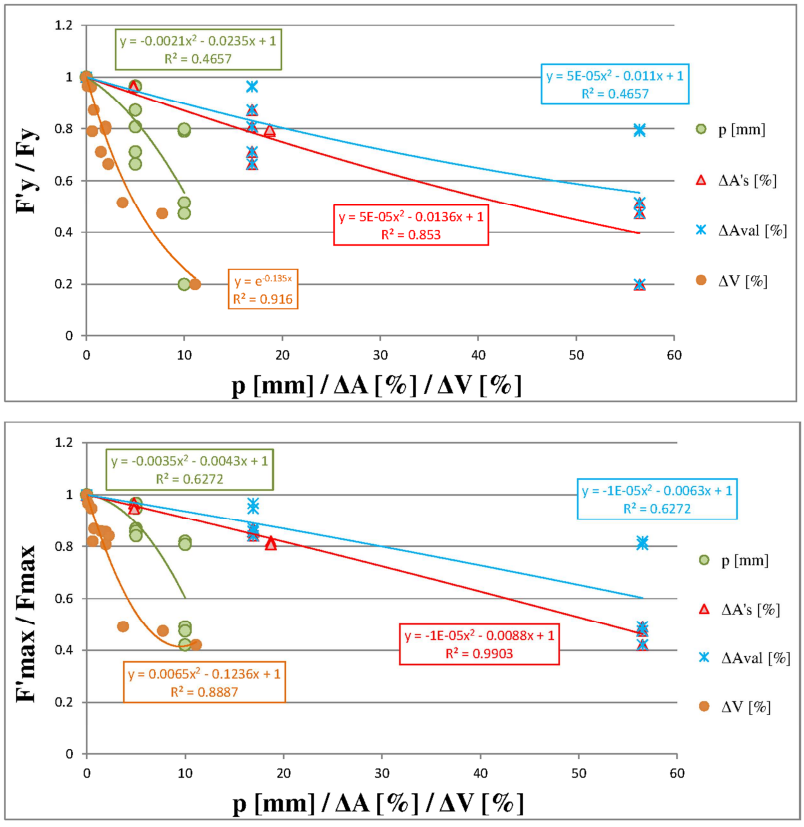

Figure 4-37. Normalised a)Yield Load and b) Maximum Load versus penetration of pitting corrosion p[mm] / loss of cross-sectional area ΔA [%] / loss of volume ΔV [%] of steel bars

For all the graphs, the best correlation between the data is found, examining three different kind of fitting functions: linear, exponential and polynomial of second degree. Only the best function found respect to R-squared is shown in the graphs. Among these, it is possible to observe that the best correlations are obtained between the normalised loads and the loss of volume ΔV [%] or the real loss of cross-sectional area $\Delta A'_s$. As expected instead, the correlations with the maximum corrosion penetration and the residual area evaluated with the Val's model present lower values of R^2. In the first case indeed, the results of the experimental data made demonstrate the variability of the value of residual area as function of the pit shape. In the second case, the Val's model allows only an estimation of the residual cross-sectional area, which may strongly differ from the real values depending on the pit shape and longitudinal distribution. Therefore in absence of the longitudinal profile of corroded bars, the loss of volume (weight) should be related to their residual strength.

In order to compare the results obtained with the results of other authors, three different kinds of graphs are made, that correlate the normalised nominal or effective strengths to the percentage of mass loss by corroded bars or to the percentage of maximum section loss (A_{pit}/A_s). In order to compare easily the results and only for this goal, linear fitting curves are added in the graphs for each set of data:

- Nominal strengths versus mass loss X [%]

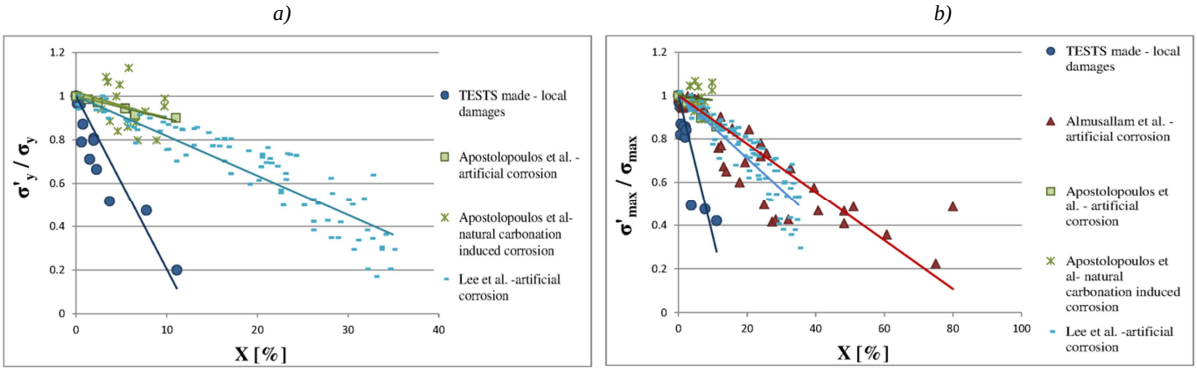

Figure 4-38. Normalised nominal a)Yield and b)Maximum strength versus mass loss [%]

It is possible to observe that considering nominal strengths versus mass loss, the results of different authors qualitatively agree: both yield and maximum strengths are strongly influenced by reinforcement corrosion and decrease with increasing degrees of corrosion. This is reasonable because the nominal strengths are equal to the forces divided by A_s and, as observed before, the loads are correlated to the volume loss ΔV[%], equal to the mass loss. Quantitatively instead the results differ mainly due to the different nature of the corrosive attack and therefore the entity of the minimum residual cross section: the tests made are comparable with pitting corrosion; the artificially corroded bars tested by Almusallam et al.[7] and Apostolopoulos et al.[14] are comparable to mixed corrosion type and the the bars exposed to natural carbonation-induced corrosion tested by Apostolopoulos et al.[14] are comparable to uniform corrosion. *Figure 4-38 a)* and *b)* show that pitting corrosion leads to a high reduction of steel strengths; mixed corrosion type leads to a quite strong reduction of steel strengths and uniform corrosion to a more moderate reduction of steel strengths, confirming the observations of Lee et al. [152]. Finally, all the data related to artificial corrosion tests are fitted with the best function possible respect to R^2, for both normalised yield and maximum strengths, which is found to be a polynomial one of second order (blue curves). The results are shown in *Figure 4-39* and compared with a linear fitting function, as proposed by Lee et al.[152]. The approximation given by the more simple linear function is

acceptable and also the coefficients found are in well agreement with the ones proposed by Lee et al.[152] (see *Figure 3-27*). For this reason, it is here suggested to adopt *Equation 3-24* and the coefficients reported in *Table 4-16* for the evaluation of the nominal strengths of reinforcing bars as function of the mass loss by the bars, in the case of mixed corrosion type.

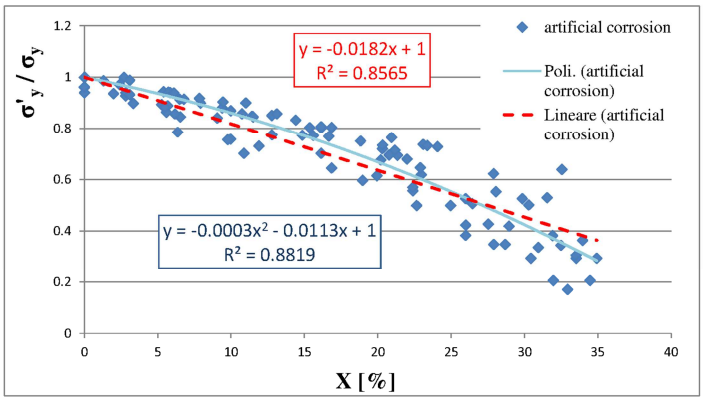

a)

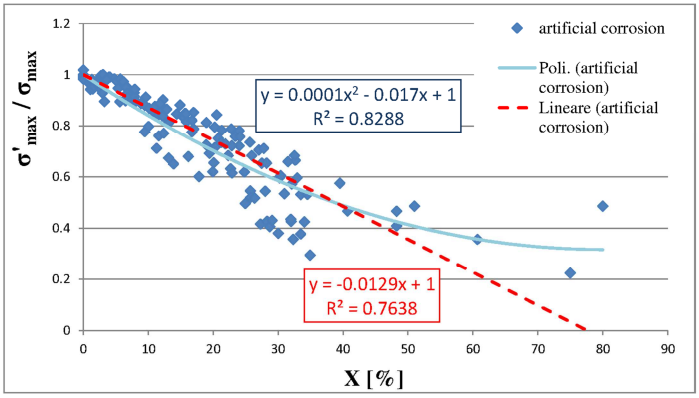

b)

Figure 4-39. Normalised nominal a)Yield and b)Maximum strength versus mass loss [%]

Table 4-16. Values of the coefficients for the evaluation of the residual strengths in the case of reinforcing bars subjected to mixed corrosion type, based on the data of Lee et al. [152], Almusallam et al.[7] and Apostolopoulos et al.[14]

Mechanical properties	*Experimental coefficient*	*Value for mixed corrosion type*
Yield strength	α_y=	*1.82*
Maximum tensile strength	α_u=	*1.29*

- Effective strengths versus mass loss X [%]

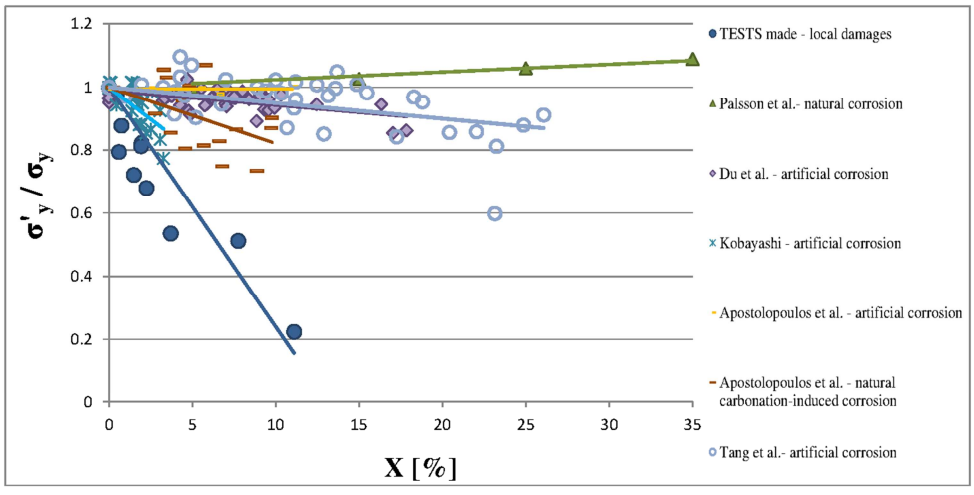

a)

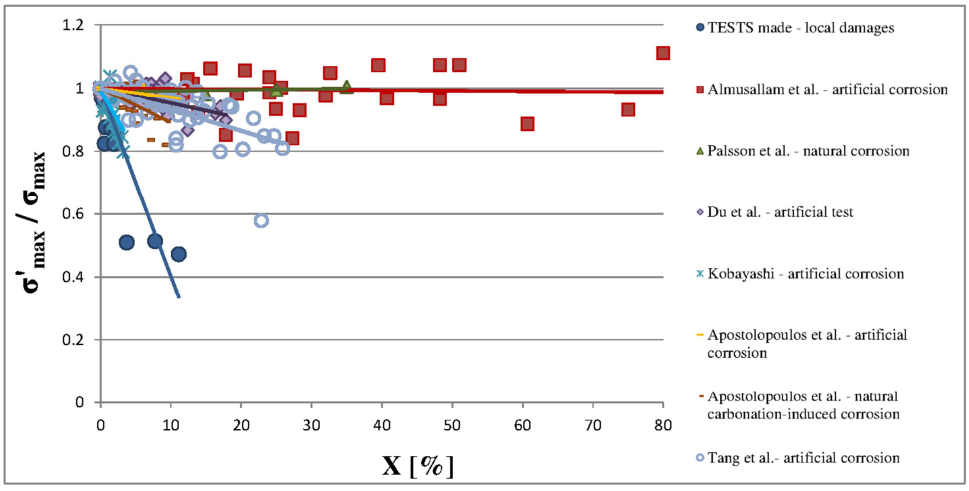

b)

Figure 4-40. Normalised effective a)Yield and b)Maximum strength versus mass loss [%]

The majority of the authors relate the effective strengths (calculated respect to A_r) to the mass loss by the corroded bars, as shown in *Figure 4-40*. It is possible to observe that in this case the results are neither qualitatively nor quantitatively in agree among them. The trend of the data is highly influenced by the corrosion type: for example in the case of naturally corroded bars the normalised strengths are not influenced by corrosion level while in the case of pitting corrosion the normalised strengths strongly decrease. In the case of bars subjected to artificial corrosion the strengths moderately or strongly reduce with increasing levels of mass loss, without the possibility to find a unique trend. This is due to the fact that the authors found the effective strengths dividing the loads by the medium cross-sectional area loss by the bars, A_r. However, A_r can decrease faster or slower than the loads, depending on corrosion type: for example in the experimental tests made A_r has very low values due to the presence of a small number of pits, therefore the loads decrease faster and consequently also the effective strengths. Both Du et al.[94] and Kobayashi[146] proposed to consider a linear correlation between the effective strengths and the mass loss by corroded bars, see paragraph 3.3.2, *Equation 3-21-Equation 3-24*. However, the coefficients found by the two authors as well as the trend of the data (see *Figure 4-39-Figure 4-40)* greatly differ. Therefore a correlation between the effective strengths and the loss of mass of corroded bars is not recommended by this Author.

- Effective strengths versus maximum section loss [%]

a) b)

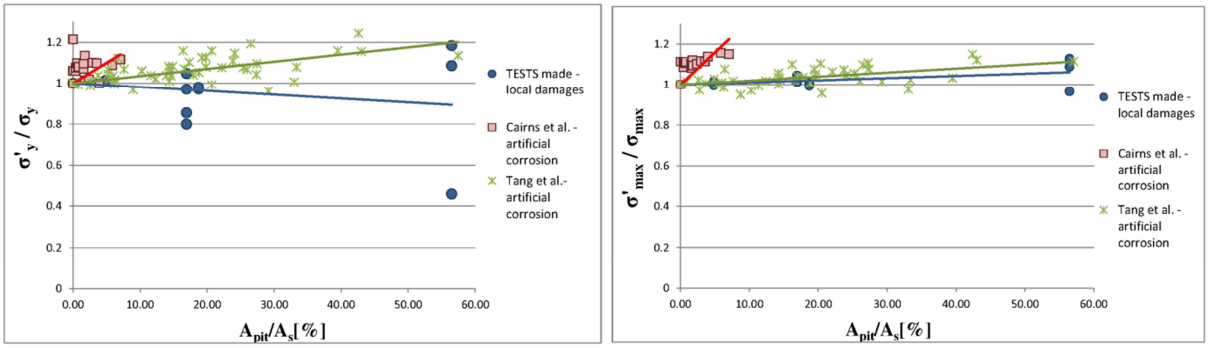

Figure 4-41. Normalised effective a)Yield; b)Maximum strength vs maximum section loss [%]

In this case the effective strengths are calculated respect to A'_s, while the maximum section loss is defined as $(A_s - A'_s)/A_s$ [%]. From the data available, reported in *Figure 4-41 a)* and *b)*, it is possible to notice that the values of normalised effective strengths slightly increase with

increasing section loss in the majority of the cases. This is due to the fact that the loads decrease slower than the residual cross-sectional area A'_s, with increasing levels of corrosion. Furthermore, the results of pitting and mixed type corrosion are found to be comparable, because the effective strengths are related to the maximum section loss that can be similar for these two corrosion types. For this reason, all the data available are plotted together in *Figure 4-42* and fitted with a linear function in order to visualize the trend. For higher safety standards, it is here proposed to do not consider any increase of the effective strengths with increasing levels of corrosion.

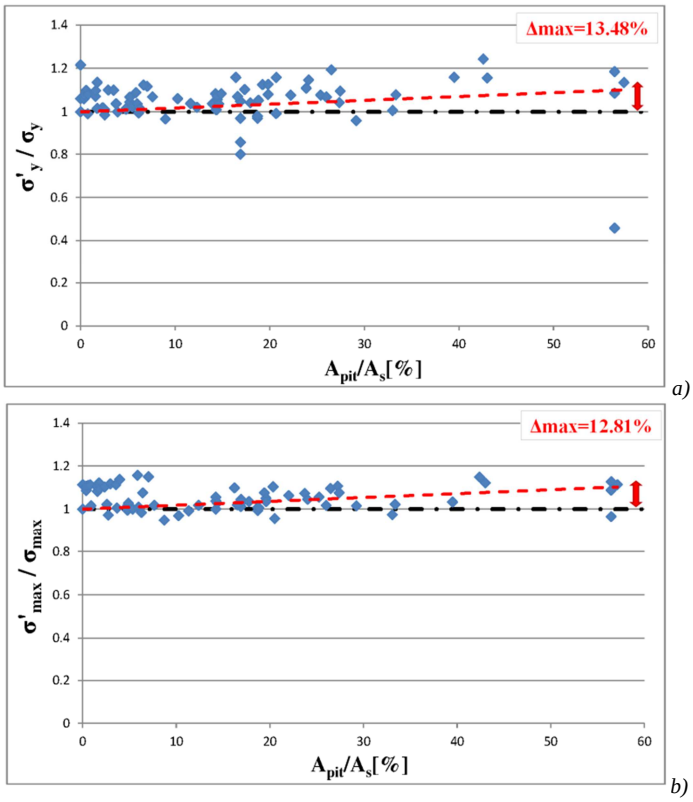

Figure 4-42. Normalised effective a)Yield; b)Maximum strength versus maximum section loss [%]

To conclude, two different approaches are here suggested, for the numerical simulation of the mechanical behaviour of corroded bars. The first one consists on considering none reduction of cross-sectional area for corroded bars but adopting a reduction of the nominal yield and maximum strengths. When reinforcing bars are subjected to mixed corrosion type, *Equation 3-24* and the coefficients reported in *Table 4-16* can be employed to calculate the residual yield and maximum strengths. This method is recommended when only the reduction of mass of corroded bars is known. The second approach instead provides that the residual cross-sectional area A'_s of corroded bars being calculated and used in the numerical simulations, while no reduction of yield or maximum strength is considered because the effective strengths are not assumed influenced by corrosion level. This method can be applied only when detailed information are available regarding the longitudinal profile of the corroded bars, in order to establish the maximum corrosion penetration. In the case of reinforcing bars subject to mixed corrosion type, *Equation 4-3* can be employed to determinate the value of the residual cross-sectional area A'_s.

Residual ductility in corroded reinforcing bars

The reduction of ductility in corroded bars is mainly function of the non-uniform distribution of residual cross sections along the bar length; in the experimental tests, due to the presence of

mainly one pit, the ductility is mainly function of the maximum corrosion penetration *p*, index of the variation of the longitudinal profile. This is confirmed by the following graphs that report the results of the experimental tests made in terms of all the three different definitions of ductility previously introduced. In detail, the values of ductility of damaged bars are normalized with respect to the values found for the undamaged bar and plot against the penetration of pitting corrosion *p* [mm], the loss of cross-sectional area *ΔA* [%] or the loss of volume *ΔV* [%]. As before, only the best fitting function found respect to R-squared is shown in the graphs. It is possible to notice that:

- The normalised strain at maximum load, ε_{sm}, is well correlated to the maximum corrosion penetration *p*, while for the normalised ratio between maximum and yield strength, a good correlation is found respect to the volume loss ΔV. Basing on such results, the definition of ductility suggested by CEB-FIP MC90[61], through these two parameters, is of difficult application for corroded bars. Further, as found also by Moreno et al.[186], the ratio between ultimate and yield strength may increase with greater corrosion levels.
- For the normalised strain-hardening deformation work A*, the best fitting is found respect the maximum corrosion penetration *p* (with a second degree polynomial). A good correlation is possible also respect to the residual cross-sectional area evaluated through Val's model, while the loss of volume is a meaningless parameter for the estimation of the residual steel ductility.
- The same conclusions made for the normalised A* are valid also for the normalised total energy W. The best fitting function is a polynomial one of second degree respect to the maximum corrosion penetration *p*.

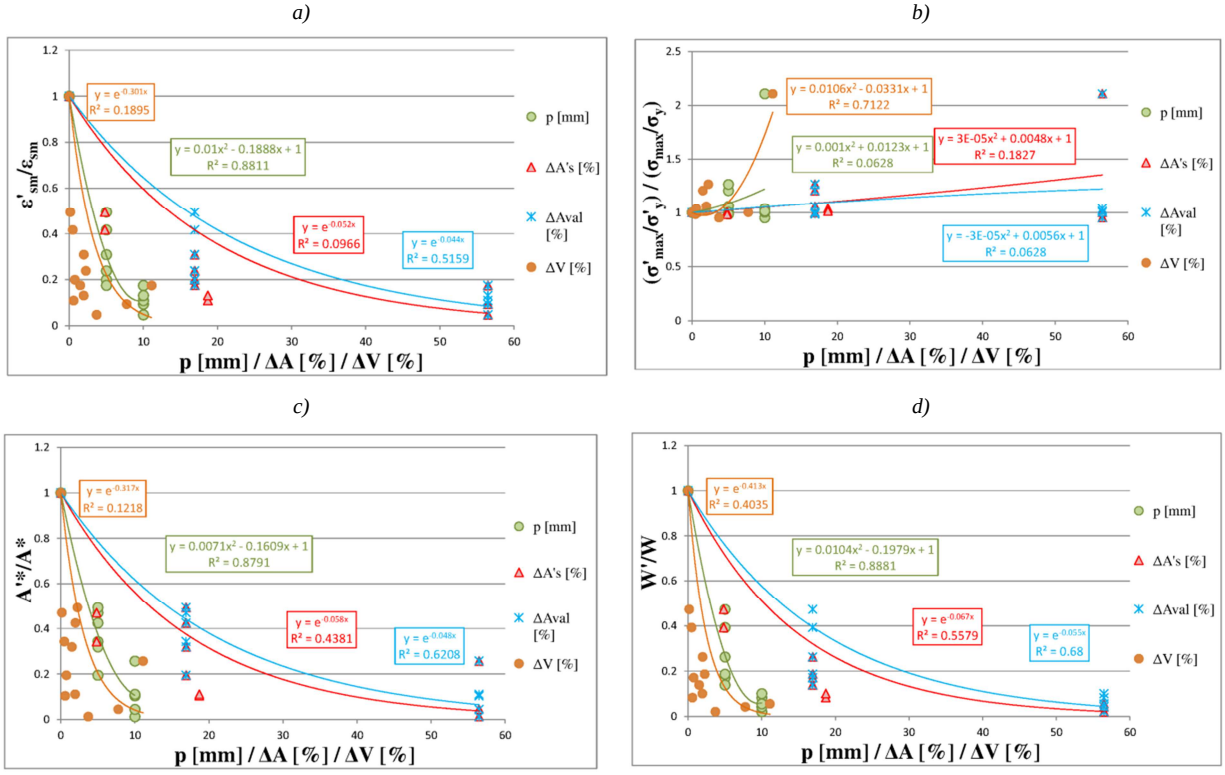

Figure 4-43. Normalised a)Strain at maximum load; b)Ratio between maximum and yield strength; c)Strain-hardening deformation work; d)Total energy, versus penetration of pitting corrosion p[mm] / loss of cross-sectional area ΔA [%] / loss of volume ΔV [%]

To conclude, for the assessment of the residual ductility of corroded bars, it is recommended to consider an energetic criterion (A* or W) and to correlate it with the maximum corrosion penetration *p*. This value is obtainable once the longitudinal profile of the corroded bar is given and therefore when the non-uniform reduction of the cross-sectional area along the bar length is known (spatial distribution of pits). Finally, it is advisable the choice of the total energy W. Indeed, as observed in paragraph 4.2.1.4, W takes into account also the length of the yield plateau, which actually plays an important role in the definition of ductility. Furthermore, W can be easily estimated also when there is not a defined yield point on the stress-strain curves, situation that is often detected for corroded bars. In the case of non-availability of stress-strain curves, the definition of ductility should be based only on the ultimate strain/elongation and not on the strength, because the two parameters depend respectively on the maximum corrosion penetration and on the mass loss, they cannot be correlated with the same parameter of corrosion level. For this reason, following, we will refer only to the ultimate strain/elongation.

The results obtained are here compared with the results of other researches, briefly described in paragraph 3.3.2. All the authors agree that reinforcement corrosion leads to a reduction of bar ductility. Some of them have proposed also equations for the evaluation of the residual strain/elongation at the maximum strength or at bar rupture. However, the proposals lead to values of residual ductility that differ strongly each other.

First of all, the results of the experimental tests made, expressed in terms of normalised displacement at maximum load versus residual area ratio A'_s/A_s, are compared with the results found by Cairns et al.[54], *Figure 4-44*. Indeed, Cairns et al.[54] made tensile tests on bars with different diameters and circular local damages (details in paragraph 3.3.2). It is possible to notice that bars with lower diameter feel more the effects of local damages but in general the effect of different diameters is negligible. Comparing the results obtained with the results of Cairns for the same bar diameter, *Figure 4-45 a)*, it is possible to observe the influence of different pit shapes and lengths on the displacement at the maximum load. A better correspondence between the results is obtainable if only the bars damaged with circular and long pits are considered, probably more similar to the local damages created by Cairns et al.[54], *Figure 4-45 b)*. In general however, the results agree well and show the same trend between the displacement at the maximum load and the residual area ratio.

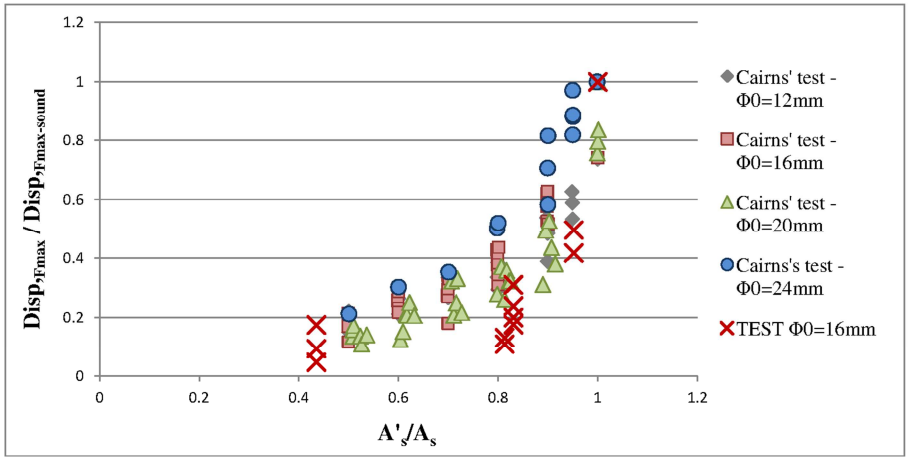

Figure 4-44. Normalised displacement at maximum load for various damage levels and geometries

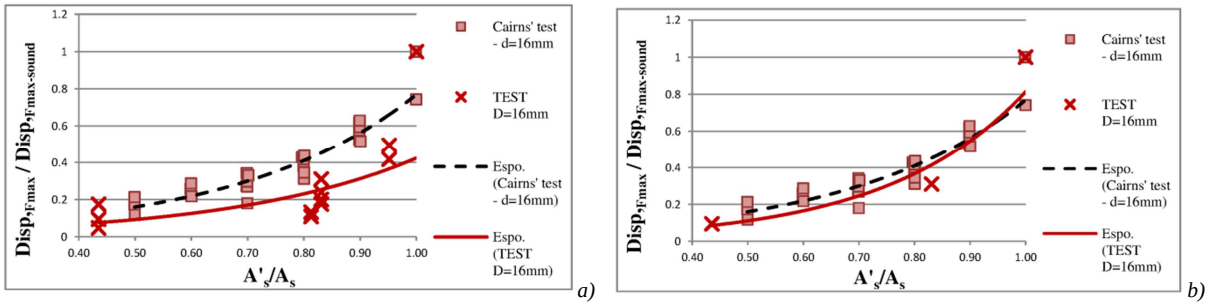

Figure 4-45. Comparison between the results of the tests made and the results of Cairn's tests

Then the results of the experimental tests made are compared with the results found by other authors in the case of naturally or artificially corroded bars. The comparison is made in terms of normalised elongation E or strain ε at maximum load versus the percentage of mass loss by corroded bars or the percentage of maximum section loss. In order to compare easily the results found by the different authors, exponential fitting curves are added in the graphs for each set of data, *Figure 4-46 a)* and *b).* The same trend is found. In *Figure 4-47* the data, reported respect to the mass loss or the maximum section loss, are fitted with an exponential function. The nonlinear relation is found to be more accurate if it associates to the maximum section loss (R-squared 0.5876 based on the maximum section loss and R-squared 0.0964 based on the on the mass loss), confirming the observation of Tang et al.[241] and the dependence found between ultimate strain and p. This is understandable, considering that a reinforcing bar with a relatively uniform cross-sectional area along its length undergoes plastic deformation over very significant lengths, but in corroded bars only a short segment may yield before the bar fractures in the pitted area.

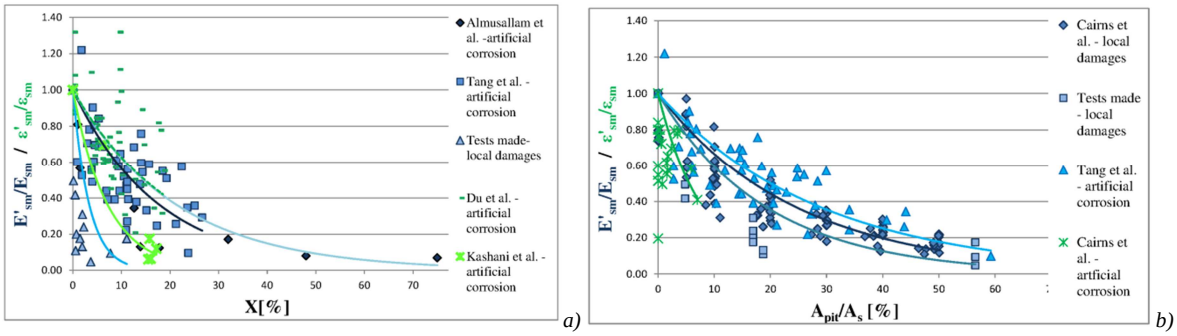

Figure 4-46. a)Normalised Elongation/Strain at maximum load versus loss of mass X [%]; b)Normalised Elongation/Strain at maximum load versus maximum section loss A_{pit}/A_s[%]

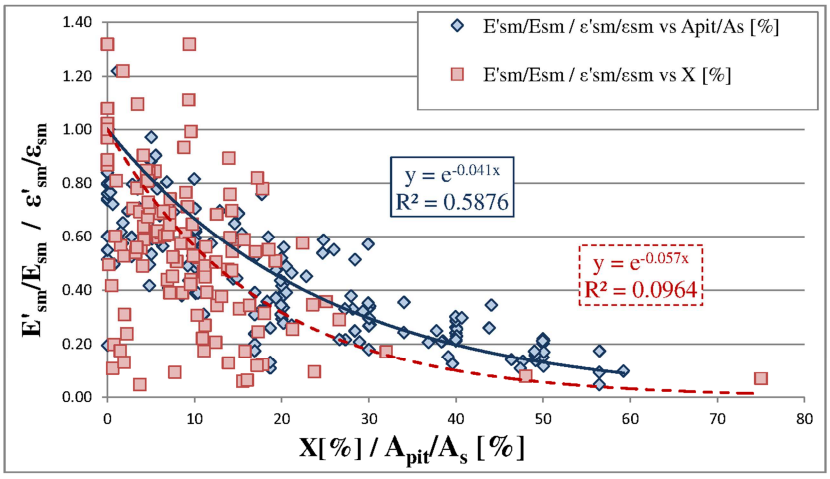

Figure 4-47. Normalised Elongation/Strain at maximum load versus loss of mass X [%] / maximum section loss A_{pit}/A_s[%]

The same kinds of graphs are made also for the normalised elongation or strain at the bar rupture. In detail, majority of researchers measured the final elongation of the corroded bars subjected to tensile tests and related it with the percentage of mass loss by the bars, *Figure 4-48 a)* and *Figure 4-49 red squares*. The best function that fits the data is an exponential one, which however presents a very low value of R-squared (R^2=0.0356–red dotted curves). This is due to the fact that strain/elongation have a bad correlation to the mass loss by the bars, as observed in *Figure 4-43 a)*. As made for the strain/elongation at maximum load, also here the normalised elongation/strain at bar rupture are correlated with the maximum section loss, *Figure 4-48 b)* and *Figure 4-49 blue diamonds*. However, also in this case the value of R-squared is found very small, probably due to the absence of enough experimental data. Indeed, only the results of the tests made and the results of Palsson et al.[198] were available. Furthermore the strains measured by Palsson e t al.[198] base on 25 mm gage length; therefore they represent very local values, more sensible to the local corrosive attack than to the global ductility of corroded bars. Finally, should be noticed that the values of the exponents, for both the correlations found, are smaller than previously (for strain/elongation at maximum load). This indicates that corrosion leads to a brittleness of the post peak branch, i.e. the local elongation during the necking phase decreases because the local concentration of strains leads to a premature rupture of the bar.

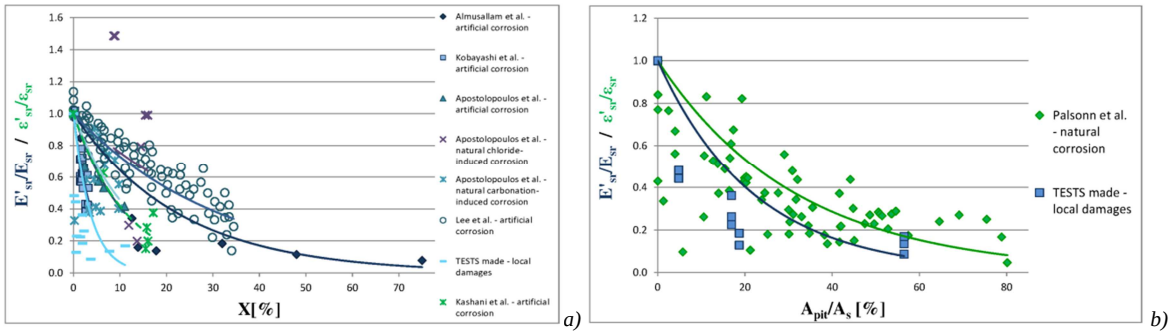

a) b)

Figure 4-48. a) Normalised Elongation/Strain at bar rupture versus loss of mass [%]; b) Normalised Elongation/Strain at bar rupture versus maximum section loss [%]

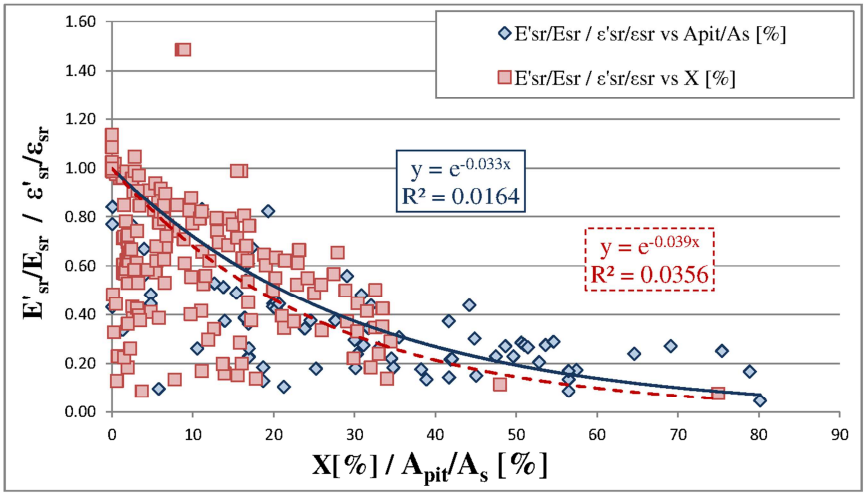

Figure 4-49. Normalised Elongation/Strain at bar rupture versus loss of mass X [%] / maximum section loss [%]

Another issue to be considered is that a better prevision of the residual ductility of corroded bars, can be made if the longitudinal profile is known. Indeed, as asserted by various authors, Palsson et al.[198], Du et al.[94], Tang et al.[241], it is the ratio between the minimum and the maximum corrosion penetration the main parameter that governs the maximum elongation of corroded bars

(e.g. *Figure 3-18 b)*). Indeed, every residual cross section will contributed to the final elongation of the corroded bar for a different amounts, also if the rupture will happen in the minimum cross section. Due to the lack of experimental data available, no conclusions can be made regarding this issue, which however represents an interesting topic for further tests and numerical models.

It should also be observed that ductility reduction verifies only for pitting or mixed corrosion, being linked to the non-uniform reduction of cross sections along the bar length. Furthermore, in real situation a perfect uniform corrosion is unlikely to occur, therefore there will be always a maximum corrosion penetration to which refer. For the same reason, for the evaluation of the residual ductility it is also not necessary to distinguish between pitting or mixed corrosion. Indeed, in both cases there will be a maximum corrosion penetration/ maximum section loss.

On the basis of the previous observations and *Figure 4-47* and *Figure 4-49*, the following proposal is made for the evaluation of the residual strains of corroded bars:

$$\varepsilon'_{sm} = e^{-0.041 \cdot \delta s}\, \varepsilon_{sm}$$
$$\varepsilon'_{sr} = e^{-0.033 \cdot \delta s}\, \varepsilon_{sr} \qquad \textit{Equation 4-5}$$

where ε_{sm} and ε_{sr} have been already defined and ε'_{sm} and ε'_{sr} are respectively the strain of the corroded bar at the maximum strength and at the bar rupture; δ_s [%] is the percentage of maximum section loss by corroded bars:

$$\delta_s = \frac{A_{pit}}{A_s} \cdot 100 \qquad \textit{Equation 4-6}$$

Finally, *Equation 4-5* is compared with the formula proposed by other authors and reported in paragraph 3.3.2. The experimental results of the tested bar 3DBc8p5 are chosen as benchmark. *Table 4-17* shows that the best agreement between experimental results and evaluation of residual strains is given by the formulas based on the pitted area: Coronelli et al.[80], Biondini et al.[40] and Equation 4-5. Regarding the equation proposed by Coronelli et al.[80], the main problem is the evaluation of the α_{pit}^{max} value, here an arbitrary value of 0.5 has been chosen. Therefore the Author recommends only Equation 4-5 or *Equation 3-28* proposed by Biondini et al.[40]. It should be noticed however that Biondini et al. [40] found this formula basing only on the test results of Apostolopoulos et al.[14], based on the average mass loss by corroded bars and not on the maximum cross section reduction.

Table 4-17. Comparison between different formula for the evaluation of ε'_{sm} and ε'_{sr}

Experimental data	ε'_{sm}	$\Delta\varepsilon'_{sm}$	ε'_{sr}	$\Delta\varepsilon'_{sr}$
3DBc8p5	*0.0307*		*0.0411*	
Model of (based on)	ε'_{sm}	$\Delta\varepsilon'_{sm}$	ε'_{sr}	$\Delta\varepsilon'_{sr}$
Coronelli et al. (A_{pit})	*0.05776*	*180.69*		
Kobayashi et al. (X)			*0.0933*	*126.97*
Lee et al. (X)			*0.1478*	*259.60*
Biondini et al. (A_{pit})	*0.04423*	*44.08*		
Du et al. (X)	*0.12043*	*292.29*		
Proposal (A_{pit})	*0.06438*	*109.70*	*0.0898*	*118.46*

In order to take into account of the ductility reduction in corroded bars, a constitutive law for steel (*Figure 4-50*) is proposed and implemented in the OpenSEES framework.

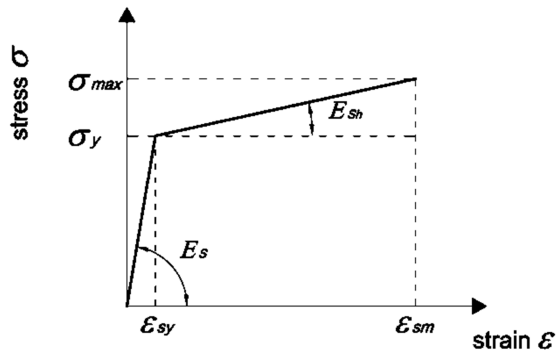

Figure 4-50. Stress-strain law for steel material under tensile load

In detail, for steel bars under tensile uniaxial load, a limit to the strain at maximum strength can be specified. Two linear branches represent the steel behaviour: the first linear branch is defined by the elastic modulus E_s of the steel and by the yield strength σ_y. The second branch is instead defined by the ultimate strain ε_{sm} and by the slope E_{sh}, which is equal to the elastic modulus E_s multiples *b*, the strain-hardening ratio (ratio between post-yield tangent and initial elastic tangent), which can be defined. In this way, it is possible to take into account of a reduction of ductility of the corroded steel bars and to maintain a general approach to the problem. When the ultimate stress is reached in the tensile bar of a RC member, the bar is not able to work anymore and the loss of convergence in the solution represents the failure of all the structure by lack of ductility.

To conclude, the residual ductility of corroded bars depends on the non-uniform distribution of residual cross sections along the bar length. However, the full longitudinal profile of a corroded bar is difficult to obtain. Basing on the previous observations, it is possible to consider the maximum section loss, A_{pit} if available. If it is not available, it can be calculated with the Val's et al.[256] model, basing on the maximum corrosion penetration (*Equation 3-15*-*Equation 3-16*). For the evaluation of the residual strain, *Equation 4-5* or *Equation 3-28* are recommended for all type of corrosion.

4.2.2.3. Premature buckling phenomena

Majority of researchers adopts a bilinear simplified constitutive law for reinforcing steel bars equal in tension and compression, which may be an elastic-perfectly plastic or an elastic-strain hardening law. This approach however is quite restrictive, because does not allow to consider eventually buckling phenomena, which may take place in the bars under compression loads. These phenomena are common in RC members with corroded reinforcement, for example in RC beams where the transverse reinforcements are not anymore able to prevent buckling of compressive bars or in RC columns where the longitudinal reinforcing bars may suffer of premature buckling. Indeed, for high levels of corrosion, stirrups may fail, the spacing among them increases and at the same time the diameter of the main bars decreases, due to the effect of cross section reduction provoked by the corrosive attack. The ratio between stirrup spacing and bar diameter, called geometrical slenderness ratio λ, may exceed the critical value λ_{crit} and buckling phenomena occur. In order to consider this possibility, in this work a new constitutive law for steel in compression is proposed and implemented in the OpenSEES framework. This law is based on both experimental evidences and previous theoretical models.

The buckling behaviour of uncorroded reinforcing bars has been studied by a number of authors, through experimental tests and analytical formulations, e.g. Dhakal et al.[92], Mendis et al.[181], Monti et al.[185] (Appendix B). The researchers agree that the slenderness ratio and the yield strength are the two most important parameters that influence the buckling strength of bars. In the

case of corrosion attack and especially pitting corrosion, the classical buckling models are however difficult to apply. Indeed, as remarked by Kashani et al.[144], corrosion damages the steel bar unsymmetrically, changing the radius of gyration in different axis and leading to formation of plastic hinges at the critical sections. Furthermore, additional bending moment will be present leading to an additional decrease in the buckling load. For all these reasons, an ad hoc model has to be defined. Reference is made on the analytical model developed by Monti et al.[185] for the behaviour of reinforcing bars in presence of buckling over the elastic threshold (Appendix B). In this model, when the critical buckling load (always greater than the yield strength) is reached, a softening branch in compression which tends to an asymptotic value, starts. In the present work the possibility of premature buckling phenomena is also included; this depends on the value of the geometrical slenderness ratio λ of the bars. The values of λ_{crit} and λ_y must be previously defined: for structural steel λ_{crit} is established equal to 5; λ_y has to be calculated as reported in Appendix B, basing on the yield strength of steel material. Then, the following monotonic stress-strain relation in compression here proposed may be considered:

- If $\lambda \leq \lambda_{crit}$ =5, the monotonic responses of bars in compression and in tension can be considered equal, because no buckling phenomena occur:

$$\begin{aligned} \sigma_s &= E_0 \cdot \varepsilon_s & 0 \leq \varepsilon_s \leq \varepsilon_{sy} \\ \sigma_s &= E_{sh} \cdot \varepsilon_s + \sigma_y & \varepsilon_{sy} \leq \varepsilon_s \leq \varepsilon_{sm} \end{aligned} \qquad \textit{Equation 4-7}$$

- If $\lambda_{crit} < \lambda \leq \lambda_y$, buckling occurs after yielding but before the achievement of the maximum strength of the steel bars. In this case, the constitutive law is composed of three branches: a first linear elastic branch, the hardening post yielding branch until the achievement of the critical buckling strength σ_{crit} at the strain ε_{crit} and the final softening branch, based Monti's et al.[185] model:

$$\begin{aligned} \sigma_s &= E_0 \cdot \varepsilon_s & 0 \leq \varepsilon_s \leq \varepsilon_{sy} \\ \sigma_s &= E_{sh} \cdot \varepsilon_s + \sigma_y & \varepsilon_{sy} \leq \varepsilon_s \leq \varepsilon_{crit} \\ \sigma_s &= \sigma_{s\infty} + (\sigma_{crit} - \sigma_{s\infty}) * e^r & \varepsilon_{crit} \leq \varepsilon_s \leq \varepsilon_{sm} \end{aligned} \qquad \textit{Equation 4-8}$$

  The exponent *r* is instead defined as:

$$r = E_{n0} \cdot \frac{(\varepsilon_{crit} - \varepsilon_s)}{(\sigma_{s\infty} - \sigma_{crit})} \qquad \textit{Equation 4-9}$$

  $\sigma_{s\infty}$ is the asymptotic value at which the softening branch tends, E_{n0} is the slope of the initial tangent of the softening branch; both are defined by Albanesi et al.[4] –Appendix B; σ_{crit} can be calculated with one of the classical inelastic buckling theories, e.g. Reduced Modulus Theory or from experimental data.

- If $\lambda > \lambda_y$, buckling occurs before the yielding of the bars:

$$\begin{aligned} \sigma_s &= E_0 \cdot \varepsilon_s & 0 \leq \varepsilon_s \leq \varepsilon_{crit} \\ \sigma_s &= \sigma_{s\infty} + (\sigma_{crit} - \sigma_{s\infty}) * e^r & \varepsilon_{crit} < \varepsilon_s \leq \varepsilon_{sm} \end{aligned} \qquad \textit{Equation 4-10}$$

Stress-strain curves obtained with this analytical model for steel bars with different values of the geometrical slenderness ratio λ are reported as an example in *Figure 4-51*.

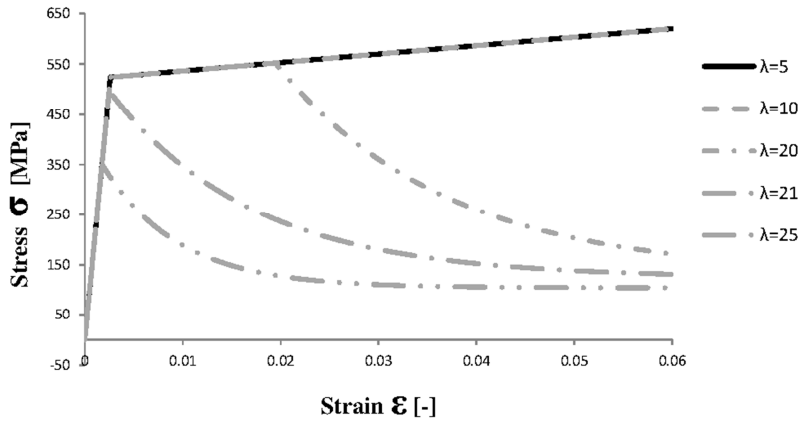

Figure 4-51. Stress-strain curves in compression obtained with the analytical model proposed

In the case of corroded reinforcing bars, the first step is the evaluation of the critical buckling load. To the Author's knowledge, only few authors faced with this problem proposing suitable equations. Rodriguez et al.[220] suggested to estimate the critical buckling load through the Euler's formula (*Equation 3-18*) or reducing the yield strength (*Equation 3-19*), see also paragraph 3.3.2. Kashani et al.[143][144] investigated the stress-strain behaviour of corrosion-damaged reinforcing bars through an extensive experimental campaign, as reported briefly in paragraph 3.3.2. The authors proposed also an equation (*Equation 3-25*) for the evaluation of the buckling strength of corroded bars, based on some coefficients that however have to be carefully selected. Indeed, the equation relates the buckling strength to the percentage of mass loss by the corroded bars and, as already demonstrated for bars in tension, this may lead to an underestimation of the residual strength. Due to the absence of other experimental data, the reliability of these two proposals is difficult to verify, but has been found that the equations give comparable results. Once defined the critical buckling load and consequently the nominal buckling strength σ_{crit}, it is possible to set up stress-strain curves for corroded bars in compression, including buckling phenomena, basing on the proposed *Equation 4-7* - *Equation 4-10*. It should be noted that in the case of corroded bars, the geometrical slenderness ratio is the ratio between the length between two consecutive intact stirrups and the residual bar diameter, λ_{corr}, which can be much lower than in sound conditions.

- If $\lambda_{corr} \leq \lambda_{crit}$ =5, the monotonic responses of the bars in compression and in tension is equal, *Equation 4-7* can be adopted.
- If $\lambda_{corr} > \lambda_{crit}$ buckling may occur:
  - If $\sigma_{crit} > \sigma_{sm}$, no buckling phenomena occur before the bar reaches the maximum strength, *Equation 4-7* can be adopted;
  - If $\sigma_y < \sigma_{crit} < \sigma_{sm}$, the softening branch starts after the yielding, but before the maximum strength of the steel bar is reached, the stress-strain curve is defined by *Equation 4-8.*
  - If $\sigma_{crit} < \sigma_y$, the softening branch starts before the yielding and the stress-strain curve is defined by *Equation 4-10.*

Actually, in the case of reinforcement corrosion of a certain amount, the most likely situation is $\sigma_{crit} < \sigma_{y,}$ as demonstrated also by the experimental tests of Kashani et al.[143][144]. The results of these tests are finally considered for the validation of the proposed model. In *Figure 4-52* is reported the comparison between the experimental data and the stress-strain curves obtained with the proposed model, for both sound and corroded bars. The analytical formulation gives curves in well agreement with the physical tests.

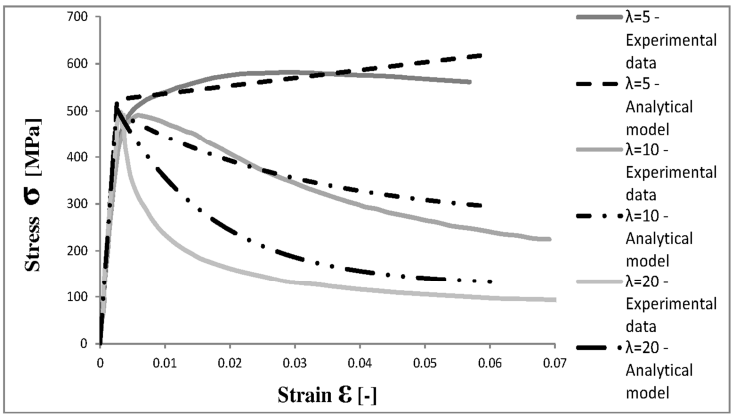

a)

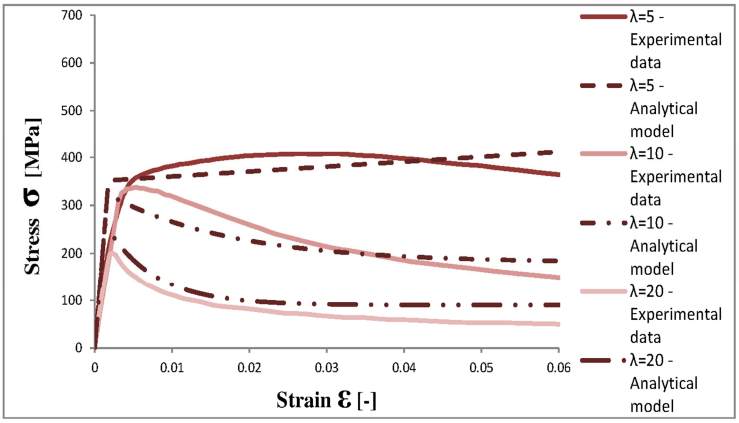

b)

Figure 4-52. Comparison between experimental data of Kashani et al.[143][144] and the analytical stress-strain curves in compression, for a) sound and b) corroded bars.

4.3. Modelling of corrosion effects on concrete

Concrete degradation may be induced by several factors, as introduced in paragraph 3.4.1. In this work, the consequences of reinforcement corrosion on concrete are considered. In detail, once corrosion initiates in reinforcing bars, the corrosion products generated by the corrosive process accumulate around the steel bar and due to their greater volume, cause pressure on the surrounding concrete (*Figure 3-37*). The expansion of the corrosion products has been found to be many times the initial steel volume. Therefore, concrete cover may crack and eventually spalling. In order to numerically model this damage on concrete, the chemical-mechanical damage model, developed by Saetta et al.[224][225] for simulating chemical attacks on concrete, is here considered and enhanced. Following, the coupled damage model is introduced and the improvements made on the model explained.

4.3.1. Environmental-mechanical damage model

Saetta et al.[224][225] developed a chemical-mechanical damage model in order to consider concrete deterioration due to chemical attacks. Some examples of chemical attacks on concrete have been briefly reported in paragraph 3.4.1. This coupled model bases on the mechanical damaged model of Faria et al.[102], then enhanced by Berto et al.[34], as reported in paragraph 2.4.1. In detail, Saetta's et al. [225] model couples the physical and the chemical deteriorations on concrete material, as following:

$$\boldsymbol{\sigma} = (1 - d_{chem})[(1 - d^{+})\bar{\boldsymbol{\sigma}}^{+} + (1 - d^{-})\bar{\boldsymbol{\sigma}}^{-}] = (1 - d^{*+})\bar{\boldsymbol{\sigma}}^{+} + (1 - d^{*-})\bar{\boldsymbol{\sigma}}^{-} \qquad \textit{Equation 4-11}$$

where:

- $\bar{\boldsymbol{\sigma}}^{+}$ and $\bar{\boldsymbol{\sigma}}^{-}$ are the tensile and the compressive components of the effective stress tensor;
- d^{+} and d^{-} are respectively the tensile and compressive mechanical damage parameters;
- d_{chem} is the chemical damage parameter related to the degree of development of the chemical reaction and the relative residual strength of the concrete material;
- d^{*+} and d^{*-} are respectively the tensile and the compressive coupled damage parameters.

The use of a single chemical damage parameter is justified by the authors, considering that the chemical-physical degradation acts in the same way in tension and in compression and it is defined as:

$$d_{chem} = (1-\varphi) - \frac{1-\varphi}{1+(2\mathcal{R})^4} \qquad \textit{Equation 4-12}$$

where $\mathcal{R}$ represents the degree of chemical reaction and φ represents the relative residual strength of the material achieved when the chemical reaction is completely developed. In particular, for break up processes, $\mathcal{R}$ can be defined as the ratio between the actual concentration c and the reference concentration of pollutant c_{ref}: $\mathcal{R}$ =[c]/[c_{ref}]. The reference concentration of diffusing specie is the concentration for which chemical degradation process reaches its maximum effect, when [c] = [c_{ref}]: $\varphi = f_{ck,damaged} / f_{ck,initial}$. Independently from its specific definition, the chemical damage parameter is assumed to be represented by an increasing function with time, which means $\dot{d}_{chem} \geq 0$.

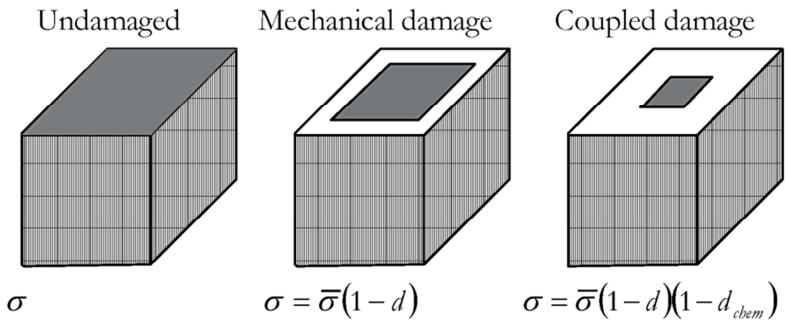

Figure 4-53. Combined action of mechanical and chemical damage, Simioni[232]

The same coupled damage model (*Equation 4-11*) was assumed by Simioni[232] in order to simulate the concrete degradation due to the chemical attacks related to reinforcement corrosion. Finally, the model of Saetta et al.[225] has been recently enhanced by Berto et al.[34] and Talledo[240], in order to consider physical damage phenomena, in particular the frost degradation of concrete. Here, the chemical damage parameter d_{chem}, was renamed as environmental damage parameter, d_{env} in order to extend its meaning. In detail, the authors related the environmental damage parameter to the number of the freeze-thaw cycles. Also in this case, it was supposed that the d_{env} parameter acts in the same way in tension and in compression. In *Figure 4-54* are shown the stress-strain curves of concrete in compression and in tension at different levels of deterioration, i.e. different values of d_{env}. As it can be seen, the parameter d_{env} controls the loss of strength and the reduction of initial stiffness (elastic modulus).

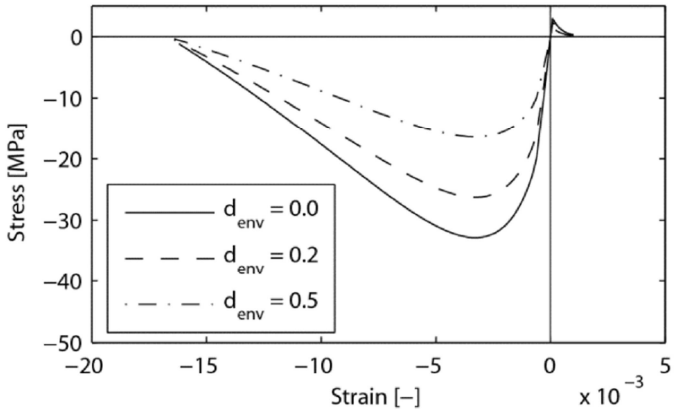

Figure 4-54. Stress-strain curves for different values of d_{env} in compression and in tension, Talledo[240]

The constitutive law of the environmental-mechanical damage model becomes then:

$$\boldsymbol{\sigma} = (1 - d_{env})[(1 - d^{+})\bar{\boldsymbol{\sigma}}^{+} + (1 - d^{-})\bar{\boldsymbol{\sigma}}^{-}] = (1 - d^{*+})\bar{\boldsymbol{\sigma}}^{+} + (1 - d^{*-})\bar{\boldsymbol{\sigma}}^{-} \qquad \textit{Equation 4-13}$$

In this way, the two coupled damage parameters d^{*+} and d^{*-} can have a more general meaning.

In this work the environmental-mechanical damage model (*Equation 4-13*) is considered for the simulation of reinforcement corrosion effects on concrete. In detail, the physical damages induced on concrete (micro and macro-cracking and spalling of the concrete cover) due to the expansion of the corrosive products are simulated, while the chemical degradation of concrete due to the agents that lead to corrosion are not considered. Indeed, as reported in paragraph 3.4.1, carbonation, chloride salts, acids, etc…change in different ways the mechanical properties of the concrete, therefore for each corrosive agent should be necessary to develop a proper d_{chem} parameter. Furthermore, the consequences of the chemical agents on concrete are more relevant in the first years of structures' life, while once cracks develop, their effects on concrete are predominant. As observed in paragraph 3.4.3, in order to adequately capture the behaviour of cracked concrete, the concrete responses in compression and in tension should be separately considered. For this reason, it is necessary to introduce the splitting of the environmental damage parameter, as below.

4.3.2. Split of the environmental damage parameter

Crack formation has different consequences on tensile and compressive concrete behaviour. Further, concrete covers, cracked by expansion of corrosion products, can be under different stress state, tensile or compressive. Therefore, it is here proposed to enhance the constitutive law of the environmental-mechanical damage, *Equation 4-13*, splitting the environmental damage parameter in two different parameters d^{+}_{env} and d^{-}_{env}, that in this way affect respectively the positive and negative part of the effective stress tensor. The environmental-mechanical damage model can be expressed then by the following relationship:

$$\boldsymbol{\sigma} = (1 - d^{+}_{env})(1 - d^{+})\bar{\boldsymbol{\sigma}}^{+} + (1 - d^{-}_{env})(1 - d^{-})\bar{\boldsymbol{\sigma}}^{-} \qquad \textit{Equation 4-14}$$

In this way, the global model is enhanced, becoming able to consider different environmental degradation and environmental-mechanical damage interaction, under compression or tension stress state. As in the previously models proposed by Saetta et al.[225] and Berto et al.[34], the environmental damage parameters are still represented by an increasing function with time: $\dot{d}^{+}_{env} \geq 0$, $\dot{d}^{-}_{env} \geq 0$.

4.3.3. Proposal for new environmental damage parameters

4.3.3.1. Environmental damage parameter for cracked concrete in compression

In the case of degraded concrete due to reinforcement corrosion, some further enhancements on the damage model are required. In Saetta et al.[225] and Berto et al.[34], d_{env} is associated to a reduction of strength and elastic modulus. Instead, the cracked concrete offers not only lower strength but also less ductility than the virgin material. This aspect has been evidenced by some authors, see paragraph 3.4.3.1, but it is still not quantified or related to reinforcement corrosion. In order to consider also this aspect, a proposal will be made following.

First, an expression for d_{env}^{-} is given, in order to capture the reduction of compressive strength of the degraded concrete. In this work, *Equation 3-34* proposed by Coronelli et al.[80] for the evaluation of the residual mean compressive strength f'_{cm} of cracked concrete is assumed together with *Equation 3-33* suggested by Molina et al.[184], which allows to evaluate the total crack width respect to the corrosion penetration x. Therefore the residual compressive strength of cracked concrete due to corrosion can be expressed as:

$$f'_{cm} = \frac{f_{cm}}{1 + k\dfrac{n_{bars} \cdot 2\pi \cdot (v_{r/s} - 1) \cdot x}{b_0 \cdot \varepsilon_{c0}}} = \frac{f_{cm}}{1 + \dfrac{n_{bars} \cdot \pi \cdot x}{5 b_0 \cdot \varepsilon_{c0}}} \qquad \textit{Equation 4-15}$$

assuming the volume of the corrosion products approximately twice the volume of the virgin steel, $\upsilon_{r/s}$=2 as proposed by Molina et al.[184] and k=0.1 as suggested by Capè[56] and Coronelli et al.[80]. The strain at the compressive stress peak f_c, ε_{co}, can be assumed equal to 0.0022 as proposed by CEB-FIP MC90[61], or assumed more realistically function of the average compressive strength f_{cm}, as suggested by fib Bulletin 1[104]:

$$\varepsilon_{c0} = 0.0017 + 0.0010\left(\frac{f_{cm}}{70}\right) \qquad \textit{Equation 4-16}$$

All the other parameters of the *Equation 3-15* have been already described in paragraph 3.4.2 and 3.4.3.1. Once defined d_{env}^{-} as:

$$d_{env}^{-} = 1 - \frac{f'_{cm}}{f_{cm}} \qquad \textit{Equation 4-17}$$

it is possible to express d_{env}^{-} as function only of the corrosion penetration x, combining *Equation 4-15* and *Equation 4-17:*

$$d_{env}^{-} = \frac{n_{bars} \cdot \pi \cdot x}{5 b_0 \varepsilon_{c0} + n_{bars} \cdot \pi \cdot x} \qquad \textit{Equation 4-18}$$

In this way d_{env}^{-} parameter is represented by an asymptotic function (*Figure 4-55*) and can assumes values between 0 and 1: when x=0, $d_{env}^{-} = 0$, when x=Φ, $d_{env}^{-} \to 1$. This last limit represents the physical limit of maximum corrosion penetration equal to the bar diameter, that actually in real cases is never reached. Finally, from *Figure 4-55* it is possible to observe that d_{env}^{-} is mainly influenced by the numbers of compressive bars n_{bars} and by the concrete section width b_0 than by the concrete strength f_{cm}.

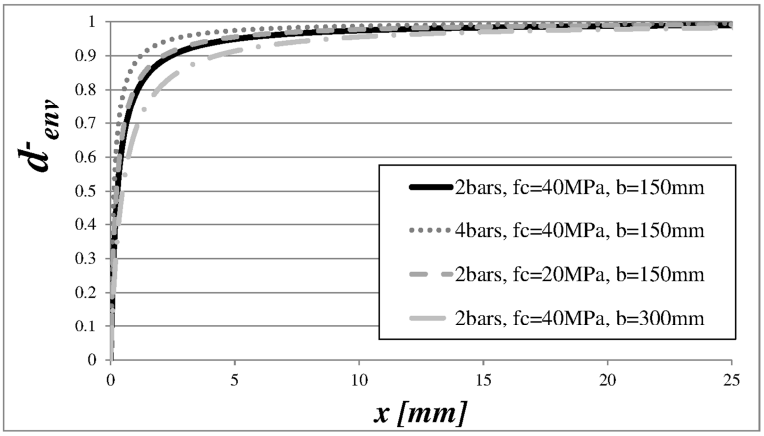

Figure 4-55. d^{-}_{env} as function of corrosion penetration x

As said, the cracked concrete is characterized by lower strength and less ductility than the virgin material. In order to consider also this second aspect, the reduction of the ultimate strain of concrete in compression is related to the corrosion level reached in the compressive reinforcing bars. In particular, the residual compressive ultimate strain of concrete ε'_{cu}, may be calculated with the formula proposed in Finozzi et al.[108]:

$$\varepsilon'_{cu} = \varepsilon_{cu}\left[1 - f\left(1 - \frac{A'_{s,tot}}{A_{s,tot}}\right)\right] \qquad \textit{Equation 4-19}$$

which relates the ultimate strain of the deteriorated concrete ε'_{cu} to the level of uniform corrosion, expressed as the ratio between the residual cross section area of all the corroded reinforcement bars $A'_{s,tot}$ and the corresponding uncorroded area $A_{s,tot}$; ε_{cu} is the ultimate strain of the sound concrete and f is a factor implicitly related to the crack width in concrete and therefore to the corrosion products expansion, $\upsilon_{r/s}$. Indeed, assuming a value of $f = \upsilon_{r/s}=2$, *Equation 4-19* can be re-written as function of the corrosion penetration x:

$$\varepsilon'_{cu} = \varepsilon_{cu}\left[1 - \frac{\varepsilon_1 \cdot b_0 \cdot (\Phi - x)}{n_{bars} \cdot \pi \cdot \Phi^2/_4}\right] \qquad \textit{Equation 4-20}$$

In this way the reduction of concrete ductility is assumed function of the physical phenomena involved in the corrosion process: the average tensile strain in cracked concrete ε_1, the concrete section width b_0, the bar diameter Φ and the numbers of compressive bars n_{bars}. Anyway the assumption of f=2 will be validated with some numerical analyses respect to experimental tests made on corroded RC beams in chapter 5.

An example of constitutive law for degraded concrete in compression obtained through the application of the new formulation of d^{-}_{env} (*Equation 4-18*) and the further reduction of ductility (*Equation 4-20*) is shown in *Figure 4-58 -dotted red line.* The curve obtained is also compared with the curve found adopting d_{chem} parameter and the constitutive law for sound concrete calibrated on the CEB-FIP MC90[61] law.

Regarding the modulus of elasticity will be reduced by d^{-}_{env} as below:

$$E'_c = E_c \cdot (1 - d^{-}_{env}) \qquad \textit{Equation 4-21}$$

Due to the lack of certain experimental data, as reported in paragraph 3.4.3.1, *Equation 4-21* provides a simplified representation of the physical phenomena.

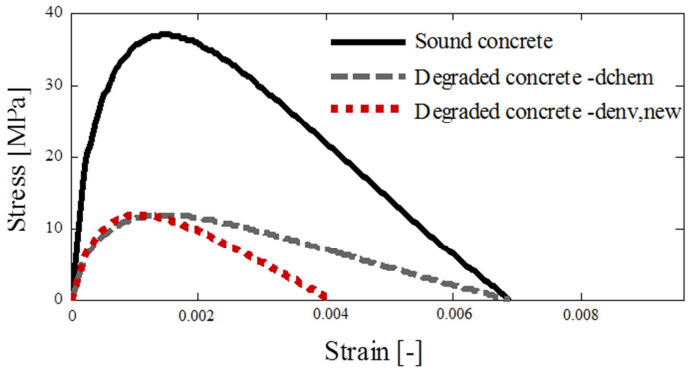

Figure 4-56. Monotonic constitutive law of sound and degraded concrete in compression

Finally, it should be noticed that in the formulations here reported all the sign are assumed positive only for the sake of simplicity of the exposition.

4.3.3.2. Environmental damage parameter for cracked concrete in tension

Regarding the tensile behaviour of degraded concrete due to reinforcement corrosion, in paragraph 3.4.3.2 different approaches adopted by other researchers and some experimental observations have been highlighted. In general, a reduction of tensile strength linked up to the reduction of compressive strength can be plausibly assumed. In this work, the tensile strength of degraded concrete is reduced through the d^{+}_{env} parameter, defined similarly to d^{-}_{env}:

$$d^{+}_{env} = 1 - \frac{f'_t}{f_t} \qquad \textit{Equation 4-22}$$

where f'_t is the mean value of tensile strength of degraded concrete, calculated from the degraded value of compressive strength f'_{cm}, according to CEB-FIP MC 90[61]:

$$f'_t = 1.4\left[\frac{(f'_{cm} - 8)}{10}\right]^{2/3} \qquad \textit{Equation 4-23}$$

In addition, a reduction of the value of fracture energy G_F is considered. In this way, the softening branch of the constitutive law of concrete in tension drops and the reduction of tension stiffening in corroded RC members is partially taken into account. In absence of certain experimental data, the equation suggested by CEB-FIP MC 90[61] for the evaluation of the fracture energy, can be adopted also for degraded concrete, as follow:

$$G'_F = G_{F0} \cdot \left(\frac{f'_{cm}}{10}\right)^{0.7} \qquad \textit{Equation 4-24}$$

where G_{F0} is the base fracture energy, which depends on the maximum aggregate size, some values are defined by CEB-FIP MC 90[61] -*table 2.1.4*.

As an example, in *Figure 4-57* the adopted constitutive law for degraded concrete in tension, obtained through the application of d^{+}_{env} parameter and further reduction of G_F (*red dotted line*), is compared with the constitutive law for sound concrete in tension (*black continuous line)* and with the law found applying only d^{+}_{env} parameter (*grey dotted line*).

Finally, a comparison between the monotonic responses of sound and degraded concrete in tension and in compression, obtained with the new proposal for the environmental-mechanical damage model, is summarized in *Figure 4-58*.

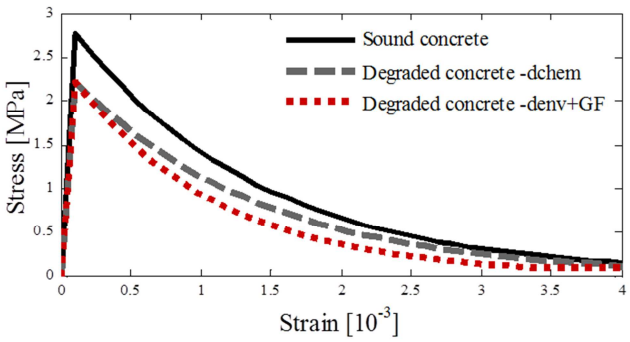

Figure 4-57. Monotonic constitutive law of sound and degraded concrete in tension

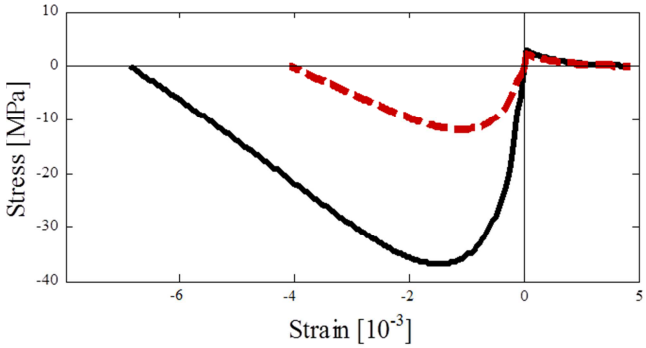

Figure 4-58. Monotonic constitutive law of sound (black curve) and degraded (red curve) concrete in tension and compression

4.4. Modelling of corrosion effects on bond

Bond influences the performances of concrete structures in several ways. At the serviceability limit state, it influences width and spacing of transverse cracks, tension stiffening and curvature. At the ultimate limit state, it is responsible for strength of end anchorages and lapped joints of reinforcement and influences rotation capacity of plastic hinge regions, *fib* MC2010[106]. The physical models able to describe the structural behaviour of concrete structures are based on perfect adherence hypothesis between steel bars and surrounding concrete, which is valid only for reinforcement in sound conditions. Nowadays the models should account bond degradation. Indeed, in existing structures the bond resistance required may turn out to be inadequate for several reasons. In practice, the lack of bond in an existing structure may be of an intrinsic or extrinsic nature and sometimes a combination of both. Dealing with intrinsic nature, it is possible to consider the lack of specific code provisions and the errors in design and execution. The lack of extrinsic nature is instead classified as bond degradation due to cracks induced by direct actions, both static and cyclic, by the corrosion of reinforcement, due to carbonation of concrete, chloride penetration or other chemical attacks, by concrete scaling and by cover damage induced by freeze/thaw cycles, Mancini and Tondolo[170]. In the next paragraph, the numerical modeling will concern only the case of bond deterioration due to reinforcement corrosion; however, a similar approach can be adopted also for other causes of bond degradation. First, the numerical approach used to simulate the steel-concrete interface is described. Then, a proposal for a new "damage type" τ-s law able to simulate splitting bond failures is introduced. Finally a comparison between experimental results of pull-out tests made by other researchers is carried out, in order to supply the bases for the development of a new proposal. Indeed, in the final paragraph, a new approach involving different τ-s laws for considering bond degradation due to reinforcement corrosion in RC structures is presented and validated against experimental results of pull-out tests.

4.4.1. Modeling of the steel-concrete interface

Within the framework of finite element method, the numerical modelling of the composite interaction between steel bar and surrounding concrete is possible at two different levels: with phenomenological modelling or detailed analysis (Lettow et al[159], Ožbolt et al.[197]). In detailed analysis the bar-concrete interaction is modeled by a three-dimensional approach formulated in the framework of continuum or discrete type modeling. In the phenomenological models concrete and steel bars are generally modeled by two or three dimensional finite elements and linked by well-defined interface elements, realized by means of discontinuous or continuous connection. In the continuous connection the macroscopic stress-strain constitutive relationship must be defined. On the other hand, the discontinuous connections consist of discrete, zero thickness elements that require stress-slip relationships. These models should take into account the most significant physical aspects of bond phenomena and geometrical characteristics of the bond zone, i.e. bar size, rib size, bar spacing, etc. that however are difficult to be considered automatically. Therefore the influence of a given bar geometry has to be assumed in advance through basic parameters of the bond model. In agreement with this approach, bond stress may be regarded as shear stress over the surface of the bar, even though implying a significant simplification of the real behaviour, described in 3.5.1. The detailed models provide instead a fine discretization of the steel bar and the of the shape of the ribs. So they allow accurate analyses, considering the influence of any geometrical characteristics involved in bond behaviour. However, they require a complex formulation and a very refined discretization to attain satisfactory accuracy in the solution.

Considering that the final aim of the current study is concerned with analyses of real structures, the phenomenological approach has been preferred instead of detailed models, which often implies excessive computational effort. In detail, a discrete modelling of the concrete-steel interface is adopted. This approach makes use of bond zero-length links that connect the reinforcing bars, which are modelled as separate truss elements, with the surrounding concrete material discretized by two dimensional finite elements. These zero-length links are defined by two nodes at the same location that are connected by multiple UnixialMaterial objects to represent the force-deformation relationship for the element. In the present work, bond force-slip laws are conferred to the zero-length links for the local *x* direction. Instead, for the local *y* direction, master-slave links are introduced between the nodes of the concrete and the nodes of the truss elements used to model the steel bars, see *Figure 4-59*. In this way, slips between concrete and steel are allowed in the local longitudinal direction of the reinforcing bars, while the steel-concrete connection perpendicular to the bar direction is assumed to be perfect.

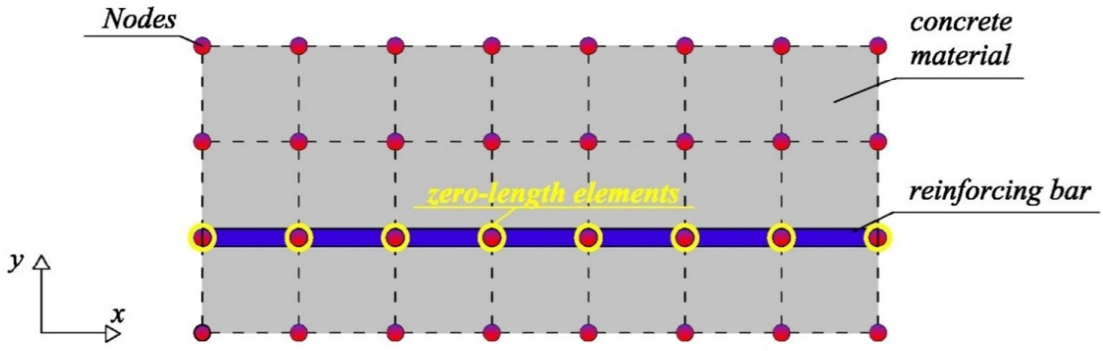

Figure 4-59. FEM modelling of RC members with zero-length links

4.4.2. Bond stress-slip laws for splitting and pull-out failures

Since the zero-length links requires the definition of a bond force-slip law, among the different approaches of literature presented in paragraph 3.5.2.3, in this work the "damage" type law proposed by Berto et al.[33] is initially assumed. The "damage" type law is selected due to its ability to well reproduce the deterioration of steel-concrete interface due to reinforcement corrosion. The authors selected the relationship, basing on the similarity between the constitutive law for concrete in compression and the τ-s law suggested by CEB-FIP MC 90[61] and they introduced a scalar damage parameter d_{bond}, for considering bond strength deterioration. In detail, the following τ-s law is proposed:

$$\tau = (1 - d_{bond})(1 - d) \cdot \bar{G} \cdot s \qquad \textit{Equation 4-25}$$

where s is the slip; d is the damage variable defined for the concrete material; $\bar{G}$ is defined as G/t, with G the elastic shear modulus and t the height of the interface elements. In this way, $\bar{G}$ results a property of the interface elements and in detail it represents the initial slope of the τ–s curve. It is worth noting that the authors used four-node plane bond elements to simulate the concrete-steel interface. Finally, d_{bond} is the corrosion bond damage parameter, its value range between 0 and 1 and it acts in a similar way as the d_{chem} parameter suggested by Saetta et al.[225].

First of all, the capacity of the "damage" type bond stress-slip law proposed by Berto et al.[33] to simulate the sound τ-s law suggested by *fib* MC2010[106] for good bond conditions and confined concrete, is following proved. As shown in *Figure 4-60*, through the calibration of some parameters of the model, the continuous numerical law well reproduces the theoretical curve. After an initial linear elastic branch, the numerical bond stress-slip law shows an ascending curve up to the maximum bond stress. Then a decreasing branch develops until the achievement of a plateau corresponding to the theoretical residual bond strength τ_{res}.

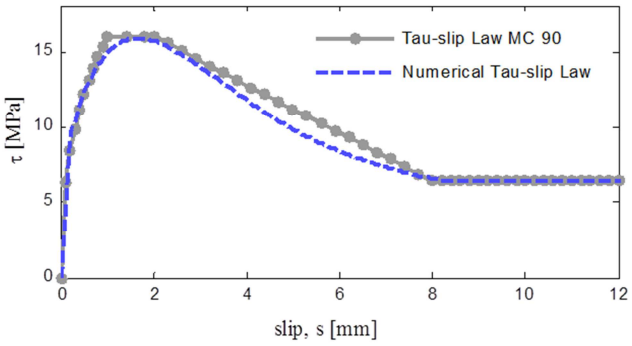

Figure 4-60. Numerical and fib MC2010[106], bond-stress relationship (pull-out failure)

On the other hand, this law is not well suited to reproduce a bond splitting failure. In the case of absence of corrosion and not well confined concrete, both CEB-FIP MC90[61] and *fib* MC2010[106] propose a different τ-s law, as described in 3.5.1.1. In order to simulate also this bond failure mode, a new bond stress-slip law is here proposed, basing on the original "damage" type one and on the theoretical law proposed by the codes. In detail, the law formulation remains the same for the first part: after the initial linear elastic branch, the law develops as an ascending curve up to the maximum bond stress τ_{max}. After the achievement of the maximum bond strength τ_{max}, a linear decreasing branch is introduced. The bond stress and the slip that define the two extremities of the linear branch, are the same defined in *fib* MC2010[106]. Then a linear constant

branch represents the residual bond strength τ_{res}. The good correspondence between new numerical law and theoretical formulation is shown in *Figure 4-61*.

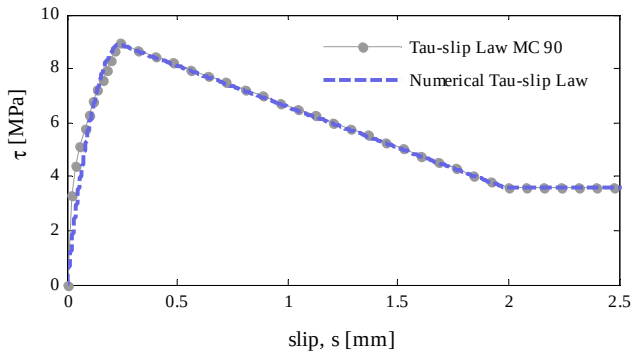

Figure 4-61. Numerical and fib MC2010[106], bond stress-slip relationship (splitting failure)

Finally, since the zero-length links adopted in this work require bond force-slip law, the bond stress τ of *Figure 4-60* and *Figure 4-61* have to be converted as follow:

$$F_\tau = 2\pi \cdot \frac{\Phi}{2} \cdot l_c \cdot n_{bars} \qquad \textit{Equation 4-26}$$

where l_c is the mesh length and n_{bars} the number of bars.

4.4.3. Comparison between experimental results

As evidenced in paragraph 3.5.2, the amount of stirrups in concrete specimens is the main factor that influences the effect of reinforcement corrosion on the composite interaction between steel bars and surrounding concrete. However, also the value of the *c/Φ* ratio has been found of great significance and should be considered. Following, a comparison of the experimental tests reported in paragraph 3.5.2 is made considering separately specimens with or without stirrups.

For specimens with stirrups, in which the transverse reinforcement is not corroded or only slightly corroded, corrosion has a minor effect on bond behaviour of longitudinal bars. Lundgren[165] observed that especially in specimens accompanied to cover cracks at uncorroded pull-out, the transverse reinforcement keeps the structure together already in sound conditions. If the cover cracks owing to corrosion, this does not have any major influence. For large corrosion penetrations, a small decrease in bond capacity can be noticed, probably mainly because the ribs are being corroded. This is confirmed by *Figure 4-62 a)*, which compares the experimental results of the authors previously considered, for corrosion levels lower than 5%. Note that in order to compare the experimental results, the bond strength $\tau_{max}^{degraded}$ is normalized with respect to the original bond strength for un-corroded specimen τ_{max}^{sound}. The corrosion level is defined as *X*, the percentage of weight loss by the corroded reinforcement. On the other hand, considering the experimental results obtained with larger levels of corrosion on the longitudinal bars, i.e. $X > 5\%$, it is possible to observe a general decrease in bond strength for *Figure 4-62 b)*.

In order to compare the experimental results, the level of concrete confinement is defined as:

$$Level\ of\ Concrete\ Confinement = \frac{c}{\Phi} \cdot \frac{A_{st}}{A_{st,min}} \qquad \textit{Equation 4-27}$$

where *c/Φ* is the cover-to-bar diameter ratio, A_{st} is the area of stirrups and $A_{st,min}$ is the minimum transverse reinforcement, as suggested by CEB-FIP MC90 [61]:

$$A_{st,min} = 0.25 \cdot n \cdot A_s \qquad \textit{Equation 4-28}$$

with n the number of bars enclosed by stirrups, and A_s area of one bar.

In *Figure 4-63*, the experimental data are interpolated through a surface with the 'nearest' interpolation method: the interpolated value at a query point is the value at the nearest sample grid point. In detail, bond strengths are reported as function of the corrosion level *X* (*X-axis*) and of the *Level of Concrete Confinement* (*Y-axis*) defined in *Equation 4-27*. As expected, higher values of bond strength are found for the higher values of the *Level of Concrete Confinement*. With increasing levels of corrosion, bond strengths decrease and tend to a same constant residual value. It is possible to observe the important role played by the *Level of Concrete Confinement* in the case of corroded specimens: with lower values of *Level of Concrete Confinement*, bond strength decreases quicker.

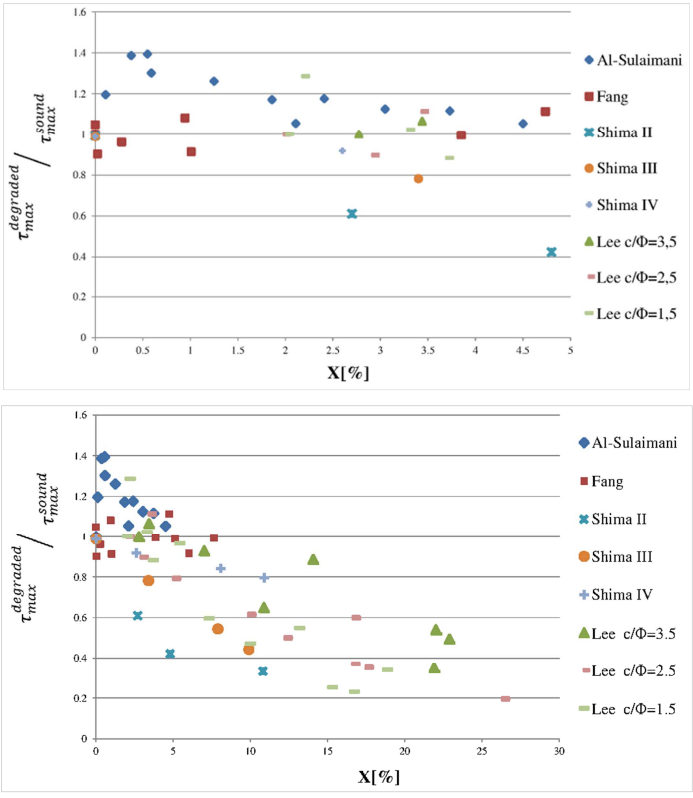

a)

b)

Figure 4-62. $\tau_{max}^{degraded} / \tau_{max}^{sound}$ *versus percentage of corrosion: a) for X<5%; b) for X<30%*

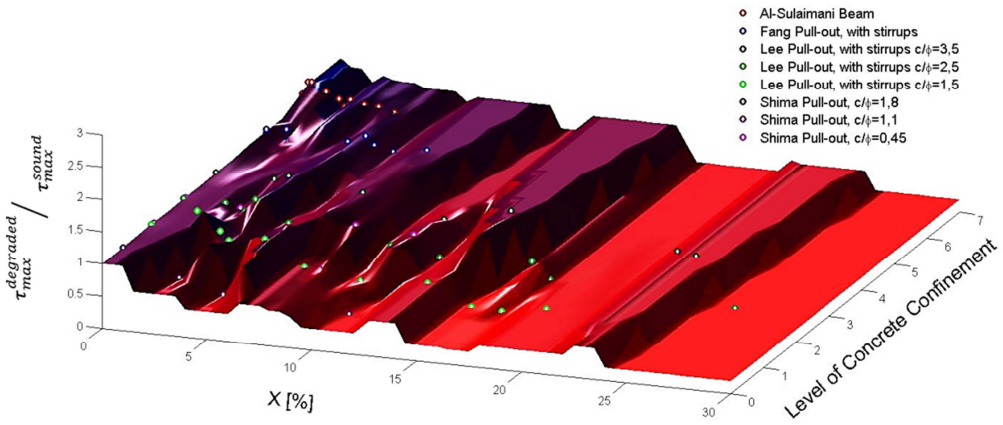

Figure 4-63: $\tau_{max}^{degraded} / \tau_{max}^{sound}$ *versus percentage of corrosion and level of Concrete Confinement – Interpolation of the experimental data*

Figure 4-64 shows the interpolation of the experimental results available in terms of bond stress normalized with respect to the maximum bond strength in sound conditions, versus the slip normalized with respect to the bar diameter, versus the percentage of corrosion.

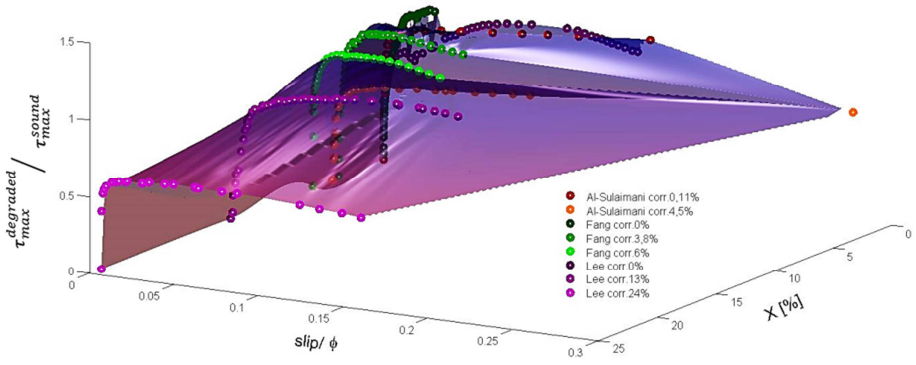

Figure 4-64: $\tau_{max}^{degraded} / \tau_{max}^{sound}$ *versus slip/Φ versus X [%]. Interpolation of experimental data*

In this way, the effects of concrete strength and bar diameter are not considered. For all the experimental tests examined, no reduction of bond stiffness, ultimate slip or change in bond failure mode is detected. As already observed, the only parameter influenced by the corrosion level is the bond strength, which decreases with the increasing of corrosion level, for *X*> 5%.

Specimens without stirrups show instead a strong reduction of bond strength with increasing levels of corrosion, *Figure 4-65 a)*, until the achievement of a very low residual value of bond strength. In *Figure 4-65 b)* is displayed the same graph, for corrosion levels up to 10%. It is possible to notice how the ratio of bond reduction strongly depends on the value of c/*Φ*: specimens with lower values of c/*Φ* exhibit a faster decrease in bond strength. Also in these graphs, in order to compare the experimental results, the bond strength: $\tau_{max}^{degraded}$ is normalized with respect to the original bond strength for un-corroded specimen τ_{max}^{sound}.

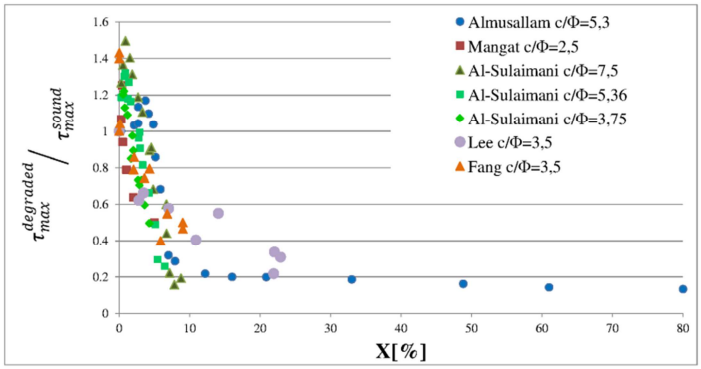

a)

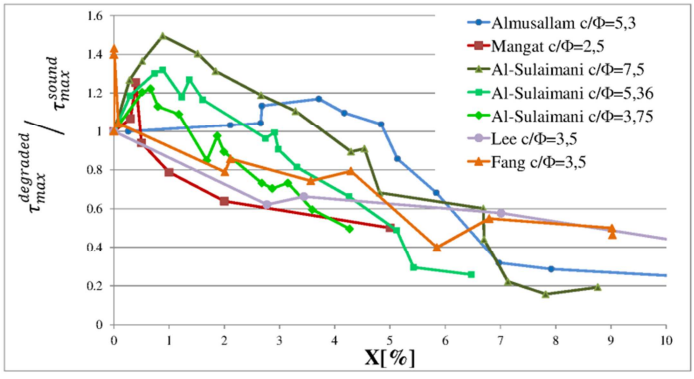

b)

Figure 4-65: $\tau_{max}^{degraded} / \tau_{max}^{sound}$ *versus X [%]: a) X< 80% of corrosion; b)X< 10% of corrosion*

In Lundgren[165] is underlined that in specimens without stirrups, where the cover cracks at uncorroded pull-out (low c/*Φ*), very limited levels of corrosion induce cracking in the cover. Thereafter, corrosion decreases drastically the bond capacity. This is confirmed by the experimental results found e.g. by Lee et al.[154] and Fang et al.[101], where the value of c/*Φ* are lower than 5: the only effects of corrosion is the reduction of the bond strength, because the bond failure is a splitting one, already in sound conditions, see *Figure 4-67*.

In all specimens without stirrups where the cover does not crack at uncorroded pull-out (high c/*Φ*), Lundgren underlined the double effect of reinforcement corrosion: both bond capacity and ultimate slip are strongly reduced when concrete cover cracks due to corrosion. These observations are confirmed by the experimental results of Al-Sulaimani et al.[9], Almusallam et al.[6] and Mangat et al.[172]. In *Figure 4-66* the experimental data are interpolated by a surface through the 'nearest' interpolation method; bond strengths are reported as function of corrosion level *X[%]* (*X-axis*) and of the *c/Φ* ratio (*Y-axis*). In the case of specimens without transverse reinforcement, for corrosion levels greater than 1-5%, depending on the value of *c/Φ*, the bond capacity decreases abruptly and the bond failure mode changes from pull-out to splitting failure, see *Figure 4-66* and *Figure 4-68*. As expected, higher values of bond strength are found for higher values of the *c/Φ*. It should be noted that in the experimental tests of Mangat et al.[172], which are characterized by a low value of *c/Φ*, the specimens without corrosion exhibited a pull-out failure, but this probably due to the presence of an external steel collar.

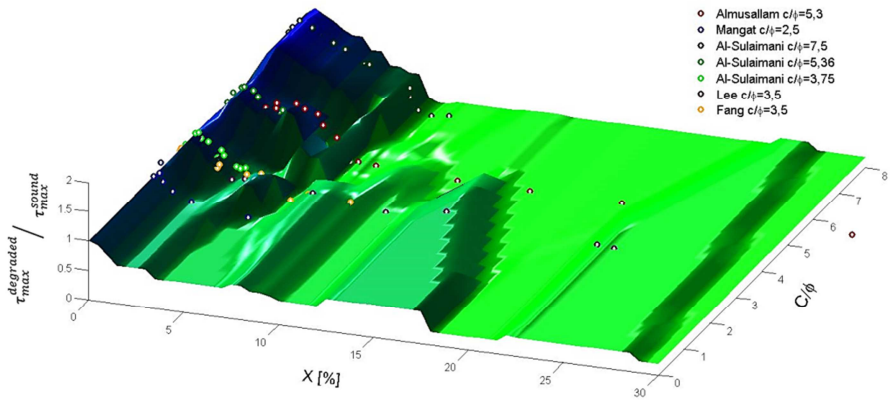

Figure 4-66: $\tau_{max}^{degraded}$ / τ_{max}^{sound} versus X [%] and level of Concrete Confinement – Interpolation of the experimental data for X<30% of corrosion

Figure 4-67 and *Figure 4-68* display the interpolation of the experimental results available in terms of bond stress normalized with respect to the maximum bond strength in sound conditions, versus the slip normalized with respect to the bar diameter, versus the percentage of corrosion.

For specimens with *c/Φ* value minor than 5, *Figure 4-67*, *w*ith increasing levels of corrosion, the experimental data show no changes or only a slight increase of the initial bond stiffness. Basing on the lack and on the uncertainties of the available data, the slip that corresponds to the achievement of the maximum bond strength cannot be considered dependent on corrosion level. It is reasonable to suppose that an increase of initial bond stiffness verifies, due to the expansion of the corrosion products. On the other side, the density of the oxide products is lower than the original material. For these reasons, the initial bond stiffness can increase or decrease with corrosion, depending also on the levels and the extension of the corrosion along the bar. As said, for these kinds of specimens, the bond failure is a splitting one already in sound conditions, therefore it can be concluded that corrosion leads only to a reduction of bond strength.

For specimens with *c/Φ* value greater than 5, *Figure 4-68*, the experimental data show a slight increase in the initial bond stiffness for low levels of corrosion and a decrease in the initial bond stiffness for high levels of corrosion. The bond failure mode clearly changes from pull-out to splitting, for high levels of corrosion. This has been underlined also by Yang et al.[274]: once the steel is corroded, due to the fact that corrosion mainly reduces the concrete confinement, it can be reasonably accepted the splitting failure as the dominant mode for corrosion-affected bond failure. Minor corrosion levels may instead increase the confinement and the pull-out failure may still be likely. Furthermore, almost all the authors have observed that low corrosion levels (until 1-5%) lead to an increase of bond strength, while higher corrosion levels cause a widening of splitting cracks, a reduction of the confinement and therefore a sharp loss of bond strength.

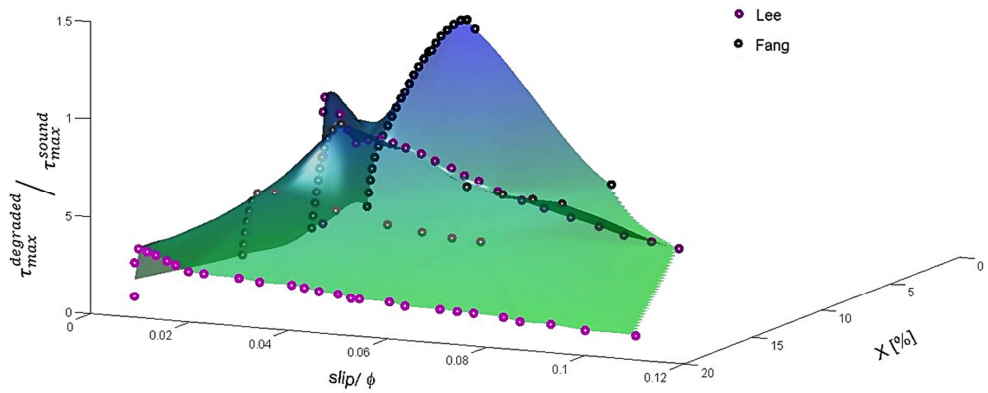

Figure 4-67: $\tau_{max}^{degraded} / \tau_{max}^{sound}$ versus slip/Φ versus X [%] – Interpolation of the experimental data of specimens with c/Φ<5

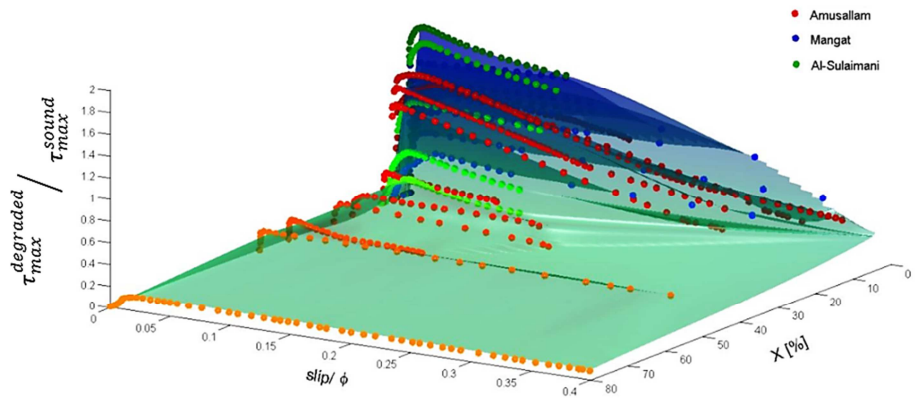

Figure 4-68: $\tau_{max}^{degraded} / \tau_{max}^{sound}$ versus slip/Φ versus X [%] – Interpolation of the experimental data of specimens with high c/Φ>5

Finally, some general remarks are here made for an accurate and exhaustive interpretation of the experimental results.

In all the experimental tests previously reported, bond degradation due to reinforcement corrosion was evaluated through accelerated tests. In this kind of tests, attention must be kept on the rate and amount of the current density, which may have a great influence on the experimental results. For example, Coronelli et al.[78] observed that bond degradation in tests made with a high level of current densities may be partly attributed to the material degradation caused by electric current. Recently experimental works, agree that a maximum current density between 200 and 400 $\mu A/cm^2$ must be applied in accelerated corrosion tests, in order to avoid an overestimation of bond

degradation due to corrosion, Mancini et al.[170]. It is worth noting that all the tests here reported were performed with higher levels of current density (800-3500 μA/cm^2). However, only few studies with natural corrosion are available for a comparison, e.g. Zhang et al.[276], therefore deeper investigations are certainly suggested.

Other variables may also influence the experimental results, as the test conditions, such as specimen submerged in chloride-contaminated water or subjected to a spray fog, or wet/dry cycles, level of moisture, porosity and strength of concrete, etc. Moreover, in actual conditions, there is always a concomitance of environmental and loading actions.

It is worth noting that published data on the effects of corrosion on bond strength may be in conflict also due to different bond test techniques. Most researchers conducted pull-out tests, which however represent bond behaviour in extreme cases of high stress concentrations. In these tests, also if short embedment lengths are adopted, the distribution of stress on the rebar length is not uniform as instead assumed. Moreover, in real RC beams, it is the concrete which transfers stresses to the steel through the interfacial bond and not the opposite as in the pull-out tests. For this reasons, alternative bond tests on beam specimens are considered to be more representative for flexural members than pull-out tests.

The same remarks and conclusions made for ribbed bars can be assumed valid also for smooth bars. Studies of bond mechanisms and effects of corrosion on bond show that the same basic mechanisms are active for both ribbed and smooth bars but with different magnitude, Lundgren[165]. As logical, the bond capacity of smooth reinforcement is lower than in ribbed bars, due to the absence of ribs that generate normal stresses at slip. For the same reason, high levels of corrosion lead to higher reduction of bond strength, especially in absence of transverse reinforcement.

4.4.4. New models for the simulation of the corrosion effects on bond

In order to capture the different effects of corrosion on bond behaviour, taking into account also the confining action of concrete and transverse reinforcement, here below a new approach involving different τ-s laws is proposed. As observed in paragraph 3.5.2.3, through analytical formulations is difficult to capture bond strength reduction/increase, change in bond failure, deterioration of bond stiffness, etc. Therefore the proposal will base on the experimental results found by other authors, analysed and compared in the previous paragraph and on the suggestions of *fib* MC2010[106]. In detail, the τ-s laws that will be formulated will automatically compute the effect of corrosion without the need of parameters calibration and: therefore they represent a good alternative or base on which calibrate the "damage" type bond stress-slip laws presented in paragraph 4.4.2. Finally the new approach will be validated against experimental results of some pull-out tests.

First, in order to capture and properly define the decrease/increase of bond strength due to corrosion, a scalar parameter has to be defined, here called d_τ.

$$d_\tau = \frac{\tau_{max}^{degraded}}{\tau_{max}^{sound}} \qquad \textit{Equation 4-29}$$

This parameter is analogous to d_{bond} parameter defined by Berto et al.[33] but it varies oppositely than normal damage parameters that assume values between 0 and 1 (0 in sound conditions and 1 in corroded conditions). Further, d_τ is not characterized by external limits, in order to capture also increments of bond strength.

Three different cases will be distinguished to properly capture the effects of corrosion on bond: confined concrete specimens with main bars corroded; unconfined concrete specimens with a value of c/Φ lower than 5 and unconfined concrete specimens with a value of c/Φ greater than 5. Instead, regarding confined concrete specimens with both main and transverse bars corroded, no experimental tests have been found in literature. However, this case presents some similarities to the unconfined concrete specimens with $c/\Phi > 5$, as we will discuss.

4.4.4.1. Confined concrete specimens with main bars corroded

In paragraph 4.4.3 the results of pull-out tests available in literature, regarding concrete specimens confined with transverse reinforcement, have been compared. Analogous to *Figure 4-62 b)*, in *Figure 4-69* the experimental results considered are reported in terms of d_τ – corrosion level X [%]. The data are then fitted through an exponential fitting curve (*Figure 4-69 black line*). The following expression is found:

$$d_\tau = 1.3e^{-0.064X} \qquad \textit{Equation 4-30}$$

However, basing on the observations extrapolated from the experimental results (paragraph 4.4.3) and on the suggestion of *fib* MC2010[106] (τ_{res}=0.4τ_{max} in the case of transverse reinforcement), a constant residual value of bond strength is more likely to be reached. Furthermore, the trendline should capture the initial increase of bond strength experimentally observed. A different fitting of the experimental data is therefore here proposed:

$$\begin{cases} d_\tau = 1 + 0.134 \cdot X & 0\% < X \leq 1.5\% \\ d_\tau = 0.4 + e^{-0.16 \cdot X} & X > 1.5\% \end{cases} \qquad \textit{Equation 4-31}$$

In order to find the curve that better fits the experimental data, the Solver tool of Excel is used to maximise the value of R-squared. The Solver tool is commonly used to solve an optimization problem by adjusting a number of input cells according to a set of criteria or constraints, which are defined by the user. In this case, the constraints are the initial bond strength increase (maximum d_τ =1.2 reached at 1.5% of corrosion level) and the residual value of bond strength equal to 0.4τ_{max}. The maximum d_τ and the corresponding value of corrosion level have been found as the average of the values experimentally reported. In *Figure 4-69* the proposed *Equation 4-31*, (*red line*), is compared with the exponential fitting curve of Equation 4-30. A better value of R-squared is found with the proposed approach.

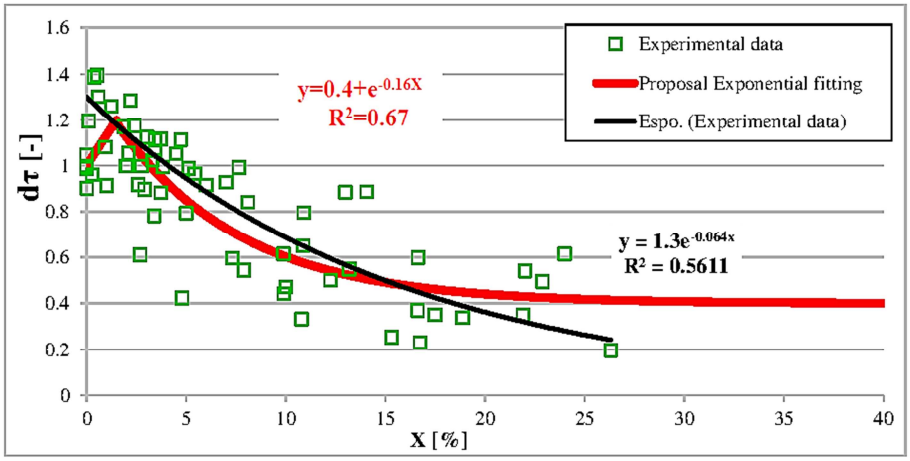

Figure 4-69. d_τ as a function of corrosion level X (%)

Once defined the reduction of bond strength due to corrosion, the effects of corrosion on the other parameters that define the bond τ-s relationship can be analysed. *fib* MC2010[106] proposes to consider a reduction of bond stiffness (first branch of the τ-s law) and an increasing length of the plateau (second branch of the τ-s law), moving from good to bad bond conditions (see *Figure 3-53 a)*). The analysis of the experimental data, have instead evidences no reduction of bond stiffness (see *Figure 4-64)*. In order to explain this difference, have to be specified that the Code gives general indications, not specifically related to a change of bond conditions due to corrosion. Moreover, in the experimental tests considered only the main bars were corroded, instead stirrups were isolated from the main bar to avoid corrosion.

It is worth noting that some authors, e.g. Croce et al.[85], pointed out that the use of CEB-FIP bond-slip model leads to an underestimation of bond stresses transfer between concrete and steel in RC members. In detail, the authors observed that in RC members the actual slips are well below those corresponding to the horizontal plateau or to the descending branch of the CEB-FIP bond-slip law. The authors explained this, arguing that the classical CEB-FIP bond-slip law is valid only when the directly loaded rebar is pulled out from a fully confined member, where the slip attains values of several millimetres. While in usual structures, like the bending beams, the slip rarely exceeds 0.0-0.2 mm, if the rebars are efficiently anchored. It is worth noting that in almost all the tests reported in paragraph 3.5.2.1, the value of s_1 was found well below the value of 1.0 mm. Horrigmoe et al.[122] made a comparison between published test data regarding the value of s_1 (the slip on which the maximum bond strength is reached in a pull-out test) and the effect of corrosion on s_1, see *Figure 4-70* and *Table 4-18*. The authors found a considerable scatter, as expected, but they gave no explanations. Also Eligehausen et al.[98] remarked that regarding bond stiffness there is a great scatter in literature. The authors showed a comparison between local bond stress-slip found by different authors, see *Figure 4-71*. The large scatter is explained due to the difficulties in measuring slip between steel and concrete correctly and due to the use of different tests specimens, with various bar diameter and deformation patterns. Also the position of the bars during casting has a great influence: bars cast horizontally show a much smaller stiffness ad a lower bond strength respect bars cast in vertical position. Finally, *fib MC2010*[106] suggests τ-s laws not normalized: the slips instead depend on bar diameter. In the proposed τ-s laws, the values of the slips, are taken lower than those proposed by the Codes and considered dependent on bar diameter, see *Figure 4-72 red dotted lines*.

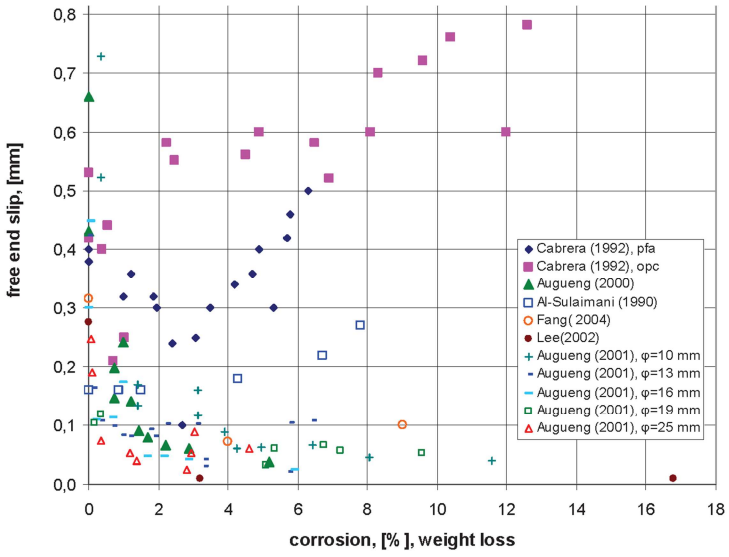

Figure 4-70. Slip s_1 versus degree of corrosion, Horrigmoe et al.[122]

Table 4-18. Fitting of tests data to CEB-FIP MC90, Horrigmoe et al.[122]

Author(s)	*Weight loss, X[%]*	*α*	*s_1 [mm]*	*τ_{max} [MPa]*
Al-Sulaimani et al. (1990)	*0*	*0.35*	*0.16*	*15.7*
	0.78	*0.4*	*0.27*	*4.0*
Tachibana et al. (1990)	*0*	*0.35*	*0.27*	*12.0*
	6 days	*0.3*	*0.08*	*9.0*
Cabrera and Ghoddouissi (1992)	*0*	*0.25*	*0.43*	*20.0*
	6.9	*0.35*	*0.52*	*15.0*
Almussallma et al. (1996)	*0*	*0.1*	*0.7*	*16.0*
	5.1	*0.01*	*0.1*	*13.5*
Auyeung et al. (2000)	*0*	*0.41*	*0.254*	*4.71*
	5.19	*0.82*	*0.038*	*1.46*
Fang et al. no stirrups (2004)	*0*	*0.44*	*0.315*	*21.95*
	4	*0.14*	*0.071*	*12.06*
Fang et al. stirrups (2004)	*0*	*0.30*	*0.5625*	*21.95*
	3.8	*0.21*	*0.65*	*20.87*
Lee et al. no stirrups (2002)	*0*	*0.65*	*0.276*	*6.15*
	0.32	*0.15*	*0.0095*	*3.95*
Lee et al. stirrups (2002)	*0*	*0.27*	*1.34*	*7.85*
	13	*0.15*	*1.34*	*6.95*

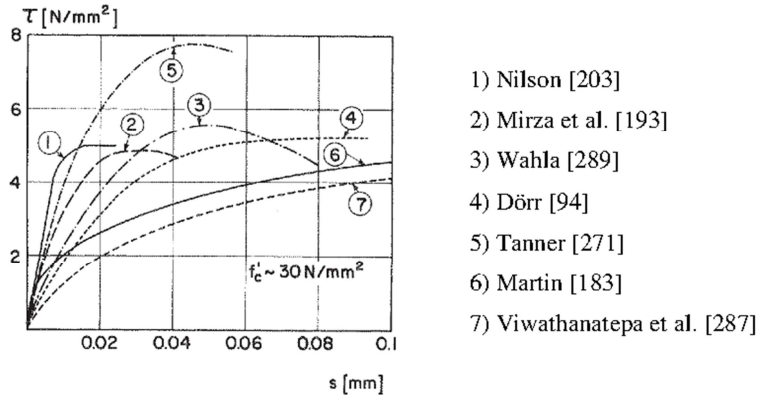

Figure 4-71. Local τ-s relationships from different researchers, Eligehausen et al.[98]

Basing on these previous remarks, the following proposal is given: with the increasing of corrosion, bond strength reduction and value of s_1, which defines indirectly the bond stiffness, are defined by d_τ parameter. The residual bond strength and the value of s_3 (value of clear rib spacing) do not change with increasing of corrosion, because they depend mainly on the transverse pressure, which in this case does not change. The plateau length increases progressively with the increasing of corrosion: in detail the value of s_2, increases linearly from the initial value to the value of s_3. Some examples of τ-s laws obtained with the proposed approach for different levels of corrosion are reported in *Figure 4-72* (*red dotted curves*) and compared with the sound τ-s law proposed by *fib* MC2010[106] for confined concrete and good bond conditions. In the graph, the bond strength is normalized with respect to the sound bond strength and the slip s respect to the bar diameter Φ. Thanks the definition of $d_\tau - X$[%] relationship given in *Equation 4-31*, the initial increases of bond strength experimentally observed can be simulated (τ-s curve obtained for X=2%). For X=3.12% the τ-s curve matches with the sound one; for increasing values of corrosion the curves go down until to reach the residual bond strength.

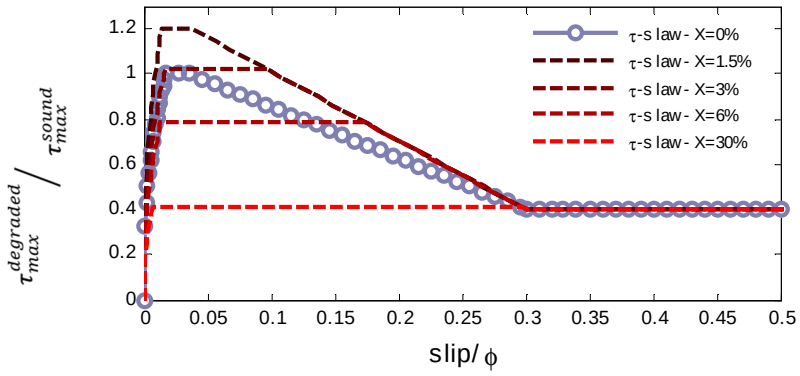

Figure 4-72. Proposal of τ-s laws for different levels of corrosion for confined concrete specimens

In order to prove the effectiveness of this proposal, the pull-out tests carried out by Fang et al.[101] for different levels of corrosion and for specimens with transverse reinforcement are numerically simulated. A brief description of the tests has been already given in paragraph 3.5.2.1. For the FE analyses, the approach described in 4.4.1 is adopted. A summary of the input data assumed for the numerical analyses is given in *Table 4-19*. A schematic drawing of the mesh adopted for the numerical simulation of the pull-out tests is shown in *Figure 4-73*.

Table 4-19. Material properties and parameters

Concrete			*Steel*		
Rcm=	*52.1*	*MPa*	*fy=*	*350.9*	*MPa*
ft=	*3.22*	*MPa*	*fu=*	*521.2*	*MPa*
Ec=	*31524*	*MPa*	*Es=*	*200000*	*MPa*
GF=	*84*	*N/m*	*b=*	*0.025*	-

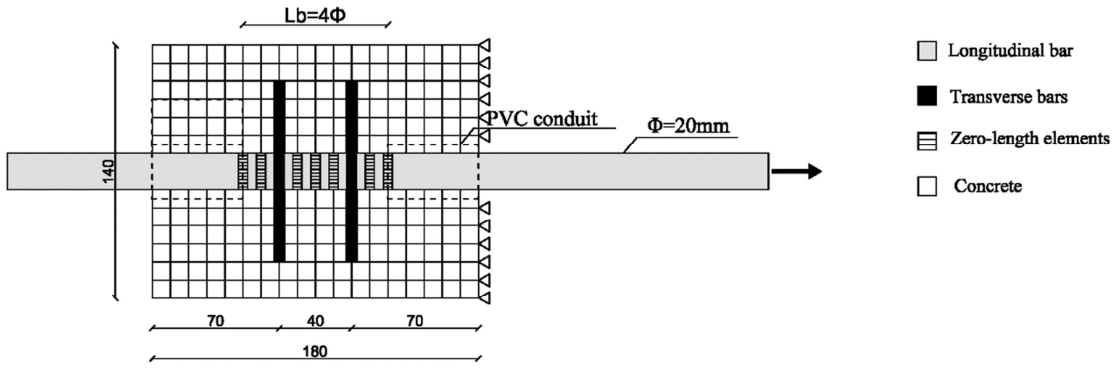

Figure 4-73. Mesh for the FE analyses of pull-out tests

For the numerical simulation of the sound pull-out test, different *τ-s* laws are adopted in order to compare the different approaches, see *Figure 4-74*. In detail, the original bond stress law proposed by *fib* MC2010[106] (*grey line*), the proposed bond stress-slip law (*dotted blue line*) and the "damage" type bond stress-slip law for pull-out bond failure mode described in 4.4.2 (*violet line*), calibrated on the previous one, are assumed. A standard value of the clear rib spacing (s_3) equal to 6.0 mm is adopted for all the bond stress-slip laws. The numerical results obtained in terms of applied load – free-end slip curves are finally compared with the experimental data available, see *Figure 4-75*. It can be observed that both the proposed bond stress-slip law and the "damage" type bond stress-slip, well reproduce the experimental results (*blue and violet curves*). The main difference between the two approaches consists on the post-peak behaviour, difficult to control in the "damage" law. Instead, the original bond stress law proposed by *fib* MC2010 [106] (*grey*

dotted curve) leads to an overestimation of the slips, as suggested by Croce et al.[85]. From these preliminary results, the approach adopted seems to better represents the bond behavior in RC members.

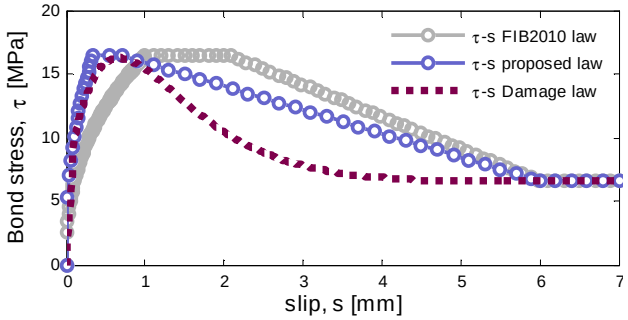

Figure 4-74. τ-s laws in numerical simulation of the sound pull-out test of Fang et al. [101]

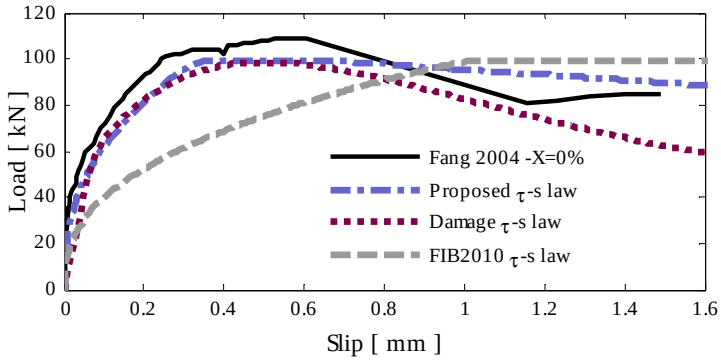

Figure 4-75. Numerical simulation of the sound Pull-out tests made by Fang et al. [101]

Regarding pull-out tests in case of reinforcement corrosion, two different levels of corrosion are considered: X=3.8% and X=6%. In the numerical simulations, the τ-s laws reported in *Figure 4-72* for these two levels of corrosion are adopted. In the numerical analyses reduction of the steel area and degradation of concrete around the reinforcing bar are also considered. In *Figure 4-76* the numerical results in terms of load – free-end slip curves are compared with the experimental data. As reported by Fang et al.[101], as the degree of corrosion increases, there is no substantial degradation in bond strength for reinforcing bar with stirrups:even if corrosion causes fine cracks in the specimen, the stirrups provided enough confinement. In the numerical simulations instead, a greater reduction of the load with increasing levels of corrosion is simulated. In detail, a maximum difference between experimental and numerical loads of 15% is found. This can be believed a good approximation, if it is considered that none calibration has been made.

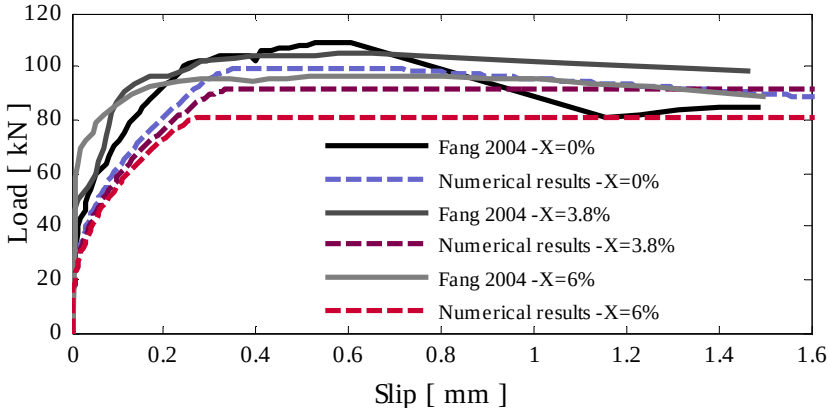

Figure 4-76. Numerical simulation of Pull-out tests made by Fang et al. [101]

4.4.4.2. Unconfined concrete specimens with main bars corroded

In paragraph 4.4.3 the results of pull-out tests available in literature, regarding concrete specimens without transverse reinforcement have been compared. Analogous to *Figure 4-65*, in *Figure 4-77* the experimental results considered are reported in terms of d_τ – corrosion level X [%]. In absence of transverse reinforcement, *fib* MC2010[106] suggests a residual bond strength equal to zero. In order to fit the experimental data and to follow the fib suggestion, an exponential fitting curve is adopted. The trendline reported in *Figure 4-77 -black line* is found, of equation:

$$d_{bond} = 0.8031e^{-0.035X} \qquad \textit{Equation 4-32}$$

The R-squared value associated to this trendline is 0.4892 which is far from 1 that represents instead the best fits of the data. Furthermore, the trendline does not capture the initial increase of bond strength experimentally observed. For these reasons, the Solver tool of Excel is used to maximise the value of R-squared and to consider an initial bond strength increase. Through this method, the following $d_\tau - X$ relationship is found:

$$\begin{cases} d_\tau = 1 + 0.227 \cdot X & 0\% < X \leq 1.1\% \\ d_\tau = 1.5e^{-0.176 \cdot X} & X > 1.1\% \end{cases} \qquad \textit{Equation 4-33}$$

The proposed relationship of *Equation 4-33* is reported in *Figure 4-77 -red dotted line*. A considerable better value of R-squared is found with this approach.

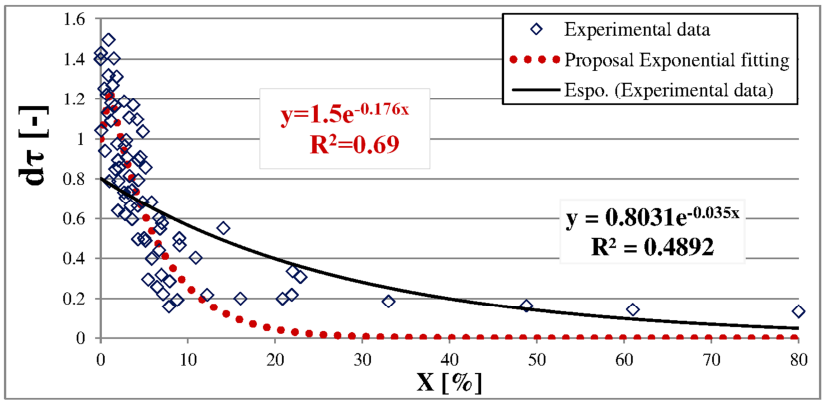

Figure 4-77. d_τ as a function of corrosion level X (%)

It is worth noting that both *fib* MC2010[106] and Lundgren[165] recognized the important role of *c/Φ* ratio. In detail *fib* MC2010[106] imposes a minimum value of *c/Φ* equal to 5 in order to consider a concrete specimen as "confined". Instead, Lundgren distinguishes two different types of specimen without stirrups: the one with low values of *c/Φ* that mostly fail by splitting also in sound condition and the one with high values of *c/Φ* that in sound conditions fail by pull-out and due to corrosion present a splitting failure. In order to investigate the effects of corrosion on bond strength for concrete specimens with different *c/Φ* values, the experimental data previously considered are divided in two groups. The first group of experimental specimens have a value of *c/Φ*<5, the second group of specimens have instead a value of *c/Φ*>5. The same procedure described before for finding the trendline that maximize the R-squared is adopted. The exponential fitting curves found are reported in *Figure 4-78 –orange dotted line –pink dotted line.* From the comparison between these two curves with the proposal of *Equation 4-33 –dotted red line*, no great differences are evident regarding the effect of corrosion on bond strength. This is probably due to the approach adopted: when we consider a fitting of experimental data, the trendlines express an average evolution, therefore the curves do not differ each other. Instead, if

we compare the single experimental results for different *c/Φ (Figure 4-65 b))* the differences can be easily noticed. Due to the lack of enough experimental data and in order to avoid excessive complications, an average trendline able to fit all the experimental data also with different *c/Φ* values, seems to be the best choice up to now. Therefore *Equation 4-33* is considered valid for the prediction of the bond strength in the case of concrete specimens without stirrups and different *c/Φ*.

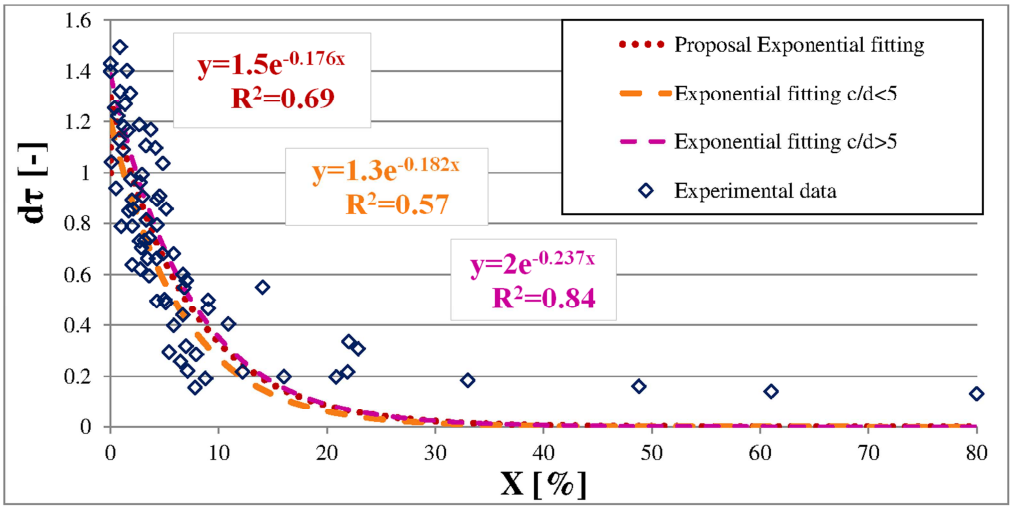

Figure 4-78. d_τ versus X[%]: specimens with c/Φ <5, specimens with c/Φ >5, all specimens

The effects of corrosion on the other parameters that define the bond *τ-s* relationship are then analysed. However, in this case it is indispensable to distinguish between the specimens with high or low *c/Φ*. This necessity is mainly due to the different bond failure mode that the two types of specimens exhibit in sound conditions: pull-out bond failure for specimens with high *c/Φ* values and splitting bond failure for specimens with low *c/Φ*.

Regarding the specimens without stirrups and with low value of *c/Φ* (an upper limit value equal to 5 is assumed), *fib* MC2010[106] considers a splitting failure likely to occur. The Code proposes to consider bond strength and bond stiffness reduction and an increment of s_1 and s_3 values, moving from good to bad bond conditions (see *Figure 3-53 b)*). The experimental data (*Figure 4-67*), have instead evidenced no reduction, but on the contrary, a slight increase of bond stiffness (see *Figure 3-62*, *Figure 3-64*). Due to the absence of a clear trend, only a slight bond stiffness reduction is here considered. Regarding the value of the ultimate slip s_3, also in this case the experimental tests do not show a clear trend, mainly for the difficulties in measuring the postpeak behaviour. For this reason s_3 is not assumed dependent on corrosion level. Finally, the experimental data showed an increase of bond strength for low levels of corrosion, *Figure 4-77*. As stated by Lundgren[165], maximum bond strength is not reduced by corrosion, for corrosion penetrations that do not crack the concrete cover. For larger corrosion penetrations, bond strength decreases rapidly to zero. This is confirmed by the experimental tests of Mangat et al.[172] and Auyeung et al.[16] that show a small increase of bond strength until that corrosion penetration reaches a critical level, thereafter bond strength decreases. Basing on these remarks, the following proposal is given: in the pre-cracking phase, $X \leq X_{crit}$, the value of d_τ increases from 1 to 1.25, bond stiffness increases and the value of s_1 decreases. After the critical level of corrosion, $X > X_{crit}$, the value of d_τ decreases with the increasing of corrosion and bond stiffness and the value of s_1, are defined by the value of d_τ. The residual bond strength is set always equal to 0 and the value of s_3 does not change with the increasing of corrosion. Some examples of *τ-s* laws obtained with

the proposed approach for different levels of corrosion are reported in *Figure 4-79* (red dotted curves) and compared with the sound τ-*s* law. It is worth noting that an average value of X_{crit} for concrete specimens with $c/\Phi<5$ is 0.4. However, *Equation 4-33* has been assumed valid for concrete specimens with every value of c/Φ, so X_{crit}=1.1% is here considered. Moreover, the τ-*s* laws proposed are displayed normalized with respect to the sound bond strength and the bar diameter, respectively for the bond strength and the slip. Thanks to the definition of $d_\tau - X$[%] relationship, given in *Equation 4-33*, the initial increases of bond strength experimentally observed can be simulated (τ-*s* curve obtained for X=1.5%). For X=2% the τ-*s* curve matches with the sound one; for increasing values of corrosion the bond strength decreases up to X=20%. At this corrosion level bond strength is negligible.

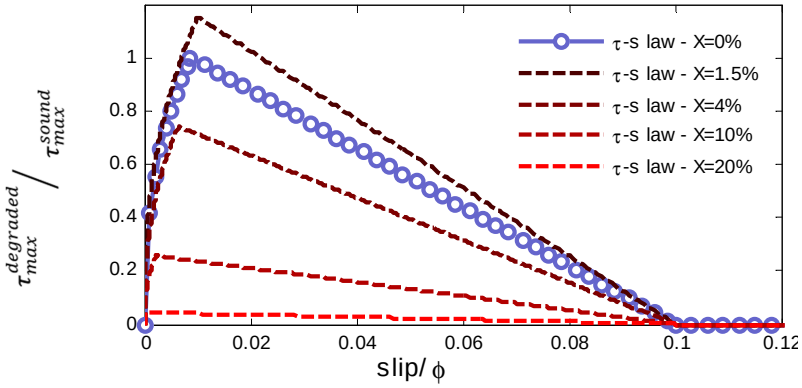

Figure 4-79. Proposed τ-s laws for different levels of corrosion, unconfined specimens with $c/\Phi<5$

In order to prove the effectiveness of this proposal, the pull-out tests carried out by Fang et al.[101] for specimens without transverse reinforcement are numerically simulated. The mesh adopted is shown in *Figure 4-73*, in this case no transverse bars were located in the concrete specimens. Also the material properties are the same of the specimens with transverse reinforcement, *Table 4-19*.

The sound Pull-out tests are firstly simulated. Also in this case, the numerical analyses are made with both the proposed bond stress-slip law and the "damage" type bond stress-slip law for splitting bond failure mode described in 4.4.2 and calibrated on the previous one. The numerical results obtained in terms of applied load – free-end slip curves are compared with the experimental data available in *Figure 4-80*. Both the τ-*s* laws considered lead to the same response (*dashed blue and dotted violet curves*). The numerical results differ from the experimental ones especially in terms of slips values. Anyway, as demonstrated in 4.4.4.1, there is a great scatter regarding the experimental value of the slip at which the maximum bond strength is reached in a pull-out test, s_1.

Regarding pull-out tests in case of reinforcement corrosion, two different levels of corrosion are considered: X=4% and X=9%. For the numerical simulations, the proposed τ-*s* laws of *Figure 4-79*, for these two levels of corrosion are adopted. In the numerical analyses reduction of the steel area and degradation of concrete around the reinforcing bar are also taken into account. Indeed, in all the corroded specimens, longitudinal corrosion-induced cracks were observed. In case of ribbed bars and specimens without stirrups, Fang et al.[101] noticed a substantial degradation of bond strength, with increasing levels of corrosion and a bond failure characterized by the splitting of the specimen along the corrosion cracks. The ultimate load decreased from 110 kN to 60 kN (-45%) as the degree of corrosion increased from 0% to 4.0%. In *Figure 4-81* the

numerical results obtained in terms of load – free-end slip curves are compared with the experimental data. If we take into account the fact that no calibration phase has been made, the numerical results can be considered a good approximation of the experimental ones. This result confirms the effectiveness of the proposal approach especially for the prediction of bond strength in the case of corroded specimens. The difference in load between experimental and numerical results is found to be between 7% and 13%.

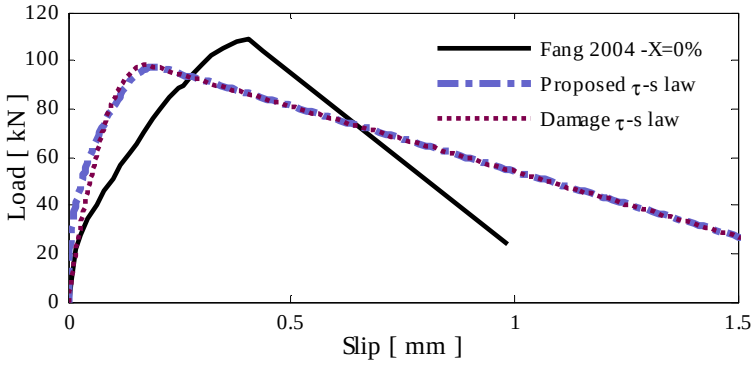

Figure 4-80. Numerical simulation of Pull-out tests made by Fang et al.[101]

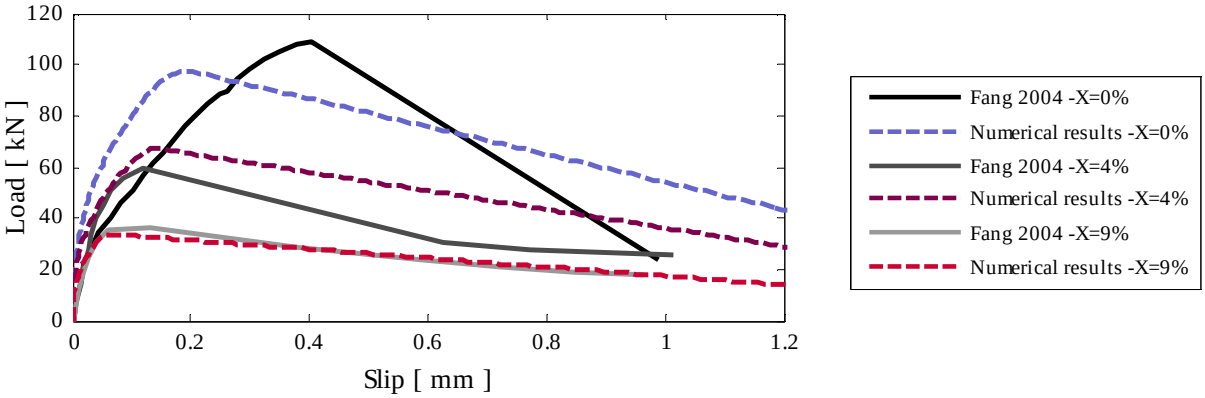

Figure 4-81. Numerical simulation of Pull-out tests made by Fang et al. [101]

Regarding specimens without stirrups and with high value of c/Φ (> 5), *fib* MC2010[106] considers a pull-out failure likely to occur in sound conditions. This case can be considered analogous to the case of specimens with transverse reinforcement, because of the confinement provided by the large concrete cover. In the case of pull-out tests in sound conditions, the concrete cover does not crack. For a certain level of reinforcement corrosion, named critical level of corrosion X_{crit}, corrosion-induced cracks can instead be observed on the surface of the concrete specimen. For corrosion penetrations smaller than X_{crit}, pre-cracking phase, bond strength and bond stiffness increase, as experimentally observed by Almusallam et al.[6], Al-Sulaimani et al.[9] and Hussein et al.[127]. For corrosion penetrations close to X_{crit}, cracking phase, as stated by Lundgren[165], the maximum bond strength is almost the same than in sound condition, but the failure mode changes from pull-out to splitting. Almusallam et al.[6] pointed out that in the cracking phase bond failure occurs suddenly at a very low free-end slip and that the slip at the ultimate bond strength decreases with increasing levels of corrosion. For corrosion penetrations greater than X_{crit}, post-cracking phase, bond strength abruptly decreases. Bond stiffness slightly decreases or remains almost constant for all the corrosion levels $X \geq X_{crit}$, as experimentally observed by Almusallam et al.[6], Al-Sulaimani et al.[9] (paragraph 3.5.2.1 and 4.4.3).

Basing on the previous remarks, the following proposal is given. The value of X_{crit} is difficult to define due to lack of enough experimental data. As observed by Almusallam et al.[6], it depends mainly on the values of c/Φ and in general for low values of c/Φ ratio, lower values of corrosion are necessary to initiate concrete cracking. In this work, a value of X_{crit} = 1.1% is assumed (obtained as average out of the experimental data available) at which corresponds a value of d_τ equal to 1.25 (see *Figure 4-77*). *Equation 4-33* is applied for the evaluation of bond strength at different corrosion levels. In order to define the variability of the other parameters of the τ-s law, the three phases experimentally observed have to be specified. The pre-cracking phase is defined for corrosion levels X ≤ X_{crit} : with the increasing of corrosion d_τ assumes values between 1 and 1.25 and bond stiffness increases. The cracking phase is defined for corrosion levels X_{crit} < X < 4%: with the increasing of corrosion d_τ varies from 1.25 to 0.75, bond stiffness decreases and bond failure changes from pull-out to splitting. The post-cracking phase is defined for corrosion levels X > 4%: with the increasing of corrosion d_τ, bond stiffness gradually decreases and bond failure remains a splitting one. Some examples of τ-*s* laws obtained with the proposed approach, for different levels of corrosion, are reported in *Figure 4-82* (*red dotted curves*) and compared with the sound τ-*s* law (*blue dots curve*).

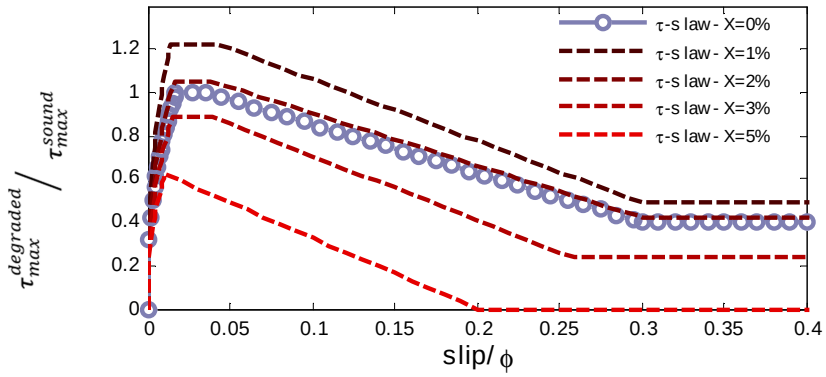

Figure 4-82. Proposal of τ-s laws for different levels of corrosion, unconfined specimens with c/Φ>5

In order to prove the effectiveness of this proposal, the pull-out tests carried out by Al-Sulaimani et al.[9] made on specimens without transverse reinforcement and high value of c/Φ are numerically simulated. A brief description of the tests has been already given in paragraph 3.5.2.2. The experimental data related to Φ=10 mm (c/Φ=7.5) are considered for the numerical simulation. For the FE analyses, the approach described in 4.4.1 is adopted. A schematic drawing of the mesh adopted for the numerical simulation of the pull-out tests is shown in *Figure 4-83*. A summary of the input data assumed in the numerical analyses is given in *Table 4-20*.

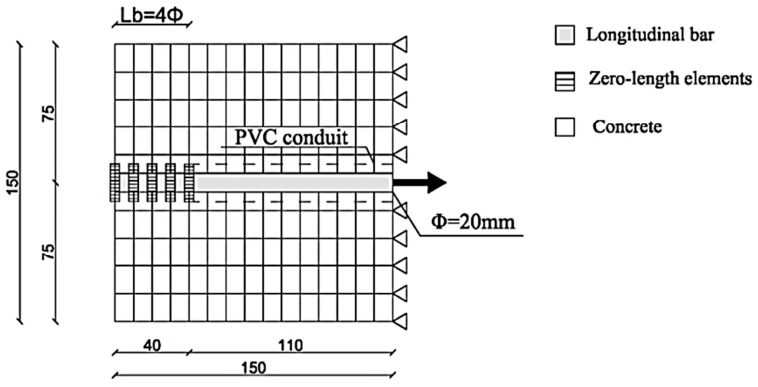

Figure 4-83. Mesh for the FEM analysis of pull-out tests

Table 4-20. Material properties and parameters

Concrete			Steel		
fc=	*30.0*	*MPa*	*fy=*	*450*	*MPa*
ft=	*2.35*	*MPa*	*fu=*	*655*	*MPa*
Ec=	*31008*	*MPa*	*Es=*	*206000*	*MPa*
GF=	*54*	*N/m*	*b=*	*0.0128*	-

Since the equivalence between the proposed τ-s laws and the "damage" type τ-s laws calibrated on the previous ones, has been previously demonstrated, here only the proposed τ-s laws are considered in the numerical simulations. The numerical results obtained in terms of applied bond stress – free-end slip curves are compared with the experimental data available, see *Figure 4-84.* The reported bond stresses are calculated from the external loads on the bar and total surface area of embedded portion of the bar, thereby they represent an average value of stress along the bonded length of the bar, as made in the experimental tests. The main problems observed in the numerical simulations are the exact prediction of X_{crit} value and the right evaluation of bond strength at low levels of corrosion. Indeed, for the lower levels of corrosion (0.87%-1.5%) the numerical simulations underestimate the maximum experimental bond strength (up to 29%). For the corrosion level close to the adopted X_{crit} =4, experimentally no change in bond failure type from pulling to splitting was detected. This is probably due to the high value of c/Φ, equal to 7.5 that leads to a delay in the change of bond type failure with respect to the considered corrosion level. However, due to the lack of experimental data, the proposed approach can be considered enough efficient, especially for corrosion levels higher than X_{crit}, as can be observed in *Figure 4-84.* The difference in bond stress between experimental and numerical results is found to be between 2 and 29%.

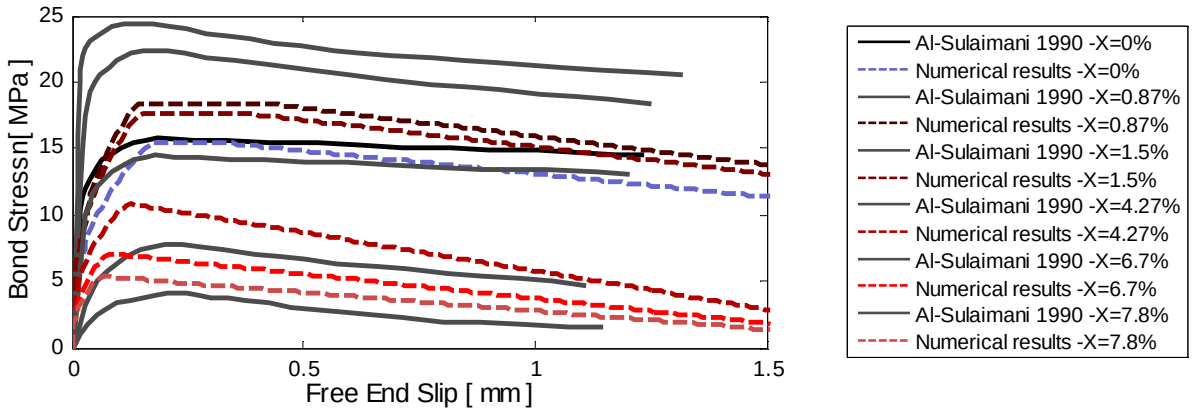

Figure 4-84. Numerical simulation of Pull-out tests made by Al-Sulaimani et al.[9]

4.4.4.3. Final remarks

The composite interaction between reinforcing bars and surrounding concrete is strongly influenced by the actual confinement conditions, given by the surrounding concrete, transverse reinforcement and transverse pressure. In specimens with stirrups, reinforcement corrosion may lead to cover spalling and in extreme cases, to the rupture of the transverse reinforcement. In this case, no confinement is provided to the longitudinal bars and a bond failure is likely to occur. In modern RC structures, the presence of stirrups is a standard structural requisite and in natural corrosive environment both longitudinal and transverse reinforcement are corroded, so this case assumes a great importance. Nevertheless, the bond capacity of corroded bars in concrete specimens with corroded stirrups has not been well studied. To the Author's knowledge, only one

experimental campaign (Hanjari et al.[117]) has been made in order to study the effect of stirrups corrosion in pull-out tests. The authors made eccentric pull-out tests, observing that bond deterioration can be expected only when the level of corrosion in stirrup is very high (rupture of the stirrups). When this happen, the confinement is loss and a splitting bond failure is likely to occur, while in sound conditions, the specimens with stirrups exhibit a pull-out bond failure. This case presents similarities with the case of specimens with high value of c/Φ and absence of stirrups, however the change in bond failure mode and the bond strength degradations are difficult to define due to the lack of experimental data.

It is worth noting that in *fib* MC2010[106] a splitting bond stress-slip law is proposed in the case of low confined concrete specimens and low c/Φ ratios. This case may theoretically happen, however no experimental data have been found until now by the Author about splitting bond failure in confined concrete specimen in pull-out tests. Anyway, this case can be well simulated following the approach suggested for unconfined concrete with low value of c/Φ and adopting a residual bond strength.

Finally, it should be noted that the same τ-s laws here proposed for the simulation of pull-out tests with tension loading, can be adopted also for compression loading. Indeed, Eligehausen et al.[98] found that the bond stress-slip relationships are almost identical in tension and in compression, paragraph 3.5.1.4.

4.6 Comprehensive approach

In order to properly model and therefore assess the structural response of corroded RC members, the local effects of reinforcement corrosion have to be adequately simulated. To this aim, in this chapter, some new proposals for the modelling of the local effects of reinforcement corrosion have been presented. In detail, these formulations are based on both original and literature analytical models, as well as experimental tests and they represent the different dowels of a more general comprehensive approach, as reported in *Figure 4-85*. This picture shows the local effects of corrosion on reinforcing bars, concrete and on the composite interaction between steel bars and surrounding concrete, emphasizing the mutual relationships. Further, the formulations developed in this chapter for taking into account of the different consequences of reinforcement corrosion, are also underlined for a better understanding of the global chapter.

The resulting comprehensive modelling approach needs to be validated in order to demonstrate its ability to predict the global effects of corrosion on RC elements at different levels of corrosion-induced degradation. To this aim, in chapter 5 the proposed comprehensive modelling approach will be applied to the simulation of the structural response of corroded RC members and the numerical results will be compared with the experimental ones.

Figure 4-85. Comprehensive modelling approach

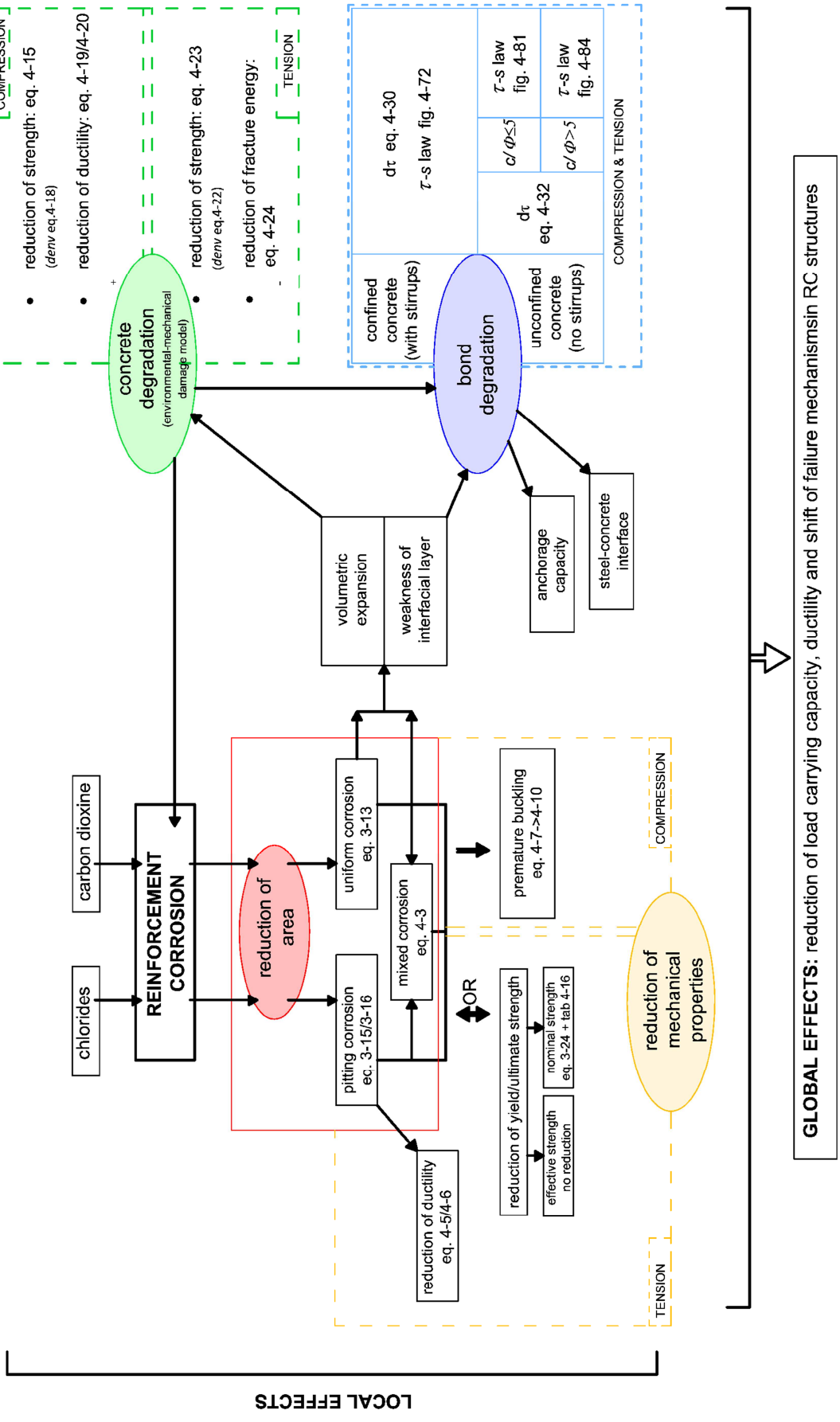

CHAPTER 5
FE MODELLING OF CORRODED RC STRUCTURES

5.1 Introduction

Corrosion of steel reinforcement in concrete may affect both load-carrying capacity and ductility of the structures themselves, leading to a reduction of their level of safety. In order to evaluate the response of corroded RC members and therefore their remaining service life, a non-linear model able to describe the evolution of the structural degradation and the progressive redistribution of stress in corroded RC structures is required. After the definition of appropriate constitutive laws for materials and relationships between material mechanical properties and corrosion level, as proposed in chapter 4, the effects of reinforcement corrosion on the global response of RC members can be analysed. In the last years, only some studies have been devoted on nonlinear finite element analysis of corroded structures. Some of them have been dealt with the problem of assessing the behaviour of corroded RC beams, e.g. Biondini et al.[40] and Coronelli et al.[80]. The main uncertainties concern the evaluation of the ductility reduction in corroded beams and the residual area of steel bars when pitting corrosion occurs. Moreover, also the relevance of bond degradation on the global structural response has not been deeply investigated, especially by varying the hypotheses of bond condition, i.e. perfect adherence and degraded bond. Finally, corrosion attack may lead to a change in failure mechanism of RC beams, from a ductile bending type to a sudden shear failure and the models available in the literature seem not able to capture this effect. Some authors have experimentally investigated also the structural consequences of corrosion on RC columns. This research topic is particularly important due to the possible structural implications of the collapse of RC columns and piles. Numerical analyses are required for the better understanding of the consequences of concrete cover degradation and premature buckling phenomena. In this chapter, the comprehensive approach presented in chapter 4 is applied for simulating the structural response of corroded RC beams and columns. The proposed approach needs to be validated in order to demonstrate its ability to reproduce the actual behaviour of RC elements in different degradation conditions. To this aim, numerical analyses are made to reproduce some case studies. In particular, the experimental tests carried out by Rodriguez et al.[221][222] and Lee et al.[153] are used as benchmark for the analysis of RC beams. Then some corroded RC columns are also simulated. Reference is made on the tests carried out by Rodriguez et al.[220].

5.2 Finite element modeling approach

The finite element modelling approach for corroded RC structures is similar to the one proposed for sound structures, paragraph 2.5.1. The concrete material is modelled with the enhanced environmental – mechanical damage model described in 4.3. In detail, the reduction of compressive ductility of cracked concrete cover, the reduction of concrete strength in compression and in tension through d^{+}_{env} and d^{-}_{env} parameters and the reduction of G_F are considered. In order to reduce the computational effort of the numerical analyses, the concrete material is modelled

with 2D plane stress elements, *Figure 5-1 -blue elements*. The stress-strain curve of reinforcing steel bars in tension is taken as for an elasto-plastic material with linear strain hardening and ultimate strength, *Figure 4-50*. In compression, premature buckling phenomena are considered through the new proposal, shown in *Figure 4-52*. Reinforcing bars and stirrups are modeled with truss elements (*Figure 5-1- red elements*). Regarding the effect of corrosion on steel, the reduction of both cross-sectional area and steel ductility are considered. The nodes of the truss elements are connected directly to the nodes of the quads representing the concrete material or when a condition different from perfect adherence is considered, through zero-length links (*Figure 5-1 - cyan links*). These links may be characterized by different τ-s laws, in order to simulate both good and bad bond conditions between steel bars and surrounding concrete. Initially, a condition of perfect adherence between concrete and steel reinforcement is assumed for all the beams. Then, an investigation regarding different bond conditions on RC beams is made and the new formulations of τ-s law are applied. Due to the symmetry, only half of the beam is modelled with proper boundary conditions, in order to reduce the computational effort. A similar FE model is applied also for the simulation of corroded RC columns. In these analyses however, only a condition of perfect adherence between concrete and steel bars is considered; therefore the nodes of concrete quads and of steel truss are in common. All the aforementioned formulations, belonging to the comprehensive modelling approach (*Figure 4-85)*, are implemented in the finite element framework OpenSEES)[179].

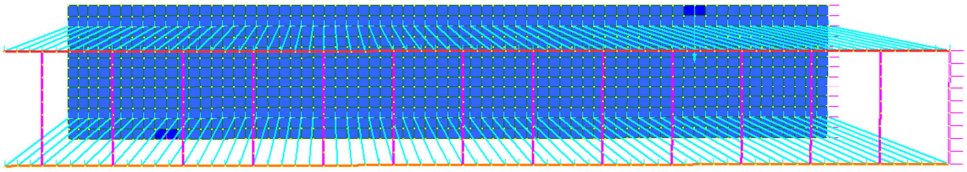

Figure 5-1. FEM model of half of RC beam, example.

5.3 Numerical simulation of corroded RC beams

The main structural consequences of reinforcement corrosion on RC beams are: reduction of ultimate displacement and of ultimate load, reduction of stiffness and change in failure mode, as introduced in paragraph 3.6. The main local effects of corrosion are profitably taken into consideration through comprehensive modelling approach. Their consequences on the global response of RC beams are here analysed.

5.3.1 Numerical simulation of the experimental tests made by Rodriguez et al.

Rodriguez et al.[221][222] tested beams with different ratio of longitudinal and transverse reinforcement and subjected to an accelerated corrosion for different periods. The beams were simply supported and two symmetrical loads were applied, a detail description is given in paragraph 3.6.1.1. In the present work, only type 11 and type 31 beams are considered. Type 11 beams are characterized by low reinforcement ratio (0.62% for tensile bars, 0.40% for compressive bars) and high stirrups spacing (170 mm), *Figure 3-76 a)*. Type 31 beams are characterized by higher reinforcement ratio (1.78% for tensile bars and 0.79% for compressive bars) and lower stirrups spacing (85 mm), *Figure 3-76 b)*. Due to the fact that d_{max}=12 mm, there is only one layer of tensile reinforcement and ρ<2%, a value of ε_{ref} =0.0004 is assumed for these beams, following the proposal reported in *Table 2-6*. Preliminary analyses are carried out on sound beams, in order to demonstrate the capacity of the damage mechanical model to well

reproduce the experimental responses of these RC beams. Concerning corroded beams, in a first phase a beam is analysed and the parameters involved in the proposed relationships, which define the effects of corrosion, verified. Then in the second phase of study, i.e. the predictive one, analyses are performed on all the other corroded beams to assess their structural response. For the validation of the predictive capacity of the model, the numerical results are compared with experimental data.

5.3.1.1 Sound RC beams

Reference beams without corroded steel bars, made with concrete type 1, of both type 11 and 31, are preliminary analysed. While the mesh size correction for concrete adopted in tension is well known and widely used, the approach adopted for the compression softening behaviour needs an additional validation. As described in paragraph 2.4.3, the constitutive law suggested by CEB-FIP MC 90[61] is amplified by the *m.s.f.*, to partially overcome the problem of mesh size dependency in compression, *Figure 5-2 -grey continuous line*. The adopted damage numerical law is calibrated on the amplified law, accordingly to *Figure 5-2 (blue continuous line)* and used for the numerical simulations of these RC beams. The mechanical characteristics adopted in the numerical model for steel and concrete are those listed respectively in *Table 5-1* and *Table 5-2* and based on CEB-FIP MC 90[61] recommendations or on the experimental data.

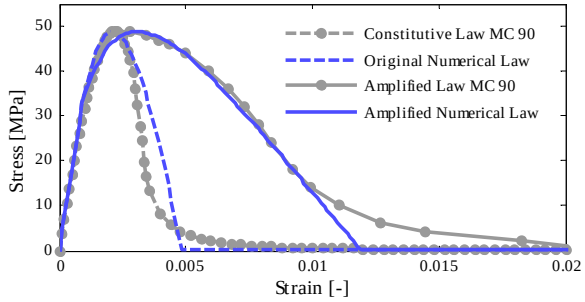

Figure 5-2. Uniaxial stress-strain laws for concrete in compression

Table 5-1. Mechanical characteristics of concrete type 1 and 2

CONCRETE	*TYPE 1*		*TYPE 2*	
f_{cm}=	*49*	*MPa*	*37*	*MPa*
f_t=	*3.59*	*MPa*	*2.85*	*MPa*
E_c=	*36518*	*MPa*	*33254*	*MPa*
G_F=	*74*	*N/m*	*58*	*N/m*

Table 5-2. Mechanical characteristics of reinforcing steel

Elastic Modulus		E_s=	*210000*	*MPa*				
Hardening Modulus		E_{sh}=	*840*	*MPa*				
Tensile bars	ϕ*12*	A_s=	*113.10*	mm^2	ϕ*10*	A_s=	*78.5*	mm^2
		σ_y=	*585*	*MPa*		σ_y =	*575*	*MPa*
		σ_{max}=	*655*	*MPa*		σ_{max}=	*655*	*MPa*
Compressive bars	ϕ*8*	A_s=	*50.27*	mm^2				
		σ_y=	*615*	*MPa*				
		σ_{max}=	*673*	*MPa*				
Stirrups	ϕ*6*	A_s=	*28.27*	mm^2				
		σ_y=	*626*	*MPa*				
		σ_{max}=	*760*	*MPa*				

For the assessment of sound RC structures, full transfer of actions between concrete and steel bars, neglecting the bond-slip effects, is a valid hypothesis. Therefore, a perfect adherence condition between the two materials can be assumed.

Figure 5-3 shows the comparison between the experimental force-deflection curves (*continuous black and grey lines*) and the numerical curve (*continuous blue line*) regarding beams 311-312. The main difference between experimental and numerical results concerns the initial stiffness, which is significantly higher in the numerical response. This could be due to a precracking phase missing in the experimental test. Indeed, the tested beams seem to start directly with the cracked stiffness. If the numerical curve is shifted of a value corrisponding to the beginning of the cracking phase (*dashed light blu line*), the stiffness of the numerical curve closely corresponds to the experimental one. The experimental failure load and the ultimate displacement are instead well captured.

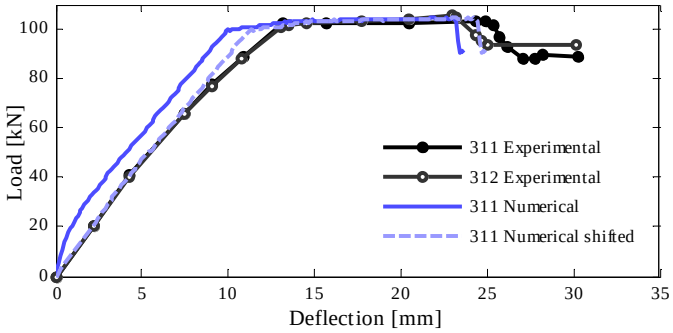

Figure 5-3. Experimental and numerical force-deflection curves for sound beams 311-312

Due to the percentage of tensile and compressive reinforcing bars and stirrups spacing, the RC beams 311-312 experimentally presented a ductile flexural mode of failure, with yielding of tensile reinforcement long before the crushing of concrete in the upper zone. The same type of failure is obtained in the finite element simulations, as shown by *Figure 5-4*, depicting the positive and negative damage contours. The long horizontal plateau, displayed in *Figure 5-3*, is characterized by the development of flexural cracks *Figure 5-4-dp* and precedes the failure by concrete crushing in the upper-central zone of the beam *Figure 5-4 -dn.*

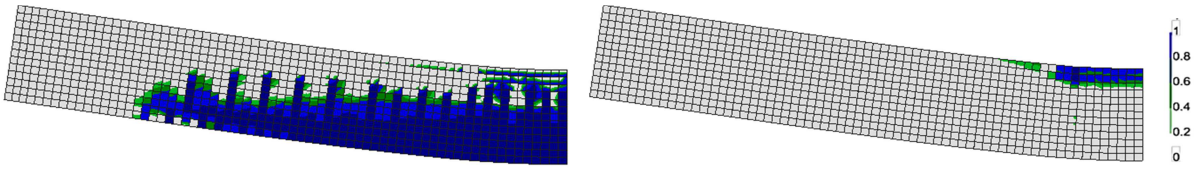

Figure 5-4. Tensile (dp) and compressive (dn) damage contours for sound beams 311-312 at failure

In order to demonstrate the validity of the approach proposed, for the bond simulation between concrete and reinforcing bars, one analysis is carried out conferring to the zero links between tensile bars and concrete a "good bond" τ-s law (*Figure 5-5*), since the beams 311-312 are not corroded. It should be noted that also a "damage" type law for pull-out bond failure could be adopted, because the two approaches are equivalent, with the only disadvantage that the "damage" type τ-s law requires the calibration of some parameters, such as d_{bond} and β. *Figure 5-6* shows the comparison between the numerical results obtained assuming a "good bond" condition and the case of perfect adherence between steel bars and concrete. The global response of the beam remains substantially unchanged, demonstrating the validity of the numerical simulation and of

the perfect adherence hypothesis. The only visible effect concerns the stiffness of the cracking phase, which is slightly lower for worst bond condition.

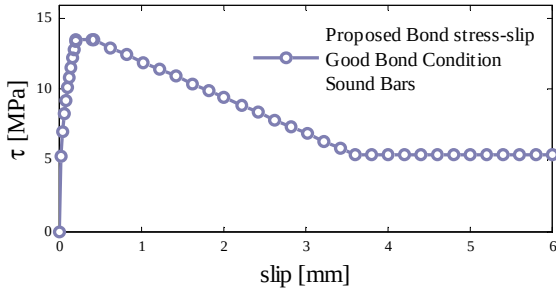

Figure 5-5. Proposed bond stress-slip law for good bond condition

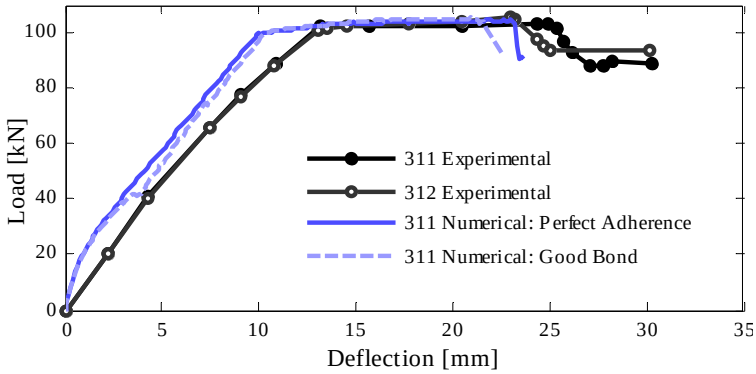

Figure 5-6. Force-deflection curves for sound beams 311-312 with different bond conditions

The sound beam 112 exhibited also a bending failure by crushing of the compressive cover concrete long after that the tensile bars had reached the yielding stress. The same behaviour is found in the numerical analysis, as evidenced by the load-deflection curves of *Figure 5-7* and by the damage maps of Figure *5-8.*

To conclude, the numerical simulations of sound RC beams demonstrate the validity of the *m.s.f.* approach and show the good agreement between experimental tests and numerical simulations.

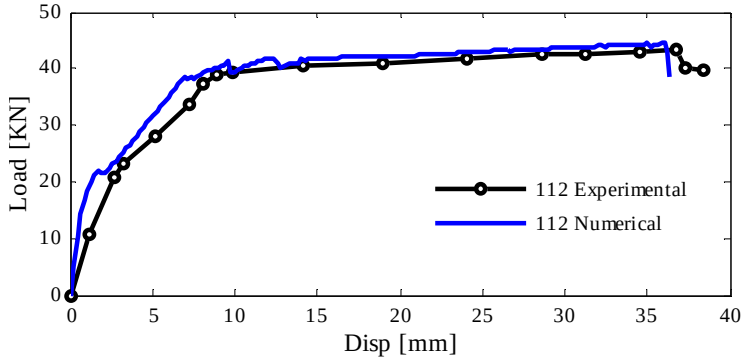

Figure 5-7. Force-deflection curves for sound beam 112

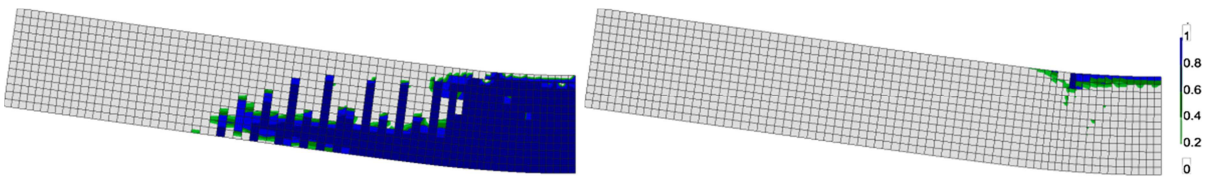

Figure 5-8. Tensile (dp) and compressive (dn) damage contours for sound beam 112 at failure

5.3.1.2 Corroded RC beams

The corroded beams were made with concrete type 2 and were subjected to an accelerated corrosion process before being loaded. Similarly to the case of concrete type 1 used for the sound beams, the constitutive law adopted for concrete type 2, based on CEB-FIP MC 90[61] law, is amplified by *m.s.f.* In order to take into account of concrete deterioration, due to formation of micro and macro cracks, the approach described in paragraph 4.3 is applied to the concrete covers. An example of constitutive laws for sound and degraded concrete in compression is shown in *Figure 5-10*.

The authors measured the corrosion attack penetration in each bar of the beams, finding that compressive bars presented only uniform corrosion, tensile bars and stirrups instead exhibited both pitting and uniform corrosion, *Table 3-8*. The authors instead did not report the longitudinal profiles of corroded bars and the exact numbers of bars affected by pitting corrosion. In the numerical simulations uniform corrosion is assumed for compressive bars and for the internal tensile bars; mixed corrosion is assumed for the external tensile bars and for all the stirrups. This can be considered a suitable hypothesis in view of the position of the bars: the two external tensile bars, located near the stirrup, are likely subjected to higher corrosion attack than the internal tensile bars.

It is worth noting that for all the numerical simulations, first a perfect adherence hypothesis between concrete and steel bars is considered. Indeed, no signals of bond degradation were pointed out by the experimental tests. The hypothesis of perfect bond is then verified: some analyses are carried out with degraded bond in order to investigate the consequences of a possible slippage between concrete and reinforcement on the behaviour of RC beams. Due to the fact that the bars were adequately anchored at support regions and that the levels of corrosion were not so high, a slight influence of bond degradation on the structural response of this RC beams is actually expected.

Validation phase

In order to verify the equations proposed in the comprehensive modelling procedure (*Figure 4-85*), for the validation phase the corroded beam 313 is deeply analysed. **Beam 313** is the one subjected to accelerated corrosion for the shortest period. The values of corrosion penetration are reported in *Table 3-8* and the values of residual cross-sectional area, for each type of bar, are shown in *Table 5-3*. It should be noticed that stirrups have the highest reduction of area, because the ratio between pitting corrosion penetration and bar diameter was higher than in other bars (around 50% of Φ).

Table 5-3. Reduction of steel cross section due to corrosion attack – Beam 313

BEAM No.	Tensile bars			Compressive bars			Stirrups		
	Initial area [mm^2]	Residual area [mm^2]	Reduction [%]	Initial area [mm^2]	Residual area [mm^2]	Reduction [%]	Initial area [mm^2]	Residual area [mm^2]	Reduction [%]
313	452.39	383.98	-15.12	201.06	181.46	-9.75	28.27	8.04	-71.56

Concerning the assessment of the residual ductility for degraded concrete in compression, for this beam different values for the factor *f* of *Equation 4-19* are assumed, in order to validate the chosen value of *f=2*. The analyses confirm that *f=2* is indeed the value that better simulates the experimental data, *Figure 5-9*, therefore this value will be maintained for all the other corroded beams. The calculated accordingly values of residual ductility for concrete covers and the values

for d^{-}_{env} evaluated with *Equation 4-18* are shown in *Table 5-4*. Finally, the constitutive laws adopted for the concrete core covers are shown in *Figure 5-10*. Due to the fact that the corroded beam 313 has lower strength than the sound beam 311, ε_{cu} is greater.

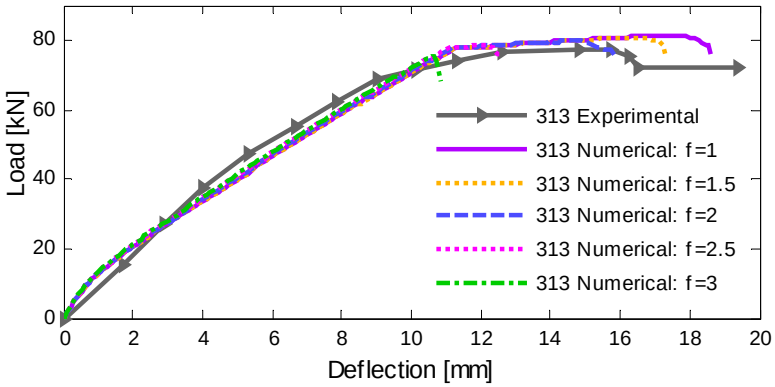

Figure 5-9. Force-deflection curves for different values of f parameter - corroded beam 313

Table 5-4. Reduction of compression strength and ductility of concrete cover - Beam 313

BEAM No.	Bottom concrete cover		Top concrete cover	
	d^{-}_{env}	Reduction ductility [%]	d^{-}_{env}	Reduction ductility [%]
313	0.69	-19.5	0.60	-19.5

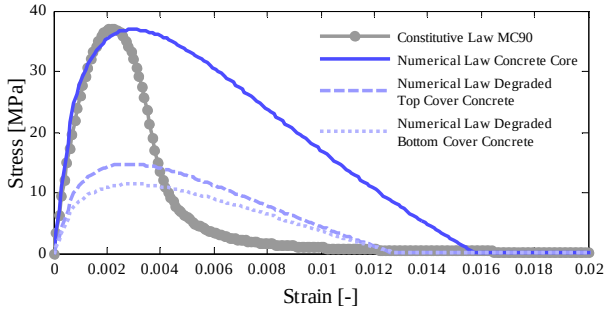

Figure 5-10. Stress-strain curve for concrete core and concrete covers in corroded beam 313

The damage contours at failure are reported in *Figure 5-11*, confirming the failure due to the crushing of concrete in compression, in the top concrete cover, as experimentally observed.

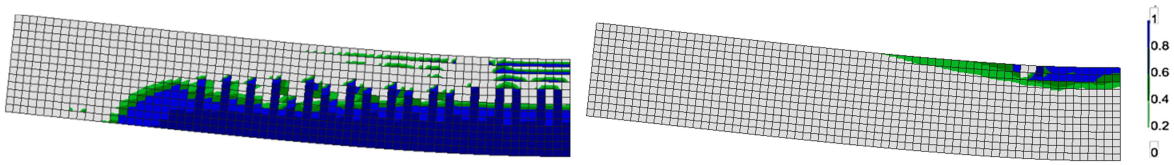

Figure 5-11. Tensile (dp) and compressive (dn) damage contours for corroded beam 313

A sensitivity analysis of the structural response to different evaluations of the residual area of corroded tensile reinforcement is also proposed. In detail, basing on the values of attack penetration reported in *Table 3-8* for beam 313, five different methods to evaluate the residual area are examined and the corresponding diagrams force-displacement obtained with the numerical simulations are compared in *Figure 5-12* (legend in *Figure 5-13*). By considering only pitting corrosion and the Val's et al. [256] model, case *(c) dark green line*, the global response is very close to the one obtained without reduction of area (*black line* – no corrosion). Otherwise, by combining such a pitting area reduction with a uniform corrosion (case *(d)*), the obtained curve (*light green curve*) gets close to the experimental ones (*continuous grey line*). Similar results are

obtained by considering only uniform corrosion (*dotted grey line*) confirming that the corroded area evaluated with the Val's et al.[256] model is very small for low pitting corrosion. The last two cases refer to the hypothesis of mixed corrosion: the residual area is evaluated with *Equation 4-3*. The *light blue line*, case *(b)*, refers to the case of all the four bars subjected to mixed corrosion; *continuous pink line*, case *(e)* (i.e. hypothesis used in this thesis) assumes the two external bars subjected to mixed corrosion and the two internal bars subjected to uniform corrosion. Both these results are in well agreement with the experimental ones, confirming the suitability of *Equation 4-3* for evaluating residual area for mixed corrosion.

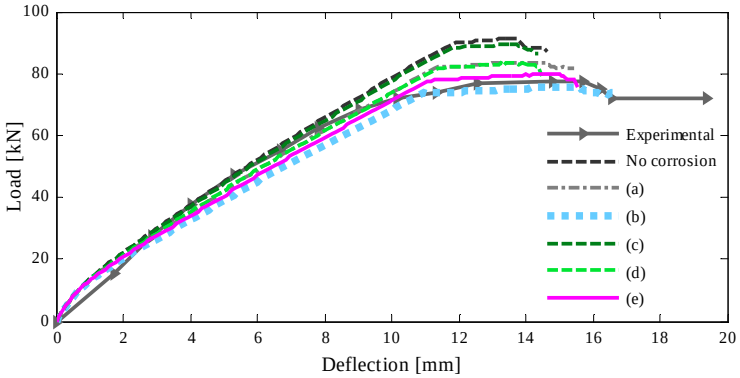

Figure 5-12. Load-deflection curves for different evaluations of residual area - beam 313

(a)	*Unifom corrosion (Equation 3-13)* $x = x_{mean} = 0.30$ *mm*	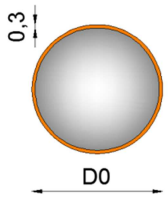	*·4 bars*
(b)	*Mixed corrosion (Equation 4-3)* $p = 1.30$ *mm*	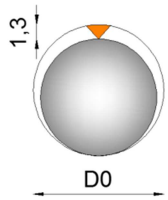	*·4 bars*
(c)	*Pitting corrosion Val & Melchers [256]* $p = 1.30$ *mm*	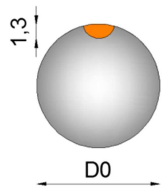	*·4 bars*
(d)	*Pitting corrosion Val & Melchers[256]* $p = 1.30$ *mm and uniform corrosion(Equation 3-13)* $x = 0.23$ *mm*	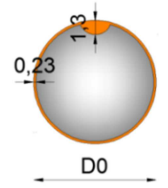	*·4 bars*
(e)	*Mixed corrosion (Equation 4-3)* $p = 1.30$ *mm and uniform corrosion (Equation 3-13)* $x = x_{mean} = 0.30$ *mm*	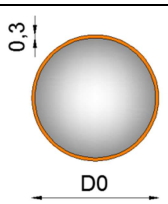 *·2 bars* 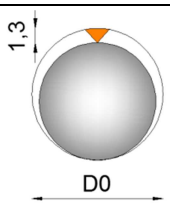	*·2 bars*

Figure 5-13. Legend of Figure 5-12

In order to investigate the structural consequences of a possible slippage between concrete and reinforcement on the behaviour of RC beams, some analyses are carried out with degraded bond stress-slip laws. Regarding beam 313, stirrups spacing was quite small and no evidences of stirrups failure were reported by the authors. For this reason, in the numerical simulations, the degraded τ-s law for confined concrete described in paragraph 4.4.4.1 is adopted (*Figure 5-14*). The numerical results obtained are compared with the results found with perfect adherence condition and "good bond" condition in terms of force-deflection curves, *Figure 5-15*. Similarly to the case of sound beams, worst bond conditions do not influence the failure load of the corroded beam 313; only a slight reduction of ultimate displacement and of stiffness in the pre-yielding phase can be observed.

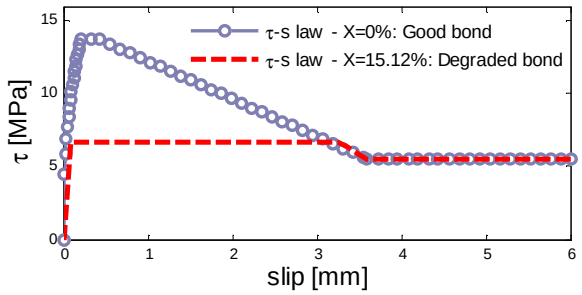

Figure 5-14. Bond stress-slip laws: good Bond and degraded Bond Conditions

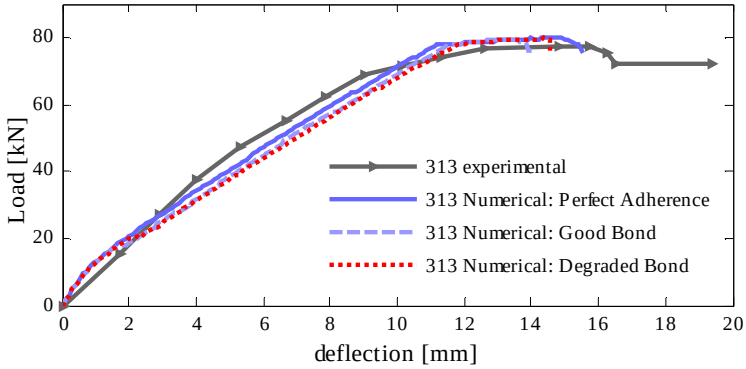

Figure 5-15. Force-deflection curves for corroded beam 313 with different bond conditions

Predictive phase

Once proved the reliability of the adopted approach for the evaluation of the residual steel area of reinforcing bars and the value of *f* equal to 2, the structural responses of corroded beams 113-114-314-315-316 are here simulated as regards the predictive phase of the numerical model. The numerical results will be then compared with the experimental ones for the final validation.

Starting from the values of corrosion penetration given in *Table 3-8*, the residual steel areas and mechanical properties of cracked concrete covers are calculated and reported in *Table 5-5* and *Table 5-6*. Some additional considerations regarding the residual ductility of steel bar and the influence of the pit spatial distribution in tensile bars will also be made. It is worth noting that bond degradation has been found not relevant for the behaviour of low corroded beams (percentage of area reduction around 15%), see *Figure 5-15*. Therefore, a perfect adherence condition is here firstly considered. Then some analyses will be made also with bond degradation, in order to investigate possible consequences on RC beams with high levels of corrosion.

Table 5-5. Reduction of steel cross section due to corrosion attack – type 11 and type 31 beams

Beam n°	Tensile bars			Compressive bars			Stirrups		
	Initial area [mm^2]	Residual area [mm^2]	Reduction [%]	Initial area [mm^2]	Residual area [mm^2]	Reduction [%]	Initial area [mm^2]	Residual area [mm^2]	Reduction [%]
113	157.08	118.89	-24.31	100.53	74.35	-26.05	28.27	3.46	-87.75
114	157.08	124.42	-20.79	100.53	76.09	-24.31	28.27	6.61	-76.64
314	452.39	364.63	-19.40	201.06	175.77	-12.58	28.27	3.14	-88.89
316	452.39	359.06	-20.63	201.06	165.59	-17.64	28.27	2.27	-91.97
315	452.39	346.46	-23.42	201.06	168.33	-16.28	28.27	0.79	-97.21

Table 5-6. Values of d^-_{env} and reduction of ductility of concrete cover – type 11 and type 31 beams

Beam n°	Bottom concrete cover		Top concrete cover	
	d^-_{env}	Reduction ductility [%]	d^-_{env}	Reduction ductility [%]
113	0.65	-37.3	0.68	-52.1
114	0.63	-34.4	0.66	-48.6
314	0.78	-30.7	0.66	-25.2
316	0.76	-27.0	0.74	-35.3
315	0.79	-32.6	0.72	-32.6

Beam 114 is first considered. This beam is characterized by a low value of corrosion penetration and exhibited a flexural failure during the experimental test. The numerical analysis shows the same kind of response: *Figure 5-16* and *Figure 5-17*. In this beam, a premature concrete crushing is observed than beam 112, due to the lower value of ductility of the concrete cover. In detail, beam 114 fails for a deflection of 18 mm long after the yielding of the tensile bars. Also in this case the bond degradation has a slight influence: it leads only to a global stiffness reduction in the pre-yielding phase, after the formation of the firsts vertical cracks in the bottom of the beam, when the bond condition is more relevant, and to a reduction of ultimate displacement (-15.8%).

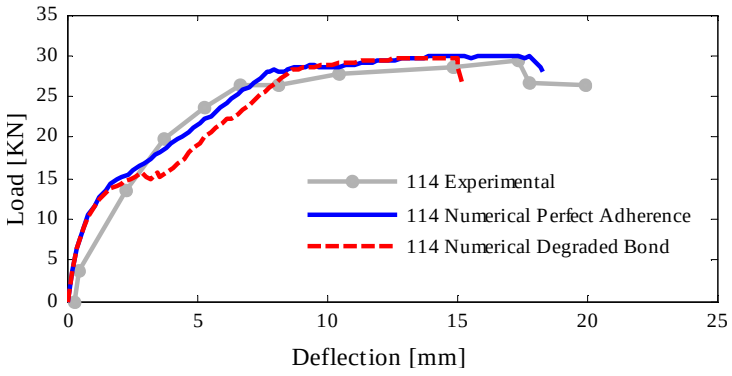

Figure 5-16. Force-deflection curves for different bond conditions - beam 114

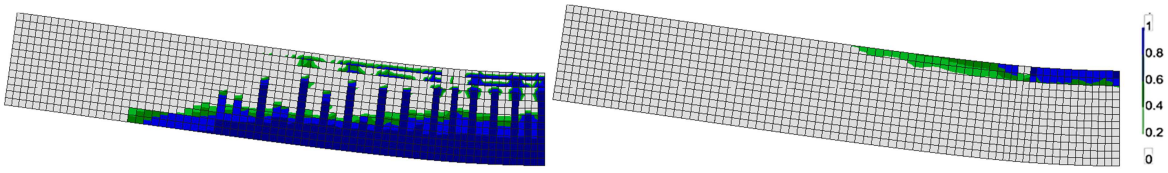

Figure 5-17. Tensile (dp) and compressive (dn) damage contours for beam 114 at failure

Beam 113 is characterized by a higher level of corrosion penetration than beam 114, especially in tensile bars, and a different failure mode. Rodriguez et al.[221] observed that beam 113 failed in

bending due to the rupture of tensile reinforcing bars at pits, before the upper concrete could crush, but still with a certain amount of ductility. This beam is therefore particularly interesting for the validation of *Equation 4-5*, which provides the ultimate strain of corroded bars in tension. The strain at bar rupture and at maximum strength of corroded tensile bars obtained with *Equation 4-5* are reported in *Table 5-7* and compared with the strain at bar rupture estimated by Rodriguez et al.[221] and the strain at maximum strength calculated with *Equation 3-28*, proposed by Biondini et al.[40]. It is possible to observe the great difference between the value reported by Rodriguez et al. and the values calculated with the others two formulas. This is due to the fact that Rodriguez et al. estimate ε'_{sr} by equilibrium considerations from the value of maximum measured compressive strain, without considering bond degradation or other effects of corrosion. Therefore, in the opinion of the Author, this value is not a reliable one. The ε'_{sm} strains evaluated with *Equation 3-28* and *Equation 4-5* are instead quite similar, around 20‰, confirming the equivalence of the two proposals. It should be noticed that the values estimated with *Equation 3-28* are lower than the ones evaluated with *Equation 4-5*, because the formula of Biondini et al.[40] was calibrated on bars that had majority of pitting corrosion than uniform corrosion. In this work a value of ultimate strain equal to 0.0219 is considered for the stress-strain law of tensile bars, reported in *Figure 4-50*.

Table 5-7. Residual strains for corroded tensile bars of beam 113

Experimental data – uncorroded tensile bars	*Analytical evaluation – corroded tensile bars beam 113*		
Rodriguez et al.[221]	*Rodriguez et al.[221]*	*Biondini et al.[40] Equation 3-28*	*Proposal Equation 4-5*
ε_{sr}=25 ‰	ε'_{sr}=13 ‰ (-48%)	ε'_{sm}=18.4 ‰	ε'_{sm}=21.9 ‰ ε'_{sr}=22.5‰ (-10%)
( ) in brachets, percentage reduction of strain at bar rupture of corroded bars respect to sound ones			

The load-deflection curve obtained restricting the steel ductility of tensile bars at ε'_{sm}=21.9‰ is compared with the case of no reduction of steel ductility, respectively *cyan dotted line* and *continuous blue line* of *Figure 5-18.* It is possible to observe that by assuming ε'_{sm}=21.9‰ the ultimate displacement of the beam slightly reduces but is still close to the experimental one. Adopting lower values of ε'_{sm}, e.g. equal to 18.4‰ as proposed by Biondini et al.[40], the beam ductility would be excessively underestimated, as we can observe in *Figure 5-18 -green dotted line*. This provides the reliability of the proposed *Equation 4-5*.

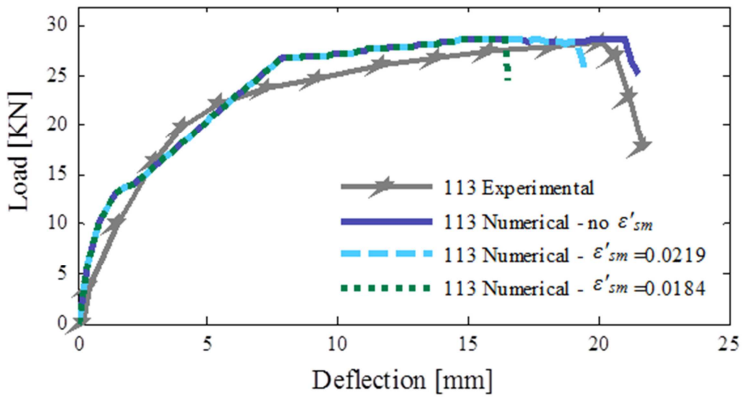

Figure 5-18. Force-deflection curves for different values of ε'_{sm} - beam 113

In *Figure 5-19* are shown the damage contours obtained when ε'_{sm} is imposed equal to 21.9‰. It is possible to observe that no concrete crushing occurs in the top concrete cover, because the tensile bars have previously reached the ultimate strain.

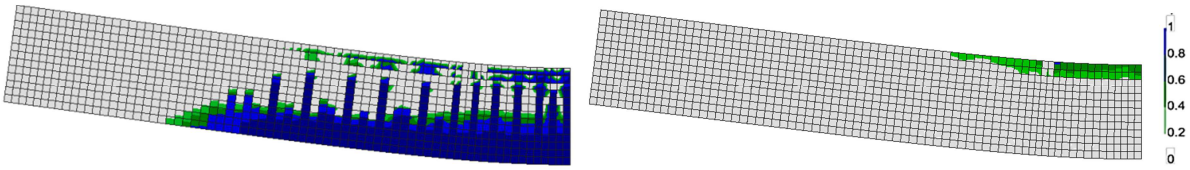

Figure 5-19. Tensile (dp) and compressive (dn) damage contours for beam 113 at failure

Also for beam 113 the condition of bond degradation is investigated. The result is reported in *Figure 5-20 -dotted red line* and compare with the case of perfect adherence (*cyan continuous line*); ε'_{sm}=21.9‰ is assumed for tensile bars in both cases. *Figure 5-20* shows that for higher levels of corrosion, the reduction of beam ductility becomes more relevant, here -25%. The reduction of beam stiffness in the pre-yielding phase is almost the same as in beam 114. It should be noticed that the force-deflection curves obtained with bond degradation for all the beams analysed so far, do not agree with the experimental results. The reason lies in the fact that probably in these beams no bond degradation took place during the experimental tests, as stated also by Rodriguez et al.[221].

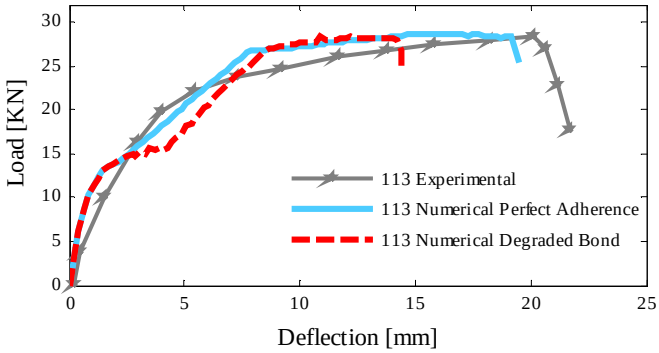

Figure 5-20. Force-deflection curves for different bond conditions -beam 113

Another important issue concerns the spatial distribution of pits in corroded bars. If the deepest pits are located in the zone of maximum bending moment of the beam, for example in the midspan, this zone will represent the weakest point of the bar, where it will break. This case corresponds to the case analysed before, because the steel bar elements situated in the beam midspan are the most stressed. If instead no pits are located in this zone, two situations are possible: the top concrete cover crushes before the rupture of the tensile bar or the bar rupture occurs in tensile bar where the deepest pit is located, for an intermediate value of beam ductility. To better explain this concept, in the next analyses, the localized reduction of steel ductility is considered in the tensile bars only at pits location. In detail ε'_{sm} is applied in the steel stress-strain law of some steel bar elements, where pits are supposed to occur. Two positions of pits are taken in the zone of maximum bending moment (sections C-under the load and D-midspan), one at the support (section A) and one at the a quarter length of the beam (section B), see *Figure 5-21*. A lower value of ε'_{sm} equal to 0.011 is considered in the constitutive law of the tensile bars of beam 113, which corresponds to δ_s=20% in *Equation 4-5*. The stress-strain law adopted for tensile bars is shown in *Figure 5-22 a)*. The results in terms of load-deflection curves reported in *Figure 5-23* confirm that reduction of global ductility in beam 113 occurs when pits are located in the area of maximum bending moment, i.e. between section C and D. When the pit is located at beam

midspan (section D), the highest reduction of beam ductility is observed, because the maximum steel strength is reached earliest by the steel bar in this section, see *Figure 5-22 b)*. When the pit is located at section A or B, the top concrete cover crushes before the rupture of the tensile bar.

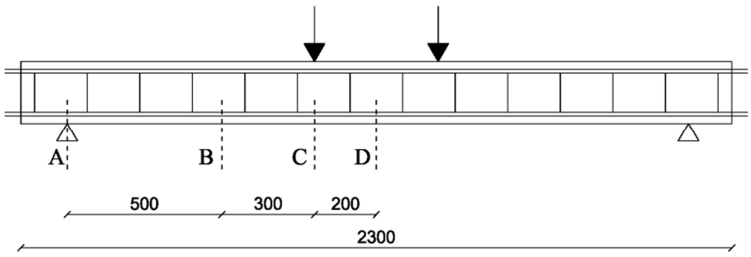

Figure 5-21. Beam 113 – location of supposed pits in tensile bars

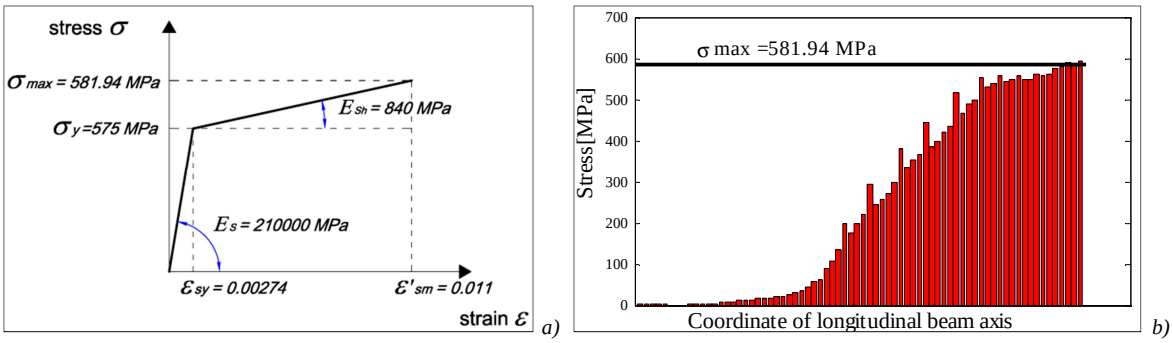

Figure 5-22. a)Constitutive law for steel of tensile bars; b)Stresses in tensile bar -beam 113

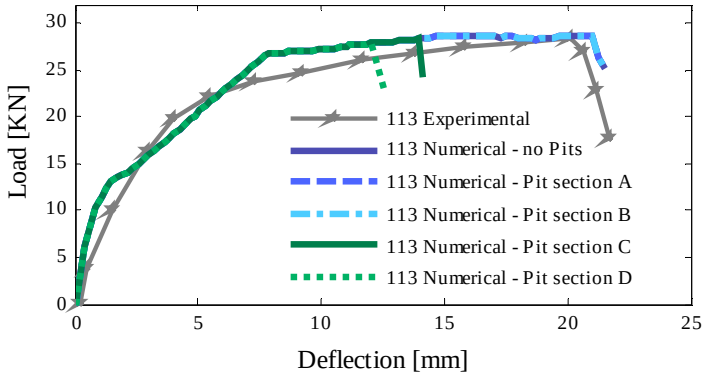

Figure 5-23. Force-deflection curves for different pits locations -beam 113

Beam 314 and **beam 316** were subjected to corrosion procedure for a medium period; therefore they present an attack penetration halfway between beams 313 and 315. For beams 314 and 316, the crushing failure of compressive concrete covers occurred before the tensile bars had reached the yield strength. This experimental observation is correctly reproduced by the numerical simulations, as shown in the force-displacement graphs of *Figure 5-25 –blue continuous line*. In detail, in *Figure 5-26* the stresses in the steel bar elements are shown: no one of them reaches the yield strength. The results shown in *Figure 5-25* confirm the absence of ductile behaviour in these beams, due to the premature crushing of concrete covers caused by the high concrete degradation. A sensitivity analysis concerning different bond conditions is carried out also for these beams. The numerical curves of *Figure 5-25* (*dotted red lines*) show that a degraded bond condition has not influence on the global response of such set of beams, because concrete crushing occurs before loss of composite interaction between tensile bars ad concrete takes place. The constitutive laws adopted for the core concrete and for the concrete covers are reported in *Figure 5-24.*

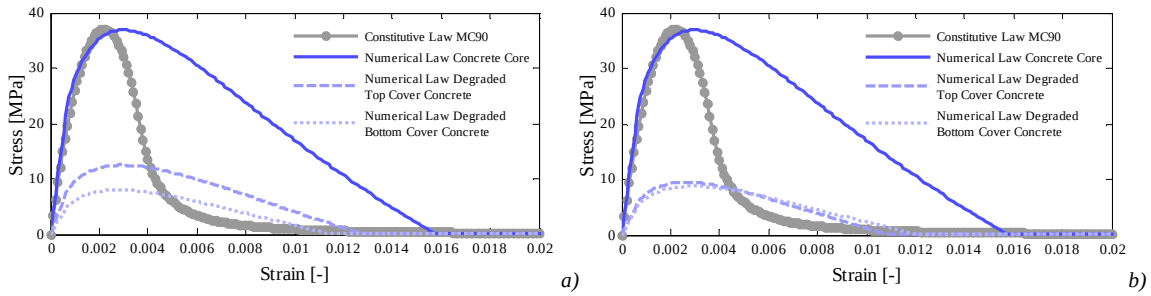

Figure 5-24. Stress-strain curve: concrete core and concrete covers; a)beam 314; b)beam 316

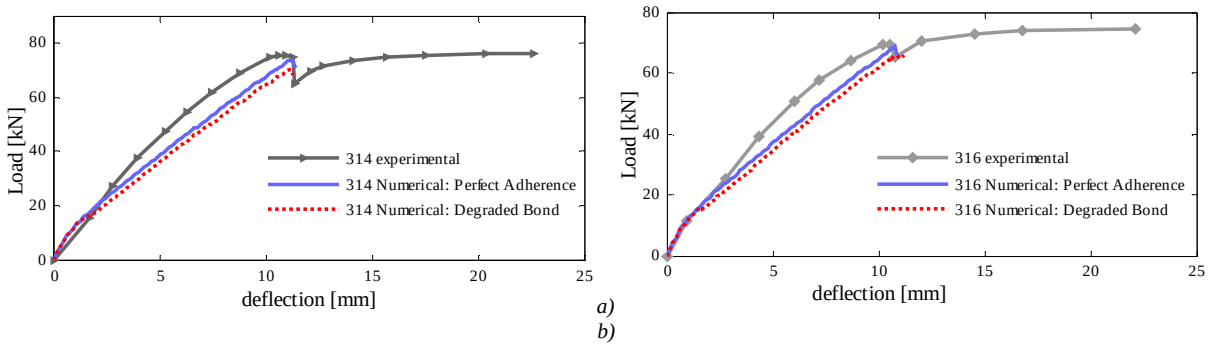

Figure 5-25. Force-deflection curves for a) corroded beam 314 and b) corroded beam 316

It is worth noting that the slight increase experimentally observed in the force-displacement graphs, after the achievement of the maximum load and the consequent decrement, is ascribed by Rodriguez "*to the collaboration of the sound part of the top concrete and the stress increase at tensile bars which had not reached the yield strength*".

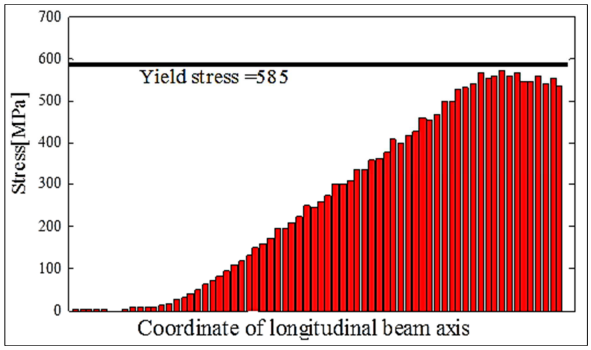

Figure 5-26. Stresses in tensile bars - beam 316

Finally *Figure 5-27* and *Figure 5-28* display the compressive and tensile damage contours for both beams, evidencing the beam failures by crushing in the compressed concrete covers.

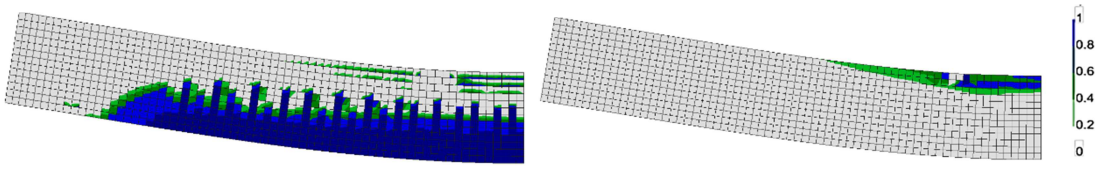

Figure 5-27. Tensile (dp) and compressive (dn) damage contours for corroded beam 314

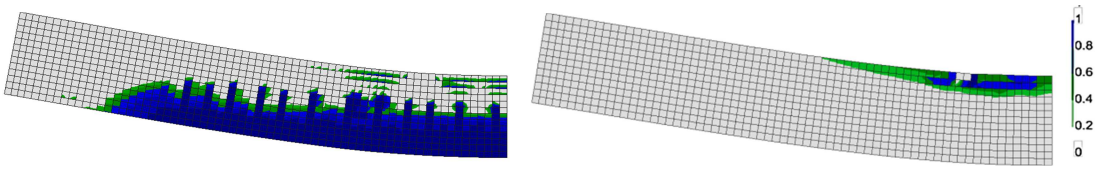

Figure 5-28. Tensile (dp) and compressive (dn) damage contours for corroded beam 316

Beam 315 was subjected to corrosion procedure for the longest period; therefore the steel bars are characterized by the highest values of corrosion penetration. While the levels of attack, due to uniform and pitting corrosion, in tensile and compressive bars are similar to beams 314 and 316, stirrups present severe values of pitting corrosion penetration: of 5 mm starting from a diameter of 6 mm. Mainly due to this reason, beam 315 exhibited a change in failure mode: indeed, it is the only beam tested that failed by shear. *Figure 5-29* depicts the numerical (*blue continuous line*) and experimental (*grey continuous line*) force-displacement curves. It is worth noting that the numerical model is able to well reproduce the brittle shear failure mode of the beam, characterized by high reduction of ductility and ultimate load, but it slightly upper estimates the residual load carrying capacity. Also in this beam, bond degradation does not influence the global response of the beam, due to the brittle anticipated failure, *Figure 5-29 –red dotted line*. Finally, due to the high reduction of cross-sectional area of stirrups, it is possible that some stirrups break. In order to investigate this scenario, one further analysis is carried out considering half number of stirrups inside the beam. In this way the stirrups spacing becomes the double. The numerical result shows a reduction of ultimate load, as expected, closer to the experimental curve *Figure 5-29 –green dotted line*.

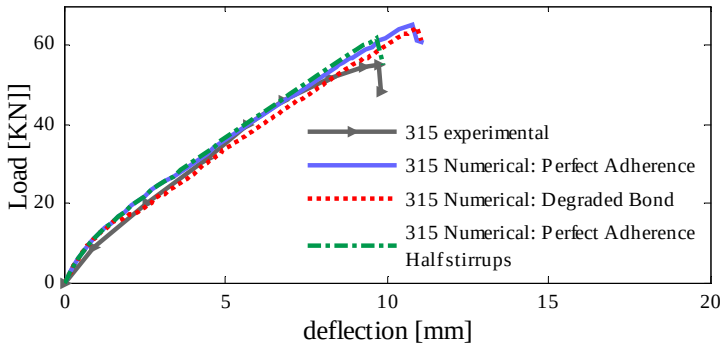

Figure 5-29. Force-deflection curves for corroded beam 315

The damage contour reported in *Figure 5-30* highlights the shear failure mode: the tensile damage map shows the development of diagonal cracks at the failure step, while the compression damage map evidences that compression damage has not yet reached the maximum value of 1. Finally, as further confirmation of the shear mode of failure, in *Figure 5-31* are compared the principal strains of beam 314 and 315. *Figure 5-31 a)* shows the principal strains of beam 314, typical of a flexural response; *Figure 5-31 b)* displays the principal strains of beam 315, disposed along the S-shaped path typical instead of the shear failure.

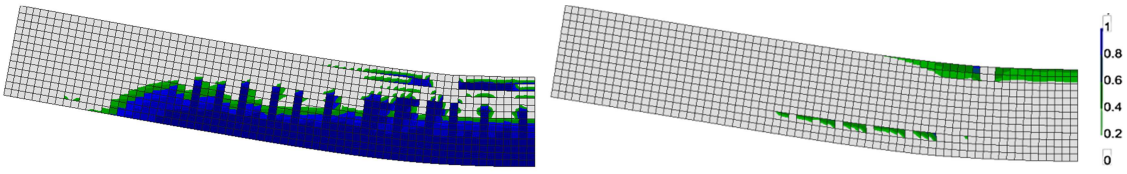

Figure 5-30. Tensile (dp) and compressive (dn) damage contours for corroded beam 315

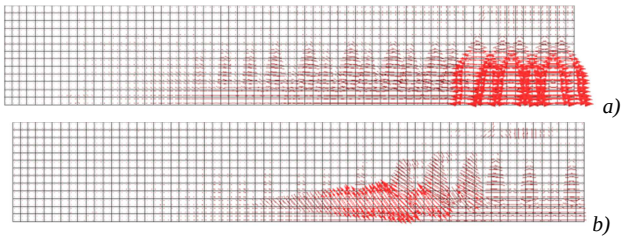

Figure 5-31. Principal strains on corroded beams 314 and 315

Finally, some comparisons between experimental and numerical results are here made. In *Figure 5-32 a)* and *b)* are reported respectively the load deflection curves obtained for type 11 and type 31 beams. It is possible to observe that the main effects of corrosion on RC beams have been the reduction of load-carrying capacity and ductility, related also to the change in failure mode. These remarks confirm the observations made by most of the researchers, as reported in paragraph 3.6.1 and *Table 3-5*.

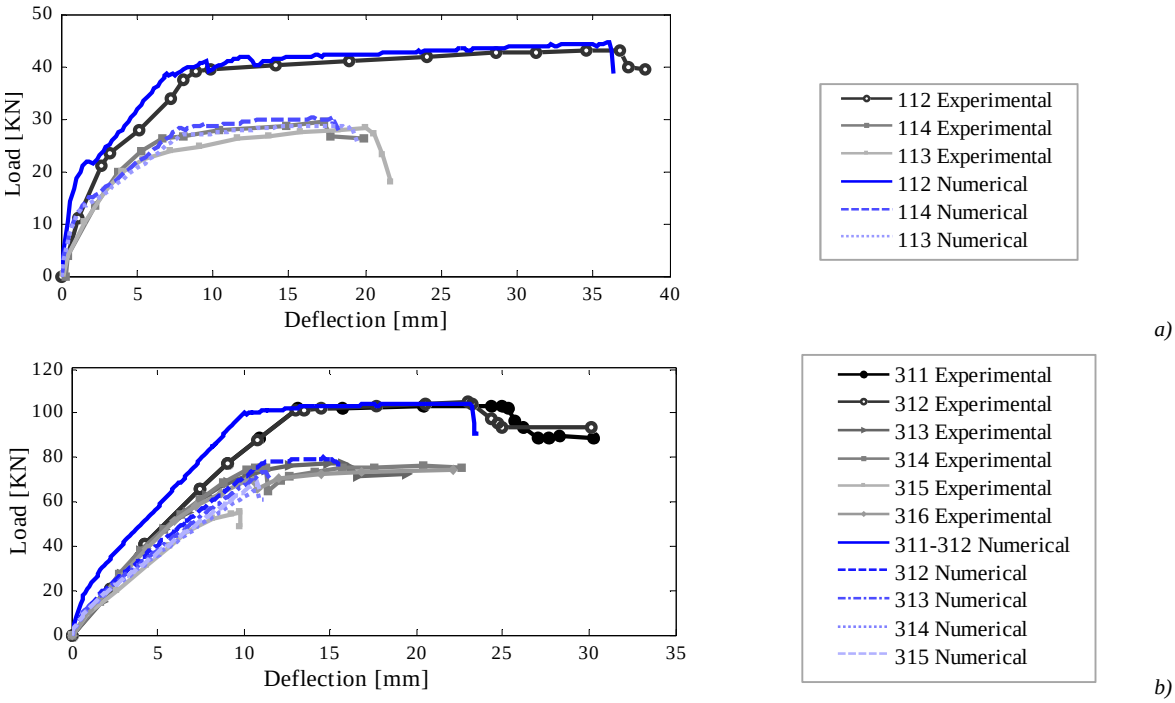

Figure 5-32. Load deflection curves for type 31 beams: numerical and experimental results

In order to quantify the effect of reinforcement corrosion on ultimate load and deflection of the beams analysed, in *Figure 5-33 a)* and *b)* the variation in ultimate load with increasing levels of corrosion in tensile bars is shown, for experimental and numerical results. The reduction in load-carrying capacity is observed to be linear from the sound beams through to the most corroded, except for beam 315 which failed in shear. The discontinuity, indicating the change in failure mechanism, is very evident in *Figure 5-33* a), less in *Figure 5-33* b), because as observed in paragraph 5.3.1.2, the numerical simulation has over-estimated the ultimate load of beam 315.

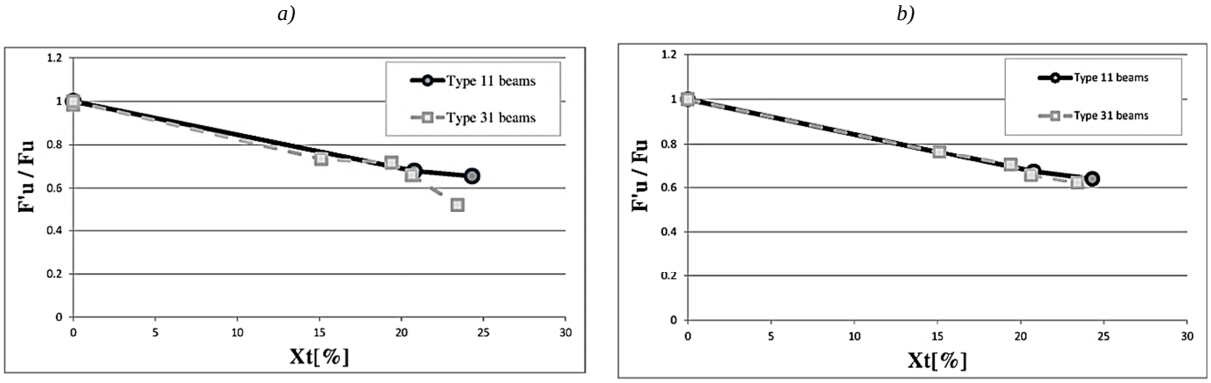

Figure 5-33. Variation in load-carrying capacity with tension reinforcement corrosion: a) experimental results; b) numerical results

In *Figure 5-34* a comparison between experimental and numerical results is reported. In general, the numerical model captures well both ultimate load and ultimate deflection of corroded beams (differences lower than 5% can be observed) except the case of beam 315. Due to the fact that Rodriguez et al.[221][222] did not report failure of stirrups, others mechanisms likely play an important role in the change in failure mode in this beam. One possibility is that corrosion influences also the secondary mechanisms of shear resistance, as stated also by Cairns[50]: *"normal assumptions of dowel action, of aggregate interlock effects, and of the state of stress in the compression zone of the beam no longer hold when concrete is broken out around tension bars"*. For this reason lower values of ε_{ref} should be adopted with increasing levels of corrosion. However, a relation between the secondary mechanisms of shear resistance and corrosion level is difficult to assess. In this work, a further analysis is carried out for beam 315, with a value of ε_{ref} reduced of 25% than the one used for the other beams (ε_{ref} = 0.0003). The numerical load-deflection curve obtained, *Figure 5-35*, confirms the previous hypothesis, showing a better correspondence with the experimental curve.

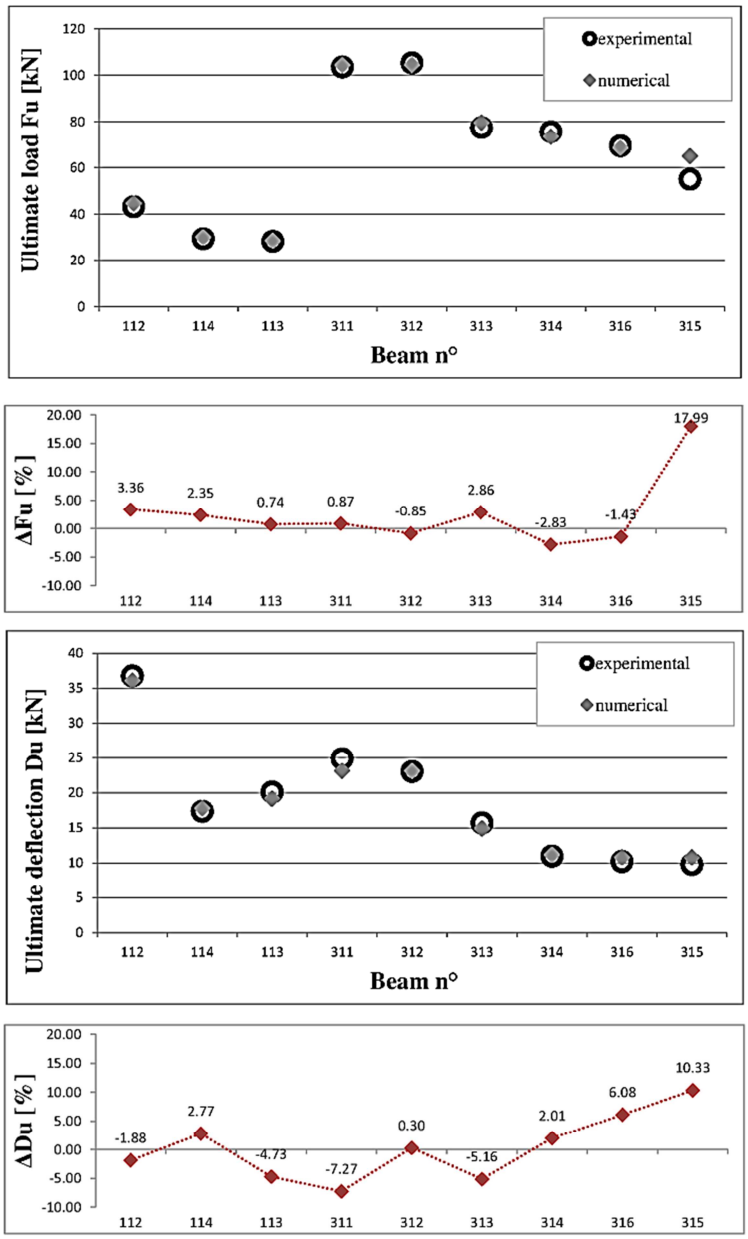

Figure 5-34. Comparison between experimental and numerical results

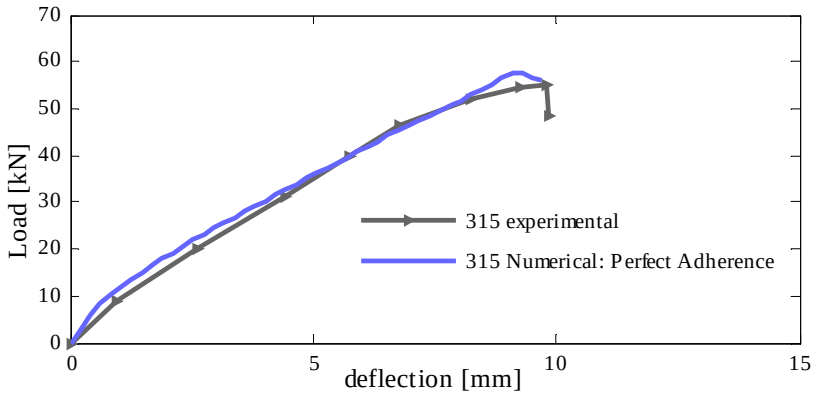

Figure 5-35. Load-deflection curve for beam 315 with reduced value of ε_{ref}

Variation in ultimate load with increasing corrosion is an useful kind of graph for the understanding of the time-dependent effect of corrosion on the ultimate limit state of damaged RC structures, for example placing in the abscissa the degradation time instead of percentage of corrosion. For corroded beams tested by Rodriguez et al.[221][222], the linear variation in load-carrying capacity with increasing section loss reported in *Figure 5-33 a)* suggests also that no debonding between steel and concrete took place. Indeed, Almusallam et al.[5] found a non-linear variation in load carrying capacity with increasing section loss due to reduction in bond strength in the RC slabs tested, *Figure 5-36*. This confirms the numerical observations made. For all the beams analysed, different conditions of composite interaction between steel bars and the surrounding concrete were investigated. It was found that bond degradation leads to a reduction of beam stiffness in the pre-yielding phase and to a reduction of beam ductility. This matches with the physical phenomena: when high bond degradation takes place, it is accompanied by longitudinal bond cracks in the concrete cover, reducing the stiffness of specimens and causing a concentration of deformation at the middle span, which resulted in the premature crushing of concrete. The premature crushing of concrete experimentally observed was found to be lower than in the numerical analyses with bond degradation and mainly related to the concrete cover degradation. Further, no strong reduction of stiffness in the pre-yielding phase was experimentally observed, confirming that the confinement provided by stirrups and the fact that the ends of the bars were adequately anchored at support regions, were sufficient to provide a residual bond strength.

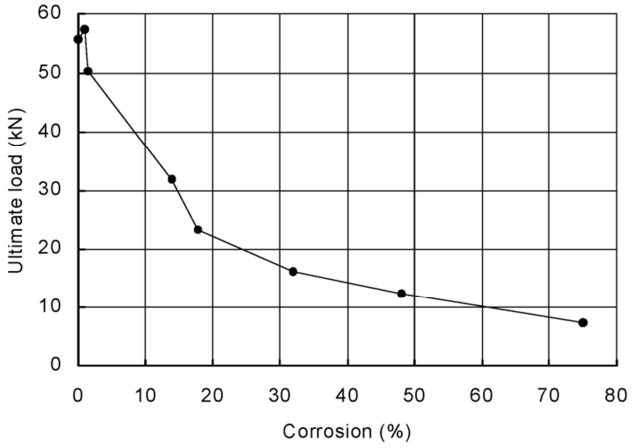

Figure 5-36. Variation in load-carrying capacity with corrosion, Almusallam et al.[5]

5.3.2 Numerical simulation of the experimental tests made by Lee et al.

In order to better understand the effect of bond degradation on the structural response of RC beams, the beams tested by Lee et al.[153] are analysed. A brief description of the experimental tests made by Lee et al.[153] has been reported in paragraph 3.6.1.2. The sound BS beam and the high corroded BCD3-0 beam are numerically simulated. The low corroded BCD1-0 beam is not considered because characterized by a flexural failure, as the reference beam. The medium corroded BCD2-0 beam has instead a similar behaviour of the BCD3-0 beam. Finally BD beam was not subjected to an accelerate corrosion procedure, therefore is not relevant for this study.

Also in these analyses, the comprehensive approach proposed in chapter 4 is adopted. It is worth noting that in the following analyses, no calibration of numerical parameters is carried out. The numerical results are finally compared with the experimental ones, in order to demonstrate the robustness and the effectiveness of the comprehensive approach. Particular attention is paid to the influence of different bond conditions on the structural response of corroded beam BCD3-0. For this particular study, no experimental observations were available, so the numerical analysis can be considered as an advanced tool for the investigation of the behaviour of RC beams.

5.3.2.1 Sound beam

The BS beam is firstly considered. The mechanical characteristics adopted in the numerical analysis for steel and concrete materials are based on the information supplied by Lee et al.[153] or are deduced basing on the CEB-FIP MC 90[61], see *Table 5-8*. The constitutive law for concrete suggested by CEB-FIP MC 90[61] is amplified by the *m.s.f* as described in paragraph *2.4.3*. A condition of perfect adherence between steel bars and surrounding concrete is initially considered. For this reason, the first analysis is carried out without zero-length links between concrete and steel bars. In the FEM analysis a displacement-increment method is used for loading.

Table 5-8. Mechanical properties of concrete and steel bars- numerical analysis of beam BS

Concrete			*Steel*				
f_c=	39.2	MPa	Type	σ_y [MPa]	σ_{max} [MPa]	E_s [MPa]	b [-]
f_t=	2.9	MPa	D13	343	477	182000	0.004
E_c=	29419	MPa	D10	289	429	187000	0.004
G_F=	65	N/m	D6	226	415	194000	0.0124

The numerical results reported in terms of load-deflection curve in Figure 5-37 - *blue dotted line*, show a satisfactory agreement with the experimental curve. However, a higher load-carrying capacity is found in the numerical simulation respect to the experimental test. This depends mainly on the mechanical properties of the tensile steel bars and particularly on σ_y. Indeed, it is possible to observe a higher yielding point in the numerical analysis. The failure mode obtained in the numerical simulation corresponds to the one described by Lee et al.[153]: BS specimen exhibits a flexural failure, characterized by the development of many flexural cracks and final rupture due to the crushing of compressive concrete cover. *Figure 5-38* shows the principal strains, typical of a flexural failure, while *Figure 5-39* depicts compressive and tensile damage contours. The numerical curve obtained with the perfect adherence condition between steel bars and concrete is then compared with the curve obtained with a "good bond" condition, Figure 5-37 - *green dotted line*. Zero length elements are introduced between quad and truss elements and the τ-*s* law defined in paragraph 4.4.4.1 for sound specimens with transverse reinforcement is adopted (see also *Figure 5-40*). The comparison between the numerical results shows the equivalence of the two bond conditions: only a slight decrease in the global ductility is detected in the case of

"good bond" condition. This confirms what has been observed in the numerical simulations of Rodriguez's beam. Also the compressive and the tensile damage contours are similar between the two bond conditions considered. For sake of brevity, are not reported.

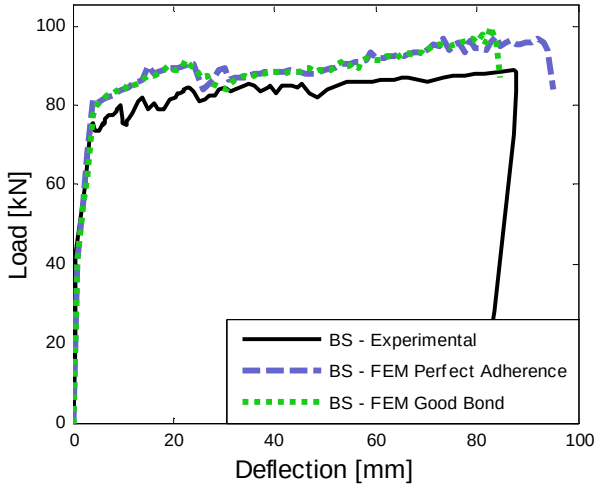

Figure 5-37. Load-deflection graph: comparison between experimental and numerical results

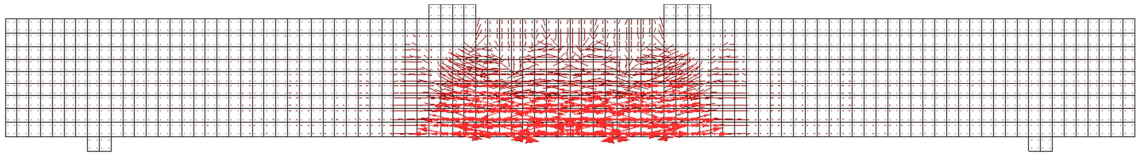

Figure 5-38. Principal strains for perfect adherence condition - BS beam.

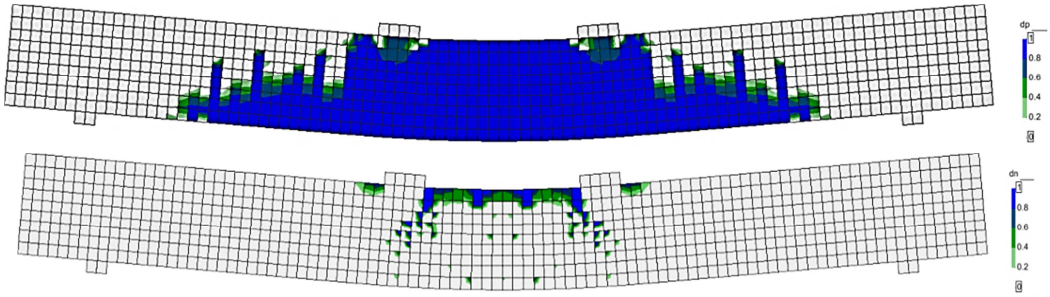

Figure 5-39. Tensile (dp) and compressive (dn) damage contour - BS beam.

5.3.2.2 Corroded beam

The high corroded BCD3-0 beam is selected for the investigation of different bond conditions on the structural response of corroded RC beams. During the experimental tests, only the tensile bars were corroded (see *Figure 3-81*) while the transverse reinforcement were isolated and remained in sound conditions. From the description of the experimental tests is not clear how the artificial corrosion process has influenced the anchorage of tensile bars. The bottom reinforcement indeed had 90° hook at the ends in order to develop better anchorage of the longitudinal bars but only a part of the hook was subjected to the corrosive attack, see also *Figure 3-82*. For this reason, both possible conditions of "good anchorage" and "bad anchorage" are investigated in the numerical analyses. Due to the fact that stirrups were not subjected to corrosion procedure, in FEM analyses the τ-s law for confined concrete without corrosion of the transverse reinforcement is adopted for the zero-length links. Finally, in order to verify the assumption of pull-out bond failure, some numerical analyses are carried out also with the τ-s law for splitting failure and the results are compared with the previous ones. In *Figure 5-40* is reported the τ-s law adopted for the BS beam, which represents "good bond" conditions (*blue line*) and compared to those assumed for

the corroded BCD3-0 beam, respectively valid in the case of pull-out bond failure of the rebars (PO) and splitting bond failure (SP).

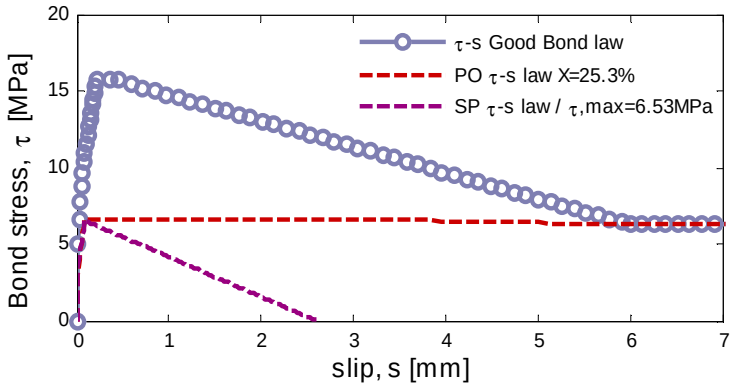

Figure 5-40. Bond stress-slip laws for sound and corroded conditions

BCD3-0: pull-out bond failure in tensile steel bars

First, some numerical analyses are carried out with τ-s laws for pull-out bond failure (PO). In *Table 5-9* are reported the data assumed for the numerical analyses: the equivalent uniform corrosion penetration x, the residual area of tensile bars $A'_{s,tot}$; the maximum bond strength τ_{max} and the compressive strength of sound and degraded concrete, f_{cm}. The information are deduced from the experimental data X =25.3%, the weight lost by tensile bars. It is worth noting that only the bottom concrete cover is degraded, indeed only here salt was added to concrete mixture (*Figure 3-82*).

Table 5-9. Characteristics of the beams tested - numerical analysis

Name of the beam	*X [%] weight loss*	*x [mm]*	*$A'_{s,tot}$ [mm^2] tensile bars*	*τ_{max} [MPa] / d_τ*	*f_{cm} [MPa] bottom concrete cover*
BS	*0*	*0*	*398.197*	*15.65*	*39.2*
BCD3-0	*25.3*	*0.882*	*297.453*	*6.53 / 0.417*	*8.38*

The numerical results in terms of load-deflection curves are reported in Figure 5-41, for both conditions of “good anchorage” of the tensile bars (*blue continuous line*) and “bad anchorage” of the tensile bars (corrosion attack involves also the hooks – *violet dotted line*). In the first case, for the zero-length links of the external nodes of the beam, a perfect adherence condition between steel and concrete is assumed. In the second case, also for the zero-length links of the external nodes, a degraded τ-s law is considered. Actually, it is unlikely that a “bad anchorage” situation has occurred during the experimental tests of Lee et al.[153], because the hooks were not completely located inside the area subjected to corrosion procedure. However, it is useful to analyze the effect of anchorage loss because it represents a situation that characterizes many real corroded structures. From Figure 5-41, it is possible to observe that experimental and numerical results, obtained in the case of “good anchorage” condition, well agree. A rather high reduction of ductility is noticed when a “bad anchorage” of tensile bars is considered. This is plausible because an adequate anchor length allows the tensile bars to reach higher stresses and it enhances the ductility of the beam, as also experimentally observed by Mousa[187]. The good anchorage condition leads to a global ductility closer to the experimental one, so it is the situation that most likely took place in beam BCD3-0.

BCD3-0 beam experimentally and numerically exhibits bond loss in tensile bars. Comparing the positive damage contours of the corroded beam with bad anchorage condition, with the damage maps of BS beam (Figure 5-42), it is possible to notice that the flexural cracks are less in number and tend to concentrate on the maximum bending moment zone, as reported by Lee et al.[153]. The positive damage is higher in the bottom concrete cover because here the material is degraded. This well represents the spalling of concrete cover due to the radial cracks that propagate along the longitudinal tensile bars, which lead to bond loss. The same type of structural behaviour was observed in the experimental tests and it is depicted in Figure 5-43, where it is shown also the comparison with the behaviour of the sound BS beam. Finally in the case of "good anchorage" of tensile bars, the structural behaviour results halfway between the other two cases examined.

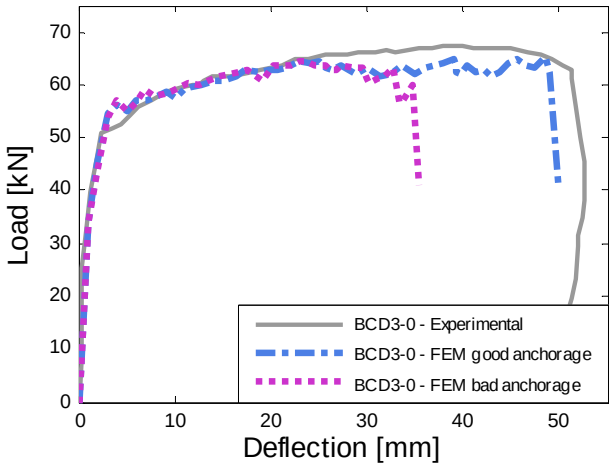

Figure 5-41. Load-deflection graph: comparison between experimental and numerical results

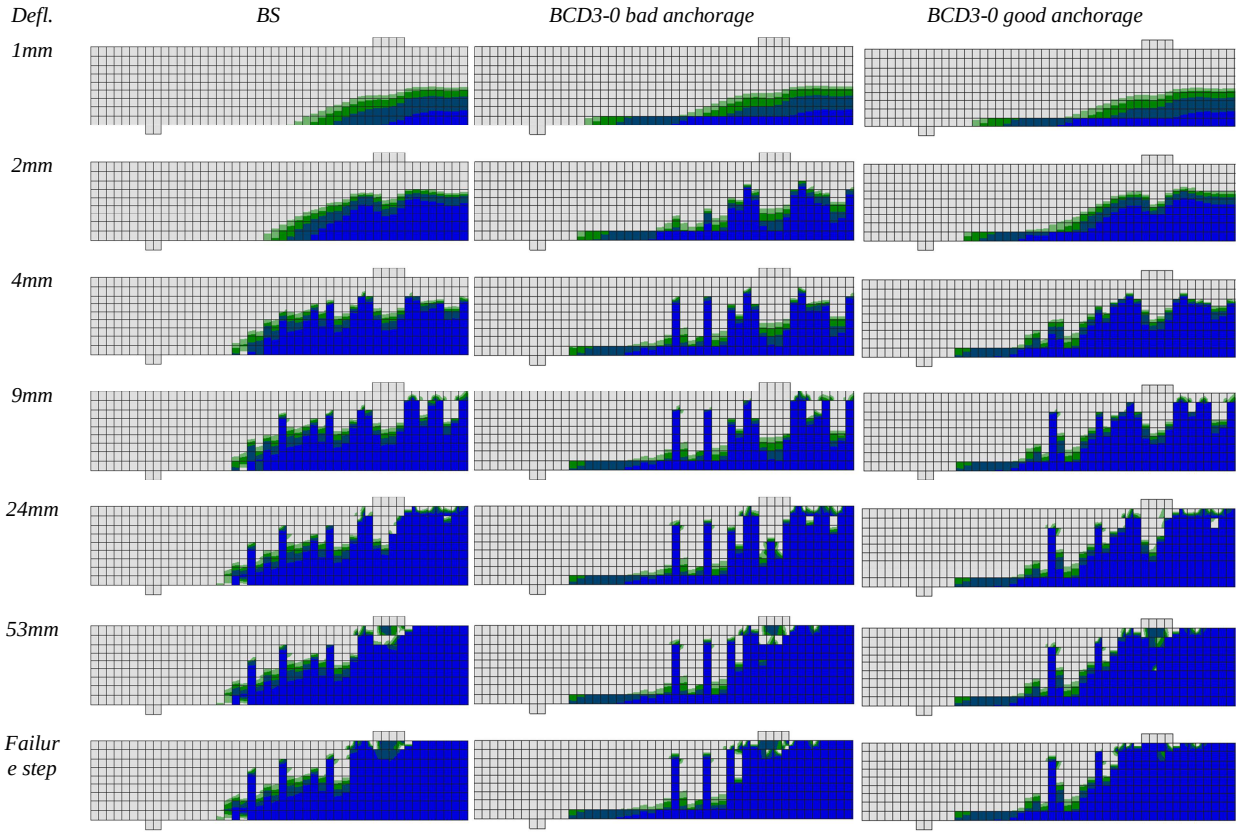

Figure 5-42. Comparison between positive damage contours numerically found for: BS beam, BCD3-0 beam in the case of bad anchorage and BCD3-0 with adequate anchorage

Figure 5-43. Experimental cracks patterns of BS and BCD3-0 at failure, Lee et al.[153]

The compression damage contours of sound and corroded beams are instead quite similar, as experimentally observed, Figure 5-43. In both BS beam and BCD3-0 beam crushing of compressive concrete occurs (Figure 5-44), but in BCD3-0 beam the bond failure in tensile bars anticipates the concrete crushing.

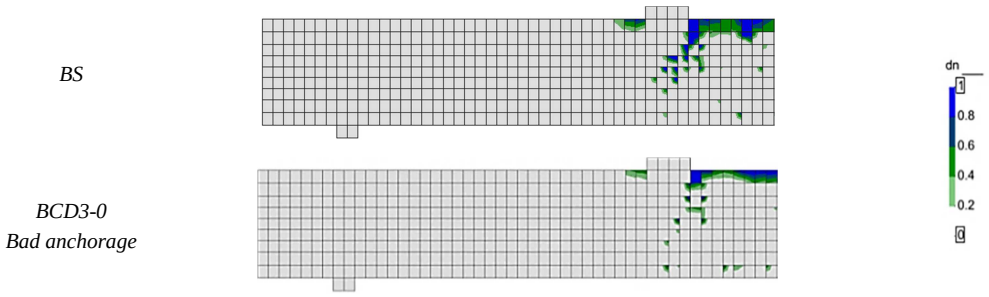

Figure 5-44. Comparison between the dn contours, numerically found for the BS beam, the BCD3-0 beam in the case of bad anchorage and the BCD3-0 with adequate anchorage.

In Figure 5-45 *a) b) c)* are reported the slips between concrete and tensile bars along the bar length for the corroded BCD3-0 beam with bad anchorage. As asserted by Leonhardt and Walther[158], a bond loss is characterized by large slips values accompanied by large bond stresses close to the open flexural cracks, and this behaviour is well captured by the numerical simulation, as it is possible to observe in the pictures.

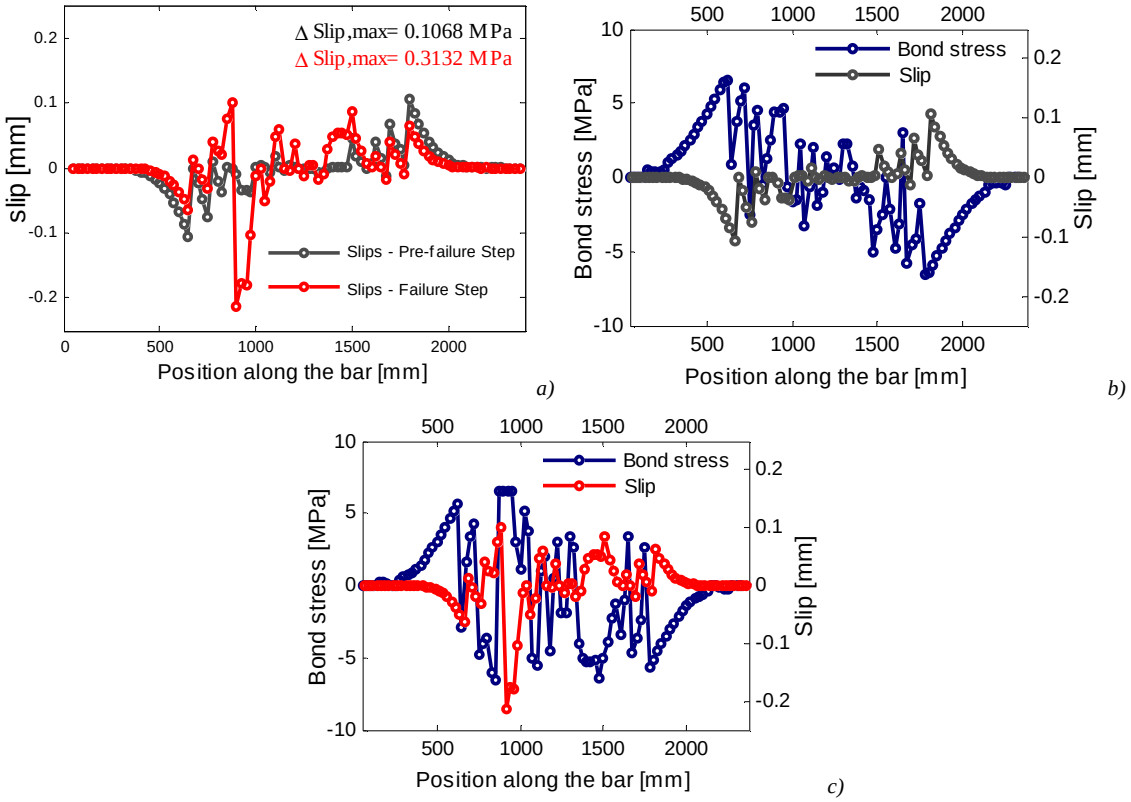

Figure 5-45. a) Slips in corroded beam BCD3-0: comparison between pre-failure and failure step; Bond stresses and slips along the tensile bar b) at pre-failure step, c) at failure step

BCD3-0: splitting bond failure in tensile steel bars

In order to analyse also a different bond condition, some numerical analyses are carried out with the τ-s law typical of a splitting failure (SP). Two different τ_{max} are assumed:

- τ_{max}=6.53 MPa as in the PO τ-s law previously considered, (*Figure 5-40*) in order to see the effect only of a different τ-s law assumed for the zero-length links;
- τ_{max}=0.3 MPa obtained for corrosion level equal to 25.3%. This numerical analysis simulates the case of corrosion attack in both tensile and transverse bars. Also in this case, two different anchorage conditions are considered: "good anchorage" and "bad anchorage" of tensile bars.

In Figure 5-46 the curves obtained for "good anchorage" and PO τ-s law (*light blue dotted line*) or "good anchorage" and SP τ-s law with equal τ_{max}=6.53 MPa (*dark blue dotted line*) are compared. As expected, a splitting τ-s law leads to a lower global ductility. In the case of SP τ-s law and "bad anchorage" (*pink dotted line)*, the beam ductility further decreases. In all the cases analysed, bond loss occurs in tensile bars. As a conclusion, if bond strength is not severely deteriorated due to reinforcement corrosion, the damaged beam is still able to develop a certain amount of deflection before to collapse.

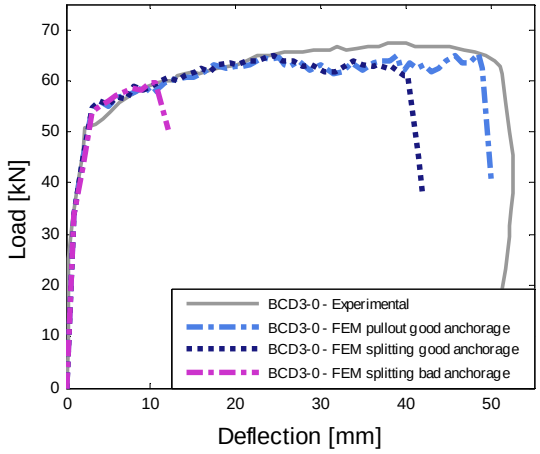

Figure 5-46. Load-deflection graph: comparison between different τ-s laws

In Figure 5-47 the results obtained with the SP τ-s law and high reduction of bond strength (τ_{max}=0.3 MPa) and different anchorage conditions, are compared with the case of PO τ-s law. In the case of "good anchorage" of tensile bars (Figure 5-47 *dotted dark blue curve*), the adopted splitting τ-s law leads to a strong reduction of beam ductility. Once that in all the zero length elements the bond strength is reached, bond stresses fall fast to zero and only the two ends of the tensile bars collaborate with concrete thanks the good end anchorages. When also in the two extremities of tensile bars the bond strength is reached, beam collapses. However, due to the good anchorages, the load-carrying capacity of the beam does not change. On the contrary, beam stiffness highly reduces after the achievement of the first flexural cracks. This perfectly matches with the statement of Coronelli et al.[80]: "*the stiffness deterioration is partly due to the progressive crushing of the concrete cover. Also the bond failure along the span contributes…<omissis>…where the maximum bond strength is reached immediately after the formation of the bending cracks, at approximately 50% of the maximum load*".

When a degraded τ-s law for splitting failure is assumed also for the zero-length links at the two extremities, "bad anchorage", the load-carrying capacity of the beam is completely lost after the development of the first flexural cracks *(*Figure 5-47 *-pink curve*). This case can be assimilated to

a beam without tensile reinforcing bars (Figure 5-47 *-red curve*), due to the incapability of the tensile bars to collaborate with the concrete.

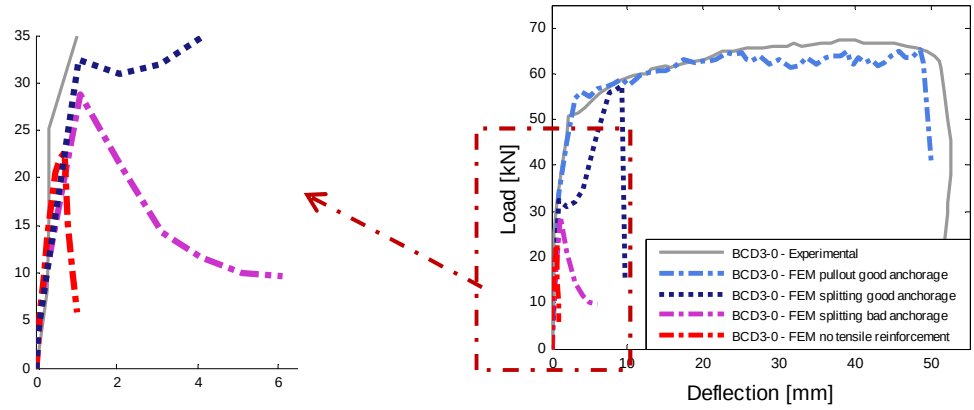

Figure 5-47. Load-deflection graph: comparison between bond conditions

In the case of tensile bars disbonded along the beam span, without impaired of anchorages at the extremities, a change of structural behaviour of the beam, from flexural towards of a tied arch may occur. In normal conditions, the loads applied to RC beams are supposed to be sustained either by the change in tensile force T, which is called *beam mechanism*, or by the change in the length of the internal lever arm Z, which is called *tie-arch mechanism*, Fenwick and Paulay[103]. For beams with long shear span, the distance between the loading point and the support weakens the tie-arch mechanism, and the beam mechanism governs the load-carrying capacity. However, in beam mechanism a perfect adherence between concrete and bars is indispensable in transferring the tensile stress. In the case of low bond degradation, bond cracks along the longitudinal bars leads to a concentration of deformation at the middle span and concrete cover in compression crushes prematurely (weakness of beam mechanism). This failure mode is called "*bond compression failure*" and has been detected in the simulation of the corroded beams tested by Rodriguez et al.[221][222] and Lee et al.[153] when a degraded PO *τ-s* law was assumed. If instead a complete loss of bond occurs along the span accompanied with efficiency of external anchorages of tensile bars, stress redistribution inside corroded beams takes place. In detail, when tensile bars are bonded, the lever arm Z is constant and stress in the bars varies in proportion to the applied moment, see Figure *5-48 a)*. When tensile bars are debonded, stress in the bars cannot vary along the portion of debonded bars (Figure *5-48 b))*, therefore Z and the depth of the neutral axis have to change in response to different levels of applied moment and to move towards the tensile bars whereas the moment is decreasing (Figure *5-49)*, Cairns[49][50].

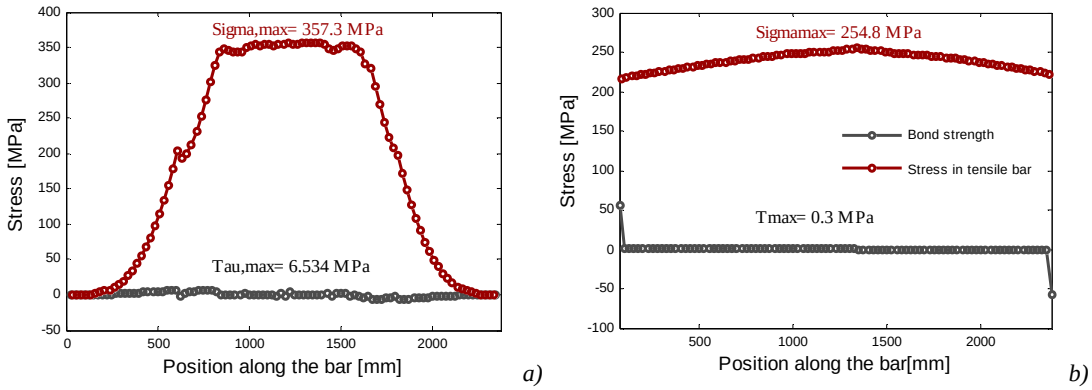

Figure 5-48. Stresses in tensile bar and bond stresses along the bar length for BCD3-0 beam: a)PO τ-s law "good anchorage" τmax=6.53MPa; b) SP τ-s law "good anchorage" τmax=0.3MPa

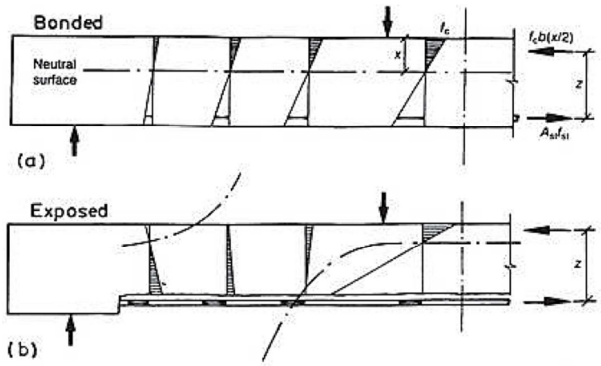

Figure 5-49. Pattern of strains in RC beams with a) embedded, b) exposed, tensile bar, Cairns[50]

Further, when tensile bars are good bonded to concrete, compatibility of deformations is satisfied (plane section behaviour). If tensile bars are debonded, plane section assumption is not anymore valid and to satisfy compatibility, an increase in elongation of concrete between anchorages has to compensate the elongation of debonded bars. The necessary increase in elongation of concrete is achieved through an increase in curvature of the concrete section near midspan, therefore here the maximum compressive strain in concrete increases, Cairns[50]. Due to the limited compressive strain capacity of concrete in degraded covers, a premature crushing takes place. In order to prove these remarks, in *Figure 5-50* the principal stress distributions for corroded beam BCD3-0, in the case of low degraded bond (*Figure 5-50 a)*) and high degraded bond (*Figure 5-50 b)*), are reported. Because of the bond loss at midspan, the arch action becomes very evident in BCD3-0 beam with SP τ-s law (τ_{max}=0.3 MPa) and "good anchorage" condition, *Figure 5-50 b)*: the crushing failure is anticipated and the ductility of the corroded beam is thus reduced. The same change of stress distribution, between beams with bonded and debonded tensile bars, was found by Coronelli et al.[80], see *Figure 5-51*.

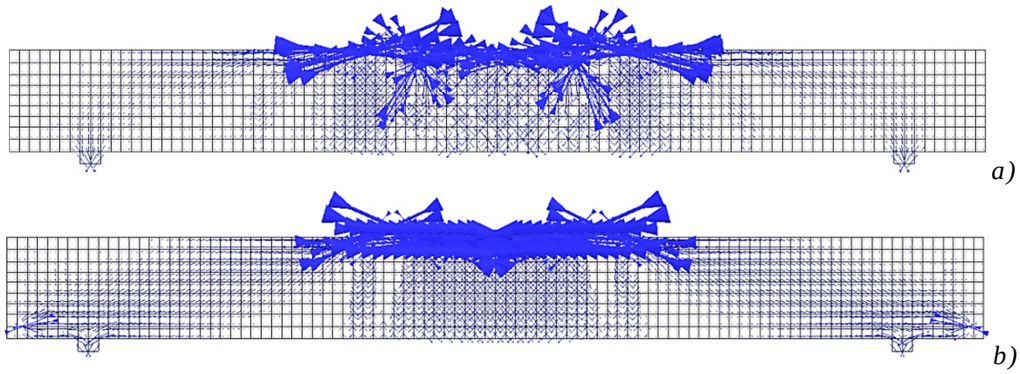

Figure 5-50. Principal stress distribution for BCD3-0 beam: a) PO τ-s law "good anchorage", τmax=6.53 MPa; b) SP τ-s law "good anchorage", τmax=0.3 MPa

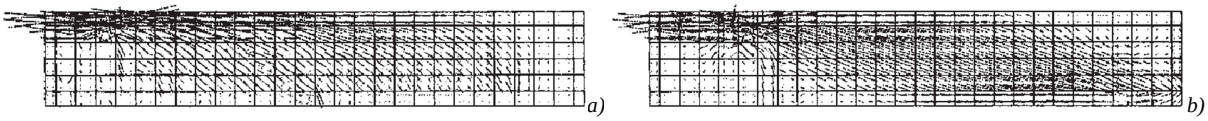

Figure 5-51. Principal stress distribution in a) sound beam (truss action); b) corroded beam (arch action favoured by bond deterioration), Coronelli et al.[80]

To conclude, the analyses carried out have first confirmed the importance of adequate composite interaction between tensile bars and the surrounding concrete in order to reach a certain level of ductility in RC beams; and second the fundamental role played by the anchorage of reinforcement to achieve the designed load-carrying capacity.

5.4 Numerical simulation of corroded RC columns

RC structures damaged by reinforcement corrosion exhibit not only a reduction of load-carrying capacity but also an alteration of the collapse mechanism: corroded structures may fail suddenly in a brittle way. The reduction of structural ductility is a critical aspect, particularly for buildings in seismic regions and especially for RC columns: indeed potential plastic hinge regions have to ensure deformations under seismic loads and moment redistribution without to collapse. However, to the Author's knowledge only few researches have been carried out on the structural implication of reinforcement corrosion on the behaviour of RC columns. The assessment of both their residual load-carrying capacity and ductility is required in order to assure adequate structural safety level and therefore to avoid loss of human life. In this paragraph, the experimental tests made by Rodriguez et al.[220] on RC columns, subjected to different levels of corrosion, are considered. The experimental data reported by the authors are then compared with the results of the numerical analyses, in order to validate the applicability of the comprehensive modelling approach also to such RC elements.

5.4.1 Numerical simulation of the experimental tests made by Rodriguez et al.

The RC columns tested by Rodriguez et al.[220] under central uniaxial load, are firstly simulated. The experimental campaign is described in paragraph 3.6.2.1. It is worth noting that during the loading tests some not expected eccentricities were measured. The columns that revealed negligible eccentricities were the sound column n°22 and the corroded column n°28. For this reason, these two columns are selected as benchmark for the numerical simulations, in order to disregard the effects of load eccentricities in this phase of study. Indeed, while the load eccentricities are small, the compressive behavior of the concrete is dominant. Therefore, it is important to accurately model the phenomena associated with compression, such as gradual spalling of concrete cover and the confining action of stirrups, which are the main aims of this study. As the load eccentricity increases, cracking gradually dominates and the properties of reinforcing steel bars become more important. Firstly, the sound column n°22 is simulated for the validation of the mesh size correction in compression also for RC columns. Then the corroded column n°28 is simulated, taking into account all the main effects of reinforcement corrosion and in particularly the premature buckling phenomena of longitudinal bars through the approach proposed in paragraph 4.2.2.3.

5.4.1.1 Sound column

The geometry of sound column n°22, of Rodriguez's et al.[220] test campaign, is shown in *Figure 3-86.* Reinforcing bars and concrete characteristics experimentally measured are reported in *Table 3-12*. For the FE model, a regular mesh of 25x25 mm is adopted, *Figure 5-52 a).* Regarding the constitutive law for concrete material, two different laws are adopted: one for the concrete core (*Figure 5-53 -continuous blue line*) and one for the concrete cover (*Figure 5-53 -dotted green line*). The mechanical properties of concrete material adopted in the numerical simulation, are reported in *Table 5-10.* The concrete core is confined by transverse reinforcement, therefore it has higher compressive strength and ultimate strain than concrete cover. These effects are particularly relevant for the modelling of concrete column and have been studied by various researchers, see Appendix C. In this study, the approach proposed by Scott et al.[228] is adopted: the authors considered greater strength and strain at peak and lower slope of the post peak branch in compression for confined concrete, depending on the level of confinement.

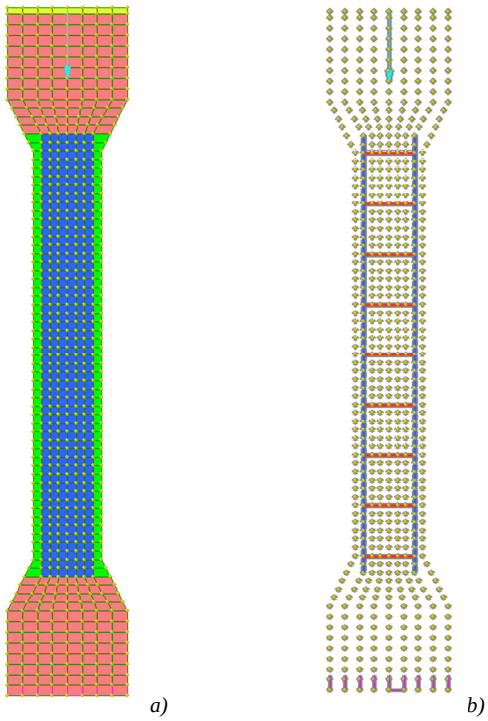

Figure 5-52. FE model of Rodriguez's et al.[220] concrete columns

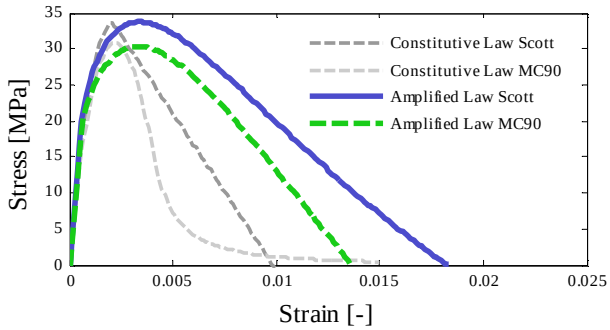

Figure 5-53. Stress-strain curves for confined and unconfined concrete

Table 5-10. Mechanical characteristics of concrete material

	Compressive strength fc[MPa]	*Tensile strength ft[MPa]*	*Fracture energy G_F[N/m]*
Confined concrete	*33.86*	*2.6*	*66*
Unconfined concrete	*30.83*	*2.4*	*52*

Longitudinal and transverse reinforcing steel bars are modelled with truss elements (*Figure 5-52 b)*) and connected directly with the nodes of concrete material, in order to reproduce a perfect adherence condition between steel bars and surrounding concrete. The constitutive laws adopted in the numerical analyses for longitudinal and transverse bars, are reported respectively in *Figure 5-54 a)* and *b)*. In detail, due to the fact that the geometrical slenderness ratio λ for longitudinal bar is 9.38, buckling phenomena are likely to occur between the yield strength and the ultimate strength. For this reason, in *Figure 5-54 a)*, a softening branch develops starting from the critical load. The yield strength and the ultimate strength of the reinforcing bars assumed in the numerical simulation are based on the experimental data, the other mechanical properties are obtained from Spanish codes UNE 36068:2011 UNE 36065:2011. Indeed, Rodriguez et al.[220] used ribbed bars AEH 500S of Spanish type.

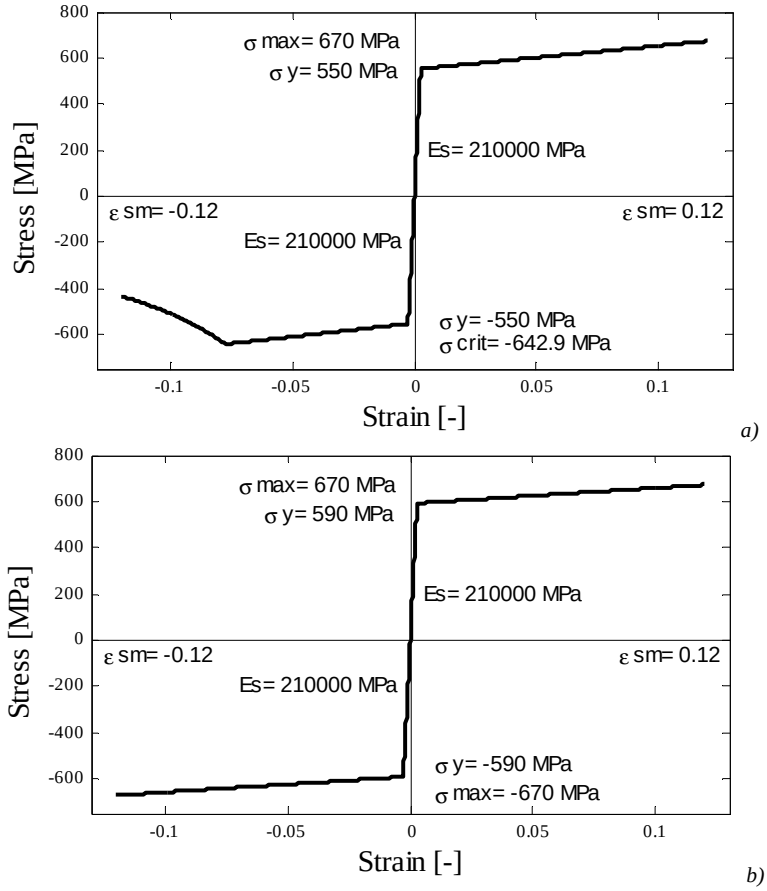

Figure 5-54. Constitutive law for a) longitudinal and b)transverse bars in tension and compression

Figure 5-55 shows the comparison between numerical and experimental load-mean strain curves. The numerical results agree well with the experimental ones, in terms of both ultimate axial load and mean strain. Regarding the failure mode, also in this case the numerical damage contours (*Figure 5-56*) well agree with the failure mode experimentally observed: delamination of concrete cover and consequent crushing and collapse of the column, due to the concrete material failure, *Figure 5-56 a)*. Due to the particular shape of the upper part of the column, tensile damages of relevant entities develop at the two ends of the column trunk, *Figure 5-56 b)*.

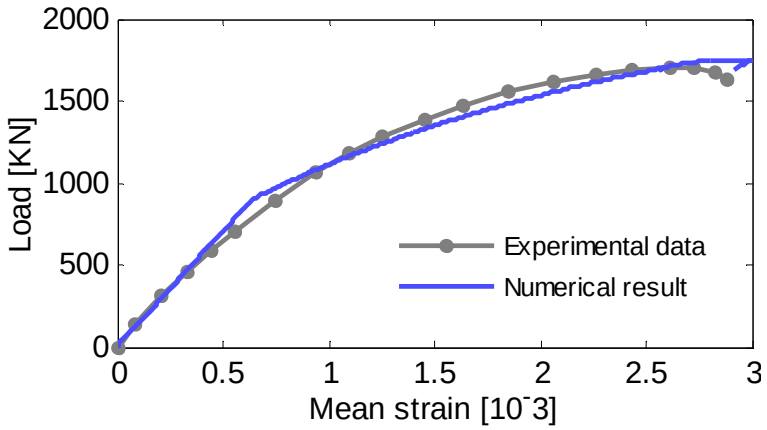

Figure 5-55. Load-mean strain curves - column n°22: numerical and experimental results

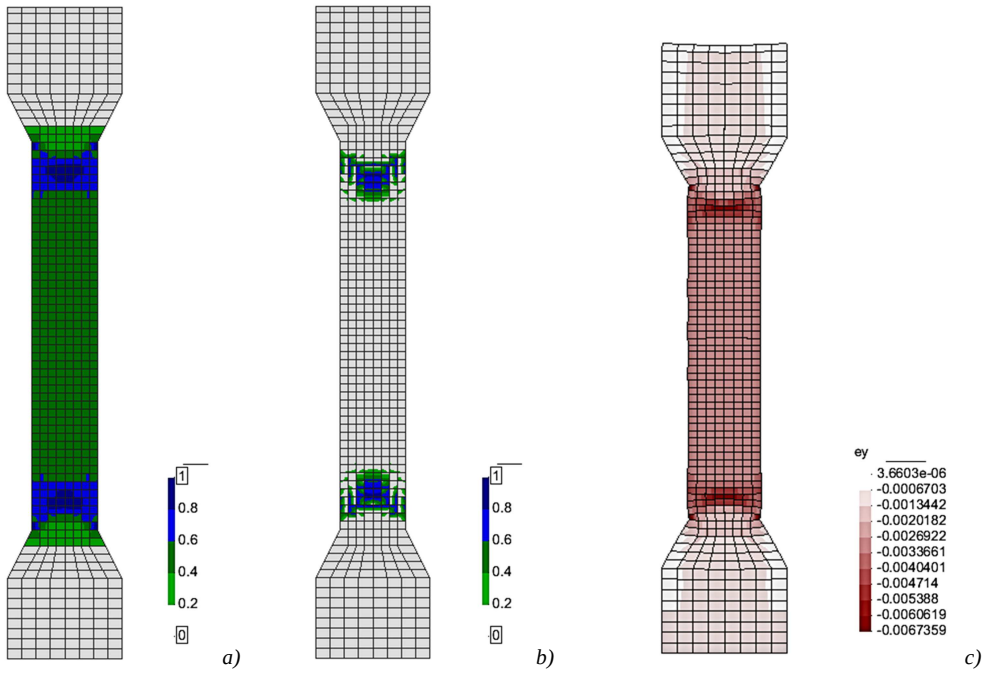

Figure 5-56. a)Compressive damage contour (dn); b)Tensile damage contour (dp); c)Vertical deformations, at the failure step – sound column n°22

5.4.1.2 Corroded column

Corroded column n°28 of Rodriguez's et al.[220] test campaign is taken as benchmark for the numerical analyses. For corroded columns the most important effects that should be considered are the reduction of the mechanical properties of concrete covers, due to cracking and spalling phenomena experimentally observed and the failure of some stirrups, which leads to premature buckling of longitudinal bars. The concrete strength of corroded columns is higher than sound columns, therefore different constitutive laws are used for concrete in column n°28. These are reported in *Figure 5-57 -continuous blue line* for confined concrete core and *dotted green line* for concrete cover. In order to simulate concrete cover deterioration, reduction of both compressive strength and ductility are considered. The stress-strain law for the deteriorated concrete cover is represented in *Figure 5-57 –red line*. The mechanical properties of the concrete material adopted in the numerical simulation, are reported in *Table 5-11*.

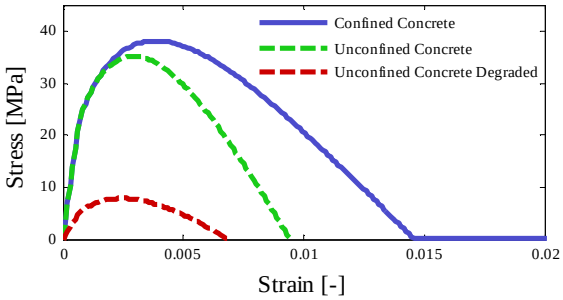

Figure 5-57. Constitutive laws for concrete cover and core, sound and deteriorated conditions

Table 5-11. Mechanical characteristics of concrete material

	Compressive strength f_c[MPa]	*Tensile strength f_t[MPa]*	*Fracture energy G_F[N/m]*
Confined concrete	*38.1*	*2.9*	*70*
Unconfined concrete	*35.6*	*2.7*	*67*
Deteriorated unconfined concrete	*7.7*	*0.0*	*2*

Uniform corrosion of 0.63 mm penetration was observed in longitudinal bars of corroded column n°28 (*Table 3-13*). Therefore the total value of residual area of these bars is assumed equal to 682.56 mm^2 in the numerical analysis. Regarding stirrups, mixed corrosion type was detected and the maximum corrosion penetration was found to be 4.7 mm. Due to this high level of pitting corrosion penetration (-95.3% of area), four stirrups failed during the loading, shortly before the ultimate load. However, the authors did not report the position of the stirrups that failed and this information is essential for the right assessment of the geometrical slenderness ratio. For this reason, two different situations are considered: failure of two consecutive stirrups and failure of alternate stirrups, *Figure 5-58 a)* and *Figure 5-58 b)*. The corresponding values of critical buckling strength calculated with the approach proposed by Kashani et al.[143][144] (*Equation 3-25*) are reported in *Table 5-12*. The constitutive laws adopted in the numerical analyses for the two cases, are reported respectively in *Figure 5-59*. The value of α for λ_{corr}=30.53 is extrapolated basing on the data given by the authors for lower λ and taken equal to 0.024.

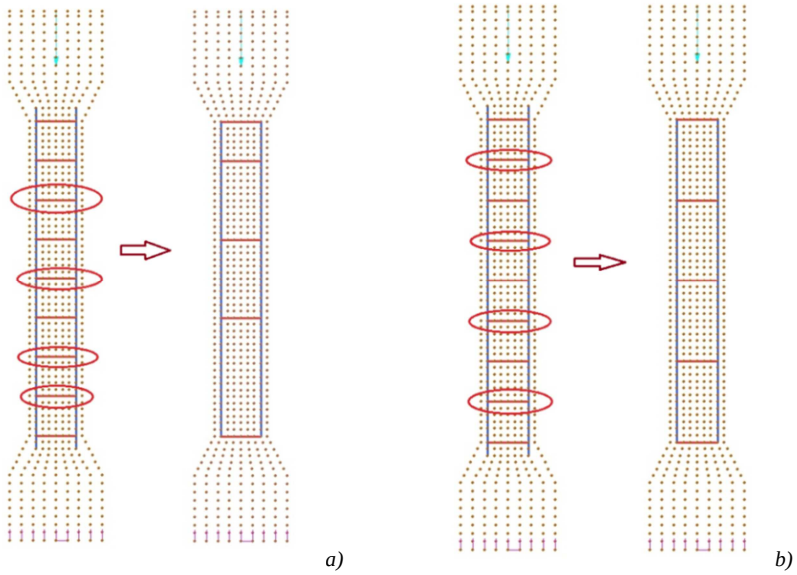

a) *b)*

Figure 5-58. a) alternate stirrups failure; b) two consecutive stirrups failure

Table 5-12. Critical buckling stresses

		1 stirrup fail	*2 consecutive stirrups fail*
Residual bar diameter [mm]	*Φ'=*	*14.74*	*14.74*
Stirrups spacing [mm]	*L=*	*300*	*450*
Geometrical slenderness ratio	λ_{corr}=	*20.35*	*30.53*
Critical buckling strength [MPa]	σ_{crit} =	*383.57*	*350.28*

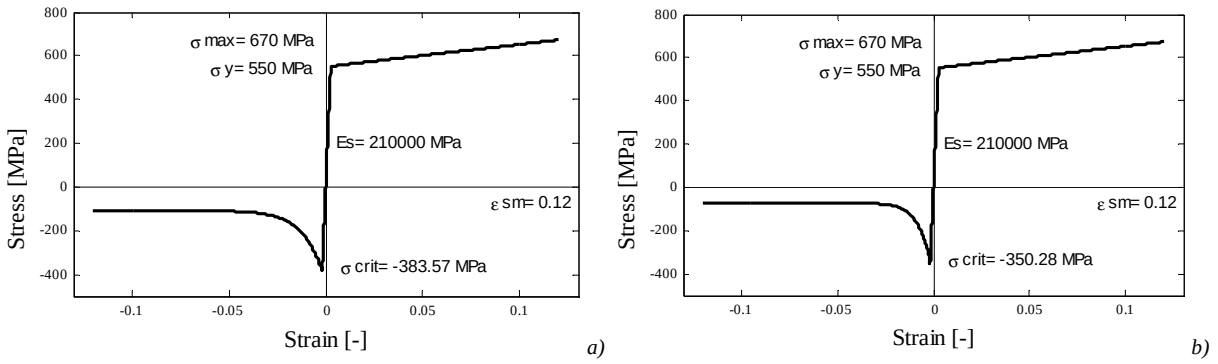

a) *b)*

Figure 5-59. Constitutive law for longitudinal corroded bars in tension and compression

Before to analyze the influence of buckling phenomena of longitudinal bars on the global behaviour of column n°28, the effectiveness of the environmental-mechanical damage model for concrete is proved. In particular, many authors, e.g. Rodriguez et al.[220], have proposed to leave out two or four sides of concrete cover, in order to take into account of spalling and cracking phenomena caused by reinforcement corrosion. The results obtained adopting this approach are compared with the analysis made with the damage model, in which concrete degradation is considered through d^{-}_{env} parameter and reduction of ductility, *Figure 5-60.* It is worth noting that the case of two consecutive stirrups failure is studied. In the Load – mean strain graph is possible to observe the better correspondence with the experimental data, obtained with the damage approach (*continuous blue line*) respect to the analysis carried out without the sides of the concrete section (*dotted green lines*).

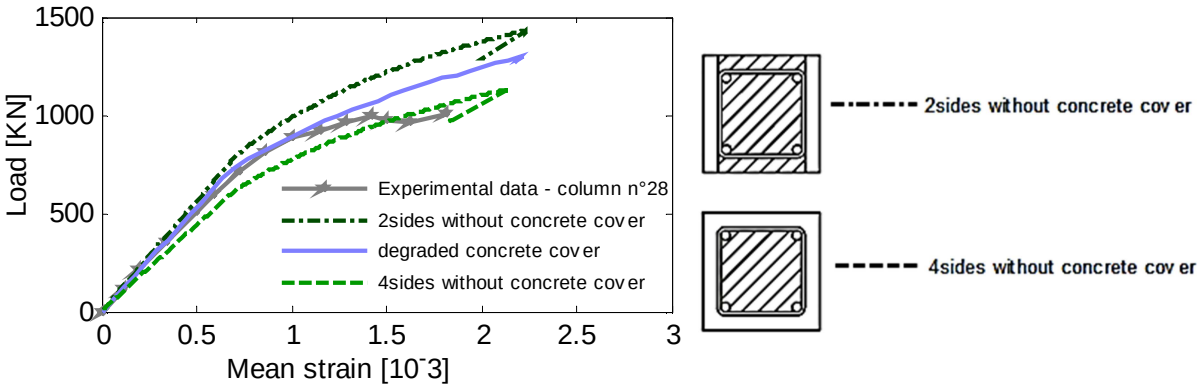

Figure 5-60. Load-mean strain graph: numerical simulation without 2 or 4 sides of concrete cover and degraded concrete cover with d^{-}_{env}

Figure 5-61 compares the numerical results obtained without to consider buckling phenomena (*continuous blue line*), and with considering premature buckling of longitudinal bars with the two critical buckling strengths calculated in *Table 5-12*, relating to the case of failure of alternate stirrups and failure of two consecutive stirrups (*black and grey lines*). It is worth noting that the constitutive law proposed for taking into account of buckling phenomena, allows achieving a significant improvement in the quality of the results. In detail, the result obtained for two consecutive stirrups with buckling phenomena is very close to the experimental curve. Finally, *Figure 5-62* shows the tensile and compressive damage contours that evidence the failure mode of the corroded column n°28. Experimentally the authors reported that the column failure was initiated by cracking and spalling of concrete cover and the rupture of stirrups, more affected by pitting corrosion. These phenomena led to buckling of longitudinal bars that developed immediately before the achievement of the maximum load. The same response is noticed in the numerical simulation: initially the negative damage reaches the maximum value of 1 in the concrete cover at the two extremities of the column, then the stresses in the longitudinal bars exceed the critical buckling load and the column is no longer able to carry the load.

To conclude, concrete cover degradation and premature buckling phenomena of longitudinal bars were found to be the most important consequences of reinforcement corrosion on RC columns. This is because they lead to a reduction of load-carrying capacity, reduction of strain at the maximum load, and reduction of compressive stiffness, see *Figure 5-63*. The numerical analyses have shown improvement in the results obtained by introducing the buckling law for steel in compression and the great influence of the number and the position of stirrups that fail on the global response of corroded columns.

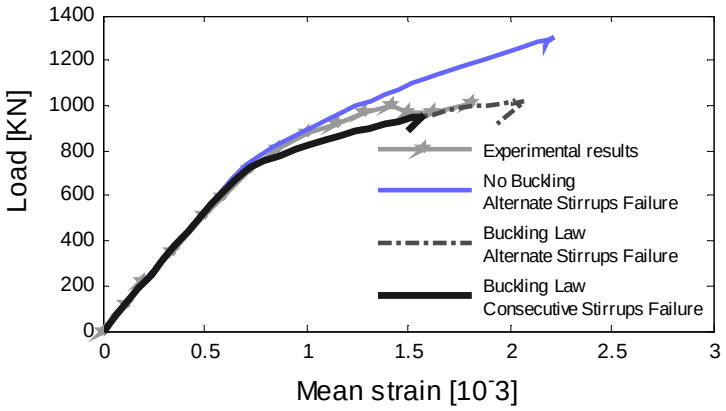

Figure 5-61. Load-mean strain graph: comparison between numerical analysis without and with buckling phenomena

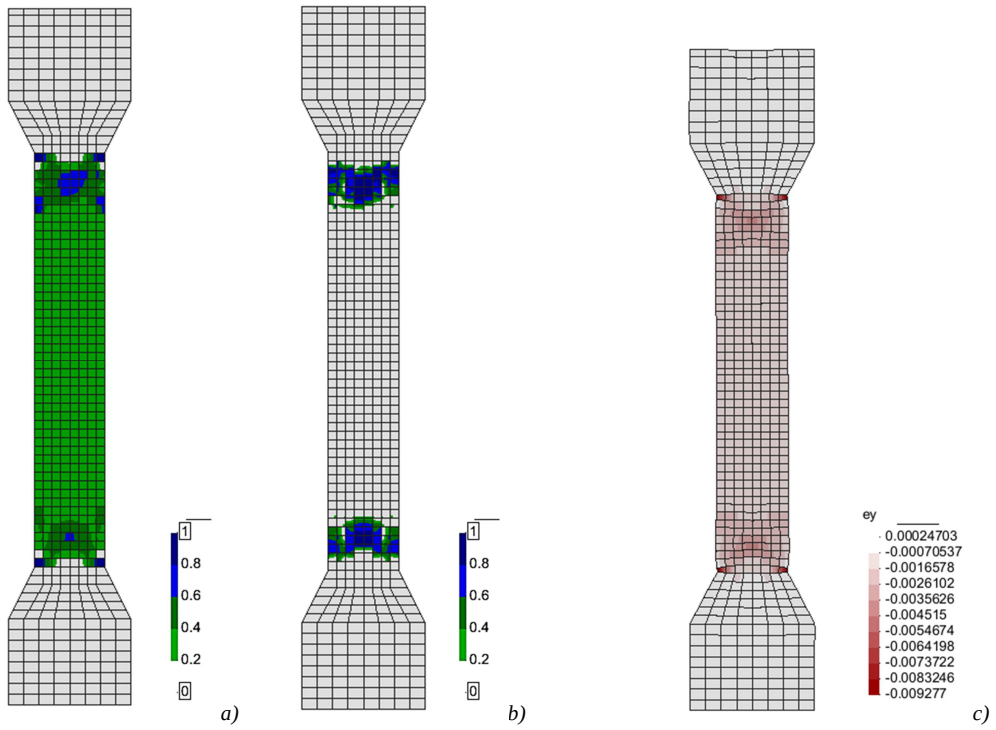

Figure 5-62. a)Compressive damage contour (dn); b)Tensile damage contour (dp); c)Vertical deformations, at the failure step – corroded column n°28

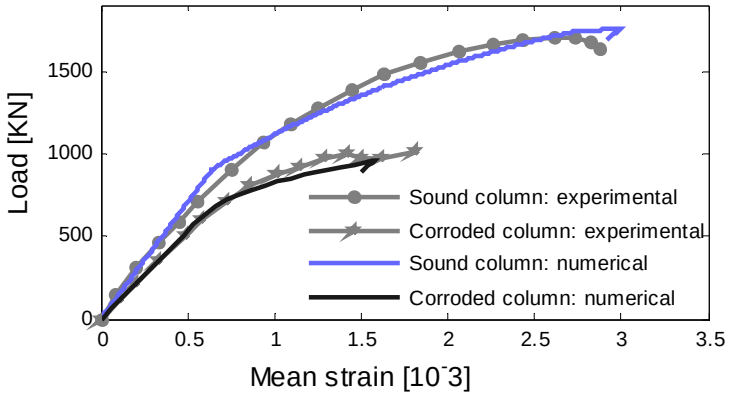

Figure 5-63. Load-mean strain graph: numerical and experimental results for sound and corroded columns

CHAPTER 6
SYNOPSIS

6.1 Summary

The problem of durability of reinforced concrete (RC) structures, exposed to both physical and chemical actions, represents an evolving research topic in the assessment of existing constructions. A reliable evaluation of the condition and behavior of a structure is an important basis for an effective service life management. Due to aggressive environments and poor construction, nowadays an increasing number of existing RC structures exhibit high levels of deterioration. Corrosion of reinforcing bars is one of the most widely encountered causes of degradation and one of the most important, because it may lead to serious structural consequences and therefore to loss of serviceability and safety level. In the present dissertation, a numerical tool for the assessment of the residual performance of RC structures affected by reinforcement corrosion was proposed, within the framework of a comprehensive approach for deteriorated RC structures analysis.

Initially, the mechanical damage model developed by Faria et al.[102] for the modelling of concrete material and enhanced by Berto et al.[34], Scotta et al.[227] and Talledo[240] was adopted and some aspects examined in depth and enhanced:

- A new method, which bases on the approach proposed by Hanjari et al.[119], to partially overcome the problem of mesh-dependency in compression of the damage model was introduced;
- The *shear retention factor* introduced by Scotta et al.[227] for one-parameter scalar damage model, then extended to two-parameter scalar damage model, was better explored. In detail, a range of values for the reference strain was proposed and correlated to some characteristics of reinforced concrete structures.

Both these aspects were investigated through a number of numerical analyses simulating experimental tests on RC beams taken from literature. It was found that the enhanced mechanical damage model well reproduced both the failure modes of RC beams considered (i.e. flexural as well as shear one) and the experimental data.

Regarding corrosion of reinforcing bars in concrete, an introduction about corrosion phenomena was made for the better understanding of the nature of this attack. Then a literature review of the main experimental tests made by different authors, regarding the local effects of corrosion on steel (reduction of cross section area and mechanical properties of reinforcing bars), on concrete (cracking and spalling of concrete cover) and on the composite interaction between concrete and steel (bond degradation) was carried out. Further, a brief summary of the effect of corrosion on the global behaviour of RC beams and columns found by other researchers was presented. Corrosion damaged structures have demonstrated lower load bearing capacity and structural ductility.

In order to take into account of the main local effects of corrosion, a comprehensive modelling approach was proposed, combining original formulations with some empirical/theoretical models derived from the literature:

- Regarding the effect of corrosion on reinforcing bars, experimental tensile tests on locally damaged bars were made by the Author for the evaluation of the residual cross-sectional area and mechanical properties of reinforcement subject to pitting corrosion. The morphology of the pits was found to be relevant. The results of these tests were compared with models of literature proposed for the estimation of the residual area, strength and ductility of corroded bars. Regarding these aspects some new relationships were also proposed, such as the equations for the estimation of the residual area in case of mixed corrosion and for the evaluation of residual steel ductility as well as the model proposed for taking into account of premature buckling in compression of bars subjected to corrosion.
- Concerning concrete, the coupled chemical – mechanical damage model developed by Saetta et al.[224][225] was adopted for modelling material deterioration and renamed environmental-mechanical damage model. The model was enhanced to consider the specific consequences of reinforcement corrosion: micro, macro-cracking and eventually spalling of concrete covers. The different material degradation in tension and in compression was introduced, splitting the environmental damage parameter into two new parameters: d^{+}_{env} and d^{-}_{env}. New formulations for the environmental parameters were proposed, in order to consider the reduction of strength for cracked concrete cover due to corrosion. Further, reduction of ultimate strain of cracked concrete in compression and reduction of fracture energy values were related to corrosion level.
- Bond deterioration between steel bars and concrete was also investigated. A new "damage" type τ-s laws for simulating splitting bond failure was formulated. Then a new approach, able to predict the maximum bond strength in degraded condition through a d_{τ} scalar parameter, was proposed. Furthermore, three different τ-s laws were introduced to consider different bond mode failure, which may verify in case of reinforcement corrosion and different confinement levels. These laws were validated by the numerical simulations of experimental pull-out tests available in the literature.

Finally, a number of corroded members, at different levels of degradation, were simulated in order to validate the new proposed formulations. The results of the numerical analysis were compared with the results of available experimental tests. The consequences of the local effects of corrosion on the structural response of RC structures were also discussed.

- First, the experimental results of the tests carried out by Rodriguez et al.[221][222] on beam 313, were used as benchmark for the verification of the *f* parameter of *Equation 4-19*, proposed for the estimation of residual ductility of cracked concrete. Second, the proposal made for the evaluation of the residual area of corroded reinforcing bars (*Equation 4-3*) was verified. The numerical results well simulated the experimental data, in terms of both load-carrying capacity and ductility behaviour. Therefore the approach was applied to predict the behaviour of the other corroded beams tested by Rodriguez et al.[221][222]. The effects of corrosion were demonstrated to depend on the amount and type of the corrosive attack. Regarding type 11 beams, in uncorroded condition failed by crushing of compressive concrete cover long after the tensile bars had reached their yielding strength. Reinforcement corrosion led to a reduction of global stiffness, ductility

and load-carrying capacity. The failure mode remained the same for low levels of corrosion (beam 114), and changed into bending failure in tensile bars (beam 113), where a high level of pitting corrosion was present. For beam 113, *Equation 4-5* for the assessment of residual ultimate strain on steel bars was proven with respect to other literature formulas and the effect of different spatial distribution of pits in tensile corroded bars was also investigated. Regarding type 31 beam, the sound beams exhibited bending failure due to compressive concrete crushing. A premature crushing of compressive concrete cover was found in beams 314-316, subjected to a medium level of corrosion and characterized by cracking of concrete covers. Beam 315 failed in shear, mainly due to the severe corrosion penetration affecting stirrups. The comparison between numerical and experimental results evidenced the reliability of the proposals made in capturing the response of corrosion damaged RC beams. Further, for all the beams analysed in the predictive phase a sensitivity analysis regarding different bond was carried out, making use of the degraded τ-s law proposed for confined concrete. It was found that bond degradation leads to a reduction of beam stiffness in the pre-yielding phase and to a reduction of beam ductility, when the failure mode was not a brittle one and especially for greater corrosion levels.

- In order to better understand the effect of bond degradation on the structural response of RC beams, the beams tested by Lee et al.[153] were also analysed. In these beams, bond loss between tensile bars and concrete was experimentally observed. The analyses carried out evidenced: first, the importance of adequate composite interaction between tensile bars and the surrounding concrete in order to reach a certain level of ductility in RC beams; and second, the fundamental role played by the anchorage of reinforcement to achieve the designed load-carrying capacity. Further, the debonding of tensile bars was observed to lead to a change of carrying mechanism inside the beam: from flexural to tied arch type, explaining the premature crushing of concrete found for beams with degraded bond.
- RC columns were also simulated, with the aim to capture the global response in corroded conditions. The results showed that the model was able to well capture the structural response of the columns by taking into account cracking of concrete covers through the environmental-mechanical damage model, stirrups failure as well as premature buckling phenomena of longitudinal bars through the proposed formulation.

To conclude, for both corroded RC beams and columns, the residual load-carrying capacity and ductility observed in the experimental tests were well captured identifying in the numerical model and in the comprehensive approach proposed, a good tool for the evaluation of the residual safety of corroded structures.

6.2 Conclusions and outlooks for further research

Regarding the mechanical damage model adopted for modelling concrete material, the investigations made on the *shear retention factor* and the new criterion proposed to partially overcome the problem of mesh-dependency in compression allowed to well simulate both flexural and shear modes of failure of RC beams. In particular, the beams tested by Bresler and Scordelis[43] represent a difficult challenge in modeling, with many finite element formulations failing to provide accurate simulations of their behavior. The proposed damage model was able to well reproduce the shear critical response of these beams. However, additional experimental data

are required to better correlate the value of the reference strain ε_{ref} to the characteristics of RC members that influence the secondary mechanisms of shear resistance. Further, it could be useful to modify the negative damage evolution law of concrete, developing a formulation that allows to have a fix value of the peak strain.

In the main part of this thesis, corrosion phenomena in RC structures were studied, because they represent the most important cause of material degradation.

In order to develop a numerical model able to assess the structural response of corroded RC members, a comprehensive approach including some innovative aspects in order to capture all the main local effects of corrosion was developed. It is worth noting the need to consider more the morphology of the local damages than the average weight loss in pitting corroded bars, for a correct evaluation of their residual mechanical properties and cross-sectional area. Further, compression tests on locally damaged bars, similarly to those made by the Author in tension, could be useful to better understand premature buckling phenomena in case of pitting corrosion in steel bars. For concrete material, the introduction of two different environmental damage parameters d^{+}_{env} and d^{-}_{env} allowed to better reproduce the behaviour of cracked concrete in tension and in compression and especially to consider not only the strength reduction of cracked concrete but also the reduction of ultimate strain. However, more experimental data are certainly necessary for the correct assessment of residual strains of degraded concrete in compression. Finally, a new bond law for splitting bond failure and a new bond damage parameter d_τ were proposed. These two innovative aspects respectively permitted to consider not only the pull-out bond failures and to predict bond degradation once the level of corrosion is known. Further, new τ-s laws based on d_τ, were developed for considering corrosion effects on composite interaction between concrete and steel bars, in different conditions of confinement. Also in this case, more experimental data would be necessary to improve and validate the proposed approach. Particularly interesting, it would be to develop a model able to relate bond with the state of the surrounding concrete, i.e. stress state, damage state, etc... . In this way the bond law would be able to consider automatically the presence of confinement stress and its variation with the degradation level, without to supply an already defined τ-s law from outside the program.

Finally, the comprehensive approach was applied to the numerical simulation of corroded RC beams and columns. The numerical investigations carried out have evidenced the importance to consider corrosion-induced degradation in the assessment of existing structures.

Regarding corrosion effects on RC beams, through the numerical analyses, it has been clarified that the reduction of load-carrying capacity in corroded RC structures is mainly related to residual cross-sectional area of reinforcing bars, to concrete strength degradation and to anchorage efficiency of the tensile bars. The reduction of global ductility of corroded structures is instead dependent on: the residual ductility of degraded concrete and of steel bars affected by pitting corrosion, and on bond degradation between steel bars and surrounding concrete. Especially bond degradation and failure of transverse reinforcement may lead to a change of the resistant mechanisms. Therefore, bond loss and cracking of concrete cannot be neglected, as instead made in recent models proposed in literature, which considered merely the steel section reduction in the evaluation of corrosion damaged RC members, among others Choe et al.[65] and Marsh and Frangopol[174]. In this dissertation, only the effects of corrosion on the flexural behaviour of RC beams were investigated. A study regarding the influence of reinforcement corrosion on shear behaviour of RC beams should be also made for the better understanding of residual capacity of corroded members.

Regarding RC columns, the numerical analyses carried out evidenced that concrete cover cracking, failure of stirrups and especially premature buckling phenomena of longitudinal bars, play the main role in the structural collapse. Starting from this study, further aspects should be investigated, such as the effect of corrosion on the P-Δ response of eccentrically loaded columns, since the asymmetric deterioration of the columns due to corrosion might lead to an increase of the eccentricity, particularly dangerous when bending is present.

In conclusion, the ability of the numerical model to capture the influence of local effects of corrosion, at different levels of degradation, on the global structural response of the RC beams and columns has been demonstrated. The agreement obtained between the numerical simulations and the experimental data proves that the proposed comprehensive approach can be applied to existing degraded structures, in order to assess their residual strength and global ductility. To this aim, data from real deteriorated structures are necessary. Starting from the results obtained in this work, the developed numerical model could be further improved for simulating the seismic response of RC members and structures, through the implementation of specific cyclic constitutive laws for concrete and steel materials and bond strength-slip laws, considering corrosion degradation.

REFERENCES

[1] ACI-ASCE Committee 426 (326). Shear and Diagonal Tension. ACI Journal, Proceedings V. 59, No. 1-3, Jan., Feb., and Mar. 1962, pp. 1-30, 227-333, and 353-395.

[2] ACI Committee 318, 2005. Building Code Requirements for Structural Concrete (ACI 318-05) and Commentary (318R-05). American Concrete Institute, Farmington Hills, Mich., 430 pp.

[3] Addessi, D., Marfia, S. and Sacco, E. (2002). A plastic nonlocal damage model. Computer Methods in Applied Mechanics and Engineering, 191:1291-1310.

[4] Albanesi T, Biondi S, Nuti M. Influenza dell'instabilità delle armature longitudinali sulla risposta d'elementi in c.a. In: Proceedings of the 10th Italian Conference on Earthquake Engineering, Potenza, Italy. Rome: Anidis, 2001 (in Italian).

[5] Almusallam, A., Al-Gahtani, A., Aziz, A., Dakhil, F., and Rasheeduzzafar. Effect of Reinforcement Corrosion on Flexural Behavior of Concrete Slabs. J. Mater. Civ. Eng., 1996; 8(3), 123–127.

[6] Almusallam A.A., Al-Gahtani A.S., Aziz A.R., Rasheeduzzafar. Effect of reinforcement corrosion on bond strength. Construction and Buildings Materials, 1996; 10(2):123–129.

[7] Almusallam A.A. Effect of degree of corrosion on the properties of reinforcing steel bars. Construction and Building Materials, 2001; 15: 361-368.

[8] Alonso C., Andrade C., Rodriguez J., Diez J.M., Factors controlling cracking of concrete affected by reinforcement corrosion, Mater. Struct. 1998; 31: 435–441.

[9] Al-Sulaimani G.J., Kaleemullah M., Basanbul. I. A., Racheeduzzafar. Influence of corrosion and cracking on bond behavior and strength of reinforced concrete members. ACI Structural Journal, 1990; 87(2):220–231.

[10] Andrade C., Alonso C. and Molina F. Cover cracking as a function of bar corrosion: Part I - Experimental test. Materials and structures, 1993; 26: 453-464.

[11] Andrade C., Alonso C. Molina, F. J. Cover cracking as a function of rebar corrosion: Part II. Numerical model. Materials and Structures 1993; 26: 532-548.

[12] Angst, U., Elsener, B., Jamali, A., Adey, B. Concrete cover cracking owing to reinforcement corrosion – theoretical considerations and practical experience. Materials and Corrosion, 2012; 63(12): 1069-1077.

[13] Apostolopoulos, C.A.,Demis, S., Papadakis, V.G. Chloride-induced corrosion of steel reinforcement-mechanical performance and pit depth analysis. Constr Build Mater, 2013; 38:139–46.

[14] Apostolopoulos C.A., Papadakis V.G. Consequences of steel corrosion on the ductility properties of reinforcement bar. Construction and Building Materials, 2008; 22: 2316-2324.

[15] Arup H. The mechanisms of the protection of steel by concrete", in "Corrosion of Reinforcement in Concrete Construction. (Crane, A. P., Ed.), Ellis Horwood Limited, UK, 1983; Chapter 10: 151-157.

[16] Auyeung, Yubun, Balaguru, P. and Chung. Lan. Bond Behaviour of Corroded Reinforcement Bars. ACI journal, 2000; 97-M28: 214-220.

[17] Bahn B.Y., Hsu C.T.T. Stress-strain behavior of concrete under cyclic loading. ACI materials journal, 1998; 95(2): 178-193.

[18] Barros, F. B. (2002). Métodos sem malha e método dos elementos finitos generalizados em análise não-linear de estruturas. PhD Thesis, Escola de Engenharia de São Carlos, Universidade de São Paulo, São Paulo.

[19] Barros F.B., Proença S. P. B. and De Barcellos C. S. Generalized finite element method in structural nonlinear analysis - a p adaptive strategy. Computational Mechanics, 2004; 33(2): 95-107.

[20] Bathe, K.J., Walczak, J., Welch, A, Mistry, N. Non linear analysis of concrete structures. Computers & Structures, 1989; 32(3/4): 563-590.

[21] Bazant, Z. P. Physical model for steel corrosion in concrete sea structures – Application. Journal of the Structural Division, Proceedings of the American Society of Civil Engineers Vol. 105, ST6, June 1979, pp. 1155-1166.

[22] Bazant, Z. P. (1994). Nonlocal damage theory based on micromechanics of crack interaction. ASCE Journal of Engineering Mechnics, 120:593-617.

[23] Bazant, Z. P., Cedolin, L. Stability of structures: elastic, inelastic, fracture, and damage theories. Oxford University Press, 1991.

[24] Bazant, Z. P. and Jirásek, M. (1994). Damage nonlocality due to micro-crack interactions: Statistical determination of crack influence function. In Bazant, Z. P., Bittnar, Z., Jirásek, M., e Mazars, J., editors, Fracture and Damage in Quasibrittle Structures: Experiment, Modelling and Computer Analysis, pp. 3-17. E and FN Spon, London.

[25] Bazant, Z. P. and Lin, F.-B. (1988). Nonlocal smeared cracking model for concrete fracture. Journal of Structural Engineering - ASCE, 114:2493-2510.

[26] Bazant, Z. P. and Oh, B.-H. (1983). Crack band theory for fracture of concrete. Materials and Structures, 16:155-177.

[27] Bazant, Z. P. and Pijaudier-Cabot, G. (1988). Nonlocal continuum damage, localization instability and convergence. Journal of Applied Mechanics, 55:287-293.

[28] Bazant, Z. P. and Pijaudier-Cabot, G. (1989). Measurement of characteristic length of nonlocal continuum. ASCE Journal of Engineering Mechanics, 115:755-767.

[29] Bazant Z. P. and Planas J. (1998). Fracture and size effect in concrete and other quasi brittle materials. CRC Press, Boca Raton, 1st edition.

[30] Bazant, Z. P. and Jirásek, M. (2002). Nonlocal integral formulations of plasticity and damage: survey of progress. ASCE Journal of Engineering Mechnics, 128:1119-1149.

[31] Beeby A.W. Ductility in reinforced concrete: why is it needed and how is it achieved? The Structural Engineer, 1997; 75(18): 311–318.

[32] Bennett E. W., Snounou I. G. Bond-slip Characteristics of plain reinforcing bars under varying stress. Bond in concrete, Edited by P. Bartos, Applied Science Publishers London, 1982: 140-150.

[33] Berto L., Simioni P., Saetta A. Numerical modelling of bond behaviour in RC structures affected by reinforcement corrosion. Eng Struct 2008; 30:1375-85.

[34] Berto L., Saetta A., Scotta R., Talledo D. A coupled damage model for RC structures: proposal for a frost deterioration model and enhancement of mixed tension domain. Construction and Building Materials, 2014; 65: 310‑320.

[35] Berto, L., Budelmann, H., Finozzi, I.B.N., Saetta, A. Talledo, D.A. (2015). Coupled Damage Model for RC elements Assessment under environmental degradation. International Workshop on Durability and Sustainability of Concrete Structures, 1-3 October 2015, Bologna, Italy.

[36] Bertolini L., Elsener B., Polder R., Pedeferri P. Corrosion of Steel in Concrete. Wiley VCH, 2004.

[37] Bhargava, K., Ghosh, A., Mori, Y., Ramanujam, S. (2006). Analytical model for time to cover cracking in RC structures due to rebar corrosion. Nucl. Eng. Des., 236(11): 1123–1139.

[38] Bhargava, K., Ghosh, A. K., Mori, Y., Ramanujam, S. Suggested Empirical Models for Corrosion-Induced Bond Degradation in Reinforced Concrete. J. of Structural Engineering, 2008; 134(2): 221-230.

[39] Bigaj A.J. Bond behaviour of deformed bars in NSC and HSC: experimental study. Delft University of Technology, Dept. of Civil Engineering, N.25.5-95-II, September 1995.

[40] Biondini, F., Vergani, M. Damage modeling and nonlinear analysis of concrete bridges under corrosion. Roc. of 6th International Conference on Bridge Maintenance, Safety and Management, 2012; 949-957.

[41] Bocca P., Carpinteri A. and Valente S. Mixed mode fracture of concrete. International Journal of Solids and Structures, 1991; 27: 1139-1153.

[42] Borino, G., Fuschi, P., and Polizzotto, C. (1999). A thermodynamic approach to nonlocal plasticity and related variational principles. Journal of Applied Mechanics, 66:952-963.

[43] Bresler, B., Scordelis, A.C. Shear Strength of Reinforced Concrete Beams. J.Am. Concr. Inst., 1963; 60(1): 51-72.

[44] Cabrera, J.G. Deterioration of concrete due to reinforcement steel corrosion. Cement and Concrete Composites, 1996; 18: 47-59.

[45] Cabrera, J., Ghoddoussi P. The Effect of Reinforcement Corrosion on Strength of Steel/Concrete Bond. Bond in Concrete, Proceedings of the International Conference, Riga-Latvia, 1992; 10:11-24.

[46] Çağatay, I.H.. Experimental evaluation of buildings damaged in recent earthquakes in Turkey. Eng. Failure An., 2005; 12: 440–452.

[47] Cai, Q. Finite element modelling of cracking in concrete gravity dams. PhD thesis, University of Pretoria, South Africa, 2007.

[48] Cairns, J. Design of concrete structures using fusion bonded epoxy coated reinforcement. Proc. Inst. Of Civil Engineers: Structures & Buildings 1992; 94(1): 93-102.

[49] Cairns, J. Consequences of Bond Loss for Behaviour of Reinforced Concrete Beams. In: Proceeding of 5th International Conference on Structural Faults and Repairs (1993) 3:149-54.

[50] Cairns, J. Strength of Concrete Beams during Concrete Breakout. IABSE reports, 1995; 73/1/73/2: 499-504

[51] Cairns, J. Bond and anchorage of embedded steel reinforcement in the fib Model Code 2010. Structural Concrete, Journal of the *fib*, 2014.

[52] Cairns, J., Du, Y., Law, D. Influence of corrosion on the friction characteristics of the steel/concrete interface. Construction and Building Materials, 2007; 21: 190-197.

[53] Cairns, J., Millard, S. Reinforcement corrosion and its effect on residual strength of concrete structures. Proceedings of the 8th International Conference on Structural Faults and Repair, Edinburgh 13-15 July 1999, Engineering Technics Press, Edinburgh.

[54] Cairns, J., Plizzari, G. A., Du, Y., Law, D.W., Franzoni. Mechanical properties of corrosion-damaged reinforcement. ACI Materials Journal, 2005; 102(4): 256-264.

[55] Camacho G. T., Ortiz M. Computational modeling of impact damage in brittle materials. International Journal of Solids and Structures, 1996; 33(20-22): 2899-2938.

[56] Cape`, M. Residual service-life assessment of existing R/C structures. MS thesis, Chalmers Univ. of Technology, Goteborg Sweden and Milan Univ. of Technology, Italy, 1999.

[57] Carpinteri, A. Mechanical damage and crack growth in concrete: plastic collapse to brittle fracture. Martinus Nijhoff Publishers, 1st edition, 1986.

[58] Castel, R. Francois, G. Arliguie. Mechanical behaviour of corroded reinforced concrete beams - Part 1: Experimental study of corroded beams. Materials and Structures, 2000; 33: 539-544.

[59] Castel, A., Francois, R., Arliguie, G. Mechanical behavior of corroded reinforced concrete beams. II: Bond and notch effects. Mater. Struct., 2000; 33: 545–551.

[60] Castel, A., Vidal, T., Viriyametanont, K., François, R. Effect of reinforcing bar orientation and location on bond with self-consolidating concrete. ACI Struct J 2006; 103(4):559–67.

[61] CEB-FIP Model Code 1990, Design Code. CEB Bulletin d'Information n. 213/214, Thomas Telford, London, 1993.

[62] Cervera, M., Oliver, J., and Faria, R. (1995). Seismic evaluation of concrete dams via continuum damage models. Earthquake Engineering and Structural Dynamics, 24:1225-1245.

[63] Chaboche, J. L. (1978). Description thermodynamique et phénoménologique de la viscoplasticité cyclique avec endommagement. PhD Thesis, Université Paris 6, Paris.

[64] Chang, J.J., Yeih, W., Huang, R., Chi, J.M. Mechanical properties of carbonated concrete. Journal of the Chinese Institute of Engineers, 2003; 26(4): 513-522.

[65] Choe, D., Gardoni, P., Rosowsky, D. Haukaas, T.Probabilistic capacity models and seismic fragility estimates for RC columns subject to corrosion. Reliability Engineering and System Safety, 2008; 93: 383–393.

[66] Chung, L., Cho, S., Kim, J. J. and Yi, S. Correction factor suggestion for ACI development length provisions based on flexural testing of RC slabs with various levels of corroded reinforcing bars. Engineering Structures, 2004; 26: 1013–1026.

[67] Chung, L., Jay Kim, J.H., & Yi, S.T. Bond strength prediction for reinforced concrete members with highly corroded reinforcing bars. Cement and Concrete Composites, 2008; 30(7): 603-611.

[68] Collepardi M., Borsoi A., Collepardi S., Troli R. Strength, shrinkage and creep of SCC and flowing concrete. In: Proc of SCC2005 conf center for advanced cement based materials, USA Northwestern University; 2005: 911–20.

[69] Comi, C. (1999). Computational modelling of gradient-enhanced damage in quasi-brittle materials. Mechanics of Cohesive-frictional Materials, 4:17-36.

[70] Comi, C. and Driemeier, L. (1998). On gradient regularization for numerical analysis in the presence of damage. In de Borst, R. and van der Giessen, E., editors, Material Instabilities in Solids, pp. 425-440. John Wiley & Sons, Chichester.

[71] Comi C., Mariani S., Perego U. An extended FE strategy for transition from continuum damage to mode I cohesive crack propagation. Int. J. Numer. Anal. Meth. Geomech. 2000; 00:1–6.

[72] Comi C., Mariani S., Perego U. From localized damage to discrete cohesive crack propagation in nonlocal continua. In Mang, H. A., Rammerstorfer, F. G., and Eberhardsteiner, J., editors, Fifth World Congress on Computational Mechanics, 2002

[73] Comi, C. and Perego, U. (2000). A bi-dissapative damage model for concrete with applications to dam engineering. In ECCOMAS 2000.

[74] Comi, C. and Perego, U. (2001). Fracture energy based bi- dissipative damage model for concrete. International Journal of Solids and Structures, 38:6427-6454.

[75] Comi, C. and Perego, U. (2001). Non-local aspects of non-local damage analyses of concrete structures. European Journal of Finite Elements, 10:227-242.

[76] Comi, C. and Perego, U. (2001). Symmetric and non-symmetric non-local damage formulations: an assessment of merits. In ECCM-2001.

[77] Cordebois, J. P. and Sidoroff, F. (1982). Anisotropic damage in elasticity and plasticity. Journal de Mécanique téorique et appliquée, 2:45-60.

[78] Coronelli, D. Bond of Corroded bars in confined concrete: test results and mechanical modeling. Studi e Ricerche, 1997; 18:187–209. (In Italian)

[79] Coronelli, D. Corrosion Cracking and Bond Strength Modeling for Corroded Bars in Reinforced Concrete. ACI Structural Journal, 2002; 99(3): 267-276.

[80] Coronelli, D., Gambarova P. Structural assessment of corroded reinforced concrete beams: modelling guidelines. J Struct Eng 2004; 130(8):1214-24.

[81] Cosenza, E., Greco, C., Manfredi, G. Remarks on defining the concept of ‘equivalent steel. Technical Report No.29. Structural Division, University of Salerno, 1992.

[82] Cotterell, B. and Mai, Y. W. (1996). Fracture mechanics of cementitious materials. Chapman and Hall, 1st edition.

[83] Cowell, A.D., Bertero, V.V., Popov, E.P. An investigation of Local Bond Slip Under Variation of Specimen Parameters. Earthquale Engineering Research Center, Report n° UCB/EERC 82/23. University of California, Berkeley; 1982.

[84] Creazza G. and Russo S. A. New proposal for defining the ductility of concrete-reinforcement steels by means of a single parameter. Materials and Structures, 1996, 29, No. 186, 406–410.

[85] Croce, P., Formichi, P. Numerical Simulation of the Behavior of Cracked Reinforced Concrete Members. Materials Sciences and Application, 2014; 5: 883-894.

[86] Dagher H. J. and Kulendran S. Finite Element Modelling of Corrosion Damage in Concrete. ACI Structural Journal, Vol. 89, November-December 1992, pp. 699-708.

[87] Daly, A. F. Effects of accelerated corrosion on the flexural strength of small scale beams. TRL Research Report PR/CE/15/94, Crowthorne, Unpublished, 1994.

[88] Dang, V.H., François, R. Influence of long-term corrosion in chloride environment on mechanical behaviour of RC beam. Engineering Structures, 2013; 48: 558–568

[89] Daoud A, Lorrain M, Elgonnounil M. Resistance à l'arrachement d'armatures ancrées dans du béton autoplaçant. Matériaux et Constructions 2002; 35:395–401.

[90] De Borst, R. Fracture in quasi-brittle materials: a review of continuum damage-based approaches, Eng. Fract. Mech., 2002; 69: 95-112

[91] Den Uijl J. A., Bigaj A. J. A bond model for ribbed bars based on concrete confinement. HERON 1996; 41(3): 201-226.

[92] Dhakal, R.P., Maekawa, K. Modeling for postyield buckling of reinforcement. J Struct Eng 2002; 128(9): 1139–47.

[93] Du, Y.G., Clark, L.A., Chan, A.H.C. Effect of corrosion on ductility of reinforcing bars. Magazine of Concrete Research, 2005; 57(7): 407-490.

[94] Du, Y.G., Clark, L.A., Chan, A.H.C. Residual capacity of corroded reinforcing bars. Magazine of Concrete Research, 2005; 57(3): 135-147.

[95] DuraCrete. Modelling of degradation. The European Union – Brite EuRam III, 1998.

[96] Eibl, J. and Neuroth U. Experimentelle und rechne-rische Untersuchung zum Einfluß örtlicher Stahl deh-nungen und Querspannungen auf das local Verbundver-halten von Betonrippenstahl," Forschungsbericht Inst. f. Massivebau der Universität Karlsruhe, Germany, 1989.

[97] Elices, M. e Planas, J. (1989). Material models. In Elfren, L., editor, Fracture Mechanics of Concrete Structures - from theory to applications, pp. 16-66. Chapman and Hall, London.

[98] Eligehausen R., Popov E.P, Bertero V.V. Local bond stress–slip relationships of deformed bars under generalized excitations. Report UCB/EERC 83/23, 1983. Earthquake Engineering Research Centre. University of California, Berkeley, pp.169.

[99] Evans R.H. and Marathe M.S. Microcracking and stress-strain curves for concrete in tension. Matériaux et Construction, 1968; 1(1). 61-64.

[100] Fan, Y.F., Chen, Y.S., Hu, Z.Q.Li, X. Experimental study on compressive strength of corroded concrete. Proceedings of 31st Conferenc on Our World in Concrete & Structures, 16-17 August 2006, Singapore.

[101] Fang C., Lundgrenb K., Chena L., Zhua C. Corrosion influence on bond in reinforced concrete. Cement and Concrete Research, 2004; 34: 2159–2167.

[102] Faria R., Oliver J., Cervera M. A strain-based plastic viscous-damage model for massive concrete structures. International Journal of Solids and Structures, 1998; 35:1533-1558.

[103] Fenwick, R. C. and Paulay, T. Mechanisms of shear resistance of concrete beams. Journal of the Structural Division, ASCE, 1968; 94(ST10): 2235-2350.

[104] *fib* International Federation of Structural Concrete. Structural Concrete: Textbook on Behaviour, Design and Performance: Updated Knowledge of the CEB/FIP Model Code 1990. Fib Bulletin No. 1, 1999.

[105] *fib* International Federation of Structural Concrete. Bond of reinforcement in concrete. Fib Bulletin No. 10, 2000.

[106] *fib* International Federation of Structural Concrete. Model Code 2010. Final draft. Fib Bulletin No. 65 & 66. Lausanne, 2012. Vol.1, Vol.2.

[107] *fib* International Federation of Structural Concrete. Bond and anchorage of embedded reinforcement: Background to the *fib* Model Code for Concrete Structures 2010. Fib Bullettin No.72. Technical report, May 2014.

[108] Finozzi I.B.N, Berto L., Saetta A., Budelmann H. Numerical modeling of the corrosion effects on reinforced concrete beams. WCCM XI, Proceedings, Barcelona, Spain, 2014; II: 880-891.

[109] Finozzi I.B.N., Berto L., Saetta A. Structural response of corroded RC beams: a comprehensive damage approach. Computers and Concrete, 2015; 15(3): 411-436.

[110] Gambarova P.G., Rosati G.P. Bond and splitting in reinforced concrete: test results on bar pull-out. Materials and Structures 1996; 29(5): 267-276.

[111] Geers, M. (2004). Course on damage mechanics, Lecture notes (4K060). Technische Universiteit Eidhoven, Eidhoven.

[112] Gestdóttir, E., Guðmundsson, T. Bond Behaviour of Naturally Corroded Reinforcement in Concrete Structures. Experimental and Numerical Study. Master's Thesis, Chalmers University of Technology, Göteborg, Sweden 2012.

[113] Giuriani E., Plizzari G., Schumm C. Role of stirrups and residual tensile strength of cracked concrete on bond. J Struct Eng 1991;117(1):1-18.

[114] Gonzales J.A., Andrade C., Alonso C. and Feliu S. Comparison of rates of general corrosion and maximum pitting penetration on concrete embedded steel reinforcement. Cement and Concrete Research, 1995; 25(2): 257–264.

[115] Gouda, V.K. Corrosion and corrosion inhibition of reinforcing steel. I. Immersed in alkaline solutions. British Corrosion Journal, 1970; 5: 198–203.

[116] Hamad B.S. Bond strength improvement of reinforcing bars with specially designed rib geometries. ACI Struct J 1995; 92(1):3–13.

[117] Hanjari, K.Z., Coronelli, D., Lundgren, K. Bond capacity of severely corroded bars with corroded stirrups. Magazine of Concrete Research, 2011; 63(12): 953-968.

[118] Hanjari KM, Kettil P, Lundgren K. Analysis of Mechanical Behavior of Corroded Reinforced Concrete Structures. ACI Structural Journal 2011;108(5):532-41.

[119] Hanjari KM, Kettil P, Lundgren K. Modelling the structural behaviour of frost-damaged reinforced concrete structures. Struct Infrastruct E: Maintenance, Management, Life-Cycle Design and Performance 2013;9(5):416-31.

[120] Haukka, M., Jakonen, M., Nivajärvi, T.and Kallinen, M. The subtle effects of iron-containing metal surfaces on the reductive carbonylation of RuCl3. Dalton Trans., 2006; 26: 3212-3220.

[121] Hillerborg A., Modeer M., and Peterson P. E. Analysis of crack propagation and crack growth in concrete by means of fracture mechanics and finite elements. Cement and Concrete Research, 1976; 6: 773-782.

[122] Horrigmoe, G., Sæther, I., Antonsen, R., Arntsen, B. Laboratory investigations of steel bar corrosion in concrete. Background document SB3.10. Sustainable bridges, 2007. Sixth Framework Programme.

[123] Huang R., Sukumar N. and Prévost J.H. Modeling quasi-static crack growth with the extended finite element method. Part II: Numerical applications. International Journal of Solid and Structures, 2003; 40: 7539-7552.

[124] Hunkeler F. Corrosion in reinforced concrete structures. Ed. Hans B., published by Woodhead publishing limited, Abington Hall, Abington Cambridge CBI 6AH, England, 2005: 1-45.

[125] Hunkeler, F., Mühlan, B., Ungricht, H. Risk of spalling of concrete due to rebar corrosion. Forschungsauftrag Nr. AGB 2002/015, Schweizerische Eidgenossenschaft, Bundesamt für Strassen 2006.
[126] Hussein, L. Analytical Modeling of Bond Stress at Steel-Concrete Interface due to Corrosion. MASc Thesis, Ryerson University, Toronto, 2011.
[127] Hussein, N.A., Yang, Y., Kawai, K., Sato, R. Time dependent bond behaviour of corroded bars. In Bond in Concrete: From Research to Standards (Balazs G. L., Bartos P. J. M., Cairns J. and Borosnyoi A. (eds)). Publishing company of Budapest University of Technology and Economics, Budapest, 2002, pp. 166–173.
[128] ISO/FDIS 15630-1. International Standard. Steel for the reinforcement and prestressing of concrete – test methods. Part 1: reinforcing bars, wire rod and wire; 2002.
[129] Jansen, D.C., Shah, S.P. Effect of length on compressive strain softening of concrete. J. Engrg. Mech., ASCE, 1997; 123(1), 25-35.
[130] Jirásek M. Nonlocal models for damage and fracture: comparison of approaches. International Journal of Solids and Structures, 1998; 35: 4133-4145.
[131] Jirásek, M. (1999). Computational aspects of non-local models. In ECCM 99.
[132] Jirásek, M. Modelling of localized damage and fracture in quasi- brittle materials. In Vermeer, P. A. and et al, editors, Continuous and discontinuous modelling of cohesive frictional materials. Springer, Berlin. Lecture Notes in Physics, 2001; 568:17-29.
[133] Jirásek M. Comparative study on finite elements with embedded cracks. Computer Methods in Applied Mechanics and Engineering, 2002; 188: 307-330.
[134] Jirásek, M. (2002). Objective modeling of strain localization. Revue française de génie civile, 6:1119-1132.
[135] Jirásek, M. (2004). Modeling of localized inelastic deformation, Lecture notes. Czech Technical University, Prague.
[136] Jirásek, M. and Patzak, B. (2002). Consistent tangent stiffness for non-local damage models. Computers & Structures, 80:1279-1293.
[137] Joyce, T.A. The effects of steel reinforcement corrosion on the flexural capacity and stiffness of reinforced concrete beams. Theses and dissertations, Ryerson University, Toronto, Canada, 2008.
[138] Kachanov L. M. (1958). Time of the rupture process under creep conditions. Izvestija Akademii Nauk SSSR, Otdelenie Techniceskich Nauk, 8:26-31.
[139] Kachanov, L. M. (1986). Introduction to continuum damage mechanics. Kluwer.
[140] Kallias AN, Rafiq MI. Finite element investigation of the structural response of corroded RC beams. Eng Struct 2010; 32: 2984-94.
[141] Kani G. N. J. The riddle of shear failure and its solution. Journal of the American Concrete Institute, 1964; 61(4): 441-467.
[142] Kankam C. Relationship of Bond Stress, Steel Stress, and Slip in Reinforced Concrete. J. Struct. Eng. 1997; 123(1): 79–85.
[143] Kashani, M.M., Crewe, A.J., Alexander, N.A. Stress-Strain Response of Corroded Reinforcing Bars under Monotonic and Cyclic Loading. Proceedings of the 15th World Conference on Earthquake Engineering, Lisbon, Portugal, 2012.
[144] Kashani, M.M., Crewe, A.J., Alexander, N.A. Nonlinear stress–strain behaviour of corrosion-damaged reinforcing bars including inelastic buckling. Engineering Structures, 2013; 48: 417–429.
[145] Khan, I., François, R., Castel, A. Prediction of reinforcement corrosion using corrosion induced cracks width in corroded reinforced concrete beams. Cement and Concrete Research, 2014; 56: 84-96.

[146] Kobayashi, K. The seismic behaviour of RC members suffering from chloride-induced corrosion. FIB 2nd Int. Congress. Naples, Italy, 2006; 15-48.
[147] Krajcinovic D. and Fonseka G. U. The continuous damage theory of brittle materials. Journal of Applied Mechanics, 1981: 48:809-824.
[148] Kupfer H., Hilsdorf H.K., and Rusch H. Behavior of concrete under biaxial stresses. ACI Journal, 1969; 66: 656–666.
[149] Kurz, J.H., Stoppel, M., Taffe, A., Boller, C. Condition assessment of reinforced concrete structures using automated multi-sensor system. Proceddings of the 18th World Conference on Nondestructive Testing, 16-20 April 2012, Durban, South Africa.
[150] Langer P. Verdrehfahigkeit Plastizierter Tragwerkbereiche in Stailbetonbau. Institute für Werkstoffe im Bauwesen der Universität Stuttgart, Stuttgart, Germany, 1997 (in German).
[151] Lee, J. and Fenves, G. L. (1998). A plastic-damage concrete model for earthquake analysis of dams. Earthquake Engineering and Structural Dynamics, 27:937-956.
[152] Lee, H.S., Cho, Y.S. Evaluation of the mechanical properties of steel reinforcement embedded in concrete specimen as a function of the degree of reinforcement corrosion. International Journal of Fracture, 2009; 157: 81-88
[153] Lee, H.S., Kage, T., Nogughi, T., Tomosawa, F. The Evaluation of Flexural Strength of RC Beams Damaged by Rebar Corrosion- Flexural strength of RC beams. Durability of Building Materials and Components 8. (1999) Edited by M.A. Lacasse and D.J. Vanier. Institute for Research in Construction, Ottawa ON, K1A 0R6, Canada, pp. 321-330.
[154] Lee, H., Noguchi, T., Tomosawa, F. Evaluation of the bond properties between concrete and reinforcement as a function of the degree of reinforcement corrosion. Cement and Concrete Research, 2002; 32:1313-1318.
[155] Lemaitre, J. (1992). A course on damage mechanics. Springer-Verlag, 1st edition.
[156] Lemaitre, J. and Chaboche, J.-L. (1985). Mécanique des matériaux solides. Dunod, 1st edition.
[157] Lemaitre, J. and Desmorat, R. (2005). Engineering Damage Mechanics: Ductile, Creep, Fracture and Brittle Failures. Springer, Berlin.
[158] Leonhardt F., Walther R. Einfluss des Momenten-Schub-Verhältnises auf die Schubtragfähigkeit bei Rechtenbalken ohne Schubbewehrung unter Einzel und Gleichlast. Beton und Stahlbeton, 1962; 2.
[159] Lettow, S., Ožbolt, J., Eligehausen, R., Mayer, U. Bond of RC members using nonlinear 3D FE analysis. FRAMCOS 5: Fifth International Conference on Fracture Mechanics of Concrete and Concrete Structures, 12-16 April 2004, Vail Colorado, USA.
[160] Li, C., Yang, S., Saafi, M. Numerical Simulation of Behavior of Reinforced Concrete Structures considering Corrosion Effects on Bonding. Journal of Structural Engineering, 2014; 140(12): 04014092.
[161] Liu, T., and Weyers, R. W. Modeling the dynamic corrosion process in chloride contaminated concrete structures." Cem. Concr. Res.,1998a; 28(3):365–379.
[162] Lowes, L.N.. Finite element modeling of reinforced concrete beam-column bridge connections. PhD thesis, Department of Civil Engineering, University of California, Berkeley, California, 1999.
[163] Lu M., Mai, Y.W. and Ye, L. (2001). Crack-tip field for fast fracture of an elastic-plastic-viscoplastic material coupled with quasi-brittle damage. Part 2. Small damage regime. International Journal of Solids and Structures, 38:9403-9420.
[164] Lubliner, J., Oliver, J., Oller, S., and Onate, E. (1989). A plastic-damage model for concrete. International Journal of Solids and Structures, 25:299-326.
[165] Lundgren, K. Effect of corrosion on the bond between steel and concrete: An overview. Magazine of Concrete Research, 2007; 59(6):447-461.

[166] Maaddaay, T. E., and Soudki, K. (2007). A model for prediction of time from corrosion initiation to corrosion cracking. Cem. Concr. Compos., 29, 168–175.
[167] Maeda M., Otani S., Aoyama H. Effect of confinement on bond splitting behaviour in reinforced concrete beams. Structural Engineering International, 1995; 3: 166-171.
[168] Mahrenholtz C. Seismic bond model for concrete reinforcement and the application to column-to-foundation connections. PhD thesis, Institut für Werkstoffe im Bauwesen, Universität Stuttgart, 2013.
[169] Malvar J.L. Confinement stress dependent bond behaviour. Proceeding of the International Conference on Bond in Concrete. Riga, 1992; 1: 79-88.
[170] Mancini G., Tondolo F. Effect of bond degradation due to corrosion – a literature survey. Structural Concrete 2014; 15: 408-418.
[171] Mander, J., Priestley, M., and Park, R. Theoretical Stress-Strain Model for Confined Concrete. J. Struct. Eng., 1988; 114(8): 1804–1826.
[172] Mangat P.S., Elgarf M.S. Bond characteristics of corroding reinforcement in concrete beams", Materials and Structures, 1999; 32: 89-97.
[173] Mariani S. and Perego U. Extended finite element method for quasi-brittle fracture. International Journal for Numerical Methods in Engineering, 2003; 58: 103-126.
[174] Marsh, P.S., Frangopol, D.M. Reinforced concrete bridge deck reliability model incorporating temporal and spatial variations of probabilistic corrosion rate sensor data. Reliability Engineering and System Safety, 2008; 93:394–409.
[175] Martin-Perez, B., Zibara, H., Hooton, R. D., and Thomas, M. D. A. A study of the effect of chloride binding on service life predictions. Cem. Concr. Res., 2000; 30: 1215–1223.
[176] Mazars, J. (1984). Application de la mécanique de l'endommagement au comportement non lineaire et à la rupture du béton de structure. PhD Thesis, Université Paris 6, Paris.
[177] Mazars J. and Pijaudier-Cabot G. Continuum damage theory - application to concrete. ASCE Journal of Engineering Mechanics, 1989; 115: 345-365.
[178] Mazars, J., Pijaudier-Cabot, G., and Saouridis, C. (1991). Size effect and continuous damage in cementitious materials. International Journal of Fracture, 51:159-173.
[179] Mckenna F, Fenves GL, Scott MH, Jeremic B. Open System for Earthquake Engineering Simulation (OpenSees). Pacific Earthquake Engineering Research Center, University of California, Berkeley, CA, 2000.
[180] Mehta and Monteiro (1993). Concrete Structure, Properties, and Materials. Prentice-Hall, Inc., Englewood Cliffs, NJ.
[181] Mendis, P.A., Kovacic, D., Setunge, S. Basis for the design of lateral reinforcement for high-strength concrete columns. Structural Engineering and Mechanics,2000; 9(6): 589-600.
[182] Mietz J., Polder R., and Elsener B. Corrosion of Reinforcement in Concrete: (EFC 31). Aachen: Maney Publishing, 2000.
[183] Moës N. and Belytshko T. Extended finite element method for cohesive crack growth. Engineering Fracture Mechanics, 2002; 69: 813-833.
[184] Molina F. J., Andrade C. and Alonso C. Cover cracking as a function of bar corrosion: Part II - Numerical model. Materials and structures, 1993; 26: 532-548.
[185] Monti, G. & Nuti, C. 1992. Nonlinear cyclic behaviour of reinforcing bars including buckling. Journal of Structural Engineering, ASCE 118 (12): 3268-3284.
[186] Moreno, E., Cobo, A., Canovas, M.F. Ductility of reinforcing steel with different degrees of corrosion and the 'equivalent steel' criterion. Mater Constr 2007; 57(286): 5–18.
[187] Mousa, M.I. Effect of bond loss of tension reinforcement on the flexural behaviour of reinforced concrete beams, HBRC Journal, 2015.
[188] Murthy, A.C., Palani, G.S. and Riyer, N. State-of-the-art review on fracture analysis of concrete structural components. Sādhanā, 2009; 34(2): 345–367.

[189] Ngala, V.T, Page, C. L. Effects of Carbonation on Pore Structure and Diffusional Properties of Hydrated Cement Pastes. Cement and Concrete Research, 1997; 27(7): 995-1007.
[190] Nakamura, H., Higai, T. Compressive fracture energy and fracture zone length of concrete. In Shing, P., Tanabe, T., editors. Modelling of inelastic behaviour of RC structures under seismic loads. American Society of Civil Engineers; 2001; 87: 471.
[191] Nilson A.H. International Measurement of Bond Slip. ACI Journal 1972; 69(7): 439-441.
[192] NTC 2008. Norme tecniche per le costruzioni, D.M. 14 Gennaio 2008 (in Italian).
[193] Oliver, J. A consistent characteristic length for smeared cracking models. International Journal for Numerical Methods in Engineering, 1989; 28:461-474.
[194] Oliver J., Huespe A.E., Pulido M.D.G. From continuum mechanics to fracture mechanics: the strong discontinuity approach. Engineering Fracture Mechanics, 2002; 69: 113-136.
[195] Ortiz, M. A constitutive theory for the inelastic behavior of concrete. Mechanics of Materials, 1985; 4: 67-93.
[196] Ouglova, M., François, Y., Berthaud, S., Caré, F., Foct. Mechanical properties of an iron oxide formed by corrosion in reinforced concrete structures, Proceedings of the NUCPERF 2006 Workshop, Cadarache, France (27–30 Mars 2006), Journal de Physique IV, 2006; 136: 99–107.
[197] Ožbolt, J., Lettow, S., Kožar, I. Discrete bond element for 3D finite element analysis of reinforced concrete Structures. In: Beiträge aus der Befestigungstechnik und dem Stahlbetonbau, Festschrift zum 60. Geb. von Prof. Dr.-Ing. R. Eligehausen. Stuttgart: ibidem-Verlag, 2002: 239-258.
[198] Palsson, R., and Mirza, M. S. Mechanical Response of Corroded Steel Reinforcement of Abandoned Concrete Bridge. ACI Structural Journal, 2002; 99(2):157-162.
[199] Pamin, J. Gradient-dependent plasticity in numerical simulation of localization phenomena. PhD Thesis, Delft Technical University, Delft, 1994.
[200] Peerlings, R. H. J., de Borst, R., Brekelmans, W. A. M., and de Vree, J. H. P. Gradient-enhanced damage for quasi-brittle materials. International Journal for Numerical Methods in Engineering, 1996; 39:3391-3403.
[201] Pijaudier-Cabot, G. and Bazant, Z. P. Nonlocal damage theory. ASCE Journal of Engineering Mechanics, 1987; 113:1512-1533.
[202] Pijaudier-Cabot, G. and Benallal, A. (1993). Strain localization and bifurcation in a nonlocal continuum. International Journal of Solids and Structures, 30:1761-1775.
[203] Planas, J., Elices, M. Asymptotic analysis of a cohesive crack: 1. Theoretical background. International Journal of Fracture,1992; 55: 153-177.
[204] Planas J., Elices M. Asymptotic analysis of a cohesive crack: 2. Influence of softening curve. International Journal of Fracture, 1993; 64: 221-237.
[205] Plizzari G.A and Schumm C. Sul Collasso dell'Aderenza per Sfilamento della Barra e Spacco del Calcestruzzo. Studi e Ricerche, School for the Design of R.C. Structures, Milan University of Technology, 12:81-116, 1990 (in Italian).
[206] Pourbaix, A. Corrosion Chemistry within Pits, Crevices and Cracks. Ed. A. Turnbull; National Physical Laboratory, Teddington, Middlesex 1984, pp. 1–15.
[207] Proença S. P. B. and Pituba, J. J. C. (2003). A damage constitutive model accounting for induced anisotropy and bimodular elastic response. Latin American Journal of Solids and Structures, São Paulo, 1(1):101-117.
[208] Proença S. P. B. and Balbo, A.R. (2004). On a regular convex solver potential for an elastic-damage constitutive model: a theoretical analysis. International Journal of Solids and Structures, 41(7):1975-1989.
[209] Rabotnov, Y. N. (1968). Creep rupture. In 12th International Congress of Applied Mechanics. Stanford.

[210] Ramtani, S., Berthaud, Y., and Mazars, J. (1992). Orthotropic behavior of concrete with directional aspects: modelling and experiments. Nuclear Engineering and Design, 133:97-111.

[211] Rehm, G. Über die Grundlagen des Verbudzwischen Stahl undBeton. Heft 138, Deutscher Ausschuss für Stahlbeton, Berlin, 1961; 59.

[212] Reinhardt H.W., Cornelissen H.A.W. Post-peak cyclic behaviour of concrete and alternating tensile and compressive loading, Cement and concrete research, 1984; 14: 263-270.

[213] Revathy, J., Suguba, K., Raghunath, P.N. Effect of Corrosion Damage on the Ductility Perofrmance of Concrete Columns. American J. of Engineering and Applied Sciences, 2009; 2(2): 324-327.

[214] Ribeiro, R.B., Silva, J.W.J., Hein, L.R.O., Pereira, M.C., Codaro, E.N. and Matias, N.T. Morphology Characterisation of Pitting Corrosion on Sensitized Austenitic Stainless Steel by Digital Image Analysis. ISRN Corrosion, vol. 2013, Article ID 905942, 7 pages, 2013.

[215] Richart F.E.A., Brandtzaeg A., Brown R.L. A study of the failure of concrete under combined compressive stresses. Technical Reports, 1928. University of Illinois, Engineering Experiment Station. Bulletin no. 185.

[216] RILEM. Essai portant sur l'adhérence des armatures de béton – Essai par traction, Matériaux et Constructions 1970; 3(15):175–178.

[217] RILEM. Recommendations for the Testing and Use of Construction Materials, 1994.

[218] Roberge P.R. Handbook of Corrosion Engineering. McGraw-Hill, 2000; 1140 pages.

[219] Rodriguez J., Ortega L. and Garcia A. Corrosion of reinforcing bars and service life of R/C structures: Corrosion and bond deterioration. Proc. Int. Conf. on Concrete across Borders, Odense, Denmark, 1994, Vol. II: 315–326.

[220] Rodriguez, J., Ortega, L. M. & Casal, J. 1996. Load-carrying capacity of concrete columns with corroded reinforcement. Fourth international symposium on the corrosion of reinforcement in concrete structures: 220-23. Cambridge, UK

[221] Rodriguez J., Ortega L.M., Casal J., Diez J.M. Assessing structural conditions of concrete structures with corroded reinforcement. In: Dhir RK, Jones MR, editors. Concrete repair, rehabilitation and protection. E&FN Spon; 1996, p. 65-78.

[222] Rodriguez J., Ortega L.M., Casal J. Load-carrying capacity of concrete structures with corroded reinforcement. Construct Building Mater 1997;11(4):239-48.

[223] Saether, I. and Sand, B. FEM simulation of reinforced concrete beams attacked by corrosion. ACI Structural Journal, 2009; 39 (3): 15-31.

[224] Saetta A., Scotta R., Vitaliani R. Mechanical behaviour of concrete under physical-chemical attacks. J Eng Mech-ASCE 1998; 124(10): 1100-9.

[225] Saetta, A., Scotta, R., Vitaliani, R. Coupled Environmental-Mechanical Damage Model of RC Structures. J. of Eng. Mech., 1999; 125(8): 930–940.

[226] Šavija, B., Luković, M., Hosseini, S.A.S., Pacheco, J., Schlangen, E. Corrosion induced cover cracking studied by X-ray computed tomography, nanoindentation, and energy dispersive X-ray spectrometry (EDS). Materials and Structures, 2015; 48(7): 2043–2062.

[227] Scotta R, Vitaliani R, Saetta A, Oñate E, Hanganu A. A scalar damage model with a shear retention factor for the analysis of reinforced concrete structures: theory and validation. J. of Computers & Structures 2001; 79 (7):737-55.

[228] Scott B.D., Park R., Priestley M.J.N. Stress-strain behaviour of concrete confined by overlapping hoops at low and high strain rates. J. of the American Concrete Institute, 1982; 79(1): 13-27.

[229] Shima H., Chou L.L., Okamura H. (b): Micro and macro models for bond in reinforced concrete. J. of the Faculty of Engrg., University of Tokio, 1987; 39(2): 133-194.

[230] Shima H. Local bond stress-slip relationship of corroded steel bars embedded in concrete. Bond in Concrete: From Research to Standards. Proceedings of the 3rd International

Symposium held at the Budapest University of Technology and Economics, Budapest, Hungary, 20-22 November 2002, pp. 153-158.

[231] Shimomura, T., Maruyama, K. Constitutive models for prediction of performance of deteriorated concrete structures. Proceedings of the 2nd International RILEM Workshop on Life Prediction and Aging Management of Concrete Structures, Paris, France, 5-6 May 2003, RILEM Proceedings PRO 29: 3-12.

[232] Simioni, P. Seismic response of reinforced concrete structures affected by reinforcement corrosion. PhD Thesis, University of Florence-TU Braunschweig, Italy-Germany, 2009.

[233] Simo, J. C., Oliver, J., and Armero, F. An analysis of strong discontinuities induced by strain softening in rate-independent inelastic solids. Computational Mechanics, 1993; 12: 277-296.

[234] Sirivivatnanon, V., Khatri, R.P. Characterising chloride penetration resistance of concrete. Durability of Building Materials and Components 8. Edited by M.A. Lacasse and D.J. Vanier. Institute for Research in Construction, Ottawa ON, K1A 0R6, Canada, 1999: 386-398.

[235] Song G., Shayan A. Corrosion of steel in concrete: causes, detection and prediction. A state-of-the-art review, Review Report 4. ARRB Transport Research Ltd; 1998.

[236] Stanish, K, Hooton, R D & Pantazopoulou, S. J. Corrosion effects on bond strength in reinforced concrete. ACI Structural Journal,1999; 96(6): 915–21.

[237] Stewart, M.G. Spatial variability of pitting corrosion and its influence on structural fragilty and reliability of RC beams in flexure. Struct Saf, 2004; 26(4): 453-470.

[238] Stewart, M.G. Mechanical behaviour of pitting corrosion of flexural and shear reinforcement and its effect on structural reliability of corroding RC beams. Structural Safety, 2009; 31: 19–30.

[239] Sukumar, N. and Prévost J.H. Modeling quasi-static crack growth with the extended finite element method. Part I: Computer implementation. International Journal of Solids and Structures, 2003; 40: 7513- 7537.

[240] Talledo, D.A. A coupled environmental-mechanical damage model for structural analysis of RC constructions. PhD Thesis, University of Florence-TU Braunschweig, Italy-Germany, 2014.

[241] Tang, F., Lin, Z., Chen, G., Yi, W. Three-dimensional corrosion pit measurement and statistical mechanical degradation analysis of deformed steel bars subjected to accelerated corrosion. Construction and Building Materials, 2014;70: 104-117

[242] Tassios, T.P. Properties of Bond Between Concrete and steel under Cycles Idealizing Seismic Actions. Proceedings of AICAP-CEB Symposium, Rome, Apr. 1979, CEB Bulletin No. 131, Paris, pp. 67-122.

[243] Tassios, T.P., Koroneos E.G. Local bond-slip by means of the moiré method. ACI Journal, 1984; 81(4): 27-34.

[244] Tepfers, R. Cracking of concrete cover along anchored deformed reinforcing bars. Mag. Concr. Res., (1979); 31(106), 3–12.

[245] Tepfers R. Lapped tensile reinforcement splices. ASCE, J. Struc. Div., 1982; 108(1): 283-301.

[246] Tesser, L, Filippou, F.C., Talledo, D.A., Scotta, R., Vitaliani, R. Nonlinear analysis of R/C panels by a two parameter concrete damage model. COMPDYN, Corfu, Greece, 26-28 May 2011.

[247] Thoft-Christensen P. & Hansen H.I. Optimal Strategy for Maintenance of Concrete Bridges Using Expert System. Proc. ICOSSAR ’93, A.A.Balkema, Rotterdam-Netherlands, 1994: 939-946.

[248] Torre-Casanova A., Jason L., Davenne L., Pinelli X. Confinement effects on the steel–concrete bond strength and pull-out failure. Engineering Fracture Mechanics, 2013; 97: 92–104.

[249] Torres-Acosta, A.A., Navarro-Gutierrez, S., Terán-Guillén, J. Residual flexure capacity of corroded reinforced concrete beams. Eng Struct, 2007; 29(6): 1145-52.

[250] Ueda, T., Sato, Y., Kakuta, Y. and Kameya, H. Analytical study of concrete cover cracking due to reinforcement corrosion. Concrete in severe environments, CONSEC '98, Norway, E & FN Spon, pp. 678-687.

[251] UNI EN 1992-1-1:2005. Eurocode 2-Design of concrete structures-part 1-1: General rules and rules for building, 225.

[252] Uomoto T. and Misra S. Behaviour of concrete beams and columns in marine environment when corrosion of reinforcing bars takes place. Concrete in marine environments, ACI SP, 1990; 109(6): 127-146.

[253] Uomoto, T., Tsuji, K., Kakizawa, T. Deterioration mechanism of concrete structures caused by corrosion of reinforcing bars. Transactions of the Japan Concrete Institute, 1984; 6: 163-170.

[254] U.S. Federal Highway Administration and National Department of Transportation. The Deleterious Chemical Effects of Concentrated Deicing Solutions on Portland Cement Concrete. Study SD2002-01, prepared by Michigan Tech Transportation Institute, 2008.

[255] Vakulenko, A. A. and Kachanov, M. L. Continuum theory of medium with cracks. Mekhanika Tverdogo Tela, 1971; 4:159-166 (in russian)

[256] Val D. V., and Melchers R. E. Reliability of deteriorating RC slab bridges. J. Struct. Eng., 1997; 123(12): 1638–1644.

[257] Van Mier, J.G.M. Strain-softening of concrete under multiaxial loading conditions. PhD thesis, Eindhoven University of Technology, Eindhoven, The Netherlands, 1984.

[258] Van Mier, J.G.M. Multiaxial strain-softening of concrete, part I: fracture, part II: load-histories, Materials and Structures, RILEM, 1986; 19: 179-200

[259] Van Mier, J.G.M. Fracture of concrete under complex stress. Heron, 1986; 31(3).

[260] Vecchio F.J., Collins M.P. (1993). Compression Response of Cracked Reinforced Concrete. Journal of Structural Engineering, 119(12): 3590-3610

[261] Vergani, M., 2010. Modellazione del degrado di strutture in calcestruzzo armato soggette a corrosione. Degree Thesis, Politecnico di Milano, Italy (in Italian).

[262] Vidal, T., Castel, A., Francois, R. Analyzing crack width to predict corrosion in reinforced concrete, Cement and Concrete Research, 2004; 34: 165-174.

[263] Vile, G.W.D. Proceedings of the International Conference on Structure of Concrete and Its Behaviour Under Load, Cement and Concrete Association, London, September, 1965: 275–288.

[264] Viwathanatepa, S., Popov, E.P., Bertero, V.V. Effects of Generalized Loadings on Bond of Reinforcing Bars Embedded in Confined Concrete Blocks. Earthquake Engineering Research Center, Report n° UCB/EERC -79/22. University of California, Berkeley; August 1979.

[265] Vonk, R.A. Softening of Concrete Loaded in Compression. PhD Thesis 1992, University of Technology Eindhoven, the Nederlands.

[266] Vonk, R.A. A micromechanical investigation of softening of concrete loaded in compression. Heron 1993; 38(3).

[267] Walraven, J.C. Aggregate interlock: A theoretical and experimental analysis. PhD thesis, Delft University, 1980.

[268] Wells G.N. and Sluys L.J. A new method for modeling cohesive cracks using finite elements. International Journal for Numerical Methods in Engineering, 2001; 50: 2667-2682.

[269] Wells, G.N., Sluys, L.J., De Borst, R. Simulating the propagation of displacement discontinuities in a regularized strain-softening medium. International Journal for Numerical Methods in Engineering, 2002; 53: 1235-1256.

[270] Wittmann, F.H. Structure of Concrete and Crack formation. Fracture of Non-Metallic Materials, 1987: 309-340.

[271] Wong, H.S., Zhao, Y.X, Karimi, A.R., Buenfeld, N.R., Jin, W.L. On the penetration of corrosion products from reinforcing steel into concrete due to chloride-induced corrosion. Corrosion Science, 2010; 52(7): 2469-2480.

[272] Wu, H. Bond Degradation and Residual Flexural Capacity of Corroded RC Beams. Theses and dissertations. Paper 708, Ryerson University, Toronto, Canada, 2012.

[273] Xu X.P. and Needleman A. Numerical simulation of fast crack growth in brittle solids, Journal of the Mechanics and Physics of Solids, 1994; 42: 1397-1434.

[274] Yang, S., Li, C. Corrosion-induced bond deterioration in reinforced concrete structures. RILEM International Symposium on Concrete Modelling, 12-14 October 2014, Beijing, China.

[275] Yankelevsky D.Z. and Reinhardt H.W. Response of plain concrete to cyclic tension. ACI Material Journal, (1987b); 84(5): 365-373.

[276] Zhang, R., Castel, A., François, R. Serviceability Limit State criteria based on steel-concrete bond loss for corroded reinforced concrete in chloride environment. Materials and Structures, 2009; 42(10):1407–1421.

[277] Zhang, R., Castel, A., François, R. Concrete cover cracking with reinforcement corrosion of RC beams during chloride-induced corrosion process. Cement and Concrete Research, 2010; 40: 415–425.

[278] Zhang, Y., Fan, Y., Li, H. Influence of Simulated Acid Rain Corrosion on the Uniaxial Tensile Mechanical Properties of Concrete. Hindawi Publishing Corporation. International Journal of Corrosion, 2012; Article ID 172394, 7 pages.

APPENDIX A: Geometrical details of the locally damaged steel bars tested

A number of locally damaged steel bars, of 16 mm diameter and 500 mm length, were subjected to tensile test at the Laboratory of the Institut für Baustoffe, Massivbau und Brandschutz (iBMB) of the Technische Universität Braunschweig. The local damage was created by a computer numerical control (CNC) milling machine, provided by the Stahlbau Institutes of the Technische Universität Braunschweig, in order to simulate pitting corrosion. Eight bars were locally damaged, creating one single pit of different shapes and lengths at the half length of the bar. In detail, for four bars the damage created had circular cross section, for the other four was narrower than deep, assuming a wedge cross section. Other three bars were created with two or three pits. The geometrical details of each local damage in the steel bars, are below provided.

- *1DBc8d5 bar*

Table 1 – Geometrical characteristics of 1DBc8d5 bar

Max pit depth	*Initial cross-sectional area*	*Max cross-sectional area of the pit*	*Min. residual cross-sectional area*	*Reduction of cross-sectional area*	*Residual volume between jacks*	*Volume of the pit*	*Reduction of volume*
p[mm]	*As[mm2]*	*Ap[mm2]*	*A's[mm2]*	*ΔAs[%]*	*Vr[mm3]*	*Vp[mm3]*	*ΔV[%]*
5	*201.06*	*34.01*	*167.05*	*16.92*	*66852.15*	*502.95*	*0.75*

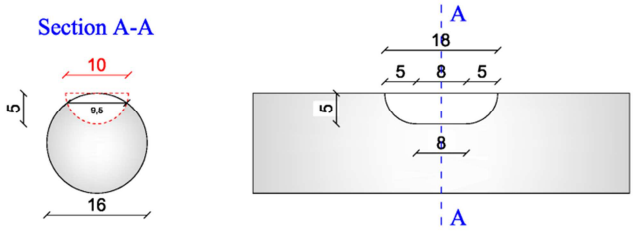

Figure 1- Geometrical characteristics of 1DBc8d5 bar

- *1DBc8d10 bar*

Table 2 – Geometrical characteristics of 1DBc8d10 bar

Max pit depth	*Initial cross-sectional area*	*Max cross-sectional area of the pit*	*Min. residual cross-sectional area*	*Reduction of cross-sectional area*	*Residual volume between jacks*	*Volume of the pit*	*Reduction of volume*
p[mm]	*As[mm2]*	*Ap[mm2]*	*A's[mm2]*	*ΔAs[%]*	*Vr[mm3]*	*Vp[mm3]*	*ΔV[%]*
10	*201.06*	*113.53*	*87.53*	*56.47*	*64861.37*	*2493.73*	*3.70*

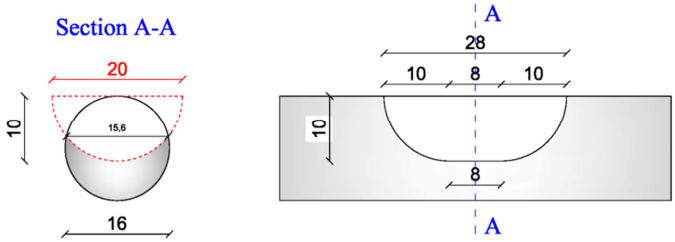

Figure 2- Geometrical characteristics of 1DBc8d10 bar

- *1DBc32d5 bar*

Table 3 – Geometrical characteristics of 1DBc32d5 bar

Max pit depth	*Initial cross-sectional area*	*Max cross-sectional area of the pit*	*Min. residual cross-sectional area*	*Reduction of cross-sectional area*	*Residual volume between jacks*	*Volume of the pit*	*Reduction of volume*
p[mm]	*As[mm2]*	*Ap[mm2]*	*A's[mm2]*	*ΔAs[%]*	*Vr[mm3]*	*Vp[mm3]*	*ΔV[%]*
5	*201.06*	*34.01*	*167.05*	*16.92*	*66035.92*	*1319.18*	*1.96*

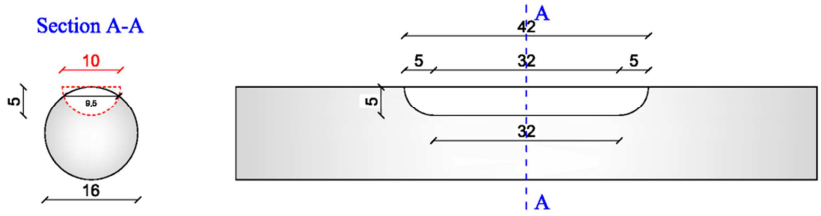

Figure 3- Geometrical characteristics of 1DBc32d5 bar

- *1DBc32d10 bar*

Table 4 – Geometrical characteristics of 1DBc32d10 bar

Max pit depth	*Initial cross-sectional area*	*Max cross-sectional area of the pit*	*Min. residual cross-sectional area*	*Reduction of cross-sectional area*	*Residual volume between jacks*	*Volume of the pit*	*Reduction of volume*
p[mm]	*A_s[mm^2]*	*A_p[mm^2]*	*A'_s[mm^2]*	*ΔA_s[%]*	*V_r[mm^3]*	*V_p[mm^3]*	*ΔV[%]*
10	*201.06*	*113.53*	*87.53*	*56.47*	*62136.65*	*5218.45*	*7.75*

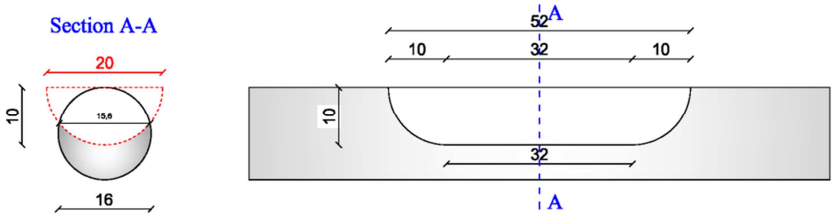

Figure 4- Geometrical characteristics of 1DBc32d10 bar

- *1DBw8d5 bar*

Table 5 – Geometrical characteristics of 1DBw8d5 bar

Max pit depth	*Initial cross-sectional area*	*Max cross-sectional area of the pit*	*Min. residual cross-sectional area*	*Reduction of cross-sectional area*	*Residual volume between jacks*	*Volume of the pit*	*Reduction of volume*
p[mm]	*As[mm2]*	*Ap[mm2]*	*A's[mm2]*	*ΔAs[%]*	*Vr[mm3]*	*Vp[mm3]*	*ΔV[%]*
5	*201.06*	*9.68*	*191.38*	*4.81*	*67262.19*	*92.91*	*0.14*

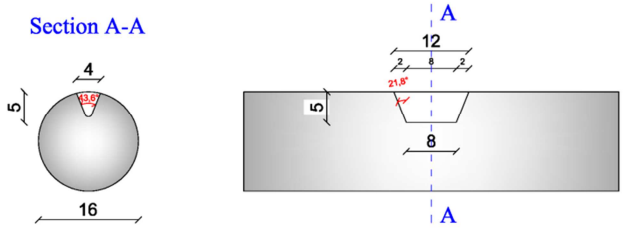

Figure 5- Geometrical characteristics of 1DBw8d5 bar

- *1DBw8d10 bar*

Table 6 – Geometrical characteristics of 1DBw8d10 bar

Max pit depth	*Initial cross-sectional area*	*Max cross-sectional area of the pit*	*Min. residual cross-sectional area*	*Reduction of cross-sectional area*	*Residual volume between jacks*	*Volume of the pit*	*Reduction of volume*
p[mm]	*As[mm2]*	*Ap[mm2]*	*A's[mm2]*	*ΔAs[%]*	*Vr[mm3]*	*Vp[mm3]*	*ΔV[%]*
10	*201.06*	*37.6*	*163.46*	*18.70*	*66954.03*	*401.07*	*0.60*

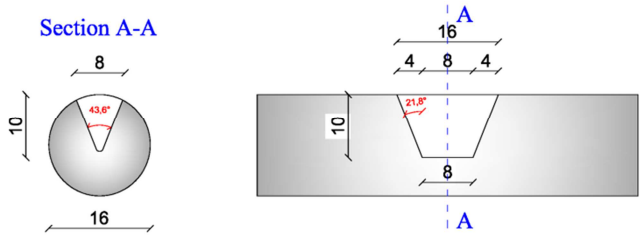

Figure 6- Geometrical characteristics of 1DBw8d10 bar

- *1DBw32d5 bar*

Table 7 – Geometrical characteristics of 1DBw32d5 bar

Max pit depth	*Initial cross-sectional area*	*Max cross-sectional area of the pit*	*Min. residual cross-sectional area*	*Reduction of cross-sectional area*	*Residual volume between jacks*	*Volume of the pit*	*Reduction of volume*
p[mm]	*As[mm2]*	*Ap[mm2]*	*A's[mm2]*	*ΔAs[%]*	*Vr[mm3]*	*Vp[mm3]*	*ΔV[%]*
5	*201.06*	*9.68*	*191.38*	*4.81*	*67032.43*	*322.67*	*0.48*

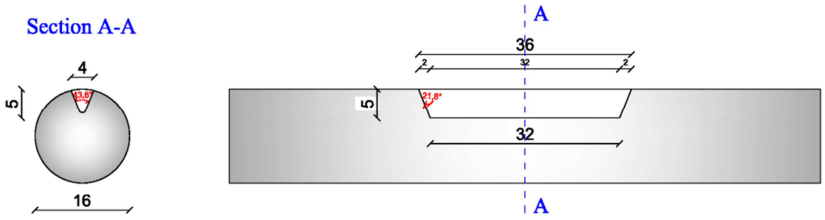

Figure 7- Geometrical characteristics of 1DBw32d5 bar

- *1DBw32d10 bar*

Table 8 – Geometrical characteristics of 1DBw32d10 bar

Max pit depth	*Initial cross-sectional area*	*Max cross-sectional area of the pit*	*Min. residual cross-sectional area*	*Reduction of cross-sectional area*	*Residual volume between jacks*	*Volume of the pit*	*Reduction of volume*
p[mm]	*As[mm2]*	*Ap[mm2]*	*A's[mm2]*	*ΔAs[%]*	*Vr[mm3]*	*Vp[mm3]*	*ΔV[%]*
10	*201.06*	*37.6*	*163.46*	*18.70*	*66051.63*	*1303.47*	*1.94*

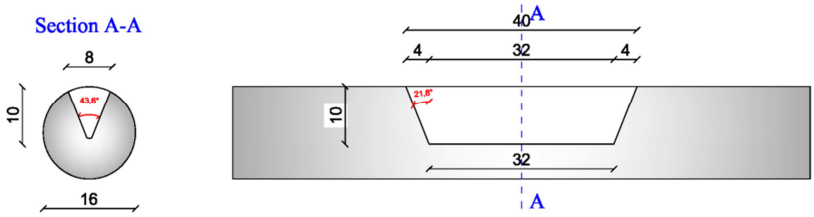

Figure 8- Geometrical characteristics of 1DBw32d10 bar

- *2DBc8d5 bar*

Table 9 – Geometrical characteristics of 2DBc8d5 bar

Max pit depth	*Initial cross-sectional area*	*Max cross-sectional area of the pit*	*Min. residual cross-sectional area*	*Reduction of cross-sectional area*	*Residual volume between jacks*	*Volume of the pit*	*Reduction of volume*
p[mm]	*As[mm2]*	*Ap[mm2]*	*A's[mm2]*	*ΔAs[%]*	*Vr[mm3]*	*Vp[mm3]*	*ΔV[%]*
5	*201.06*	*34.01*	*167.05*	*16.92*	*66349.20*	*1005.90*	*1.49*

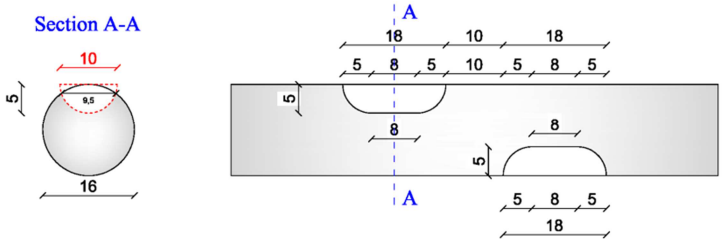

Figure 9- Geometrical characteristics of 2DBc8d5 bar

- *3DBc8d5 bar*

Table 10 – Geometrical characteristics of 3DBc8d5 bar

Max pit depth	*Initial cross-sectional area*	*Max cross-sectional area of the pit*	*Min. residual cross-sectional area*	*Reduction of cross-sectional area*	*Residual volume between jacks*	*Volume of the pit*	*Reduction of volume*
p[mm]	*As[mm2]*	*Ap[mm2]*	*A's[mm2]*	*ΔAs[%]*	*Vr[mm3]*	*Vp[mm3]*	*ΔV[%]*
5	*201.06*	*34.01*	*167.05*	*16.92*	*65846.25*	*1508.85*	*2.24*

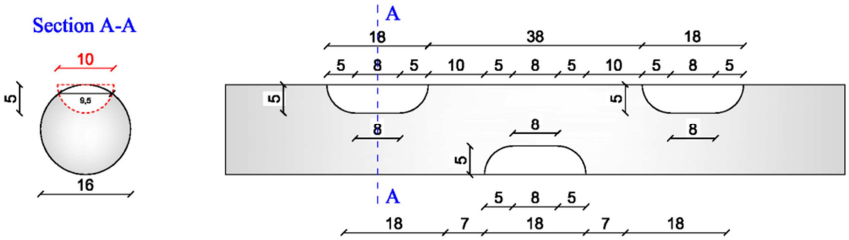

Figure 10- Geometrical characteristics of 3DBc8d5 bar

- *3DBc8d10 bar*

Table 11 – Geometrical characteristics of 3DBc8d10 bar

Max pit depth	*Initial cross-sectional area*	*Max cross-sectional area of the pit*	*Min. residual cross-sectional area*	*Reduction of cross-sectional area*	*Residual volume between jacks*	*Volume of the pit*	*Reduction of volume*
p[mm]	*As[mm2]*	*Ap[mm2]*	*A's[mm2]*	*ΔAs[%]*	*Vr[mm3]*	*Vp[mm3]*	*ΔV[%]*
10	*201.06*	*113.53*	*87.53*	*56.47*	*59873.91*	*7481.19*	*11.11*

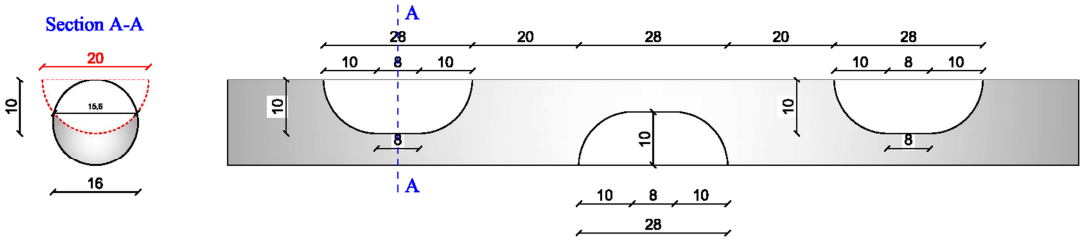

Figure 11- Geometrical characteristics of 3DBc8d10 bar

APPENDIX B: Buckling of uncorroded reinforcing steel bars

Reinforcing steel bars in RC structures carry load primarily along their axis. While the response of steel bars under tension load has been well investigated and it is easily to be defined, the strength of bars in compression depends on both the geometrical and material properties of the bars.

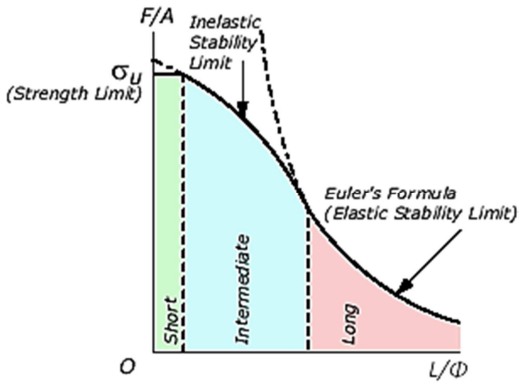

Figure 1 – Critical buckling load as function of the slenderness ratio

In case of short-length bars (*Figure 1*), the ultimate compression strength is not geometry-related and depends only on the material properties. This is the case of reinforcing bars with a geometrical slenderness ratio $\lambda=L/\Phi$ minor than about 5 for structural steel (λ_{crit}); where L is the bar length between two consecutive stirrups and Φ is the bar diameter. The monotonic response of the bars in compression and tension is essentially the same.

In case of long-length bars (*Figure 1*), buckling phenomena may occur before that the stresses reach the yield strength of the material. The compression strength depends on both the geometry of the bar and on the material properties and can be calculated with the Euler's formula for the evaluation of the critical buckling load:

$$N_{crit} = \frac{\pi^2 E_s I}{{L_0}^2} \qquad \textit{Equation 1}$$

where L_0 is the effective length, equal to the bar length L multiplied by the coefficient K, which takes into account of end constraint conditions (*Figure 2*).

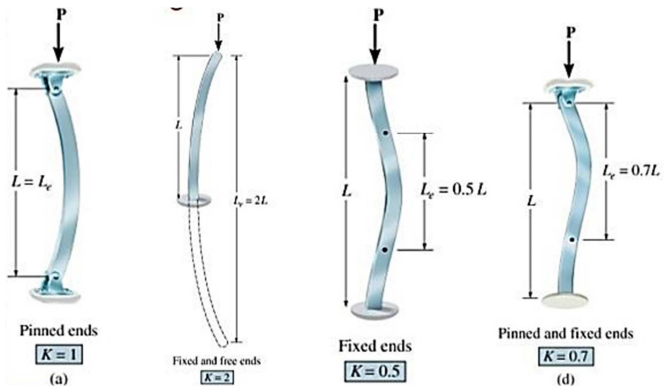

Figure 2 – Values of K coefficient for different end constraint conditions

Due to the fact that the cross section shape of steel bars is circular, the Area Moment of Inertia I is equal to $\pi\ \Phi^4/64$. *Equation 1* can be then re-written as critical buckling strength:

$$\sigma_{crit} = \frac{E_s}{16}\left(\frac{\pi \cdot \Phi}{K \cdot L}\right)^2$$ *Equation 2*

which is function only of the steel stiffness E_s and of the geometrical slenderness ratio λ. A defined reinforcing bar can be considered long, if the slenderness ratio assumes values greater than λ_y, calculated fixing the critical buckling strength equal to the yield strength:

$$\lambda_y = \sqrt{\frac{E_s \cdot \pi^2}{16 \cdot \sigma_y \cdot K^2}}$$ *Equation 3*

For example, for a steel bar B500B with σ_y=520 MPa and E_s=210000 MPa, K=2/3 (typical value assumed for safety reason), λ_y is equal to 23.7. All the bars B500B with slenderness ratio greater than this value likely buckle in the elastic field at the critical buckling strength. For these bars, the monotonic responses in compression and tension considerably differ.

When reinforcing bars have value of slenderness ratio between λ_y and λ_{crit}, intermediate-length bars (*Figure 1*), buckling occurs after that the stresses reach the yield strength but before that they reach the ultimate compression strength of the steel material. This kind of situation is called inelastic buckling: the monotonic response of bars in compression and tension is similar until the achievement of the critical buckling strength. In the years, many researchers have elaborated inelastic buckling theories. The most famous ones are the *Tangent-Modulus Theory* and the *Reduced Modulus Theory* developed by Engesser[4][5]. In the first method the elastic modulus E_s of steel is replaced by the post-yield tangent modulus E_{sh}, defined as the slope of the stress-strain curve at the start of the plastic strain range, in *Equation 1*:

$$N_{crit} = \frac{\pi^2 E_{sh} I}{{L_0}^2}$$ *Equation 4*

In the *Reduced Modulus Theory*, a reduced elastic modulus of steel is defined. This method was developed to compensate the underestimation of the critical buckling load given by the *Tangent-Modulus Theory* (see *Figure 3*). In detail, the reduced elastic modulus E_r, can be evaluated as follow:

$$E_r = \frac{4E_s E_t}{\left(\sqrt{E_s} + \sqrt{E_t}\right)^2}$$ *Equation 5*

where E_t is the tangent modulus at the buckling stress value.

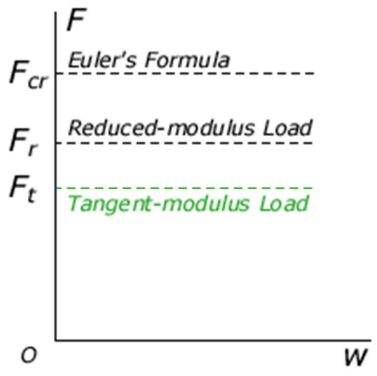

Figure 3 - Critical buckling load calculated with different theories

Over the last years, many models have been proposed to describe the behaviour of reinforcing bars in compression including buckling, under cyclic and monotonic loads (e.g. Dhakal et al.[2][1][3], Gomes and Appleton[6], Mau and El-Mabsout[7] and Mau[8], Mendis et al.[9], Monti and Nuti[10], Papia and Russo[11], Rodriguez et al.[12], Scribner[13]). One of the most reliable and complete model, based on several experimental results, is the one developed by Monti and Nuti[10]. This model is able to describe the monotonic and cyclic behavior of reinforcing bars in presence of buckling over the elastic threshold, i.e. for $\lambda \geq \lambda_{crit}$ =5 (*Figure 4*). Regarding the monotonic response, the authors observed the same behaviour previously reported: absence of buckling in case of $\lambda < \lambda_{crit}$ =5; buckling after a short superposition, equal to γ_s, of compressive and tensile response (λ_{crit} =5 ≤ $\lambda < \lambda_y$=*11);* and buckling before the yield point for $\lambda \geq \lambda_y$=*11*. For the evaluation of γ_s, the following empirical relation was proposed:

$$\gamma_s = \frac{\lambda_y - \lambda}{e^{c\lambda} - 1} \geq 0 \qquad \textit{Equation 6}$$

In case of buckling, a softening branch was experimentally observed after the achievement of the critical buckling strength. The softening branch tends to an asymptotic value, which reduces with increasing values of λ, with an exponential law, according to the following relation:

$$\sigma_{s\infty} = 6 \cdot \frac{f_y}{\lambda} \qquad \textit{Equation 7}$$

Immediately after the achievement of the buckling strength, the softening branch is tangent to the straight line of E_{n0} slope, defined as $b^- \cdot E_s$, where b^- also decreases with increasing λ:

$$b^- = a\,(\lambda_h - \lambda) \qquad \textit{Equation 8}$$

The following values were proposed by the authors: c=0.5; a=0.006-0.008. For more details, refer to Monti and Nuti[10]. It should be noticed that the value of λ_y differs from the previously defined (λ_y =23.7), because the steel material used in the tests of Monti and Nuti[10] was Feb44 (σ_y=440 MPa).

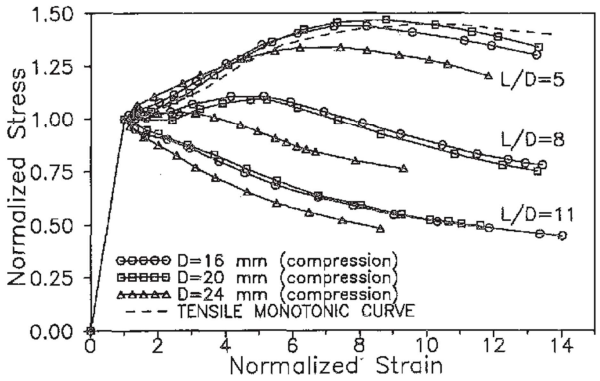

Figure 4 – Experimental monotonic compressive curves, Monti and Nuti[10]

Some years later, Albanesi et al.[1] proposed some improvements. In order to have a general expression, they suggested to calculate the c parameter and the asymptotic value $\sigma_{s\infty}$, as:

$$c = \frac{1}{5} ln\left(\frac{6}{|\varepsilon_{sr} - \varepsilon_{sy}|} + 1\right) \qquad \textit{Equation 9}$$

$$\sigma_{s\infty} = 5 \cdot \frac{f_y}{\lambda}$$ *Equation 10*

In absence of buckling, they proposed a law for steel in which the monotonic curves in compression and in tension are equal and opposite. The monotonic stress-strain curve consists of three branches:

$$\sigma_s = \begin{cases} E_s \cdot \varepsilon_s & 0 \le \varepsilon_s < \varepsilon_{sy} \\ \sigma_y + E_{sy}(\varepsilon_s - \varepsilon_{sy}) & \varepsilon_{sy} \le \varepsilon_s < \varepsilon_{sh} \\ \sigma_B(\varepsilon_1^{(i)}, \varepsilon_{sm}, \sigma_1^{(i)}, \sigma_{max}, E_1^{(i)}, \varepsilon_s) & \varepsilon_{sh} \le \varepsilon_s < \varepsilon_{su}^{(i)} \end{cases}$$ *Equation 11*

where ε_s is the current strain; E_s the initial elastic modulus; ε_{sy} and σ_y the yield strain and strength; E_{sy} is the initial elastic modulus of plateau; ε_{sh} is the strain at the onset of hardening; ε_{sr} is the strain at the bar rupture; ε_{sm} and σ_{max} are the peak strain and strength; $\varepsilon_1^{(i)}$ and $\sigma_1^{(i)}$ are the points of the Brisighella curve with slope $E_1^{(i)}$. Different monotonic curves can be defined through the choice of ε_{sm} and σ_{max} according to $\varepsilon_1^{(i)}$, $\sigma_1^{(i)}$, $E_1^{(i)}$parameters. For example the strain peak can be assumed equal to ε_{sr} or a symmetric post-elastic branch with respect to strain at the peak can be defined.

In case of buckling, the following expression for the softening branch is proposed by the authors:

$$\sigma_n(\varepsilon_{sy}, \gamma_s, \sigma_{max}, \sigma_{s\infty}, E_{n0,}\varepsilon_s) = \sigma_{s\infty} + (\sigma_{max} - \sigma_{s\infty}) \cdot e^{E_{n0}\frac{(\varepsilon_{sy}+\gamma_s)-\varepsilon_s}{\sigma_{s\infty}-\sigma_{max}}}$$ *Equation 12*

The softening branch can start before the yield point, in the plateau or in the hardening/softening branch. An example of the compressive curve for steel bars in which buckling occurs during the hardening branch is displayed in *Figure 5*. For more details, refer to Albanesi et al.[4].

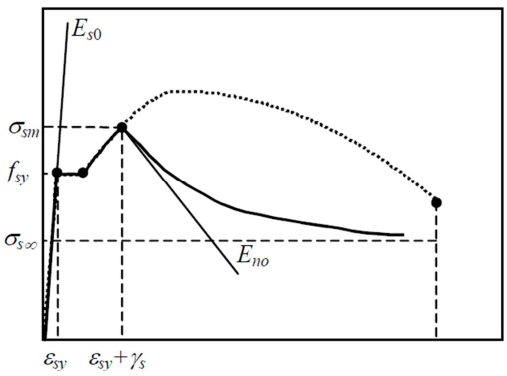

Figure 5 - Stress-strain model of Albanesi et al.[1]

References

[1] Albanesi T, Biondi S, Nuti M. Influenza dell'instabilità delle armature longitudinali sulla risposta d'elementi in c.a.. In: Proceedings of the 10th Italian Conference on Earthquake Engineering, Potenza, Italy. Rome: Anidis, 2001 (in Italian).

[2] Dhakal, R.P., Maekawa, K. Modeling for postyield buckling of reinforcement. J Struct Eng 2002;128 (9):1139–47.

[3] Dhakal, R.P., Maekawa, K. Path-dependent cyclic stress–strain relationship of reinforcing bar including buckling. Eng Struct 2002; 24:1139–47.

[4] Engesser, F. Über die Knickfestigkeit gerader Stäbe, Zeitschrift für Architektur und Ingenieurwesen. 1899; vol. 35 (4): 455-462.
[5] Engesser, F. Z. ver. deut. Ingr. 42, (1898) 927; see also 1899, Uber die Knickfestigkeit gerader Sätbe. Zeitschrift für Architecktur und Ingenieurwesen, 35.
[6] Gomes, A., Appleton, J. Nonlinear cyclic stress–strain relationship of reinforcing bars including buckling. Eng Struct 1997; 19:822–6.
[7] Mau, S.T., El-Mabsout, M. Inelastic buckling of reinforcing bars. J Eng Mech 1989; 115(1):1–17.
[8] Mau, S.T. Effect of tie spacing on inelastic buckling of reinforcing bars. ACI Struct J 1990; 87(6):671–8.
[9] Mendis, P.A., Kovacic, D., Setunge, S. Basis for the design of lateral reinforcement for high-strength concrete columns. Structural Engineering and Mechanics,2000; 9(6): 589-600.
[10] Monti, G., Nuti, C. Nonlinear cyclic behavior of reinforcing bars including buckling. J Struct Eng 1992; 118(12):3268–84.
[11] Papia, M., Russo, G. Compressive concrete strain at buckling of longitudinal reinforcement. J Struct Eng 1989; 115(2):382–97.
[12] Rodriguez, M.E., Botero, J.C., Villa, J. Cyclic stress–strain behavior of reinforcing steel including the effect of buckling. J Struct Eng 1999; 125(6):605–12.
[13] Scribner, C.F. Reinforcement buckling in reinforced concrete flexural members. ACI J 1986; 83(6):966–73.

APPENDIX C: Constitutive laws for confined concrete

In the last decades, many studies have been made on the effect of different arrangements of transverse reinforcement on the confinement of concrete. Experimental tests have demonstrated that a suitable amount and configuration of transverse reinforcement can result in a significant increase in both the strength and the ductility of compressed concrete. The increasing in ductility has a considerable influence on the ductility of RC columns. As a result of the experimental remarks, material models that take into account the effect of confinement on concrete have been proposed. In many cases a confinement-dependent uniaxial constitutive model is sufficiently accurate, also if a 3-D material model can better represent the stress-state in the confined elements, Claeson[1]. In order to accurately model the confining action of transverse reinforcement, a number of researchers have proposed compressive concrete models, among others the model proposed by Scott et al.[6] is one of the most widespread. This model based on the previous model for confined concrete proposed by Kent and Park[3], which however considered the same concrete strength for confined and unconfined concrete, *Figure 1 a)*. Scott et al.[6] demonstrated with experimental tests on square section columns that concrete strength is enhanced by the presence of good confining reinforcement details, thus they modified the model of Kent and Park[3] in order to incorporate also this aspect, *Figure 1 b)*. In detail, through a defined parameter called *K*, both the slope of the post-peak branch and the maximum strength are affected by the level of transverse confinement, as below reported:

$$f_c = Kf'_c\left[\frac{2\varepsilon_c}{0.002K} - \left(\frac{\varepsilon_c}{0.002K}\right)^2\right] \qquad \varepsilon_c \le 0.002K \qquad \textit{Equation 1}$$

$$f_c = Kf'_c[1 - Z_m(\varepsilon_c - 0.002K)] > 0.2Kf'_c \qquad \varepsilon_c > 0.002K \qquad \textit{Equation 2}$$

where f'_c is the unconfined concrete strength [MPa]; ρ_s is the ratio of volume of rectangular steel stirrups to volume of concrete core measured to the outside of the peripheral stirrup; h'' is the width of concrete core measured to the outside of the peripheral stirrups; s_h is the center-to-center spacing of stirrups set; f_{yh} is the yield strength of the transverse reinforcement and Z_m and K are so defined:

$$Z_m = \frac{0.5}{\frac{3 + 0.29f'_c}{145f'_c - 1000} + \frac{3}{4}\rho_s\sqrt{\frac{h''}{s_h}} - 0.002K} \qquad \textit{Equation 3}$$

$$K = 1 + \frac{\rho_s f_{yh}}{f'_c} \qquad \textit{Equation 4}$$

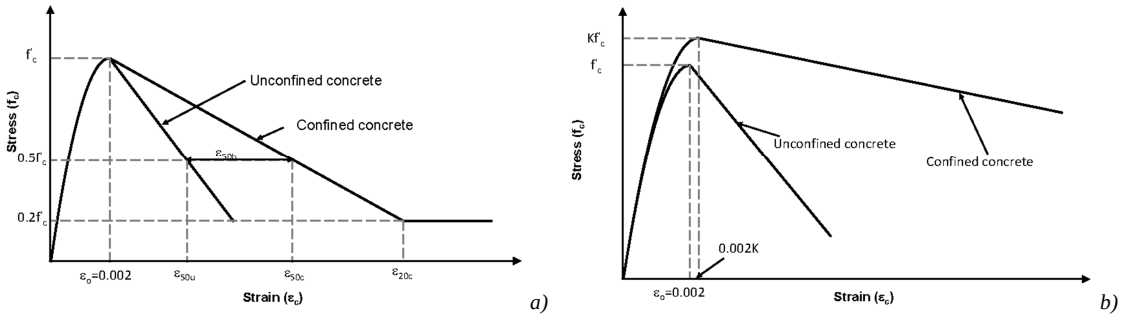

Figure 1- Stress-strain model for monotonic loading of confined and unconfined concrete in compression, Scott et al.[6]

Another model commonly used is the one proposed by Mander et al.[4]. The authors tested square, rectangular and circular columns with different arrangements of transverse reinforcement.

To describe the axial compressive stress f_c – axial strain ε_c law of confined concrete, they adopted the 3-parameter equation proposed by Popovics[5], considering the effect of confinement as follow:

$$f_c = \frac{f'_{cc} \cdot r\left(\frac{\varepsilon_c}{\varepsilon_{cc}}\right)}{r - 1 + \left(\frac{\varepsilon_c}{\varepsilon_{cc}}\right)^r} \qquad \textit{Equation 5}$$

Where f'_{co} is the compressive strength and ε_{co} the corresponding strain of unconfined concrete; ε_c is the longitudinal compressive strain; ε_{cc} is the strain at the peak stress of confined concrete (f'_{cc}) and can be found with the empirical equation given by Gerstle et al.[2]; $r = \frac{E_c}{E_c - E_{sec}}$, where $E_c[MPa] = 5000\sqrt{f'_{co}}$ and $E_{sec} = \frac{f'_{cc}}{\varepsilon_{cc}}$. The effective lateral confining pressure is defined as:

$$f'_l = \frac{1}{2} k_e \cdot \rho_s \cdot f_{yh} \qquad \textit{Equation 6}$$

Where f_{yh} and ρ_s have been lready defined and k_e is the confinement coefficient, for more detail see Mander et al.[4]. The confined compressive strength f'_{cc} can now be calculated using the effective lateral pressure f'_l and the unconfined concrete compressive strength f'_{co}:

$$f'_{cc} = f'_{co}\left(-10254 + 2.254\sqrt{1 + \frac{7.94 f'_l}{f'_{co}}} - 2\frac{f'_l}{f'_{co}}\right) \qquad \textit{Equation 7}$$

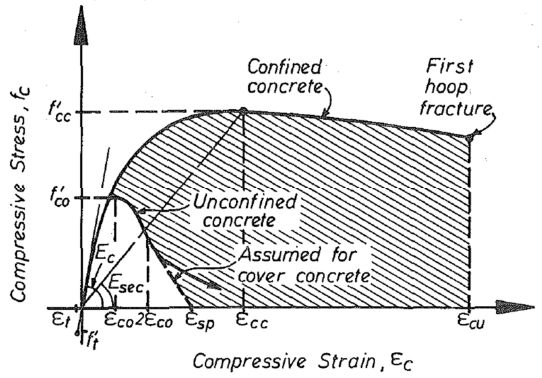

Figure 2- Stress-strain model for monotonic loading of confined and unconfined concrete in compression, Mander et al.[4]

References

[1] Claeson C. Finite element analysis of confined concrete columns. Nordic Concrete research publications, 1999; 22:1-20.

[2] Gerstle, K.H. Material behaviour under various types of loading. Proceedings, National Science Foundation Workshop on High Strength Concrete, University of Illinois at Chicago Circle, Pub. No. PB79-210057, S.P. Shah ed., NTIS Washington D.C., 43-78.

[3] Kent, D.C., and Park, R. Flexural members with confined concrete. Journal of the Structural Division, Proc. of the American Society of Civil Engineers, 97(ST7), 1971: 1969-1990.

[4] Mander, J., Priestley, M., and Park, R. Theoretical Stress-Strain Model for Confined Concrete. Journal of Structural Engineering, 1988; 114(8): 1804–1826.

[5] Popovics, S. A numerical approach to the complete stress-strain curves of concrete. Cement and Concrete Research, 1973; 3(5), 583-599.

[6] Scott, B.D., Park, R., Priestley, M.J.N. Stress-strain behaviour of concrete confined by overlapping hoops at low and high strain rates. Journal of the American Concrete Institute, 1982; 79(1): 13-27.